UNIVERSITY OF CAPE TOWN
IYUNIVESITHI YASEKAPA • UNIVERSITEIT VAN KAAPSTAD

On the Evaluation of Common Design Metrics for the Optimization of Non-Axisymmetric Endwall Contours for a 1-Stage Turbine Rotor

Author: Jonathan Bergh

Supervisor: Prof B. D. Reddy
Co-supervisor: Dr G. C. Snedden

Thesis presented for the Degree of
Doctor of Philosophy in the Department of Mechanical Engineering
University of Cape Town
September 24, 2018

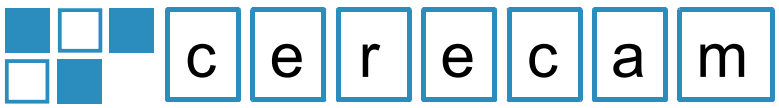

"**It is not the critic who counts**; not the man who points out how the strong man stumbles, or where the doer of deeds could have done them better. The credit belongs to the man who is actually in the arena, whose face is marred by dust and sweat and blood; who strives valiantly; who errs, who comes short again and again, because there is no effort without error and shortcoming; but who does actually strive to do the deeds; who knows great enthusiasms, the great devotions; who spends himself in a worthy cause; who at the best knows in the end the triumph of high achievement, and who at the worst, if he fails, at least fails while daring greatly, so that his place shall never be with those cold and timid souls who neither know victory nor defeat."

Theodore Roosevelt
Sorbonne, 1910

Abstract

With the continued economic and socio-political pressure on aircraft manufacturers to produce more profitable and environmentally-friendly aircraft, the drive towards increasingly more efficient aircraft engines remains of prime importance to aircraft engine manufacturers.

While the majority of axial flow turbomachines use cylindrically shaped endwalls between the blades on the hub or shroud, non-axisymmetric endwall contouring is a reasonably recent technique which relaxes this constraint, and allows the geometry of the endwalls to depart from that of a plain cylinder. Although a number of studies have shown non-axisymmetric endwall contouring to be an effective mechanism for the reduction of secondary flows (and the losses associated with them), within the open literature there still remains a general lack of detailed information relating to the optimal design of these devices. Among some of the most important issues which remain unresolved, are uncertainties such as: *"What is the best way to identify and thereafter quantify the strength of turbine secondary flows?"*, and thereafter, as a natural progression from this, *"Of the metrics which are currently found within the literature, which are best for use in the design of secondary loss mitigating endwall contours for a real turbine?"*.

Some of the reasons for the lack of information as described above, result from the undertaking of many of the investigations into the design of endwall contours by or on behalf of the major engine manufacturers, and therefore, a general inability or perhaps even unwillingness to divulge many of the specific details related to the methodologies and quantities used as a result of the commercial sensitivity of these investigations. In addition to this, as a result of the relatively large number and diverse nature of groups involved in non-axisymmetric endwall contouring research, within the literature which has been made available, there exists a wide variety of different test geometries as well as conditions which have been used, making a neutral determination of the most successful approach to endwall contouring considerably more difficult.

This thesis documents the design and testing of a number of different non-axisymmetric endwall configurations intended to produce flow conditions optimized using a selection of the metrics commonly found in the literature, for the rotor of a low speed, research turbine, whose baseline as well as performance using contoured endwalls has been reported on previously, in order to establish which of these metrics is the most effective.

As part of this process, a fully validated computational fluid dynamics model of the turbine downstream of the first nozzle was developed and incorporated into an automated non-axisymmetric end-

wall design routine, capable of producing endwall contours optimized for various objective functions. Numerical testing showed that, in order to distinguish accurately between the various endwall configurations, relatively fine computational meshes were required and therefore, as a result of corresponding computational expense associated with these meshes, the implementation of a *surrogate* modelling procedure in which part of this computational cost is offset by mathematical modelling, was necessary.

Altogether, a total of 8 endwall designs were produced - 6 using a single metric each as the basis of their objective functions (the 'simple' designs) and a further 2 so-called 'compound' designs. Of the simple designs, the best performing endwalls in terms of improvements to the rotor exit efficiency were the η_{tt}-, C_{ske}- & β_{dev}-based designs, which were based in turn on the rotor total-total efficiency (η_{tt}), coefficient of secondary kinetic energy (C_{ske}) and flow deviation from design angle (β_{dev}) respectively. All three of these designs were predicted to result in very similar changes to the secondary flow characteristics although the increasing bias towards flow correction was found to have an inverse correlation with the overall efficiencies predicted for each rotor. Of these designs, the numerical predictions for both the η_{tt}- & C_{ske}-based designs (which were included in the experimental subset), were found to be validated, at both the rotor exit as well as downstream measurement planes. Further to this (with the exception of the $C_{p0,rel}$-based case), although the remainder of the simple designs (i.e. the $SKEH$ & η_{de}-based designs) were also predicted to improve the overall rotor efficiency, either the form or the performance of these endwalls resulted in the final corresponding designs for these metrics being considered unsatisfactory.

Finally, the two 'compound' metrics were both formulated to to include a term designed to target the secondary flow within the target blade row, as well as an additional term which was designed to promote improvement in the flow into the downstream blade row. While both designs produced using the compound design objective functions were predicted to improve both the conditions for the target blade row, as well as the flow quality at the exit of the blade row, flow separations at the exit of the contoured regions for both designs resulted in only partial validation of each design when tested experimentally. Finally, although both designs were once again predicted to perform very well at the 'mixed-out' measurement plane, these predictions were found to be only partially validated by the experiment.

Keywords: 1½ stage turbine, non-axisymmetric, endwall, contouring, optimization, annular

Declaration

I, _____,

(a) hereby declare that:

(i) the work on which this thesis is based is my original work (except where acknowledgements indicate otherwise), and that;

(ii) neither the whole work, nor any part of it has been, is being, or is to be submitted for another degree in this or any other university.

(b) authorise the University to reproduce for the purpose of research either the whole or any portion of the contents in any manner whatsoever.

(c) am now presenting this thesis for examination for the degree of PhD.

Acknowledgements

In the first instance, I would like to extend my sincerest thanks to my supervisor Professor Daya Reddy, Director of the University of Cape Town's Centre for Research in Applied and Computational Mechanics. I have been most privileged to be a student at the Cerecam, not only a fantastic academic home, but one which I feel very fortunate to have been able to be part of.

To Dr Glen Snedden, who faithfully met with me on a Friday afternoon for 4 years via Skype, and who was always willing to make his best effort at understanding and then advising me during this journey, and who consistently reigned me in and kept this work focussed on the 'big picture', I owe a huge debt of gratitude.

To the support staff, Ms Olivia Goodhind, Mr Graham Inggs, Mrs Mama Gladys Stuurman, Ms Florence Nozuku and more recently Ms Natalie Bent, I extend my thanks for always making sure there was coffee and tea to drink, the incidental chats and that the lab was always well run.

To my student colleagues, it has been a great experience to meet many new people in Cape Town as well as discuss and share the experience of postgraduate study together. I would like to extend special thanks to some of the 'older' students, including Bev, Jean-Paul, Milo, James, Andie, Evan, Maien and Ritesh - thanks for all the discussions and chats we had to break to long hours as well as so willingly sharing your friendship.

In addition to the above, I would like to acknowledge Dr Dwain Dunn for his assistance with the experimental testing conducted for this work as well as Dr Glen Snedden for preparing the CAD models used in the manufacture of the test blades.

This document is the result of a research effort funded by Armscor in terms of order KT471040

Conference proceedings and Presentations

Peer-reviewed conference proceedings

Bergh, J., Snedden, G., (2015). Evaluation of the effectiveness of various metrics used in the design of non-axisymmetric turbine endwall contours. In: Proceedings of 22nd International Symposium on Air Breathing Engines: ISABE2015, October 25-30, Phoenix, Arizona, USA. ISABE-2015-20023. ISABE.

Bergh, J., Snedden, G., Meyer, C., (2012). Optimization of non-axisymmetric end wall contours for the rotor of a low speed, 1 1/2 stage research turbine with unshrouded blades. In: Proceedings of ASME Turbo Expo 2012: GT2012, June 11-15, Copenhagen, Denmark. GT2012-68569. ASME.

Conference presentations

Bergh, J., Snedden, G., Meyer, C., (2013) Design of non-axisymmetric end wall contours for the rotor row of a low speed 1 1/2 stage turbine using different objective functions. Third African Conference on Computational Mechanics - An International Conference: AfriCOMP13, July 30 - August 2, Livingstone, Zambia. ISBN 978-0-620-57539-3

Bergh, J., Bindon, J., Brooks, M., Snedden, G., (2010). Computational analysis of non-axisymmetric contoured turbine end walls. International Aerospace Symposium of South Africa 2010: IASSA 2010 Putting Ideas into Motion, November 23 - 25, 2010, Gordon's Bay, South Africa. Aeronautical Society of South Africa (AeSSA). ISBN 978-0-620-46354-6

Contents

List of Figures

List of Tables

Turbine Coordinates

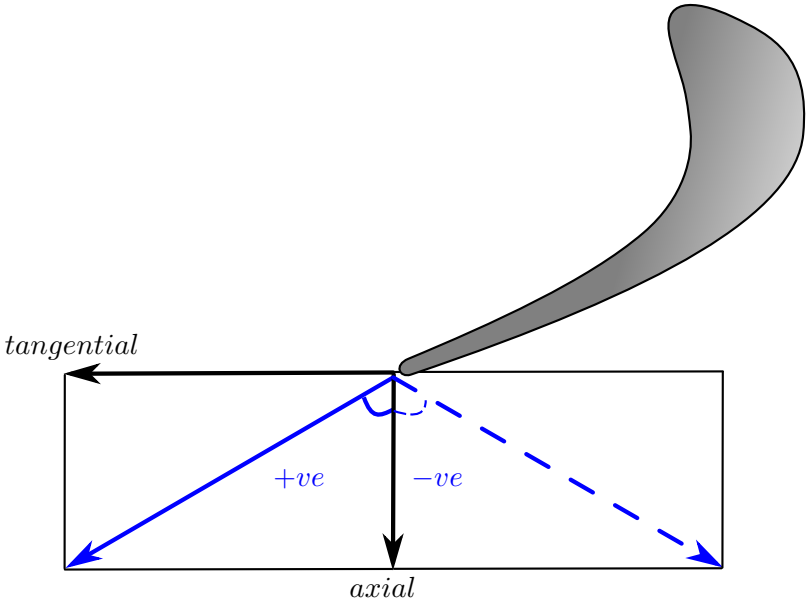

Fig. 0.1: Definition of positive and negative yaw in the blade-to-blade plane

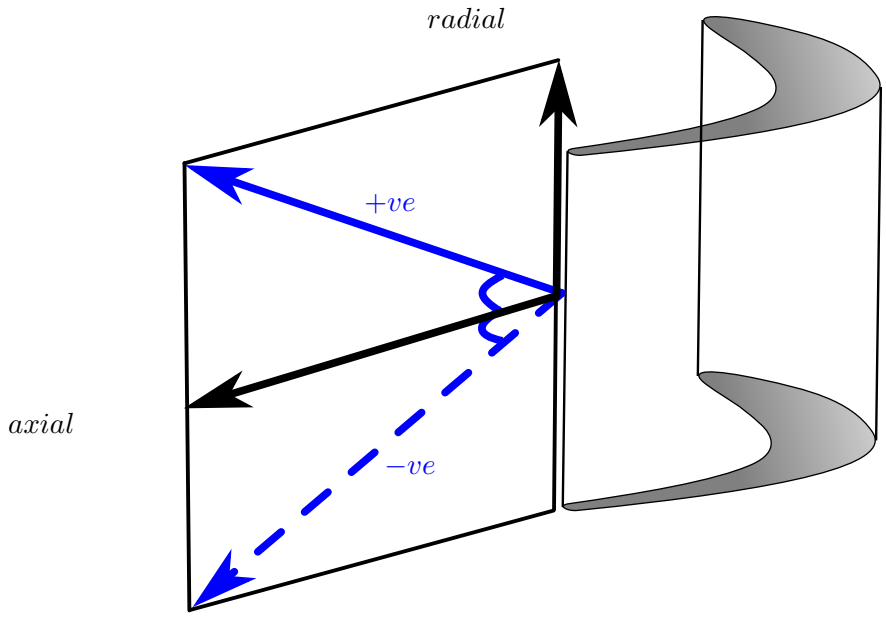

Fig. 0.2: Definition of positive and negative pitch in the meridional plane

1

Introduction

From the design and manufacture of the first self-sustaining gas turbine by Norwegian inventor Ægidus Elling in 1903 to the development of the modern day, high bypass ratio engine, the gas turbine has undergone one of the most rapid courses of development in recent mechanical engineering history. While driven initially by the military's recognition of its potential to power the next generation of high speed military aircraft, in more recent times the development of the gas turbine has been advanced by the growing pressure on aircraft and aircraft engine manufacturers to produce increasingly more efficient and environmentally friendly aircraft as a result of (in particular): increased fuel costs, requirements (especially in Europe and North America) to reduce the environmental impact of air travel, as well as the competitive nature of the market in which modern aircraft operators must survive (Cumpsty (2009)).

1.1 Overview

The nature of some of the circumstances which have led towards the drive towards more efficient aircraft and aircraft engines, are perhaps most clearly illustrated by estimates made by the United States Bureau of Transportation Statistics (BTS). For the year 2009, it was reported that the overall consumption of jet fuel by United States-based airlines alone was of the order of 16,234 million gallons, at a estimated cost of approximately US$30,682 million to the industry collectively (BTS (2010)). In addition, for the same period, it was estimated that for a single typical US passenger airline, the fuel expenditure alone accounted for between $10 - 15\%$ of the total business operating cost, making the fuel and operational efficiency of any existing and future aircraft, a non-trivial consideration for any serious operator.

In light of the above, although some authors argue that the financial case for increased engine efficiency can be made by simply noting the large number of gas turbine engines in active service - for example, Ingram (2003) puts this figure at approximately $55,000$ for Rolls Royce powerplants alone - it is perhaps Cumpsty (1997), who makes one of the most poignant observations relating to the benefits of improved fuel efficiency. In what is a surprisingly simple analysis, he showed that a reduction of as little as 1% in overall fuel weight as a result of reduced fuel consumption, can result in as much as a 5% increase in aircraft payload - a factor which is likely to have a far larger effect on overall airline profitability than all the direct savings arising from the reduction in fuel costs noted above.

Using basic thermodynamics, it can be shown that the overall performance of the simple gas turbine cycle (in terms of cycle efficiency and net power output), is primarily dependent on three factors (Cumpsty (1997)):-

1. the engine pressure ratio (p_3/p_a),
2. the maximum turbine (inlet) temperature (or more specifically, the ratio of the turbine and compressor inlet temperatures (T_4/T_2)), *and*
3. the efficiencies of the individual engine components

In response to the aforementioned demand for more efficient aircraft, in recent years, the majority of efforts in aero-engine development have been directed primarily at 1) and 2), by improving compressor design (in an effort to increase the overall engine pressure ratio), and in the development of new high performance, high temperature materials and engine cooling systems (in order to allow for increased combustion and turbine inlet temperatures). Although probably less numerous, there have also been a number of efforts made to improve the performance of the remaining engine components, such as the combustor (in an effort to increase combustion efficiency and decrease emission of undesirable by-products), as well as the aerodynamics of the turbine, where concepts such as blade work distribution management through three-dimensional blade shaping (including blade lean and sweep) have been topics for development.

In more recent times, one of the most promising advances in turbine design has been the development of *non-axisymmetric endwall contouring* (or *profiling*) - a method aimed specifically at decreasing the aerodynamic losses generated by the highly three-dimensional *secondary flows* which develop in the blade rows of these devices. Although initially conceived as a method for reducing turbine disc leakage flows (Rose (1994)), the recognition of the potential of non-axisymmetric endwall contouring as a means for the reduction of secondary flows and - more importantly, *the losses associated with them* - resulted in it been taken up very rapidly for development by various groups as a method specifically to reduce the effects of secondary flow.

Despite demonstration of the viability of the concept, as well as being developed fairly extensively by various groups since its conception, within the broader turbomachinery community there still remains a general lack of information relating to what might be considered as some of the fundamental questions surrounding the design of non-axisymmetric endwall contours. For instance, within the published literature, there is often a lack of detailed information relating to the specifics of the endwall design methodologies used (e.g. Torre et al. (2006)), while in others, detailed information relating to the actual designs generated is absent (e.g. Praisner et al. (2007)). Still others include partially complete information, for instance Nagel et al. (2001) and Germain et al. (2008), in which the general form of the functions used to parametrise the endwalls were given, but specific details of the functions themselves were not. As indicated by MacPherson and Ingram (2010), this is most probably as a result of the undertaking of many of the research efforts into endwall contouring by or on behalf of the major engine manufacturers, and therefore the commercial sensitivity associated with the work. In addition, as a result of the varied and independent nature of many of the groups who have been involved in non-axisymmetric endwall contouring research (and whose work has *not* been subject to embargo), it is sometimes difficult to draw definite conclusions between the pros and cons of the various

methodologies used as well as the effectiveness of the designs produced because of the wide variety of test configurations and conditions utilised.

Perhaps one of the greatest challenges which has been faced by nearly all groups in the field has been the question of *how best to design* non-axisymmetric endwall contours. This issue is well evidenced by the ample selection of design approaches, endwall parametrisations and objective functions (or design metrics) available in the open literature for generation of endwall contours.

Inevitably, the above issue leads to two further questions:- *firstly*,

1. What is the best approach for identifying and then quantifying the strength of the secondary flows within the blade passage?

and *secondly* (and perhaps more importantly),

2. How does one best relate reductions in the metrics above to the overall reduction in secondary loss and ultimately, the goal of any loss reduction exercise - increased efficiency?

Amongst the reasons for the difficulties listed in 1) and 2) above, has been the inability of current day computational fluid dynamics (CFD) codes to predict either the magnitudes and / or the trends in secondary loss reduction accurately, and therefore the absence of a reliable design metric for use during the endwall design process. While the details of the response to this issue are described more fully in the body of this thesis, it is this issue which has led almost directly to the development of a selection of alternative metrics for use in endwall design which act as either descriptors of the *quality* of the flow or as *proxies* for loss.

1.2 Aims of this thesis

In the light of the discussion above, this study was initiated to address as many of the points of difficulty above as possible. This was done by undertaking a fully documented investigation into the design of non-axisymmetric endwall contours for a previously characterised turbine test case and using a selection of the most popular so-called 'design metrics' from the literature as the basis of the target design (objective) functions. Thereafter, a systematic evaluation of the performance of each of the endwalls generated using each design metric was done in order to assess the relative performance and suitability of each of the metrics for the design of non-axisymmetric endwall contours.

In summary then, the major objectives of this project have been:-

- the development of an automated non-axisymmetric endwall contour design routine capable of producing endwall contours, optimized using different objective functions based on various quantities found in the literature, for a common, previously documented test case more representative of a real turbine environment than many of the linear cascades which have been commonly used in secondary flow and endwall contouring design,
- the generation of non-axisymmetric endwall contours as globally optimal as possible for the rotor row of the test turbine corresponding to the objective functions above, *and*

- the completion of an experimentally validated and systematic evaluation of the performance of as many of the generated endwalls as possible with respect to secondary flow reduction (and ultimately, increased turbine efficiency) in order to assess the unbiased, comparative performance of each of the so-called 'design metrics' commonly used in the literature for the design of non-axisymmetric endwall contours.

1.3 Layout of this thesis

This thesis comprises the following chapters:-

1. **Introduction** - provides a short introduction to the origins of non-axisymmetric endwall contouring, the reasons for the undertaking of the project and the major goals of the work.
2. **Literature survey** - describes some of the relevant prior academic work in the fields of gas turbine development, secondary flow, sources of loss in turbines and loss mitigation. Also presented is a summary of the prior work on endwall design techniques, numerical optimization, as well as the results of previous optimization attempts used in the generation of non-axisymmetric endwall contours. Finally some discussion on the origin and basis of various of the metrics used in the characterisation and design of non-axisymmetric endwall contours is presented.
3. **Objective functions** - provides definitions of the fundamental quantities used as part of the endwall design objective functions, as well as the discussion on the actual objective functions used to produce each of the endwalls tested in this investigation.
4. **Experimental test case** - provides details of the experimental test platform used in this project (the CSIR 1½ turbine) and the experimental methodology used for the characterisation of the performance of each set of endwalls.
5. **Endwall design routine** - because of the large computational expense associated with the production of each optimized design, the use of a meta- or surrogate model-based design framework was essential in this work, and the details of this framework - including the parametrisation of the endwall, the optimization methodology employed (including details of the surrogate modelling technique used), and the dataflow and linkages between the individual components of the routine, are included in this chapter.
6. **Numerical modelling** - presents the details of the computational fluid dynamics (CFD) approach used in the modelling of the turbine for the optimization routine, validation of the model, details of the model discretization, simplifications, turbulence modelling and solution methodology.
7. **Results** - presents the results of the CFD modelling and experimental testing of each set of endwalls in terms of mass- and circumferentially- (pitchwise) averaged at the rotor exit (X3) and downstream ('mixed-out') (X4) measurement planes.
8. **Discussion** - provides a discussion of the performance of each endwall design in terms of the blade loading and torque changes, changes to the structure of the secondary flow system, predicted loss (entropy) generation rates as well as the changes to the efficiency for each endwall design.

9. **Observations** - draws together the main results from the previous two chapters and provides overall observations of the use and effectiveness of each metric used in the design process, including their predictability and convergence properties.
10. **Conclusions and Recommendations** - the conclusions and recommendations associated with the findings of this investigation.

Additional details, such as the final endwall geometries (including endwall geometry coefficients), optimization and convergence data are included in various Appendices.

2

Literature Survey

In this Chapter, the existing literature relevant to the work undertaken in this thesis is examined. Initially, the motivation for pursuing increased turbine efficiency is discussed and placed in context with other activities which seek to increase the overall efficiency of the modern gas turbine engine. A review of the fundamentals of secondary flow and loss, as well as other deleterious flows commonly found in turbomachines is undertaken. In addition, discussion of the previous work relating to the mitigation of these losses through the use of various design practices and devices is included. In particular, non-axisymmetric endwall contouring is discussed, with particular reference to the parametrisations, optimization methodologies and objective functions used during endwall design.

Finally, the Chapter is concluded with a short review of the predominant optimization algorithm used in this thesis.

2.1 Axial flow gas turbines

2.1.1 The need for turbine efficiency

Conceptually, the gas turbine engine is one of the simplest heat engines in use today. Despite its relative simplicity however, the modern gas turbine is capable of producing large amounts of shaft power[1] and as a result of its compact form, very attractive power-to-weight ratios. Together, these characteristics have made the modern-day variants of the engine the prime movers of choice in a variety of applications, including perhaps most ostensibly, but not limited to, the aviation industry (Cohen et al. (1996)).

Despite its potential to produce impressive amounts of thrust and shaft horsepower, the basic arrangement of the conventional gas turbine engine (Fig. 2.1) is relatively simple, consisting of a compressor, a combuster, and a turbine. Like its mechanical arrangement, the fundamentals of its ideal thermodynamic cycle are equally as straightforward, consisting of only four processes (Fig. 2.2):- an *isentropic* compression (2 - 3), *isobaric* heat addition (3 - 4), an *isentropic* expansion (4 - 5), and an *isobaric* heat rejection (5 - 2), in which the waste heat of the cycle is rejected to the atmosphere.

In the simple cycle, a portion of the mechanical work extracted from the working fluid ($\dot{W}_{back}$) by the turbine is directed back to the inlet portion of the engine, where it is used to drive the rotor blades of the compressor so no additional external energy is required to drive these components. Any remaining work not absorbed by the compressor is available as a net work output ($\dot{W}_{net}$) from the

[1] or thrust

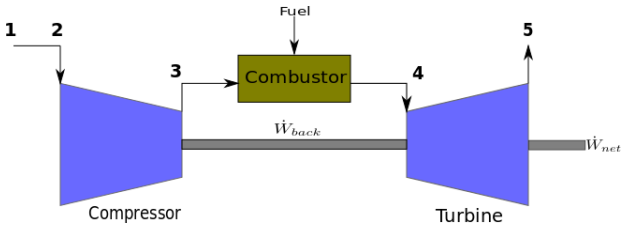

Fig. 2.1: Schematic of the simple, open-cycle gas turbine engine

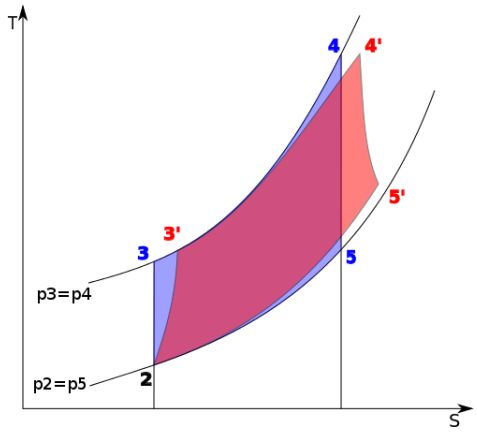

Fig. 2.2: $T - s$ diagrams for the ideal (blue) and real (red) gas turbine cycles

machine, and in modern engines there are a number of methods in which this energy is extracted and utilised.

As indicated previously, the performance of the gas turbine (i.e. net work output and cycle efficiency) can be shown to be a strong function of the engine pressure ratio (p_3/p_a), the turbine inlet temperature ratio (T_4/T_2) and the efficiencies of the individual components. Since the topic of this thesis is concerned with increasing the aerodynamic efficiency of the turbine, it is informative to investigate the effect of changes in this parameter on the two performance measures above.

Following the analysis of Cumpsty (1997), Figs. 2.3a & 2.3b show the effect of increasing turbine efficiency (η_t) with increasing pressure ratio on the non-dimensional net work output and overall cycle efficiency of an idealised machine for different compressor efficiencies (η_c) and for a constant turbine inlet temperature ratio ($T_4/T_2 = 5.5$). In addition, Figs. 2.4a & 2.4b show the effects of increasing turbine efficiency and temperature ratio (T_4/T_2) on overall cycle efficiency for a constant pressure ratio ($p_3/p_a = 40$) and compressor efficiency ($\eta_c = 0.85$) respectively, the constants having been chosen as they are representative of modern high bypass ratio engines.

From Figs. 2.3a & 2.3b it is clear that, despite the already relatively high individual turbine and compressor isentropic efficiencies, increases in the efficiency of either of the components still result in relatively lucrative increases in both the net power output and cycle efficiency of the machine. As discussed by Denton (1993), this is because the net power output of a gas turbine engine is the difference between the turbine and compressor work, which in the typical engine, are in a ratio of approximately 2:1, and therefore even small changes in efficiency of either component result in a disproportionately larger change in the net power output (and consequently cycle efficiency).

An inspection of Figs. 2.4a and 2.4b reveals an even more interesting situation. For a constant compressor efficiency and pressure ratio, Fig. 2.4a shows that an increase of approximately $\sim 1\%$ in turbine efficiency equates to an increase in cycle efficiency of approximately $\sim 1.6\%$, while for the same result, an increase in turbine inlet temperature of approximately $\sim 60K$ is required. In the latter case, this is without accounting for the additional cooling requirements (and the losses associated with them) which would be required. Finally, while the rate of cycle efficiency increase with respect to

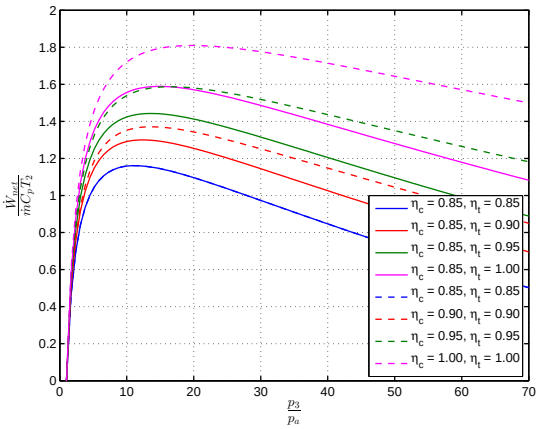

(a) Non-dimensional net work output $\left(\frac{\dot{W}_{net}}{\dot{m}C_pT_2}\right)$ plotted against pressure ratio (p_3/p_a) for different values of η_c and η_t and $T_4/T_2 = 5.5$

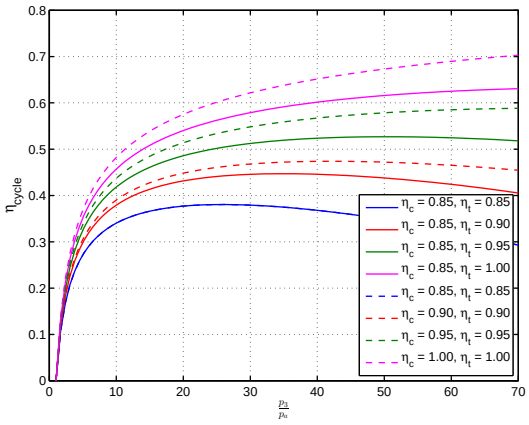

(b) Cycle efficiency (η_{cycle}) plotted against pressure ratio (p_3/p_a) for different values of η_c and η_t and $T_4/T_2 = 5.5$

Fig. 2.3: Effects of turbine and compressor isentropic efficiency on the non-dimensional net work output and overall cycle efficiency of a simple gas turbine

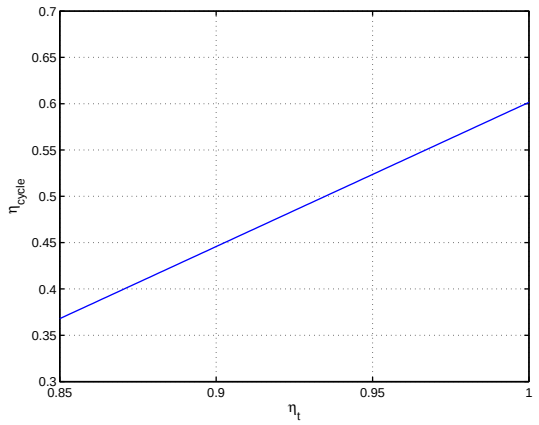

(a) Cycle efficiency (η_{cycle}) plotted against turbine efficiency with $\eta_c = 0.85$, $T_4/T_2 = 5.5$ and $p_3/p_a = 40$

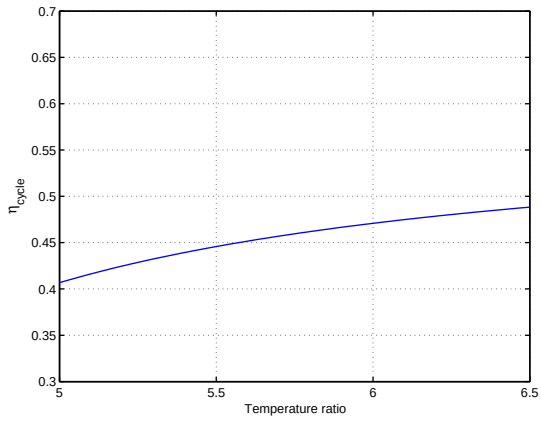

(b) Cycle efficiency (η_{cycle}) plotted against temperature ratio with $\eta_c = 0.85$, $\eta_t = 0.9$ and $p_3/p_a = 40$

Fig. 2.4: Effects of turbine efficiency and temperature ratio on overall cycle efficiency for a constant pressure ratio

turbine efficiency remains approximately constant, Fig. 2.4b shows that the rate at which the cycle efficiency increases with respect to temperature ratio *decreases* with increasing temperature ratio.

Therefore, with compressor performance and therefore pressure ratios likely to only increase over time (especially for commercial aircraft), it is clear that pursuing increases in turbine efficiency remain worthwhile, regardless of the already high isentropic turbine efficiencies currently seen in modern day engines.

2.1.2 Axial turbine operation

According to Harman (1981), the turbine is probably the most universal method of extracting energy from a flow of pressurised fluid and is used extensively in engineering applications in both axial and radial configurations. As indicated above, it is an integral component of the gas turbine engine, where as part of the gas generator, it is used to extract energy from the flow of the hot combustion gases to drive the compressor as well as any accessory shafts necessary to maintain the engine function, as well as to drive the output shaft as part of a turboshaft configuration.

The methods by which energy is extracted from the working fluid in the turbine, can be divided into two broad mechanisms:-

1. impulse, *and*
2. reaction

In the former, a momentum exchange between the gas flow and the blade is achieved by the *turning* of the fluid as it passes through the blade row, and in the latter, the torque on the blades is achieved as a result of the action of the *reaction* forces generated on the blade surfaces by the *acceleration* of the fluid in the blade passages. In general, in a real gas turbine the extraction of energy from the flow by the rotor blades is accomplished by a combination of both of these effects, with a gradual increase in reaction occurring with increasing blade radius. Both the turning and acceleration of the flow in the blade rows is important, because both mechanisms have a direct effect on the fluid pressure variations within the blade rows, which in turn, are important not only for the operation of the turbine, but also as a result of their secondary effects on the flows in the blade passages.

While the detailed variations of the pressure field within the blade passages of a typical axial turbine stage are complex, it is possible to make some general comments about the static pressure in the axial, radial and circumferential directions:-

- In the axial direction, the general action of the turbine is to *reduce* the static pressure of the flow as it moves through the machine. It is in part as a result of this favourable pressure gradient, that the typical turbine stage is able to deflect, and therefore extract, considerably more energy from the working fluid per stage than a corresponding row of compressor blades in the same engine is able to absorb (Harman (1981)). In practice therefore, it not uncommon that in a typical gas turbine engine, a single turbine stage may drive up to six compressor stages in the same engine.
- As a result of the predominantly axial nature of the flow entering the first turbine blade row, there is little initial variation of pressure in the radial direction. However, as the circumferential velocity of the flow is increased as a result of its deflection and acceleration of the flow in the first blade row (i.e. the NGV's), an *increasing* pressure gradient is seen to develop in the radial direction at the exit of the blade row.
- Downstream of the NGV's, the flow in the 1^{st} rotor row inherits the radial pressure variation generated by the upstream guide vanes, and is then turned and accelerated in the usual fashion as it moves through the blade passages. Depending on the detailed design, the flow may or may not leave the rotor row with reduced circumferential velocity with respect to its inlet flow, although in

either event, there remains some variation in the static pressure field at the exit of the rotor rows as a result of this circumferential flow.

- Having left the upstream rotor row, the flow then enters the following stationary blade row, where it is again accelerated and turned, and the radial and axial pressure variations discussed for the upstream blade rows are largely repeated.

Apart from the generation of lift, and therefore torque on the blades of the rotor, one of the main unintended effects of the various pressure gradients discussed above, is to cause the migration of low momentum boundary layer fluid on the various blade and endwall surfaces of the turbine in the direction of the decreasing pressure gradient, including flow from (Ingram (2003)):-

1. *tip* to *hub* on the stationary (*stator*) blade surfaces
2. *hub* to *tip* on the moving (*rotor*) blade surfaces, *and*
3. from the *pressure* to *suction* surface of the blades on the *endwalls* of both the stationary and rotating blade rows

In the context of this thesis, it is the last effect (that is, the migration of endwall boundary layer fluid across the blade passage) which is of most significance, as it is, in part, the migration of this fluid which gives rise to a system of flows and losses which is of great significance to turbine efficiency.

These flows are well-known as *endwall* or *secondary flows*, and their origins and characteristics are now discussed in detail.

2.2 Secondary flow

Over the last 60 years, the origins and characteristics of secondary flow have been investigated thoroughly, through numerous theoretical, experimental and more recently, computational efforts. Given their importance in turbomachinery design, it is perhaps easy to forget that they are in fact found in a wide variety of situations, having been documented as early as 1877 by Thomson in curved streams of water (Hawthorne (1951)).

With this broad context in mind, it is perhaps Ingram's definition of the phenomenon which is most appropriate (Ingram (2003)):-

> "Secondary flows can be looked at as a small disturbance on a primary flow where the primary flow is the main two dimensional flow."

Despite the attractiveness of the above definition as a result of its simplicity, within the context of turbomachinery, definitions for secondary flows are usually more complex, in order to allow them to be differentiated from the various other off-axis flows commonly found with the blade passages. In this context then, secondary flows are usually understood to be only those flows which form as a result of the presence of the endwalls, and therefore in connection with the presence of hub and casing boundary layers.

Under these circumstances, it is probably Sieverding's definition which is most appropriate (Sieverding (1985)):-

"[Secondary flows form when] ... a flow with inlet vorticity is deflected through a cascade ... [and] which occur due to the distortion of the vortex filaments of the inlet boundary layer passing through a curved passage."

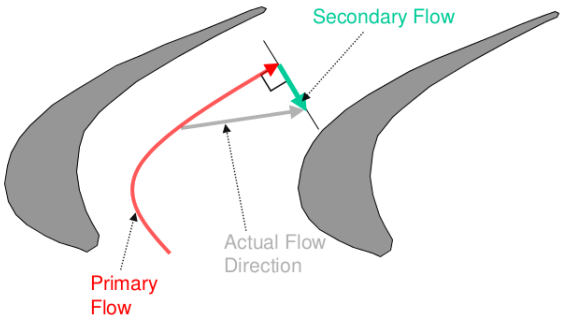

Fig. 2.5: Secondary flow definition of Ingram (2003) for a cascade [Reproduced from Ingram (2003)]

Amongst the earliest investigators of turbine secondary flows, were authors such as Squire and Winter (1949), Hawthorne (1951, 1955) and Hawthorne and Armstrong (1955), all of whom investigated the formation of the flows in curved passages and cascades of aerofoils, primarily from a mathematical standpoint. Following these early investigations, a great deal of effort was expended on experimental investigations, including numerous works to determine the detailed structure of the flow at the exit, as well as within the blade passages. Amongst these investigations included work such as that by:-

- Gaugler and Russell (1982), who with the aid of a gas bubble injection, assisted in the understanding of the general nature of the vortex systems and their interaction with one another;
- Sieverding and Van den Bosch (1983) who used smoke visualisations to show the growth and interaction of the horseshoe and passage vortices with one another; and,
- Aunapu et al. (2000a,b), who used methods such as oil and black powder as well as ink dot and solvent methods, to establish the formation and separation location of the horseshoe vortex on the turbine endwall and its impingement on the suction surface of the adjacent blade, the endwall saddle point, and the migration of low momentum fluid across the blade passage.

Finally, with the advent of computers and CFD codes powerful enough to tackle the problem with reasonable resolution and accuracy, a raft of simulation-based investigations have been undertaken, particularly for the design and 3-dimensional analysis of blade passages.

With all these efforts, the development of progressively more detailed models of the secondary flow regime has been the inevitable result, and this is well evidenced by the development of the flow models as shown in chronological order in Fig. 2.6, from the early model of Hawthorne (Fig. 2.6a) to those of later workers such as Sharma and Butler (1987) (Fig. 2.6b), Goldstein and Spores (1988) (Fig. 2.6c), Wang et al. (1997) (Fig. 2.6d) and Moon and Koh (2001) (Fig. 2.6e).

To this end, Harvey et al. (2000), in their paper dealing with the reduction of secondary flow in a large scale, 2-dimensional cascade, stated that in addition to having identified all of the major

flow features, the mechanisms leading to the development of secondary flows were by now also well documented and understood. As a result, in their paper the authors listed the following 4 features as being the major constituents of secondary flow:-

- the *endwall boundary layer cross flow* and *passage vortex*
- the *horseshoe vortices*
- and the *corner vortices*

2.2.1 Endwall boundary layer flow and the passage vortex

As indicated by Lampart (2009), Hawthorne (1951) made some of the earliest descriptions of the passage vortex within a cascade of aerofoils and included a description of a re-circulating flow which formed within the passages of a row of aerofoils. In a later paper, the same author described the creation of vorticity in the curved passages of a turbine cascade, identifying 3 main components of the vorticity in the streamwise direction (Hawthorne (1955)):-

1. two found to be lying in the trailing edge stagnation streamline behind each blade, identified as *trailing filament circulation* (formed due to the stretching of vortex filaments between the suction and pressure surfaces of the blade) and the *trailing shed vorticity* (formed as a result of the change of circulation along the span of the blade) respectively, *and*
2. a third component distributed within the free stream.

This third component was described by Hawthorne to be as a result of the flow of non-uniform velocity fluid through a curved passage and is now well-known within the literature as the so-called *passage vortex*.

One of the simplest explanations for the generation of the streamwise vorticity described above was explained by Squire and Winter (1949) who derived their now well-known formula (Eqn. 2.1) which predicted the downstream vorticity (Ω_{str}) to be a function predominantly of the inlet vorticity, ratio of the turning to mean passage radius, and the deflection angle of the flow.

More specifically, if the inlet flow to a turbine with non-uniform vorticity in the radial plane only and whose vorticity vectors are normal to the streamwise direction, as a result of the acceleration of the flow at the suction surface of the blade and deceleration adjacent to the pressure surface, the vectors are rotated with respect to the original inlet plane and a component of vorticity is then generated in the streamwise direction.

$$\Omega_{str} = -2\epsilon \cdot \frac{\partial U}{\partial z} \frac{r}{r_0} \tag{2.1}$$

where:-

Ω_{str} is downstream streamwise vorticity,
ϵ is the total turning of the flow in the cascade
U is the inlet velocity,
z is the radial coordinate, *and*

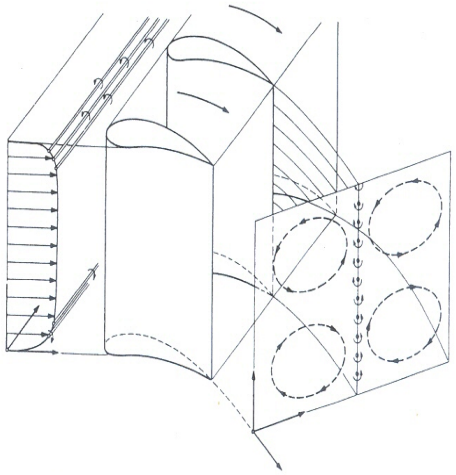

(a) Model of Hawthorne (1955) (Reproduced from Sieverding (1985))

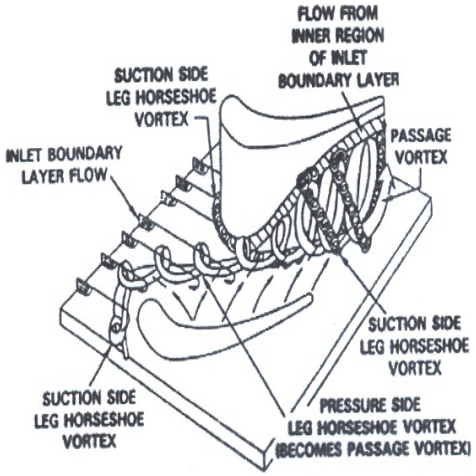

(b) Model of Sharma and Butler (1987)

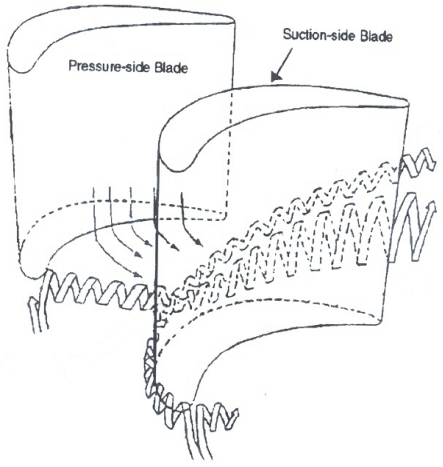

(c) Model of Goldstein and Spores (1988)

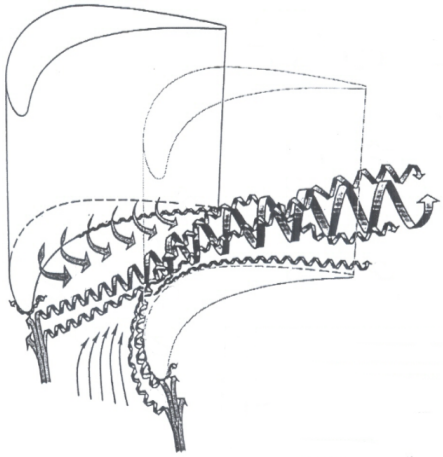

(d) Model of Wang et al. (1997)

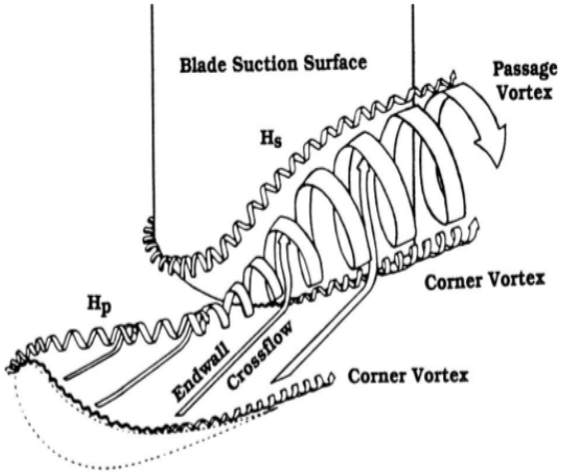

(e) Model of Moon and Koh (2001)

Fig. 2.6: Development of turbine secondary flow models from 1955 to the present day

r and r_0 are the radius and mean radius[2]

In his more recent paper, Lampart (2009) used a more physical approach to explain the formation of the passage vortex. In the absence of viscous and body forces, the momentum equation in the normal direction (in streamline co-ordinates) can be written as:-

$$\frac{\partial p}{\partial n} = \frac{\rho v^2}{r} \tag{2.2}$$

where:-

p is the fluid pressure,
n is the coordinate in the direction normal to the streamwise flow,
ρ is the fluid density,
v is the fluid velocity, *and*
r is the radius of curvature of the streamline

According to Eqn. 2.2, along with the reduction of the fluid velocity as it enters the boundary layer, a reduction in the streamline curvature of this fluid from that of the primary flow is also required to balance the cross passage pressure gradient. This results in the greater turning of the boundary layer fluid in comparison to the free stream, consequently giving rise to a boundary layer flow from the pressure side of a blade to the suction side of its adjacent blade. Thereafter, in order to preserve continuity, a return flow back towards the original blade's pressure surface must occur at some distance from the hub, giving rise to a re-circulating flow within the blade passage and the downstream streamwise vorticity.

As a result of its role in the formation of the cross passage flow, the blade passage pressure gradient (i.e. $\partial p/\partial n$ in Eqn. 2.2), is often identified as being the driving force of the secondary flow.

2.2.2 The horseshoe vortices

As indicated by Sieverding (1985), the existence of the horseshoe vortices was first shown by Fritsche (1955) reasonably early on, although only formally documented sometime later by Klein (1966). Despite this however, as indicated by Sieverding, the existence of the vortices did not receive any significant attention until a change in the general method of experimentation used for the examination of secondary flows occurred in the mid-1970's, when the general experimental approach evolved from one in which flow traverses were conducted at the inlet and exit of blade passages only, to one in which the detailed nature of the flow *within* the blade passages was examined.

The origin of the horseshoe vortices can be explained as being a phenomenon similar to that which occurs ahead of a stationary cylinder attached to the flat plate immersed in a flow. Following Lampart (2009) and referring to Fig. 2.7:-

[2] Eqn. 2.1 reduces to the more familiar version:- $\Omega_{str} = -2\epsilon \cdot \partial U/\partial z$ quoted by many authors if the passage is narrow, since $r/r_0 \sim 1$

- as a result of the inlet flow's boundary layer being forced to decelerate and stagnate in response to the increasing pressure gradient ahead of the leading edge of each blade, the flow separates at separation line s_1 and forms a reverse re-circulating cell of low energy fluid ahead of the leading edge
- thereafter, after a further separation further downstream (s_2), the fluid is rolled up into a vortex structure and forced downstream of the leading edge of each blade in two legs (the pressure (PS) and suction-side (SS) horseshoe vortices) either side of each blade surface

Sabatino and Smith (2007) presented a more complex model of the leading edge horseshoe vortex system (Fig. 2.8) in which a total of 4 vortical structures at the leading edge, including the previously discussed horseshoe, as well as a *secondary*, *tertiary* and finally, a *corner* vortex[3] were included. The authors also produced 2-dimensional probability density plots corresponding to the location of the vortices, whose bimodal nature indicated the variability of the vortices location ahead of the blade leading edge.

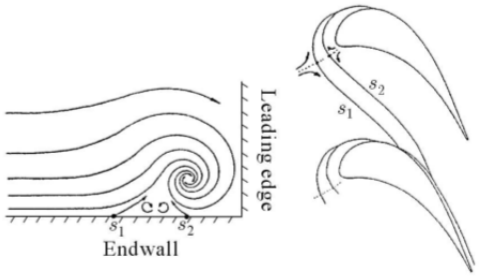

Fig. 2.7: Horseshoe vortex formation and boundary layer separation lines (s_1 & s_2) ahead of turbine blade (Marchal and Sieverding (1977))

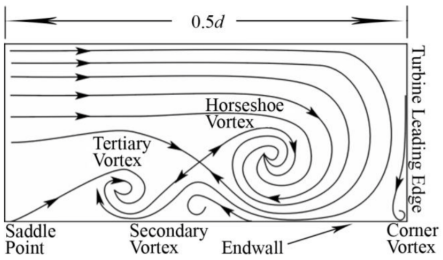

Fig. 2.8: Horseshoe vortex system of Sabatino and Smith (2007)

The point at which the boundary layer flow stagnates and divides into its respective pressure and suction-side legs is known as the *saddle point*, and is clearly visible in investigations such as those of Aunapu et al. (2000b) (Fig. 2.9), as mentioned previously. In addition, visualisations of the boundary layer flow on the suction surface of cascade blades also show the location of the impingement position of the vortices on the blade surface and its tendency to climb the suction surface during its passage through the cascade.

Finally, in addition to the above, the interactive nature of the horseshoe vortices with other secondary flow features such as the passage vortex, has also been shown to be of significant importance in the overall development of the secondary flows in turbines. In their paper, Sieverding and Van den Bosch (1983) discussed the so-called 'synchronous evolution' of the pressure side horseshoe vortex and the passage vortex discussed previously (Fig. 2.10), and in particular, showed the pressure side leg of the horseshoe vortex's tendency to locate itself near the suction surface of the adjacent blade where it formed a central vortex core, while the counter-rotating suction side leg was seen to 'orbit' around the main body of the main passage vortex structure. The central core formed by the pressure side

[3] not to be confused with the blade pressure and suction surface corner vortices as discussed in Section 2.2.3

leg, was then seen to be enlarged by the addition of supplementary fluid convected across the blade passage by the boundary layer cross-flow, finally giving rise to the well-known passage vortex discussed previously.

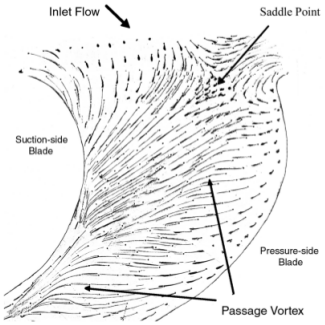

Fig. 2.9: Ink dot visualisation of turbine endwall boundary layer flow including boundary layer saddle point (Aunapu et al. (2000b))

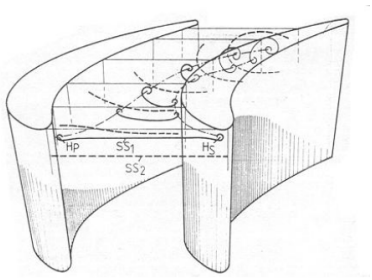

Fig. 2.10: Synchronous evolution of the pressure (PS) and suction side (SS) horseshoe and passage vortices (Sieverding and Van den Bosch (1983))

2.2.3 The corner vortices

The final set of secondary flow features which have been documented are the so-called corner vortices. In the majority of cases, these vortices have been seen to form primarily at the junction of the suction surface of each blade and the hub end wall where the end wall boundary layer flow first impinges on the adjacent blade's surface (i.e. near the mid-chord of the blade). As discussed by authors such as Sieverding (1985) & Ingram (2003), because of their relatively small size, the corner vortices are usually somewhat more difficult to distinguish in experimental studies, although despite this, their existence may often be inferred as a result of their relatively large influence on various parameters of the flow, especially the reduced overturning of the flow near the end wall of the blade passage.

This effect of the corner vortex was well documented by Harvey et al. (2000), who also attempted to exploit it to reduce the losses of downstream blade rows during a study involving non-axisymmetric endwall contouring, by using a set of specially positioned endwall contours designed to enhance the strength of the vortex, consequently reducing the increased flow overturning usually associated with the introduction of endwall contours and therefore providing more uniform flow to the downstream blade row.

2.3 Other flows

In addition to the secondary flows as described above, there also exist a number of additional flow features within the turbine flow field, including tip gap flows, disc leakage and cooling flows, as well as shed and trailing vorticity.

2.3.1 Tip gap flow

The tip gap leakage flows are among the most prominent of the additional flows commonly seen in and behind the blade passages of unshrouded blade rows. These flows form as a result of leakage of primary fluid from the high pressure side of the blade through the tip clearance gap into the suction side region of the tip where they are seen to roll up into an additional vortex structure. Extensive work on tip leakage flows was conducted by researchers such as Bindon (1987), Morphis (1993), and Kaiser (1996) resulting in a relatively complete understanding of the flows in that region.

In his work, Kaiser (1996) (Fig. 2.11) provided an excellent summary of the basic mechanisms which lead to the creation of the tip gap flows under consideration in his study:-

1. For an unshrouded blade, a bulk flow of fluid is seen to form near the blade tip as the fluid moved around the blade (tip) corner on the pressure side, and into the tip gap,
2. In the vicinity of the blade corner, the local static pressure of the fluid is seen to drop dramatically and was explained by Bindon (1987) to be as a result of the fluid remaining attached as it flowed around the blade tip corner despite the relatively sharp nature of the blade corner and the corresponding high fluid velocities in that region,
3. Upon entering the tip gap, the fluid is seen to decelerate sharply, leading to a separation of the flow on the tip surface and the formation of a separation bubble along the length of the blade tip,
4. The bulk flow then accelerates once again (as a result of the reduction in flow area caused by the development of the separation bubble) before decelerating once again as the fluid moved over the bubble and reattaches to the top surface of the blade once more,
5. In addition to the bulk fluid movements described above, low momentum fluid *within* the separation bubble is seen to migrate towards the centre of the tip surface as a result of a chord-wise pressure gradient with its low pressure located near the mid-chord of the surface,
6. This fluid was then seen to stagnate near the mid-chord and then mix with the bulk tip leakage flow, before finally being ejected from the tip gap on the suction surface side as a leakage jet,
7. Upon ejection from the tip gap, the leakage jet is seen to form a vortex rotating with a sense opposite sense to that of the passage vortex

While many modern day gas turbines incorporate shrouded blade designs and therefore mitigate the formation of tip gap flows, in the test rig used in this investigation, for historical reasons, tip clearances are present in both the stationary and rotating blade rows. In addition, the tip gaps for the rig are relatively large ($\sim 1.67\%$ & $\sim 0.83\%$ span for the rotor and stators respectively) and so the tip gap flows form a significant portion of the blade passage off-axis flows in this turbine.

2.3.2 Disc leakage and cooling flows

Cohen et al. (1996) estimated that in an advanced engine, bleed flows for the cooling of the stationary and rotating blade rows, as well as preventing the ingress of hot gas down the face of the turbine discs, could account for as much as $\sim 15\%$ of the compressor delivery flow. Denton (1993) showed that for an idealised cycle in which coolant was added to the main flow at a constant rate along the cooled

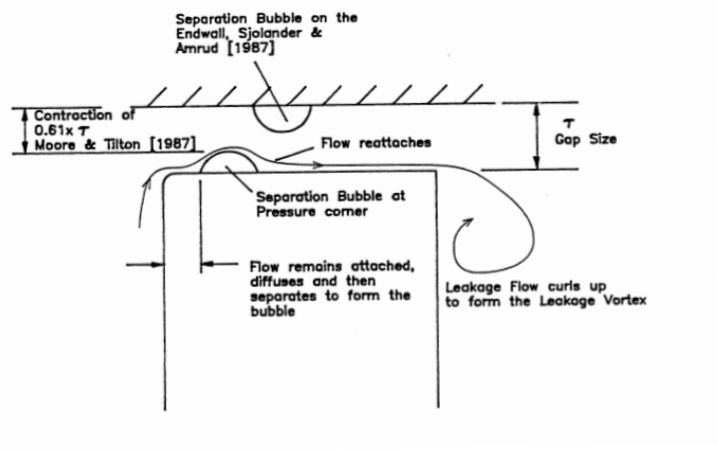

Fig. 2.11: Schematic of tip leakage flow after Kaiser (1996)

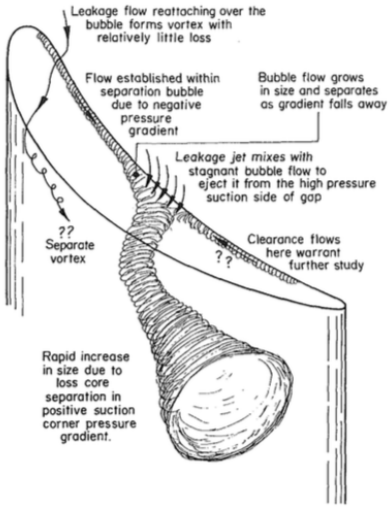

Fig. 2.12: Tip leakage flow model proposed by Bindon (1989)

portion of the expansion in the turbine, the change in overall engine efficiency was likely to be most significantly affected by the reductions in turbine efficiency due to the introduction of cooling flows[4], and so this explains at least some of the emphasis of the work which has gone into trying to reduce these effects.

Gier et al. (2003) considered the interaction of shroud leakage and the main flow in a 3-stage low pressure turbine in order to better understand the nature of the interactions. The investigation compared numerical results to experimental data gathered for the same turbine and showed that the majority of the total cavity (leakage) related losses were due to mixing of the leakage and main streams, while so-called 'by-pass' and 'step' losses were estimated to make up a smaller fraction of the total. The losses due to changes in incidence and the secondary flow due to the leakage were estimated to be smaller again. Colban et al. (2003) investigated the influence of cooling flows from the liner of a large scale combustor simulator as well as the leakage flow which originates from the interface between the combustor-turbine interface in a real machine. Unlike the majority of previous studies, in their work, the authors considered the ejection of leakage flow from a step-type slot (rather than flush arrangements) as well as the effects of coolant ejection from multiple rows of liner cooling holes upstream of the NGV blade row. Strong interactions between the adiabatic effectiveness of the slot cooling and secondary flows were noted, with the majority of the slot flow being swept onto the suction side of the blade by the secondary flows.

Piggush and Simon (2005) investigated the effects of leakage flows and more realistic turbine geometries on the flow in a NGV with axisymmetric endwall contouring, and in particular, assessed the influence of the upstream combustor-turbine transition slot geometry, as well as misalignment of the so-called *slashface* slot at the junction between adjacent vane castings. The authors used a conventional $n - factorial$ DoE to assess which of the features produced the most significant effect on the passage losses. In their conclusions, the authors found that leakage through the mid-pitch slashface slots resulted in the most significant increase in loss over the baseline case as well as complex changes

[4] Denton (1993) puts this figure at around 1% efficiency reduction per 1% cooling flow

in the passage (secondary) flow, with approximately $\sim 1\%$ of the passage mass flow being sucked *into* the slashface gap in the forward portion of the blade passage, with the same amount (including the additional blowing amount) being ejected *from* the gap further downstream in the blade passage. The increase in loss was found to be primarily due to the ejection of low momentum streamwise fluid into the blade passage as well as the thickening of the endwall boundary layer as a result thereof.

Various other investigations concerned with incorporating various additional details to the the flow path calculations have also been undertaken, including:-

- Cherry et al. (2005) considered the effects of including endwall gaps, seals and clearance features on design type calculations,
- Cardwell et al. (2005) considered the effects of endwall misalignment, slashface gap, and surface roughness on endwall film cooling,
- de la Rosa Blanco et al. (2005) considered the effect of upstream platform geometry on the secondary flows of a turbine cascade, *and*
- Ong et al. (2006) considered the effect of coolant ejection on the secondary flows of a low speed, research turbine ($LSRT$)

2.3.3 Trailing filament and shed vorticity

As with any wing of finite span, there exists in the flow behind the turbine blades, a sheet of trailing vorticity. In his paper on rotational flow through cascades, Hawthorne (1955) discussed the sources of three distinct components of vorticity, including a sheet of trailing vorticity behind the blade comprised of two components:-

1. trailing shed vorticity as a result of the change in circulation along the span of the blade, *as well as*
2. the trailing filament circulation, due to the stretching of the vortex filaments carried with the flow between the upper and lower stagnation streamlines in the wake of each blade.

As indicated by Hawthorne and Armstrong (1955), because both the shed vorticity as well as the trailing filament vorticity have the same sense of rotation, at the trailing edge they are seen to combine and form a trailing vortex sheet, which separates the flow from the pressure and suction sides of the wing. As reported by Ingram (2003), in many cases the trailing vortex sheet is seen to roll up into one or two additional vortices downstream of the trailing edge which further complicates the flow field.

2.4 Loss

In his now well-known IGTI Scholar Lecture on the subject, Denton (1993) defined loss in turbomachines as:-

> "... any flow feature which reduces the efficiency of a turbomachine ... "

with the express exclusion of those factors which reduced the efficiency of the gas turbine cycle, such as the temperature or pressure ratios.

Historically, the losses in turbomachines have been divided into three categories, with each contributing an approximately equal amount (i.e. 1/3) to the total. In no particular order, these are:-

1. the *profile losses*, identified as those losses associated with the two dimensional flow over the blade aerofoil (usually measured at the blade mid-span)
2. the *tip gap* or *tip leakage losses*, being those losses associated with the flow through the gap between the turbine shroud and the blade tip; *and finally*,
3. the *secondary* or *endwall losses*.

With regards to the secondary losses specifically, Denton went on to state that approximately 2/3 of the total secondary loss could be attributed to the generation of entropy in the various boundary layers on the hub and shroud, while a further 1/4 of the total was attributable to the dissipation of the so-called *secondary kinetic energy* (SKE) associated with the secondary flow structures.

Finally, he stated that other contributions could also arise from local flow separations as well as early transition and thickening of boundary layers as a result of the interaction with the secondary flows with the various annulus boundary layers (Denton (1993)).

2.4.1 Loss coefficients

In addition to the above, in the same paper, Denton also concluded that the only rational measure of loss in a real turbine was entropy. This was because the residence time of the working fluid in a typical machine is short resulting in a flow that is essentially adiabatic and as a result, the only possible sources of entropy in the fluid would be as a result of flow irreversibilities.

In addition to defining an *entropy loss coefficient* (ζ_s), Denton also defined two other measures for loss, including a *stagnation pressure loss* (Y), and an *energy* (or *enthalpy) loss coefficient* (ζ). Further to this, since only the entropy coefficient remains unaffected by the effects of rotation in the rotating frame of reference, only the entropy coefficient could be used successfully in both cascade and rotating test environments (Denton (1993)).

Denton also showed that, the difference between the *energy* and *entropy* loss coefficients is always of the order 10^{-3} and therefore always negligibly small. As a result, he concluded that there was little point in distinguishing between them. In addition, he also stated that at low Mach numbers ($M < 0.3$), the difference between the stagnation pressure loss coefficient and the remaining two coefficients was also small, and therefore, under these conditions there was little benefit from distinguishing between them (Denton (1993)).

2.4.2 Sensitivity of loss coefficients

Although in a conventional turbomachine, both the energy and entropy loss coefficients, are well suited to the characterisation of the loss, using a simple analysis, it can be shown that as the temperature and pressure ratio's of the turbine decrease, the sensitivity of both coefficients with respect to errors in measurement of either the pressure or temperature, becomes large, and therefore, both coefficients require highly accurate measurements to characterise them correctly.

As an example, Table 2.1 shows the sensitivity of both the energy (ζ) and entropy (ζ_s) coefficients to errors in temperature measurement for two different turbine operating regimes, one typical of a real turbine stage and one more representative of a low speed research turbine as used in this investigation:-

Table 2.1: Sensitivity of the energy (ζ) and entropy loss (ζ_s) coefficients to temperature measurement error

Coefficient	$T_1 = 1400$K, $p_1 = 109,325$Pa $p_1/p_2 = 8$	$T_1 = 298$K, $p_1 = 102,825$Pa $p_1/p_2 = 1.5$
$T_{error} = \pm 0.05°$C		
% error ζ	$\sim 1.66\%$	$\sim 40.05\%$
% error ζ_s	$\sim 2.15\%$	$\sim 40.55\%$

Clearly then, in a low speed, low pressure ratio turbine, the energy and entropy loss coefficients require a high degree of accuracy in the temperature measurement for accurate characterisation of the loss, and are not suitable for the characterisation of the loss in the turbine studied in this investigation.

2.4.3 Proxies for loss

Initially, non-axisymmetric endwall contours were designed by examining the static pressure contours on the hub and shroud of the blade rows. This is probably because the early investigations into endwall contouring developed out of the work of Rose (1994) who was primarily concerned with reducing the pressure gradient at the exit of an HP NGV blade row.

However, since those initial efforts, a number of different quantities have been derived to act as *proxies* for the loss in the blade passage. As indicated by Ingram (2003), this is because, despite the rapid development of computational methods for the calculation of 3-dimensional turbine flows, contemporary CFD methods were still regarded as too unreliable in their prediction of flow losses to be used in design calculations. As reported by Ingram, this included both a reported inability to predict the magnitudes of the losses, as well as, in many cases, even the *trends* of change in loss, rendering the approach useless in many groups opinions.

Despite the reported poor performance of CFD for loss prediction by a number of groups, more recently, a small number of researchers *have* reported relatively good agreement between predicted and measured loss levels in some cases, as well as successful endwall designs exercises in which loss coefficients were used as the target objective function. A reasonably recent example of this is the work of Praisner et al. (2007), who justified their use of a loss-based objective function for their endwall

design partly on the relatively successful loss predictions of Becz et al. (2004), who used it for leading edge modifications to a row of cascade blades, and partly on the good agreement between the predicted and measured spanwise loss predictions for the set of high lift aerofoil designs which formed part of their investigation. In the final analysis of their work, although the authors reported that their design approach had been effective in producing loss-reducing endwall contours, they conceded that although the CFD predictions had predicted the correct trends for the change in loss coefficients, they were not sufficiently accurate to predict either the overall loss magnitudes or the losses associated with the individual features of the flow. Similarly, in their work, Germain et al. (2008) also used a loss-based objective function (although in conjunction with another secondary flow proxy) and reported an increase in turbine efficiency of $1 \pm 0.4\%$ after experimental testing. However, again, this change in the efficiency was not predicted well by the CFD, which predicted a benefit of only $+0.2\%$, prompting the authors to confirm, in part, the difficulties associated with the use of loss as an endwall design metric.

To date, almost all the metrics which have been used as proxies for secondary loss, have been based on combinations of flow velocities and angles, as it was felt that despite the poor loss predictions, contemporary CFD codes *were* sufficiently good at predicting these quantities. A selection of these are now discussed.

Yaw angle

As indicated above, while the early researchers used static pressure are their initial design metric, Harvey et al. (2000) used it in conjunction with the blade row exit whirl angle as a measure of the reduction in secondary flow deviations. This was done specifically because of the authors confidence in the prediction of these quantities, but also because it was consistent with the practice of improving overall turbine efficiency by improving the quality of the flow into the downstream blade rows.

While the authors above used the flow whirl angle directly as a design quantity, a number of more recent researchers have used the quantity as a type of penalty measure, to prevent underturning of the flow as a result of the endwall contouring during design optimizations. Researchers who have taken this approach, include:- Schuepbach et al. (2009), MacPherson and Ingram (2010), McIntosh et al. (2011) and Hilfer et al. (2012).

Secondary kinetic energy (SKE)

The so-called flow *secondary kinetic energy*, is probably the most commonly used proxy for loss used in the design and analysis of non-axisymmetric endwall contours and may be viewed as the kinetic energy associated with the non-primary flow. This quantity is usually presented in non-dimensionalised form (i.e. a coefficient) using (usually) the upstream flow kinetic energy as the non-dimensionalising quantity. Although conceptually, SKE is a simple quantity to understand, practically, the difficulties related to its use lie in the determination of the direction of the primary flow, the result of which is required for the calculation of the secondary flow.

In his thesis, in which he investigated the performance of several non-axisymmetric endwall designs (in a linear cascade), Ingram (2003) defined the *coefficient of secondary kinetic energy* (C_{ske}) to be:-

$$C_{ske} = \frac{V_{sec}^2 + V_r^2}{V_{ups}^2} \tag{2.3}$$

where:-

V_{sec} is the secondary flow velocity magnitude defined as $V_{sec} = V.\sin(\alpha - \alpha_{mid})$,
α and α_{mid} are the flow angle and the midspan flow angle respectively,
V_r is the radial velocity magnitude, *and*
V_{ups} is the upstream flow velocity magnitude

In this definition, the direction of the primary flow was defined by the midspan flow angle (α_{mid}) and which was recalculated at each traverse position behind the blade.

$SKEH_B$[5]

While the above quantity was found to work sufficiently well in linear cascades, a number of shortcomings related to its use in 3-dimensional environments were identified by researchers at Rolls-Royce (Brennan et al. (2001), Rose et al. (2001)), who pointed out the inability of the method to distinguish between the secondary flow and the potential flow around aerofoils, particularly in the vicinity of the leading and trailing edges of the blade. To this end, their approach was to assemble a quantity based on the *dot product* of the secondary kinetic energy, and the *helicity* (being defined as the flux of the streamwise vorticity) of the flow which was used to focus the design routine more on the vortical components of the flow.

SKE_C

Although the $SKEH_B$ approach of Brennan et al. (2001) was used successfully to optimize endwalls for a single stage cold flow test turbine, as pointed out by Germain et al. (2007), the combination of SKE with the flow helicity was effectively equivalent to introducing an arbitrary weighting to the secondary kinetic energy without any physical justification. As a result, the researchers proposed two additional SKE definitions, of which only the so-called SKE_C derivative was applicable to general turbine flows.

Essentially, this approach could be likened to a filtering process, in which the unwanted flow features (i.e. potential flow effects, boundary layer vorticity etc) were removed from the field using a series of averaging procedures performed in the radial and circumferential (pitchwise) directions respectively. In the first step, the local circumferential (θ) and axial (z) velocity components were subtracted from the average of the velocity averaged over a preselected radial window at each pitchwise position, while in a second step, the variations computed in step 1 were then averaged in the circumferential direction over an entire blade pitch. Finally then, the secondary velocities were computed as the difference between the results of the first and second steps.

[5] In Brennan et al. (2001) and accompanying papers, this quantity was referred to as simply $\boldsymbol{SKEH}$, but to differentiate it from following definitions, it was referred as to $\boldsymbol{SKEH_B}$ by Germain et al. (2007) and the same is done here

Because in an ideal flow the radial velocities are assumed to be circumferentially uniform and the contributions to the radial velocities due to the secondary flow are assumed to be small, these were treated in a similar, but slightly modified way. Finally, the total secondary kinetic energy was computed in the usual way (as the sum of the kinetic energies in each of the secondary flow velocities).

In the first step above, the radial slice used for the averaging procedure was selected to be smaller than the desired swirl variation, but larger than the vortices within the flow. This allowed the first sweep to capture the over- and underturning of the flow caused by the secondary flow, but remove large scale effects introduced by the 3-dimensional nature of a real turbine. In addition, the radial slices were reduced in size as the spanwise position under consideration approached the casing and hub endwalls, in order to remove the vorticity associated with the boundary layers which would otherwise manifest as secondary flow.

Other quantities

Endwall transverse pressure gradient

Because it is well known that it is the action of the cross-passage or transverse pressure gradient within the blade passage which results in the migration of the low momentum boundary layer fluid across the endwall surface, and which therefore is a major source of secondary flow generation, Germain et al. (2007) proposed a further metric based on the transverse pressure gradient as a further means to characterise the strength of the secondary flow.

While the model only took into account the formation of the passage vortex as well as relied on a number of simplifications in its formulation, the authors showed that the secondary kinetic energy generated within the passage could be related to the velocity and normal pressure gradient of the flow by:-

$$SKE = \iiint_{bl} \left(\mathbf{v}^T \mathbf{f}\right) dxdydz \tag{2.4}$$

where:-

$\mathbf{f}$ is the force of the pressure gradient normal to the endwall ($\frac{\partial p}{\partial n}\mathbf{u}_n$),
$\mathbf{v}$ is the flow velocity,
p is the static pressure and $\mathbf{u}_n$ is the unit normal vector.

Although this approach represented a truly new approach to quantification of the secondary flow strength, because it retained the requirement to ascertain the primary flow direction of the freestream and therefore shares some of the difficulties associated with classical secondary kinetic energy-based approaches.

Design efficacy

One further and relatively new quantity, is the so-called *design efficacy* (η_{de}) of Dunn (2014). This metric was developed as an attempt to quantify the performance of a blade row in a means similar to that of efficiency, but without the difficulties associated with prediction of the loss or changes in the temperature of the flow. More specifically, in his work, Dunn found that because of the relatively small temperature and pressure ratios in his turbine, the total-total efficiency of a stage could be found to

vary as much as $\eta_{tt} = 10.8\%$ for an error in temperature prediction as small as $\Delta T = 0.1°C$. Similarly, he was able to show a similar but slightly smaller change in the efficiency when the same magnitude error (0.1%) was applied to the stagnation pressure.

Essentially the design efficacy approach is based on the assumption that for a given mass flow, the design condition for a given blade row can be considered the ideal flow condition for that blade row and that which provides the maximum amount of work output for that given mass flow (Dunn (2014)). This assumption was considered valid because, since blade design is usually undertaken using two-dimensional velocity triangles in the plane of the blade cross-section at the radius of interest, for a given mass flow any off-design flow would have to result from a decrease in either the axial or tangential (or both) velocity of the flow.

An inspection of Dunn's formulation showed that, at each radial location, the actual design flow vector ($\mathbf{v}$) was weighted by the design flow angle ($\boldsymbol{\theta}_D$), and subsequently normalized by the maximum design velocity at that station ($\mathbf{v}_{D,max}$). This normalization was done to produce a value close to 1 when the design flow was achieved. The design efficacy may be interpreted as a measure of agreement between the design and actual flow fields, which, when is seen to approach unity, represents the optimal flow field with the maximum work output from the blade row.

2.5 Loss reduction devices

Over the years, there have been many attempts made to reduce the losses associated with secondary flow. Amongst the most common in the literature are:-

- *boundary layer fences* and *grooves*
- *three dimensional blade design*, such as blade lean and sweep
- *leading edge bulbs* or *fillets*
- *axisymmetric endwall contouring*
- and *non-axisymmetric endwall contouring*

2.5.1 Boundary layer devices

Boundary layer devices, such as boundary layer fences and grooves, are a method proposed to reduce generation of secondary losses, by presenting a physical obstruction to the migratory flow of boundary layer fluid on the internal surfaces of the turbine. This approach has been investigated by a number of authors, including Kawai and Adachi (1987), who showed that fences on the suction surface of a turbine blade had the ability to reduce secondary losses, as well as Prumper (1972), who suggested that boundary layer fences on the hub endwall of an axial flow turbine might have the ability to reduce secondary losses as well. In response to the work of Prumper, Kawai et al. (1989) also investigated the use of boundary layer fences on the hub of an axial flow turbine, and found that fences placed optimally on the end wall surface of a linear cascade, had the ability to reduce the secondary loss by approximately $\sim$22%.

Sometime later, Moon and Koh (2001) also investigated the effects of endwall fences in a turbine cascade numerically, and especially, the details of the interaction of the horseshoe vortex legs with an endwall fence, as well as the formation of a counter-rotating streamwise vortex in the region directly above the fence. From this investigation it was concluded that an endwall fence height equal to $1/3$ of the inlet boundary layer thickness was optimum, having produced the least streamwise vorticity.

2.5.2 Three-dimensional blade design

Three dimensional blade design, such as the use of blade stacking, lean and sweep, has also been investigated by various researchers, such as Denton and Xu (1999) in the late 1990's, as well as more recently by groups such as Bagshaw et al. (2008a) and Bagshaw et al. (2008b).

In their paper, Denton and Xu (1999) commented that, as the effects of 3-dimensional blade design, such as lean and sweep produce 3-dimensional effects in the flow field, it is only as a result of the development of fully three dimensional flow calculation methods that the effects of these design features can be effectively harnessed to reduce losses and improve turbine performance. As the authors went on to explain, the effect of forward sweep of the leading edge near the hub and tip of a turbine blade, was to reduce the blade loading at these extremities, while conversely, the effect of backward sweep near the trailing edge (also at the endwalls), was to reduce the loading of the profile in these areas.

In their work, Bagshaw et al. (2008a) explained that that the use of reverse compound lean (RCL), in which blades were allowed to 'bow' in the direction of the pressure surface, resulted in an increase in the intensity of secondary flows near the hub and tip, but also a reduction in the blade profile loss near the mid-section. As a result therefore, their work was intended to be an exploration of the potential benefits of utilising the RCL to reduce the losses near the mid-chord, along with leading edge sweep and non-axisymmetric endwall contouring at the endwalls, to offset the increased losses produced by the RCL near the endwalls (Bagshaw et al. (2008a)).

Experimental testing of the blades designed by Bagshaw et al. (2008a) showed that, although the interactions between the 3-dimensional blade shaping and endwall contouring were complex, the results indicated that the synergistic use of the technologies produced greater benefits than that which would have been produced through the use technologies such as endwall contouring alone (Bagshaw et al. (2008b)).

2.5.3 Leading edge bulbs and fillets

Leading edge modifications have also been a topic of recent investigation for the reduction of secondary loss, with authors such as Sauer et al. (2001), Zess and Thole (2002), Hoeger et al. (2002) and Muller et al. (2002) all investigating the influence of leading edge bulbs and/or fillets on the secondary flows in either turbine or compressor cascades. Others, such as Shih and Lin (2003), Lethander (2003) & Lethander et al. (2003) investigated the influence of leading edge modifications on the secondary flow with more specific emphasis on reducing the heat transfer and adiabatic temperature of the endwall.

In his work, Lethander explained that the intention of modified leading edge geometry was to reduce the strength of the individual horseshoe vortices ahead of each blade (and in so doing, ultimately the

overall strength of the secondary flow), by accelerating the stagnating boundary layer fluid ahead of each blade, thereby reducing the leading edge total pressure profile and preventing the formation of the vortices in the first place (Lethander (2003)).

2.5.4 Axisymmetric endwall contouring

Axisymmetric endwall contouring, also known as the *Russian kink*, is a technique characterised by a contraction of the blade passage in an axisymmetric fashion near to the exit of the blade row, in an attempt to utilise the "turn *then* accelerate" philosophy, rather than the conventional "turn *and* accelerate" approach used in the majority of turbine designs.

As described by Harvey et al. (2000), in most cases, researchers attributed the small increases in efficiency measured for turbines modified with axisymmetric endwalls, to a redistribution of pressure and therefore loading near the endwalls of the passage, and therefore small reductions in loss, although some also indicated a portion of the improvement may also have been as a result of a reduction in the outlet flow angle variation of the profiled blade passages, and therefore, a small increase in the efficiency of the downstream blade rows.

In his work, Ingram (2003) also indicated that some authors attributed the reductions in loss to a thinning of the boundary layers on the end wall surfaces within the contraction as a result of the acceleration of the fluid in the region.

2.6 Non-axisymmetric endwall contouring

Non-axisymmetric endwall contouring, as a method specifically for the reduction of secondary losses, developed as a byproduct of the early work of Rose (1994), who was concerned primarily with reducing turbine disc coolant leakage flows by controlling the static pressure distribution at the exit of turbine blade rows, rather than reducing secondary loss.

However, following the application of the concept by Harvey et al. (2000) and Hartland et al. (2000) to a cascade model of the high pressure turbine rotor of the Rolls-Royce RB211 aero-engine (the so-called *Durham cascade*) which showed that the method was able to reduce the secondary kinetic energy and exit angle deviations, as well as to a lesser degree, the secondary loss, the technique was investigated almost immediately as a means specifically for the reduction of the secondary loss in commercial gas turbine applications.

Among the first of these commercial investigations were the efforts of Brennan et al. (2001), Rose et al. (2001) and Harvey et al. (2002) at Rolls-Royce, who investigated the technique for the reduction of secondary loss in the high (HP) and intermediate (IP) pressure turbine stages of a model Rolls-Royce Trent 500 aero-engine. Following application of the endwalls, increases in efficiency of approximately 0.59% and 0.9% were experimentally verified for the two turbine stages respectively. As would be expected, following the release of these initial findings, a raft of other investigations soon followed resulting ultimately in efforts from all the other major turbine manufacturers including both major North American operators, Pratt & Whitney and General Electric.

2.6.1 The basic idea

In summary, the method by which non-axisymmetric endwall contouring is most commonly explained to function, is through a reduction of the local endwall static pressure gradient (which was described in Section 2.2.1 as being the driving force of the cross-passage boundary layer flows and therefore the larger so-called passage vortex) through the introduction of 3-dimensional curvature to the endwall surface. In the vicinity of convex curvature, curvature of the local streamlines results in an acceleration of the flow, and a corresponding decrease in local static pressure, and in regions of concave curvature, a local deceleration of the flow and a corresponding increase in local fluid pressure.

Despite the simplicity of the above definition as well as the fact that this explanation was certainly the most common early on in the development of endwall contouring, it is now also relatively well-known that endwall contours may also interact with the formation of the so-called horseshoe vortices, as well as the corner vortices, both of which having been shown by various authors to play a part in the development of downstream streamwise vorticity, and therefore the secondary flow.

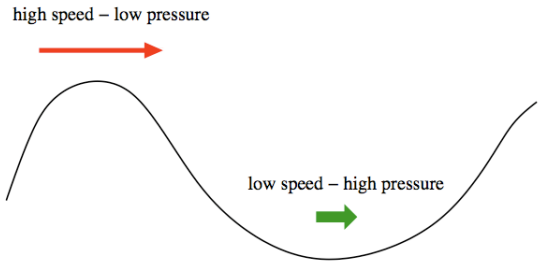

Fig. 2.13: The basic idea used in non-axisymmetric endwall contouring [Reproduced from Ingram (2003)]

2.6.2 Endwall design

The process of non-axisymmetric endwall design, usually entails a combination of procedures, including:-

1. a parametrisation, in which the curvature of the endwall surface is defined in the directions of the parimary blade passage coordinates, *and*
2. an optimization, in which the actual values of the endwall parameters are deduced, usually to produce some preferred flow field.

Parametrisation

Within the literature, one of the most popular methods of endwall parametrisation, at least early on, was the method developed by Harvey et al. (2000) and Hartland et al. (2000). As indicated, this parametrisation was used by Harvey et al. (2000) and Hartland et al. (2000) originally, but also subsequently by Brennan et al. (2001), Rose et al. (2001) and Harvey et al. (2002) at Rolls-Royce,

as well as MacPherson and Ingram (2010), McIntosh et al. (2011) and Hilfer et al. (2012) at the University of Durham.

In this parametrisation, the curvature of the endwall in the circumferential direction was defined using a truncated Fourier series, and in the axial direction, by non-uniform rational B-splines (NURBS) fitted through each various control points on each circumferential curve.

In the circumferential direction, the form of the endwall curves was given by:-

$$\delta r(\theta) = \frac{1}{C} \sum_{n=1}^{k} \left(a_n \sin\left(\frac{n\pi\theta}{P}\right) + b_n \cos\left(\frac{n\pi\theta}{P}\right) \right) \tag{2.5}$$

where:-

$\delta r(\theta)$ is the local endwall perturbation height at θ,
C is a normalising coefficient,
k is the number of harmonics used in the series,
a_n and b_n are constants related to the amplitude and phase of each curve, *and*
P is the blade pitch.

As indicated by the authors, the use of the Fourier series expression was justified as it helped to preserve the flow area of the blade passage thereby limiting throat errors in compressible flows, but also because as the pressure distribution within the blade row is often sinusoidal, it was felt it may be advantageous to have a definition for the endwall curvature which included sinusoidal functions in an attempt to cancel them out. Finally, the authors also realised that even limiting the number of harmonics included in the endwall definition to a relatively modest number (i.e. 3), still allowed for an almost any shape to be generated. The authors also justified the use of B-splines in the axial direction as a result of their increased responsiveness to changes in the local endwall height in the vicinity of each control point compared with other types of parameterised curves.

The continued emphasis on non-axisymmetric endwall contouring also led to the development of a number of other parametrisations. In their relatively recent work, Poehler et al. (2010), used an approach in which the curvature of the endwall adjacent to the blade pressure and suction surfaces was defined using two 7^{th}-order polynomials, while in the circumferential direction, a sinusoidal function was used to link the two polynomials. In order to ensure a smooth transition between the pressure and suction surface polynomials, a linear blending function of the form:-

$$A = \theta_{rel} \cdot f_1(x)_{ps} + (1 - \theta_{rel}) \cdot f_2(x)_{ss} \tag{2.6}$$

where:-

A is the endwall amplitude coefficient,
θ_{rel} is the relative circumferential coordinate given by $\frac{\theta - \theta_{ss}}{\theta_{ps} - \theta_{ss}}$,
f_1, f_2 are the pressure and suction side polynomials, *and*
x is the axial coordinate

was used to define the amplitude of the endwall sinusoids. The final circumferential endwall height was given by:-

$$\delta r(\theta_{rel}) = A \cdot (\sin(\zeta_1 \cdot \theta_{rel} + \varsigma_1) + \sin(\zeta_2 \cdot \theta_{rel} + \varsigma_2)) \tag{2.7}$$

Finally, in the axial direction, at the edges of the contoured region, zero displacement and gradient boundary conditions were enforced to ensure the smooth transition of the endwall between the annular (i.e. *uncontoured*) and contoured portions of the end wall.

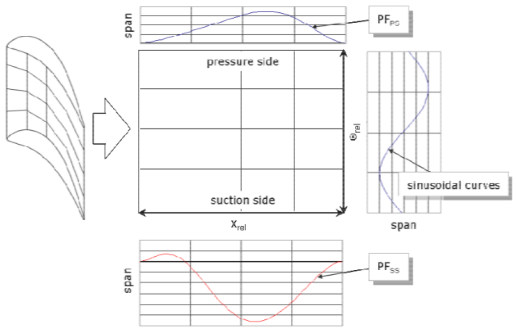

(a) Endwall parametrisation of Poehler et al. (2010)

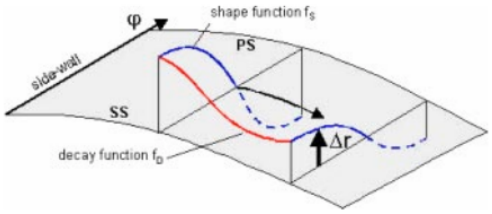

(b) Endwall parametrisation of Nagel and Baier (2005)

Fig. 2.14: Endwall parametrisations of Poehler et al. (2010) and Nagel and Baier (2005)

Nagel and Baier (2005) (Fig. 2.14b) used a similar approach to that of Poehler et al. (2010), although they used two additional spline segments to describe the axisymmetric variation of the endwall in the axial direction, and a pair of logically orthogonal basis functions, which - when multiplied together - defined the curvature of the endwalls in the circumferential direction. The actual details of the basis functions were not disclosed. Nagel and Baier's parametrisation was also subsequently used by Germain et al. (2008) for improving the efficiency of a 1½ stage, high work turbine, although the underlying basis functions used in the parametrisation were modified to allow more complex and adjustable endwall shapes to be produced.

Finally, in order to free final endwall geometries of any predetermined characteristics, other authors, such as Praisner et al. (2007) (Fig. 2.15a) and Dorfner et al. (2011) (Fig. 2.15b) opted for 'function free' endwall parametrisations, in which grids of control points are set out on the blade passage endwall and subject to various constraints, adjustments to the coordinates of each control point are made by the optimization routine. Subject to the actual details of the various constraints (such as $d = \pm\Delta y$ or $d = \pm\Delta z$ only), this allows for extremely complex endwall curvature to be defined, although this approach can greatly increase the number of geometry parameters to be optimized.

Parameter selection

Within the literature, a number of different approaches have been used for the actual selection of parameters used in the various endwall parametrisations. Initially, the selection of the parameters

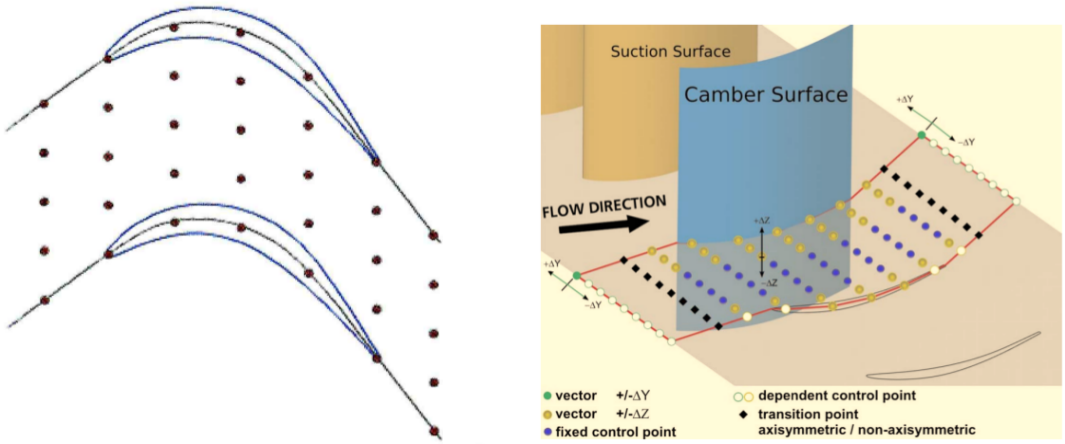

(a) Control point parametrisation grid of Praisner et al. (2007)

(b) 'Free' parametrisation of Dorfner et al. (2011) showing fixed and constrained control points

Fig. 2.15: 'Free' endwall parametrisations of Praisner et al. (2007) and Dorfner et al. (2011)

were made using manual approaches, however, as the parametrisations have become more elaborate, the procedures used for their selection have become increasingly more autonomous.

In his early work, Rose (1994) generated three endwall designs for the NGV of a HP turbine, using a total of four parameters for each design. Although in the search for his parameters, Rose did not appear to utilise any systematic domain search procedure, the parameters for the initial design were selected in order to produce pressure variations close to the endwall at a height of approximately $\sim 0.48\%$ span, while the parameters of the remaining two designs were selected to remove various undesirable features which were noticed in the pressure profile of the blade suction surface.

In the subsequent work of Harvey et al. (2000) and Hartland et al. (2000), the authors used an extended version of a linear superposition design procedure named $FAITH$ (originally described by Shahpar and Lapworth (1998) for the design of turbomachinery aerofoils) for the selection of their endwall parameters. In this approach, an initial set of 36 design perturbations were set up and the fully viscous, 3-dimensional flow solutions for each profile computed. Thereafter, the sensitivity of the flow field to each of the parameters was calculated using numerical differentiation, from which a linear sensitivity matrix could be constructed. Finally, linear superposition was used to generate *new* endwall designs, with a focus on controlling the local endwall static pressure and exit whirl angle distributions of the blade row. Although in theory, the first 3 harmonics of the Fourier series parametrisation were available for the endwall design, in the actual investigation, only the 1^{st} harmonics of the series were used. This was done because the complexity of the shapes produced using the 2^{nd} and 3^{rd} harmonics (as well as the flow profiles they produced), were found to be too great to work with manually.

In a subsequent investigation, Hartland and Gregory-Smith (2002) used an equally manual process for the design of their endwalls after having defined the axial curvature of the hub using the mean camber of the adjacent blade aerofoil as a guide. The actual axial curvature was then defined by rotating the blade mean camberline about its trailing edge, and then re-scaling the profile to match the axial chord of the blade. The height and fine details of the endwalls were then again adjusted manually to produce the desired pressure profiles.

In contrast to the above efforts, later researchers, having used increasingly more complex endwall parametrisations, have tended towards automated design routines in which the values of the design parameters are selected by some systematic search process, usually to optimize some flow quantity.

Praisner et al. (2007) used a fully automated endwall design procedure to optimize the locations of the control points used to design their 'free' endwall parametrisation - this being the gradient-based *sequential quadratic programming* (SQP) method. This was done because the number of iterations required to optimize the number of control points used in their parametrisation was estimated to be in excess of 1000 per endwall, and would therefore be impractical to undertake manually. Shortly thereafter, Germain et al. (2008) also used an SQP-based routine to select the geometry parameters for their endwalls, which, because they included about 15 parameters per endwall 'feature', would also have required considerable effort to optimize manually.

One problem common to the gradient-based SQP methodologies used by Praisner et al. (2007) & Germain et al. (2008) above, is the inability of such algorithms to escape *local* optima on the objective function surfaces and therefore effectively optimize the design objective function in a *global* manner (Haupt and Haupt (2004)). This is because gradient-based routines usually progress in a direction guided by local topology of the objective function surface only and therefore cannot distinguish between local and global optima.

One remedy to this situation is the use of so-called *evolutionary alogrithms* for selection of the endwall parameters, as were implemented by MacPherson and Ingram (2010) and McIntosh et al. (2011) for the design of their endwalls. In their investigations, the researchers used the parametrisation of Harvey et al. (2000), but incorporated all 3 harmonics in their endwall expression, thereby effectively increasing the number of endwall parameters to be optimized for each endwall in comparison to Harvey et al. (2000) significantly. Because of this increase in complexity, as well as to avoid the aforementioned pitfalls associated with gradient-based methods, the researchers employed a single-objective, multi-parameter version of the so-called *genetic algorithm* (GA) (Holland (1975)) as the parameter search algorithm in the design routine. Although no experimental validation of the resulting designs were undertaken, both groups of researchers predicted favourable reductions in secondary flow strength and loss. In both cases however, the use of the higher order parametrisation did result in extremely complex endwall shapes[6].

Although the endwall of MacPherson and Ingram (2010) was clearly too complex for actual use, the design approach demonstrated the usefulness of the globally searching algorithms for the selection of the endwall geometry parameter values and their ability to search widely through the parameter vector space for potentially indistinct or obscure geometries.

Objective functions used in the design of non-axisymmetric endwalls

Within the literature to date, there appears not to be a single, consistently used flow parameter which has been used as the basis of objective functions for the optimization of non-axisymmetric endwall contours. Instead, there have been a selection of quantities which have been used as either proxies for loss or as indicators of flow quality or machine efficiency. In some cases, true optimization approaches

[6] McIntosh et al. (2011) ultimately reduced their parametrisation complexity as a result of this complexity

were not used at all, and instead, judicious selection of parameters to reduce various features, such as the endwall pressure gradient, were used.

In their early work, Harvey et al. (2000) and Hartland et al. (2000) developed a design which was shown to adequately control the endwall surface static pressure distribution of a blade row and which reduced the exit whirl angle of the flow. As indicated by the authors, these quantities were used as design parameters as a result of the perceived superior accuracy of the design tools used in the investigation (i.e. CFD) to predict these quantities.

In the same investigation, in the experimental qualification of their design, the final endwalls were tested in a large scale, linear cascade turbine cascade, where the researchers used a total pressure loss (C_{p0}) and secondary kinetic energy (C_{ske}) coefficient, as well as flow yaw angle, to gauge the effectiveness of the contours. At the conclusion of the testing, the introduction of the endwalls to the blade row corresponded to a reduction in magnitude in all of the aforementioned performance criteria, and most importantly, a reduction in secondary loss of approximately $\sim 30\%$ at the blade exit plane and $\sim 34\%$ in mixed out terms. Importantly, the CFD predictions of the endwall static pressure distribution, coefficient of secondary kinetic energy and yaw angle, were seen to correspond well to the actual measured experimental results, in contrast to the total loss coefficient, in which no change despite the addition of the profiled endwall was predicted. In conclusion, since the contours were designed primarily to reduce over- and underturning of the flow at the blade exit (in order to improve the performance of a downstream row), the reductions in secondary loss associated with the endwall contours were unexpected. In conclusion, the poor performance of the numerical predictions with respect to the secondary loss prediction were attributed to deficiencies in the turbulence modelling of the flow, although this was seen to decrease even further when a higher order turbulence closure was utilised.

In the following and now well-known investigation at Rolls-Royce, Brennan et al. (2001) in the design of their endwall contours, for a rotating cold flow analogue of the Trent 500 aero-engine, elected to use a more complex quantity as their target optimization metric, based on the vector dot product of the secondary kinetic energy (as used by Harvey et al. (2000)), and the flow helicity (H) - itself defined as the dot product of flow velocity and vorticity - a quantity which was subsequently abbreviated to $SKEH$.

One of the principal reasons given for the use of this quantity rather than the coefficient of secondary kinetic energy used by their predecessors, was as a result, in part, of the difficulties associated with the definition of secondary kinetic energy for a real machine and more specifically, the difficulties associated with defining the primary flow direction in a 3-dimensional blade environment, but also as a result of the tendency for the regions of potential flow around the leading and trailing edges of the aerofoil to appear as secondary flow when the 'standard' definition was used. A further benefit associated with this new quantity, as noted by the authors, was the increased ability of the new quantity to isolate the secondary kinetic energy associated with the main vortical structures of the secondary flow.

Using the above mentioned design metric, Brennan et al. (2001) as well as Harvey et al. (2002) in a later study, were able to produce contoured endwall designs which resulted in experimentally validated increases in stage efficiency of $0.59\% \pm 0.25\%$ for the HP turbine, and $0.9\% \pm 0.4\%$ for the IP turbine.

Despite the experiences of those authors above, Praisner et al. (2007) reported a successful optimization for a linear cascade of high lift, LP turbine blades using an objective function based only

Table 2.2: Summary of endwall design quantities used by various researchers

Researcher	*Design quantity*	*Constraints*	*Performance measures*
Rose (1994)	static pressure		static pressure
Hartland et al. (1998)	static pressure		static pressure, yaw angle, C_{p0}
Harvey et al. (2000), Hartland et al. (2000)	static pressure, yaw angle		C_{ske}, C_{p0}, static pressure, yaw angle
Gregory-Smith et al. (2001)	C_{ske}		C_{ske},yaw angle, C_{p0}
Brennan et al. (2001), Rose et al. (2001)	$SKEH_B$		$SKEH_B$, yaw angle, efficiency
Harvey et al. (2002)	$SKEH_B$		$SKEH_B$, efficiency
Hartland and Gregory-Smith (2002)	blade camberline		C_{p0}, yaw angle, C_{ske}
Torre et al. (2006)	not given		C_{p0}, yaw deviation angle, $SKEH$
Praisner et al. (2007)	C_{p0}	yaw angle	C_{p0}, blade loading
Germain et al. (2008), Schuepbach et al. (2008)	$SKE_C + C_{p0}$	yaw angle	C_{p0}, yaw angle, SKE_C, efficiency
Bagshaw et al. (2008a), Bagshaw et al. (2008b)	$SKEH_B$		C_{p0}, yaw angle, $SKEH_B$
Schuepbach et al. (2009)	SKE_C	yaw angle (torque)	C_{p0}, yaw angle, SKE_C, efficiency, Ω_{str}
Sonoda et al. (2009)[a]	C_{p0}	β_{dev}, $\dot{m}$	C_{p0}, yaw angle
MacPherson and Ingram (2010)	C_{ske}	yaw angle	C_{ske}
Poehler et al. (2010)	$SKEH$		efficiency, C_{p0}, ω_s
Vazquez and Fidalgo (2010)	$SKEH$		C_{p0}, yaw angle, KSI, helicity, $SKEH$
McIntosh et al. (2011)	C_{ske}, $\int U^3 dA$	yaw angle	C_{ske}, $\int U^3 dA$, C_{p0}
Kumar and Goverdhan (2011)[b]	C_{ske}		yaw angle, C_{p0}, Ω_{str}, wall shear
Dorfner et al. (2011)[c]	C_{p0}		C_{p0}, Tu, $AVDR$
Bergh et al. (2012)	C_{ske} + yaw angle deviation		C_{ske}, $C_{p0,rel}$, efficiency, static pressure
Hilfer et al. (2012)	C_{ske}	yaw angle, $\dot{m}$	C_{p0}, C_{ske}, yaw angle
Miyoshi and Higuchi (2013)	ε (enstrophy)		C_{p0}

[a] Sonoda et al. (2009) actually investigated *axi*-symmetric endwall contouring of a low aspect ratio *NGV*

[b] Kumar and Goverdhan (2011) designed an endwall fence but in an effort to reduce secondary loss

[c] Dorfner et al. (2011) conducted their work on a linear *compressor* cascade

on a mass-averaged total pressure loss coefficient. Although the researchers checked various other quantities, including TKE, SKE and $SKEH$, to confirm that their optimized geometry produced reductions in these quantities as well, the primary parameter selection for the endwall geometry was guided purely on the loss-based objective function. Although the authors' final designs were successful, with reductions in the both the spanwise as well as complete exit plane mass-averaged total pressure

loss coefficients measured, this result was somewhat surprising as it is contrary to the experiences of a number of other workers in the field. In summary, the authors concluded that although the CFD had predicted the correct *trends* for the blade row loss, it lacked significant accuracy to predict the loss for individual flow features, as well as the ability to predict the overall loss magnitude accurately.

Germain et al. (2008) also used a loss component in their optimization of endwall parameters for their 1½ stage turbine, although this was in conjunction with a modified definition of secondary kinetic energy, as developed by Germain et al. (2007). The researchers contoured an upstream nozzle row, as well as a rotor, but found the endwall contouring to be most effective in the stationary row, partly as a result of changes to the midspan blade loss as well as small reductions in secondary loss. The changes to the midspan were apportioned to wholespan effect of the endwall contouring on the blade pressure profiles, especially on the suction surfaces, which resulted in significant aft-loading of the blade sections. Ultimately the efficiency of the turbine was increased by $\sim 1\% \pm 0.4\%$, which was more than was expected from the initial performance predictions of the design.

Within the remainder of the literature, a number of other endwall design optimizations have been undertaken, such as MacPherson and Ingram (2010), Poehler et al. (2010), Kumar and Goverdhan (2011) and Dorfner et al. (2011)[7], with the majority of these investigations being undertaken in cascade environments. For these design attempts, a selection of the usual quantities was used, although McIntosh et al. (2011) did perform an endwall design for a linear cascade using an objective function not commonly used to date. In this work, the authors undertook an endwall design which utilised an objective function based on the so-called U^3-integral of Denton, which was explained to be effectively a measure of the total entropy generation in the boundary layers of the turbine surfaces. The integral was implemented as a compound objective function including a measure of the blade row exit yaw angle to prevent underturning of the flow. As reported by the authors however, since the objective function was calculated as the sum of the entropy generation on both the endwall as well as the blade surfaces, the optimization scheme was able only to change the geometry of the endwall and the outcome of the optimization was somewhat limited.

Table 2.2 gives a summary of the various design metrics and performance measures used to design and characterise non-axisymmetric endwall contours for various investigations from original investigation of Rose (1994), to the present day.

2.6.3 Optimization routines used in this thesis

In this investigation, optimizations were performed at two main points during the endwall generation procedure:- firstly, as part of the *Maximum Likelihood Estimate*[8] procedure for the fitting of the so-called *Design and Analysis of Computer Experiments*[9] (*DACE*) metamodel, and secondly, during the actual searching of the objective function surface for the optimum endwall designs.

Because both the objective function used in the evaluation the optimum *DACE* metamodel hyperparameters as well as the objective functions used for the design of the optimum endwall contours were known to be nonlinear and multimodal, the routine chosen to complete these optimizations was

[7] Although the actual work of Dorfner et al. (2011) was undertaken for a *compressor* cascade, the approach was similar to that used for turbine profiled endwalls, and so is included here

[8] The use of Maximum Likelihood Estimation for the fitting of the model hyperparameters discussed in Section 5.2.3

[9] As discussed in Chapter 5 and used as the basis of the endwall design routine developed in this investigation

required to be capable of dealing with both of these requirements effectively. In addition, as various constraints were applied to the optimization subproblem (as discussed in Sections 5.3.1 and 5.6.5), a method capable of dealing effectively with these requirements was also required.

The Differential Evolution (*DE*) algorithm of Storn and Price (1995), although a relatively new routine, was selected for these tasks as it is capable of dealing with a wide variety of optimization problem types, including nonlinear and multimodal objective functions, disconnected feasible regions, and the application of constraints is relatively straightforward. In addition, when initialised uniformly across the parameter space, the algorithm was found to converge faster and more reliably to the global optimum than similar algorithms it was tested against, including the Genetic Algorithm of Holland (1975).

The */rand/1/bin*[10] variant of the *DE* algorithm used in this thesis is discussed in more detail in Section 2.6.3 below.

Differential Evolution

Differential Evolution (*DE*) is a relatively new optimization algorithm (Storn and Price (1995)), and as its name suggests, is a member of the evolutionary algorithm's (*EA*) family of metaheuristic optimizers. Although the routine shares some similarities with other EA's (such as the genetic algorithm (*GA*) and evolutionary strategy (*ES*) algorithms), the *mutation* and *crossover* routines of *DE* provide its major points of difference from other EA's.

In summary, the steps of Differential Evolution are:-

1. generate an initial population ($\mathbf{X}_0$) of vectors ($\mathbf{x}$) in the feasible region
2. mutate each member of the population to produce a new *mutant vector* ($\mathbf{v}$) where $\mathbf{v}_g = \mathbf{x}_{g,r0} + F \cdot (\mathbf{x}_{g,r1} - \mathbf{x}_{g,r2})$, and $\mathbf{x}_{r0/r1/r2}$ are randomly chosen *different* vectors from the population and g represents the generation number and r signifies each vector is chosen at random
3. perform component-wise crossover to produce *trial vector* $\mathbf{u}$ using $\mathbf{x}$ and $\mathbf{v}$ where the components of the trial vector (u_i) are given by:-

$$u_i = \begin{cases} v_i & \text{if } rand_i(0,1) \leq Cr \text{ or } i = i_{rand} \\ x_i & \text{otherwise} \end{cases} \tag{2.8}$$

4. perform selection to generate next vector population:-

$$\mathbf{x}_{g+1} = \begin{cases} \mathbf{u}_g & \text{if } f(\mathbf{u}_g) \leq f(\mathbf{x}_g) \\ \mathbf{x}_g & \text{otherwise} \end{cases} \tag{2.9}$$

5. repeat until some convergence criteria is met

[10] This is the standard methodology of Price et al. (2005) for describing the Differential Evolution variant used:- *rand* → indicates the base vector is *rand*omly chosen; *1* → indicates a single vector difference is added to each base vector; *bin* → indicates the vector mutation closely follows a *bin*omial probability distribution

As can be seen from the algorithm steps above, *DE* has two tunable parameters, the scale factor, F, which is a weighting applied to the difference between the difference vectors used in the mutant vector construction, and the so-called crossover constant, Cr, which controls the fraction of vector components of the new trial vector ($\mathbf{u}$) which come from the mutant vector ($\mathbf{v}$) and its corresponding base population vector ($\mathbf{x}$). While $Cr \in [0, 1]$, there is no strict upper limit on F, although as suggested by Price et al. (2005), it is seldom set greater than 1.0.

Since its initial development, *DE* has been found to be an effective global optimizer, with authors such as Tusar and Filipic (2007) comparing it to various state-of-the-art implementations of the well-known *genetic algorithm* (*GA*) (Holland (1975)), and finding in most cases that the *DE* performed significantly better than the corresponding *GA* implementation.

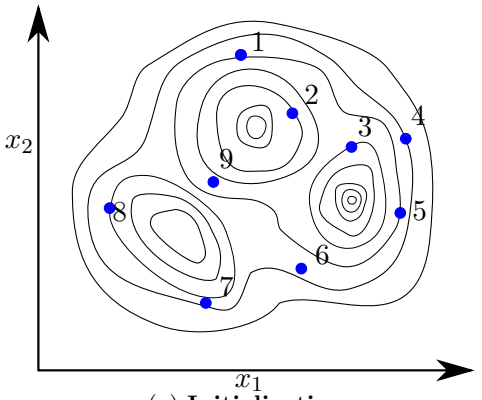

(a) **Initialization**

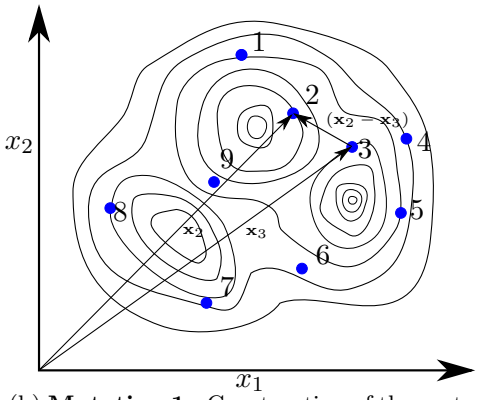

(b) **Mutation 1**:- Construction of the vector difference $(\mathbf{x}_2 - \mathbf{x}_3)$

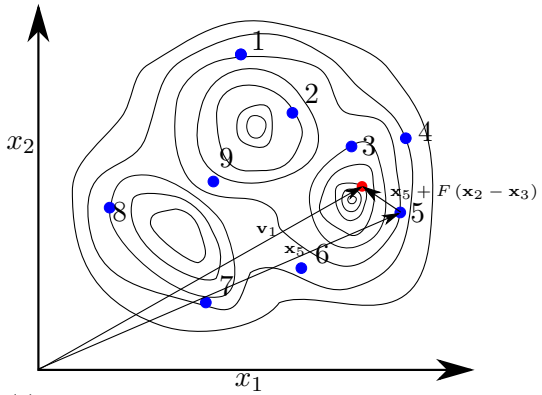

(c) **Mutation 2**:- Construction of *mutant* vector $\mathbf{v}_1 = \mathbf{x}_5 + F \cdot (\mathbf{x}_2 - \mathbf{x}_3)$

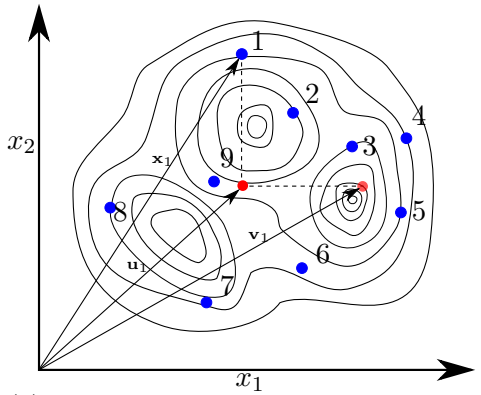

(d) **Crossover**:- Construction of *trial* vector $\mathbf{u}_1$ using components of $\mathbf{v}_1$ & $\mathbf{x}_1$ (if $rand_i(0,1) \leq Cr$ or $i = i_{rand}$, $u_i = v_i$ else $u_i = x_i$)

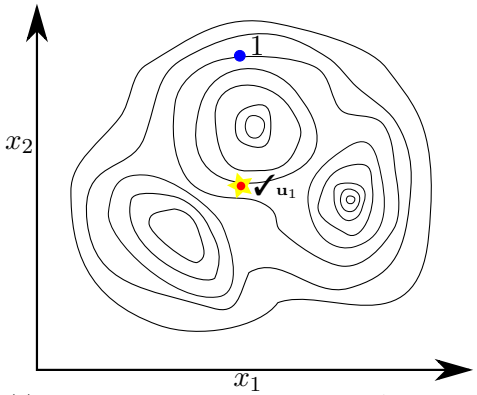

(e) **Selection**:- Test between $\mathbf{u}_1$ & $\mathbf{x}_1$ and lowest value OF vector is selected

Repeat until converged

(f) **Convergence**

Fig. 2.16: The basic steps involved in Differential Evolution optimization

3

Objective functions

In this Chapter, flow metrics as well as the objective functions which were used as the basis for the endwall designs investigated in this thesis are described. Although many authors have reported on the design of successful endwall contours, there is a great deal of variability in the quantities used, and more importantly, in the precise definition of even conceptually identical quantities. As a result of this, after having presented a brief overview of optimization and various concepts associated with it, the fundamental quantities that were used for the design of the endwall contours in this investigation were defined. Thereafter, the use of each of these quantities in the various objective functions which formed the basis of each endwall design produced for this investigation, as well as any constraints which were applied to the objective functions as part of the optimization procedure, are discussed.

3.1 Overview of optimization and objective functions

3.1.1 Single-objective optimization (*SOO*)

In the context of this work, optimization was important because, in order to compare the effectiveness of the various metrics used for the design of non-axisymmetric endwalls, it was necessary to be able to produce designs of as high (and therefore, similar) a degree of optimality as possible .

Qualitatively, the purpose of any optimization routine is to return a vector of solution variables ($\mathbf{x}$) which, when applied to a particular *target* or *objective function*, will result in the minimization or maximization of that function's value, while satisfying any constraints placed on them.

Mathematically, the problem (expressed here as a minimization problem) can be given by the following:-

$$\min_{x \in \mathbb{R}} : f(x) \tag{3.1}$$

subject to:-

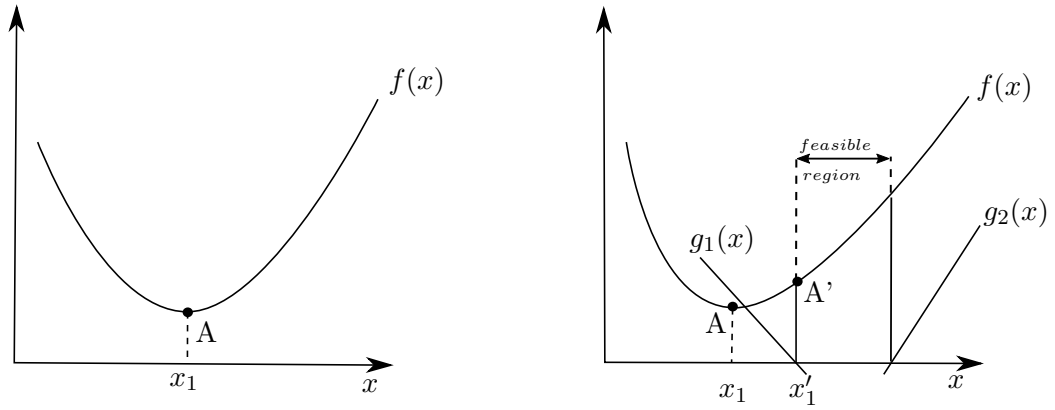

(a) Unconstrained (b) Constrained

Fig. 3.1: Elementary unconstrained and constrained optimization (minimization) problems

$$c_m(x) = 0 \tag{3.2}$$

$$g_m(x) < 0 \tag{3.3}$$

$$x_l \leq x \leq x_h \tag{3.4}$$

where:-

$f(x)$ is the so-called *objective function*,
x is the input parameter,
c_m / g_m are equality and inequality *constraint functions*, *and*
x_l, x_h are upper and lower *variable / boundary constraints* on x

In the event that the maximum of the objective function is sought, the problem above may simply be expressed as a minimization of the *negative* of the objective function, i.e:-

$$\min_{x \in \mathbb{R}} : -f(x) \tag{3.5}$$

A typical 1-dimensional unconstrained minimization problem is illustrated in Fig. 3.1a, where the global optimum of the objective function $f(x)$ is indicated by point A which in turn corresponds to a value x_1 for the input parameter x. Fig. 3.1b shows the same problem, however in this case, including the constraint functions $g_1(x)$ & $g_2(x)$ as defined by Eqn. 3.3. In this example, the unconstrained optimum A is then shifted to the so-called constrained optimum (A') to satisfy the $g_1(x) < 0$ inequality constraint.

3.1.2 Constraint handling

As indicated above, the classic optimization problem may be subject to a set of constraints, where Eqns. 3.2 and 3.3 represent the set of equality and inequality *constraint functions* and Eqn. 3.4 represents the *variable / boundary constraints*. In constrained optimization, a candidate vector $\mathbf{x}$ is

termed *feasible* if the vector satisfies all the variable and constraint functions of the problem (Fletcher (1987)).

Within the literature, there are two main techniques which are commonly used for the handling of boundary and constraint functions:-

1. *direct* constraint handling, *and*
2. *transformation methods*, in which a constrained optimization problem is transformed into an unconstrained problem

Direct methods

In the direct constraint handling approach, while a candidate vector is feasible, the optimization proceeds on the objective function as usual. However, if a candidate vector becomes infeasible, the optimization proceeds on the constraint function directly, instead of on the objective function.

Schematically, direct constraint handling is shown in Fig. 3.2a, where the objective function is given by $f(x)$ and system of constraint functions are $g_1(x)$, $g_2(x)$ where the $g_1(x), g_2(x) < 0$. Since the unconstrained optimizer A is infeasible, the optimization proceeds in the direction of reducing $g_1(x)$ constraint function value and consequently towards the constrained optimum (A') as indicated.

Transformation methods (Penalty and barrier functions)

As indicated, transformation methods involve the transformation of the constrained problem to an unconstrained one which then allows the application of unconstrained optimization methods to the solution of the problem.

Penalty and barrier methods are amongst the earliest methods of dealing with non-linear optimization problems (Fletcher (1987)). Classically, the penalty method approach transforms the constrained objective function into a modified objective or 'merit' function through the addition of a penalty term. This term balances the objectives of reducing the objective function while still attempting to satisfy the constraints.

For the penalty approach, the merit function can be given by:-

$$\tilde{f}(\mathbf{x}) = f(\mathbf{x}) + \sum_{m=1}^{M} w_m \cdot p_m(\mathbf{x}) \tag{3.6}$$

where:-

$f(\mathbf{x})$ is the original objective function,
w_m is a non-negative weighting applied to the m^{th} penalty,
p_m is a penalty function

In general two distinct penalty methods exist:- 1) the interior, and 2) exterior methods.

The so-called interior penalties or barrier functions are mathematical functions which are active while the candidate vector is *within* the feasible region. As a result, the classic barrier function is

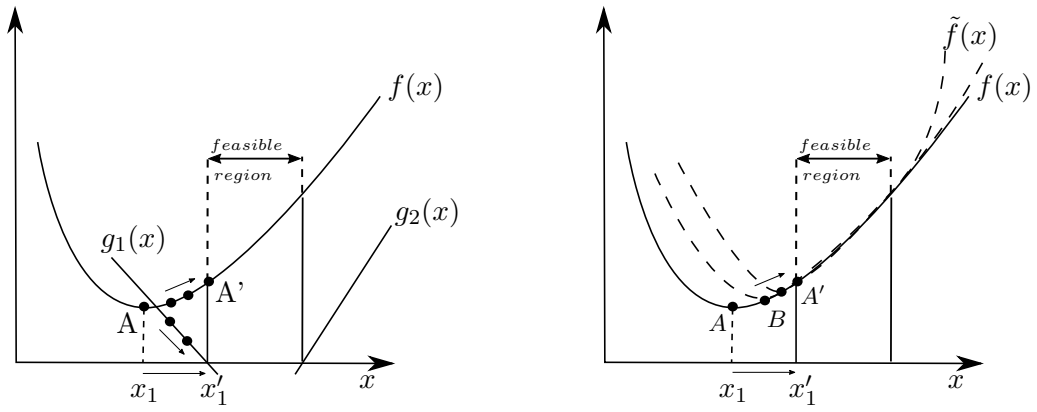

(a) Direct constraint handling

(b) Penalty constraint handling

Fig. 3.2: The direct and penalty (transformation) approaches for constraint handling

formulated so that the penalty is small in the feasible region but increasingly large near the constraint boundary. As indicated by Price et al. (2005), the biggest issue related to the use of barrier functions is that the method cannot be applied to candidate vectors which are already infeasible and therefore in this event, the input vector needs to be re-initialized within the feasible region for the algorithm to proceed.

In contrast, exterior penalty methods are methods in which the penalty term is active in the *infeasible* region, and therefore these methods effectively attempt to steer infeasible input vectors back into the feasible space rather than preventing them from becoming infeasible in the first instance. However, as indicated by Fig. 3.2b, since the exterior penalty function formulation is a weak formulation of the constrained problem, even exact optimization of the modified objective function ($\tilde{f}(\mathbf{x})$) can still result in a final solution which violates one or more of the original problem constraints (Verstraete et al. (2012)).

In the penalty approaches, the penalty weightings (w_m) dictate the bias of the transformed problem towards satisfying the original problem constraints as well as the stability of the problem. In general, while larger penalties give greater precedence to the constraint functions resulting in turn in better satisfaction of the constraints, very large penalties can result in the ill-conditioning of modified objective function $\tilde{f}(\mathbf{x})$, making the modified problem more difficult to handle numerically. In addition, as indicated by Price et al. (2005), over-penalising of the constraint functions can also result in premature convergence of the optimization routine while under-penalising may result in slow algorithm convergence.

Typical formulations for the interior (barrier and log barrier functions) and exterior (quadratic) penalty functions are given by Eqns. 3.8 and 3.9.

Barrier function

$$p_m(\mathbf{x}) = \frac{-1}{g_m(\mathbf{x})} \tag{3.7}$$

Log barrier function

$$p_m(\mathbf{x}) = -\ln\left(g_m(\mathbf{x})\right) \tag{3.8}$$

Quadratic penalty function

$$p_m(\mathbf{x}) = \begin{cases} g_m^2(\mathbf{x}) & \text{for } g_m(\mathbf{x}) > 0 \\ 0 & \text{otherwise} \end{cases} \tag{3.9}$$

where:-

$p_m(\mathbf{x})$ is the penalty term,
$\mathbf{x}$ is the parameter vector, *and*
g_m are the constraint functions

3.1.3 Boundary / variable constraints

Boundary constraints are used often in real-world optimizations as they typically relate to physical components or quantities which have natural bounds, for instance length or mass both of which must be non-negative (Price et al. (2005)). In general, there are two approaches to the implementation of boundary constraints:-

1. *resetting schemes* which modify out-of-bounds variables so that they are once again feasible, *and*
2. *penalty methods* which are similar to those discussed previously for dealing with the problem constraint functions $g_m(\mathbf{x})$ and which attempt to move candidate vectors which have become infeasible back towards the feasible region

Of the resetting schemes, among the most common are methods such as random re-initialisation and bounce-back schemes. Random re-initialisation is the least biased of the schemes since it replaces an infeasible candidate vector with one which is randomly selected from the feasible region. However, because this results in radical changes to the value of the parameter vector, this approach can easily disrupt the convergence of an algorithm to optima which lie near the variable boundary (Price et al. (2005)). The so-called bounce-back methods operate somewhat differently in that these methods attempt to replace out-of-bounds parameters with replacements which are *near* to the violated boundaries. One simple bounce-back strategy is simply to reset the out-of-bounds parameter to a value which is effectively the midpoint between the violated constraint and the previous candidate vector.

The penalty methods for boundary constraints will not be discussed in detail as these are virtually identical to those described above, with the exception that unlike the constraint penalty functions, it is possible to utilise the so-called *brick-wall* penalty as there is no requirement for the *parameter space* to remain smooth as is required by some of the gradient-based methods discussed above.

3.1.4 Multi-objective optimization (*MOO*)

Multi-objective optimization (MOO) is the process of selecting the input vector ($\mathbf{x}$) which results in the best value of more than one objective function ($f_i(\mathbf{x})$) that can be attained without adversely any

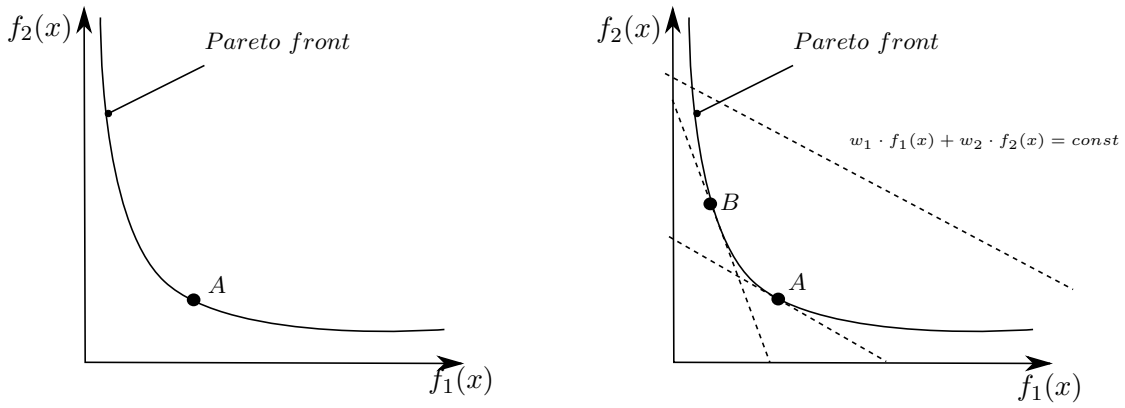

(a) Pareto front

(b) Pseudo objective function approach

Fig. 3.3: Pareto front and pseudo objective function approach for multi-objective optimization [Modified from Verstraete et al. (2012)]

one other objective function. Since in many cases, the target functions may have competing objectives, the values of these objective functions form a 'front' of equally optimal solutions, the so-called *Pareto front*. Candidate vectors which result in positions on the Pareto front are known as *non-dominated* or *Pareto optimal* solutions.

Since the complete characterisation of the Pareto front is practically impossible, in most cases the shape of the front is approximated by finding a a discrete set of Pareto optimal solutions from which the nature of the true front can be inferred (Price et al. (2005)).

One approach to the solution of so-called *MOO* problems, is the transformation of the multi-objective problem into a single-objective optimization (*SOO*) problem through the use of a so-called *pseudo* objective function comprising the weighted sum of the original individual objective function values. In this approach then, the optimization procedure becomes a search for a single non-dominated point on the Pareto front whose location is influenced by the magnitude of the weights assigned to each individual objective function.

Mathematically, this can be expressed by:-

$$F(\mathbf{x}) = \sum_{i=1}^{l} w_i \cdot f_i(\mathbf{x}) \tag{3.10}$$

where:

$F(\mathbf{x})$ is the pseudo objective,
f_i are the original *MOO* objective functions, *and*
w_i are weights assigned to each objective function.

Fig. 3.3a shows the Pareto front for hypothetical objective functions $f_1(x)$ and $f_2(x)$. At point A, no candidate solution vector can be found which produces a better objective function value for $f_1(x)$ which does not result in a worse value of $f_2(x)$ indicating that this point is Pareto optimal and lies

on the Pareto front. Similarly, Fig. 3.3b shows the same functions and Pareto front but also the line along which the sum of the objective functions multiplied by their respective weightings (w_1 & w_2) is constant. The optimal solution for the transformed MOO problem given by Eqn. 3.10 is then the point at which this line is tangent to the Pareto front (point A). Changes to the objective function weightings (for instance, an increase in w_2 and corresponding decrease in w_1) results in a change in the gradient of this line, shifting the location of the overall optimum point up the Pareto front to point B.

3.2 Objective functions used in endwall design

3.2.1 Early objective functions

In the early endwall contouring attempts of Harvey et al. (2000) & Hartland et al. (2000), the focus was placed largely on reducing the cross-passage static pressure gradient, in order to reduce the formation of the passage vortex and the reduction of the tangential deviations in flow angle at the blade exit. Following the first design iteration in Harvey et al's work, the authors, noted that while the underturning due to the secondary flows had been reduced, the delayed overturning of the endwall boundary layer resulted in less of this fluid being rolled up into the passage vortex *within* the blade passage and as a result, a more overturned boundary layer at the *exit* of the blade passage. Therefore, in the same investigation, the authors considered a second design which concentrated on correcting *only* the yaw angle deviations at the blade row exit, resulting in the generation of an additional downstream contour, the effect of which was to produce a counter-rotating corner vortex which counteracted the increased overturning of the endwall boundary layer flow.

The use of these quantities was as a direct result of the investigators' greater confidence in the numerical procedures used as part of the design system to predict these in comparison to the other quantities such as the total pressure loss. As was subsequently reported, upon testing the authors measured a significant reduction in the blade row net secondary loss of approximately $\sim 30\%$ at rotor exit and $\sim 34\%$ in 'mixed out' terms. In addition, the sought after reductions in the blade row exit whirl angle deviations were also realised.

While the measured reductions in secondary loss were not predicted by the CFD utilised during the design of the endwall, the investigators did note a positive correlation between the reductions in the coefficient of secondary kinetic energy (C_{ske}) (defined as the local SKE normalised by the upstream mainstream kinetic energy) and the reduction in secondary loss and this was hypothesised to be as a result of lower 'scraping' velocities on the endwall and blade suction surfaces by the passage vortex as well as a reduction in the mixing losses associated with the secondary flow features themselves (Hartland et al. (2000)). In addition and as discussed, the emphasis on correcting the yaw angle deviations led to the introduction of an additional counterrotating corner vortex, which although effectively reduced the mass-averaged flow angle deviations, was found to be an additional source of unwanted loss and therefore promoted some discussion on whether a better, lower loss design was achievable.

3.2.2 'Secondary kinetic energy'-based objective functions (C_{ske}, SKE, $SKEH$)

The shortcomings of the first generation endwall described above prompted the use of a different quantity for the design of the following endwalls. Based on the traditional correlation between the secondary kinetic energy and the secondary loss discussed above, a second generation endwall, in which the secondary kinetic energy rather than the yaw angle deviations of the blade row was minimized, was designed. While the original testing of the endwall suggested that, despite the larger reductions in secondary kinetic energy in comparison to that of Harvey et al. (2000), the second generation design was *less* effective in terms of reducing the secondary loss (Gregory-Smith et al. (2001)). Later measurements by Ingram et al. (2002) showed this was not the case when more accurate traverses with finer measurements of the wall adjacent fluid were conducted.

Encouraged by the successes of the work described above, Brennan et al. (2001) & Harvey et al. (2002) attempted to achieve a similar result in an engine representative and multistage rig respectively - only this time using a slightly more complex objective function (the scalar product of helicity (H) and the secondary kinetic energy (SKE)), where H was defined as the flux of streamwise vorticity. As indicated by the authors, the reason for the modification of the original quantity was to better focus the design routine on the vortical components of the flow and to reduce the influence of the blade potential flow on the design procedure. Based on the relationship between secondary kinetic energy and loss demonstrated by the Hartland et al. (2000), the authors estimated an increase in stage efficiency of +0.4% (corresponding to reductions in $SKEH$ of 30% & 17% for the NGV and rotor respectively), along with the expected reductions in yaw angle deviations.

As a likely result of the successes of the initial investigations discussed above, the majority of subsequent contoured endwall design attempts have followed a similar approach to that discussed above as evidenced by Table 2.2, although, in many cases, this included variations to actual definitions to the secondary kinetic energy itself. Examples of this are Germain et al. (2008), Schuepbach et al. (2008) & Schuepbach et al. (2009), who used a combination objective function including SKE which was based on the modified definition of Germain et al. (2007), while Poehler et al. (2010) used Brennan et al's $SKEH$ approach but with a modified definition of the primary flow direction.

The use of secondary kinetic energy has not been without its own shortcomings. Ingram et al. (2005) reported on a 'third generation' endwall designed for the Durham cascade, which, despite having been predicted to reduce the secondary kinetic energy for the flow (-15.1%), resulted in a $+9.2\%$ increase in loss over the annular case. Somewhat similarly, Vazquez and Fidalgo (2010) reported on the effects of Reynolds and Mach Number changes on the performance of non-axisymmetric endwalls and secondary flow in general, but found the endwalls designed for their investigation produced an additional loss core which negated any benefits of the contouring, despite measuring a reduction in the $SKEH$-based objective function they used.

3.2.3 'Loss'-based objective functions (C_{p0}, $C_{p0,rel}$)

In contrast to the above, some authors have elected to design contours more in line with the philosophy of increasing aerodynamic efficiency of a particular blade row *directly* by reducing the loss for that blade row. Perhaps most notably in this group was the work of Praisner et al. (2007), who used the coefficient of total pressure loss (C_{p0}) in conjunction with constraints which prevented the contouring

from increasing the flow overturning too significantly, to design non-axisymmetric endwall contours for a set of forward, aft and conventionally loaded, high lift, turbine aerofoils.

As indicated by the authors, confidence in the use of loss, rather than the quantities already discussed above, was fostered by the successful completion of a similar investigation by Nagel and Baier (2005) who managed to predict - *and confirm* - a reduction in the loss of a cascade blade row of $\sim 22\%$ as part of the three-dimensional optimization of a turbine vane (including non-axisymmetric endwall contouring) using a loss-based objective function. Further confidence in the approach was garnered by the authors as a result of their own predictions of the loss profiles of the aerofoils they intended to test, as well as by the results of Becz et al. (2004), who managed to predict reductions in loss broadly coherent with those measured experimentally for a test case in which leading edge fillets were applied to a cascade blade row. In conclusion, despite their predictions of the loss being accurate largely only in respect of the *trends* in the quantity measured during the experiment, the authors confirmed decreases in the secondary loss of $\sim 25\%$ & $\sim 10\%$ for the forward loaded and conventional high lift blades respectively. Experimental testing of the aft loaded blades was not completed at the time the work was published and so was not reported on by the authors.

3.2.4 'Compound' objective functions

In addition to the cases discussed above, a few investigators have utilised 'compound' objective functions, in which the target optimization metric was the weighted sum of two distinct quantities. As discussed in Section 3.1.4, non-dominated solutions to cost functions of this sort in fact represent a single point on the so-called Pareto front.

In Germain et al. (2008)'s investigation, a compound objective function comprised of a combination of both the secondary kinetic energy and total pressure loss was used. Bergh et al. (2012) used a similar approach, but in their optimization, constructed an objective function comprising of the weighted sum of the coefficient of secondary kinetic energy (C_{ske}) and yaw deviation (β_{dev}) from the rotor exit design angle.

MacPherson and Ingram (2010) & McIntosh et al. (2011) also all used a similar approach, basing their objective functions on the coefficient of secondary kinetic energy and yaw angle, although since the yaw angle contribution was only included in the cost function if the overall mass-averaged turning of the blade row was less than the annular case, this component more closely resembled a penalty term rather than a multiobjective optimization. The method of Hilfer et al. (2012) was the same, although, in addition to penalising underturning, endwall changes which resulted in reductions in the overall mass flow rate through their cascade were also penalised.

Finally, as discussed above, although Nagel and Baier (2005) predominantly considered a cost function designed to reduce the integral flux-averaged loss, the authors also included the maximum deviation and integrated difference between the distribution of the calculated outflow and secondary flow free outflow angles. Finally, a small contribution based on the secondary kinetic energy was also included.

3.2.5 Other quantities

Following the renewed interest in *non-axisymmetric* endwall contouring as a result of the work of Rose (1994), relatively few quantities aside from those discussed above, have been used for the design of three-dimensional endwall profiles. Despite this, in the interests of completeness, a brief overview of these attempts is given here.

Following the successful so-called 1^{st} & 2^{nd} generation designs produced at Durham University, Hartland and Gregory-Smith (2002) hypothesized that since it is in effect the curvature of the *blade* which induces the cross-passage pressure gradient, mirroring that shape on the endwall should assist in reducing that effect. With this in mind, the authors produced three alternative endwall designs based on the mean camberline of the blade row to be contoured with each design being the product of an axial component derived from the blade mean camberline, and a circumferential component, defined as a half cosine curve. The profiles were arranged to locate the maximum height of the convex endwall curvature adjacent to the pressure surface, and the minimum height adjacent to the suction surface. CFD was used to predict the performance of each design, and although no experimental validation was conducted, the most promising design was predicted to reduce the strength of the secondary flow[1] by 61% and the secondary loss, by $\sim 6\%$.

In an different approach, McIntosh et al. (2011) used Denton's (Denton (1993)) observations relating to the entropy generation in turbine boundary layers, to formulate an objective function in which the a measure of the entropy generation rate per unit surface area of the blade passage, $\dot{S}_a$, formed the basis of the cost function. Although the resulting so-called 'U^3' design[2] was predicted to reduce the overall entropy generation rate of the blade passage surfaces (since it neglected the contributions to the overall loss as a result of the 3-dimensional secondary flow structures (such as the passage vortex)), the *total* loss of the system was predicted to increase, and it was not clear whether such an approach would be beneficial.

Finally, Miyoshi and Higuchi (2013) used the concept of *enstrophy* (ϵ) - defined as the integral of the vorticity of the flow squared - as the basis of their objective function. As discussed by the authors, the principal motivation for the development of the enstrophy-based optimization criteria, was to avoid the reported difficulties associated with the direct prediction of loss by the numerical simulations. From the transport equation for enstrophy, the authors derived 2 terms:- the first related to the *diffusion* of the enstrophy (which was closely related to the generation or reduction of vorticity in the flow) in the vicinity of the endwall, and the second, related to the *production* of enstrophy in the passage (which was related to the streching of vortex filaments *within* the blade passage as is the case in the passage vortex). The two terms were derived specifically to target i) the formation of the horseshoe vortex which forms adjacent to the endwall in the vicinity of the blade leading edge, and ii) the development of the passage vortex found in the free stream. The contouring was performed for the *NGV* of a HP gas turbine stage, and at the conclusion of the procedure, a reduction in the total pressure loss coefficient of approximately $\sim 35\%$ was reported. This was in comparison to a predicted reduction of $\sim 27\%$.

[1] Determined by the reduction of the coefficient of secondary kinetic energy

[2] So named because the entropy generation rate within a boundary layer can be shown to be proportional to the cube of the velocity

3.2.6 Summary

Snedden et al. (2010a), in their observations on various quantities for the design of non-axisymmetric endwalls, indicated that non-axisymmetric endwall contouring was effective in increasing the efficiency of gas turbines through two main processes:-

- reducing the secondary kinetic energy (*i.e. reducing the strength of the secondary flow*) directly, *within* the blade row under consideration, *and*
- improving the flow quality and consistency (in terms of both pressure and flow angle profiles) entering the *downstream* blade row

Although the results of their investigation were mixed[3], the authors recommended that an objective function which formed the basis of any endwall optimization attempt, should be one which:-

1. promoted the achievement of the flow outlet design angles,
2. limited flow angle variability, *and*
3. used some C_{ske} or $SKEH$ formulation

As a potential extension, the authors also suggested that the inclusion of some measure of the tangential pressure variation at the rotor exit to reduce the impact of leakage flows, as well as the inclusion of some measure of the off-design performance of any contoured turbine may be warranted.

The design metrics used as the basis of the various objective functions tested in this investigation were selected to be broadly coherent with the suggestions given above. In particular, since improved aerodynamic efficiency is often the goal of any endwall profiling attempt, the *rotor total-total efficiency* and the *relative rotor total pressure loss* were selected as the basis of $\boldsymbol{\eta_{tt}-}$ and $\mathbf{C_{p0,rel}-based}$ objective functions respectively. In addition, the rotor exit coefficient of secondary kinetic energy, was selected as the basis of the $\mathbf{C_{ske}-based}$ objective function as this was by far one of the most common proxies in use within the literature for the secondary loss. Similarly, based on its usage by various groups at Rolls-Royce, as well as others such as Vazquez and Fidalgo (2010), a further target function (the $\mathbf{SKEH-based}$ objective function), based on the so-called secondary kinetic energy helicity proposed by Brennan et al. (2001), was formulated. Finally, in line with the discussions relating to the improvement of the downstream flow profiles above, $\times 2$ additional objective functions (the $\boldsymbol{\beta_{dev}-}$ & $\boldsymbol{\eta_{de}-based}$ objective functions), based on the flow deviation angle from design and the so-called design efficacy of Dunn, were also formulated.

In addition to the 'simple' objective functions discussed above, an additional pair of 'compound' target functions, based on the recommendations of Snedden et al. (2010a) discussed above, were also developed. In both cases, the weighted sum of a metric designed to reduce the secondary loss (the relative total pressure loss, $C_{p0,rel}$ and its most common proxy, C_{ske}) was combined with a term intended to promote an improvement in the flow quality at the exit of the rotor blade row. These objective functions were named the $\mathbf{C_{p0,rel,1}+\beta_{dev,0.7}}$ and $\mathbf{C_{ske,1}+\beta_{dev,0.7}}$ respectively. In both

[3] This was later found to be as a result of the averaging technique employed during the processing of the mass- and circumferentially-averaged results (Snedden (2015))

cases, the 'loss' term was given a weighting of unity, while the flow quality term, was given a lesser weighting of 0.7.

Finally, while the use of a single flow metric for each of the 'simple' objective functions described above resulted in the formulation of a single-objective optimization (i.e. *SOO*) problem, the use of the weighted sum approach for each of the 'compound' objective functions which - as described - was consistent with the *pseudo* objective function approach for multi-objective optimization, meant that a total of 8 single unconstrained *SOO* problems were solved for the the set of flow metrics studied in this investigation.

3.3 Definition of flow metrics

3.3.1 Rotor (total-total) efficiency (η_{tt})

As indicated by Snedden et al. (2010a), the ultimate aim of any endwall contouring endeavour is the maximization of efficiency. This is because (as discussed in Section 2.1.1 and illustrated by Figures 2.3 & 2.4), for the non-ideal gas turbine cycle (i.e. one in which component efficiencies are less than unity), the efficiencies of the individual elements of the cycle can have a large impact on the overall efficiency of the cycle. As indicated by Denton (1993), this is especially true in the context of gas turbine engines because the magnitude of the ratio of the *turbine : compressor* work in a typical engine is relatively large, and therefore even relatively small changes in the efficiency of either component result in a much larger proportional change in the net work output of the machine.

It is well-known that for turbomachines, the efficiency of a blade row may be quantified by either a *total-total* or *total-static* formulation, depending on whether the kinetic energy at the exit of the blade row is to be utilised by a downstream row or 'lost'. Although in this investigation, the downstream blade row was removed in order to allow for additional downstream measurements to be made, since this would not normally be the case, in this investigation, the *total-total* efficiency was considered the most appropriate formulation. The definition of the efficiency used in this investigation, was identical to that of Snedden (2011), which was in turn, the same as that used by authors such as Morphis (1993) & Kaiser (1996) for the same test rig.

Following Snedden (2011) and referring to Figure 3.4, the enthalpy at the rotor inlet (02) and outlet (03) can be expressed using individual quantities as:-

$$h_{02} = C_v T_2 + \frac{p_{02}}{\rho_2} \tag{3.11}$$

$$h_{03is} = C_v T_{3is} + \frac{p_{03is}}{\rho_{3is}} \tag{3.12}$$

Assuming flow is isothermal:-

$$T_2 = T_{3is} = T \tag{3.13}$$

and therefore:-

$$u_2 = u_{3is} = u \tag{3.14}$$

Also, if the flow is incompressible:-

$$\rho_2 = \rho_{3is} = \rho \tag{3.15}$$

the enthalpies can be re-expressed as:-

$$h_{02} = u + \frac{p_{02}}{\rho} \tag{3.16}$$

$$h_{03is} = u + \frac{p_{03is}}{\rho} \tag{3.17}$$

If the rotor total-total efficiency is given by:-

$$\eta_{tt} = \frac{w}{h_{02} - h_{03is}} \tag{3.18}$$

$$= \frac{w}{(h_{02} - h_{3is}) - {}^1\!/_2 V_{3is}^2} \tag{3.19}$$

then by substitution, Eqn. 3.19 can be expressed by:-

$$\eta_{tt} = \frac{\rho w}{p_{02} - p_{03is}} \tag{3.20}$$

$$= \frac{\rho w}{(p_{02} - p_{3is}) - {}^1\!/_2 V_{3is}^2} \tag{3.21}$$

Now, since from Figure 3.4:-

$$p_{3is} = p_3$$

$${}^1\!/_2 V_{3is}^2 \approx {}^1\!/_2 V_3^2$$

the final rotor exit (X3) total-total efficiency can be given by:-

$$\eta_{tt,X3} = \frac{\rho w}{(p_{02} - p_3) - {}^1\!/_2 V_3^2} \tag{3.22}$$

where:

w is the rotor work[4],

[4] Computed using $(\frac{2\pi N\tau}{60})$, where N is the rotor RPM and τ is the rotor torque

p_{02} & p_3 are the total and static pressures at the rotor inlet and outlet, *and* V_3 is the velocity magnitude at the rotor exit.

Similarly, the downstream ('mixed-out', X4) rotor total-total efficiency is given by:

$$\eta_{tt,X4} = \frac{\rho w}{(p_{02} - p_4) - {}^1\!/_2 V_4^2} \tag{3.23}$$

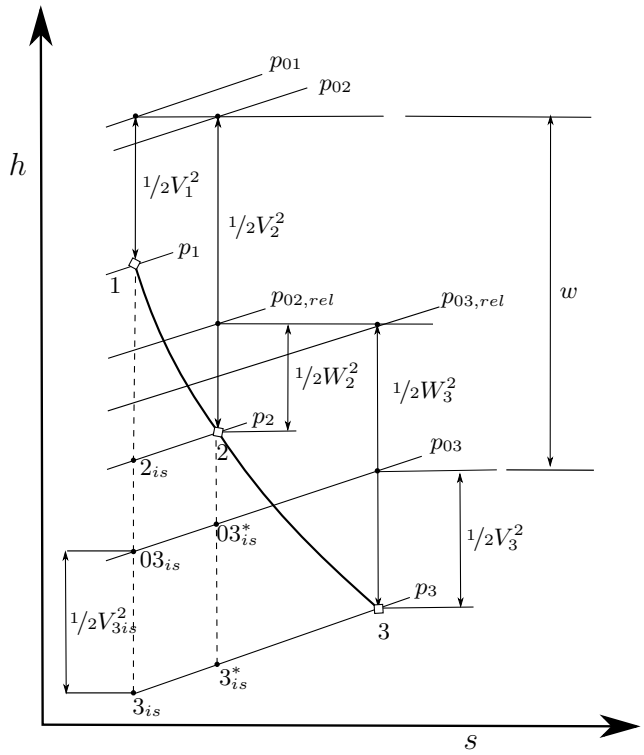

Fig. 3.4: $h-s$ diagram for the 1^{st} stage of the CSIR $1^1/_2$ stage turbine [Modified from Snedden (2011)]

3.3.2 Coefficient of secondary kinetic energy (C_{ske})

The definition of the secondary kinetic vectors, and thereafter energy followed closely after that of Ingram (2003), and was identical to that used by Snedden (2011) in his PhD thesis. Although there are a number of more exotic definitions of the quantity, the relatively simple definition used in this thesis was selected in order to maintain consistency with the previous endwall contouring work which has been undertaken in the $1^1/_2$ stage test turbine which was also the subject of this investigation. In addition, because of the similarity of the current definition to that of Ingram (2003), some degree of comparison could also then be made between previous studies undertaken in the Durham cascade[5].

[5] It should also be noted that the test turbine which was the subject of endwall contouring in *this* thesis, was also designed deliberately to use the same aerofoil profile as that of the Durham cascade at the hub of the rotor and 2^{nd} stator for the same reason

Figure 3.5 shows velocity vector ($\mathbf{v}$) at an arbitrary point in the blade passage in turbine coordinates. Since for the CSIR turbine, the pressure ratio through the stage is small (~ 1.04), the hub and shroud radii are constant, and therefore the streamwise ($\mathbf{v}_{str}$, not shown) and axial ($\mathbf{v}_{ax}$) velocities as well as the spanwise ($\mathbf{v}_{spn}$, not shown) and radial ($\mathbf{v}_{rad}$) velocities are the coincident.

If V, V_{b2b}, V_{rad} & V_{ups} are the corresponding magnitudes (i.e. $\|\mathbf{v}\|_2$) of $\mathbf{v}$, $\mathbf{v}_{b2b}$, $\mathbf{v}_{rad}$ & $\mathbf{v}_{ups}$ respectively, then the coefficient of secondary kinetic energy may be calculated from:-

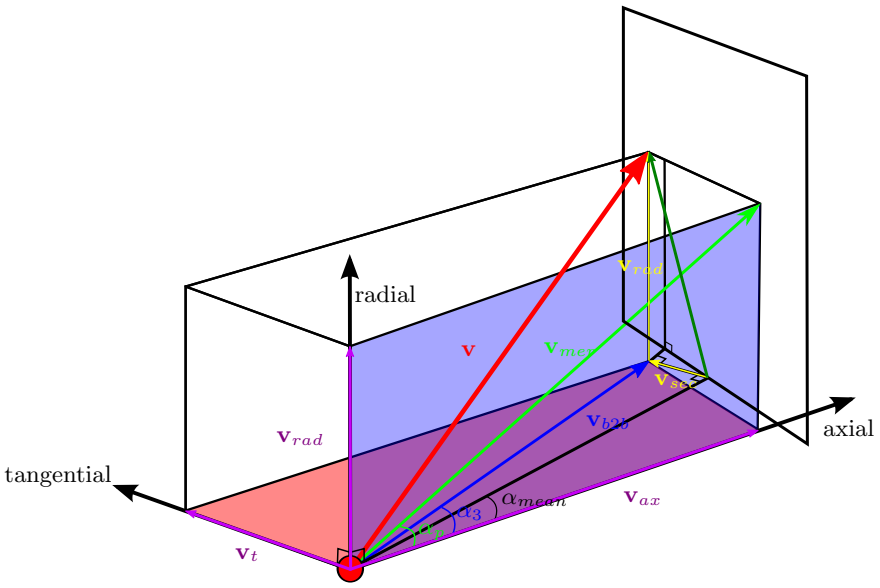

Fig. 3.5: Definition of secondary vectors used in this investigation

$$C_{ske} = \frac{V_{sec}^2 + V_{rad}^2}{V_{ups}^2} \tag{3.24}$$

where:-

V_{sec} is the secondary flow velocity magnitude, $V_{b2b}\sin(\alpha_3 - \alpha_{mean})$,
V_{b2b} is the blade-to-blade velocity magnitude,
V_{rad} is the radial velocity magnitude, $V\sin(\alpha_p)$,
V_{ups} is the inlet velocity magnitude,
α_p is the rotor exit flow pitch angle,
α_3 is the rotor exit flow angle, *and*
α_{mean} is the *mean* flow angle over the entire span

As indicated above, this definition of the coefficient of secondary kinetic energy was identical to that used by Snedden (2011) as well as Ingram (2003), except that in both this work as well as that of Snedden, the mean rotor exit flow angle (α_{mean}) rather than the midspan (α_{mid}) flow angle was used.

3.3.3 Coefficient of relative total pressure loss ($C_{p0,rel}$)

The coefficient of relative total pressure loss in this investigation was calculated using the definition of Moustapha et al. (1986). This was done, because, despite the fact that this method would be affected by the effects of rotation as discussed previously, this has been been used extensively by a number of researchers (including both Snedden (2011) & Dunn (2014) for their PhD work) and has become the *de facto* standard approach in this rig.

Following Moustapha et al. (1986), the relative total pressure loss coefficient for a rotor row may be defined as:-

$$C_{p0,rel} = \frac{p_{02rel} - p_{03rel}}{p_{03rel,mean} - p_{3,mean}} \tag{3.25}$$

where:-

$p_{02/03rel}$ are the *relative* total pressures at the rotor inlet & outlet respectively, *and* $p_{03rel,mean/3,mean}$ are the *mean* relative total and static pressures at rotor outlet.

3.3.4 Flow deviation angle (β_{dev})

The flow deviation angle from design (β_{dev}) at the rotor exit was calculated in a simple fashion, as the absolute value of difference between the predicted (β_3) and design (β_{design}) at each radial station at the rotor exit measurement plane (X3).

The rotor design flow angle (in degrees) was defined as a quadratic function of blade span (S) given by:-

$$\beta_{design}(S) = -0.0002S^2 + 0.0540S + 65.1700 \tag{3.26}$$

The flow deviation angle was then given at each radial station by:-

$$\beta_{dev}(S) = |\beta_3(S) - \beta_{design}(S)| \tag{3.27}$$

3.3.5 Secondary kinetic energy helicity ($SKEH$)

As discussed previously, the secondary kinetic energy helicity ($SKEH$) was a modification of the original C_{ske} criteria used by various authors for cascade tests, developed in order to better isolate the secondary flow in a real (i.e. 3-dimensional) turbine as well as remove the potential effects of the blade aerofoil on the secondary flow prediction.

The definition used in this investigation was identical to that used originally by Brennan et al. (2001) and Harvey et al. (2002), as well as later by Bagshaw et al. (2008a) except that the secondary kinetic energy was calculated using the same method as that used in Section 3.3.2 above.

$$SKEH = (SKE) \cdot H \tag{3.28}$$

where:-

SKE is the secondary kinetic energy, $V_{sec}^2 + V_{rad}^2$, *and*
H is the flow helicity $(\mathbf{v} \cdot (\nabla \times \mathbf{v}))$.

3.3.6 Design efficacy (η_{de})

Although it has not yet been used as part of any turbomachinery optimizations to date, the so-called design efficacy (η_{de}) was developed by Dunn (2014) as an alternative means to quantity the effects of unsteadiness on the effectiveness of non-axisymmetric endwall contouring instead of the traditional quantities such as efficiency and the total pressure loss coefficient. As discussed by the author, this was necessary because, for the test case with which he was concerned, it was noted that even relatively small errors of $\sim 0.1\%$ in the measurement of the rotor exit temperature, would translate to changes in the stage total-total efficiency of $\sim 10.8\%$. A similar error ($\sim 0.1\%$) in the corresponding total pressure measurements were shown to result in an error in the stage total-total efficiency of -2.7%.

The metric was based on the approach of Watanabe and Harada (1999) but was extended to include all three velocity components (i.e. the axial, radial and tangential components). As indicated by Dunn, the approach presupposes that the *design condition of any blade row can be considered to be the ideal flow condition for a given mass flow and provides the maximum work output for that mass flow rate*, and therefore, maximizing the design efficacy for a blade row would have the effect of maximizing the performance of that blade row, as well as providing an indication of how much of the blade exit flow conforms to the design flow condition.

Following Dunn (2014), the so-called *design efficacy* used in this investigation was computed using:-

$$\eta_{de} = \frac{\mathbf{v} \cdot \boldsymbol{\theta}_d}{V_{d,max}} \tag{3.29}$$

where:-

$$\boldsymbol{\theta}_d = \cos(\alpha_d) \cdot \mathbf{i} + \sin(\alpha_d) \cdot \mathbf{j} + \sin(\phi_d) \cdot \mathbf{k} \tag{3.30}$$

and:-

$\mathbf{v}$ is the actual velocity vector,
α_d is the design yaw angle,
ϕ_d is the design pitch angle[6],
$V_{d,max}$ is the maximum design velocity magnitude for the location under consideration, *and*
$\boldsymbol{\theta}_d$ is a unit vector as discussed below.

Since for the test case used in this study, the design pitch angle, ϕ_d was zero, $\boldsymbol{\theta}_d$ may be interpreted as a unit vector in the direction of the design flow vector $\mathbf{v}_d$ (Fig. 3.6). As such, the vector dot product

[6] Which was $\phi_d = 0$ for this turbine

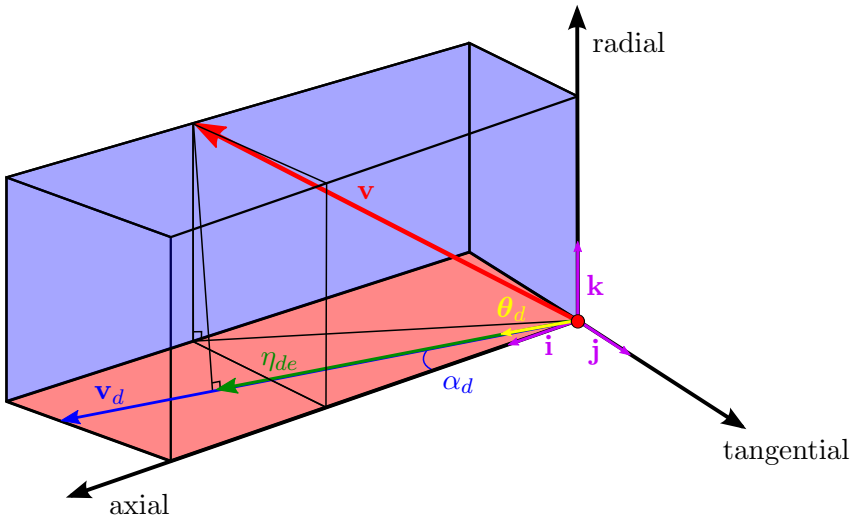

Fig. 3.6: Definition of design efficacy (η_{de}) used in this investigation (NB $\phi_d = 0$)

of $\boldsymbol{\theta}_d$ and the true velocity vector $\mathbf{v}$ (i.e. $\mathbf{v} \cdot \boldsymbol{\theta}_\mathbf{d}$) represents the projection of the actual velocity vector in the design flow direction for each point at which it is evaluated. As indicated by Eqn. 3.29, this quantity is then normalised by the maximum design velocity for that location. As a result, values of the design efficacy greater than unity (i.e $\eta_{de} > 1$) indicate locations at which the design conditions for the turbine are exceeded by the actual conditions, and vice versa.

3.4 Objective functions

The final form of each objective function used in the endwall designs are given below. The endwall design routine was formulated strictly as a minimization procedure, and therefore, in cases where the intention was to *maximize* the quantity at hand (i.e. η_{tt}), appropriate reformulation of the objective function was necessary. In most cases, the quantities which were used as the basis of the optimizations were multiplied by a magnification factor in order to ensure that all metrics were of the same order of magnitude, as well as an individual weighting factor which was used to apply increased or reduced emphasis on that particular metric.

Weightings for 'simple' objective functions (i.e. objective functions which comprised of only a single metric), were set to 1.

3.4.1 'Simple' objective functions

η_{tt}-based

$$Cost = 1 \times (1 - \eta_{tt}) \times 100 \tag{3.31}$$

C_{ske}-based

$$Cost = 1 \times (C_{ske}) \times 100 \tag{3.32}$$

$C_{p0,rel}$-based

$$Cost = 1 \times (C_{p0,rel}) \times 100 \tag{3.33}$$

β_{dev}-based

$$Cost = 1 \times (\beta_{dev}) \times 1 \tag{3.34}$$

$SKEH$-based

$$Cost = 1 \times (SKEH) \div 1 \times 10^5 \tag{3.35}$$

η_{de}-based

$$Cost = 1 \times (|1 - \eta_{de}|) \times 100 \tag{3.36}$$

3.4.2 'Compound' objective functions

$C_{ske,1} + \beta_{dev,0.7}$-based

$$Cost = 1 \times (C_{ske}) \times 100 + 0.7 \times (\beta_{dev}) \times 1 \tag{3.37}$$

$C_{p0,rel,1} + \beta_{dev,0.7}$-based

$$Cost = 1 \times (C_{p0,rel}) \times 100 + 0.7 \times (\beta_{dev}) \times 1 \tag{3.38}$$

4

Experimental test case

This Chapter discusses the test case and experimental equipment used to validate the numerical results predicted for the various endwall configurations designed and analysed in Chapters 5 & 6 respectively. In addition, the performance of the baseline (i.e. annular) case, the measurement procedure and data reduction method used to extract the fundamental quantities of the flow are presented.

4.1 Background

The test turbine used in this investigation was used formerly at the University of Natal for the study of tip gap leakage flows. In its original configuration, the rig was set up as an annular cascade with the option to rotate the casing, which allowed for the investigation of tip gap flows behind both stationary and 'rotating' blade rows (Morphis and Bindon (1988), Morphis (1993), Kaiser (1996)). Later, the rig was reconfigured as a $1^1/_2$ stage turbine and again used for the study of tip gap flows and their associated losses, although for these investigations, emphasis was placed on the effects of different tip clearance sizes and geometries on stage and downstream blade row performance (Morphis and Bindon (1994a,b)).

The rig, in its current form as a low speed, $1^1/_2$ stage experiment specifically for the study of secondary (i.e. endwall) flows, was developed as part of the PhD work of Snedden, who reported on the refurbishment as well as baseline performance of the apparatus in Snedden et al. (2007) and later on the on- and off-design performance of the turbine equipped with a set of 'generic' nonaxisymmetric endwall contours (Snedden et al. (2009a, 2010b), Snedden (2011)). As part of its recommissioning, the rig was equipped with three new blade sets, one for each of the turbine's blade rows. As part of the re-blading, the rotor and 2^{nd} stator rows were designed specifically to use the same blade profile at the hub as that used in the so-called Durham cascade, which is a well known turbomachinery test case and one which has been used extensively for the investigation of secondary flows. This was done in part, because this profile is well-known for its production of strong secondary flows (Hartland and Gregory-Smith (2002)), but also to allow for the interchange of endwall contours designed for the cascade to be implemented in the turbine (and vice versa) relatively easily.

Since its recommissioning, the turbine has been the subject of a number of endwall contouring and secondary flow related investigations, including in addition to the original work of Snedden (Snedden et al. (2009a, 2010b), Snedden (2011)) discussed above, the PhD study of Dunn (Dunn (2014)), in

which the effects of upstream wakes and flow unsteadiness on endwall contouring was investigated, as well as the work of Bergh et al. (2012), in which a first attempt at producing optimized endwalls for the rotor row were designed using a genetic algorithm coupled directly to the CFD procedure.

4.2 Turbine overview

Table 4.1 and Fig. 4.1 below provide a summary of the overall turbine design in its secondary flow research configuration with special emphasis on the details of its redesigned blading and an overview of the rig respectively. At the hub, the rotor blades have a relatively large turning angle ($\sim 111°$) and therefore as indicated above, generate strong secondary flows. In addition, the rotor aspect ratio is relatively low (~ 1.44) meaning that the tip gap and endwall flows occupy a comparatively large portion of the flow passage.

Although the rig has the ability to be configured as a 1½ stage experiment, as discussed above in this investigation the downstream stator row was removed and replaced with a blank hub to allow for 'mixed-out' measurements (X4) to be made in addition to those conducted immediately downstream of the rotor (X3). Fig. 4.2 shows a cross-sectional view of the rig configuration used in this investigation, including the NGV, rotor and blank hub used in place of the S2 blade row.

Table 4.1: Turbine design specifications

Inlet		
Axial velocity		21.38 m/s
Rotational speed		2300 RPM
NGV		
No of blades		30
Inlet angle	Hub	0°
	Tip	0°
Outlet angle	Hub	68.26°
	Tip	61.20°
Rotor		
No of blades		20
Inlet angle	Hub	42.75°
	Tip	−23.98°
Outlet angle	Hub	−68.00°
	Tip	−71.15°
Stage		
Power		3.42 kW
Pressure ratio		1.0393
Exit Reynolds Number		127,500
2nd Stator		
Not included		

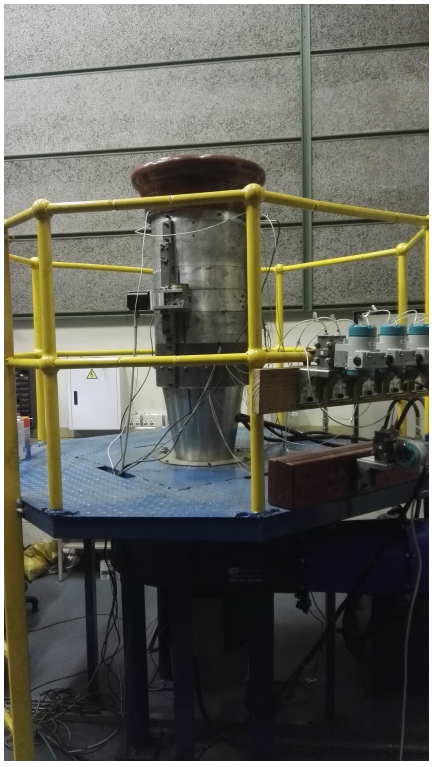

Fig. 4.1: The CSIR 1½ stage turbine

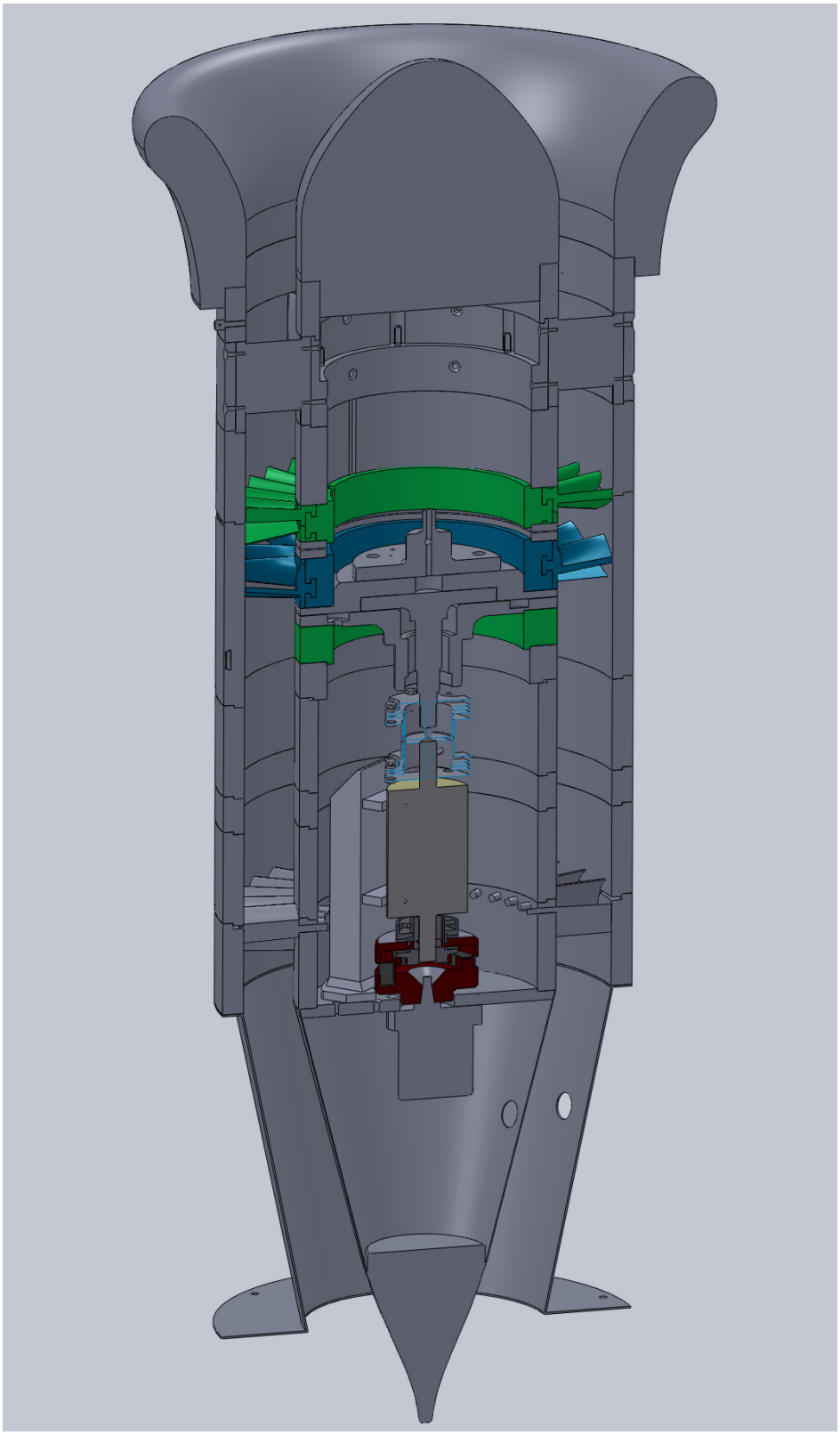

Fig. 4.2: Cross-sectional view of the CSIR 1½ stage turbine in its 1 stage configuration, showing the NGV (green) and rotor (blue) blade rows. The blank hub used in place of the 2^{nd} stator is visible (also green) aft of the rotor.

4.3 Principle of operation

The turbine is operated by drawing atmospheric air through the rig using a blower located downstream of the test section. Both the rotor RPM and inlet flow velocity are able to be controlled independently of one another, effectively allowing the flow (ϕ) and loading (ψ) coefficients of the experiment to be set explicitly for each case. The rotor RPM is set by absorbing the rotor power in a hydraulic pump fitted with two (coarse and fine) variable flow rate valves, while the inlet flow velocity is controlled by adjusting the speed of the blower using a frequency controlled VSD[1] unit.

The flow velocity is calculated using the dynamic pressure and air density at the turbine inlet - the former measured using a combination of the total inlet pressure (measured using a Kiel total pressure probe) and the inlet static pressure (measured using 3 equi-spaced static pressure ports (0.5mm diameter) located immediately downstream of the inlet bellmouth), and the latter being calculated using the ideal gas law and the inlet air temperature, measured using a further 3 RTD temperature probes located between each static pressure port.

In its current configuration, the rig can attain a maximum rotor speed of 3000 RPM and an inlet velocity of approximately $\sim 30\ ^{m}/_{s}$, which corresponds to a mass flow of approximately $\sim 2\ ^{kg}/_{s}$. The test conditions used for the current investigation are discussed in Section 4.6 below.

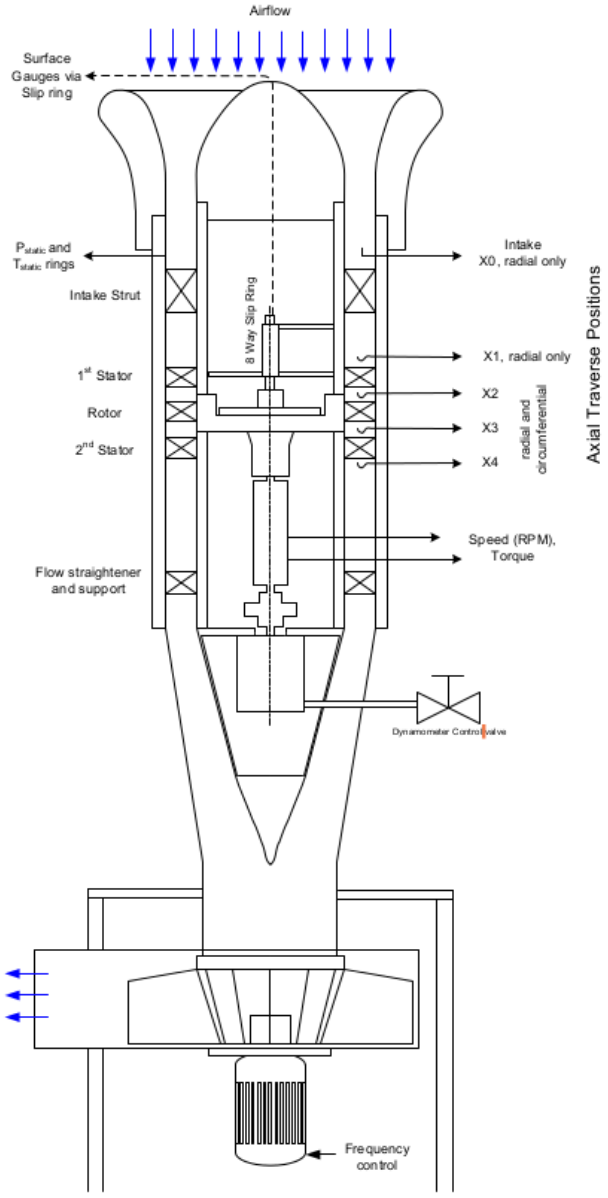

Fig. 4.3: Schematic of CSIR 1½ stage turbine [Reproduced from Snedden (2011)]

[1] Variable Speed Drive

4.4 Instrumentation

The turbine can be configured to allow for a wide variety of measurements including inlet turbulence, steady and unsteady flow measurements forward and aft of the NGV, rotor and 2^{nd} stators using 3h- & 5h-hole pressure and hot-wire probes respectively, as well as surface film investigations for both stationary and rotating blade rows via an internal 8-way slip ring device. In this investigation, measurements were limited to steady-state 5-hole pressure probe measurements and so Table 4.2 provides details of the primary and secondary instrumentation required for these measurements only.

Table 4.2: Steady-state flow measurement instrumentation [Modified from Snedden (2011)]

Measurement	**Instrument**	**Uncertainty**
Primary		
Torque Speed	Himmelstein MCRT 28002T(5-2)CNA-G + Model 721 Mechanical Power Instrument	±0.03Nm 2 RPM
Pressure (barometric)	×1 Siemens Sitrans P 7MF4233-1FA10-1AB6-Z A02+B11	0.075% of full scale
Pressure (differential)	×6 Siemens Sitrans P 7MF4433-1CA02-1AB6-Z A02+B11	0.075% of full scale
Temperature	×3 PT1000 RTD's	±0.05°C
Secondary		
Steady-state flow mapping	Aeroprobe 5-hole Drilled Elbow Probe Model No P-C05D01E-SX-S-305-1180 (⌀1.59mm, 3mm tip length)	1% or $\pm 1^{m}/_{s}$ in average velocity Better than 1° in angle
Inlet turbulence	TSI 1211-20 single component film	0.77% of mean flow velocity
Tangential traverse	Custom designed cable operated system used to rotate the outer casing of the rig	Better than 0.01%
Radial & yaw traverse s	Custom designed two component traverse driven by Cool Muscle® actuators	0.01mm (radial) 0.1° (yaw)

4.4.1 Pressure probe

The probe used in this investigation was a drilled elbow 5-hole aerodynamic probe (Fig. 4.4) with a tip diameter of 1.59mm and a cone angle of 60°. This represented a change from the probe type used in previous investigations conducted in the rig, but was necessitated as a result of leaks being detected in the original cobra-style probe and an inability to source an exact replacement.

Of the available substitutes, the drilled elbow probe offers a geometry most similar to the functionality of the original with the probe head being located as close as possible to its axis of rotation (+0.62 mm) and one therefore which in turn minimizes the amount by which the head translates when it is yawed.

As with its predecessor, the drilled elbow probe provides maximum accuracy whilst resulting in minimum blockage due to its small head diameter as well as a relatively large flow cone angle of receptivity of 60° as a result of its 5-hole configuration, although, because of its increased secondary

shaft length of 50.24mm, the maximum blockage (i.e. when fully extended) of the probe is reduced to approximately $\sim 0.19\%$ of the total flow area.

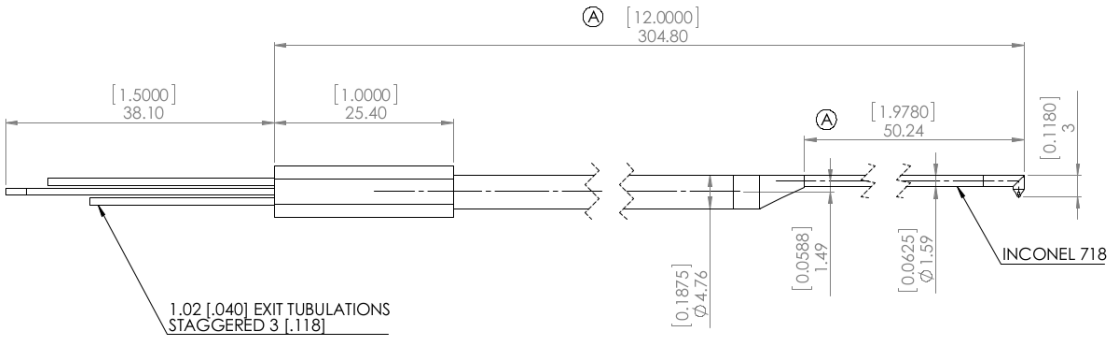

Fig. 4.4: Aeroprobe drilled elbow aerodynamic probe used for steady-state flow measurements

4.4.2 Probe calibration

The probe was calibrated using a special test stand, and the method of Snedden (2011). Briefly, the pitch and yaw axis characteristics were characterised over the entire specified cone of receptivity (i.e. $-30°$ to $+30°$) in 5° increments (including additional points at $\pm 2.5°$) for the pitch direction, and in 3° increments (including additional points at $\pm 1°$ & $\pm 2°$) in the yaw direction, giving a total of 15 points in the pitch direction and 25 points in the yaw direction, and a total of 375 points for the entire calibration procedure.

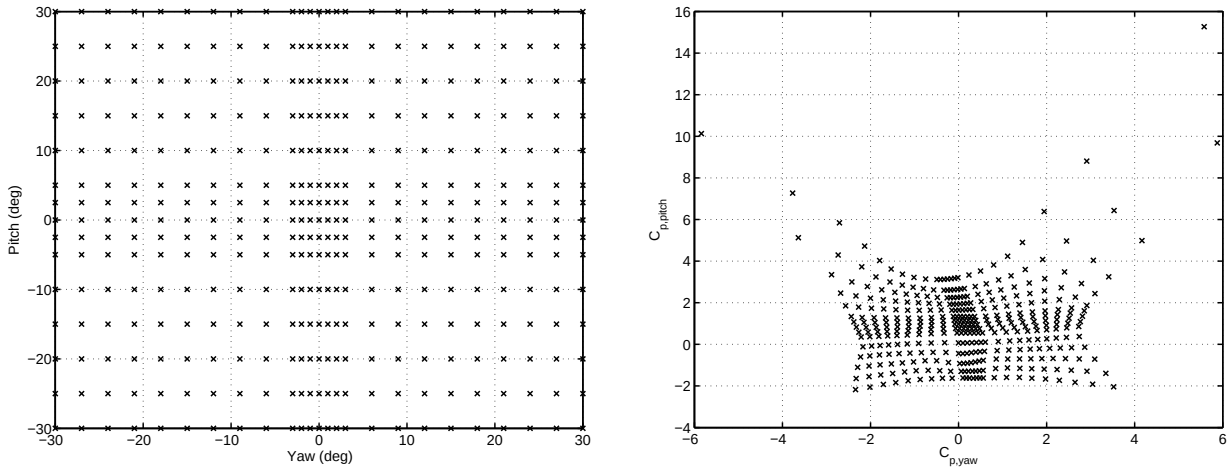

(a) Calibration traverse grid

(b) $C_{p,pitch}$ vs $C_{p,yaw}$ calibration map

Fig. 4.5: Full calibration traverse grid and map for the 5-hole probe

4.4.3 Traverse planes

Several access points located in the rig casing are available through which flow traverses can be conducted.

In addition to the rotor exit (X3) and downstream (X4) 'mixed-out' positions, access ports are also located in the intake region of the rig, ahead of the intake support struts (X0) as well as immediately upstream and downstream of the *NGV* blade row (X1 & X2). The *NGV* inlet & exit, as well as the rotor exit and 'mixed-out' measurement locations are shown in Fig. 4.6 as well as their approximate locations relative to the trailing edges of the *NGV* and rotor blade rows.

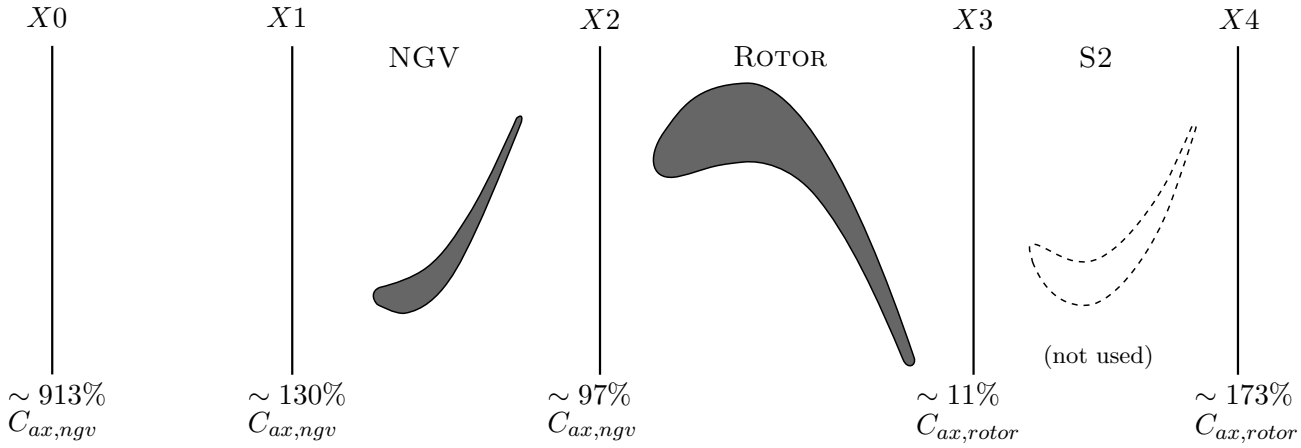

Fig. 4.6: Turbine inlet (X0), *NGV* inlet (X1) & exit (X2), rotor exit (X3) and downstream (X4) 'mixed-out' measurement planes in terms of the *NGV* & rotor axial chords ($C_{ax,ngv}$ & $C_{ax,rotor}$), measured from the trailing edge of the *NGV* and rotor (*N.B. not to scale*)

Because only the casing above the *NGV* exit, rotor and 2^{nd} stator was able to be rotated, only traverses conducted using the X2, X3 & X4 access ports included tangential points in their traverse map, with the remaining traverses (X0 & X1) consisting of radial measurements only.

4.4.4 Traverse grids

Behind the stationary blade rows (X2 & X4), the traverse grid consists of 990 points arranged in ×33 radial lines, with each consisting of 30 points 0.5° apart. Each stationary blade has a pitch of 12° and therefore the X2 & X4 measurement grids cover a region equivalent to approximately ×1.375 pitches each.

Behind the rotor (X3), the traverses consist of 3 radial lines spaced 9° apart, each consisting of 30 points (and therefore 90 points in total), covering a total of 1.5 pitches.

Figs. 4.10 shows the measurement grids used for measurements taken at the X2/X4 & X3 measurement planes as well the pitch length for the NGV/S2 and rotor blade rows respectively.

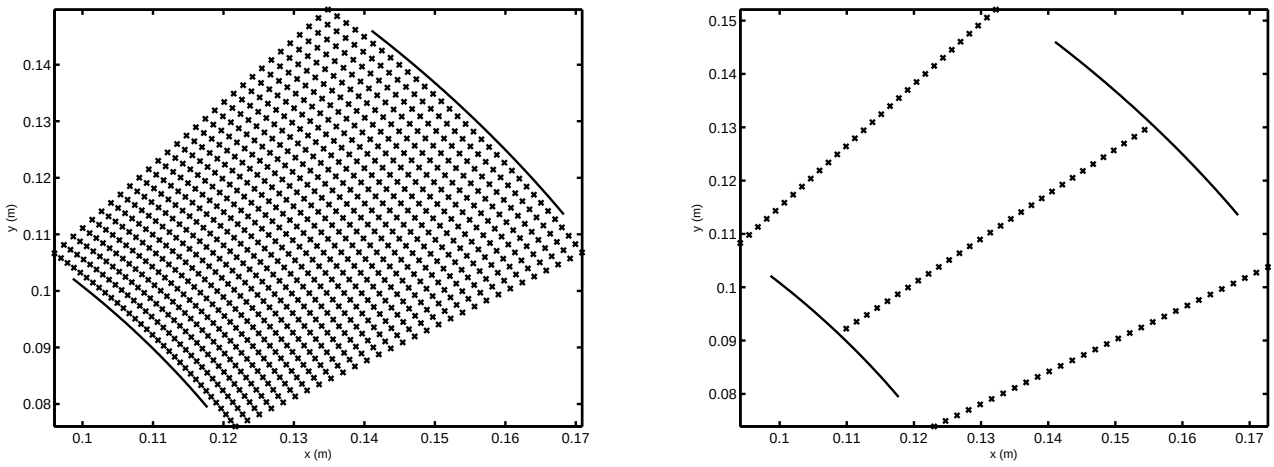

(a) X2

(b) X3 / X4

Fig. 4.7: Measurement grids for X2, X3 and X4 'mixed-out' measurement planes

Since the S2 blade row was not used in this investigation, the traverses used to capture the 'mixed-out' values at the X4 measurement plane, were conducted using the 90-point X3 traverse grid. This was deemed to be acceptable since, in the absence of the S2 blade row, the differences between the full 990-point and 90-point traverses are small. This also allowed considerable time-savings to be realised as each full 990-point traverse takes approximately $\sim$ 10hrs to complete in comparison to the 90-point traverses, which require approximately $\sim$ 1.5hrs to complete.

4.5 Blades

Each of the contoured rotor blade sets was manufactured from Fine Polyamide PA2200 using direct laser sintering with the same aerofoil designs as those used by Snedden (2011). The technique is able to provide finished articles with a high degree of accuracy and a final manufacturing tolerance of approximately ±0.2mm, which was deemed to be sufficiently small to be suitable for this study.

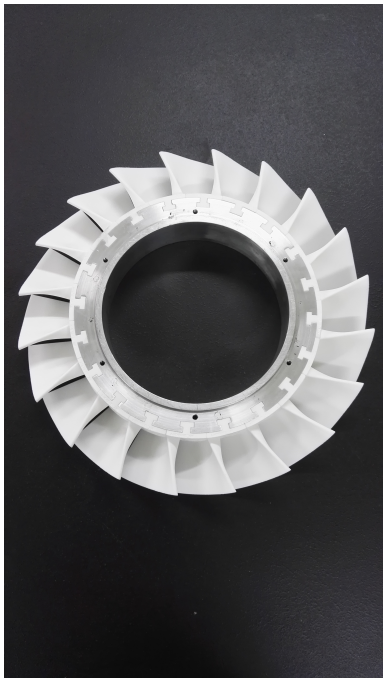

(a) Rotor attachment ring with installed blades

(b) Rotor disc and retaining ring

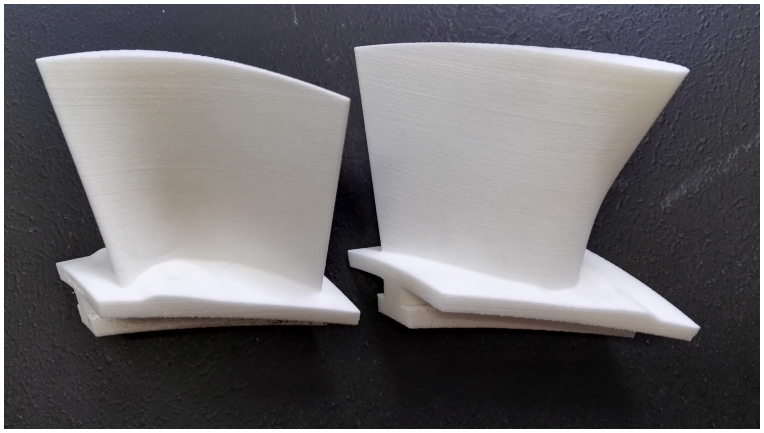

(c) Manufactured blades - pressure and suction surfaces (η_{tt}-based design)

Fig. 4.8: a) Rotor attachment ring (with installed blades), b) rotor disc and forward retaining ring and c) a pair of rotor blades prior to installation in the attachment ring

The blades make use of a T-slot attachment mechanism to locate them within the rotor attachment ring, and are then 'locked' into position using the rotor disc and a retaining ring, which are secured to the aft and forward faces of the blade attachment ring respectively. Prior to locking the blades into position, a flat block was used to ensure that the forward face of each blade's platform as well as T-slot/fir tree was flush with the forward face of the attachment ring, and therefore equivalently axially located within the attachment ring.

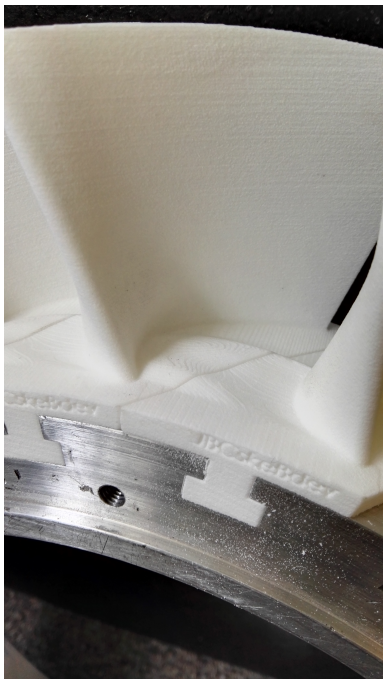

Fig. 4.9: Detail of contoured rotor endwall ready for installation into the turbine.

4.6 Test conditions

Both the annular and contoured rotor designs tested in this investigation were characterised at the aerodynamic design point of the baseline turbine. Table 4.3 shows the corresponding rotor wheel speed, inlet velocity and rotor incidence angle while the associated degree of reaction (Λ), flow (ϕ) and loading (ψ) coefficients at the midspan and hub are shown in Table 4.4.

Table 4.3: Test conditions

Property	**Value**
Inlet velocity	21.38 m/s
Rotor speed	2300 RPM
Incidence	0°

As indicated by Table 4.3 and 4.4, the test conditions correspond to a rotor incidence angle of approximately 0° and a mass flow rate for a standard day in Pretoria, South Africa, of approximately

~ 1.43 $^{kg}/_{s}$ through the turbine as well as midspan and hub flow coefficients (degree of reaction (Λ), flow (ϕ) and loading (ψ) coefficients) of 0.60, 0.52 & 0.70 and 0.38, 0.63 & 1.08 respectively.

Table 4.4: Degree of reaction (Λ), flow (ϕ) and blade loading (ψ) coefficients at test conditions

Property		**Value**
Degree of reaction (Λ)	hub	0.38
	midspan	0.60
Flow coefficient (ϕ)	hub	0.63
	midspan	0.52
Loading coefficient (ψ)	hub	1.08
	midspan	0.70

While the nominal (midspan) loading coefficient is lower than that which can be expected from a typical HP turbine, this is symptomatic of the 'model' nature of the rig and the lower associated wheel speeds and stage / overall pressure ratio. Despite this, in the secondary flow (i.e. hub) region the loading is higher and therefore more representative of the conditions likely to be used in a commercial engine design.

4.7 Repeatability

Figs. 4.10a - 4.10d show the rotor exit (X3) pitch, relative velocity and flow angles and coefficient of secondary kinetic energy for three independent measurement runs for the baseline (annular) case, and give an indication of the repeatability of the experimental measurements. The largest differences between the measurements occur in regions of high shear flow and are most noticeable in the vicinity of the tip vortex, although smaller deviations are also detectable in the secondary flow region.

Although the rig was not broken down between each measurement, the repeat measurements were conducted on different days and the rig was allowed to settle between each measurement. In addition, the probe calibration used for the measurements above was different to that used for the characterisation of the endwalls produced during this investigation, and so show some differences to those presented in Chapter 7.

4.8 Pressure probe measurements

4.8.1 Setup

The pneumatic connections used in conjunction with the 5-hole probe were identical to those used by Snedden (2011), which were in turn derived from Kaiser (1996) who developed them to minimize measurement uncertainty associated with the system. As discussed by Snedden (2011), this approach attempts to measure the smallest possible differentials for each transducer, thereby allowing the ranges on each instrument to be set to as small a value as possible, which in turn allows for high accuracy readings.

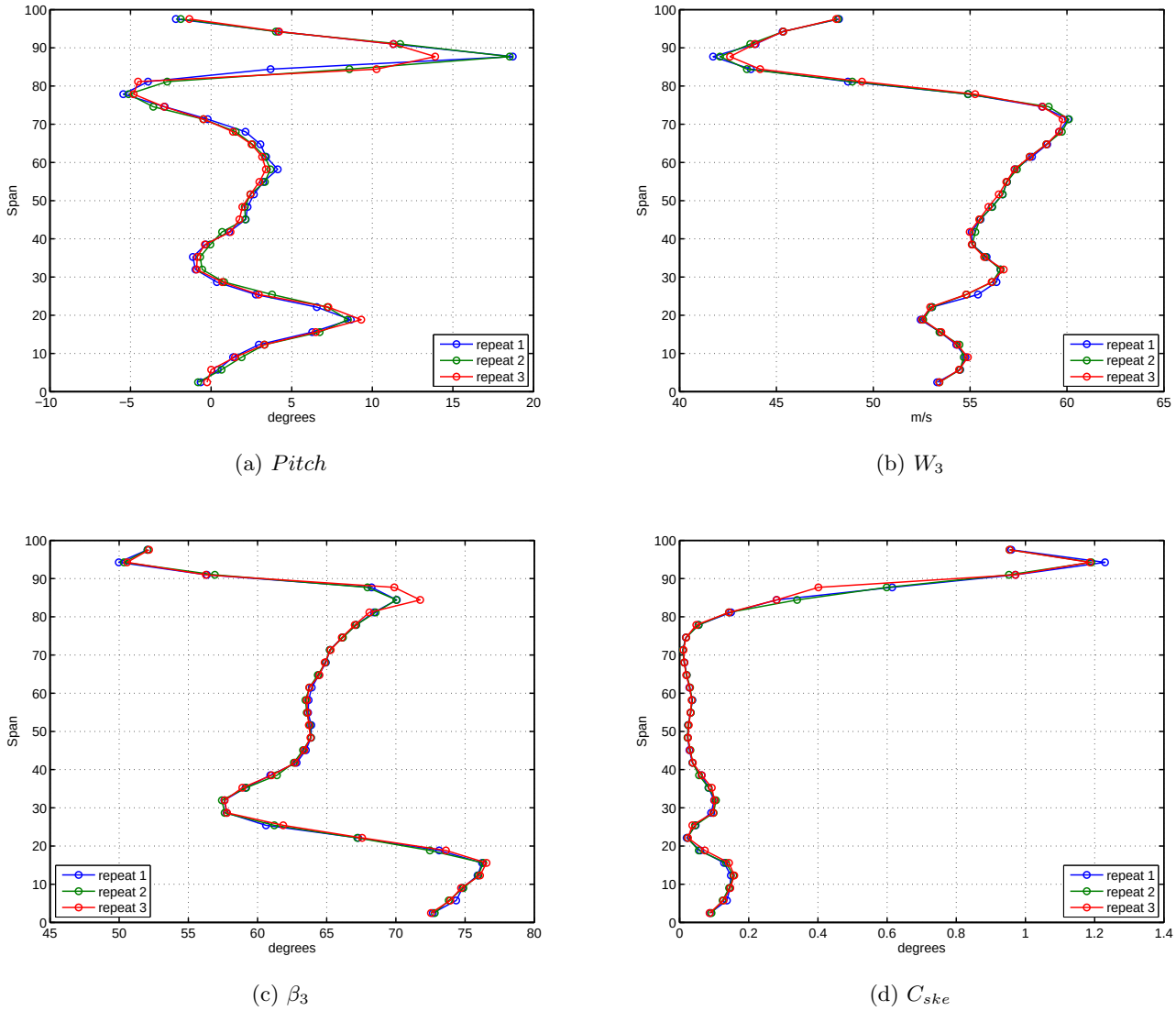

(a) *Pitch*

(b) W_3

(c) β_3

(d) C_{ske}

Fig. 4.10: Rotor exit (X3) pitch, relative velocity (W_3) & angle (β_3) and C_{ske} measurements

In this investigation however, an additional transducer (DP6) was used to connect the *left* yaw port of the probe to the upstream total pressure, allowing the actual left and right yaw pressures (P_{left} & P_{right}) to be extracted. A schematic of the pneumatic connections, as well as the measurement range set for each transducer are shown in Fig. 4.11.

The $C_{p,pitch}$, $C_{p,yaw}$, $C_{p,total}$ and $C_{p,static}$ coefficients are defined similarly to those of Snedden (2011), although as a result of the addition of the DP6 pressure transducer, P_{ave} was now defined using all of the available side ports (pitch and yaw) and not only the pitch ports as was previously the case.

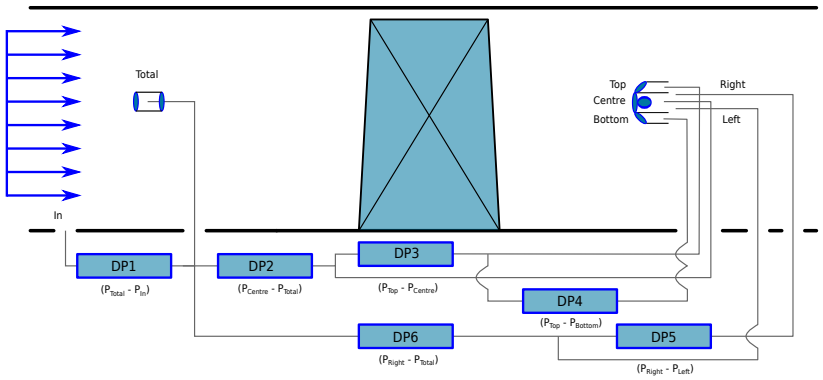

Transducer	Range
DP1	$0 \longleftrightarrow 0.5$ kPa
DP2	$0 \longleftrightarrow 4$ kPa
DP3	$-4 \longleftrightarrow 4$ kPa
DP4	$-4 \longleftrightarrow 4$ kPa
DP5	$-4 \longleftrightarrow 4$ kPa
DP6	$-5 \longleftrightarrow 5$ kPa

Fig. 4.11: Pneumatic connections and differential pressure transducer settings used for the 5-hole probe measurements [Modified from Kaiser (1996)]

$$C_{p,yaw} = \frac{P_{left} - P_{right}}{P_{centre} - P_{ave}} \tag{4.1}$$

$$C_{p,pitch} = \frac{P_{bottom} - P_{top}}{P_{centre} - P_{ave}} \tag{4.2}$$

$$C_{p,total} = \frac{P_{centre} - P_{abs}}{P_{centre} - P_{ave}} \tag{4.3}$$

$$C_{p,static} = \frac{P_{ave} - P_{static}}{P_{centre} - P_{ave}} \tag{4.4}$$

where:-

$$P_{centre} = P_{total} - DP_2 \tag{4.5}$$

$$P_{bottom} = P_{top} - DP_4 \tag{4.6}$$

$$P_{right} = P_{total} + DP_6 \tag{4.7}$$

$$P_{static} = P_{abs} - (P_{total} - P_{in}) \tag{4.8}$$

$$P_{top} = P_{centre} - DP_3 \tag{4.9}$$

$$P_{left} = P_{right} - DP_5 \tag{4.10}$$

$$P_{ave} = \frac{P_{left} + P_{right} + P_{bottom} + P_{top}}{4} \tag{4.11}$$

$$P_{abs} = \text{barometric pressure} \tag{4.12}$$

4.8.2 Data extraction

Pitch, yaw and velocity

Extraction of the actual velocity, pitch and yaw angles at each traverse point was facilitated by custom code written by Dunn (2014) which was based on the method of Ingram and Gregory-Smith (2005).

This was the same approach as that used by Snedden (2011), although, as discussed above, in this work the probe average pressure (P_{ave}) was calculated using all four probe side ports, rather than the pitch ports only.

Briefly, the method works by calculating the pitch and yaw coefficients and locating the 'box' on the calibration map within which this point lies. Bilinear interpolation is then used to calculate actual values of the pitch and yaw angles as well as the total and static pressure ($C_{p,static}$, $C_{p,total}$) coefficients. From the values of $C_{p,static}$ & $C_{p,total}$, the actual values of the total and static pressures can be calculated, from which the velocity at the probe head can be calculated using:-

$$V_{probe} = \sqrt{\frac{2}{\rho} \times (P_{total} - P_{static})} \tag{4.13}$$

Standard day conditions

In order to compensate for differences in atmospheric conditions between different days during the testing, all values were multiplied by the ratio of the rig inlet dynamic pressure (P_{dyn}) on the day of testing to the inlet dynamic pressure on the Standard Day ($P_{dyn,std}$).

Experimental vs. Numerical data

The data extraction techniques described above were applied to the 5-hole pressure probe data only as a result of the primitive flow variables for the numerical simulations being available by default at the centre of every grid point of the computational meshes used as part of the numerical simulations described in Chapter 6.

4.9 Calculation method

4.9.1 Overview

Once the primitive flow variables had been extracted from the experimental data using the method described above, additional processing and averaging techniques could be applied in order to produce the final flow quantities required for the objective function calculations and plotting requirements.

The methods used were applied identically to the above-mentioned numerical (i.e. computational fluid dynamics (CFD)) data as well as the experimental data in order to maintain consistency between the two sets of results. However, since the grid centers for the numerical meshes used in the CFD simulations did not necessarily coincide with locations of the traverse measurement points, a small amount of preprocessing was required in order to make this data available at the same grid locations as those used in the experimental measurements.

Although the methods were identical, partly because of the formats in which the data sets were available, as well as the fact that the numerical data was processed as part of the endwall design routine, the experimental and numerical calculation routines were implemented using a Microsoft Excel® spreadsheet and the MATLAB® programming language respectively.

4.9.2 Method

Once the velocity, static & total pressures, pitch and yaw angles of the flow were known, the secondary quantities used in calculation of the endwall objective functions, as well as the analysis of the flow could be undertaken.

The calculation methods used for each of the secondary quantities used in this thesis are given in Chapter 3, as well as the composition of the objective functions in which they were used. As indicated above, both the CFD and experimental data were processed identically, using the definitions provided in Chapter 3, and since their definitions are given there, no more time is spent discussing these calculations in this section. What is discussed below are the approaches used for the calculation of the mass-averages which were used to characterise spanwise changes in quantities (circumferential mass-averaging) for analysis and plotting purposes as well as the the approach which was used to provide single values for the objective function calculations.

Mass-averaging

In order to produce more meaningful results for the flow field at each measurement plane, the 2-dimensional data at each traverse plane must be mass-averaged either completely over each traverse grid to produce total mass-averaged results or partially in the circumferential direction to produce radial profiles for each flow quantity.

The circumferential and total mass-averages for any flow quantity were therefore calculated using Eqns. 4.14 & 4.15 respectively:-

Circumferential mass-average:

$$\overline{Y}_j = \frac{\sum_i Y_{ij} C_{\dot{m},ij}}{\sum_i C_{\dot{m},ij}} \tag{4.14}$$

Total mass-average:

$$\overline{Y} = \frac{\sum_i \sum_j Y_{ij} C_{\dot{m},ij}}{\sum_i \sum_j C_{\dot{m},ij}} \tag{4.15}$$

where

Y is any quantity extracted from the traverse data or calculated at a grid point, *and*
$C_{\dot{m},ij}$ is a mass flow coefficient given by Eqn. 4.16 below

In the equations above, the mass flow coefficient ($C_{\dot{m},ij}$) is used to remove the variation in atmospheric conditions from the measurements, and is given by:-

$$C_{\dot{m},ij} = \frac{\dot{m}_{ij}}{\dot{m}_{ref,ij}} \tag{4.16}$$

where

$$\dot{m}_{ref,ij} = \rho_{ref,ij} \cdot A_{ij} \cdot V_{ref,ij} \tag{4.17}$$

With reference to Eqn. 4.17 above:-

1. $\dot{m}_{ref,ij}$ corresponds to the time the $(i,j)^{th}$ data point measurement was taken,
2. A_{ij} corresponds to an area extending halfway between adjacent measurement points, and all the way to the wall at solid boundaries,
3. The velocity at solid boundaries is assumed to be zero,
4. $V_{ref,ij}$ is assumed to be the inlet velocity, and the axial velocity at the current measurement point is used in the calculation of the $(i,j)^{th}$ grid point mass flow.

5

Endwall design routine

In order to allow for a comparison of the effectiveness of each metric used in the design of the endwall contours in this investigation, it was necessary to be able to generate a final endwall geometry for each objective function with as substantial a degree of optimality as possible. In order to achieve this, and because each objective function evaluation in the optimization process required the completion of a fully viscous, 3-dimensional CFD simulation, a surrogate-based non-axisymmetric endwall design system capable of producing optimized endwalls for the rotor of the test case discussed in the previous Chapter (i.e. the CSIR turbine), was developed. This Chapter describes the design and implementation of such a system.

5.1 Background

The optimization of engineering problems often requires the computationally expensive and time-consuming simulation of physical systems as part of their objective function evaluations (Sacks et al. (1989)). In many cases, this places a practical limit on the number of objective function evaluations permissible as part of the optimization procedure. This is especially true in the context of *global* optimization, where the number of objective function evaluations required by the majority of existing algorithms, is often considerably more than those required by local methods, or in cases where the necessary computations are computationally expensive and time-consuming to complete (Jones et al. (1998)).

One solution to this problem is the use of *surrogate-based optimization* (*SBO*) methods, in which the cost of each expensive objective function evaluation is reduced by the replacement of the computationally expensive simulation procedure with a less expensive mathematical model. Since, in the procedure, the expensive models (which are themselves usually models) are substituted by computationally more tractable ones, the approach is often also referred as *meta*modelling.

As indicated by Gregory-Smith et al. (2008), the physical complexity of turbomachinery secondary flows means that modern computational techniques are required for their prediction, and therefore, any optimization of non-axisymmetric endwall contours for the reduction of secondary loss would naturally involve the use of computer simulations. A brief review of the computational requirements required for the solution of the steady-state, Reynolds Averaged Navier-Stokes (*RANS*) equations for a single rotor blade passage (such as that investigated in this project) with sufficient accuracy to predict fully mesh independent results for the objective functions studied in this investigation,

revealed a walltime requirement of approximately $\sim$ 4 hours per simulation[1], for the provision of a fully converged solution. For groups such as MacPherson and Ingram (2010) and McIntosh et al. (2011) who used an evolutionary algorithm-based routine for the global optimization of various non-axisymmetric endwalls, this could result in a requirement of as many as $\sim$ 2400 objective function evaluations, or approximately 9,600 hours *per objective function*[2], which in the absence of large-scale parallel computing facilities, was infeasible[3].

As a result of this, as well as the optimality requirements of this project discussed previously, the endwall design routine developed for this project was based on the so-called *DACE* (*Design and Analysis of Computer Experiments*) surrogate model of Sacks et al. (1989) and the accompanying *EGO* global search algorithm of Jones et al. (1998). The *DACE* model is based largely on the Kriging response surface methodology (Krige (1951)). Since its initial development, Kriging and its derivatives (i.e. *DACE*), have become increasingly more popular approaches for the modelling of complex engineering systems primarily because of their ability to model the often non-linear and multi-modal functions often found in engineering problems without special modification (Forrester et al. (2006)).

Several different approaches, including Artificial Neural Networks (*ANN*) and Radial Basis Functions (*RBF*) were trialled during the development of the endwall design procedure developed in this investigation. However, ultimately the *DACE* approach was selected as the underlying metamodeling technique to be used for the following principal reason: of the approaches investigated, only this model was able to provide an estimate of its own uncertainty of the predictions it makes, and was therefore able guarantee the true global optimization of each endwall objective function by searching in regions of known low surrogate model veracity as well as re-exploring previously explored regions of already known high objective function improvement, for even greater improvement. In addition, and also as a result of the availabilty of internal model error estimates, the use of a multiphase optimization procedure in which the overall veracity of the underlying model could be improved in an initial optimization phase using an appropriate initial search criteria, the most promising areas of improvement indicated by this higher fidelity model could then be investigated for the highest improvement design without requirement for an exhaustive brute force (and therefore computationally prohibitive) approach to be used. The approaches mentioned above are now discussed in more detail.

5.2 The *DACE* surrogate model

5.2.1 Overview

The *DACE* surrogate model is a metamodel in which the objective and constraint functions of the optimization problem are modelled as stochastic processes, meaning that their behaviour is modelled as the sum of an underlying *process trend* and stochastic or random *deviations* from this trend (Eqn. 5.1).

[1] On an Intel Xeon dual socket (2 CPU, 8 core) workstation (E5640 @ 2.66GHz, 32GB RAM @ 1060 MHz)
[2] For the mesh density used in this investigation
[3] Although more powerful computing resources were subsequently secured to perform the CFD calculations required by this investigation (reducing the walltime requirements for each simulation to approximately $\sim$ 70mins per design), the corresponding walltime of approximately $\sim 2,800$ hours per endwall optimization was still significantly too long to be undertaken without the use of some sort of surrogate modelling technique

$$y\left(\mathbf{x}^i\right) = \sum_m \underbrace{\beta_m f_m\left(\mathbf{x}^i\right)}_{\text{trend model}} + \underbrace{\epsilon(\mathbf{x})^i}_{\text{deviation}} \tag{5.1}$$

where:-

$y\left(\mathbf{x}^i\right) = y^i$ is the function value at sample point i, for $i = (1, ..., n)$
$\mathbf{x}^i = \left(x_1^i, ..., x_k^i\right)$ is a sample point i in k-dimensions
β_m is an unknown trend function coefficient,
$f_m\left(\mathbf{x}^i\right)$ is some linear or non-linear function of $\mathbf{x}$, *and*
$\epsilon(\mathbf{x})^i$ is a normally distributed, independent error term with $N\left(0, \sigma^2\right)$

In many stochastic models, the deviations in Eqn. 5.1 (otherwise described as *errors*) are modelled as random, *uncorrelated* departures from the trend, making the approach useful for the modelling of processes such as component manufacture where the exact weight of a component could be modelled as the sum of some nominal value (i.e. the trend - in this case a constant function of zero gradient) and a term representing the small, random deviations from the nominal dimension as a result of the manufacturing process. In the *DACE* model however, the process deviations are modelled as random but *correlated* variations, so that the deviations from the process trend are no longer independent, but related to each other in some way.

It is this distinction which sets the *DACE* method apart from other stochastic models but more importantly, one which makes it particularly attractive for the modelling of *deterministic* systems, such as computer simulations. This is because, as indicated by Jones et al. (1998):-

- if the process (i.e. simulation) to be modelled is indeed deterministic, any deviations from the underlying trend would be as a result of terms left out of the trend model (and *not* measurement or manufacturing error), *and*
- if this first assumption is true and the function being modelled is continuous, the error term $\epsilon(\mathbf{x}^i)$ too is continuous, and therefore, it would be reasonable to expect that two input vectors (i.e. $[(\mathbf{x}^i), (\mathbf{x}^j)]$) *close* to one another in the parameter space, would share some correlation in their deviation terms in the objective function space.

In many surrogate modelling methodologies, a great deal of emphasis is placed on the selection of the correct form of the underlying trend function, f_m, as well as on the estimation of the fitting coefficients, β_m. However, in the *DACE* approach, a comparatively small amount of effort is placed on the form of the trend function, and instead, the majority of the effort is placed on accurate estimation of the process errors. As indicated previously, one consequence of this is that in the *DACE* approach, it is usually unnecessary to know much about the functional form of the objective function, and therefore the response of the system being modelled to changes in its input variables prior to the fitting of the model.

This characteristic is particularly attractive in engineering applications, where the response of a complex physical system (such as the changes in secondary flows as a result of perturbations in the endwall geometry as encountered in this investigation), would most likely be complex itself, and therefore difficult to model accurately if the specific form of these relationships was required to be known

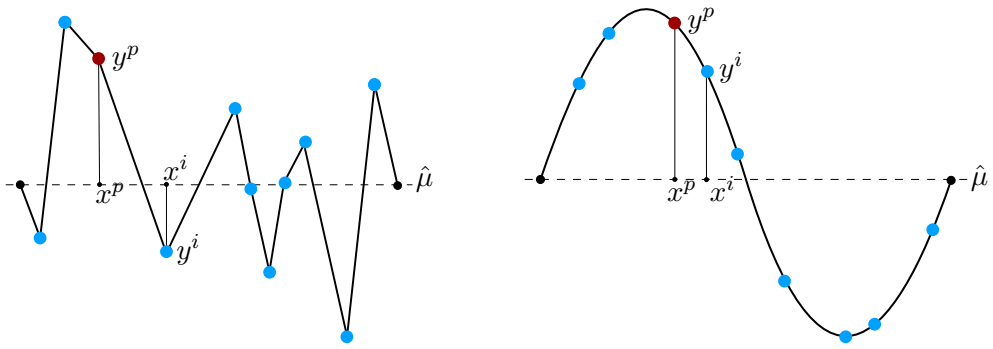

(a) Uncorrelated stochastic process

(b) Correlated stochastic process

Fig. 5.1: The *DACE* concept - uncorrelated vs. correlated modelling of errors, where $\hat{\mu}$ represents the *process mean*, x^i & y^i are a *known* data sample point and its value respectively, and y^p is the predicted value for nearby datapoint x^p. Whereas in the *DACE* model (b), the deviation from the process mean ($\hat{\mu}$) at x^p is correlated to the deviation at x^i (and therefore similar in magnitude), in (a), there is no correlation between the deviations at neighbouring datapoints.

ahead of time. Furthermore, as indicated by Jones et al. (1998), in the event that the specific form of these relationships *was* known *a priori*, there would be little point in using simulation techniques (such as CFD) to predict the responses of the system in the first place, which in turn necessitate the use of the surrogate models during the optimization process

5.2.2 Error correlation

In the *DACE* model, the correlation between the process deviations is based on the *weighted* distance between two distinct input vectors ($d(\mathbf{x}^i, \mathbf{x}^j)$). As discussed by Jones et al. (1998), this approach, rather than the use of a more simple metric such as the Euclidean distance, is preferred as this allows an individual rather than a uniform weighting to be applied to the individual input vectors components, and in so doing, allows for the influencing of the so-called 'activity' level of the individual vector components to be manipulated.

Following Jones et al. (1998), the general form of distance between input vectors is given by Eqn. 5.2, where it can be seen that each pair of component differences is individually weighted by a parameter, θ_h.

$$d\left(\mathbf{x}^i, \mathbf{x}^j\right) = \sum_{h=1}^{k} \theta_h \left| x_h^i - x_h^j \right|^{p_h} \tag{5.2}$$

where:-

$\mathbf{x}^i, \mathbf{x}^j$ are the i^{th} and j^{th} input vectors,
k is the dimensionality of the problem (i.e. the length each input vector),
θ_h is the weighting applied to the h^{th} vector component difference,
x_h^i, x_h^j are the h^{th} component of the i^{th} and j^{th} input vectors,

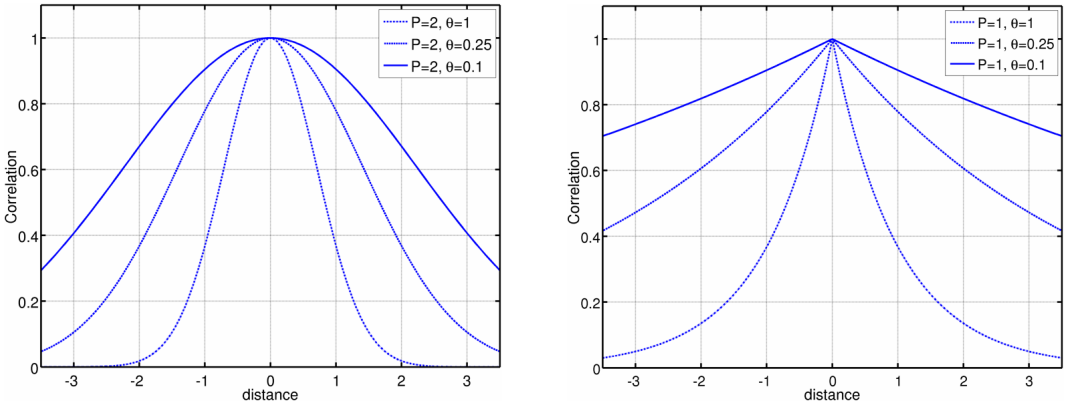

(a) Gaussian correlation function ($\mathbf{p} = \mathbf{2}$) (b) Exponential correlation function ($\mathbf{p} = \mathbf{1}$)

Fig. 5.2: Common *DACE* Spatial Correlation Functions (*SCF*'s) for highly active ($\theta = 1$), moderately active ($\theta = 0.25$) and relatively inactive ($\theta = 0.1$) variables

p_h is a smoothness parameter, *and*
$\theta_h \geq 0$

Once the distances between vectors have been calculated, the correlations between the deviation terms ($\left[\epsilon\left(\mathbf{x}^i\right), \epsilon\left(\mathbf{x}^j\right)\right]$), may be computed using one of a number of so-called *spatial correlation functions* (*SCF*'s). Sacks et al. (1989) and Lophaven et al. (2002) discuss several possible correlation functions, each of which can be categorised into two groups:- 1) those which exhibit parabolic (i.e. *smooth*) behaviour near the origin, and 2) those which display linear (i.e. *non-smooth*) characteristics at the same point.

Among the most common *SCF*'s, are the so-called *exponential correlation functions*, whose general form is given by Eqn. 5.3, and whose parameters p_h in Eqn. 5.2 are $\mathbf{p} \in [1, 2]$.

$$Corr\left[\epsilon\left(\mathbf{x}^i\right), \epsilon\left(\mathbf{x}^j\right)\right] = exp\left[-d\left(\mathbf{x}^i, \mathbf{x}^j\right)\right] \tag{5.3}$$

Within the engineering community, the Gaussian exponential *SCF* ($\mathbf{p} = \mathbf{2}$) has become a popular correlation function, primarily because of its infinite differentiability and therefore its ability to be used by many of the gradient-based optimization algorithms (Song et al. (2013)) and this correlation function was selected for use in this investigation as well. Despite its popularity, the Gaussian correlation function is well-known to cause numerical ill-conditioning in the so-called correlation matrix ($\mathbf{R}$) (Kok (2012), Zimmerman (2015)), and the implications and methods used to minimize these effects are discussed in Section 5.3.2.

The effects of the $\mathbf{p}$ hyperparameters in Eqn. 5.2 are shown in Fig. 5.2, for which Eqn. 5.3 is plotted for different values of $\boldsymbol{\theta}$ and $\mathbf{p} = \mathbf{2}$ (Fig. 5.2a) and $\mathbf{p} = \mathbf{1}$ (Fig. 5.2b).

From Fig. 5.2, the effect of the θ_h weightings is clear. While large θ_h values are seen to reduce the range of the correlation, smaller values are seen to extend it. Jones et al. (1998) explained that the magnitude of the individual weightings may be interpreted as a measure of the 'activity' of a particular component, with large weights translating small differences between the components into

large *effective distances* (and hence low correlations), resulting in large changes in the *DACE* model output for relatively small changes in the input vector positions, and vice versa.

5.2.3 Parameter estimation

In their most general form, the kriging-type surrogate models (including the *DACE* model) require the definition of a total of $(3k+1)$ parameters, including the trend function coefficients ($\boldsymbol{\beta}$), variance (σ^2), and $\boldsymbol{\theta}$ and $\mathbf{p}$ hyperparameters, where k is once again the dimensionality of the problem at hand. In order to construct a fully defined model, the value of each parameter must be estimated using some or other estimation or fitting technique.

Maximum Likelihood Estimation

Although there exist a number of methods for the estimation of each of the model parameters, the most common approach is that of Maximum Likelihood Estimation (*MLE*), in which the estimates of the optimum model parameters are those which result in a model which is most likely to include the observed data (Martin and Simpson (2004)). Practically, *MLE* involves the estimation of the model parameters which maximize the so-called *likelihood function*, which as discussed by Everitt (1987), is the joint probability of the observed data regarded as a function of the model parameters.

With the various model parameters defined as above, the likelihood function ($\mathcal{L}$) for the *DACE* model as described so far is given by:-

$$\mathcal{L}\left(\boldsymbol{\beta}, \sigma^2, \boldsymbol{\theta}, \mathbf{p}\right) = \frac{1}{(2\pi)^{n/2}\left(\sigma^2\right)^{n/2}\left|\mathbf{R}\right|^{\frac{1}{2}}} exp\left[-\frac{\left(\mathbf{y}-\mathbf{F}\boldsymbol{\beta}\right)^T \mathbf{R}^{-1}\left(\mathbf{y}-\mathbf{F}\boldsymbol{\beta}\right)}{2\sigma^2}\right] \tag{5.4}$$

where:-

n is the number of points in the data sample
σ^2 is the variance of the process model errors
$\boldsymbol{\beta} = (\beta_1, ..., \beta_m)^T$ is a vector of the trend function coefficients
$\mathbf{R}$ is a matrix with entries $(R_{i,j}) = Corr\left[\epsilon\left(\mathbf{x}^i\right), \epsilon\left(\mathbf{x}^j\right)\right]$
$\mathbf{y} = (y_1, ..., y_n)^T$ is a vector of the observed objective function values, *and*
$\mathbf{F}$ is a matrix with entries $(F_{i,m}) = f_m(\mathbf{x}^i)$

If $\boldsymbol{\theta}$ and $\mathbf{p}$ are known, the trend function coefficients and variance which maximize the likelihood of the sample data may be solved for in closed form by taking the derivatives of Eqn. 5.4 with respect to $\boldsymbol{\beta}$ and σ^2, and solving for the function stationary points. This in turn leads to the following expressions for the optimal trend coefficients and variance:-

$$\boldsymbol{\beta} = \left(\mathbf{F}^T\mathbf{R}^{-1}\mathbf{y}\right)\mathbf{F}^T\mathbf{R}^{-1}\mathbf{F} \tag{5.5}$$

$$\sigma^2 = \frac{\left(\mathbf{y}-\mathbf{F}\boldsymbol{\beta}\right)^T\mathbf{R}^{-1}\left(\mathbf{y}-\mathbf{F}\boldsymbol{\beta}\right)}{n} \tag{5.6}$$

If Eqns. 5.5 and 5.6 are substituted back into Eqn. 5.4, the resulting function is known as the concentrated likelihood function ($\mathcal{L}_c$), and is one which is then dependent only on the $\boldsymbol{\theta}$ and $\mathbf{p}$ hyperparameters. Furthermore, if the *SCF* for a particular model are selected *a priori*, $\mathcal{L}_c$ becomes a function of the $\boldsymbol{\theta}$ weights only and the *MLE* optimization problem reduces to one with dimensionality (k), equal to the number of weighting parameters.

As indicated by Everitt (1987), in practice it is often simpler to work with the logarithm of $\mathcal{L}_c$, and since both $\mathcal{L}_c$ and $\ln(\mathcal{L}_c)$ have their optima in the same positions, maximization of the latter will lead to the same estimates of the optimum model hyperparameters as that of the former. Therefore, in practice, the likelihood function which is used is:-

$$\ln\left(\mathcal{L}_c\left(\boldsymbol{\theta}\right)\right) = -\frac{n\ln\left(\sigma^2\right) + \ln\left(|\mathbf{R}|\right)}{2} \tag{5.7}$$

In this investigation, the *MLE* problem was posed as a minimization problem, and therefore finally, the model parameter estimation problem was given by:-

$$\min_{\boldsymbol{\theta}\in\mathbb{R}^k} : -\ln\left(\mathcal{L}_c\left(\boldsymbol{\theta}\right)\right) \tag{5.8}$$

subject to:-

$$\theta_h > 0$$

where:-

$$h = 1, 2, ..., k$$

Because, for the majority of correlation models available, there are no closed form solutions for finding the maximum of the likelihood function (i.e. it is often not possible to establish closed form expressions for $\frac{\partial\mathcal{L}_c}{\partial\theta_k} = 0$ and $\frac{\partial^2\mathcal{L}_c}{\partial\theta_k^2} < 0$), Eqn. 5.8 is usually solved using some numerical optimization technique. The techniques used in this investigation are discussed in Section 5.3.

5.2.4 Trend modelling

In conventional regression analysis, the trend function used to model the sampled data is often specified to best fit the form of the observed function values. In the kriging method, the underlying trend may also be specified and it is the variation in this specification which gives rise to the so-called kriging variants. In the simplest approach, known as *Simple Kriging*, the underlying trend is modelled as a known, constant quantity. When the trend is modelled as a constant but *unknown* value, the method is known as *Ordindary Kriging*, and the value of the constant is calculated as part of the model fitting process.

In some cases, it is advantageous to use a trend model with some non-constant functional form, in which case, the method is referred to as *Universal Kriging*.

In their paper, Warnes and Ripley (1987) outlined some difficulties associated with the estimation of Gaussian process models (i.e. kriging models) using the Maximum Likelihood Estimation approach,

Table 5.1: Kriging variants

Method	*Trend model*	*Characteristics*
Simple	μ	known, constant
Ordinary	$\hat{\mu}$	unknown, constant
Universal	$\sum_m \beta_m f_m$	unknown, linear / non-linear

including the convergence of various approaches used to solve the *MLE* problem to one of the many local optima of the likelihood function. In their discussion, they concluded one of the root issues for the multimodality of the likelihood function, was that although while *by intent*, the spatial correlation functions of the model were intended to model the short range (or local) deviations (ϵ) of the observed objective function values from the process mean or trend, in fact, in many cases the estimated model hyperparameters were attempting to model the *global* topographical variation of the objective function. This conclusion was discussed and subsequently corroborated by Martin and Simpson (2004), who in addition to testing the merits of various fitting techniques for the tuning of kriging-type models, also investigated the effects of increasing the complexity of the underlying kriging trend model on the ability of the models to approximate deterministic computer models. In their conclusions, the authors found (similarly to Warnes and Ripley (1987)) that not only did increasing the complexity of the underlying trend models improve the accuracy of the models, but also appeared to reduce the complexity of the likelihood function, making it easier to estimate the optimum model hyperparameters using the *MLE* approach.

In the *DACE* model, the underlying data trend is modelled using the *Ordinary Kriging* methodology, and is therefore assumed to be a constant but unknown quantity. In these circumstances, matrix $\mathbf{F}$ in Eqn. 5.5 reduces to a column vector of ones (i.e. $\mathbf{1} = (1_1, ..., 1_n)^T$) since a constant trend is used, and the trend coefficient vector $\boldsymbol{\beta}$ reduces to a scalar $\hat{\mu}$, which is effectively the generalised least squares estimate of the mean of the data, given by:-

$$\hat{\mu} = \left(\mathbf{1}^T \mathbf{R}^{-1} \mathbf{1}\right)^{-1} \mathbf{1}^T \mathbf{R}^{-1} \mathbf{y} \tag{5.9}$$

where:-

$\mathbf{R}$ is the correlation matrix,
$\mathbf{1} = (1_1, ..., 1_n)^T$ is a vector of ones, *and*,
$\mathbf{y} = (y_1, ..., y_n)^T$ is the vector of observed function values.

Since no significant model fitting issues were encountered during the design and testing of the various *DACE* model databases required for this investigation, the standard *DACE* model based on the *Ordinary Kriging* variant as given by Eqn. 5.9 was used.

5.2.5 The *DACE* predictor

The *DACE* predictor, since it is based on *Ordinary Kriging* variant, consists only of a constant ($\hat{\mu}$) and the deviation term (ϵ), to model the objective function.

For an unknown design site with input vector $\mathbf{x}^p$, the form of the *DACE* predictor can be shown to be (Jones et al. (1998)):-

$$y\left(\mathbf{x}^p\right) = \hat{\mu} + \epsilon(\mathbf{x}^p) \tag{5.10}$$

Further to this, if $\mathbf{r}$ is a vector of correlations between the deviation at the unknown design site ($\epsilon\left(\mathbf{x}^p\right)$) and the deviation at the known sample points ($\epsilon\left(\mathbf{x}^i\right)$), then the final form of the predictor is given by Eqn. 5.11:-

$$y\left(\mathbf{x}^p\right) = \hat{\mu} + \mathbf{r}^T\mathbf{R}^{-1}\left(\mathbf{y} - \mathbf{1}\hat{\mu}\right) \tag{5.11}$$

where:-

$\mathbf{r} = (r_1, ..., r_n)^T$ with $r_i = Corr\left[\epsilon\left(\mathbf{x}^p\right), \epsilon\left(\mathbf{x}^i\right)\right]$, *and*
$\mathbf{R}, \mathbf{y}, \mathbf{1}$ and $\hat{\mu}$ are as defined previously.

5.2.6 Model error and validation

Due to the construction of the *DACE* model using only discrete data about the true objective function in conjunction with some form of interpolation strategy, it is entirely reasonable to expect the model to exhibit some form of inaccuracy, and therefore also requires some form of model validation.

Model error

One advantage of the kriging-based metamodels, is the ability of these models to make some kind of estimate of the uncertainty of their own predictions of the true objective function.

Following from Jones et al. (1998), given the model variance (σ^2) and assuming a constant trend function, the *Mean Square Error* (*MSE*) of the *DACE* model predictor is given by:-

$$s^2\left(\mathbf{x}^p\right) = \sigma^2\left[1 - \mathbf{r}^T\mathbf{R}^{-1}\mathbf{r} + \frac{\left(1 - \mathbf{1}^T\mathbf{R}^{-1}\mathbf{r}\right)^2}{\mathbf{1}^T\mathbf{R}^{-1}\mathbf{1}}\right] \tag{5.12}$$

In Eqn. 5.12, the model error can be seen to be an estimate of the model variance (σ^2) adjusted by terms representing:- 1) a reduction in the uncertainty of the variance due to correlation with known data points ($\mathbf{r}^T\mathbf{R}^{-1}\mathbf{r}$), and 2) the model uncertainty due to the estimation of $\hat{\mu}$ ($\left(1-\mathbf{1}^T\mathbf{R}^{-1}\mathbf{r}\right)^2/\mathbf{1}^T\mathbf{R}^{-1}\mathbf{1}$).

Because at a known data point, the correlation between a point and itself is equal to 1, $\mathbf{r}^T\mathbf{R}^{-1}\mathbf{r} = 1$ and $\mathbf{1}^T\mathbf{R}^{-1}\mathbf{r} = 1$, and so it can be shown that at known data points, the Mean Square Error of the model $s^2\left(\mathbf{x}^*\right) \to 0$. In addition, since at a prediction point far from the known data points, the correlation between the points roughly equal to 0 (i.e. $\mathbf{r} \sim \mathbf{0}$), $\mathbf{r}^T\mathbf{R}^{-1}\mathbf{r} = 0$ and $\left(1-\mathbf{1}^T\mathbf{R}^{-1}\mathbf{r}\right)^2/\mathbf{1}^T\mathbf{R}^{-1}\mathbf{1} \sim 0$, so that the *MSE* of the model is roughly equivalent to the model variance (i.e. $s^2\left(\mathbf{x}^*\right) \to \sigma^2$).

Cross-validation

Within the literature, a number of methods have been presented for the validation of surrogate models. One of the most common for the *DACE* metamodel is the so-called *Leave-One-Out* (*LOO*) cross-validation approach. In this method, the hyperparameters which maximize the likelihood of the full data sample are estimated using some suitable technique. Thereafter, a single sample point is removed from the dataset, and then the corresponding objective function value of the removed sample point is estimated using only the remaining database sample points within the correlation matrix ($\mathbf{R}$). This process is then repeated for all the points in the database, whereafter various metrics representing the quality of the model may be calculated.

In summary then, the *LOO* cross-validation procedure may be given as follows:-

1. Generate a database of known objective function values and associated input vectors,
2. Estimate the model hyperparameters which maximize the likelihood of the dataset using method given in Section 5.2.3,
3. Remove a sample (say $y\left(\mathbf{x}^i\right)$) from the dataset, and reformulate the *DACE* parameters ($\mathbf{R}_{-i}$, $\mathbf{r}_{-i}$, $\mathbf{y}_{-i}$) using the remaining reduced dataset,
4. Estimate the value of the removed sample point ($y_{-i}\left(\mathbf{x}^i\right)$) using the reduced correlation matrix ($\mathbf{R}_{-i}$) and compare this with the known objective function value at that point, ($y\left(\mathbf{x}^i\right)$).

It is common for the difference in value between the reduced model objective function prediction of the objective function ($y_{-i}\left(\mathbf{x}^i\right)$) and the known function value ($y\left(\mathbf{x}^i\right)$) to be expressed as a 'standardized cross-validated residual'. Following Jones et al. (1998), if the standard error of the model calculated using the reduced dataset is given by $s_{-i}\left(\mathbf{x}^i\right)$, the standardized residual (R_{std}) may be found from:-

$$R_{std} = \frac{y\left(\mathbf{x}^i\right) - y_{-i}\left(\mathbf{x}^i\right)}{s_{-i}\left(\mathbf{x}^i\right)} \tag{5.13}$$

Since the *DACE* model is 99.7% confident that its prediction of $y_{-i}\left(\mathbf{x}\right)^i$ lies within 3 standard deviations of the true function value, it is therefore easy to validate the accuracy of the model by verifying that $-3 \leq R_{std} \leq +3$.

In addition to calculation of the standard residuals, it is also useful to compare the actual value of the objective function ($y(x^i)$) with the predicted value from the cross-validation ($\hat{y}_{-i}(x^i)$). Because in a well fitted model, these values should be similar, the point whose coordinates correspond to [$y(x^i)$,$\hat{y}_{-i}(x^i)$] should lie close to a line which traverses the plot at 45° on a pair of linear axes.

Finally, since the standardised residuals should behave like normal deviates, if these values are plotted against a random sample of n independent standard normal variables, the corresponding data points should again lie close to the line $y = x$ on a pair of linear axes.

A set of sample plots corresponding to the comparison between the actual versus cross-validated prediction values (y_{actual} vs $y_{predicted}$), standardised residual (R_{std} vs $y_{predicted}$), and a plot of the

ordered standardised residuals versus standard normal quartiles (Q-Q plot[4]), for a well and poorly fitted *DACE* model, are shown in Fig. 5.3, where the underlying data for these models was generated by running CFD calculations on a random selection of endwall geometries and using the lost efficiency (i.e. $(1 - \eta_{tt})$ as the evaluation function.

As can be clearly seen, the well-fitted model shows an almost linear relationship between the predicted and actual objective function values (Fig. 5.3a), while the weak predictive ability of the poorly fitted model is apparent with the clustering of predicted values around $y_{predicted} \sim 20.55$ in Fig. 5.3b. Again, while Fig. 5.3c shows all the predicted objective functions to lie within ± 3 standard deviations of the mean, at least two extreme values corresponding to ($R_{std} > 4$) may be seen for the poorly fitted model (Fig. 5.3d). Finally, while for the well-fitted mode, the standard residuals were seen to behave as standard normal deviates (Fig. 5.3e), for the poorly fitted model, the standard residuals show poor agreement with the 45° line on the Q-Q plot, indicating the residuals *do not* act like standard normal deviates.

5.3 Numerical issues

As discussed previously, in the *DACE* methodology, there are a number of difficulties related to the estimation of the optimum model hyperparameters using the *MLE* approach. As alluded to briefly above, these include:-

1. difficulties in solving the *MLE* optimization subproblem as given by Eqn. 5.8, as a result of the complex topology of the concentrated likelihood function ($\mathcal{L}_c$), *and*
2. the rapid degeneration in the numerical conditioning of the correlation matrix ($\mathbf{R}$) with the use of the so-called Gaussian *SCF* and the decrease in the magnitude of the $\boldsymbol{\theta}$ hyperparameters as well as as a result of the repeated sampling of the objective function as part of the *EGO* search algorithm (used to locate the point maximum improvement in the objective function and as the primary search method in this investigation) (Section 5.4) in a concentrated region of the parameter search space.

5.3.1 Difficulties in solving the *MLE* optimization problem

As indicated above, among the difficulties associated with the model fitting problem (as described previously in Section 5.2.3), the most significant are those related to the multimodality and complex topology of the concentrated likelihood function ($\mathcal{L}_c$).

In particular, as noted by various authors, among the most common difficulties are:-

- the multi-modal and non-linear characteristics of the concentrated ln-likelihood function in the vicinity of the maximum, as well as the presence of elongated ridges and large flat regions in other portions of the function surface, *and*

[4] Quantile-quantile plot

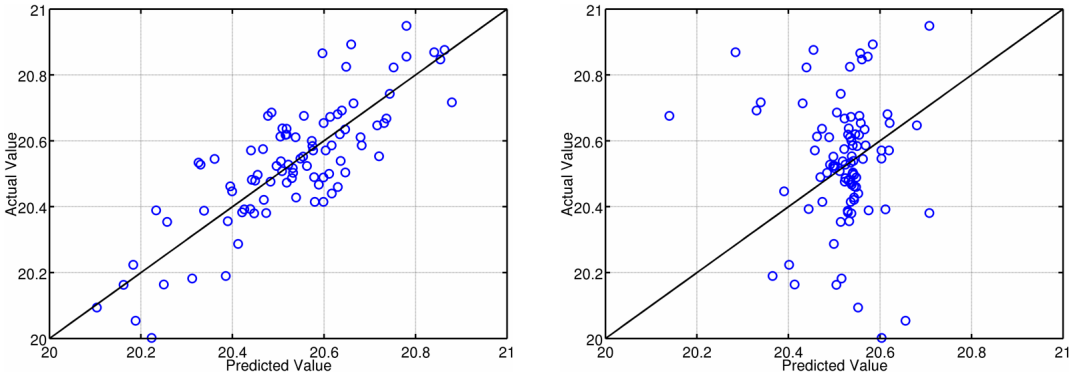

(a) y_{actual} vs $y_{predicted}$

(b) y_{actual} vs $y_{predicted}$

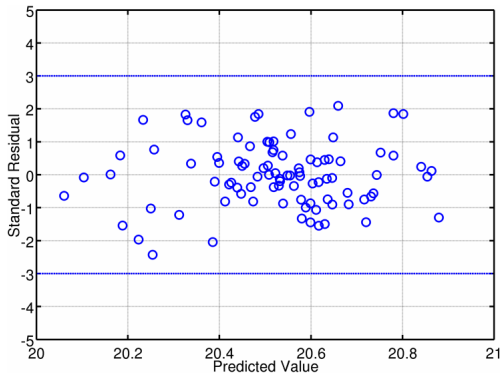

(c) Standard cross-validated residuals (R_{std})

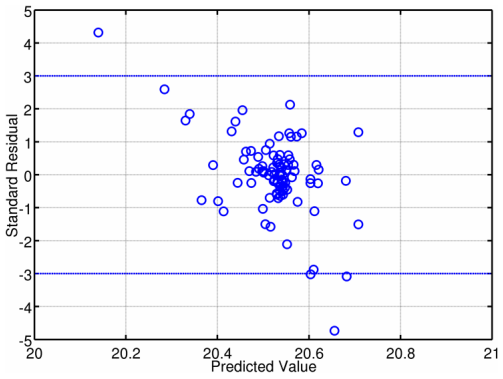

(d) Standard cross-validated residuals (R_{std})

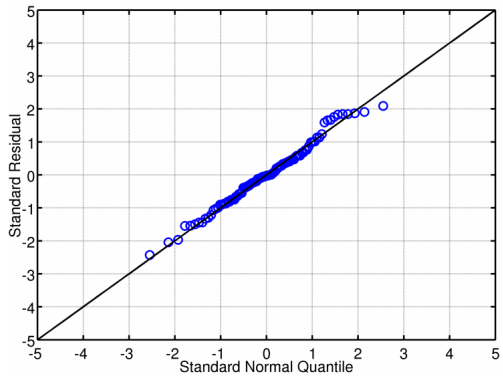

(e) Q-Q plot

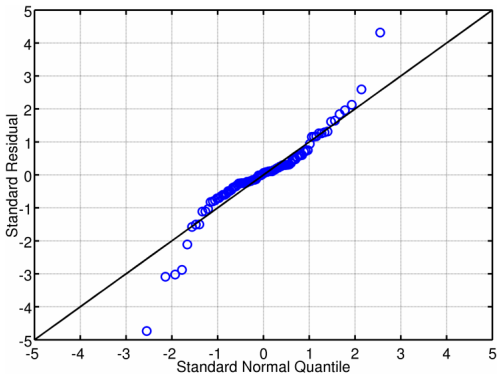

(f) Q-Q plot

Fig. 5.3: *DACE* model Leave-One-Out cross-validation metrics for a well (left) and poorly (right) fitted model

- the possibility for the likelihood function to be monotonically increasing or decreasing (and therefore contain no local optimizers) with an increase in the magnitude of the model hyperparameters, which is in turn as a result of the exact composition of the database used to construct the model.

The multi-modality and non-linearity issues discussed above make the solution of the *MLE* problem using traditional gradient-based and hill-climbing optimization routines often difficult, since these routines are highly susceptible to being trapped in local optima as well as to premature convergence in the flat portions of the likelihood function where there is little gradient information available to drive the successive steps of the algorithm. As a result, one of the most popular approaches to solve the so-called *MLE* problem of Eqn. 5.8, is the use of population-based metaheuristic optimization algorithms. In particular, this has included the use of a number of population-based, evolutionary algorithms since these algorithms (as discussed previously) are known to be powerful *global* optimizers and therefore significantly less prone to suboptimal convergence as well the issues associated with the likelihood function discussed above (because they do not rely on gradient information from the objective function surface (Haupt and Haupt (2004), Luke (2009))).

The monotonicity of the likelihood function under certain conditions, also makes the selection of the optimum model parameters difficult, since in these cases, it is possible that no internal optimizers for the likelihood function exist. More specifically, Kok (2012) was able to show, using a relatively simple 1-dimensional example, that the concentrated likelihood function ($\mathcal{L}_c$) could be shown to increase monotonically with either increasing $\boldsymbol{\theta}$ - leading to an estimate of the optimum hyperparameters as as large a number as possible - or with decreasing $\boldsymbol{\theta}$ - leading to an estimate of the model weights as small as practically possible - depending on the composition of the database on which the model was built[5]. In both cases, the likelihood function contained no internal optimizers.

In the case where the likelihood function is found to be monotonically *decreasing* with $\boldsymbol{\theta}$, the limit on the minimum size of the hyperparameters is usually determined by the numerical conditioning of the correlation matrix as described in 2) above, and so this issue is discussed in the following section (Section 5.3.2). Conversely however, in the monotonically *increasing* case, where the hyperparameters are estimated to be *as large a number as possible*, no such ill-conditioning issues occur, and instead the limit on the maximum size of the hyperparameters is related to the predictive capability of the metamodel, where the estimates of the modelled function degenerate to a constant global trend with large deviations from it in the vicinity of the known database points.

In order to illustrate the issues discussed above, Fiqures 5.4a & 5.4b show the concentrated ln-likelihood function of Rosenbrock's so-called *banana test function* (Rosenbrock (1960)) plotted for an initial random dataset ($n_{points} = 10$) using linear and logarithmic coordinate systems. When plotted in linear coordinates, the large $\sim$0 gradient portions of the function are clear, in logarithmic coordinates, the complex topology of the function is evident including at least different optima, as well as a long ridge of equal likelihood adjacent to the global optimum. Finally, Fig. 5.4c shows the likelihood for the same function as used above, but plotted for an initial database comprised of $n_{points} = 2$. In this case, it can be seen that $\mathcal{L}_c$ is monotonically increasing with $\boldsymbol{\theta}$ and then where the $\boldsymbol{\theta}$ weights for the *DACE*

[5] In his investigation, Kok (2012) actually formulated the likelihood function as $\Phi(\boldsymbol{\theta}) = -\ln(\mathcal{L}_c)$ and so he reported a monotonically *decreasing* likelihood function with either increasing or decreasing $\boldsymbol{\theta}$ weights depending on the database composition under consideration

model computed using the *MLE* approach would be estimated to be as large a number as possible. All figures are plotted for $\theta_{1/2} \in [10^{-10}, 10^{2}]$.

Remedies used in this investigation for the *MLE* optimization problem

In order to deal with the difficulties associated with estimating the *DACE* model parameters using the *MLE* approach as discussed above, a number of different strategies were trialled. In particular, in order to deal with the potential non-linearity and multi-modality as well as the large zero gradient portions of the concentrated ln-likelihood function, two different population-based metaheuristic optimizers were tested as part of the *DACE* model fitting procedure used in this investigation:-

1. a continuous Genetic Algorithm, incorporating elitism and single point cross-over (Haupt and Haupt (2004)), *and*
2. the */rand/1/bin* Differential Evolution algorithm (Price et al. (2005))

In order to deal with the presence of the large ~ 0 gradient portions of the likelihood function, the populations of both algorithms were initialised using a random point distribution in logarithmic space, rather than linear space. This ensured that at least some of the starting population vectors were initialised in the non-zero gradient portions of the function space and thereby reducing the change of premature convergence on the flat portions of the ln-likelihood function. This approach is illustrated in Fig. 5.5.

Thereafter, the effectiveness of each algorithm in solving the *MLE* problem was established by using each algorithm to maximize the likelihood of three sets of CFD generated aerodynamic data. This was done by recording the estimate of the maximum likelihood found by each algorithm for each dataset and computing the associated Root Mean Square (*RMSE*) and Maximum Errors corresponding to each estimate thereafter using the standard *LOO* and cross-validation procedures discussed in Section 5.2.6. In addition, the efficiency of each algorithm in converging to the location of each maximum likelihood estimate was noted in terms of the total number of iterations required to converge to the predicted optima. For each dataset, the fitting procedure was repeated 5 times, and the maximum, minimum and mean for each quantity was calculated.

The results for each dataset are shown in Table 5.2 below. For the majority of the cases, the Differential Evolution algorithm was found to converge both faster and to a better (i.e higher) *MLE* value than the GA-based approach, although this was not the case for dataset 2. However, in all cases, the *DE* algorithm was found to converge more consistently to its predicted optimum point, with each of the five runs for each dataset converging to the same point in each case. For all three datasets, the models fitted using the *DE* algorithm resulted in lower mean *RMSE* values although, as indicated in the table, for datasets 1 & 2, the average *Max Errors* for *DE*-fitted models were slightly higher than those for the GA-fitted models.

Despite the slightly lower mean *Max Errors* noted for datasets 1 & 2 produced by the GA-fitted models, the Differential Evolution routine was selected as the basis of the *DACE* model fitting procedure in this investigation. This was due primarily to the more consistent convergence displayed by the algorithm, faster convergence and higher *MLE* values located for the majority of the cases tested. For a review of the Differential Evolution algorithm, the reader is directed to Section 2.6.3.

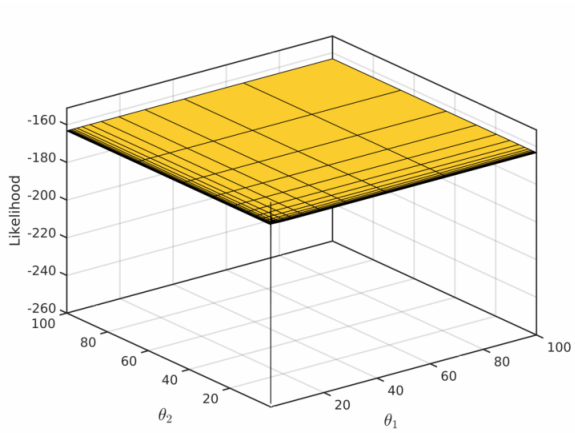

(a) Linear coordinates ($n_{points} = 10$)

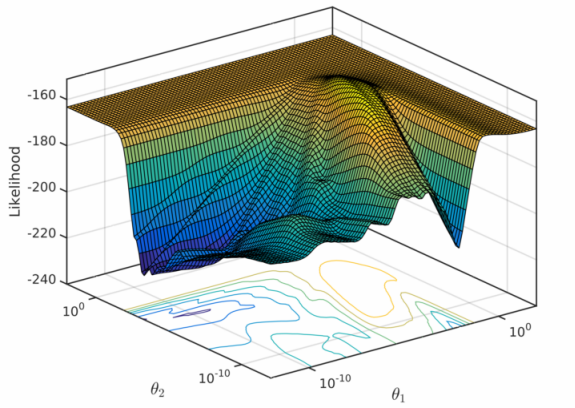

(b) Logarithmic coordinates ($n_{points} = 10$)

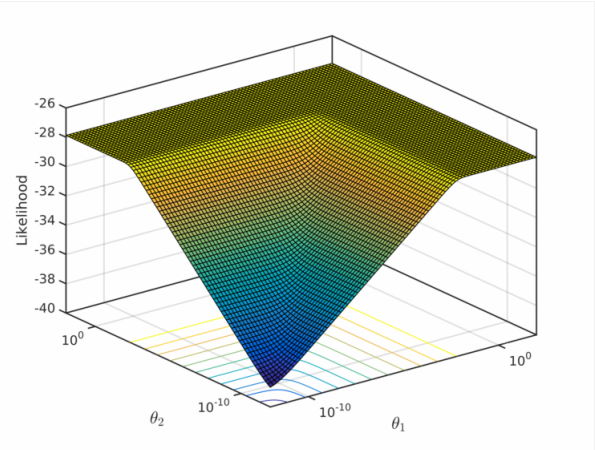

(c) Monotonically increasing case with increasing $\boldsymbol{\theta}$ ($n_{points} = 2$)

Fig. 5.4: Concentrated ln-likelihood function ($\mathcal{L}_c$) for Rosenbrock's so-called Banana Test Function with a dataset of $n_{points} = 10$ (a & b) and $n_{points} = 2$ (c) chosen randomly where $\mathbf{x} \in [-30, 30]$

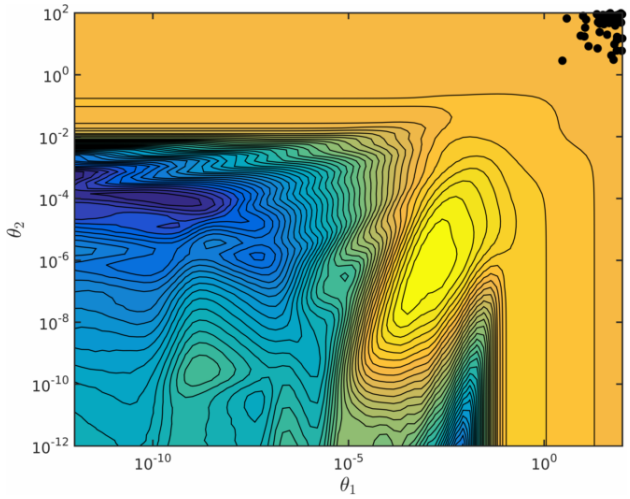

(a) Random initialisation in linear space (i.e. $x_h = (1, 2, 3 \ldots n)$

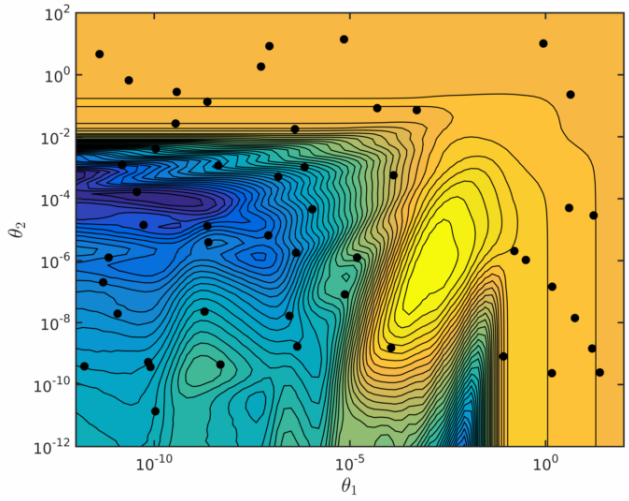

(b) Random initialisation in logarithmic space (i.e. $x_h = 10^1, 10^2, 10^3 \ldots 10^n$)

Fig. 5.5: Effects of quasi-uniform (random) point initialisation in linear & logarithmic parameter space on the location of the starting population vectors in the concentrated ln-likelihood function space

In order to deal with the cases in which the likelihood function was seen to increase monotonically with either increasing or decreasing model weights, a system of function and boundary constraints was added to the optimization problem given by Eqn. 5.8 to prevent excessively high or low values of the $\boldsymbol{\theta}$ from being returned in these cases.

Specifically, the constraints added were:-

Function

Table 5.2: Summary of averaged GA and DE-based fitting statistics for 3 CFD-generated aerodynamic datasets based on 5 independent runs on each dataset

Dataset	*Max* $\ln(\mathcal{L}_c)$		*RMSE*		*Max error*		*Iterations*	
	GA	DE	GA	DE	GA	DE	GA	DE
Dataset 1								
Min	179.46	181.07	0.1159	0.1137	0.2370	0.2829	+3500	∼1250
Max	180.49	181.07	0.1209	0.1137	0.2806	0.2829	+3500	∼1250
Mean	179.92	181.07	0.1189	0.1137	0.2605	0.2829	+3500	∼1420
Dataset 2								
Min	125.13	124.17	0.2155	0.2002	0.4692	0.6198	+3500	∼1350
Max	125.38	124.17	0.2190	0.2002	0.5033	0.6198	+3500	∼2150
Mean	125.25	124.17	0.2173	0.2002	0.4898	0.6198	+3500	∼1610
Dataset 3								
Min	23.24	26.30	0.5702	0.5724	1.4049	1.7030	+3500	∼2200
Max	25.99	26.30	0.5809	0.5724	1.8920	1.7030	+3500	∼1850
Mean	25.26	26.30	0.5751	0.5724	1.6816	1.7030	+3500	∼1940

$$c_1(\boldsymbol{\theta}) : \ln(\mathcal{L}_c) \geq -1 \times 10^{15} \tag{5.14}$$

$$c_2(\boldsymbol{\theta}) : \ln(\mathcal{L}_c) \leq 1 \times 10^{15} \tag{5.15}$$

$$c_3(\boldsymbol{\theta}) : \kappa(\tilde{\mathbf{R}}) \leq 1 \times 10^{13} \tag{5.16}$$

and

Boundary

$$b_1 : \boldsymbol{\theta} \leq 10^2 \tag{5.17}$$

$$b_2 : \boldsymbol{\theta} \geq 10^{-12} \tag{5.18}$$

Although theoretically, the boundary constraints b_1 & b_2 on the $\boldsymbol{\theta}$ weights imply a limit on the value of the likelihood function, because there is a practical limit on the size of the largest and smallest numbers representable in a finite precision computer code (and it is not known *a priori* at what rate the likelihood function will increase with increasing or decreasing $\boldsymbol{\theta}$), the c_1 & c_2 constraints were implemented to limit the maximum and minimum objective function values, and in so doing, prevent numerical overflow errors. The sizes of the maximum and minimum objective function values were chosen somewhat arbitrarily although running the endwall design procedure (Section 5.6) showed that in the majority of cases, the only active constraints (if any) on the magnitude of the *DACE* model hyperparameters at the point of maximum *MLE* were imposed by c_3 (i.e. the constraint on the condition of the *regularised* correlation matrix ($\tilde{\mathbf{R}}$), discussed below), and in some isolated cases, constraint b_2 which imposed a hard limit on the lower value of the components of $\boldsymbol{\theta}$.

The function and boundary constraints for the MLE subproblem were imposed using a combination of quadratic and 'brick-wall' penalty constraints respectively as described in Sections 3.1.2 & 3.1.3 respectively.

5.3.2 Difficulties related to the ill-conditioning of correlation matrix R

As discussed above, a second difficulty related to the estimation of the model hyperparameters, is the rapid degeneration of the numerical condition of the correlation matrix ($\mathbf{R}$) with the reduction in the magnitude of the $\boldsymbol{\theta}$ model weights. Because, for example, in Eqns. 5.5 & 5.6 as well as Eqns. 5.11 & 5.12, numerical inversion of $\mathbf{R}$ is required, as the conditioning of the matrix becomes worse, the inversion of $\mathbf{R}$ as required in the above equations becomes increasingly more difficult to perform accurately.

The *condition number* (κ) of a symmetric matrix $\mathbf{A}$ is given by:-

$$\kappa(\mathbf{A}) = \frac{|\lambda|_{max}}{|\lambda|_{min}} \tag{5.19}$$

where:-

$\mathbf{A} \in \mathbb{R}^{m \times m}$, *and*
λ_{max} and λ_{min} are the largest and smallest eigenvalues of $\mathbf{A}$ respectively

In order to understand the reasons for the increase in κ for the correlation matrix with the reduction in the model weights discussed above, it is useful to redefine Eqn. 5.2 as follows:-

$$d\left(\mathbf{x}^i, \mathbf{x}^j\right) = \sum_{h=1}^{k} \left| \frac{x_h^i - x_h^j}{b_h} \right|^{p_h} \tag{5.20}$$

where b_h is the so-called *range parameter* which indicates the strength of influence or correlation length of point i on point j and which $b_h \to \infty$ as $\theta_h \to 0$, and $b_h \to 0$ as $\theta_h \to \infty$.

Following Kok (2012), with the increase in the $\boldsymbol{\theta}$ weights in Eqn. 5.2 and therefore a decrease in the range parameter in Eqn. 5.20, the correlation matrix tends towards the identity matrix ($\mathbf{R} \to \mathbf{I}$), and all the corresponding eigenvalues of $\mathbf{R}$ tend towards 1, resulting in a condition number of $\kappa(\mathbf{R}) \sim 1$ indicating it is well-conditioned. However, with a decrease in the $\boldsymbol{\theta}$ weights in Eqn. 5.2 and therefore an increase in the correlation range (or range parameter) in Eqn. 5.20, the correlation matrix tends towards the unit matrix, all of whose eigenvalues tend towards 0, except for one which tends towards m. Therefore, as the correlation length increases, the condition number of $\mathbf{R}$ also tends towards ∞, indicating a decrease in the conditioning of $\mathbf{R}$.

As discussed by Andrianakis and Challenor (2012), this may be interpreted as equivalent to the design points of the model database getting closer and closer to one another, until in the limit, the columns of $\mathbf{R}$ become linearly dependent and offer no information to the error term (ϵ) of Eqn. 5.1.

Although not related to the size of the model hyperparameters as discussed above, the sampling of the objective function in successive iterations of the *EGO* algorithm (as discussed in Section 5.4), may also result in a reduction in the linear independence of the columns of $\mathbf{R}$ resulting in a subsequent

reduction in the overal conditioning of the matrix. Since towards the end of an optimization run, it is reasonable to expect that the points selected for sampling on the objective function surface converge in the vicinity of the optimum resulting in dense sampling of the function in that area. This results in a corresponding reduction in the independence of the columns of the correlation matrix, which would ultimately have the same effect as those discussed for the θ-hyperparameters above (and therefore present similar difficulties to the optimization procedure towards the end of any optimization attempt).

Remedies used in this investigation for the ill-conditioning of R

The effects of ill-conditioning of the correlation matrix as a result of both the reduction in the $\boldsymbol{\theta}$ model weights as part of the model fitting procedure, as well as as a result of the convergence of the *EGO* algorithm towards the end of an optimization run, were reduced using the so-called *nugget* approach, in which a small positive number (ν) is added to the diagonal of the correlation matrix in order to improve its condition.

Following Lophaven et al. (2002) and Andrianakis and Challenor (2012), if a *regularised correlation matrix* ($\tilde{\mathbf{R}}$) is defined as:-

$$\tilde{\mathbf{R}} = \mathbf{R} + \nu\mathbf{I} \tag{5.21}$$

then it can be shown that the j^{th} eigenvalue of $\tilde{\mathbf{R}}$ (i.e. $\tilde{\lambda}_j$), is related to λ_j (the j^{th} eigenvalue of $\mathbf{R}$) by:-

$$\tilde{\lambda}_j = \lambda_j + \nu \tag{5.22}$$

Since the condition number of $\tilde{\mathbf{R}}$ is now given by:-

$$\kappa(\tilde{\mathbf{R}}) = \frac{|\lambda|_{max} + \nu}{|\lambda|_{min} + \nu} \tag{5.23}$$

and it can be shown that:-

$$\left(\frac{|\lambda|_{max} + \nu}{|\lambda|_{min} + \nu}\right) \underset{always}{<} \left(\frac{|\lambda|_{max}}{|\lambda|_{min}}\right) \tag{5.24}$$

this implies that that $\tilde{\mathbf{R}}$ is always better conditioned that $\mathbf{R}$. In addition, in the worst case scenario, if $\boldsymbol{\theta} \to 0$, $\kappa(\tilde{\mathbf{R}}_{\boldsymbol{\theta}\to 0}) = \frac{m+\nu}{\nu}$ guaranteeing that $\tilde{\mathbf{R}}$ is always invertible.

Following Lophaven et al. (2002), the nugget used in this investigation was set to:-

$$\nu = (10 + m)\epsilon_m \tag{5.25}$$

where:-

m is the number of design sites in the *DACE* model database, *and*

ϵ_m is the machine accuracy equivalent to $\sim 2.2204e^{-16}$

Despite the addition of the so-called nugget to the correlation matrix and therefore the improvement of the conditioning of the correlation matrix in the circumstances discussed above, an additional function constraint (c_3) was used to limit the selection of model hyperparameters to those which resulted in condition numbers for the regularised correlation matrix below a value of 1×10^{13}. This figure was based on the fact that a matrix can be considered ill-conditioned if the reciprocal of its condition number ($1/\kappa$) approaches the precision of computer code used (Andrianakis and Challenor (2012)). Since the computations associated with the *DACE* model were computed using binary64 format, which gives approximately 15 digits of precision, the limit set of 10^{-12} as indicated above was considered acceptable. Although this limit was set slightly higher than that used by Andrianakis and Challenor (2012) (who considered a matrix whose condition number exceeded 10^{12} to be ill-conditioned), this limit was still less than the reciprocal of the machine precision and no warning messages were produced by the software during the matrix inversion procedures.

The effect using the 'nugget' approach as discussed above is illustrated by Figs. 5.6b & 5.6a, which show a comparison between the concentrated ln-likelihood ($\ln(\mathcal{L}_c)$) function for Rosenbrock's Banana Function computed *with* and *without* the addition of the nugget. The regions of the spurious ln-likelihood function values where θ_1 & θ_2 are small indicate the onset of the numerical difficulties discussed above, and in particular the difficulties associated with the inversion of $\mathbf{R}$.

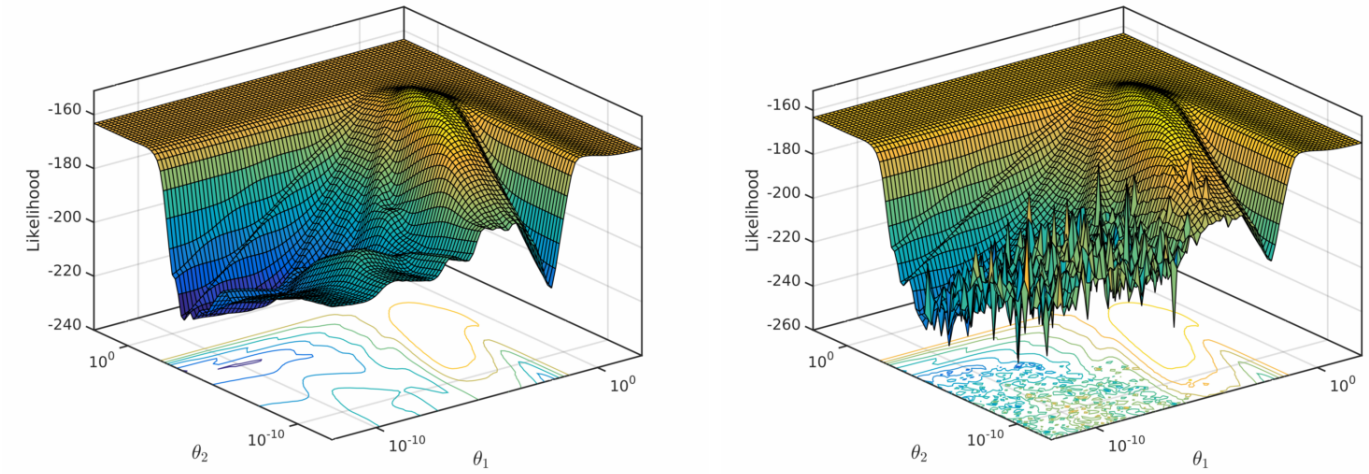

(a) $\ln(\mathcal{L}_c)$ computed using $\tilde{\mathbf{R}}$ (i.e. with 'nugget')

(b) $\ln(\mathcal{L}_c)$ computed using $\mathbf{R}$ (i.e. without 'nugget')

Fig. 5.6: Comparison of the concentrated ln-likelihood function ($\ln(\mathcal{L}_c)$) of Rosenbrock's Banana Function computed *with* and *without* the addition of the 'nugget'

5.4 The *EGO* algorithm

The Efficient Global Optimization (*EGO*) algorithm is the search methodology originally developed by Jones et al. (1998) for use with the *DACE* metamodel and as suggested by its name, was intended for the global optimization of systems incorporating expensive objective functions. In this thesis, a modified version of the original *EGO* was used as the search procedure to find the optimum parameters for the turbine endwall contours.

Since the algorithm was developed for the efficient optimization of systems with expensive objective functions, the methodology was developed to minimize the number of objective function evaluations required during the optimization procedure by making use of so-called Infill Search Criteria (*ISC*) to determine the most efficient location at which the objective function should be evaluated.

The basic *EGO* algorithm is illustrated in Fig. 5.7, and following Jones et al. (1998), may be described by the following steps:-

- Fit an initial *DACE* model using a set of existing database points
- Conduct the model validation tests to confirm an appropriate model fit
  - If the model fit is poor, re-fit the model, or
  - Apply a suitable function transformation (i.e. log) to the function and re-fit the model
- Search the selected Infill Search Criteria (*ISC*) for the initial *DACE* model and return the point at which the criterion is optimal
- Evaluate the value of the true objective function value at the point of optimal *ISC* and add the point coordinates and true objective function value to the model database
- Re-evaluate (re-fit) the *DACE* model parameters for the augmented database, *and*
- Repeat until some pre-determined stopping criteria is met

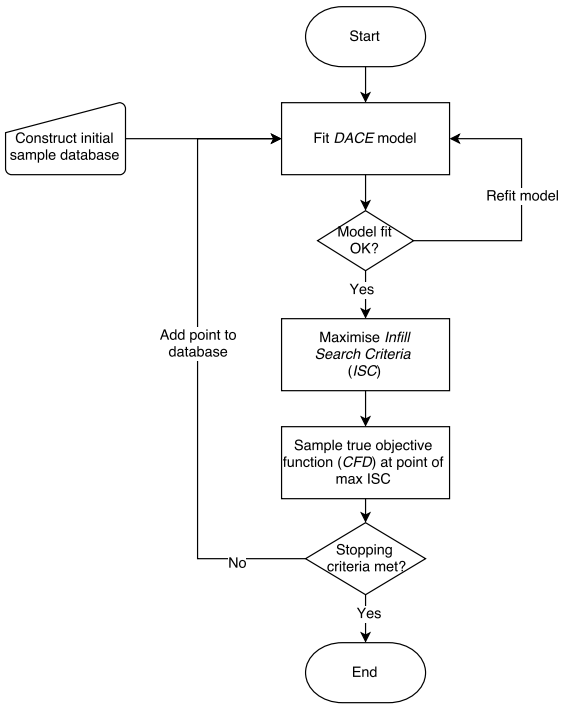

Fig. 5.7: The *EGO* algorithm

5.4.1 Infill search criteria (*ISC*)

Expected Improvement criteria

Searching the metamodel prediction of the objective function surface can lead to the convergence of the optimization procedure to a false optimum. This is because the predicted and actual shape of the objective function surface may differ substantially due to poor model generalisation.

One of the strengths of the kriging-based models in this context then is their ability to formulate a reasonably accurate estimate of error associated with the surface prediction (provided the model meets the validation criteria of Section 5.2.6). As indicated above, the search criteria used to sample the *DACE* metamodel surface as part of the *EGO* algorithm was the so-called *EI* criterion, in which the predicted objective function value is combined with the an estimate of the uncertainty by the *DACE* model itself in order to determine at which locations the an improved objective function value was likely to be found.

The *EI* criterion attempts to subvert the problems associated with poor metamodel generalisation by sampling the true objective function surface at locations where the possibility of reducing the current best function value is greatest, including regions of already known favourable performance as well as regions with high model uncertainty.

Following Sasena et al. (2000), the Improvement of the objective function can be defined by:-

$$I = \max[0, f_{min}^n - Y] \tag{5.26}$$

where:-

I is the improvement,
f_{min}^n is the actual current lowest objective function value, *and*
Y is the predicted function value treated as a normal random variable with $N(\hat{y}(\mathbf{x}), s^2(\mathbf{x}))$,

The Expected Improvement can then be defined as:-

$$E(I) = \int_{-\infty}^{f_{min}^n} (f_{min}^n - Y)\phi(Y)dY \tag{5.27}$$

where:-

$E(I)$ is the expected improvement, *and*
$\phi(\cdot)$ is the normal probability density function

Computing the appropriate integrals, the Expected Improvement can be expressed in closed form by:-

$$E(I) = \begin{cases} (f_{min}^n - \hat{y}(\mathbf{x}))\Phi\left(\frac{f_{min}^n - \hat{y}(\mathbf{x})}{s(\mathbf{x})}\right) + s(\mathbf{x})\phi\left(\frac{f_{min}^n - \hat{y}(\mathbf{x})}{s(\mathbf{x})}\right) & \text{if } s > 0 \\ 0 & \text{if } s = 0 \end{cases} \tag{5.28}$$

where:-

$\hat{y}(\mathbf{x})$ and $s(\mathbf{x})$ are the mean and standard deviation of Y at $\mathbf{x}$,
$\Phi(\cdot)$ is the normal cumulative distribution function, *and*

Inspection of Eqn. 5.28 shows that the first term of the expression will be large where there is a high likelihood that the predicted objective function value ($\hat{y}(\mathbf{x})$) will be higher than the current best realised value (f_{min}^n), while the second term, will be large in areas of high uncertainty in the

metamodel prediction. Significantly, since there is no uncertainty in the metamodel at known data points, the Expected Improvement at these locations is 0.

Watson & Barnes WB1 criteria

Sasena et al. (2000) investigated alternative infill criteria to the traditional Expected Improvement approach, and specifically the criteria proposed by Watson and Barnes (1995) for locating extremes for geostatistical applications. One of the criteria proposed by the authors, was the so-called $WB1$ criteria, which was described by Watson & Barnes as a search criteria for locating *threshold-bounded extremes* (i.e. locating regions, if they exist, in which a pre-specified value is exceeded).

In the context of objective function optimization, Sasena et al. (2000) specified the threshold to be the improvement of over the current best objective function, in which case the $WB1$ can be defined as:-

$$WB1 = \Phi\left(\frac{f^n_{min} - \hat{y}(\mathbf{x})}{s(\mathbf{x})}\right) \tag{5.29}$$

where:-

$\Phi(\cdot)$, f^n_{min}, $\hat{y}(\mathbf{x})$ and $s(\mathbf{x})$ are as defined previously.

One method of understanding the significance of the $WB1$ criteria in relation to the original Expected Improvement criteria as developed by Jones et al. (1998), is by generalising the Expected Improvement criteria. Following Sasena et al. (2002), the Improvement of the objective function can be redefined as:-

$$I^g = \max[0, (f^n_{min} - Y)^g] \tag{5.30}$$

where g is a positive integer.

The closed form expression for the Expected Improvement (Eqn. 5.28) can then be re-derived as a recursive formula given by:-

$$E(I^g) = \begin{cases} s^g(\mathbf{x}) \sum_{k=0}^{g} (-1)^k \left(\frac{g!}{k!(g-k)!}\right) (f'^n_{min})^{g-k} T_k & \text{if } s > 0 \\ 0 & \text{if } s = 0 \end{cases} \tag{5.31}$$

where:-

$f'^n_{min} = \left(\frac{f^n_{min} - \hat{y}(\mathbf{x})}{s(\mathbf{x})}\right)$, *and*
$T_k = -\phi\left(f'^n_{min}\right)\left(f'^n_{min}\right)^{k-1} + (k-1)T_{k-2}$.

starting with $T_0 = \Phi\left(f'^n_{min}\right)$ and $T_1 = -\phi\left(f'^n_{min}\right)$.

As discussed by Sasena et al. (2002), the effect increasing g in Eqn. 5.31 is to bias the infill criteria towards a more global search, while lower values result in a more local searching criteria.

Since setting $g = 1$ and 0 in Eqn. 5.31 results in Equations 5.28 & 5.29 respectively, it can be understood that the original Expected Improvement represents a relatively balanced search criterion (between local and global search bias), while the $WB1$ criteria of Watson & Barnes represents a significantly more local search criteria.

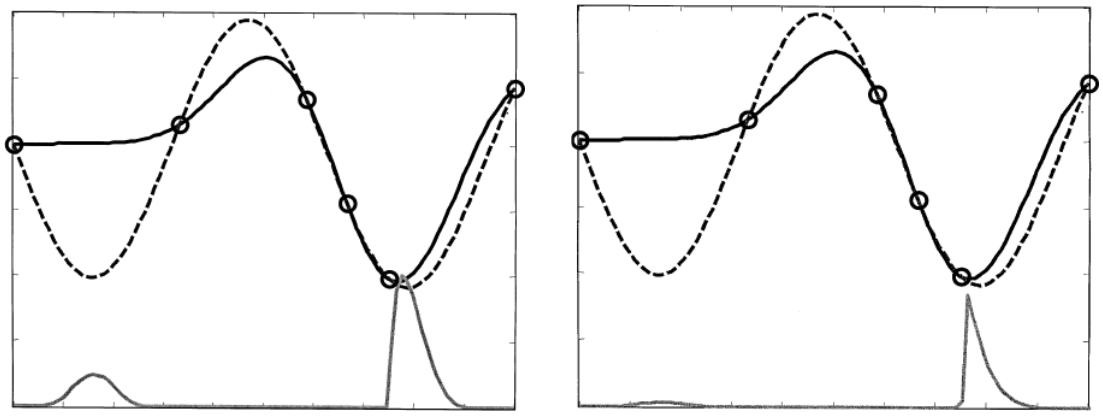

(a) Expected Improvement ($g = 1$) (b) Watson & Barnes WB1 ($g = 0$)

Fig. 5.8: True (dashed), *DACE* (black) and Expected Improvement (grey) curves for the 1-dimensional Test Function # 1 of Sasena (2002) corresponding to EI_1 ($g = 1$) & $WB1$ ($g = 0$) infill search criteria of Jones et al. (1998) and Watson and Barnes (1995) respectively. Known datapoints are marked by ∘. [Reproduced from Sasena et al. (2002)]

In this investigation then, a combination between the balanced local-global search bias of the EI_1 criteria and the local search bias of the WB_1 criteria was used to optimize the various objective functions considered. Firstly, the EI_1 criterion was used to establish the location of the global optimum for each objective function, and thereafter, the WB_1 criterion was used in an attempt to locate the vicinity of the true function optimum within the region of the global optimum, by searching for the location of extremes of the objective function values within the region of the global optimum.

The total number of *EGO* iterations used for each search criteria was based on the number of iterations used for the optimization of various test objective functions with the same number of dimensions as the endwall optimization problem considered in this thesis (i.e. $k = 12$). In addition, traces of the current best *true* objective function value were plotted against the number of iterations used in each phase of the endwall generation process, which gave a qualitative indication of the degree of convergence of each *EGO* phase.

Similar to the so-called *Cool* approach of Sasena (2002) then, the complete optimization procedure used in this investigation comprised of:-

Table 5.3: *EGO* optimization schedule

Iteration	*g value*
1 - 150	1
150 - 300	0
≥ 300 [a]	0

[a] if required

5.4.2 Searching the *DACE* model: Differential Evolution

In the original *EGO* procedure, a Branch & Bound-type (B&B) algorithm (Land and Doig (1960)) was used to maximize the Expected Improvement, which required the identification of appropriate lower (y^L) and upper (s^U) bounds on the objective function prediction ($\hat{y}(\mathbf{x})$) and the root mean squared error ($s(\mathbf{x})$) respectively. These estimates were then subsequently substituted into Eqn. 5.28 whereafter the Expected Improvement could then be calculated. Although the original B&B methodology proposed by Jones et al. (1998) was sufficient for dealing with the multimodality of the *ISC* function, as well as guaranteed optimality of the *EI* criterion, the process of constructing y^L and s^U for the predictor and the mean square error was found to be difficult and also entailed the solution of 2 additional sub-optimization problems in addition to the solution of the *ISC* problem. In addition, the authors did not report on the use of their approach in problems which included constraints or in situations where disconnected regions of feasibility in the parameter and objective function space existed[6].

As a result of the above, in this investigation, the above-mentioned approach was replaced with the *Differential Evolution* algorithm of Storn and Price (1995), which was the same algorithm discussed previously for the solution of the *MLE* optimization problem. Although this approach does not *guarantee* optimality of the so-called *ISC* function, as discussed previously, the *DE* algorithm is a well known global optimizer and one which can easily be applied to objective function spaces with disconnected regions of feasibility and constraints other than simple variable constraints. In addition, in order to prevent the premature convergence of the *DE* routine to a local optimum, or in the large flat portions of the *ISC* function space (see Fig. 5.8), the routine was programmed to complete a mandatory 1000 iterations of the *ISC* function, before checking for convergence to a maximum point.

Once again, for a review of the Differential Evolution algorithm, the reader is directed to Section 2.6.3.

5.4.3 Test examples

In order to assess the ability of the optimization procedure implemented for this investigation, the procedure was tested on a number of test cases for which the global (as well as various local optima, if applicable) optimum were known. The test functions were selected specifically to evaluate the routine's ability to deal with a number of different scenarios which were identified as being potentially related to the endwall design problem at hand (especially since for the optimization of so-called 'black-box'

[6] Which may have occurred in this investigation as a result of the constraints applied to the endwall geometry parameters

systems such as that encountered in this investigation, the specific nature of the objective function hypersurface cannot easily be known *a priori*), including:-

- 2 *unimodal* functions designed to validate the routine with an initial case (**DeJong #1 (2D)**) for which the vicinity and convergence to the global optimum is trivial, as well as a more difficult case in which locating the global optimum is again trivial, but for which convergence to the exact location of the optimum can be difficult (**Rosenbrock's valley (2D)**). In addition, in order to test the routines ability to deal with both cases under conditions more representative of the problem at hand, each case was repeated in the same dimensional space as that of the endwall problem (**DeJong #1 (12D), Rosenbrock's valley (12D)**)
- a set of 2 additional test functions (**Michaelwicz's function, Ackley's function**) selected primarily as a result of their *multimodal* characteristics, for which **Michaelwicz's function (2D)** was used to present a deceptive case in which the general objective function topology provides very little assistance to the identification of the region of global optimality, and **Ackley's function (2D)**, which is characterised by a large number of local optima which surround the global value. Again, both functions were extended to dimensions more representative of those of the problem investigated in this thesis (**10D**[7]**/12D** respectively)

A summary of the test cases and objectives of each approach are included in Table 5.4.

Table 5.4: Summary of *DE*-based *EGO* optimization test cases

Type	*Test case*	*Function*	*Objective*
Unimodal			
	1	DeJong's function #1 (2D)	Adaptation to increased dimensionality
	2	DeJong's function #1 (12D)	
	3	Rosenbrock's valley (2D)	Convergence to difficult global optimum
	4	Rosenbrock's valley (12D)	
Multimodal			
	5	Michaelwicz's function (2D)	Optimization of deceptive function
	6	Michaelwicz's function (10D)	
	7	Ackley's function (2D)	Optimization of hugely multi-modal function
	8	Ackley's function (12D)	

Metrics

As shown in Table 5.5, a selection of metrics, as originally implemented by Sasena et al. (2002) were implemented in order to characterise the performance of the optimization routine for each of the test cases. In order to provide a better understanding of their significance, a brief summary of each metric is included below:-

[7] Michalewicz's function was tested in 10-dimensional space due to a lack of information relating to its true optimum at 12D

$f(\mathbf{x}^*)$ - true function minimum
The true *global* minimum of the test function.

$f(\hat{\mathbf{x}}^*)$ - predicted function minimum
The *predicted* minimum of the test function as returned by the optimization routine.

f_n - no. of function evaluations (total)
The *total* number of function evaluations undertaken by the optimization routine as part of the test optimization, recorded as a fraction of the total allowed for each test case. A total of 20 iterations (function evaluations) were allowed for each 2D case, while for the higher dimensional cases, the full two-step procedure as discussed in Section 5.4.1 was implemented.

$x_{1\%}$ - no. of function evaluations required to sample within 1% of true $\mathbf{x}^*$
The number of iterations required before the test function was sampled by the optimization routine within 1% of the true optimum location. The distance between each sample vector and the location of the true optimum location, was calculated on a *component-wise* basis, and was only considered to meet the 1% criteria once **all** components of the vector difference were less than 1% of the total sample domain size. As such, this metric presents a relatively challenging criteria to the optimization routine since a high dregree of accuracy is required in *all* the problem spatial dimensions.

$f_{1\%}$ - no. of function evaluations required to sample within 1% of true $f(\mathbf{x}^*)$
Similarly, the $f_{1\%}$ metric records the number of iterations required by the optimization routine to sample the test function within 1% of its true minimum value, where the metric is calculated using the difference between the maximum and minimum test function values for the given search space.

x_* - distance between the predicted and true optimum points
The distance between the final predicted optimum point and true function optimum calculated as the Euclidean[8] distance between the two points.

DeJong 2*D*/12*D*

For the 2D case, the DeJong test function #1 presented little difficulty for the optimization routine. In fact, the predicted optimum ($f(\hat{\mathbf{x}}^*)$) was estimated to within 2 decimal places, within a single algorithm iteration. Correspondingly, the $f_{1\%}$ and $x_{1\%}$ metrics were also met within a single iteration, with the norm of the distance between the true and predicted optimum points approximately ~ 0.

For the higher dimensional case (i.e. 12D), the optimization algorithm showed very good convergence to the test function optimum, and as such, required only the use of a single additional iteration within the first step (i.e. the EI_1 step) of the search before the function was sampled to within the

[8] i.e. 2-norm

Table 5.5: Summary of test example results

Type	*Test case*	$f(\mathbf{x}^*)$	EI_1		WB_1		*Metrics* [a]		
			$f(\hat{\mathbf{x}}^*)$	f_n	$f(\hat{\mathbf{x}}^*)$	f_n	$x_{1\%}$	$f_{1\%}$	x_* [b]
Unimodal									
	DeJong (2D)	0	0.00	$^1/_{20}$			1	1	0.00
	DeJong (12D)	0	0.16	$^2/_{150}$			2	2	0.41
	Rosenbrock (2D)	0	0.24	$^{20}/_{20}$			-	1	0.40
	Rosenbrock (12D)	0	28.12	$^{150}/_{300}$	14.76	$^{300}/_{300}$	-	2	3.18
Multimodal									
	Michalewicz (2D)	-1.80	-1.80	$^{14}/_{20}$			9	10	0.00
	Michalewicz (10D)[c]	-9.66	-6.32	$^{150}/_{300}$	-7.77	$^{300}/_{300}$	$^{n}/_{a}$	-	$^{n}/_{a}$
	Ackley (2D)	0	0.10	$^{20}/_{20}$			11	16	0.03
	Ackley (12D)	0	11.50	$^{150}/_{300}$	10.27	$^{300}/_{300}$	-	-	10.93

[a] as implemented Sasena et al. (2002)

[b] x_* is defined as the 2-norm of the difference between the true and predicted optimum points, $x_* = \|\mathbf{x}^* - \hat{\mathbf{x}}^*\|_2$

[c] optimal vectors (i.e. $\mathbf{x}^*$) are not given for Michalewicz's function in higher dimensions

tolerances specified for the various metrics. The error in the final predicted function optimum was only ~ 0.16 and the solution vector error (x_*), was approximately ~ 0.41.

Rosenbrock 2D/12D

As indicated previously, Rosenbrock's test function presents a case in which locating the general region in which the global optimum is contained is trivial, while convergence to the exact optimum is difficult.

For both test cases (2D & 12D), the maximum number of permissible iterations (20 & 300 respectively) were used by the optimizer. For the 2D case specifically, a best predicted optimum value of 0.24 with an error in the predicted optimum location (x_*) of approximately ~ 0.40. Inspection of 2-dimensional plots of the test results showed that although the true function was sampled consistently within the valley within which the global optimum point was located, as is common for this test function, some difficulty in locating the position of the global minimum was encountered.

Similar behaviour was noted for the higher dimensional case. Again, although the maximum number of iterations were utilised by the procedure, a best predicted function value of 14.76 was returned after 300 iterations, without the true function being sampled within 1% of the true function value ($f_{1\%}$) or location ($x_{1\%}$). The corresponding error between the true and predicted optimum location (x_*) was approximately ~ 3.18 which represented an error in location of approximately $\sim 22\%$ when compared to the overall size of the search domain.

Michalewicz 2D/10D

The Michalewicz test function is formulated with a tunable parameter m, which determines the steepness of the network of valleys which traverse the function space. For this test, this parameter was set to the recommended value of $m = 10$, which resulted in a relatively steep sided system and therefore

a reasonably challenging case.Although not as efficient as the 2-dimensional DeJong test case, for this case the optimizer returned a predicted optimum function value and location to within 2 decimal place accuracy while requiring only 14 *EGO* iterations. Additionally, the algorithm was found to meet the $x_{1\%}$ and $f_{1\%}$ criteria within 9 & 10 iterations respectively.

As with the previous test function, the higher dimensional case presented a slightly greater challenge for the optimization routine, where predicted optimum function values of -6.32 and -7.77 were returned after the initial (EI_1) and final (WB_1) optimization steps respectively. As indicated previously, the location of the global optimum point for higher dimensional cases is not given, and so the corresponding value of the $x_{1\%}$ was not computed.

Ackley 2*D*/12*D*

As indicated previously, Ackley's test function is a massively multimodal test case which is characterised by a single global optimum surrounded by a large number of smaller local optima.

Once again for the lower dimensional case (i.e. 2D case), the optimizer performed relatively well, with a final predicted optimum value of approximately ~ 0.1 in comparison to the true function minimum of 0 and requiring a total of 11 & 16 iterations to meet the $x_{1\%}$ & $f_{1\%}$ criteria respectively. The final distance between the predicted and given optimum points (i.e. x_*) was again small (~ 0.03).

The higher dimensional case once again provided a more difficult test for the optimization routine, with the maximum number of iterations for both the EI_1 & WB_1 steps being used without either of the $x_{1\%}$ of $f_{1\%}$ metrics being met. The final predicted optimum for the test function was estimated to be 10.27, which although was not particularly close the true value (i.e. 0), still represented a decrease in the overall average starting values used for the optimization by a factor of 2.

Critique of optimizer performance

While the results of test optimizations showed that in a number of cases, not all of the target metrics used to characterise the performance of the optimizer were met, the performance of the routine was deemed acceptable for further use within the endwall design procedure, based on the following observations:-

- In lower dimensions, the routine performed exceptionally well, meeting all the specified criteria set for it without requiring in any cases even the switch to the more locally searching criteria to be made
- While in the higher dimensions, in all cases but one, the routine was noted to use all the available iterations for both optimization steps, the errors between the actual and final predicted optimum points (i.e. x_*) for all cases (with the exception of the Ackley 12D test case) were small, indicating that despite the substantial increase in dimensionality, the routine was still able to locate the approximate vicinity of the true optimum reasonably well
- Finally, with the exception of the DeJong test function, **all** the test functions used in characterisation of the proposed optimization procedure represented test cases well-known for presenting non-trivial difficulties to candidate optimization algorithms even in relatively low dimensional

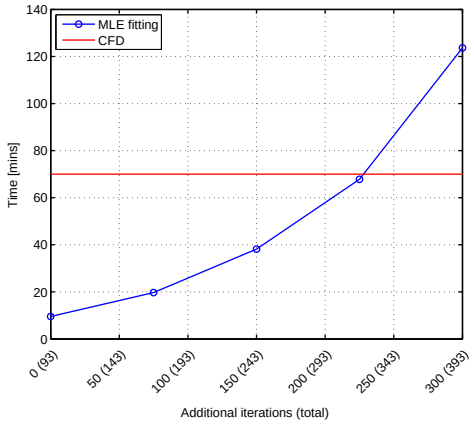

Fig. 5.9: Comparison of time requirements for *DACE* model parameter tuning with database size

Table 5.6: Temporal requirements of *DACE* model fitting & (CFD) simulation sub-problems

Iterations	*Total database size*	*Time*	*Predicted optimization time*
0	(93)	9.52 min	$\sim$ 0 days
75	(168)	19.73 min	$\sim$ 4.3 days
150	(243)	38.15 min	$\sim$ 9.2 days
225	(318)	67.82 min	$\sim$ 15.6 days
CFD	-	**70.00 min**	-
300	(393)	123.68 min	$\sim$ 24.2 days

space, and so the excellent performance of the routine for the 2D cases, as well as its reasonable performance for the higher dimensional cases, was pleasing

5.4.4 Stopping criteria

Queipo et al. (2009), in the process of formulating an assessment criteria for determining the potential benefit of additional iterations of surrogate-based optimization attempts, found that in many cases, attempts had been truncated after a predetermined number of iterations with very few being allowed to proceed to full convergence. This was because, in the majority of circumstances, the computational costs associated with additional cycles of the optimization routines were prohibitively expensive.

As an example, Jones et al. (1998), in their original work, suggested that the *EGO* search procedure be stopped when the value of the maximum *EI* as returned by the *ISC* maximization procedure was less than 1% of the lowest actual objective function value, indicating a very small chance of improvement in the true objective function with additional iterations. While this was feasible with the majority of their lower dimensional test examples, when applied to a higher dimensional test function, the overall computational expense associated with the fitting of the underlying surrogate model and maximizing of the *ISC* criteria, meant that the progression of the algorithm was too slow to be run to full convergence.

More recently, Forrester et al. (2007), limited the number of iterations used for the design of a transonic aircraft wing to a total of 200, at which point the computational cost of tuning the metamodel hyperparameters became equivalent to that used for the actual CFD simulations.

Table 5.7: Summary of stopping rules used in various investigations ordered by problem dimensionality

Investigator(s)	*Problem dimension*	*Surrogate*	*Iterations*
Verstraete et al. (2012)	5D	ANN	17[a]
Jeong and Obayashi (2005)	10D	DACE	5
Jeong et al. (2006)	10D	DACE	6 (43)[b]
Goinis et al. (2013)	11D	DACE / ANN	300
Verstraete (2008)	15D	ANN / RBF	30
Chahine et al. (2012)	23D	ANN	89
Deng et al. (2013)	24D	DACE	50
Jeong and Obayashi (2005)	26D	DACE	26
Van den Braembussche et al. (2012)	31D	ANN	50

[a] The CFD model used by Verstraete et al. (2012) consisted of $\sim 10M$ cells requiring that the number objective function evaluations be limited to a relatively small number

[b] Jeong et al. (2006) solved a multiobjective *EGO* (*EGOMOP*) optimization problem in which each iteration consisted of multiple objective function evaluations

In view of the above, the total number of algorithm iterations used in the optimization of the rotor endwalls in this investigation was based on the greatest number which could be performed within a realistic time frame. As was the case with Forrester et al. (2007), the major costs associated with the optimizations performed in this investigation were associated with the *DACE* model fitting procedure, as well as the solution of CFD simulations used as part of the objective function evaluation. While the computational cost of the CFD simulations were independent of the total number of iterations undertaken by the algorithm, the costs associated with the model fitting subproblem are directly related to the current iteration number as a result of the coupling between the total number of algorithm iterations and the corresponding size of the surrogate model database ($\mathbf{X}_{database}$).

Figs. 5.9 and Table 5.6 show the temporal requirements associated with both the *DACE* model fitting and CFD subproblems, where it can be seen that the total amount of time to fit the *DACE* model begins to exceed that of the CFD after approximately ~ 225 iterations and a predicted total optimization time of approximately ~ 15 days. Additionally, Table 5.7 provides a summary of the problem dimensionality and total number of design iterations used by various other researchers for similar problems.

Based on the results of the above surveys, a target number of 300 iterations were selected for the optimization of each rotor endwall. Although this was somewhat more than similar investigations (Table 5.7) and incurred a corresponding increase in overall optimization time, it was determined that the increase in optimization time and effort was reasonable given the need to produce designs with as high a degree of optimality as possible.

5.5 Endwall parametrisation

Overview

As indicated by Sonoda et al. (2009), the parametrisation of the geometry to be optimized is a crucial part of the optimization procedure since (along with any constraints), it determines the set of all possible designs as well as the topology and quality of the design space. In addition, the authors suggested that any proposed parametrisation meet the following criteria:-

- *flexibility* - the parametrisation should be flexible enough to represent a wide range of different designs,
- *compactness* - the number of parameters used in the parametrisation should be as low as possible in order to allow for reasonable convergence of the chosen optimization algorithm, *and*
- *locality* - variations in a (single) parameter should result in only *local* variations of the model geometry and *not* the global model shape

In the development of the parametrisation used in this investigation, attempts were made to meet all three of these conditions, although, the generality (i.e. flexibility) of the parametrisation was - *by design* - restricted to a smaller design space than those which have been used in some other investigations. This was done intentionally as, as shown by other authors (such as Bagshaw et al. (2008a), Ingram et al. (2005), Vazquez and Fidalgo (2010)), it is relatively easy to design poorly performing endwalls if overly complex or aggressive design features are allowed to propagate into the final design.

The parametrisation used in this investigation was based on the method of Harvey et al. (2000) and Hartland et al. (2000) discussed previously, although the parts of it (i.e. the reduced periodicity requirements, see below) were modified for the current work.

In their parametrisation, Harvey et al. (2000) constructed their endwall through the manual, superposition of the harmonics of a Fourier series, in which the adjustable parameters were the coefficients of the individual sinusoidal terms. As discussed by the authors, this method was used mainly as a result of the large number of geometries which could be generated using only relatively small number of harmonic terms but also because the periodicity of the function helped to preserve the blade passage flow area which was important for compressible flows. In the actual work, the number of terms used in the series was limited to the first 3 harmonics only, as this was considered enough to provide variation in the geometry required. In the subsequent investigations of Brennan et al. (2001) & Harvey et al. (2002), the number of terms used was reduced to 0^{th} and 1^{st}-order harmonics only, in order to reduce the size of the design space to one which was easier to work with. This was also the case in the work of McIntosh et al. (2011) & Hilfer et al. (2012), who used the same parametrisation but with only the 1^{st}-order harmonic (setting the 0^{th}-order component to 0), as a result of the geometrically complex designs which resulted from the use of higher order harmonics in the previous attempt (MacPherson and Ingram (2010)).

If the 0^{th} term of the so-called 'Fourier series' parametrisation of Harvey et al. (2000) discussed previously is set to zero, Eqn. 2.5 can be represented without loss of generality by:-

$$\delta r_j(\theta) = \sum_{n=1}^{k} c_n \sin\left(\frac{n\pi\theta}{P} + \Psi_n\right) \tag{5.32}$$

where:-

δr_j is the local perturbation height of curve j,
θ is the circumferential coordinate,
n is the current harmonic,
k is the total number of harmonics included in the curve,
c_n is the amplitude of the curve,
P is the blade pitch, *and*
Ψ_n is the phase of the curve.

The benefit of Eqn. 5.32 is that the amplitude (i.e. height) as well as the phase of each harmonic is expressed explicitly, rather than as a combination of the variables. This, in turn, reduces the interaction (or *epistatis*) between the variables which can make the system more amenable to being solved using simpler methods (Haupt and Haupt (2004)).

Parametrisation used in this investigation

For these reasons, in this investigation therefore, the endwall parametrisation was based on the form of Eqn. 5.32, and was defined by:-

$$\delta r_j(\theta) = c \sin\left(\frac{n\pi\theta}{P} + \left(\Psi_1 + \sum_{i=2, i\neq 1}^{j} \psi_i\right)\right) \tag{5.33}$$

where:-

δr_j is the local perturbation height of curve j,
θ is the circumferential coordinate,
c is the amplitude of the curve,
n is the period of the curve,
P is the blade pitch,
Ψ_1 is the phase of the curve 1,
ψ_i is the phase shift of curve i.

The final height of the endwall surface above the machine axis was then given by:-

$$r_j(\theta) = R_0 + \delta r_j(\theta) \tag{5.34}$$

where:-

$r_j(\theta)$ is the endwall height,
R_0 is the mean turbine hub radius, *and*
$\delta r_j(\theta)$ is the local endwall perturbation height given by Eqn. 5.33

In order to apply the parametrisation described above to the turbine rotor, the endwall surface was divided into four axial stations, with the basic curvature of the endwall in the circumferential direction at each successive station being defined by Eqn. 5.33. In addition, two additional sets of annular curves were specified at the beginning and end of the contoured region, in order to return the endwall geometry to that of a cylinder outside of the contoured region.

In the axial direction, the endwall curvature was defined by non-uniform rational B-spline (*NURBS*) curves. As indicated by Harvey et al. (2000), in comparison to other parametric curves, B-splines display greater local response to changes in control point location, and therefore are advantageous at modelling the endwall curvature where the amplitude of the endwalls change rapidly. However, while this behaviour is beneficial for defining rapid amplitude changes, this can lead to 'drooping' of the axial curvature between the curves defining the endwall curvature of a similar amplitude in the circumferential direction if the curves are spaced too far apart.

In order to reduce this effect, 3 additional intermediate *'driven'* curves were located between the non-annular interior *'driving'* curves (i.e. those curves under direct control of the optimization algorithm). The constants defining the *driven* curves, were calculated as the numerical average of their two adjacent *driving* curves, and therefore promoted the smooth transition of the endwall in the axial direction between successive *driving* curves.

The formulations for the coefficients of the additional curves, 2_a, 3_a and 4_a are given in Table 5.8 below.

Table 5.8: Driven curve parameters

Curve number	*Amplitude* (c_n)	*Period* (n_n)	*Phase shift terms* (ψ_i)
2_a	$\frac{(c_2+c_3)}{2}$	$\frac{(n_2+n_3)}{2}$	$\frac{\sum_{i=1}^{1}\psi_i+\sum_{i=1}^{2}\psi_i}{2}$
3_a	$\frac{(c_3+c_4)}{2}$	$\frac{(n_3+n_4)}{2}$	$\frac{\sum_{i=1}^{2}\psi_i+\sum_{i=1}^{3}\psi_i}{2}$
4_a	$\frac{(c_4+c_5)}{2}$	$\frac{(n_4+n_5)}{2}$	$\frac{\sum_{i=1}^{3}\psi_i+\sum_{i=1}^{4}\psi_i}{2}$

Summary

In total then, the complete three dimensional curvature of the endwall within the contoured region was fully described by a 12-dimensional vector, $\mathbf{x}$, where:-

$$\mathbf{x} = \begin{bmatrix} x_1 \\ x_2 \\ x_3 \\ x_4 \\ x_5 \\ x_6 \\ x_7 \\ x_8 \\ x_9 \\ x_{10} \\ x_{11} \\ x_{12} \end{bmatrix} = \begin{bmatrix} c_1 \\ n_1 \\ \Psi_1 \\ c_2 \\ n_2 \\ \psi_2 \\ c_3 \\ n_3 \\ \psi_3 \\ c_4 \\ n_4 \\ \psi_4 \end{bmatrix} \tag{5.35}$$

where:-

$c_{1,2,3,4}$ are the amplitudes of each curve,
$n_{1,2,3,4}$ are the periods of each curve,
Ψ_1 is the phase of curve 1, *and*
$\psi_{2,3,4}$ are the phase shifts of curves 2, 3 and 4 respectively with respect to Ψ_1

As a result of the parametrisation selected for this investigation as discussed above, the endwalls produced in this study were expected to take on the same general (and familiar) 'hump-and-dip' configuration as those created by a number of researchers previously. This however, was not of particular concern, as the intention of this work was to determine the *effectiveness* of the various objective functions used in the design of each endwall, rather than to investigate new endwall parametrisations. In addition, an inspection of Eqn. 5.33 indicates that the manipulation of the optimization variables, may be described as having the following effects on the final character of each endwall:-

1. the location of the 'hump' and 'dip' in the circumferential direction within the blade passage is determined by the *phase angle*, Ψ_1, of the first curve (curve 1),
2. the initial amplitude of this hump is then defined by the constant c_1,
3. the subsequent amplitude and change in location of the hump peak are adjusted through parameters $c_{2,3,4}$ and the phase shift variables $\psi_{2,3,4}$
4. finally, control of the periodicity of each individual line, $n_{1,2,3,4}$, provides some control over the steepness of the transistion between the 'hump' and 'dip' features

In previous investigations in which sinusoidal type parametrisations have been used for defining the circumferential endwall curvature, the periodicity of the curves used was limited to a set of positive integers, which ensured that any positive perturbation in the local endwall height was balanced with a corresponding negative dip of the same magnitude in order to limit the changes to the throat area and hence mass flow changes through the machine. However, for the test case used in this investigation the mass flow through the turbine is set directly, and therefore would not be affected by any changes to the passage flow area (if they are present). Therefore, the introduction of the variables $n_{1,2,3,4}$ as optimization variables was not considered to be problematic. In addition, since in this parametrisation, the periodicity variables were allowed to vary as positive real numbers, this

also resulted in the possibility of producing a number of additional endwall geometries which have not been described before.

5.6 Design procedure: TurbineOpti

5.6.1 Database design

As part of the *DACE* procedure, an initial database of points (i.e. the set $\mathbf{X}$ of parameter vectors $\mathbf{x}$) and their corresponding vector of true objective function values ($\mathbf{y}$) are required, from which the initial metamodel surface is constructed. Once the model has been constructed, the first iteration of the *EGO* algorithm may be started.

Historically, the sample locations used for the construction of surrogate models of computer experiments were generated using traditional Design of Experiment (DoE) techniques.

Viana (2013) listed the principal differences between DoE's for physical and computer experiments as:-

- DoE's for physical experiments tend to be designed to deal with *non-deterministic* problems of a relatively *low* dimensional nature[9], while computer experiments tend to be *deterministic* and often involve *many* dimensions (i.e. many input variables)
- computer experiments are relatively more cheap to conduct than their physical equivalents and tend be utilised in investigations such as reliability assessments and design optimization where there is little previous knowledge and analysts are interested in exploring large design spaces requiring many function evaluations, whereas physical experiments are more expensive and are used when very little is known about the system (i.e. in the early phase of material development) and in the validation of final designs

As a result of the growing disparity between the needs of the physical and computer experimenters, and in particular as a result of the need for computer experimenters to model both local and global effects of large design spaces, techniques directed specifically at the needs of computer investigators were inevitably developed.

The most common DoE's for computer experiments are the so-called *space-filling* designs, in which the goal is to provide the most efficient coverage of the parameter (input) space for a given number of database points.

As an illustration of the above, Fig. 5.10 (a) shows the well known 2^3 full factorial (plus $\times 1$ centre point, n_{centre}) sampling plan for physical experiments on the unit cube (i.e. $n_{dim} = 3$), while (b) shows its space-filling equivalent.

Despite the presence of n_{centre}, Fig. 5.10 (b) is clearly more capable of capturing local details (i.e. local optima) of the modelled function *as well as to some extent, the global function trends.*

For this investigation, two space-filling methods were considered:-

[9] Usually due to cost

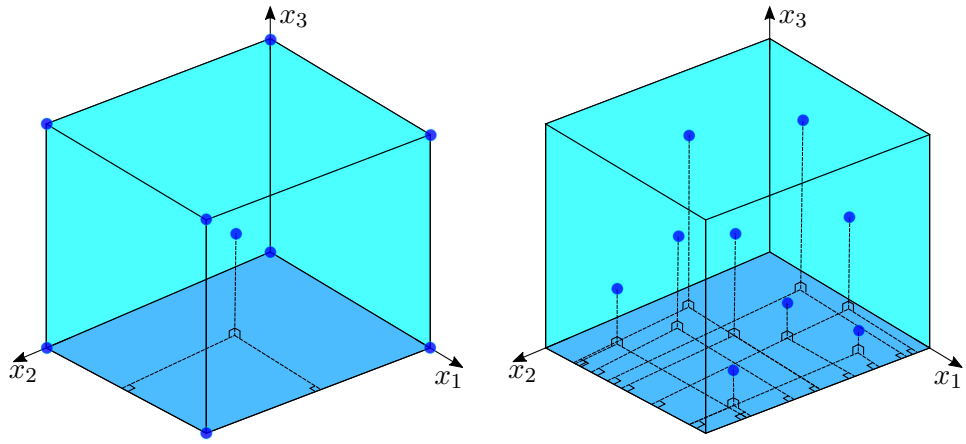

(a) 2^3 full factorial design (b) Space-filling design

Fig. 5.10: Comparison of traditional 2^3 full factorial (plus $n_{centre} = 1$) and a typical space-filling DoE for $k = 3$ & $n_{points} = 9$

1. the pseudo-random Halton sequence, *and*
2. the Latin Hypercube Sampling (*LHS*)

Halton sequence

Pseudo-random number sequences such as the Hammersley (Hammersley (1960)) and Halton (Halton (1960)) sequences are attractive space-filling methods as they are deterministic and easy to calculate. This is in contrast to other techniques (such as *LHS*, see below) in which some additional sub-optimization is required in order to produce a good design. In addition the point distribution produced by the quasi-random sequences are *uniform*, but *irregular* and with *low discrepancy* (i.e. do not produce points in close proximity to one another) (Simpson et al. (2001), Price et al. (2005)).

The so-called Halton sequence is based on prime numbers, and was calculated for this investigation using the algorithm of Price et al. (2005).

Briefly:-

- given a vector $\mathbf{x}_{prime} = [x_1, x_2, ..., x_k]$ of prime numbers, where $k = no.\ of\ dimensions$, and n_{points} is the required number of database points, (e.g. $\mathbf{x}_{prime} = [2, 3]$ for $m = 2$, and $n_{points} = 4$)
- the unit interval $(0, 1)$ is divided into sub-intervals $\frac{1}{x_1}$ & $\frac{1}{x_2}$, corresponding to $\frac{1}{2}$ & $\frac{1}{3}$ respectively
- the subsequent sets of sub-intervals $\left(0, \frac{1}{2}\right)$ & $\left(\frac{1}{2}, 1\right)$ and $\left(0, \frac{1}{3}\right)$ & $\left(\frac{1}{3}, 1\right)$ are then divided into further intervals corresponding to:- $\frac{1}{x_1^{ic}}$ & $\frac{1}{x_2^{ic}}$, (i.e. $\frac{1}{4}$ & $\frac{1}{9}$) where $ic = the\ current\ interval\ subdivision\ iteration$ (i.e. $k = 1, 2, 3...$)
- the algorithm is repeated until the *no. of intervals less 1* is equal to the number of points required, (i.e. $n_{points} = n_{intervals} - 1$) whereafter the upper values of each set of intervals are paired forming a set of coordinate points $\mathbf{X}_{database}$, i.e. $\mathbf{X}_{database} = \left[\left(\frac{1}{2}, \frac{1}{3}\right), \left(\frac{1}{4}, \frac{2}{3}\right), \left(\frac{3}{4}, \frac{1}{9}\right), \left(\frac{1}{8}, \frac{4}{9}\right) ...\text{etc}\right]$

Latin Hypercube Sampling

Latin Hypercube Sampling (*LHS*) is a further well known space-filling technique which was designed especially for use with computer experiments and can be seen as an extension of so-called *Latin Square* sampling into k-dimensional space (McKay et al. (1979)). In the original work, the method was compared to two other techniques (*random* and *stratified random* sampling), and was to found to perform favourably for modelling a fluid dynamics code in which the blowdown depressurisation of a straight pipe was modelled.

As discussed by the authors, the method was based on the same reasoning as that of stratified sampling (which ensures each portion of the sample space ($\mathbf{S}$) is sampled), however *LHS* additionally ensures that the sampling plan is stratified on all of its dimensions (Forrester et al. (2008)).

In short, an *LHS* design may be constructed by:-

- dividing the *range* of each input variable into N strata of equally marginal probability $1/N$, from each of which 1 sample is then taken
- each of the samples is then matched to another in a random fashion to form the coordinates of the overall DoE sample point

As a means of illustration, Figs. 5.11 (a) & (b) show *random* and *optimized LHS* sampling plans on the unit square with individual dimensions $\mathbf{x} = [x_1, x_2]$ respectively. Whereas in Fig. 5.11 (a), the coordinates of each of the sample points are selected at random from the *entire* range of each component, in *LHS*, the ranges of each component (x_1, x_2) are divided into N strata of equal probability from which a random sample is then drawn. Each strata sample is then paired at random with one other, to form the coordinates of the overall sample point.

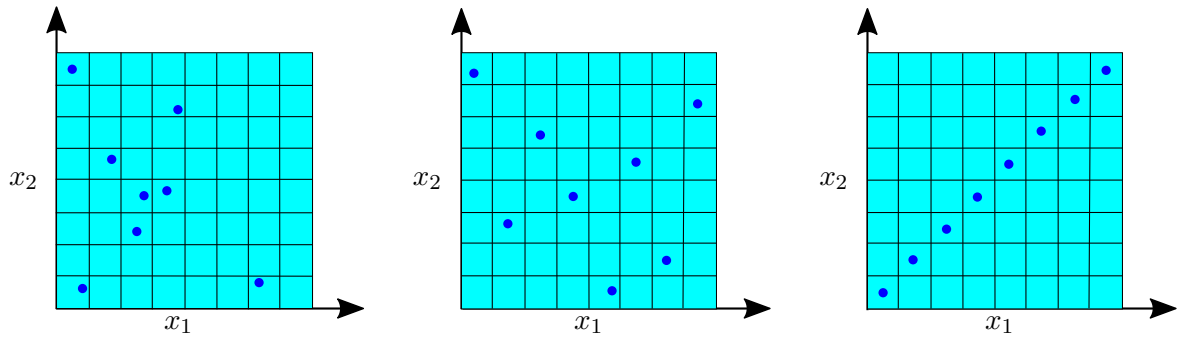

(a) Random sampling (b) *Optimized LHS* design (c) *Non*-optimized *LHS* design

Fig. 5.11: Comparison of random and optimized & non-optimized *LHS* database designs on the unit square (i.e. $n_{dim} = 2$)

Because of the random pairing of in the construction of the various sample point coordinates *LHS*, despite a guarantee that all points will be stratified, the approach *does not* guarantee the resultant design will be adequately space-filling. This is demonstrated in Fig. 5.11 (c), where despite the plan being a valid *LHS* design, it exhibits very poor space-filling properties.

As a result of the potential scenario illustrated in Fig. 5.11 (c), significant effort has been invested in the optimization of *LHS* sampling plans. The optimization of a k-dimensional *LHS* design is a combinatorial problem with a search space of order $(n_{points}!)^k$, and therefore, as alluded to previously, the additional computational expense associated with producing an acceptable space-filling design can be significant (Viana (2013)).

Within the literature, a myriad of approaches have been used, including coordinate exchange, genetic algorithms, enhanced evolutionary algorithms, iterated local search and simulated annealing algorithms. In addition, as discussed by Forrester and Jones (2008) & Viana (2013), a number of different objective functions, including maximum entropy, potential energy and ϕ_p criteria, integrated mean square error (IMSE) and 1- and infinite-norm criteria, are used.

Database design for this investigation

Although, as discussed previously, the Halton sequence is capable of producing good space-filling designs at minimal cost, for higher dimensions it can be shown that the linear correlation between points exists. Upon extension to the number of dimensions required in this investigation (i.e. 12), a distinct correlation between database points was noted and therefore, despite the extra computational effort required, the *LHS* method was selected as the database design approach for this investigation.

In order to generate the points in the initial *DACE* database, an $(n \times k)$ where $k = 12$ matrix of data points was generated using the built-in MATLAB® function *lhsdesign.m*. Since *lhsdesign.m* produces *LHS* sampling plans on the unit hypercube, each function call to the *lhsdesign.m* was made from within a wrapper function (*lhsGen.m*), which then scaled the coordinates of each sample point in the design to the range allowed for each variable by the endwall parametrisation scheme (Table 5.9).

Table 5.9: Database variable scaling limits

Endwall variable	*Lower limit*	*Upper limit*
$c_{1,2,3,4}$	0	3.5
$n_{1,2,3,4}$	0.5	1
Ψ_1	-3.1416	3.1416
$\psi_{2,3,4}$	-0.7854	0.7854

lhsdesign.m provides two *LHS* optimization options which can be accessed by passing additional flags to the function. These include the optimization *'criterion'* flag which specifies the criterion used to adjudicate between successive designs during the optimization process, and the *'iterations'* which determines the number of optimization iterations to be used in the optimization procedure.

The *'criterion'* flag has two options:- *'maximin'* and *'correlation'*, which score competing designs according to the magnitude of the minimum distance between the two nearest sample points (thereby seeking to maximize the distance between points and steer the design towards a more space-filling design), and the correlation between points. Since it was considered more important in this investigation to produce the best space-filling design possible, the *'maximin'* criterion was used in the *LHS* design

optimizations. In addition, because of the relative lack of sophistication of the optimization method used by *lhsdesign.m* (optimization is achieved by creating an initial design, and then randomly generating and comparing a selection of successive designs to the original, replacing it where advantageous), a large number of iterations (specified using the *'iterations'* flag) corresponding to $(500 \times n)$ (where n was the number of datapoints in the requested), was used. For this investigation then, this meant approximately 60,000 *LHS* designs were evaluated with the best performing design returned for use in construction of the *DACE* model database.

Table 5.10: *lhsdesign.m* options

Parameter	*Value*
'criterion'	'maximin'
'iterations'	$500 \times n$

5.6.2 Database construction

The total number of sampling points included in the initial *DACE* database, was based on $n_{points} = 10k$ rule of thumb as suggested by Jones et al. (1998) (and used by various other authors such as Forrester et al. (2007, 2008), Haderlie and Crossley (2010)) where k is once again the number of dimensions of the problem. Therefore, the initial *DACE* model database was populated with a 120 sampling points $(\mathbf{x}_1, ..., \mathbf{x}_{120})$ and inputs (c_i, n_i, Φ_i), $(i = 1, ..., 4)$.

Once the database had been generated, the space-filling characteristics of the design were checked by visually inspecting the dispersion of points in 2-dimensional planes corresponding to each of the input variable pairs and confirming that in each instance, the variables were relatively evenly arranged. Figs. 5.12a to 5.12d show a sample of the final location of the database points for the first and last four dimensions (i.e. input variables). Thereafter, computational meshes for each endwall and corresponding flow solutions for each geometry were produced and the solutions for each sample point were then inspected to verify that each solution was adequately converged. Any unsuitable solutions were isolated and their corresponding input vectors were removed from the database[10].

In order to confirm that the final databases for each objective function were sufficiently accurate, as well as met the validity criteria discussed in Section 5.2.6, a *Leave-One-Out* cross-validation exercise was performed for each starting database, the principal results of which are summarised in Table 5.11 below. In addition, the full set of validation plots as discussed in Section 5.2.6 are included in Appendix C.

[10] In contrast to the removal of *dimensions* from an existing *LHS* design,in which case the DoE remains a true Latin Hypercube, removal of individual sampling points / input vectors from the database *does* mean the resulting design is no longer a true Latin Hypercube. The removal of the sampling points associated with the poorly converged therefore resulted in a reduced database which was not strictly an *LHS* design, however, as discussed the reduction in the database effectiveness was expected to be small

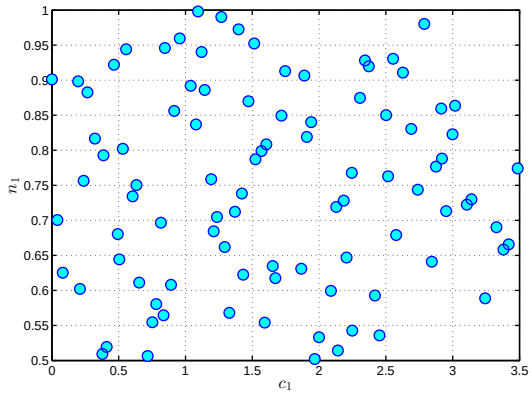

(a) $\mathbf{X}_{database}$ projected onto the $c_1 - n_1$ $(k = 1, 2)$ plane

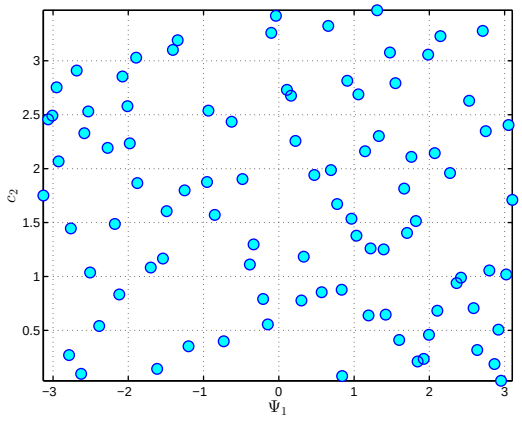

(b) $\mathbf{X}_{database}$ projected onto the $\Psi_1 - c_2$ $(k = 3, 4)$ plane

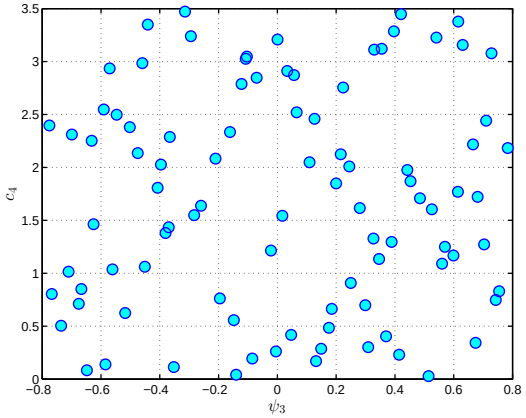

(c) $\mathbf{X}_{database}$ projected onto $\psi_3 - c_4$ $(k = 9, 10)$ plane

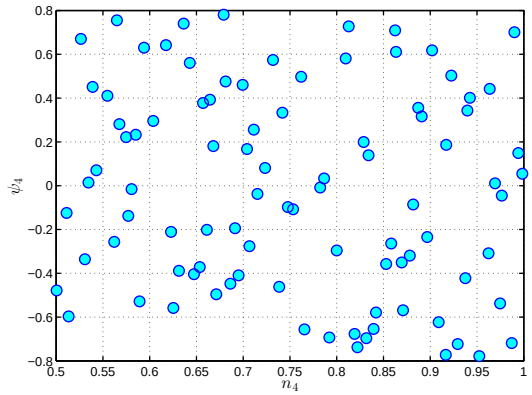

(d) $\mathbf{X}_{database}$ projected onto the $n_4 - \psi_4$ $(k = 11, 12)$ plane

Fig. 5.12: Sampling points of the final *LHS* design projected onto various planes

5.6.3 Endwall design routine

The endwall design routine, including the various geometry generation, discretization, simulation and optimization procedures as discussed previously, were implemented using the MATLAB® programming language and controlled via a custom graphical user interface (*GUI*).

An overview of the general procedural flow and program logic is shown in Fig. 5.13. Briefly, the principal steps of the procedure were:-

1. Turbine, CFD, endwall and metamodel (*DACE*) parameters were input into the routine
2. The starting database of sample points ($\mathbf{X}_{database}$) and a corresponding vector of objective function values ($\mathbf{Y}_{database}$) were loaded into the metamodel.
3. A corresponding set of *DACE* model optimized hyperparameters ($\boldsymbol{\theta}$) for the initial dataset were then generated by selecting an appropriate optimization algorithm and fitting the model using the

Table 5.11: Comparison of *LOO* cross-validated *RMSE*, *Max Error* & $Max\ R_{std}$ values for each objective function for the initial *DACE* model database ($\mathbf{X}_{database}$)

Flow metric	$n_{points,final}$	*Leave-One-Out cross-validation*			
		Mean	*RMSE*	*Max Error*	$Max\ R_{std}$
η_{tt}	93	20.52	0.55% (0.11)	1.38% (0.28)	2.43
C_{ske}	93	10.61	5.39% (0.57)	16.04% (1.70)	2.37
$C_{p0,rel}$	92	14.92	1.36% (0.20)	4.10% (0.61)	2.74
β_{dev}	93	5.02	4.08% (0.20)	13.13% (0.65)	2.82
$SKEH$	93	28.58	7.81% (2.23)	22.37% (6.39)	2.68
η_{de}	93	4.41	5.36% (0.23)	15.22% (0.67)	3.06
$C_{ske,1} + \beta_{dev,0.7}$	93	14.09	5.04% (0.71)	15.93% (2.24)	2.53
$C_{p0,rel,1} + \beta_{dev,0.7}$	92	18.40	1.25% (0.23)	2.50% (0.46)	2.60

Maximum Likelihood approach (Section 5.2.3). Although a selection of either a continuous Genetic Algorithm (GA) or Differential Evolution (DE) optimization scheme was possible in the software, all the designs produced in this investigation were produced using the Differential Evolution algorithm as described in Section 2.6.3. The settings for the both the *MLE* and *ISC* sub-problems are discussed in Section 5.6.4 below.

4. As discussed, each endwall design run was configured by setting a maximum number of iterations rather than by implementing a particular convergence rule, with an initial 150 iterations completed using the *EI1* criterion, whereafter an additional 150 iterations were completed using the *WB1* criterion.

5. Following the solution of the *ISC* subproblem, the meshing (**mesh.sh**) and CFD (**CFD.sh**) scripts were run. In both cases, the outputs of the mesher and CFD routines were checked to ensure that the mesh was valid mesh and met the basic quality criteria for the CFD solver and that the CFD routine had converged acceptably. If mesh or CFD errors were detected, the user was alerted and manual intervention was used to correct the specific error at hand, either by manually re-meshing the flow domain, or adjusting the CFD solver settings and re-running the solution manually.

6. Once an acceptable flow solution had been obtained, solution data at the rotor inlet (X2), exit (X3) and downstream 'mixed-out' (X4) measurement planes was exported to file and the data processed and the results screened again to confirm no spurious results were present.

7. Following the successful post-processing of the flow data, the input vector $\mathbf{x}$ corresponding to the endwall geometry analysed, as well as the value of the objective function vector were added to the model database

Table 5.12: Optimizer settings for the *MLE* optimization subproblem

Setting	*Value*
Population size (*popsize*)	48
Scaling factor (F)	0.8
Cross-over rate (Cr)	0.8
$Var_{hi/lo}$	10^2 / 10^{-12}
Min / Max iterations ($it_{min/max}$)	- / 3500

Table 5.13: Optimizer settings for the *ISC* optimization subproblem

Setting	*Value*
Population size (*popsize*)	48
Scaling factor (F)	0.8
Cross-over rate (Cr)	0.8
$Var_{hi/lo}$	as per Table 5.14
Min / Max iterations ($it_{min/max}$)	1000 / 5000

8. Thereafter, a new *DACE* model and hyperparameters corresponding to the augmented database was constructed and the *LOO* cross-validated fitting metrics recalculated to ensure that the model was valid.
9. Finally, since the stopping criteria for the procedure was based on the number of total iterations rather than a predefined convergence criteria, the procedure was stopped if the required number of iterations had been completed ($EI1 \rightarrow {}^{150}/_{300}$, $WB1 \rightarrow {}^{300}/_{300}$) in accordance with Table 5.3.

5.6.4 Optimizer settings

The specific settings used in conjunction with the Differential Evolution optimizer for the *MLE* and *ISC* optimization subproblems are given in Tables 5.12 & 5.13.

The settings were based on the recommendations given by Price et al. (2005).

5.6.5 Constraints

Previous experience in automated endwall design has shown that it is relatively easy to produce designs with significant (and sometimes unanticipated) geometric complexity. In addition, the pitfalls of so-called 'aggressive' contouring, in which large changes in endwall contour amplitudes are allowed, were shown by Ingram et al. (2005) to have the potential to result in poor actual endwall performance.

To avoid the pitfalls mentioned above, in conjunction with the relatively simple approach used to parametrise the endwall surface, a system of constraints was placed on the design vector components, intended to limit the design of endwalls to those which could be easily manufactured and used in the test rig with a relatively high degree of confidence.

Since the limits were applied to the design vector components (i.e. the individual endwall design variables) only, the constraints could be applied as a set of simple (variable) *boundary constraints*, with simple upper and lower bounds on each variable.

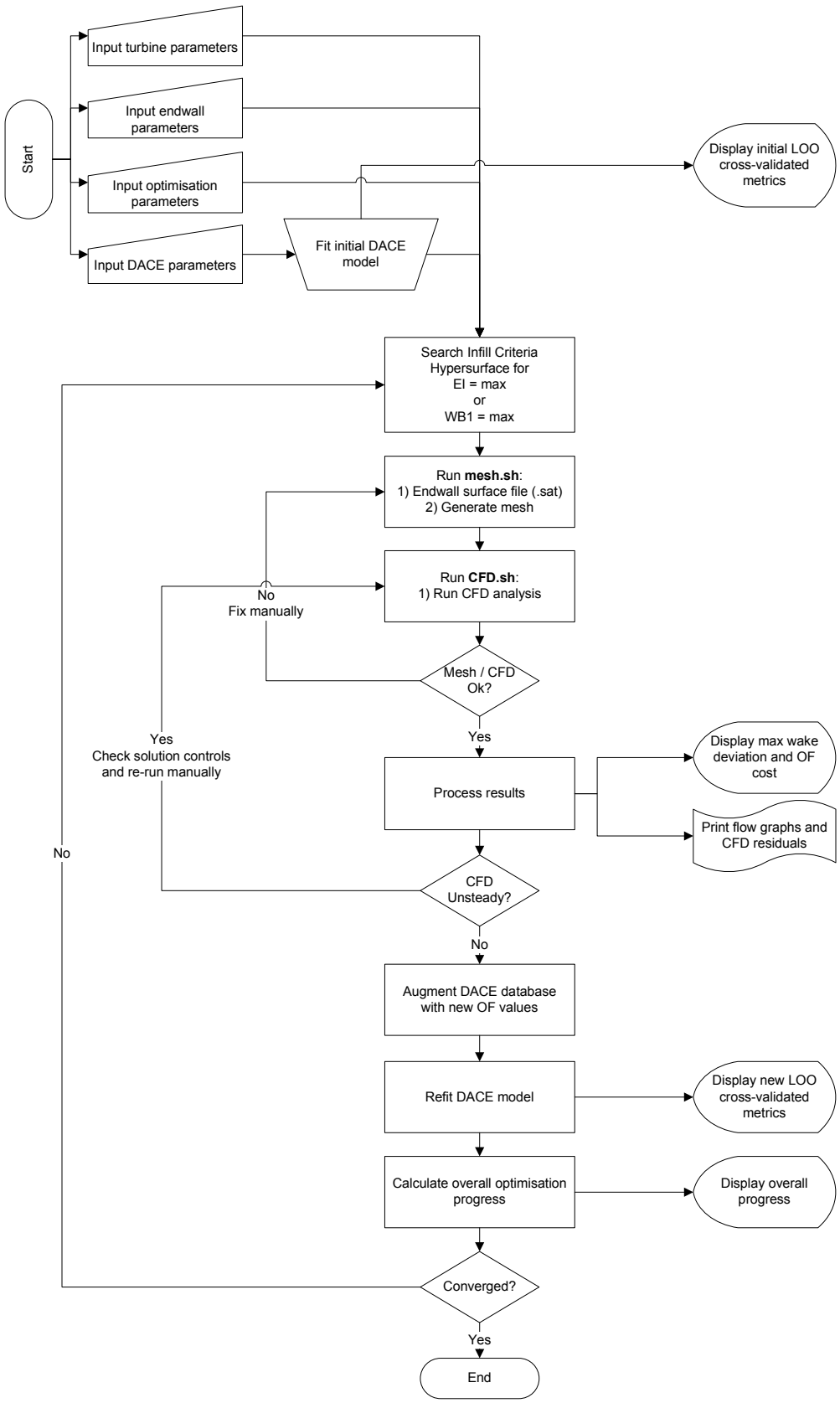

Fig. 5.13: Schematic of the TurbineOpti optimization procedure

Boundary

$$b_{e1} : c_1 \geq 0 \quad (5.36)$$
$$b_{e2} : c_2 \geq 0 \quad (5.37)$$
$$b_{e3} : c_3 \geq 0 \quad (5.38)$$
$$b_{e4} : c_4 \geq 0 \quad (5.39)$$
$$b_{e5} : c_1 \leq 3.5 \quad (5.40)$$
$$b_{e6} : c_2 \leq 3.5 \quad (5.41)$$
$$b_{e7} : c_3 \leq 3.5 \quad (5.42)$$
$$b_{e8} : c_4 \leq 3.5 \quad (5.43)$$
$$b_{e9} : c_2 - c_1 \geq -2 \quad (5.44)$$
$$b_{e10} : c_3 - c_2 \geq -2 \quad (5.45)$$
$$b_{e11} : c_4 - c_3 \geq -2 \quad (5.46)$$
$$b_{e12} : c_2 - c_1 \leq 2 \quad (5.47)$$
$$b_{e13} : c_3 - c_2 \leq 2 \quad (5.48)$$
$$b_{e14} : c_4 - c_3 \leq 2 \quad (5.49)$$
$$b_{e15} : \Psi_1 \geq -3.1416 \quad (5.50)$$
$$b_{e16} : \Psi_1 \leq 3.1416 \quad (5.51)$$
$$b_{e17} : \psi_2 \geq -0.7854 \quad (5.52)$$
$$b_{e18} : \psi_3 \geq -0.7854 \quad (5.53)$$
$$b_{e19} : \psi_4 \geq -0.7854 \quad (5.54)$$
$$b_{e20} : \psi_2 \leq 0.7854 \quad (5.55)$$
$$b_{e21} : \psi_3 \leq 0.7854 \quad (5.56)$$
$$b_{e22} : \psi_4 \leq 0.7854 \quad (5.57)$$
$$b_{e23} : n_1 \geq 0.5 \quad (5.58)$$
$$b_{e24} : n_2 \geq 0.5 \quad (5.59)$$
$$b_{e25} : n_3 \geq 0.5 \quad (5.60)$$
$$b_{e26} : n_4 \geq 0.5 \quad (5.61)$$
$$b_{e27} : n_1 \leq 1 \quad (5.62)$$
$$b_{e28} : n_2 \leq 1 \quad (5.63)$$
$$b_{e29} : n_3 \leq 1 \quad (5.64)$$
$$b_{e30} : n_4 \leq 1 \quad (5.65)$$
$$b_{e31} : n_2 - n_1 \geq -0.25 \quad (5.66)$$
$$b_{e32} : n_3 - n_2 \geq -0.25 \quad (5.67)$$
$$b_{e33} : n_4 - n_3 \geq -0.25 \quad (5.68)$$
$$b_{e34} : n_2 - n_1 \leq 0.25 \quad (5.69)$$
$$b_{e35} : n_3 - n_2 \leq 0.25 \quad (5.70)$$
$$b_{e36} : n_4 - n_3 \leq 0.25 \quad (5.71)$$

where:-

each c, Ψ, ψ & n are defined by Eqn. 5.35

Referring to the equations above, the constraints may be interpreted as:-

1. Constraints 5.36 to 5.43 were used to limit to the maximum amplitude of each circumferential endwall curve to 3.5mm above the nominal turbine radius (0.142m)
2. Additionally, constraints 5.44 to 5.49 were used to ensure that the *change* in amplitude *between* successive curves was limited to 2mm
3. Constraints 5.50 & 5.51 limited the phase angle (Ψ) of the first circumferential curve to a $\sim 360°$ range (i.e. $\pm\pi$ rads). Although at first these limits may seem extraneous, they are important to place upper and lower bounds on the Ψ_1 variable
4. Similarly to constraints 5.44 - 5.49, constraints 5.52 - 5.57 were imposed to limit the *change* in the phase angle of each downstream circumferential endwall curve from the initial Ψ_1 value in an attempt to ensure a smooth transition in the circumferential location of the endwall 'hump' and 'dip' features. For this investigation, the maximum phase angle change between successive endwall curves was set to $\pm\pi/2$ rads
5. Like constraints 5.36 to 5.43 which imposed variable bounds on the endwall curve amplitudes, constraints 5.58 to 5.65 imposed an upper and lower limit on the periodicity of each circumferential

endwall curve, with the period of each curve being allowed to vary from a minimum value of 0.5 to a maximum of 1 respectively

6. Constraints 5.66 to 5.71 again imposed upper and lower limits on the *change* in the periodicity between the successive endwall curves

Finally, all the endwall variable boundary constraints were imposed using a 'brick-wall' penalty scheme in which each variable was reset to the nearest feasible boundary value (as described in Section 3.1.3).

A summary of Eqns. 5.36 - 5.71 is included in Table 5.14 below for overall clarity.

Table 5.14: Summary of endwall parameter contraints

Parameter	*Constraint*	*Units*
Endwall amplitude[a]	$0 \leq c_k \leq 3.5$	mm
Amplitude change	$-2 \leq \Delta c_{k,k-1} \leq 2$	mm
Phase angle	$-3.1416 \leq \Psi_1 \leq 3.1416$	rad
Phase angle change	$-0.7854 \leq \psi_i \leq 0.7854$	rad
Curve periodicity	$0.5 \leq n_k \leq 1$	–
Periodicity change	$-0.25 \leq \Delta n_{k,k-1} \leq 0.25$	–

[a] Although c_k was constrained to be positive, '*negative*' endwall curvature was possible by allowing the *phase angle* (Ψ_1) of curve 1 to vary from $-180°$ to $180°$

6

Numerical modelling

This Chapter describes the numerical method used to model the turbine as part of the endwall design procedure used in this investigation. More specifically, it describes the endwall geometry and mesh generation, as well as the computational fluid dynamics (CFD) methodologies used.

Since the endwall design procedure was intended to require minimal user intervention, the procedures described in this Chapter were designed to execute as autonomously as possible using input journal files containing predetermined sequences of program commands, thereby removing the need for user intervention. However, due to complexity of some of the procedures involved (for example, meshing of complex endwall curvature), various checks were built into the procedures to ensure that the user was alerted if various criteria were not met or potential issues encountered by the geometry, meshing and simulation routines.

6.1 Geometry generation

The curves used to define the endwall curvature of the rotor passage in the circumferential direction were described in Section 5.5. This section describes the use of these curves together with additional curves which defined the curvature of the endwall in the axial direction, in the construction of the 3-dimensional endwall geometry from which the CFD models were then produced.

As discussed in Section 5.5, the axial and circumferential curvature of the rotor endwalls was defined using a network of logically orthogonal curves, constructed by fitting two sets of interpolating non-uniform rational basis splines (*NURBS*) curves through formatted data points defined by Eqn. 5.33 in the circumferential direction and by a set of control points placed at predetermined intervals along each circumferential curve in the axial direction. Thereafter, the 3-dimensional endwall surface was generated by constructing a bi-directional interpolating surface through the curve network.

As discussed previously, the 2^{nd} stator (S2) was *not* considered as part of the CFD model for the rotor endwall optimizations, and so this portion of the geometry was not generated as part of the geometry generation procedure described here. Instead, the S2 row *without* the turning vane was added as part of the mesh generation procedure described in the following section (Section 6.2).

In summary, the procedure used to generate the rotor endwall surfaces for each candidate endwall was as follows:-

1. formatted point data generated at 0.1 *rads* intervals for each *driving* (2, 3, 4 & 5) and *driven* (2a, 3a & 4a) curve was generated using Eqn. 5.33 using the curve parameters produced by the optimization routine as well as the interpolation formulae of Table 5.8. In addition, 2 sets of purely annular curve data (1 & 6) were also generated and located at approximately 0% C_{ax} and 60% C_{ax} in order to limit the profiled region of the endwall to the forward portion of the blade passage[1]
2. once the point data had been imported, interpolating *NURBS* curves were fitted to each set of points to create curves from which the endwall surface could be generated
3. once the circumferential curvature of the endwall (contoured and annular) had been defined, control points located at 0, 12.5, 25, 37.5, 50, 62.5, 75, 87.5 and 100% length along each circumferential curve (1, 2, 2a, 3, 3a, 4, 4a, 5 & 6) (as well as through each construction curve) were created, and interpolating *NURBS* curves fitted through each set of points in order to define the endwall curvature in the axial direction ($axial_{1-9}$)
4. finally, the 2-dimensional endwall surface was generated by creating a bi-directional interpolating 'net' surface through the curve network using a fitting tolerance of $t = 0.001mm$

Following the generation of the rotor endwall surface, the pressure and suction side blade surfaces were generated in a similar manner:-

1. formatted point data defining the blade tip suction and pressure surfaces was imported at $r = 202.5mm$ and hub at $r = 137mm$ and interpolating *NURBS* splines fitted through each set of points
2. the blade pressure and suction surfaces were then generated using the 'wireframe' tool, duplicated and then rotated by $\pm 9^{\circ}$ until the mean blade camberline of each blade was coincident with the outermost axial curves ($axial_{1,0\%}$ & $axial_{9,100\%}$) of the endwall surface
3. all surfaces (rotor pressure/suction & endwall) were then exported to *.sat* (ACIS, rel 16.0) format for use in the meshing procedure

As indicated above, the blade root profiles for each blade were generated at approximately $-5mm$ below the mean turbine hub datum (i.e. $r = 142mm$) in order to make allowance for the reduced hub radius in the lowered (i.e. 'dip') regions of the endwall surface.

Figs. 6.1a - 6.1c below show the curve network and dimensions used to construct the contoured endwall surface for each design iteration, while the Figs. 6.2a & 6.2b give a general overview of the rotor passage geometry from the leading and trailing perspectives respectively.

[1] In addition to the limiting annular curves 1 & 6, additional annular 'construction' curves were also generated forward and aft of the contoured portion of the endwall to ensure remainder of the endwall was completely annular

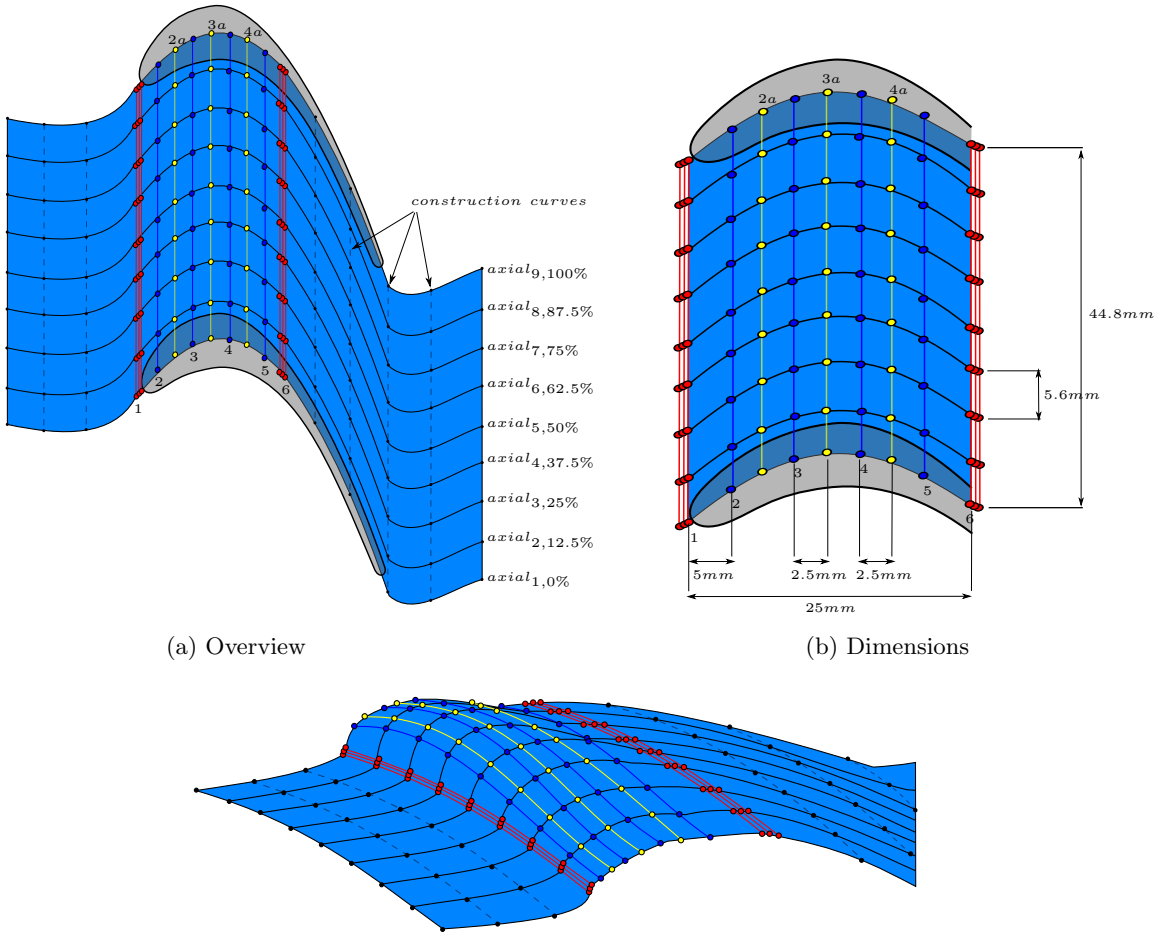

(a) Overview

(b) Dimensions

(c) Perspective

Fig. 6.1: Curve network used to generate the rotor non-axisymmetric endwall surface. The circumferential curvature defined by the *driving* (2, 3, 4 & 5) (blue) & *driven* (2a, 3a & 4a) (yellow) curves. The axial curvature was defined by the *NURBS* curves ($axial_{1-9}$) (black) fitted through control points at 12.5% intervals along each circumferential curve. The limiting annular curves (1 & 6) and construction curves are shown in (red) and (grey, dashed) respectively

6.2 Meshing

6.2.1 Overview

Once the rotor blade passage geometry had been generated, the rotor passage geometry was imported into the meshing software and the flow domain was discretized using the IcemCfd® meshing software (ANSYS (2014)). This particular software package was selected for use as a result of its availability but also as a result of its ability to:-

1. discretize relatively complex flow domains using high quality hexahedral cells using the Hexa domain decomposition tool, *and*

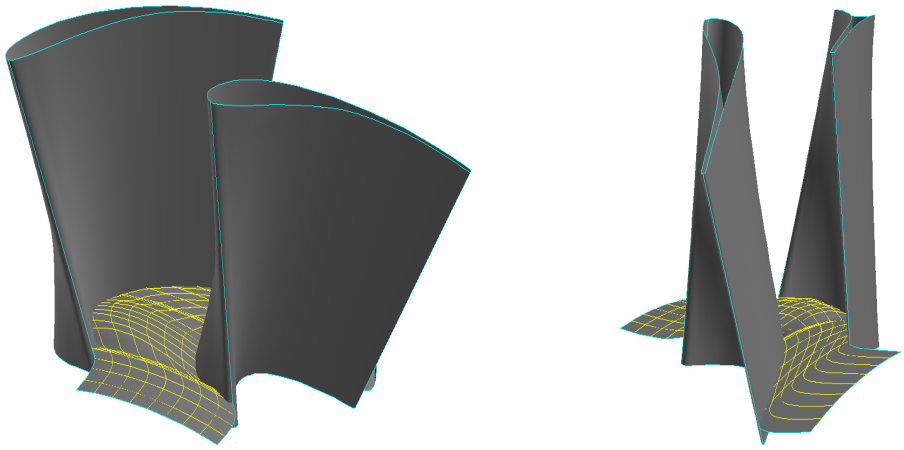

(a) Leading edge view (b) Trailing edge view

Fig. 6.2: Rotor blade and non-axisymmetric endwall geometry generated by the geometry generation routine (excluding the rotor casing and S2 passage geometry, which was generated during the meshing procedure)

2. be run autonomously using a series of flags (`-batch -script`) and input scripts containing predetermined meshing instructions therefore removing the need for direct user interaction

The flow domain was decomposed using a conventional HOH-grid scheme, although this was adapted to accomodate a blade-to-blade domain topology in which the extremities of the flow domain in the circumferential direction were defined by the pressure and suction surfaces of an adjacent pair of blades. This topology was used in order to allow the curves from which the circumferential curvature of the endwalls was produced to be constructed as single smooth interpolating splines without large changes in radius at their centre points (i.e. on the blade mean camber line).

In order to ensure the results from each endwall simulation were not affected by variations in the architecture of the flow domain discretization, a single prototype mesh was developed for the datum (i.e annular) case, the endwall region of which was then adjusted to fit the endwall geometry of each intermediate design.

Potential effects

Under the operating conditions at which this investigation was undertaken, the potential effects of the rotor blades on the upstream NGV row were found to be very small. As a result, in order to reduce the size and therefore computational expense of the CFD model used in conjunction with the endwall design procedure, the upstream NGV blade row was not included in the optimization CFD model. Instead, the exit flow from the NGV blade row was calculated using a steady state simulation of the full turbine and was used to generate pitchwise-averaged inlet profiles for the inlet flow and turbulence quantities. The profiles were then applied to the inlet of the rotor flow domain, whereafter the flow simulations were completed. In principle, this approach was very similar to the well known mixing

plane model (MPM) approach, although as discussed, any potential effects of the downstream blade row are not propagated upstream into the NGV blade row.

2^{nd} stator

As mentioned previously, the 2^{nd} stator blade was not included in the CFD or experimental testing of the rotor hub endwall effectiveness in this investigation. Many authors (Harvey et al. (2000), Ingram (2003)) have characterised the effectiveness of endwall contouring of a blade row in terms of the changes in loss (or whatever proxy was in use) at the exit of the blade row, as well as a function of the so-called *mixed-out* loss at some point infinitely downstream of the row under consideration. As a result, in this investigation, the same approach as that which was used by Snedden (2011) to characterise the 'mixed-out' performance of a contoured rotor was followed (in which the second stator was removed from the test rig, and measurements made at a downstream measurement plane) and the meshes used for the optimization of the rotor non-axisymmetric endwall *did not* include the downstream blade row.

Tip gap

Finally, in this investigation, it was decided that the best approach for the modelling of the tip gap was the use of a fully gridded tip. Although this approach has the potential to add some degree of meshing and numerical complexity (the high velocity gradients in the tip region can add some difficulty in obtaining a stable solution of the numerical model), it was used because it was felt it would provide the most accurate prediction of the flow. This was particularly in comparison to other approaches, such as the use of 'periodic' boundaries at the entry and exit of the tip gip, which, although reduce the model complexity, do not accurately model various features such as the chordwise transport of fluid *on* the tip of the blade (a mechanism which was described by researchers such as Bindon (1987)) or the detailed formation of the tip leakage jet flow (Denton (2010)).

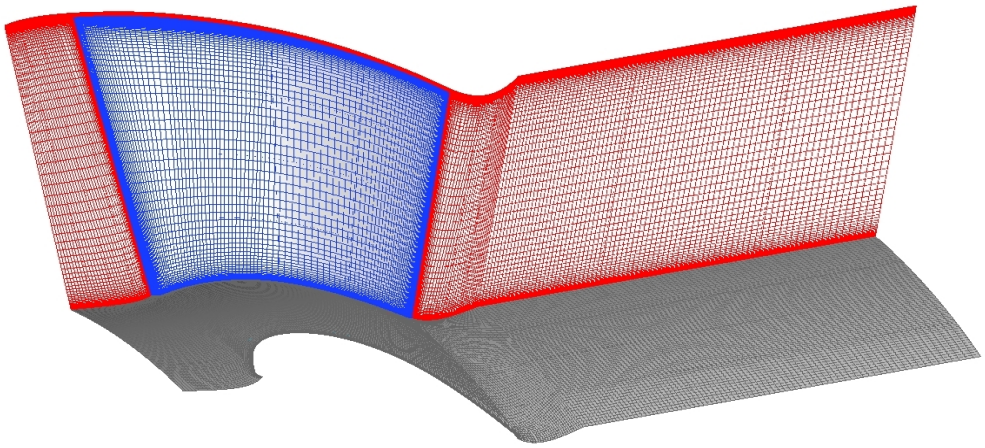

(a) Overview

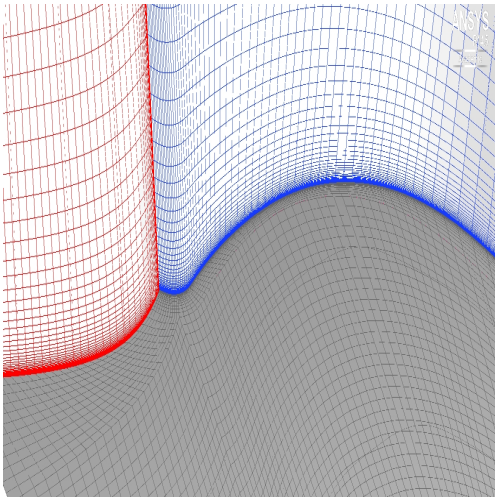

(b) Leading edge detail (hub)

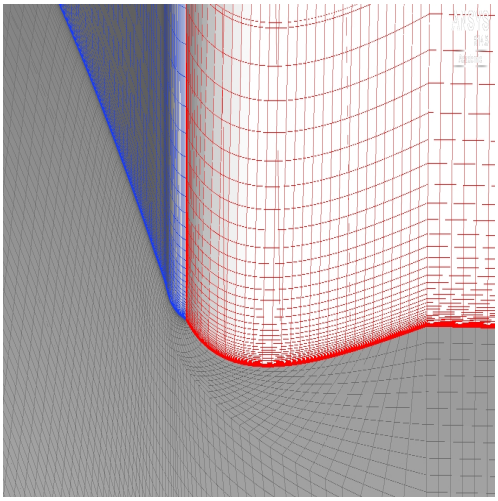

(c) Trailing edge detail (hub)

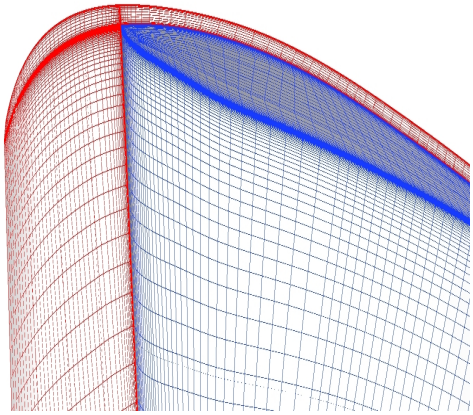

(d) Leading edge detail (tip)

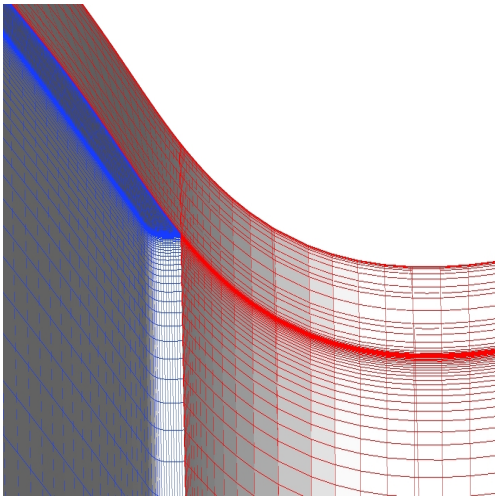

(e) Trailing edge detail (tip)

Fig. 6.3: Computational mesh used in CFD calculations showing rotor blade pressure and tip surface (blue), rotor and second stator hub (grey) and periodic surfaces (red). NB Rotor suction surface not shown.

6.2.2 Mesh generation procedure

The general mesh generation procedure followed the following steps:-

- import endwall and blade geometry files (*endwall.sat*) and convert to local IcemCfd® (*.tin*) format
- trim the contoured endwall to remove those portions of within the blades themselves
- generate rotor & S2 casing, inlet, outlet and S2 hub surfaces
- generate forward, aft and rotor tip periodic surfaces, as well as blade o-grid curves
- import flow domain mesh template and associate endwall mesh points with the current contoured endwall surface
- deform mesh template onto the contoured endwall and generate the mesh
- run mesh check diagnostics to check for mesh defects and adequate mesh quality
  - if mesh defects exist, alert user *else*,
  - print mesh statistics and continue
- export final contoured mesh to Fluent® (*.msh*) format for solving

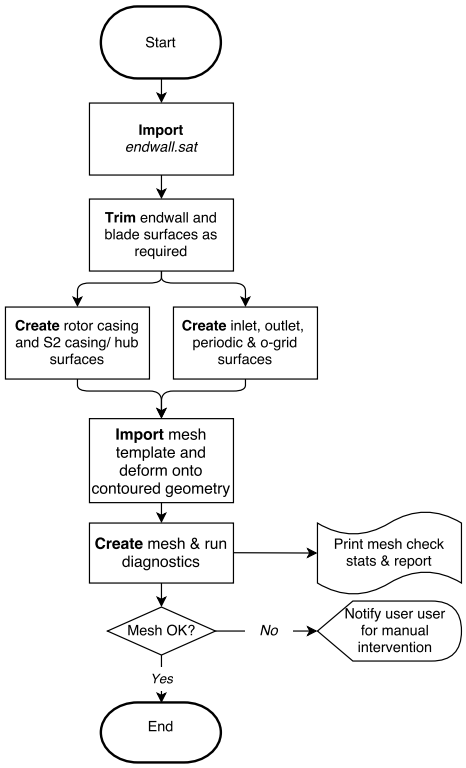

Fig. 6.4: Mesh generation procedure

Similarly to the geometry generation procedure, the meshing procedure described above was also fully automated, and was implemented to only require user intervention in the event that geometry or mesh quality errors were detected.

The general overview of the computational mesh, as applied to the annular case is shown in Fig. 6.3a, while Figs. 6.3b & 6.3c and 6.3d & 6.3e show details of mesh in the vicinty of the leading and trailing edges, at the hub and tip respectively.

6.2.3 Mesh sensitivity

In order to ensure that the predictions of the various flow quantities to be used as part of the endwall optimization procedures were independent of the flow domain discretization, a mesh sensitivity study was conducted. In addition, in order to give some indication of the relative *changes* between various flow quantities which could be expected between various important quantities for different mesh sizes, the same quantities were calculated using the final optimization mesh as applied to the annular case, as well as a rotor equipped with the 'generic' endwall previously tested by Snedden (2011).

The circumferentially (pitchwise) -averaged rotor exit (X3) profiles for rotor relative outlet angle (β_3), velocity (W_3) and coefficient of secondary kinetic energy (C_{ske}) for the annular and generic endwalls are shown in Figs. 6.5a - 6.5f, while in addition, the mass-averaged rotor exit results for the

rotor torque, total-total efficiency (η_{tt}), coefficient of secondary kinetic energy (C_{ske}), loss ($C_{p0,rel}$), design efficacy (η_{de}), flow deviation from design (β_{dev}) and $SKEH$ are shown in Figs. 6.6a - 6.6g.

Finally, the experimental uncertainties for each of the quantities as measured by Snedden (2011) (excluding the $SKEH$ & η_{de}), are summarised in Table 6.1.

Circumferentially-averaged sensitivities (X3)

The circumferentially-averaged X3 profiles (Figs. 6.5a - 6.5f) show the rotor exit CFD predictions converge well for both the annular and generically contoured cases once a mesh size of approximately $\sim 2.4M$ cells is exceeded. In addition, for both the annular and contoured cases, the CFD appears to predict the bulk changes to the rotor exit flow with acceptable accuracy. For both endwalls, and all the metrics, some differences between the predicted and experimental results were evident, most noticeably in the tip gap (β_3 (Fig. 6.5a) & C_{ske} (Fig. 6.5e)). These differences were also noted by other researchers (Snedden (2011) who measured the flow for the *same* turbine and were subsequently explained by Dunn (2014) in his PhD thesis as being as a result of the very high shear in combination with the connection method they used for their measurements (in which the steady state static pressure was calculated using only the 2 pitch ports). Although, in this investigation, this connection methodology was changed to use of all 4 side ports (i.e. both pitch and yaw ports) for the calculation of the static pressure, and this resulted in significantly better resolution of flow in regions of moderate to high levels of shear (for instance between $20 - 40\%$ span), some issues still remained in the regions of very high shear (such as in the tip gap) as mentioned previously.

Mass-averaged sensitivities (X3)

Figs. 6.6a - 6.6f show that for the majority of quantities, the influence of increasing the mesh size beyond $\sim 2.4M$ cells was relatively small, although some small depedency on mesh size appeared to remain for the secondary kinetic energy-based quantities (C_{ske} (Fig. 6.6c) & $SKEH$ (Fig. 6.6g)), although this dependency appeared more apparent for the mass-averaged $SKEH$. Despite this, in both cases, the *differences* between the mass-averaged values for each endwall were clearly discernible and exhibited the correct trends (i.e. lower values for the contoured endwall and higher for the baseline case).

Fig. 6.6a also appears to show that the rotor torque also displays some residual dependency on the mesh density, although noting the scale of the figure, this was of the order of approximately -0.0136 Nm for the coarsest mesh and -0.0012 Nm for the finest and so was considered effectively negligible.

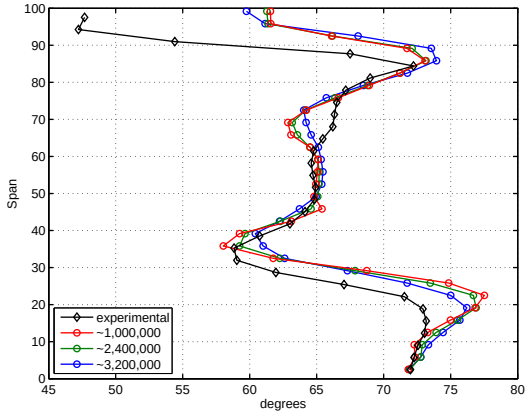

(a) β_3 (annular)

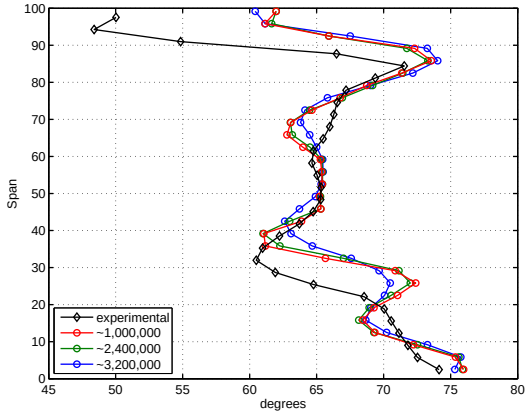

(b) β_3 (contoured)

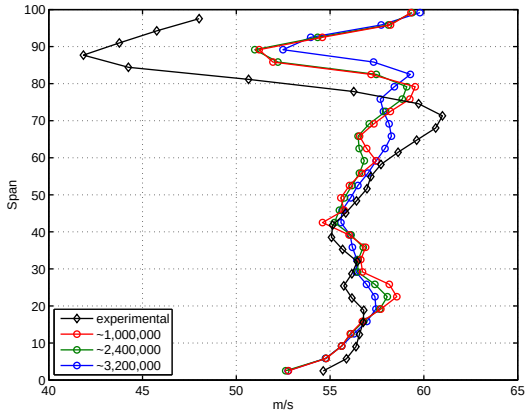

(c) W_3 (annular)

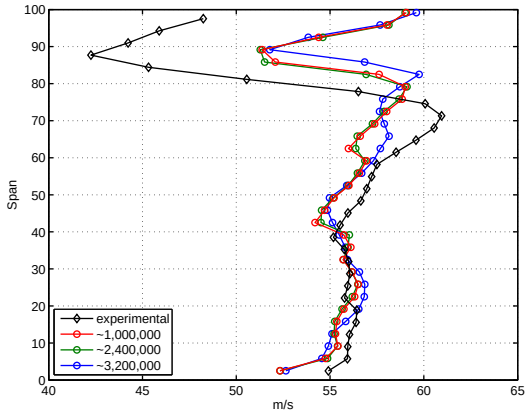

(d) W_3 (contoured)

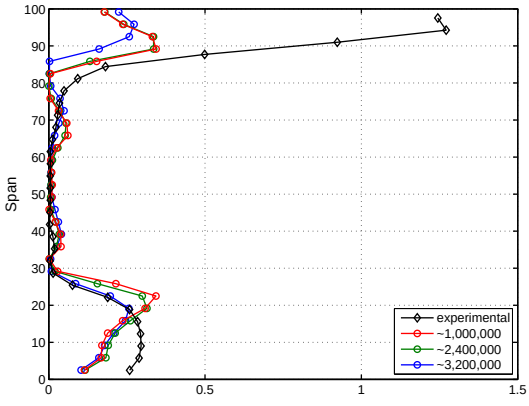

(e) C_{ske} (annular)

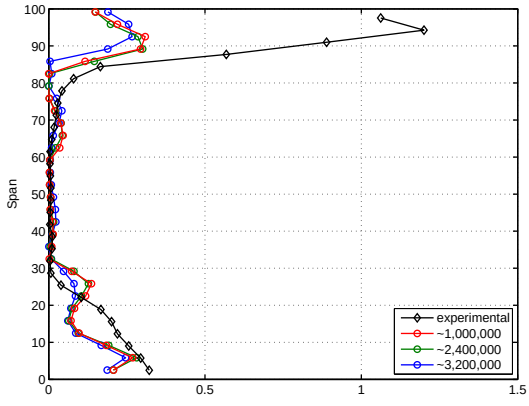

(f) C_{ske} (contoured)

Fig. 6.5: Radial profiles of various flow and optimization quantities at rotor exit (X_3) for the annular (left) contoured (right) case for meshes of different mesh densities

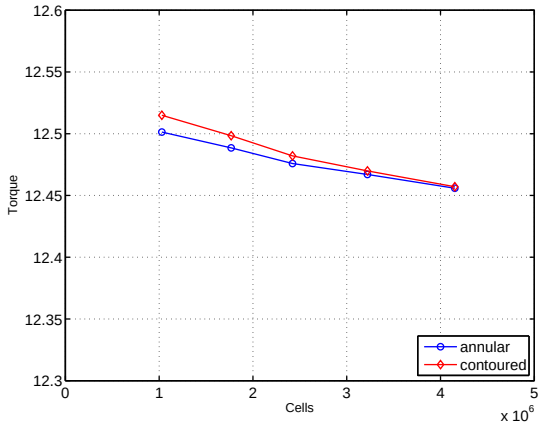

(a) torque

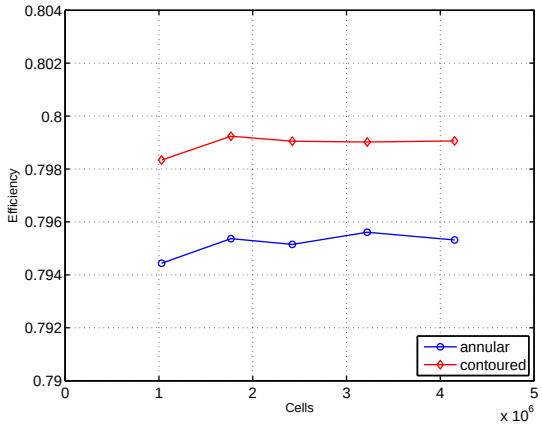

(b) η_{tt}

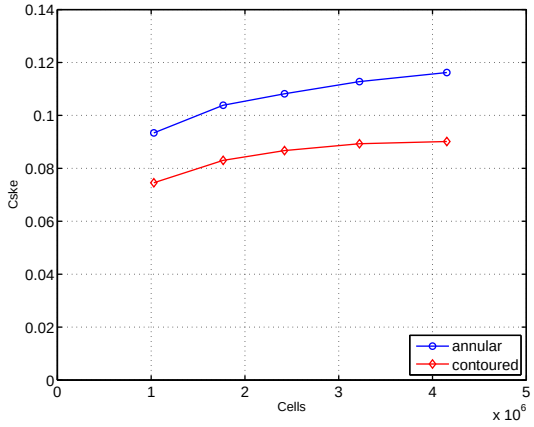

(c) C_{ske}

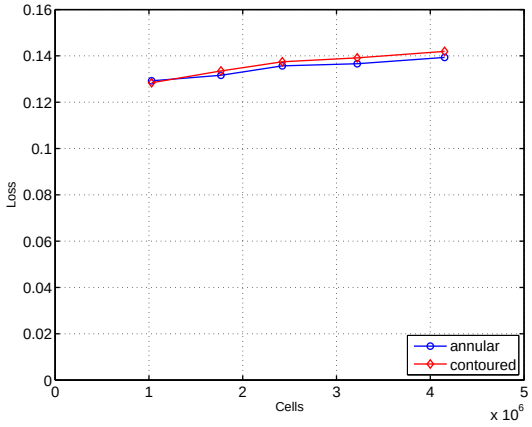

(d) $C_{p0,rel}$

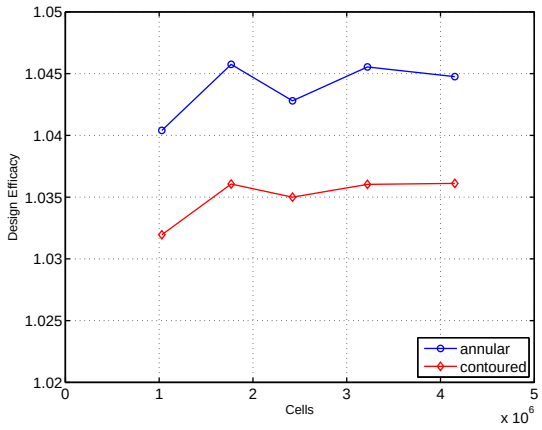

(e) η_{de}

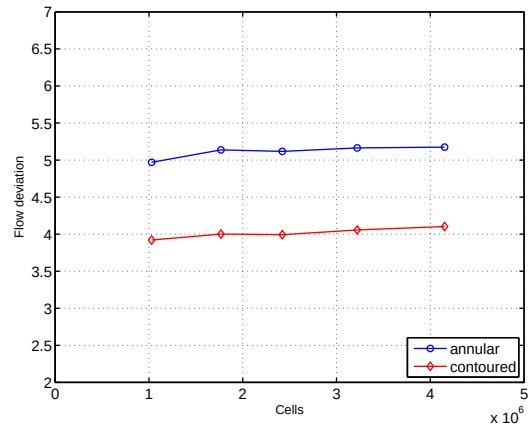

(f) β_{dev}

Fig. 6.6: Mass-averaged magnitudes for various quantities calculated at the rotor exit plane (X3) using meshes of increasing cell density for an annular and contoured endwall

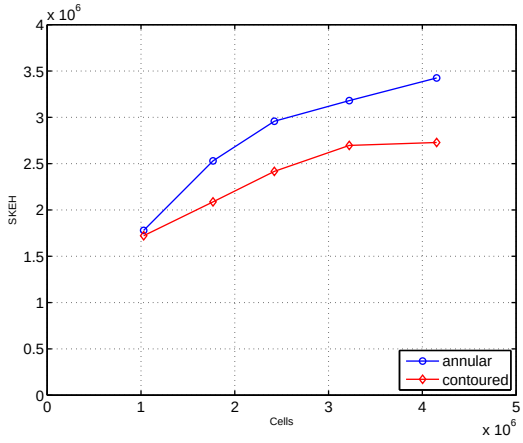

(g) $SKEH$

Fig. 6.6: Mass-averaged magnitudes for various quantities calculated at the rotor exit plane (X3) using meshes of increasing cell density for an annular and contoured endwall (cont)

Experimental uncertainties

The experimental uncertainties associated with the CSIR turbine were calculated by Snedden (2011) by taking multiple measurements downstream of the rotor blade whilst breaking down and reassembling the turbine between measurements. In addition, the measurement sequences of individual points for each flow traverse were also altered between measurements, and the mean, averaged and standard deviations from which the final uncertainty was determined, were calculated.

They are important as they provide an indication of the resolution at which different candidate endwall designs produced by the design routine can be differentiated from each other.

Table 6.1: Experimental uncertainties for CSIR turbine (as per Snedden (2011)

Quantity	*Uncertainty*
torque	$\pm 0.03\ Nm$
η_{tt}	$\pm 0.126\%$
C_{ske}	$\pm 0.074\%$
$C_{p0,rel}$	$\pm 0.136\%$
η_{de}	-[a]
β_{dev}	$\pm 0.4°$
$SKEH$	-[a]

[a] Values for η_{de} & $SKEH$ were not given by Snedden (2011) as η_{de} was not investigated by him and the measurement of helicity (H) for the calculation of $SKEH$ for a rotating blade row is not trivial

6.2.4 Summary

The final mesh size selected for the endwall optimization procedure was approximately 2.4×10^6 cells with an average Near Wall Reynolds Number (y^+) of ~ 0.497. This value was below the recommended threshold for accurate resolution of the boundary layer flow ($y^+ \leq 1$) and although this figure was in fact valid only for the annular case, it was not expected that this would vary significantly with the application of the 3-dimensional profiling to the hub for each intermediate endwall design. Fruther, the formulation for the solver used in this investigation was set to use *enhanced wall treatment*[2], in which the turbulence model formulations for the laminar and logarithmic layers are blended together smoothly guaranteeing correct asymptotic behaviour of the turbulence quantities for regions of the model where $y^+ \approx 1$ and reasonable accuracy where y^+ falls in the buffer layer ($3 \leq y^+ \leq 11.2$). The maximum y^+ on the endwall for the annular case was $y^+ = 0.564$.

A total of 108 cells were used in the radial direction, while in the circumferential direction, 38 cells were used for each blade passage. A total of 20 cells were used on the blade and endwall surfaces and 25 used in the tip gap region to capture the boundary layer flows in these regions. For all boundary layer cells, a bi-geometric bunching law was used meaning the mesh nodes are distributed in a parabolic fashion adjacent to the wall boundaries and linearly once the tangents of each parabola are equal. The initial cell height for all wall adjacent cells was set to 0.005 mm and a constant cell growth ratio of 1.2 was used as recommended by the IcemCfd® user guide.

A summary of the final mesh specifications is given in Table 6.2.

Table 6.2: Summary of final optimization mesh specifications

Parameter	*Value*
Total cell count	$\sim 2.4M$
Radial	108
Circumferential	38
Boundary layer cells	
Blade	20
Endwall	20
Tip gap	25
Near wall Re Number (y^+) (endwall)	
Avg	0.497
Min	0.004
Max	0.564

[2] It should be noted that enhanced wall *treatment* use here is *not* synonymous with enhanced wall *functions*, with the former referring to the proprietary blending algorithm introduced by the manufacturers of the Fluent® software used in this investigation and the latter, the modelling of the near turbulence properties using appropriate model relationships. For a more detailed discussed, the interested reader is referred to pg12-7 of the Ansys Fluent® User Guide.

6.3 Computational fluid dynamics

6.3.1 Discussion on reduced (rotor only) model

Despite the use of the surrogate modelling techniques discussed in Chapter 5, the average time taken to perform a single endwall contour optimization was approximately $\sim 20-25$ days. This is because, as discussed previously, with the growth in size of the underlying surrogate model database with the progression of the optimization procedure, the computational effort required for the tuning of the *DACE* model hyperparameters can approach (or even exceed) the computational demands of the simulation procedure itself (Forrester et al. (2007)), effectively doubling the walltime required for each iteration.

Using the computing hardware available for this investigation[3], the average calculation time for a single CFD simulation was ~ 1 hr, while the model tuning procedure varied from approximately ~ 7 mins at the start of the procedure (and with an initial metamodel database size of $\mathbf{X}_{database} = 93$ design sites) to in excess of ~ 120 mins after approximately 300 iterations.

As a result of the above, as discussed in Section 6.2, in order to reduce the computational expense of the endwall generation routine as much as possible, the computational expense associated with the individual objective function evaluations was reduced by *not* including the upstream *NGV* blade row in the endwall optimization model. Instead, the outlet flow and turbulence parameters of the upstream blade row were circumferentially-averaged and applied to the inlet of the rotor blade row in a manner identical to that used in the well known mixing plane approach. However, in contrast to the mixing plane approach where the downstream static pressure is propagated upstream and any potential effects generated by changes to the endwall shape can therefore potentially have an effect on the rotor inlet velocity profile. Since this was not possible with the approach used in this investigation, any potential effects generated by the downstream rotor contouring were neglected in the optimization of the endwalls.

In order to confirm that the potential effects of the downstream blade row on the rotor inlet flow were negligible, the inlet velocity magnitude (V_2), angle (α_2) and static pressure (p_2) at the rotor inlet plane (X2) for a full 1-stage model (full model) and the optimization model (reduced model) solved using the *NGV* outlet flow profiles were extracted were compared (Figs. 6.7). Contours of the rotor endwall and inlet static pressures as well as the inlet velocities are also shown (Fig. 6.8 & 6.9).

6.3.2 Fluid properties

The maximum flow velocity at the rotor exit was calculated to be approximately ~ 42 $^{m}/_{s}$ which corresponded to a Mach number of approximately $M \approx 0.12$. Although a small portion of the flow in the vicinity of the pressure side tip gap corner was found to have a velocity which corresponded to a Mach number of approximately $M = 0.303$, this was limited to a few cells only and represented velocities atypical of those of the bulk of the flow. As a result, the air passing through the turbine was modelled as an incompressible fluid, the properties of which are given in Table 6.3 and were based on the average atmospheric conditions for the test site as reported by Snedden (2011).

[3] Dell PowerEdge R815 server, Quad AMD Opteron 6380 2.5GHz CPU (64 core), 128GB DDR3-1600MHz RAM

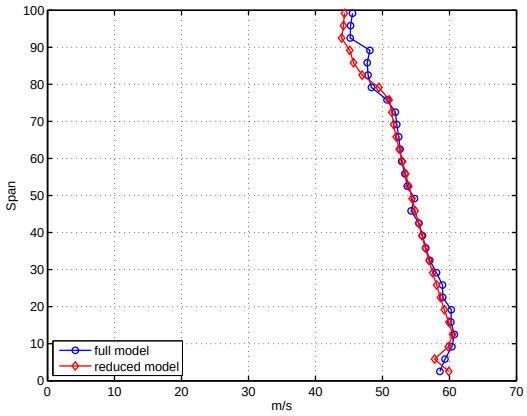

(a) V_2 (annular)

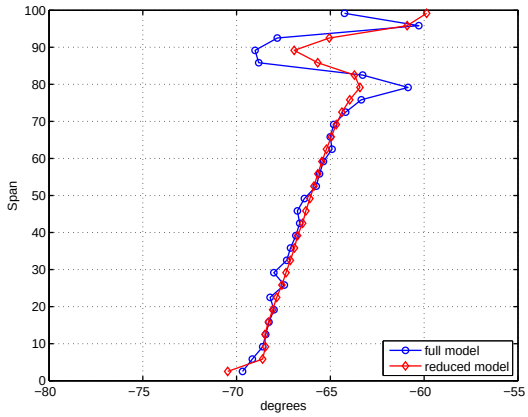

(b) α_2 (annular)

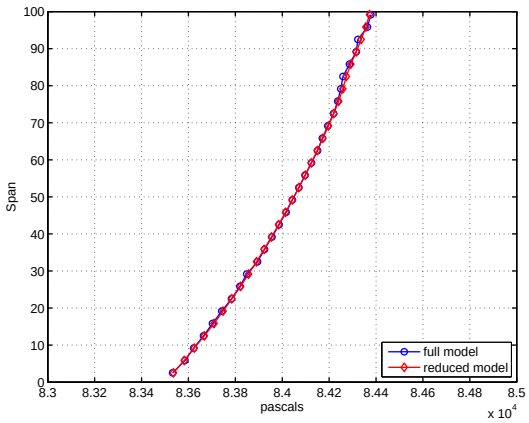

(c) p_2 (annular)

Fig. 6.7: Comparison of rotor inlet profiles (X2) for the reduced (optimization) model and full (1-stage) models for the annular endwall

Table 6.3: Summary of CFD fluid properties

Quantity	*Value*	*Note*
$P_{operating}$	86.4 kPa	Average $P_{atmospheric}$ at test site
T_{in}	25°C	Average $T_{atmospheric}$ at test site
ρ	1.010 kg/m^3	
μ	$1.814e^{-5}$ kg/ms	

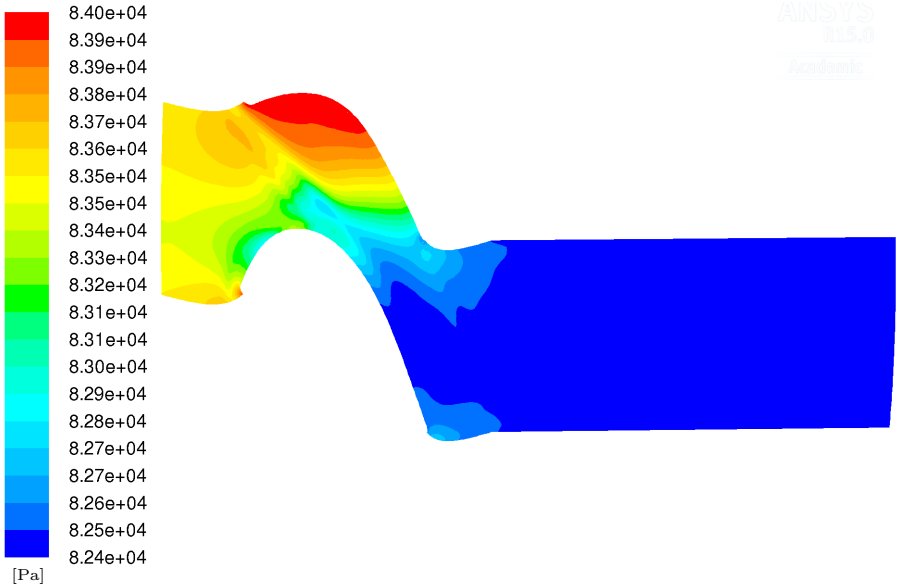

(a) Full model

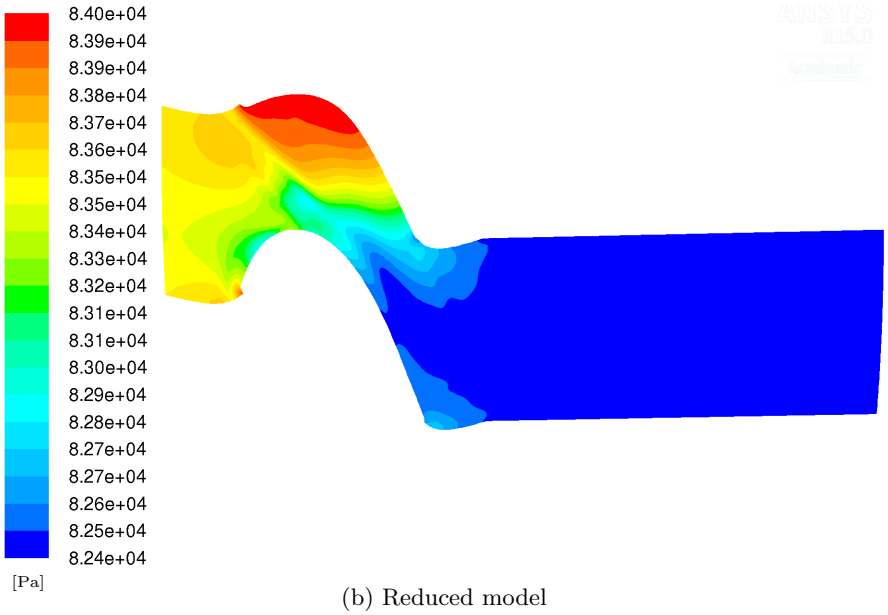

(b) Reduced model

Fig. 6.8: Comparison of endwall static pressures for full and reduced (optimization) models (*NGV* row not shown)

6.3.3 Solution method and controls

Two CFD solution packages were investigated as part of the numerical procedure of this investigation:- the commercial package ANSYS FLUENT®, which is a multipurpose, cell-centred finite volume code; and OPENFOAM®, which is an opensource c++ library developed by CFD Direct and distributed under the GNU General Public License (GPL) (F.S.F (2007)). While both packages were found to perform adequately, ultimately, ANSYS FLUENT® was selected for use primarily because of its access to the so-called coupled solver (in which the equations governing the fluid flow are solved in a monolithic

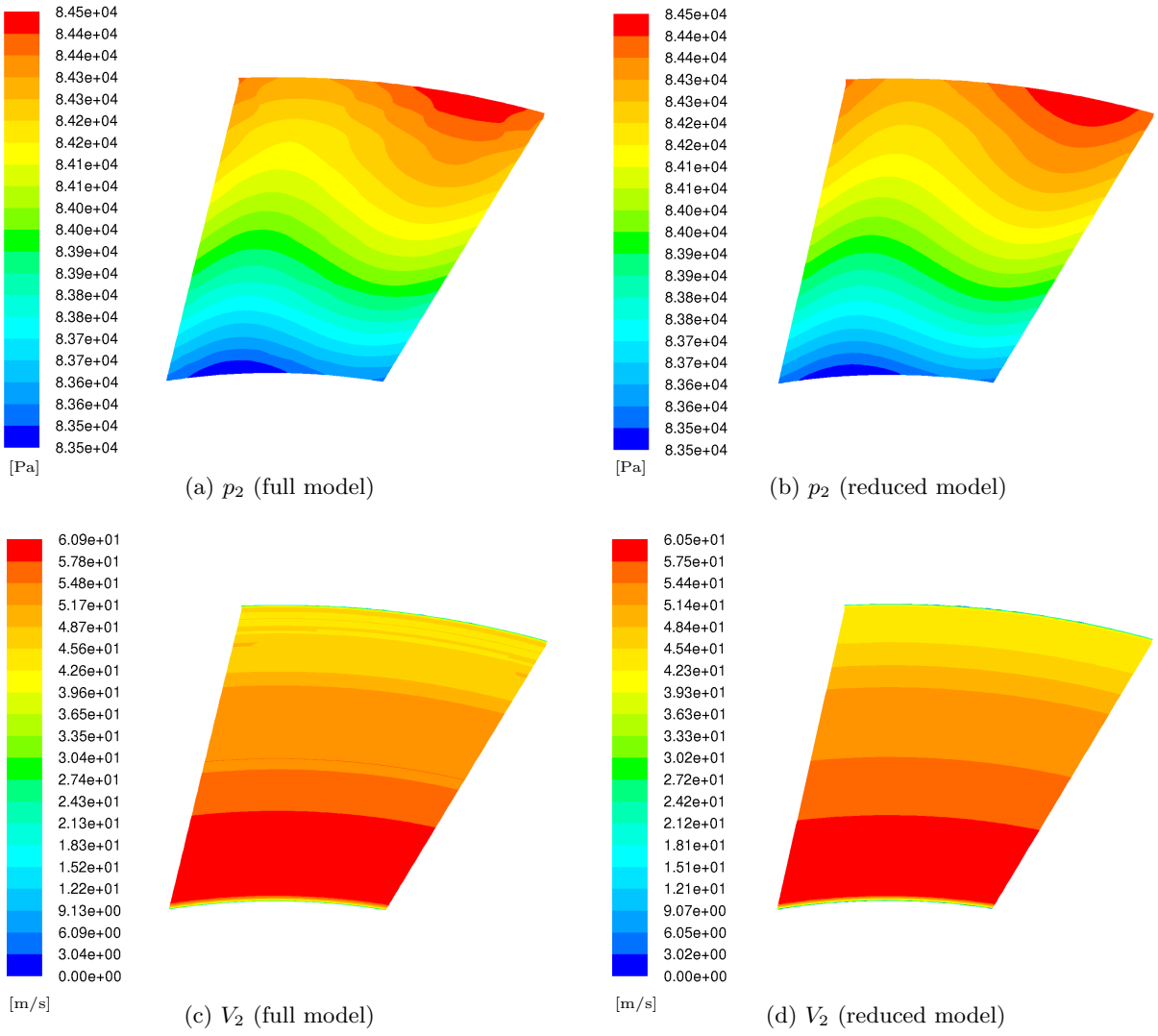

(a) p_2 (full model) (b) p_2 (reduced model)

(c) V_2 (full model) (d) V_2 (reduced model)

Fig. 6.9: Comparison of rotor inlet pressure (p_2) and velocity (V_2) conditions for the full (a, c) and reduced (optimization) (b, d) models

fashion) which provided a significant reduction in solution time relative to the traditional segregated approach. All equations were solved using second order accurate up-winding, with the exception of the pressure correction (continuity) equation, which was solved using the PRESTO! pressure interpolation scheme and is recommended for flows in curved domains or rotating flows (ANSYS (2014)).

Because the endwall optimization procedure was intended to operate without user intervention, the CFD solver settings were selected to ensure as stable as possible solution of the equations as possible, without dramatically adversely affecting the convergence speed of the algorithm.

6.3.4 Boundary conditions

Inlet

As discussed previously, in order to reduce the overall computational effort required for each intermediate CFD run, the numerical domain used in the endwall optimization routine was limited to the rotor and S2 rows only, with the upstream NGV row not explicitly modelled. Instead, the flow from the upstream NGV blade row was modelled by applying 1D radial profiles for the flow velocity, turbulent kinetic energy and specific turbulence dissipation rate to the inlet of the rotor domain. The profiles were produced by modelling the flow through the full turbine and by averaging the properties of the flow at a predetermined number of points in the radial direction at the outlet of the NGV blade row.

Since it is well known that the inlet boundary layer to a blade row can have a large effect on the prediction of the secondary flows (Walsh (1987), Denton (2010)), a number of boundary layer profiles with different levels of radial refinement were trialled in conjunction with the final optimization mesh. In particular, an initial profile (*rotor_inlet_Vel4.prof*) consisting of a number of points (100) consistent with the number of points used by default with the mixing plane approach of the solver was constructed, while the second (*rotor_inlet_Vel5.prof*) was constructed to ensure that the number of points (+500) within the profile not only exceeded the number of cells on the rotor inlet in the radial direction but in addition ensured that at least one value for each rotor inlet quantity was available at the same radial height as the correpsonding centroid of each inlet boundary face and therefore foregoing the requirement of the solver to interpolate between heights at which the profile data was specified.

CFD solutions for the annular case were calculated using each of the inlet profiles and the final optimization mesh, and the results for various rotor exit quantities as well as computed oilflow streamlines are shown in Fig. 6.10. From the figures, the effect of the number of sampling points within the inlet profiles is clear, with the more densely sampled profile (*rotor_inlet_Vel5.prof*) appearing to capture the rotor exit flow more accurately, particularly the rotor exit relative flow angle (β_3) (Fig. 6.10a). In addition, in the secondary flow region ($0-25\%$ span), the use of the finer profile results in greater levels of off-axis flow (as quantitified by the coefficient of secondary kinetic energy, Fig. 6.10c), while the computed oilflow streamlines for each case show a shift in the circumferential position of the boundary layer saddle point, as well as more prominent skewing of the inlet boundary layer at the inlet to the blade row.

These results were entirely consistent with those published by authors such as Walsh and Gregory-Smith (1989), who found by skewing the inlet boundary layer to a large scale, linear cascade, that so-called 'negative' boundary layer skew (such as that found in a turbine) resulted in an *increase* in the magnitude of the secondary flow at the exit of the blade row in comparison to the zero skew case.

Outlet

The outlet of the turbine downstream of the S2 blade row was modelled using a radial equilibrium pressure boundary condition, where the static pressure on the outlet is specified at the position of minimum radius (i.e. at the hub) and the pressure on the remainder of the boundary is calculated so that:-

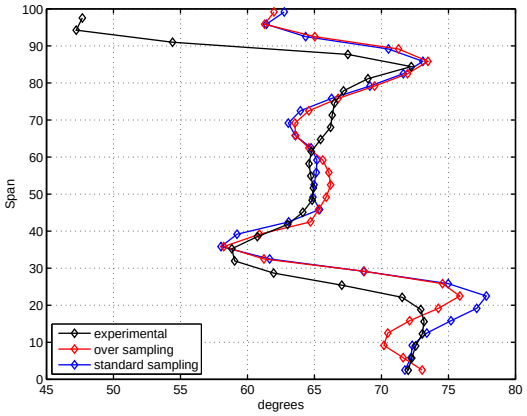

(a) β_3

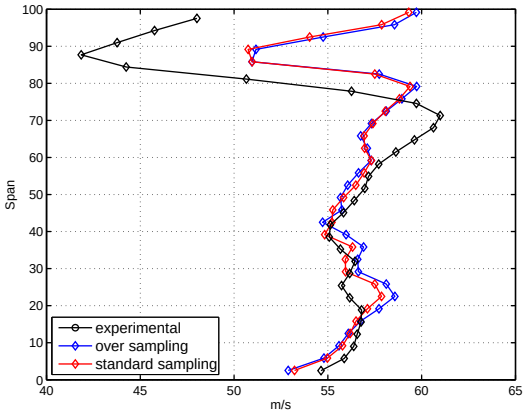

(b) W_3

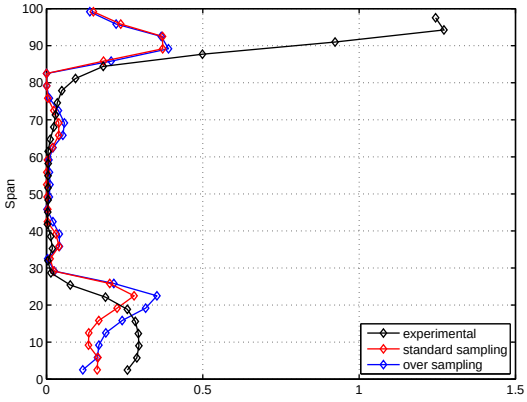

(c) C_{ske}

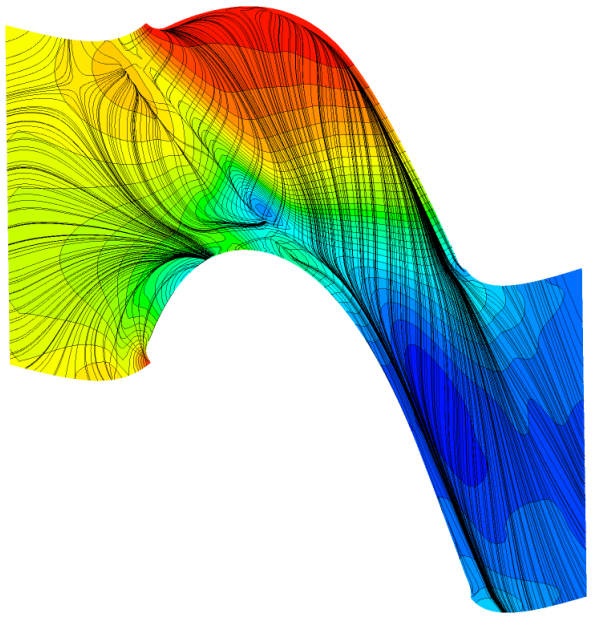

100 point profile

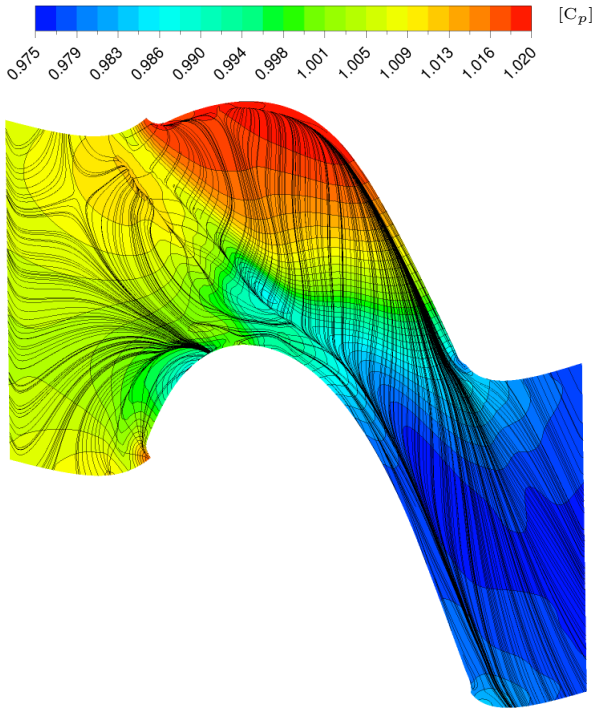

+500 point profile

Fig. 6.10: Comparison between computed oilflow streamlines and various rotor exit (X3) quantities for the 100 & +500-point inlet boundary layer profiles

$$\frac{\partial p_r}{\partial r} = \frac{\rho v_\theta^2}{r} \tag{6.1}$$

where:-

p_r is the static pressure at radius r,
ρ is the fluid density,
v_θ is the component of the outlet velocity in the circumferential direction, *and*
r is the radial coordinate

Integration of Eqn. 6.1 above results in the introduction of a constant of integration (i.e. a pressure term), which in this context represented the static pressure of the outlet at the hub.

The radial equilibrium boundary condition assumes negligible flow in the radial direction and although this is not strictly the case, the use of this boundary condition is common practice for the modelling of turbomachinery components (Denton (2010)). Tests in which alternative outlet boundary conditions were trialled (i.e. average (integrated), uniform pressure) showed the radial equilibrium condition to be the most satisfactory and since it has been used without issue in a number of cases for calculating turbine secondary flows by researchers (Harvey et al. (2000), Snedden (2011) and more recently Dunn (2014)), it was considered the most appropriate boundary condition for this case.

Summary

In summary, the boundary conditions used for the optimization model were as follows:-

Table 6.4: Summary of CFD boundary conditions

Boundary	*Value / Type*
Inlet	
Velocity (v_z, v_θ, v_r)	1D radial profile
Turbulence (k, ω)	1D radial profile
Outlet	
Pressure	Radial equilibrium
Pressure @ hub	82.4 kPa
Walls	
Endwall, blades	-240.8554 $^{rad}/_{s}$, no slip
Casing, S2 hub	0 $^{rad}/_{s}$, no slip
No. of rotor blades	20

6.3.5 Turbulence modelling

Overview

Within the literature, a wide variety of models have been used for the prediction of secondary flow and loss, including simple mixing-length models by researchers such as Moore and Gregory-Smith (1996), Harvey et al. (2000), Bagshaw et al. (2008b) & Denton (2010), to more industry standard two-equation

models by researchers such as MacPherson and Ingram (2010), McIntosh et al. (2011) & Hilfer et al. (2012) ($k-\epsilon$ RNG), Snedden (2011), Poehler et al. (2010) & Dunn (2014) ($k-\omega$ SST). More recently, more exotic models incorporating transition have also been used by various groups including Germain et al. (2007), Germain et al. (2010), Praisner et al. (2007) & Praisner et al. (2008).

In addition to the variety in turbulence closures used, there has also been variety in the approach used to the model the near wall physics of the flow. Naturally, those researchers who have chosen to use models which are incapable of being integrated into the near wall region have used the wall function approach (Harvey et al. (2000)) while a number of the later researchers in the field have tended towards low Reynolds implementations of the various turbulence models (Torre et al. (2006), Praisner et al. (2007, 2008), Germain et al. (2008), Kumar and Goverdhan (2011)).

Model survey

In the selection of a turbulence closure model for this work, a survey of closure models was conducted including the 'standard' $k-\epsilon$ model (Launder and Spalding (1974)) and RNG $k-\epsilon$ models (Yakhot et al. (1992)), Menter's $k-\omega$ SST model (Menter (1994)) as well as Spalart & Allmaras's one equation model (Spalart and Allmaras (1992)). For each turbulence model, the upstream flow through NGV was recalculated using the turbulence model under consideration and the inlet flow and turbulence profiles for the rotor row were recreated as discussed in Section 6.3.4. These profiles were then applied to the optimization model and the rotor exit values calculated.

Fig. 6.11 shows a comparison of the circumferentially-averaged rotor exit (X3) rotor relative outlet flow angle (β_3) and velocity (W_3) as well as two optimization quantities (C_{ske} and $C_{p0,rel}$) for the annular endwall case. The rotor exit relative flow angle and velocity (Figs. 6.11a & 6.11b) were chosen as comaprison parameters in order to evaluate each model's ability to capture the secondary flow structures, while the coefficient of secondary kinetic energy (C_{ske}) (Fig. 6.11c) and rotor loss coefficient ($C_{p0,rel}$) (Fig.6.11d) were selected to give an indication of each model's ability to predict a relatively simple secondary flow proxy, as well as a more complex quantity, such as the total pressure loss.

Although all the models tested appeared to capture the overall form of of the rotor exit flow, relative to the remainder of the models, the standard $k-\epsilon$ model was the least sensitive to the effects of the secondary flow, with this model showing the smallest changes in rotor relative exit velocity and angle at $\sim 15-20\%$ span. In contrast, and relative to the more complex two-equation models, the one-equation Spalart-Allmaras (SA) model appeared to perform overall disproportionately better than the standard and RNG $k-\epsilon$ models, and appeared to predict both the location of the magnitude and location of the over- and underturning turning peaks at $\sim 20\%$ and $\sim 35\%$ span, as well as the overall magnitude of the secondary kinetic energy, with significantly better accuracy.

Of the two remaining models, both the RNG $k-\epsilon$ and $k-\omega$ SST were the most sensitive to the presence of the secondary flows, with both models predicting the largest changes in rotor exit velocity at $\sim 25\%$ span, as well as the largest changes to the rotor relative exit flow angle at both $\sim 20\%$ and $\sim 35\%$ span respectively. Although both models overpredicted the magnitude of the flow angle, as discussed by Snedden (2011), this greater sensitivity to the presence of secondary flows may make

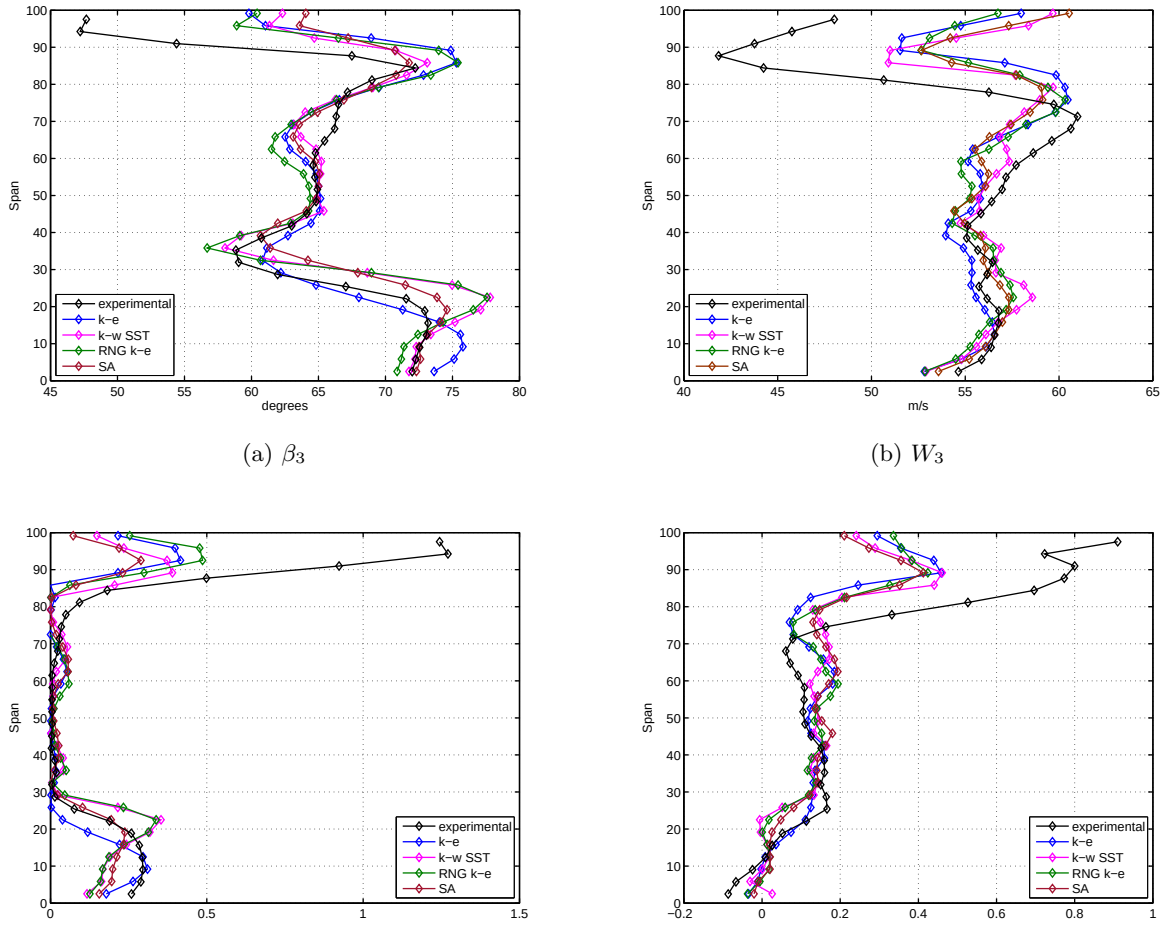

(a) β_3 (b) W_3

(c) C_{ske} (d) $C_{p0,rel}$

Fig. 6.11: Comparison of various rotor exit quantities for different turbulence closure models for the annular case

these types of model more attractive than others in scenarios where the identification of secondary flows (such as in optimization) is more important than accuracy.

Higher order closure and anisotropy

The so-called Reynolds decomposition and averaging of the Navier-Stokes equations result in the well-known Reynolds Averaged Navier-Stokes ($RANS$) equations:-

$$\begin{aligned} \frac{\partial U_i}{\partial x_i} &= 0 \\ \rho\frac{\partial U_i}{\partial t} + \rho U_j\frac{\partial U_i}{\partial x_j} &= -\frac{\partial P}{\partial x_i} + \frac{\partial}{\partial x_j}\left(\mu\left(\frac{\partial U_j}{x_i} + \frac{\partial U_i}{x_j}\right) - \rho\overline{u_j' u_i'}\right) \end{aligned} \tag{6.2}$$

in which the additional so-called Reynolds stress tensor ($\rho\overline{u_j' u_i'}$) is present and where:-

U_i is the mean flow velocity,
u_i' & u_j' are the instantaneous velocities, *and*
ρ & μ are the fluid density and molecular viscosity respectively,

and where repeated indices in a term imply summation over those indices[4]

In all the turbulence closures discussed in the preceding section, the unknown Reynolds stresses are assumed to be directly proportional to the mean flow velocity gradients, where δ_{ji} is the well-known Kronecker delta and the constant of proportionality is the so-called *turbulent viscosity* (μ_t) i.e:-

$$-\rho\overline{u_j' u_i'} = \mu_t \left(\frac{\partial U_j}{\partial x_i} + \frac{\partial U_i}{\partial x_j} \right) - \frac{2}{3}\rho k \delta_{ji} \tag{6.3}$$

This is the well-known Boussinesq approximation, the net result of which implies isotropy of the normal Reynolds stresses, an assumption which may not be valid in cases where (Wilcox (1994b)):-

- flows experience sudden changes in mean strain rate,
- flows follow curved paths over geometry,
- flows in ducts give rise to secondary flows,
- flows are exposed to body forces (i.e. such as those in rotating domains), *and*
- flows undergo boundary layer separation

Given that in a rotating blade row, at least three of the above conditions are always present (flow over curved surfaces, flows with secondary flows and exposure to body forces) with the potential for a fourth (flow separations) depending on the design of the aerofoils, it may be expected that a closure model which takes into account the anisotropy of the Reynolds stresses may perform better than those based on the Boussinesq approximation.

The Reynolds Stress Model (RSM) is a so-called second order closure model in which an additional transport equation is solved explicity for each of the normal and shear Reynolds stresses, as well a further equation which provides a means for the determination of the turbulent length scale (i.e. ϵ, ω). In most cases, the equations solved for each of the Reynolds stresses are derived from their exact counterparts, although a number of the remaining terms, namely the dissipation (ϵ_{ij}), turbulent transport (C_{ijk}) and pressure-strain (Π_{ij}) tensors, are modelled (Wilcox (1994b)).

As with the previous models, the flow through the rotor domain was solved using boundary conditions generated by solving the flow through the upstream *NGV* row with the RSM model, and the pressure strain tensor was modelled using the Linear Pressure-Strain model which includes linear contributions of the i) slow & ii) rapid *return-to-isotropy* as well as iii) wall-reflection terms.

Figs. 6.12a - 6.12d show the rotor exit relative flow angle (β_3), velocity (W_3), coefficient of secondary kinetic energy (C_{ske}) and coefficient of total pressure loss ($C_{p0,rel}$) alongside the results for Menter's

[4] i.e. $\frac{\partial U_i}{\partial x_i} = \sum_{i=1}^{3} \frac{\partial U_i}{\partial x_i}$ and $\frac{\partial^2}{\partial x_j}\left(\frac{\partial U_j}{\partial x_i}\right) = \sum_{j=1}^{3} \frac{\partial U_j}{\partial x_j x_i}$ etc

$k-\omega$ SST model for the annular case. Although some differences at the mid-span are apparent, from the figures it can be seen that the RSM model predicted very similar results to the $k-\omega$ SST model particularly in the region of the endwall secondary flow where the spanwise location of the over- & underturning peaks were largely coincident. As mentioned above, the most significant differences between the flow predictions occured in the mid-span region, where the $k-\omega$ SST model appeared to capture the flow trends and angle magnitudes at $\sim 45-60\%$ span better than the RSM model. Above $\sim 60\%$ span, the prediction of the relative flow angle and coefficient of total pressure loss of both models were largely alike, although some differences in the tip gap region persisted for the relative flow velocity and coefficient of secondary kinetic energy.

Ultimately, from the figures, it is clear that no great enhancement in prediction accuracy was obtained by increasing the complexity of the turbulence closure model to one which included the anisotropic effects of the Reynold's stresses. As a result, given the similarity between the results and the significant increase in computational expense required for the solution of the Reynolds stress equations, it was determined that the additional expense of the RSM approach was not warranted for this investigation.

Transition modelling

The flow in a turbine blade row is well known to be transitional (Moore (1995), Moore and Gregory-Smith (1996), Denton (2010)). In his work, Ingram confirmed this was still the case for non-axisymmetric contoured endwalls while investigating whether the reductions in loss measured in a turbine cascade equipped with non-axisymmetric endwalls were as a result of changes to the state of the endwall and suction surface boundary layers (Ingram (2003)). In a similar study, Snedden et al. (2009b) confirmed that this was still the case for a rotating blade row, despite some difficulty in interpreting the results.

Since standard turbulence models treat all flows within the computational domain as fully turbulent, they are unlikely to predict the loss in a turbine blade row accurately. Further to this, in cases such as the relatively well known Pratt & Whitney PAK-B low pressure turbine blade, in which a separation bubble is often found to form towards the trailing edge of the suction surface (Praisner et al. (2008)), the use of a fully turbulent simulation may preclude this feature from being resolved at all, further reducing the accuracy of the calculations (Menter et al. (2015)).

In order to investigate the effects of transition on the predicted turbine loss, the γ-transition model (Menter et al. (2015)) which is an extension of the previously discussed $k-\omega$ SST turbulence model, was trialled in addition to the models already discussed.

The γ-transition model is a revision of the $\gamma - Re_\theta$ model of Menter et al. (2006) which removes the need for the solution of an additional equation for the transition momentum thickness Reynolds Number (Re_θ) and which also rendered the original model Galilean invariant and therefore not suitable in situations including relative motion between different wall boundaries.

The model is a Local Correlation-based Transition Model ($LCTM$) in which magnitude of the turbulence production term ($\tilde{P}_k$) in the accompanying turbulence model's turbulent kinetic energy equation is controlled by the level of turbulence intermittency (γ) in the flow field. The distribution of intermittency within the flow field is calculated using a transport equation (the γ-equation), the

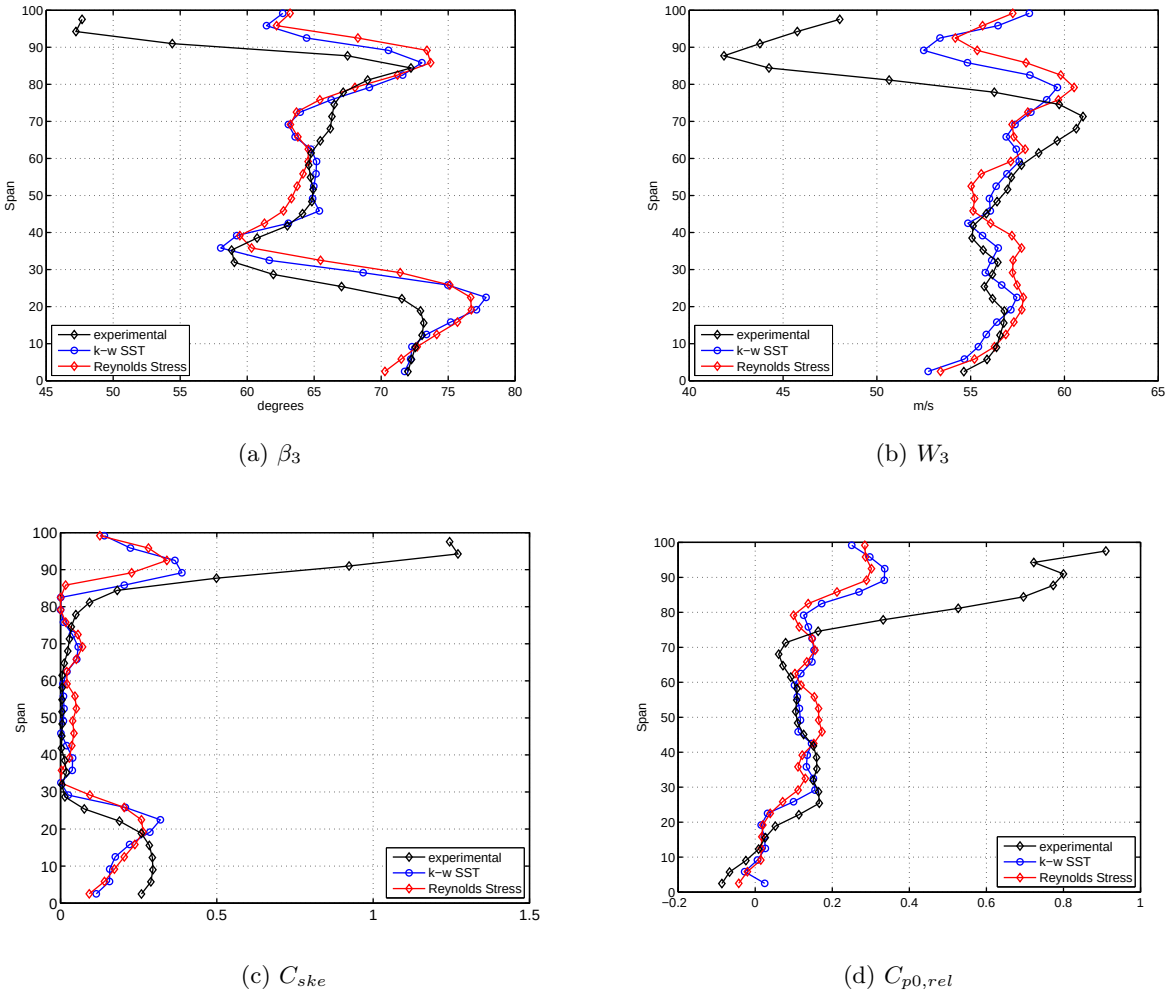

(a) β_3 (b) W_3

(c) C_{ske} (d) $C_{p0,rel}$

Fig. 6.12: Comparison of rotor exit results for the 2-equation $k-\omega$ SST and Reynolds Stress Model (RSM)

production of which itself is controlled by the critical momentum thickness Reynolds number ($Re_{\theta,c}$) which is calculated algebraically using transition correlations.

The results of the transitional simulations are shown in Figs. 6.13a - 6.13d. Like the Reynolds stress model, in the lower portion of the blade passage, the rotor exit results for the transition sensitized $k-\omega$ SST model showed considerable similarities to the baseline case, although Fig. 6.13a showed the degree of underturning predicted by the transitional model at $\sim 35\%$ span which was noticeably reduced in comparison to the fully turbulent $k-\omega$ SST model. Although some minor differences were also evident in the midspan region, the most significant differences between the baseline and transitional SST models were found within the tip gap region, where the relative rotor exit velocity (W_3) (Fig. 6.13b), coefficient of secondary kinetic energy (C_{ske}) (Fig. 6.13c) and loss coefficient ($C_{p0,rel}$) (Fig. 6.13d) were all severely underpredicted by the transitional model. This was not the case for the relative flow angle (β_3) (Fig. 6.13a) which was seen to mimic the fully turbulent results closely.

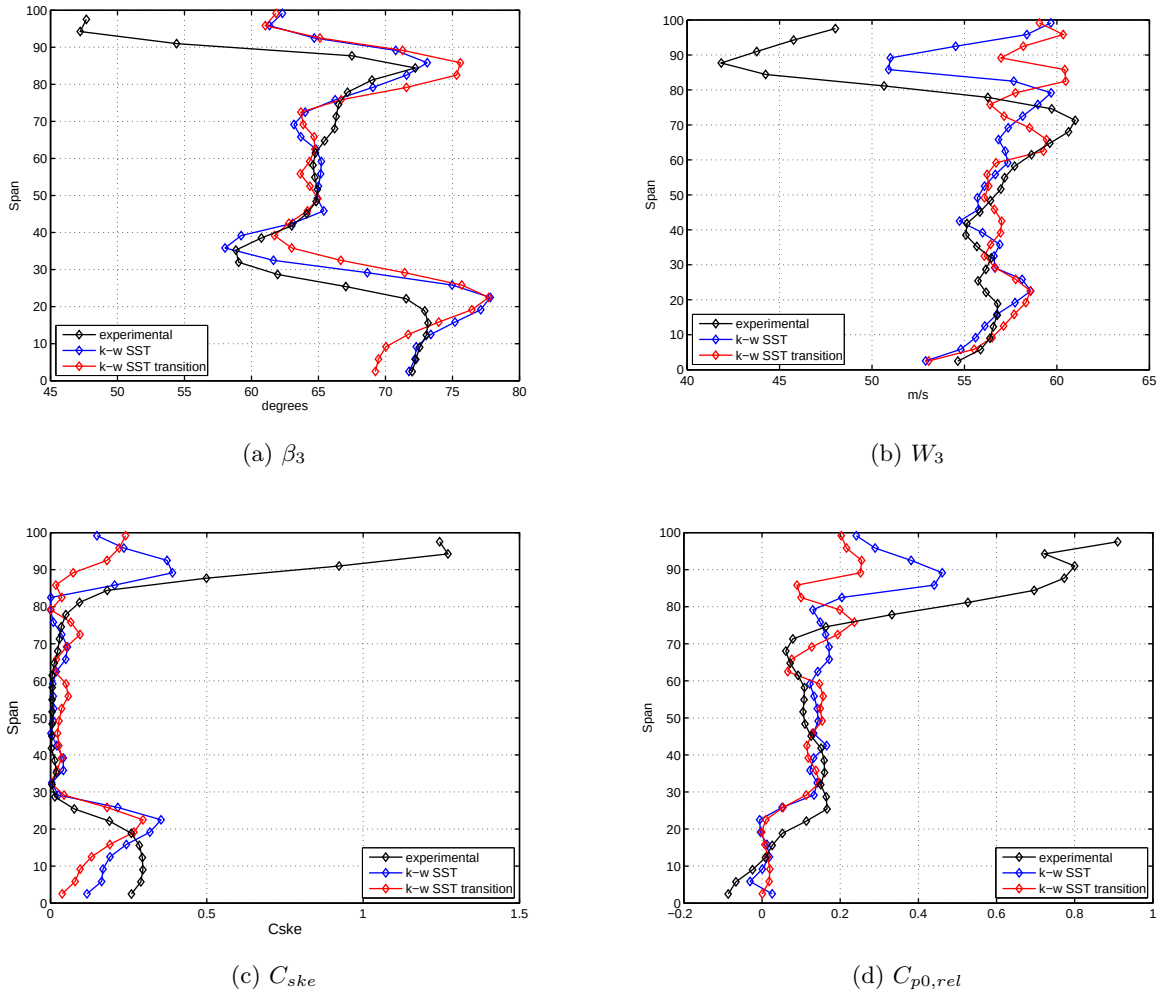

(a) β_3

(b) W_3

(c) C_{ske}

(d) $C_{p0,rel}$

Fig. 6.13: Comparison of rotor exit results for the standard $k-\omega$ *SST* model and the $k-\omega$ *SST* model coupled with the 1-equation γ-transition closure model

Critique of turbulence models

In summary, a variety of turbulence closures and one transition model were tested to ascertain their ability to predict the various flows expected in the rotor optimization model. Perhaps the best performing model relative to its complexity, was the one-equation model of Spalart & Allmaras. This result gave much credibility to comments by some authors relating to its usefulness in turbomachinery calculations, and explains its use by authors such as Denton and Pullan (2012). However, it was felt that for this application, the most appropriate models for use would be those models which provided an adequate blend of accuracy in terms of absolute velocity and angle magnitudes, but also those models which displayed the greatest sensitivity to the presence of the secondary flows. In this regard, the *RNG* $k-\epsilon$ and $k-\omega$ *SST* models were found to be most useful.

Higher order closure models which account for anisotropy in the Reynolds stress tensor (the RSM model) and transition models, which account for transitional behaviour of the flow, did not provide

significant improvements to the overall prediction of the flow when compared with the simpler one and two-equation models.

As a result, the best performing two-equation model, the $k-\omega$ SST model was selected as the most appropriate model for this work as this would provide some measure of continuity between the work of previous authors who have studied secondary flows using this model using the same turbine as was under consideration in this work. In addition, the sensitivity of the model to the presence of the secondary flows was seen as an advantage in the current work since this model was more likely to pick up even subtle changes to the secondary flow profiles therefore aiding the endwall optimization process.

The model was found to predict the secondary flows best when using the Wilcox's low Reynolds corrections (Wilcox (1994a)) and with Menter's production limiter (Menter et al. (2003)). The remainder of the model constants were left unchanged from their recommended values.

7

Results of Endwall Optimizations

In this Chapter, the results of the endwall contouring optimizations are discussed. As a prerequisite to this, some discussion on the convergence of the endwall design routine for each objective function is included, with the intention of providing additional insight into the performance of each objective function in the context of the overall performance of the endwall generation routine. Thereafter, the predicted (CFD) mass- and circumferentially-averaged results at the rotor exit (X3) and downstream ('mixed-out') (X4) measurement planes are presented. As an aid to the understanding of these results, 2-dimensional contour plots for each quantity at each measurement location are included alongside the circumferentially-averaged results.

After presentation of the numerical results, the mass- and circumferentially-averaged experimental results for a selection of the optimized endwalls, at the same measurement locations are presented, with the intent to validate as many of the computed results presented earlier. Finally, the overall results are summarised and the chapter is concluded by isolating the most significant results from the numerical and experimental test process.

7.1 Convergence

7.1.1 Cost function convergence and scatter plots

The following section contains information relating to the convergence of the optimization routine for each objective function. First, for each endwall, a plot of the convergence of each objective function quantity versus algorithm iteration is included (along with contour plots which show graphically, the convergence of each endwall to its final design) and thereafter, a set of scatter plots (Appendix B, Figs. B.1 - B.32), in which the sampling of the design space by the optimization algorithm and subsequent 'clustering' of sample points is used to show regions in which 'successful' designs were found. Each point in the scatter plots was also assigned a color using a **blue** ● → **red** ● colour map with the 'cool' portion of the map indicating poor objective function values and vice versa.

In this way, not only does the density of sampling points give an idea of the overall convergence of the scheme to its final optimum, but also the location of additional regions (if present) within the design space in which alternative designs of similar performance may be found. Additionally, on each plot, the location of the first and last (i.e. best) sampling points in which the objective function was seen decrease is marked (first - **blue box** □, last - **black box** □). Added to that, the trajectory of

the endwall optimization routine taken through the design space between 'successful' samples (i.e. samples at which the cost function was seen to decrease) is shown. In some cases, additional points of interest in the design space are marked (◇) along with text indicating the iteration number of the marked point.

Finally, in order to provide some context to the location of the infill sampling points selected by the design routine during each optimization, the original *LHS* database points on which the *DACE* surrogate model was built, are indicated by black dots of reduced size (i.e. ●).

Marker	Description
□	first sample point
□	last sample point
●	database point
●	high OF-value point (bad)
●	low OF-value point (good)
◇ It 225	specific iteration point

Table 7.1: Plot legend - optimization scatter plots

η_{tt}-based

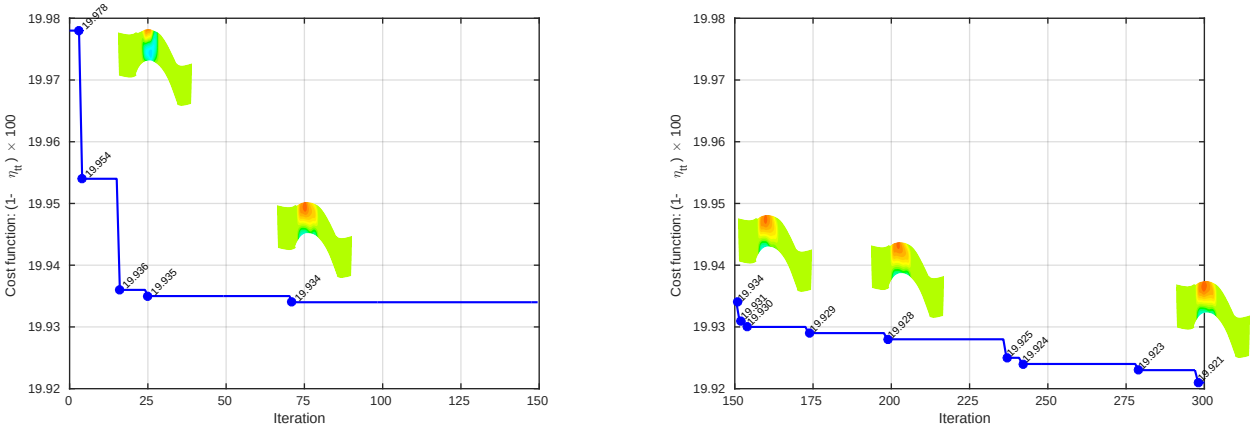

(a) Iterations 1-150 (EI_1)

(b) Iterations 150-300 (WB_1)

Fig. 7.1: Cost function convergence for the η_{tt}-based endwall

Figs. 7.1a & 7.1b show the reduction in the cost function formulated for the η_{tt}-based endwall. The influence of the two stage optimization is clear - the procedure commences with a number of large reductions in the objective function early on (consistent with the isolating the appropximate location of the global optimum), followed by a series of steady reductions in the overall cost function consistent with the 'fine-tuning' of the design once the infill search criteria had been switched to the highly localised searching criteria (WB_1).

The corresponding scatter plots (Figs. B.1 - B.4) show the convergence of the individual parameters of each of the 4 driven curves by which the circumferential endwall curvature was defined. As was the case for the majority of the remaining endwall designs, the optimum parameters for the first driven curve (curve 2), were found to lie along the c_1 constraint boundary, indicating a preference for the maximum allowable amplitude of the first driven curve, with the optimum phase angle (Ψ_1) of that curve being found to be that which located the point of maximum amplitude adjacent to the blade pressure surface. Despite the relatively concentrated sampling of the design space near to where the optimum parameters were found, the routine was seen to sample relatively evenly throughout the remainder of the $c_1 - n_1 - \Psi_1$ feasible region indicating that the search for the optimum parameters did include the correct balance between explorative & exploitative behaviour.

For the remainder of driven curves (3, 4 & 5), the scatter plots again appeared to show a relatively thorough search of the feasible space for each parameter, although in each case, the region in which the best performing parameters were found appeared to form a well-defined subregion of the overall design space indicating that, at least for the blade and endwall parametrisation used in this investigation, the geometry for the maximum efficiency endwall was well defined.

C_{ske} − based

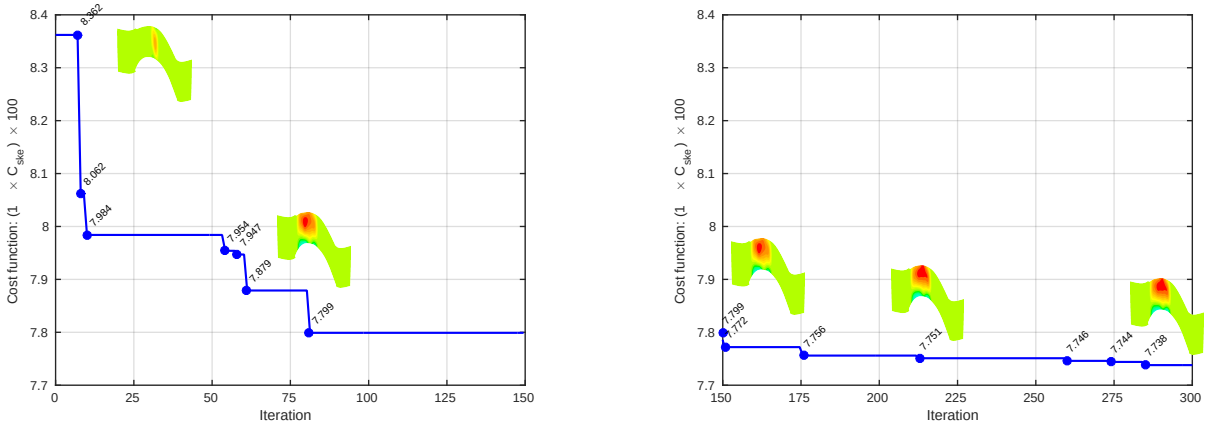

(a) Iterations 1-150 (EI_1)

(b) Iterations 150-300 (WB_1)

Fig. 7.2: Cost function convergence for the C_{ske}-based endwall

The convergence behaviour of the C_{ske}-based objective function (Figs. 7.2a & 7.2b) appeared to be very similar in character to that of the η_{tt}-based objective function, although slightly more iterations were required to locate the region of minimum C_{ske} ($\sim$ 17 for the η_{tt}-based c.f. $\sim$ 82 for the C_{ske}-based). Again, the optimization was characterised by a number of large initial reductions in the cost function, followed by a series of small, progressive improvements once the infill criteria was switched to the local search criteria.

The driven curve scatter plots (Figs. B.5 - B.8) also showed similar trends to the η_{tt}-based objective function - with the near-optimum parameters of the initial endwall curve (curve 2) again found to

be densely clustered along the c_1 constraint boundary. In contrast to the η_{tt}-based endwall, Fig. B.5 showed that the optimizer searched less uniformly through the $c_1 - n_1 - \Psi_1$ design space, and instead expended almost its entire sampling budget in the neighbourhood where the optimal design parameters were finally located. In addition, the C_{ske}-based objective function was also seen to sample at both the upper and lower limits of the curve periodicity (n_2) as well as at the maximum curve phase angle (Ψ_1).

Despite the differences between the searches for the optimum curve 2 parameters of the η_{tt}- and C_{ske}-based endwalls, the characteristics of the parameter searches for the remaining C_{ske} endwall curves (3, 4 & 5) were again very similar to those noted for the η_{tt}-based objective function. Again, each of the feasible regions for the remaining curves were explored in a relatively uniform fashion, whilst the regions of lowest C_{ske} were relatively well-defined, with similar overall locations to those found for the η_{tt}-based objective function.

$C_{p0,rel}$ − based

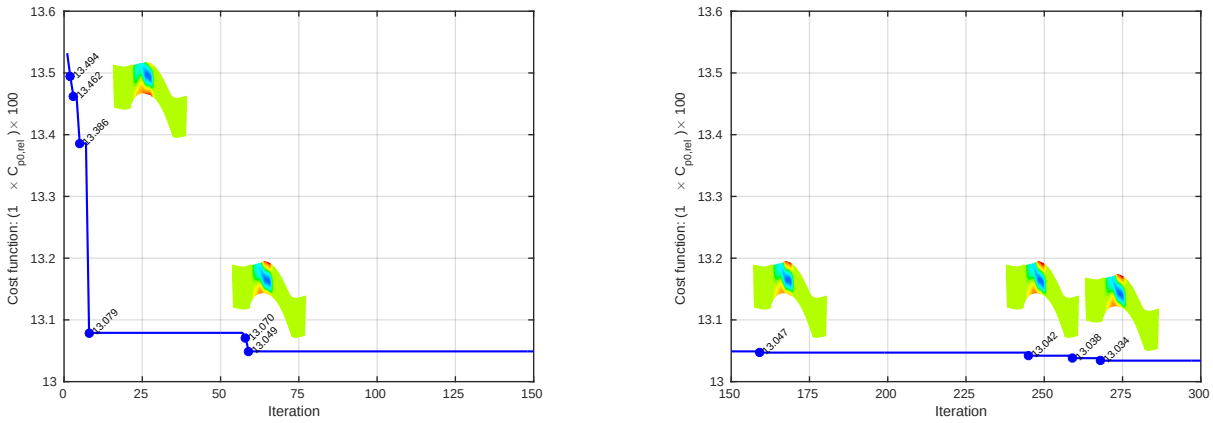

(a) Iterations 1-150 (EI_1)

(b) Iterations 150-300 (WB_1)

Fig. 7.3: Cost function convergence of $C_{p0,rel}$-based endwall

The $C_{p0,rel}$-based convergence plots (Figs. 7.3a - 7.3b) once again showed the typical behaviour discussed for the previously discussed C_{ske}- & η_{tt}-based endwalls, although the routine appeared to locate the region of minimum loss coefficient even more efficiently (than the previous cases) while the remainder of the sampling budget was expended almost exclusively on refining the initial design. The scatter plots (Figs. B.9 - B.9) tell a similar story, with the region of predicted low loss appearing to be relatively well defined by the obvious clustering of the infill sampling locations for each driven circumferential curve. In addition, the trajectory plots for each curve show the relatively small region in which decreases in the $C_{p0,rel}$-based cost function were located.

In contrast to all the previous designs though, the $C_{p0,rel}$-based design did not sample as consistently along the boundary of the c_1 parameter. Instead, the parameters for the first endwall curve were

selected to produce a reversed version of the well-known 'hump-and-dip' configuration, with the dip located immediately aft to the blade leading edge on the pressure side and a slight 'hill' feature correspondingly located adjacent to the suction surface. Similarly, the optimum parameters for curve 3 appeared to be selected to progress the formation of the reverse 'hump-and-dip' feature initiated by the curve 2 parameters by increasing the amplitude of the curve as well as shifting it towards the suction surface by approximately 25°. This created a narrow valley which traversed the endwall surface in approximately the same trajectory as the pressure side horseshoe vortex, the effect of which is discussed later. Finally, the parameters of the remaining curves (curve 4 & 5) were selected to extend the above-mentioned feature, with the maximum allowable curve amplitudes (c_3 & c_4) being selected for both the remaining curves and the phase shift terms (ψ_3 & ψ_4) selected to shift the position of the maximum depth to a location approximately adjacent to the suction surface.

β_{dev} − based

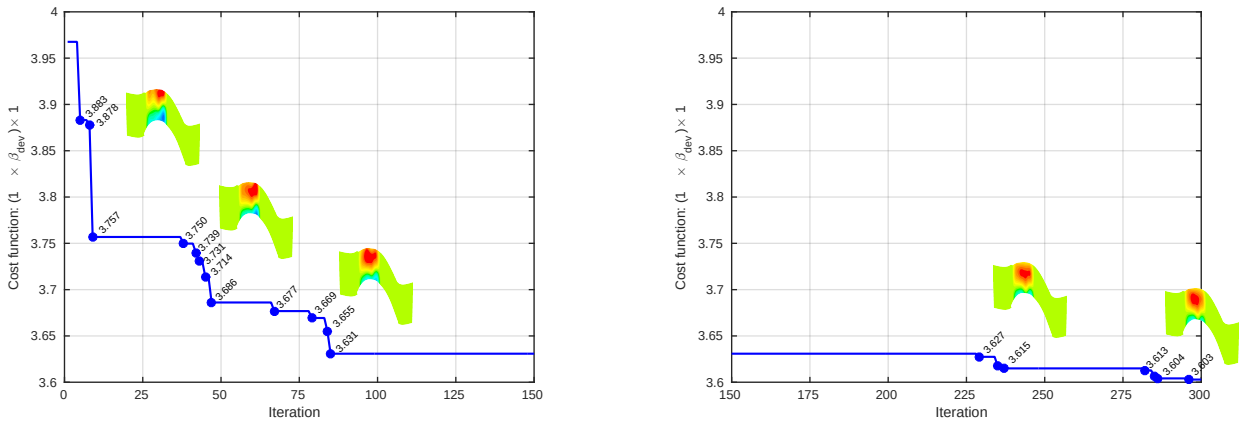

(a) Iterations 1-150 (EI_1)

(b) Iterations 150-300 (WB_1)

Fig. 7.4: Cost function convergence of the β_{dev}-based endwall

As was the case for all the previous quantities, the convergence behaviour of the β_{dev}-based cost function was characterised by a large number of initial decreases, consistent with the discovery of a series of regions within the design space corresponding to low mass-averaged flow deviation from design. Unlike the preceding endwalls though, the β_{dev}-based cost function appeared to contain a number of local optima, in which favourable mass-averaged values of the cost function were found. This assertion appeared to be corroborated by the series of step-like reductions in the magnitude of the cost function (Fig. 7.4a) which were seen to correspond to fairly significant changes in the overall characteristics of the endwall shape. After having appeared to locate the vicinity of the optimum parameters (corresponding to the lowest mass-averaged flow deviation from design β_{dev}) and a switch to the more locally exploitative *ISC* criteria, a series of small reductions in the cost function (corresponding to relatively minor changes in the geometry of the endwall, as evidenced by the inset figures), was noted.

While the scatter plots for the first driving endwall curve (Fig. B.13) showed similar characteristics to all of the previous endwalls (with the exception of the $C_{p0,rel}$-based design), the plots for the 3^{rd} & 4^{th} curves (Figs. B.14 - B.15) corroborated the narrative discussed above, with the optimization trajectory showing that the algorithm investigated a number of distinct regions of the design space before finally locating the region of the lowest objective function values which corresponded to the optimum parameters returned by the endwall design routine. Finally, the scatter plots for the final endwall curve (curve 5) (Fig. B.16) showed a significantly more concentrated sampling of the design space indicating much reduced variability in the selection of the parameters for the final endwall curve.

SKEH − based

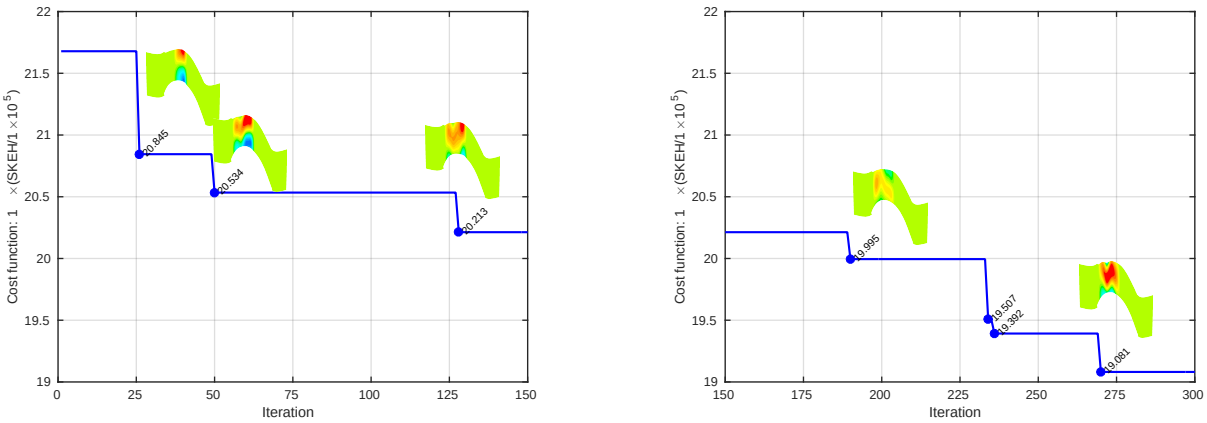

(a) Iterations 1-150 (EI_1)

(b) Iterations 150-300 (WB_1)

Fig. 7.5: Cost function convergence of the $SKEH$-based endwall

The convergence behaviour of the $SKEH$-based endwall did not appear to be as well-defined, in that, in contrast to the initial large decreases in the cost function which were then followed by a succession of smaller incremental improvements in the overall design as was noted for a number of the previous objective functions, Figs. 7.5a & 7.5b both show a series of relatively large reductions in the cost function at approximately equal junctures during the optimization process, suggesting that even after 300 iterations, the optimal solution had still not been found. This position appears to be corroborated by a review of the actual endwall shapes (Fig. 7.5a & 7.5b inset) associated with each reduction in the objective function which show considerable changes in the physical nature of the endwall with each reduction in the objective function.

A review of the optimization scatter plots (Figs. B.17 - B.20) tells a similar story. With the exception of endwall curve 2 which showed some similarities to those for previous endwalls (with relatively concentrated sampling of the design space in the vicinity of the final optimum point), the plots appeared to show no particular affinity for any particular region of the parameter space with apparently indiscriminate and spatially isolated portions of the space all resulting in reduced objective function magnitudes without any particular affinity for one particular region. Further, as is evidenced by the

traces plotted in Figs. B.18, B.19 & B.20, the optimizer was seen to traverse the majority of the design space with no apparent particular restrictions resulting in the large changes in the physical endwall shape as mentioned above.

$\eta_{de} - based$

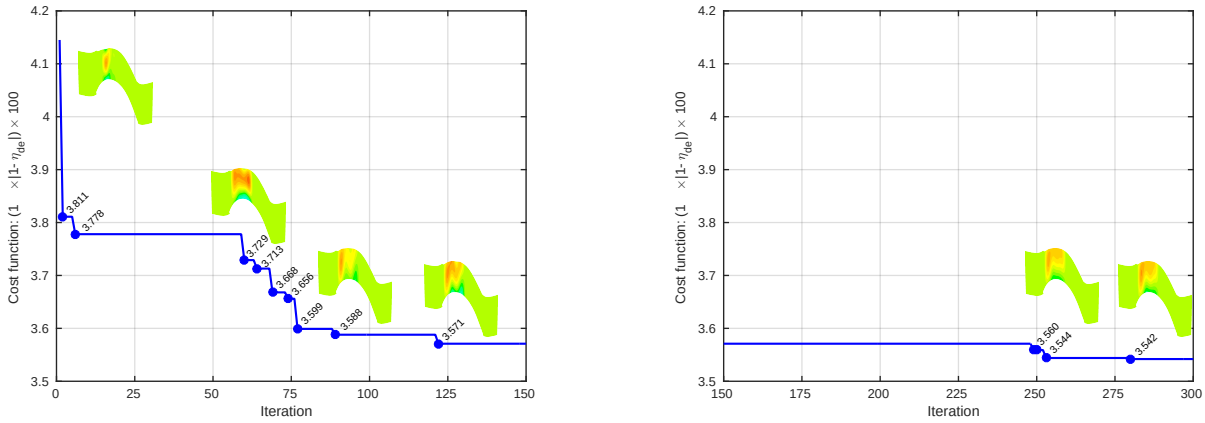

(a) Iterations 1-150 (EI_1)

(b) Iterations 150-300 (WB_1)

Fig. 7.6: Cost function convergence of the η_{de}-based endwall

The convergence plots for the η_{de}-based endwall (Fig. 7.6) showed a return to the more conventional convergence behaviour previously noted for the majority the endwalls discussed to date. More specifically, during the early iterations of the optimization procedure (Fig. 7.6a), the process was dominated by the characteristically rapid decrease in the target objective function, followed by a second phase in which the initial design was further refined. Further to this, similar to the previously mentioned C_{ske}- & β_{dev}-based designs, and in contrast to the η_{tt}- & $C_{p0,rel}$-based designs, the final characteristic shape of the design appeared to be located relatively late in the initial exploratory phase of the optimization (after approximately $\sim$ 76 iterations), while for the latter endwalls, the characteristic shape of the final design was isolated much earlier.

As was the case for the convergence plots above, the scatter plots (Fig. B.21 to B.24) again showed significantly more similarity to the previous endwalls than was the case for the $SKEH$-based design, with the design routine appearing to initially sample the entire design space (with the exception of curve 2, Fig. B.21) relatively uniformly, before isolating and re-sampling the design space in regions where favourable objective function values were found.

$C_{ske,1} + \beta_{dev,0.7} - based$

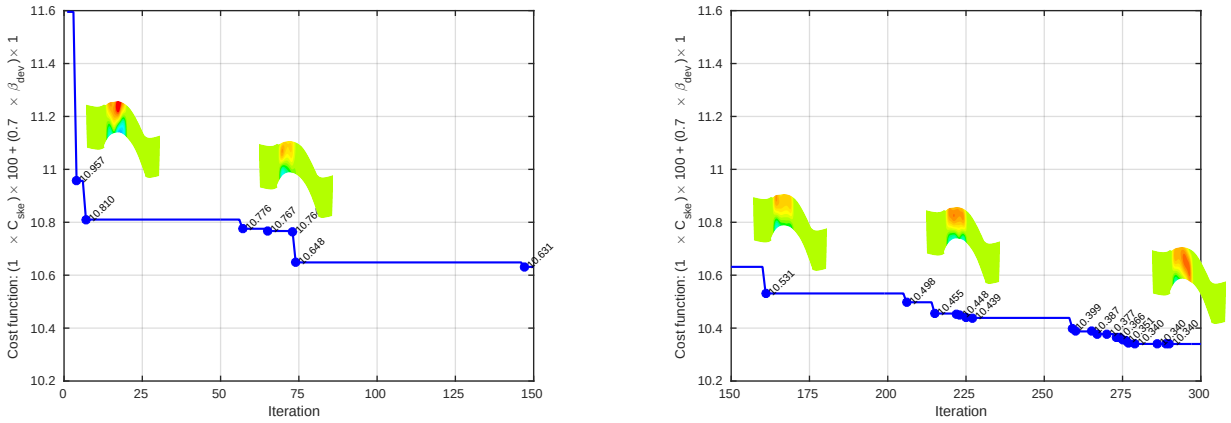

(a) Iterations 1-150 (EI_1)

(b) Iterations 150-300 (WB_1)

Fig. 7.7: Cost function convergence for the $C_{ske,1} + \beta_{dev,0.7}$-based endwall

Similar to the η_{tt}- and C_{ske}-based endwalls, the $C_{ske,1} + \beta_{dev,0.7}$-based endwall also showed initial large reductions in the cost function as well as a gradual refinement of the design once the *ISC* search function had been changed. However, unlike the previous designs, the incremental refinement of the design was halted after approximately $\sim$ 259 iterations, whereafter the routine located a previously undiscovered region of low objective function values, which was then more fully explored and exploited. This occurrence was well illustrated by the succession of of rapid reductions in the objective function spanning from iterations $\sim$ 259 - 290 in Fig. 7.7b as well as accompanying changes of the endwall profile itself (see inset).

In terms of the *ISC* scatter plots (Figs. B.25 - B.25), the initial endwall curve (curve 2) once again showed very similar sampling characteristics to the C_{ske}-only based endwall. In particular, in the search for the optimum curve 2 parameters, both the upper and lower limits of the n_1 periodicity parameter were sampled, as well the upper limit of the curve phase shift angle (Ψ_1). Again, the c_1 parameter was most often sampled at its maximum constrained value ($c_1 = 2mm$). As with the previous endwalls, the remainder of the endwall curves showed some clustering at various points in the design space, although this appeared to be less distinct than for the previous designs. In addition, consistent with the discovery of the 'new' region of low cost function values, in contrast to the previous designs, two distinct regions of favourable objective function values are discernible for almost all of the remaining endwall parameters. The fundamental change in character of the endwall at approximately 259 iterations is also distinguishable by plotting the last favourable design point located immediately prior to the change (iteration 227) whereupon the change in the general locality of the sampling objective function sampling was changed.

$C_{p0,rel,1} + \beta_{dev,0.7} - based$

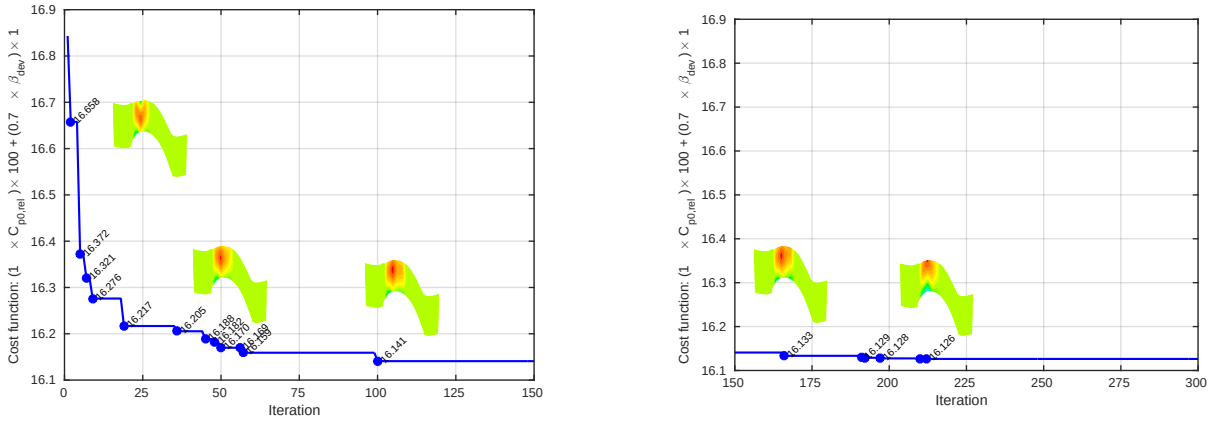

(a) Iterations 1-150 (EI_1)

(b) Iterations 150-300 (WB_1)

Fig. 7.8: Cost function convergence of the $C_{p0,rel,1} + \beta_{dev,0.7}$-based endwall

Finally, although not necessarily well illustrated by the plots of the cost function reductions (Figs. 7.8a - 7.8b), the optimization of the $C_{p0,rel,1} + \beta_{dev,0.7}$-based endwall proceeded in a manner very similar to that of the $C_{ske,1} + \beta_{dev,0.7}$-based design, in which the design routine was seen to converge fairly readily to an initial optimum¿ After this the routine located a previously undiscovered region of low cost function magnitudes from which the final optimum parameters were finally selected. Despite the relatively fundamental change in the overall characteristics of the endwall, the corresponding reduction in the magnitude of the cost function was fairly small, as evidenced by the comparatively small change in the cost function value between iterations 166 & 191 ($\sim 16.133 \rightarrow \sim 16.129$). Unlike the $C_{ske,1} + \beta_{dev,0.7}$-based endwall, where the change in endwall characteristics was driven by the discovery of a region of reduced flow deviation from design angle (i.e. β_{dev}), in the current case the rearrangement of the endwall configuration between iterations 166 & 191 was consistent with a slight *increase* in the mass averaged flow deviation from design, and by a correspondingly larger *reduction* in the mass-averaged rotor exit loss coefficient ($C_{p0,rel}$).

The scatter plots for the initial circumferential endwall curve (curve 2) (Fig. B.29) are fairly similar to all the preceding designs (apart from the $C_{p0,rel}$-based endwall), and limited to a relatively dense subregion of each parameter's feasible region, while the change in the fundamental configuration of the endwall as described above was well illustrated by the presence of a number of distinct regions of low overall objective function values (particularly for curves 3 & 4).

7.1.2 Comparison of *DACE* and CFD predicted final objective function values

In addition to the analysis of each optimization run as discussed above, an additional convergence test in which the final objective function sample point was removed from the surrogate model database, and a prediction of that point then made using the database and model hyperparameters for the $n-1$

(i.e. the 299^{th}) iteration, was performed. The value of the predicted final point was then compared with the actual value calculated by the CFD for each objective function during the final (i.e. 300^{th}) iteration. This test was undertaken in order to gain an idea of the accuracy of the surrogate model prediction accuracy and the results are presented in Table 7.2 below :-

Table 7.2: Summary of *DACE* and CFD predicted objective function values

Cost function	*Final point*		$\Delta_{metamodel/cfd}$
	DACE[a]	CFD	
η_{tt}-based	19.9010	19.8990	+0.01% (+0.0020)
C_{ske}-based	7.7403	7.7410	−0.01% (−0.0007)
$C_{p0,rel}$-based	13.0840	13.0853	−0.01% (−0.0013)
β_{dev}-based	3.6412	3.6410	+0.01% (+0.0002)
$SKEH$-based	21.9793	21.3741	+2.83% (+0.6052)
η_{de}-based	3.6318	3.6176	+0.39% (+0.0142)
$C_{ske,1} + \beta_{dev,0.7}$-based	10.4587	10.4587	$\sim$ 0.00% ($\sim$ 0.0000)
$C_{p0,rel,1} + \beta_{dev,0.7}$-based	16.1891	16.1890	$\sim$ 0.00% (+0.0001)

[a] Predicted using *DACE* model parameters from iteration 299 (θ_{299})

From the comparisons for each objective function above, it is clear that at the end of each optimization run, the accuracy of the *DACE* model was very good with the best agreement between the predictions of the objective functions realised for the $C_{ske,1} + \beta_{dev,0.7}$ & $C_{p0,rel,1} + \beta_{dev,0.7}$ objective functions. In addition, the error between the metamodel and CFD predictions of the final iteration objective function value for the η_{tt}-, C_{ske}-, $C_{p0,rel}$-, β_{dev}- & η_{de}-based objective functions was considerably less than 1% of the final predicted value. Consistent with its poorer convergence behaviour as evidenced by its cost function convergence graphs, the greatest discrepancy between the metamodel and predicted model values was noted for the $SKEH$-based objective function, with an error of approximately +2.83%.

7.2 Mass-averaged CFD results

The mass-averaged CFD results for each endwall at the rotor exit (X3) and downstream ('mixed-out') (X4) measurement planes are included in Sections 7.2.1 & 7.2.2. For each endwall and each measurement location, the predicted results were mass-averaged over the entire blade span using the techniques discussed in Section 4.8.2 and reported as the percentage change from the annular case for each quantity.

Finally, summaries of the overall mass-averaged rotor exit (X3) and 'mixed-out' results (X4), including the percent changes from the annular case, are shown in Figs. 7.9 & 7.9.

Line	Description
	CFD (change from annular)

Table 7.3: Plot legend - CFD mass-averaged results

7.2.1 Rotor exit (X3)

η_{tt} − based

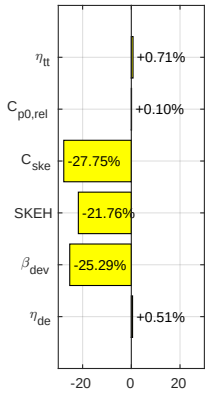

In terms of increasing the overall rotor efficiency, the η_{tt}-based endwall was predicted to perform the best of all those endwalls designed, with an increase in mass-averaged total-total rotor efficiency of +0.71% predicted for the design. Accompanying the predicted increase in rotor efficiency, were fairly significant predicted decreases in the mass-averaged rotor exit coefficient of secondary kinetic energy (C_{ske}) (−27.75%) and the flow deviation angle from design (β_{dev}) (−25.29%). Further to this, a decrease in the mass-averaged $SKEH$ of approximately −21.76% was also predicted, consistent with the decreased coefficient of secondary kinetic energy although not as significant. The rotor exit loss ($C_{p0,rel}$) was predicted to remain largely equivalent to the baseline case, with only a small increase in the overall magnitude predicted (+0.10%). Finally, a small increase in the mass-averaged design efficacy (η_{de}) at the rotor exit was also predicted (+0.51%).

C_{ske} − based

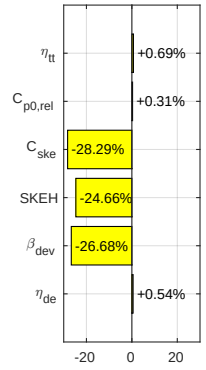

In general, the C_{ske}-based endwall was predicted to perform very similarly to the η_{tt}-based design, with only minor differences in their performance being predicted. More specifically, for the fully optimized C_{ske}-based endwall, the predicted reductions in the coefficient of secondary kinetic energy (C_{ske}) were slightly larger than those of the η_{tt}-based endwall (−28.29%), whilst the predicted increase in loss coefficient ($C_{p0,rel}$) as a result of the endwall contouring was slightly increased (+0.31%) in comparison to the η_{tt}-based design. Further, consistent with the increased reductions in the coefficient of secondary kinetic energy, for the C_{ske}-based endwall, slightly larger reductions in the flow angle deviation from design were predicted (−26.68%), as well as slightly increased reductions in the rotor exit mass-averaged $SKEH$ (−24.66%). Finally, as was the case for the η_{tt}-based design, a small improvement (+0.54%) in the design efficacy (η_{de}) was also predicted for this endwall.

$C_{p0,rel}$ − based

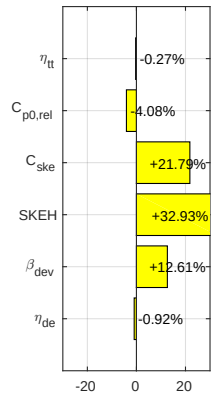

In contrast to the C_{ske}-based design, the predicted results for the $C_{p0,rel}$-based endwall were considerably different from those of the η_{tt}-based design. More specifically, the results for the $C_{p0,rel}$-based design included a predicted reduction in the overall mass-averaged rotor efficiency (-0.27%), as well as substantial increases in the mass-averaged coefficient of secondary kinetic energy ($+21.79\%$), flow angle deviation for design ($+12.61\%$) and $SKEH$ ($+32.93\%$). Again, in contrast to the previous designs, a moderate decrease in the rotor exit relative total pressure loss coefficient ($C_{p0,rel}$) was predicted as a consequence of the optimization (-4.08%). Finally, and again in contrast to the previous cases, a reasonably large decrease in the mass-averaged rotor design efficacy of -0.92% was predicted.

β_{dev} − based

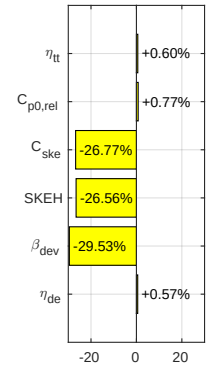

A review of the predicted changes in the various mass-averaged rotor exit quantities showed that the β_{dev}-based endwall resulted in the same general changes in the flow as the η_{tt}- & C_{ske}-based designs, although the relative magnitudes of the changes between the current endwall and the annular, was somewhat different to those which were predicted for the previous designs. More specifically, the β_{dev}-based endwall was predicted to result in an increase in total-total efficiency of $+0.60\%$ which was significant, but not as great as those increases predicted for the aforementioned designs. Further to this, for the present case, the predicted reduction in the coefficient of secondary kinetic energy was smaller than that predicted for the previous designs (-26.77%), while the reduction in the flow deviation from design - as could be expected - was slightly larger than both those of the η_{tt}- & C_{ske}-based designs respectively (-29.53%). Again in contrast to the preceding η_{tt}- & C_{ske}-based designs, the increase in the predicted rotor exit loss coefficient was slightly increased ($+0.77\%$). The mass-averaged reduction in $SKEH$ and increase in η_{de} at the rotor exit were predicted to be -26.56% & $+0.57\%$ respectively, which were very similar to the those predicted for the C_{ske}-based endwall.

$SKEH - based$

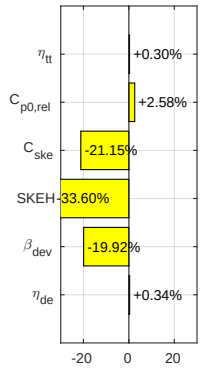

While the predicted results of the $SKEH$-based design showed some similarity to the a number of the previously discussed endwalls, the most significant difference between the $SKEH$-based design and its predecessors, was the significant increase in the reduction in the mass-averaged $SKEH$ (-33.60%) at the rotor exit. This was expected given the formulation of the objective function for this endwall with this quantity, and the similar effects for each of the endwalls for which a single quantity was used as the basis of the design function, although unlike the C_{ske}-based design, this reduction in $SKEH$ was not predicted to translate into a significant increase in the rotor efficiency, and only a moderate increase was predicted for this endwall ($+0.30\%$). While reductions in the mass-averaged C_{ske} & β_{dev}were predicted for the current endwall (-21.15% & -19.92%), these were considerably less than those predicted for the both the η_{tt}- as well as the C_{ske}-only based designs. As was the case for both the η_{tt}- as well as the C_{ske}-based designs, an increase in the mass-averaged rotor exit $C_{p0,rel}$ was predicted, although this increase was significantly larger than that predicted for any of the previous designs ($+2.58\%$) with the exception of the $C_{p0,rel}$-only based design. Finally, as was the case for all the endwalls investigated to date (again, with the exception of the $C_{p0,rel}$-based design), a small increase in the design efficacy (η_{de}) was predicted for the current endwall ($+0.34\%$), although as was the case for the efficiency, this was relatively small in comparison to the majority of the previous designs.

$\eta_{de} - based$

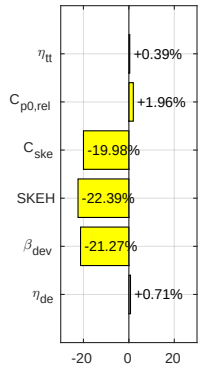

As would be expected, at the rotor exit measurement plane, the η_{de}-based endwall showed the greatest improvement in the mass-averaged design efficacy (η_{de}), with a reasonably significant increase in comparison the annular case of approximately $+0.71\%$. This was accompanied by relatively moderate reductions in the mass-averaged coefficient of secondary kinetic energy (C_{ske}) and secondary kinetic energy helicity ($SKEH$), as well as the flow deviation from design angle (β_{dev}) of -19.98%, -22.39% & -21.27% respectively. Similar to the $SKEH$-based design, the η_{de}-based design resulted in a fairly large predicted increase in the rotor exit loss coefficient ($C_{p0,rel}$) ($+1.96\%$) and despite the reductions in the various measures of secondary flow, only a relatively small increase in the predicted rotor total-total efficiency ($+0.39\%$).

$C_{ske,1} + \beta_{dev,0.7} - based$

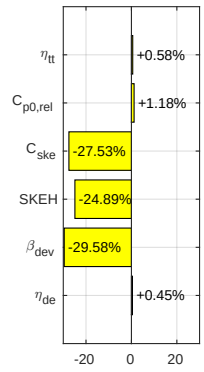

The results of the $C_{ske,1} + \beta_{dev,0.7}$-based design were largely similar to those of the C_{ske}-based endwall, although the effect of the added β_{dev} component to the cost function was clearly evident. In particular, while the predicted reductions in the coefficient of secondary kinetic energy (C_{ske}) were largely similar to those of the C_{ske}-only design (i.e. -27.53%), the mass-averaged flow deviation from design (β_{dev}) was predicted to be decreased by a further 3% relative to the C_{ske}-only endwall. This additional reduction in flow deviation was accompanied by a fairly substantial increase in the overall predicted rotor exit loss coefficient relative to both the η_{tt}- & C_{ske}-only based designs (+0.87%) as well as a reduction in the overall predicted increase in rotor total-total efficiency relative to the η_{tt}- & C_{ske}-based designs. Finally, the predicted reduction in the mass-averaged $SKEH$ as well as the increase in design efficacy (η_{de}) were largely unchanged from the η_{tt}- & C_{ske}-based cases (-24.89% & $+0.45\%$) respectively.

$C_{p0,rel,1} + \beta_{dev,0.7} - based$

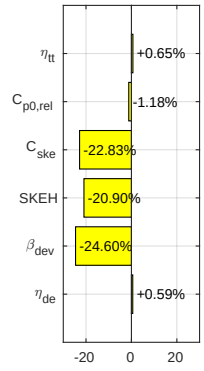

Finally, as was the case with the $C_{ske,1}+\beta_{dev,0.7}$-based endwall, the $C_{p0,rel,1}+\beta_{dev,0.7}$-based design shared some similarity with the η_{tt}- & C_{ske}- as well as the $C_{ske,1} + \beta_{dev,0.7}$-based design itself, although the predicted magnitudes of the changes in each of rotor exit quantities were slightly different. More specifically, while predicted to be less than that of the η_{tt}- & C_{ske}-based endwalls, the increase in the rotor efficiency was predicted to be moderately more than that predicted for the $C_{ske,1} + \beta_{dev,0.7}$-based design. In addition, instead of the large increase in the mass-averaged rotor exit loss coefficient predicted for $C_{ske,1} + \beta_{dev,0.7}$-based design, the combination of the $C_{p0,rel}$ & β_{dev} components for the current objective function was predicted to result in an overall reduction in the rotor exit loss coefficient. Once again, an overall reduction in the mass-averaged coefficient of secondary kinetic energy (-22.83%) was predicted for this endwall, although this was less than that predicted for both the η_{tt}-, C_{ske}-, β_{dev}- as well as $C_{ske,1} + \beta_{dev,0.7}$-based designs. The predicted reductions in the rotor exit mass-averaged $SKEH$, and β_{dev} were similar to those predicted for the above-mentioned designs, although in all cases, these were smaller than the aforementioned designs (-20.90% & -24.60% respectively). Finally, an overall increase in the mass-averaged design efficacy (η_{de}) was predicted for this design (+0.59%).

7.2.2 Downstream (X4)

At the downstream measurement plane (X4), only the rotor total-total efficiency (η_{tt}), pressure loss coefficient ($C_{p0,rel}$), coefficient of secondary kinetic energy (C_{ske}) and secondary kinetic energy helicity ($SKEH$) are reported, since the remaining quantities (i.e. the relative flow angle from design (β_{dev}) and design efficacy (η_{de})) rely on the design flow angle for their calculation which was not available at the downstream plane.

η_{tt} − based

In comparison to the annular case, at the downstream plane, the η_{tt}-based endwall was once again predicted to the greatest increase in rotor total-total efficiency (+0.86%). This was accompanied by significant reductions in the mass-averaged coefficient of secondary kinetic energy (C_{ske}) (−33.53%) and secondary kinetic energy helicity ($SKEH$) (−49.26%). In contrast to the rotor exit results however, at the downstream measurement plane, in addition to the aforementioned reductions in the C_{ske} & $SKEH$, a relatively large reduction in the relative total pressure loss coefficient ($C_{p0,rel}$) (−6.86%) was also predicted.

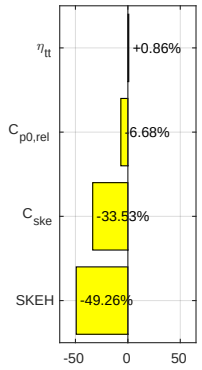

C_{ske} − based

As was the case at the rotor exit, at the downstream measurement plane, the C_{ske}-based design was predicted to produce very similar results to the η_{tt}-based endwall. In particular, in addition to a significant increase in rotor total-total efficiency (+0.83%), fairly significant reductions in both the downstream secondary kinetic energy (C_{ske}) as well as the secondary kinetic energy helicity ($SKEH$) were predicted (−34.94% & −53.99% respectively). In addition, as was the case for the η_{tt}-based case, at the downstream measurement plane, a reasonably large decrease in the overall mass-averaged loss coefficient of approximately −6.32% was also predicted.

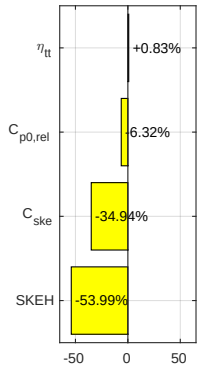

$C_{p0,rel}$ − based

At the downstream measurement plane, the results for the $C_{p0,rel}$-based endwall were once again noted to be in stark contrast to those predicted for the η_{tt}- & C_{ske}-based designs. More specifically, at the downstream plane, the predicted rotor total-total efficiency was again predicted to be reduced in comparison to the annular case (−0.39%), while both the mass-averaged coefficient of secondary kinetic energy (C_{ske}) as well as the secondary kinetic energy helicity ($SKEH$) were both predicted to increase significantly (+23.25% & +24.32%). Finally, in contrast to the upstream result, at the downstream plane, the $C_{p0,rel}$-based endwall was predicted to result in an overall increase in the mass-averaged relative total pressure loss coefficient ($C_{p0,rel}$) (+1.88%).

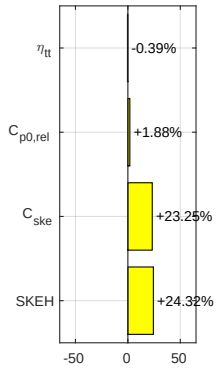

β_{dev} − based

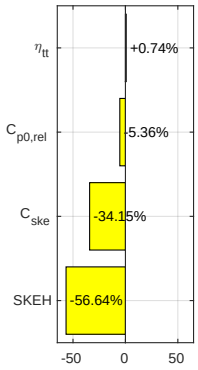

At the downstream plane, the β_{dev}-based endwall once again was predicted to show some similarity to the η_{tt}- & C_{ske}-based designs, although because no design angles were available at the X4 measurement plane, the increased reduction in the flow deviation from design (noted for the β_{dev}-based endwall at the rotor exit), could not be compared with the same result at the downstream plane. However, in terms of the remainder of the quantities, as was the case for the η_{tt}- as well as the C_{ske}-based designs, at the downstream measurement plane, the β_{dev}-based design was predicted to increase the rotor efficiency by approximately +0.74% in comparison to the annular case. This was accompanied by relatively large reductions in the mass-averaged relative total pressure loss (−5.36%) and secondary kinetic energy (C_{ske}) (−34.15%) coefficients. Finally, as was the case for both the η_{tt}- as well as the C_{ske}-based endwalls, at the downstream measurement plane, an overall reduction in the mass-averaged secondary kinetic energy helicity ($SKEH$) of approximately −56.96% was also predicted.

$SKEH$ − based

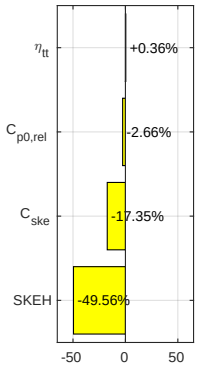

Once again, as was the case at the rotor exit measurement plane, the $SKEH$-based design resulted in similar trends in the changes to the overall mass-averaged magnitudes of the various flow metrics (with the exception of the $C_{p0,rel}$-based design), although as was the case at the rotor exit measurement plane, the increase in the rotor total-total efficiency (+0.36%) was significantly less than those predicted for the majority of the preceding designs. In addition, while a reduction in the mass-averaged 'mixed-out' loss coefficient was predicted (−2.66%), this was also significantly less than that predicted for the all of the previous endwalls (again with the exception of the $C_{p0,rel}$-based design). A similar result was also noted for the mixed-out coefficient of secondary kinetic energy which was predicted to be reduced by only −17.35% in comparison to the datum case. Finally, despite the quantity being used as the basis of the objective function for this endwall, at the downstream measurement plane, the reductions in the predicted secondary kinetic energy helicity ($SKEH$) (−49.56%) was somewhat smaller than that predicted for the majority of the preceding designs (with the exception of the η_{tt}- & $C_{p0,rel}$-based designs).

$\eta_{de} - based$

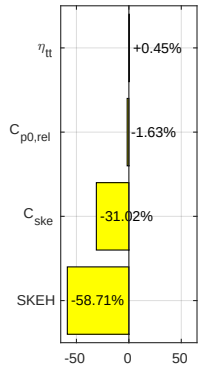

At the downstream measurement plane, the η_{de}-based design was predicted to result in an increase in the rotor total-total efficiency (+0.45%), as well as a decrease in the overall mass-averaged relative total pressure loss coefficient ($C_{p0,rel}$) (−1.63%). It should be noted that, although a reduction in the loss coefficient at the downstream measurement plane was predicted for this design, this was considerably smaller than the reductions which were predicted for the all of the previous designs, with the exception of the $C_{p0,rel}$-based design. Further to this, at the downstream plane, the η_{de}-based design was predicted to result in decreases in the mass-averaged coefficient of secondary kinetic energy (C_{ske}) and secondary kinetic helicity ($SKEH$) similar to those predicted for the C_{ske} & β_{dev}-based designs (−31.02% & −58.71%). Finally, as was the case for the β_{dev}-only endwall, because of a lack of design flow angles at the 'mixed-out' measurement plane, no comparison for the changes in the design efficacy (η_{de}) could be made at this location.

$C_{ske,1} + \beta_{dev,0.7} - based$

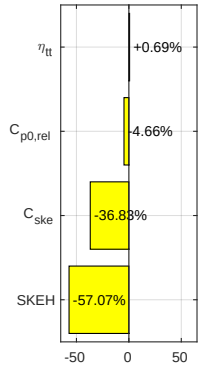

Like the η_{tt}- and C_{ske}-based endwalls, the $C_{ske,1} + \beta_{dev,0.7}$ endwall resulted in a predicted increase in the rotor exit total-total efficiency as well as reductions in all of the remaining flow metrics. However, although the reductions in the coefficient of secondary kinetic energy and $SKEH$ were predicted to be greater than the preceding designs (−36.83%) & (57.07%), the reduction in the total relative pressure loss coefficient was slightly reduced in comparison to the η_{tt}- and C_{ske}-based designs (−4.66%), while the increase in rotor efficiency was slightly smaller than those of the previous endwalls at approximately +0.69%.

$C_{p0,rel,1} + \beta_{dev,0.7} - based$

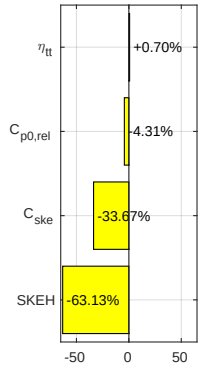

Finally, with the addition of the β_{dev} parameter to the $C_{p0,rel,1} + \beta_{dev,0.7}$-based objective function, the predicted results for the endwall at the downstream plane once again resembled those of the previous η_{tt}-, C_{ske}- & $C_{ske,1}+\beta_{dev,0.7}$-based designs. In fact, the results were largely equivalent to the $C_{ske,1} + \beta_{dev,0.7}$-based design, although interestingly, the $C_{p0,rel,1} + \beta_{dev,0.7}$-based endwall was in fact predicted to result in the lowest magnitude of mass-averaged $SKEH$ at the X4 measurement plane (−63.13%). As indicated, the remainder of the downstream results were largely equivalent to those of the $C_{ske,1} + \beta_{dev,0.7}$-based endwall ($\eta_{tt}$, +0.70%, $C_{p0,rel}$, −4.31%, & C_{ske}, −33.67%).

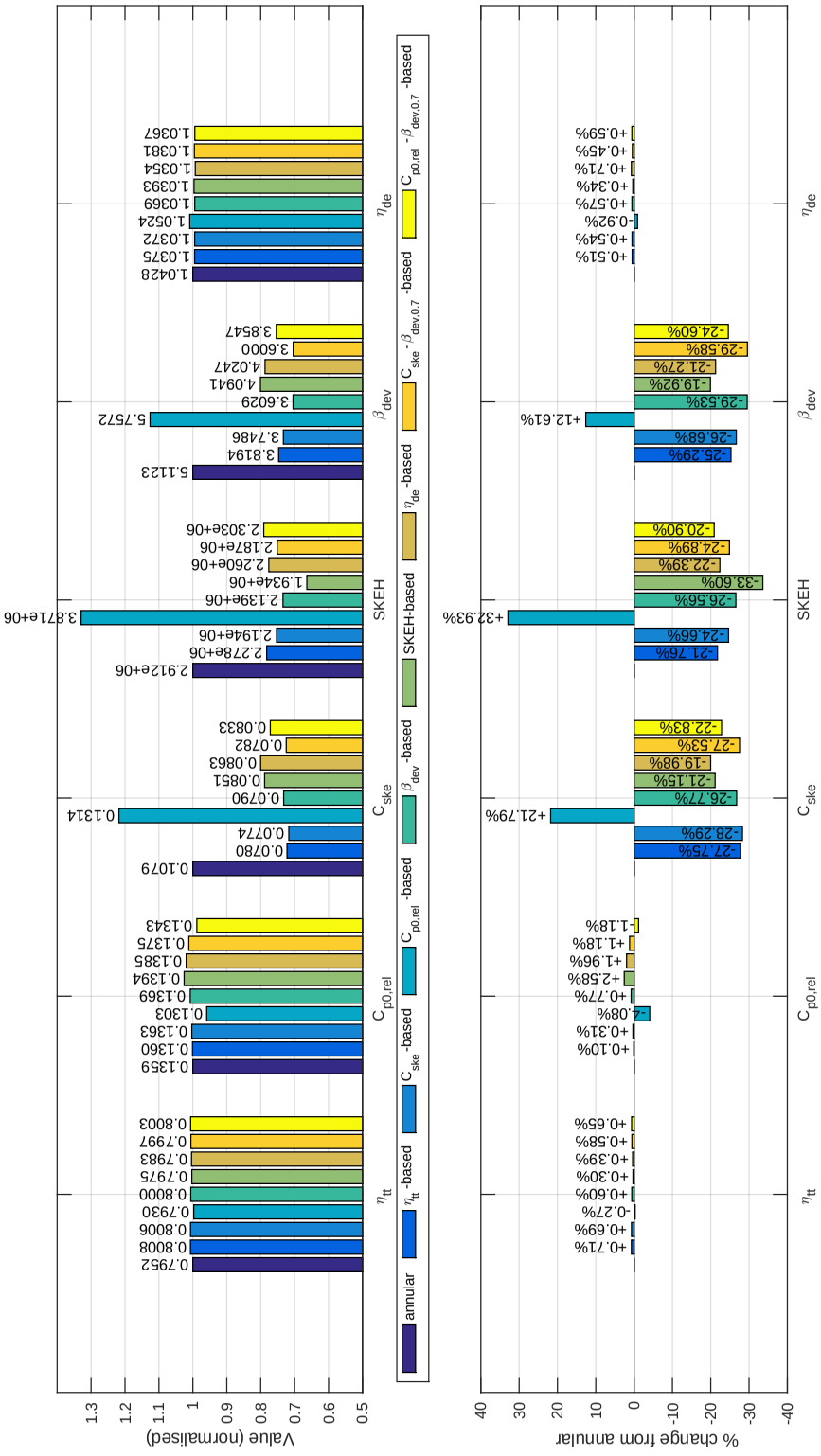

Fig. 7.9: Summary of mass-averaged CFD results at the rotor exit (X3) measurement plane

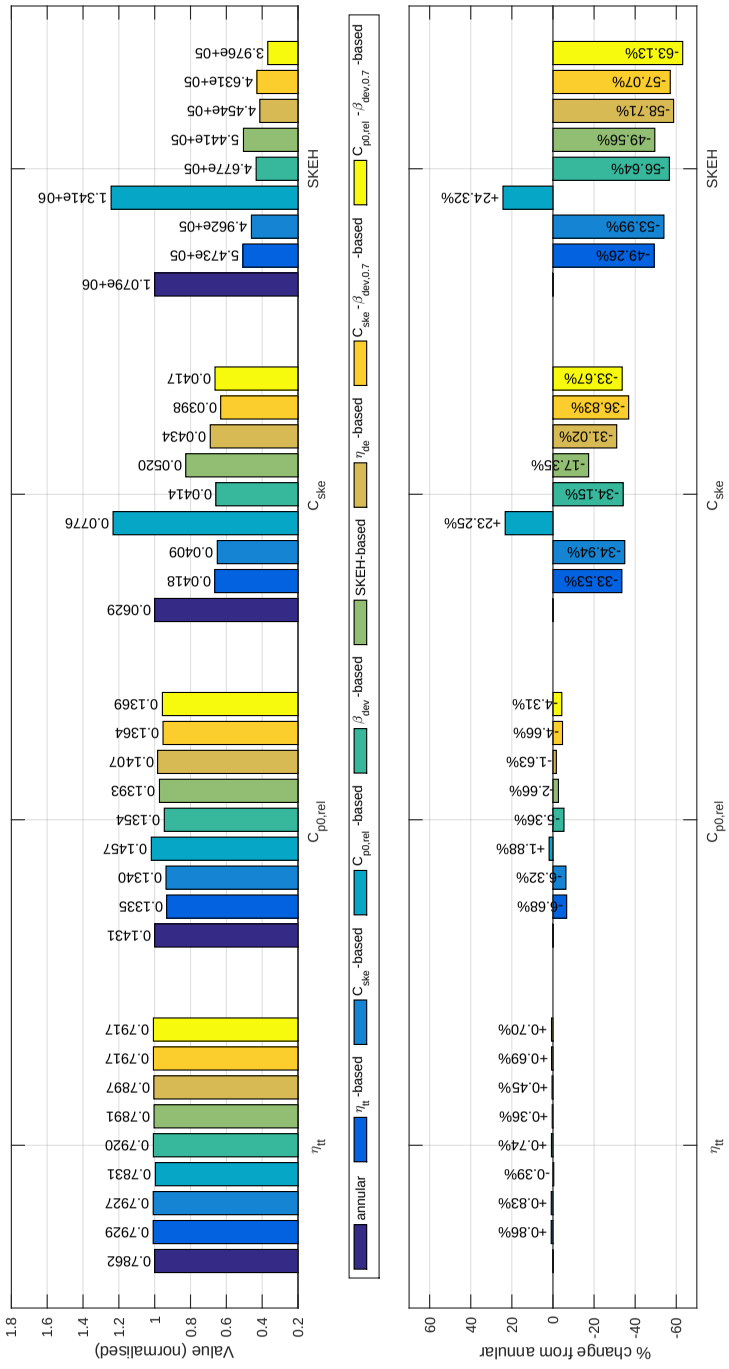

Fig. 7.10: Summary of mass-averaged CFD results at the downstream (X4) measurement plane

7.3 Circumferentially-averaged CFD results

The circumferentially-averaged spanwise rotor exit and downstream predicted flow profiles, and their corresponding contour plots for each endwall (including the annular case), are presented in this section in order to document the changes to the flow more physically than is allowed by the mass-averaged results, but also as an aid to understanding the reasons for the changes in the mass-averaged results. Although each endwall design is discussed, in contrast to the mass-averaged results, the circumferentially-averaged results are presented on a 'per metric' basis rather than on an 'endwall' basis, in an attempt to present the results as compactly as possible, in what would otherwise result in a large number of endwall / metric combinations.

Line	Marker	Description
———	none	Design
———	○	Annular (CFD)
———	◇	Contoured (CFD)

Table 7.4: Plot legend - Annular vs contoured CFD circumferentially-averaged results

7.3.1 Rotor exit (X3)

The circumferentially-averaged (spanwise) CFD results for each endwall design (including the annular case) at the rotor exit plane (X3), for each of the various design metrics used by the endwall generation routine, are shown in Figs. 7.11 to 7.17[1].

Relative flow (β_3) / flow deviation ($\beta_{dev,3}$) angles

Figs. 7.11a - 7.11r show the rotor exit (X3) spanwise profiles and contour plots of relative flow (β) and flow deviation (β_{dev}) angles for the annular and contoured cases. In general, in comparison to the annular case, all the designs (with the exception of the $C_{p0,rel}$-based endwall) were predicted to improve the overall rotor exit flow and deviation angles with all cases showing at least some degree of consistency to equivalent plots produced by other authors for 'successful' non-axisymmetric endwall contours, including:-

- a reduction in the underturning produced by the passage vortex,
- a suppression of the overturned flow in the lower portion of the passage to a spanwise region closer to the endwall surface, as well as an increase in the maximum degree of overturning immediately adjacent to the endwall surface, and
- a general improvement in the quality of the flow angle in the vicinity of the midspan ($\sim 40-60\%$ span).

[1] In addition to the various design quantities including the flow deviation (i.e. β_{dev}) angle, at the rotor exit (X3), spanwise and contour plots of the rotor relative flow angle (β) were also included for additional clarity

In addition to the above, while the η_{tt}- and C_{ske}-based designs closely resemble the aforementioned spanwise profiles, the circumferentially-averaged profiles for the remaining designs, all included an additional feature which was seen to manifest as an inflection point in the rotor exit relative flow angle profiles and as an additional peak of overturned fluid between the endwall and peak of underturned flow closer to the midspan in the corresponding contour plots (Figs. 7.11i - 7.11r).

Finally, in contrast to the above, the spanwise plots of rotor exit relative flow (Fig. 7.11g) and flow deviation (Fig. 7.12g) angles for the $C_{p0,rel}$-based case showed an overall decrease in the flow quality, with increases in the rotor exit flow over- and underturning (at $\sim 30\%$ & $\sim 41\%$ span respectively).

Coefficient of secondary kinetic energy ($C_{ske,3}$)

The calculated spanwise profiles and contour plots of C_{ske} for the annular and contoured cases at the rotor exit (X3) are shown in Figs. 7.13a - 7.13r.

- As was the case the for the rotor relative flow (β) and deviation (β_{dev}) angles, below the midspan, all the contoured designs (again with the exception of the $C_{p0,rel}$-based case) were predicted to result in a reduction in the coefficient of secondary kinetic energy close to the midspan ($\sim 30-40\%$ span) with an accompanying restriction of the C_{ske} to a region closer to the endwall surface but with a clear increase in its the peak value
- In addition, and in contrast to the η_{tt}- & C_{ske}-based cases, the profiles for all the remaining designs (again with the exclusion of the $C_{p0,rel}$-based case) were all seen to include a region of slightly increased C_{ske} between approximately $\sim 10-30\%$ span consistent with the additional overturning peak mentioned above for these endwalls, with the $SKEH$-, η_{de}- and $C_{p0,rel,1} + \beta_{dev,0.7}$-based (Figs. 7.13k, 7.13m & 7.13q) designs showing this most obviously.
- Finally, again in contrast to all the previous cases, the calculated magnitudes of local circumferentially-averaged C_{ske} peaks for the $C_{p0,rel}$-based case (Fig. 7.13g) were predicted to increase as a result of the that endwall's contouring, both close to the midspan as well as in the region between $\sim 0-30\%$ span.

Loss ($C_{p0,rel,3}$)

In comparison to the flow angle and C_{ske} quantities, the rotor exit loss profiles (Figs. 7.14a - 7.14r) showed a greater degree of differentiation between the endwalls.

- As expected, the η_{tt}- & C_{ske}-based designs showed a high degree of similarity, with a slight reduction in the loss generated through the midspan, as well as a distinct peak located close to the endwall, corresponding to the region of increased overturning and C_{ske} discussed previously.
- Similarly, the $C_{p0,rel}$-based design showed a great deal of similarity to the baseline case, with the loss profiles immediately adjacent to the hub and shrouds effectively unchanged, although while the bulk of the loss close to the midspan was noted to migrate clearly towards the midspan, the radial extent of this region was reduced, resulting in a smaller spanwise region of elevated loss.

- In contrast to the above, the β_{dev}-, $SKEH$-, $C_{ske,1}+\beta_{dev,0.7}$- & $C_{p0,rel,1}+\beta_{dev,0.7}$-based designs all showed some degree of similarity to the η_{tt}- and C_{ske}-based designs, although the loss core associated with the additional overturned flow peak located at approximately $\sim 30\%$ span, resulted in a general increase in the magnitude of the loss profile in this region. Additionally, for the $SKEH$-based design, the lower loss core consistent with the overturned fluid close the endwall noted for all cases, was slightly reduced in comparison to the remaining cases, consistent with the reduced peak overturning predicted for this design.
- Finally, despite the previously reported changes to the flow angle and C_{ske} profiles, the rotor exit loss profile for the η_{de}-based design was predicted to be largely unchanged from the baseline case.

Efficiency ($\eta_{tt,3}$)

Fig. 7.15a - 7.15r show the rotor exit of the predicted spanwise profiles of rotor total-total efficiency. Once again, as was the case for all the quantities to date, above the midspan, no differences between the annular and contoured designs were predicted. More specifically:-

- Both the η_{tt}- and C_{ske}-based designs showed a high degree of similarity to one another, with the bulk of the predicted efficiency improvements corresponding to the spanwise region in which the predicted loss coefficient was decreased ($\sim 20-40\%$ span) as well as close to the endwall, where the predicted loss coefficients were significantly larger¿
- Similarly, and as was the case for the predicted rotor exit loss coefficient, the β_{dev}-, $SKEH$-, $C_{ske,1}+\beta_{dev,0.7}$- & $C_{p0,rel,1}+\beta_{dev,0.7}$-based designs (Figs. 7.15i, 7.15k, 7.15o, 7.15q) all showed more complex behaviour in the aforementioned region produced as a result of the combination of the region of improved spanwise efficiency which was seen to form behind the blade offset by the effects of the additional peak of reduced efficiency (at approximately $\sim 25\%$ span) seen to form for these endwalls. It should be noted that although present, this effect was somewhat smaller for the $SKEH$-based design.
- Finally, while behind the rotor, the efficiency predictions for the $C_{p0,rel}$-based design were seen to manifest as a similar but intensified version of the baseline (annular) case, the predictions for the η_{de}-based design showed a relatively simple profile with a limited but non-trivial improvement in the efficiency between $\sim 20-30\%$ span, as well as a slightly radial migration of this peak towards the midspan.

Secondary kinetic energy helicity ($SKEH_3$)

The predicted rotor exit spanwise profiles and contour plots of secondary kinetic energy helicity for each endwall and the annular case are shown in Figs. 7.16a - 7.16r. Inspection of these results showed that, generally the spanwise profiles were similar to the plots of previously discussed rotor exit C_{ske}, with the exception of that of the $SKEH$-based design.

In short:-

- The η_{tt}- & C_{ske}-based designs (Figs. 7.16c & 7.16e) showed a great deal of similarity to one another, with a reduction of the local $SKEH$ peak close to the midspan (located at approxi-

mately $\sim 40\%$ span), as well as a suppression of the bulk of the secondary kinetic energy to a region close to the endwall surface itself (i.e. $\sim 0 - 20\%$ span).

- Further, as was the case for the rotor exit C_{ske}, the profiles of $SKEH$ for the β_{dev}-, $SKEH$-, η_{de}-, $C_{ske,1} + \beta_{dev,0.7}$ and $C_{p0,rel,1} + \beta_{dev,0.7}$-based designs (Figs. 7.16i - 7.16q) all showed an additional region of elevated $SKEH$ above the aforementioned endwall adjacent region (i.e. between $\sim 20 - 30\%$ span), although for the β_{dev}- & $C_{p0,rel,1} + \beta_{dev,0.7}$-based designs, the circumferentially-averaged magnitudes of the $SKEH$ in this region were considerably more muted than for the remaining designs.
- Finally, the $C_{p0,rel}$-based endwall once again showed a considerable departure from the previous designs, with a great deal of similarity to the annular case, but with an increase in the peak circumferentially-averaged magnitudes of $SKEH$, as well as a migration of the secondary flow peaks closer to the midspan.

Despite the similarities to the rotor exit C_{ske}, one difference between the current quantity and the former was that, the magnitude of the wall adjacent $SKEH$ peak for the $SKEH$-based case was considerably smaller than those predicted for the remainder of the designs, especially when compared to the same predictions made for the rotor exit C_{ske}.

Design efficacy ($\eta_{de,3}$)

Lastly, the profiles of predicted design efficacy and associated contour plots are shown in Figs. 7.17a - 7.17r. As expected, these profiles shared some degree of similarity to those predicted for the flow and flow deviation angles (β & β_{dev}) on which they are based.

- Again the η_{tt}- and C_{ske}-based profiles (Figs. 7.17c, 7.17e) showed a high degree of similarity to one another, with improvements in the η_{de} predicted in the vicinity of the passage vortex as well as a slight decrease immediately adjacent to the endwall where the rotor outlet flow overturning was predicted to be increased as a result of the endwall contouring. Closer to the midspan, the region of increased uniformity of the flow angle (seen to be between $\sim 40 - 60\%$ span for the η_{tt}-based design, Fig. 7.11c) was also reflected in the η_{de} profiles for both designs, with a similar improvement in the design efficacy in this region.
- Once again, the increased complexity of the flow angles of the remaining designs discussed previously (again with the exception of the $C_{p0,rel}$-based case) was reflected in the η_{de} profiles shown in Figs. 7.17i, 7.17k, 7.17m, 7.17o & 7.17q, with the η_{de}-based design as expected showing the greatest degree of adjustment towards the optimal (i.e. design) profile.
- Finally, consistent with all the previously discussed profiles as well as the mass-averaged results for that endwall, the rotor exit design efficacy profile for the $C_{p0,rel}$-based case showed reductions in the circumferentially-averaged η_{de} in the vicinity of the passage vortex (i.e. $\sim 30\%$ & $\sim 40\%$ span) and where the rotor exit flow deviations (Fig. 7.17g) were predicted to increase as a result of the optimized contours, while close to the endwall, the reduced overturning predicted previously for this design corresponded to slight improvements in the circumferentially-averaged η_{de} magnitudes.

7.3.2 Downstream (X4)

The corresponding circumferentially-averaged CFD results for the downstream (X4) measurement plane, are shown in Figs. 7.18 to 7.22[2]. The downstream profiles showed the same overall spanwise trends for each quantity as those at the rotor exit (X3) although as expected, the 'mixed out' nature of the profiles (resulting in generally less extreme profiles), was clear.

In general then:-

Relative flow angle (β_4)

As indicated above, at the downstream measurement plane, the general shape of the predicted profiles of mixed-out relative flow angle for each endwall (Figs. 7.18a - 7.18r) remained largely consistent with those noted for the same design at the rotor exit. In addition, and again for all cases, the profiles also showed overall reductions in the under- and overturning peaks associated with the secondary flow, as well as a general migration of the location of these peaks towards the midspan. Once again, as was the case at the rotor exit, in the tip gap region, no differences of note between the contoured and annular cases was predicted.

Coefficient of secondary kinetic energy ($C_{ske,4}$)

Once again and for all the cases, at the downstream measurement plane, the circumferentially-averaged magnitudes of peak C_{ske} (Figs. 7.19a - 7.19r) were seen to reduce as a result of the mixing out of the flow, although (and again for all cases), the average C_{ske} magnitudes predominantly in the midspan region, were seen to increase. Whilst this was expected for the $C_{p0,rel}$-based (as a result of the increased secondary kinetic energy seen at the rotor exit for this endwall), this effect was less expected but still noticeable for the remaining designs, and was largest for the β_{dev}-, $SKEH$-, η_{de}-, $C_{ske,1} + \beta_{dev,0.7}$- & $C_{p0,rel,1} + \beta_{dev,0.7}$-based designs and less so for the η_{tt}- & C_{ske}-based endwalls. Once again, the spanwise locations of the various C_{ske} peaks were also seen to migrate away from the endwall, although somewhat less obviously than was noted for the relative flow angle as described above. Once again, no differences of significance were noted for any of the designs in the tip gap region.

Loss ($C_{p0,rel,4}$)

In contrast to the previous metrics, at the downstream plane, the spanwise profiles of the rotor loss coefficient (Figs. 7.20a - 7.20r) showed a great deal more variation in their overall characteristic shape in comparison to the results for the rotor exit. In particular, the increases in the loss coefficient close to the endwall ($\sim 10 - 20\%$ span) predicted for all the cases (again with the exception of the $C_{p0,rel}$-based but also the η_{de}-based design in this case), were considerably reduced at the downstream measurement plane, with the bulk of the loss seen to locate rather almost

[2] Further, at the downstream plane (X4), as was done for the mass-averaged results (and for the same reasons), the β_{dev} and η_{de} plots are not shown

exactly at the midspan. Again, this effect was most noticeable for the η_{tt}-, C_{ske}-, β_{dev}- & $C_{ske,1} + \beta_{dev,0.7}$-based designs but was also noted for the $SKEH$- & $C_{p0,rel,1} + \beta_{dev,0.7}$-based cases. While as was the case at the rotor exit, at the downstream plane, all the changes to the loss profile for the $C_{p0,rel}$-based case were noted close to the midspan, almost no changes to the loss profile at the 'mixed-out' measurement plane were predicted for the η_{de}-based design.

Efficiency ($\eta_{tt,4}$)

At the downstream measurement plane, the changes to the rotor 'mixed-out' efficiencies (Figs. 7.21a - 7.21r) were predicted to be occur only below the midspan, with the results for all endwalls (again with the express exception of only the $C_{p0,rel}$-based case), showing an improvement in this vicinity (particularly between $\sim 10-40\%$ span), with the most prominent improvements predicted for the η_{tt}- & C_{ske}-based designs. Further to this, for a number of the designs, immediately adjacent to the endwall surface, the 'mixed-out' efficiencies were actually predicted to be reduced in comparison to the datum case, again with the most notable of these being, the η_{tt}-, C_{ske}-, β_{dev} and $C_{ske,1} + \beta_{dev,0.7}$-based cases. In contrast, once again the $C_{p0,rel}$-based design showed a distinct departure from the behaviour predicted for the previous designs, with no changes of siginificance predicted below approximately $\sim 25\%$ span and only a slight *increase* in the efficiency above the midspan persisting to a spanwise height of $\sim 60\%$ span. Instead, for this design, between the radial positions of $\sim 25 - 40\%$ span, a distinct decrease in the overall efficiency profile was predicted. Finally, one further exception to the general trends described above was noted, and that was for the η_{de}-based design. In contrast to the majority of previous endwalls, for this design, the predicted improvements in the secondary flow region (and below the midspan) were predicted to extend to the endwall surface completely, with no reductions in the circumferentially-averaged efficiency predicted close to the endwall surface (as was the case for the majority of the previous designs).

Secondary kinetic energy helicity ($SKEH_4$)

Finally, in general, the mixed-out profiles of secondary kinetic energy helicity ($SKEH$) (Figs. 7.22a - 7.22r) echoed those already noted for the C_{ske} previously, with a overall reduction in the magnitude of the circumferentially-averaged values associated with the secondary flow structures, as well as a general increase in the magnitudes of the $SKEH$ through the midspan. In contrast however, for the present metric, the increases near the midspan, although noteworthy, were considerably smaller than those noted for the simple C_{ske} metric.

7.4 Summary: CFD results

The mass- and circumferentially-averaged CFD results showed a natural grouping emerge from the overall body of designs.

The first and most obvious group consisted of the η_{tt}-, C_{ske}- & β_{dev}-based designs, not only produced similar reductions in each of the mass-averaged quantities, but also very similar spanwise profiles

for each of the different quantities studied. In particular, all three of these designs were predicted to produce non-trivial increases in the rotor efficiency, but also significant reductions in the overall rotor exit C_{ske}, $SKEH$ and flow deviations, as well as improvements in the mass-averaged rotor design efficacies. In addition to this, in accomplishing these reductions, each of these designs was also predicted to result in small, but non-negligible increases in the rotor exit loss coefficient. In terms of these increased losses, both a positive correlation between the magnitude of the increase in the rotor exit loss and the degree to which the rotor exit flow was 'corrected' as well as an inverse correlation between the degree of flow quality correction and the overall predicted increase in efficiency, with the smallest efficiency improvement predicted for the β_{dev}-based case but also the greatest reductions in the flow deviations from design, $SKEH$ and secondary kinetic energy. In addition, for each of these designs, the spanwise flow profiles showed a consistent suppression of the secondary flow toward the endwall surface which was naturally accompanied by a increase in the local loss coefficient in each of the rotor exit spanwise loss profiles in this region.

In contrast to the above, a seconding grouping of designs appeared to emerge, consisting of the $C_{p0,rel}$, $SKEH$ & η_{de}-based designs. Within this group, the $C_{p0,rel}$-based design was predicted to produce results significantly different to the remainder of the designs, being the only design in which the secondary flow strength, flow deviations and $SKEH$ were increased. In addition, these increases in the secondary flow intensity were noted to correspond to a reduction in both the rotor efficiency as well as the rotor exit design efficacy. In contrast however, despite the increase in the secondary flow strength, the both the overall mass-averaged as well as local circumferentially-averaged loss coefficient in the vicinity of the intensified secondary flow region, were predicted to decrease for this design.

Further to the above, and within the second grouping of designs, the $SKEH$- & η_{de}-based designs seemed to naturally aggregate together with both designs predicted to result in smaller overall, but similar increases in the rotor efficiency in comparison to the initial grouping discussed above. In addition, these designs also resulted in increases in the rotor exit loss coefficient which were slightly larger than those of the η_{tt}- / C_{ske}- / β_{dev}-based grouping. While both designs were predicted to result in decreases in the mass-averaged C_{ske} and flow deviations, in both cases, reductions in the overall mass-averaged averaged $SKEH$ appeared to be favoured. The spanwise profiles for these designs both showed local corrections to the rotor exit relative flow angle (β_3) as well as the flow deviation angles.

Finally, a final grouping, consisting of the so-called 'compound' designs (comprising the $C_{ske,1}$ + $\beta_{dev,0.7}$- & $C_{p0,rel,1}$ + $\beta_{dev,0.7}$-based designs) was noted. For both of these cases, the overall mass-averaged rotor efficiencies were predicted to be improved, along with corresponding reductions in the secondary flow and flow deviations. Further, for both designs, improvements in the design efficacy were also predicted. As would be expected, the spanwise profiles for both cases showed considerable emphasis on the correction of the rotor exit flow (as a result of the inclusion of the flow deviation term), but also reductions in the local spanwise rotor exit loss profiles.

At the downstream measurement plane, the 'mixed-out' mass-averages and spanwise profiles generally showed an extension of the rotor exit results, although special mention should be made of the non-trivial increase in the overall mass-averaged loss for the $C_{p0,rel}$-based case at the 'mixed-out' measurement plane, which was seen to originate primarily in the spanwise region corresponding to the location of the increased secondary flow predicted for this design at the rotor exit.

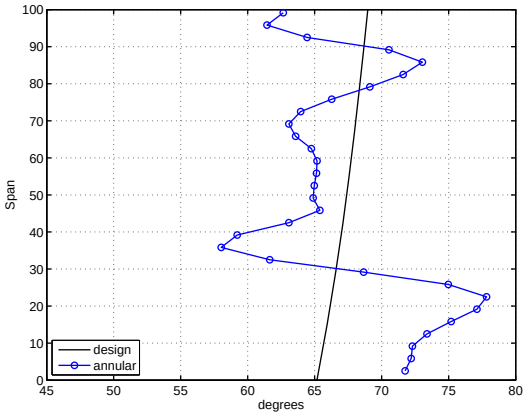

(a) annular

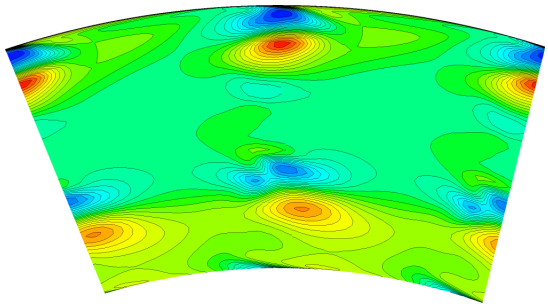

(b)

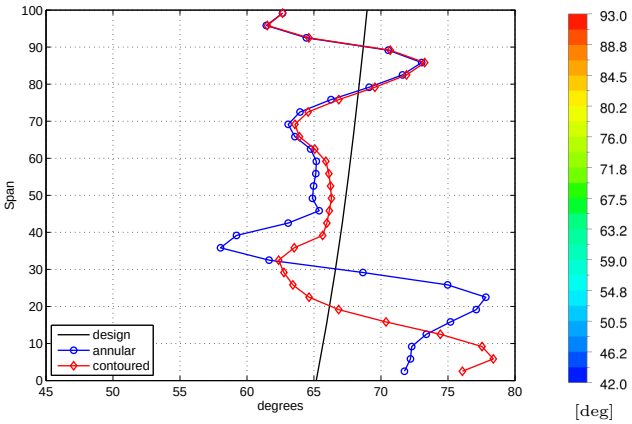

(c) $\eta_{tt} - based$

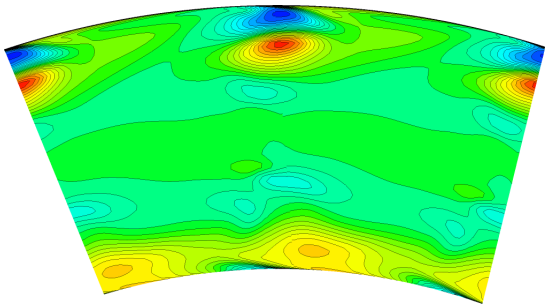

(d)

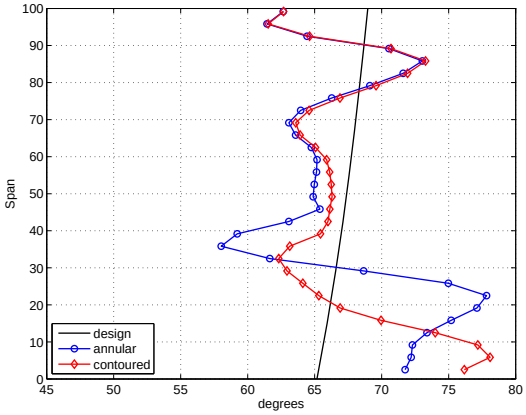

(e) $C_{ske-based}$

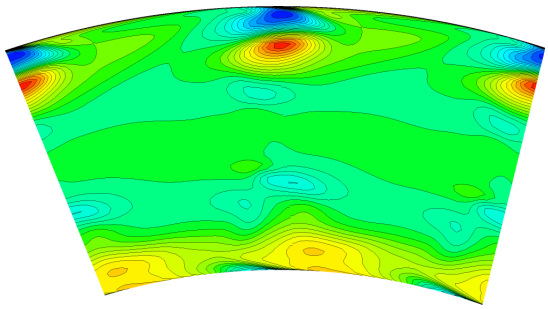

(f)

Fig. 7.11: Relative flow angle (β_3) at rotor exit (X3)

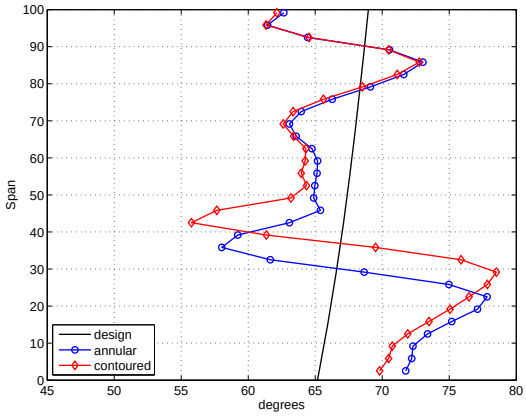

(g) $C_{p0,rel} - based$

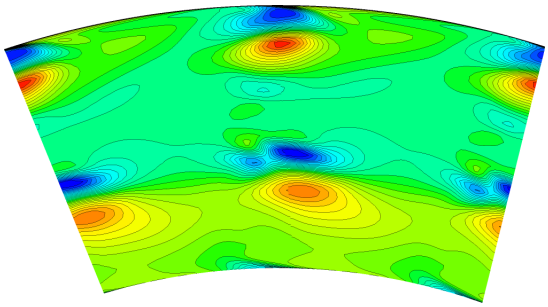

(h)

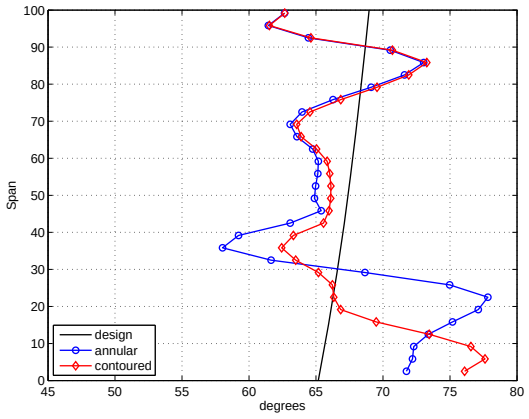

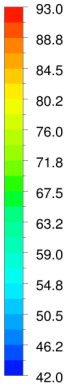

(i) $\beta_{dev} - based$

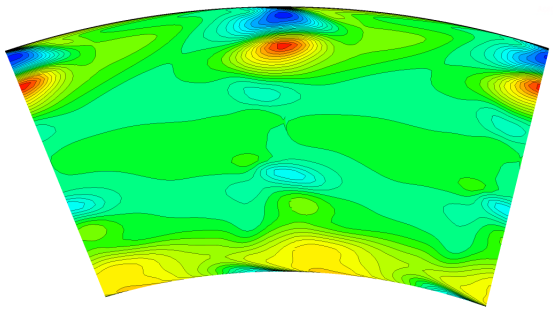

(j)

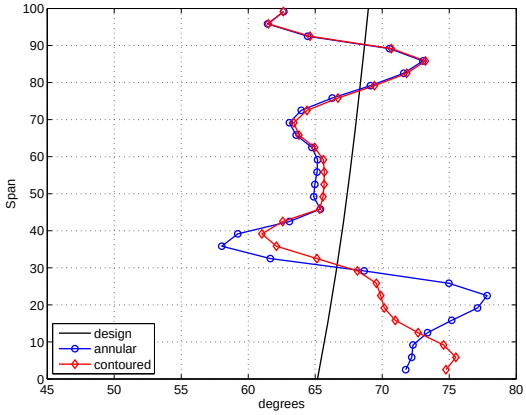

(k) $SKEH - based$

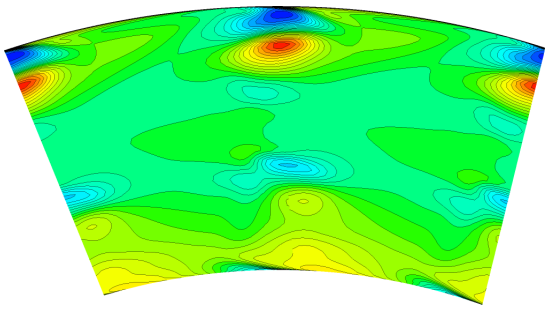

(l)

Fig. 7.11: Relative flow angle (β_3) at rotor exit (X3) (cont)

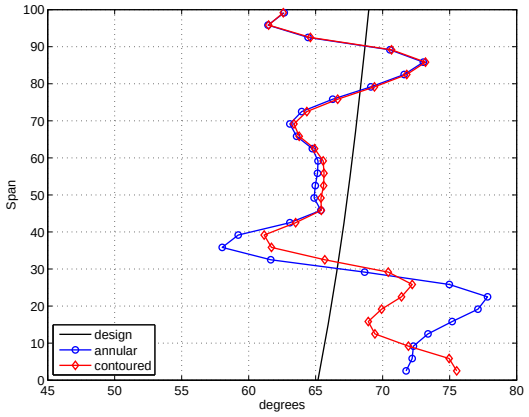

(m) $\eta_{de} - based$

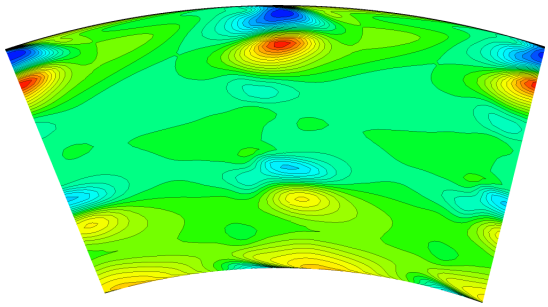

(n)

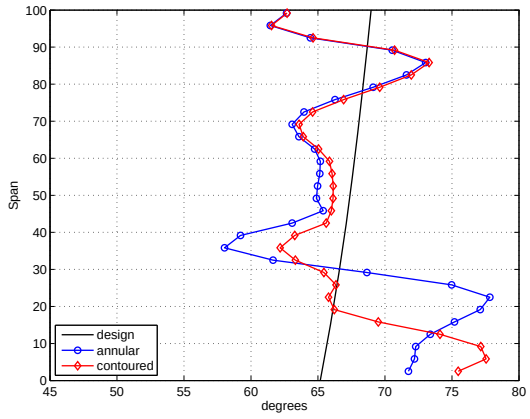

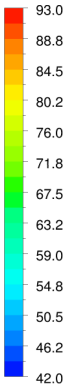

(o) $C_{ske,1} + \beta_{dev,0.7} - based$

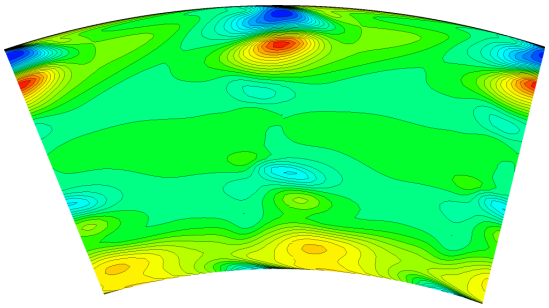

(p)

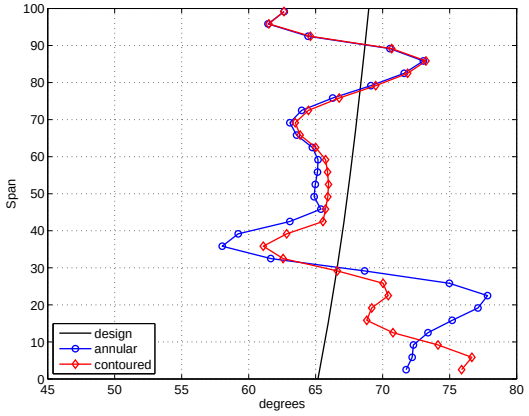

(q) $C_{p0,rel} + \beta_{dev,0.7} - based$

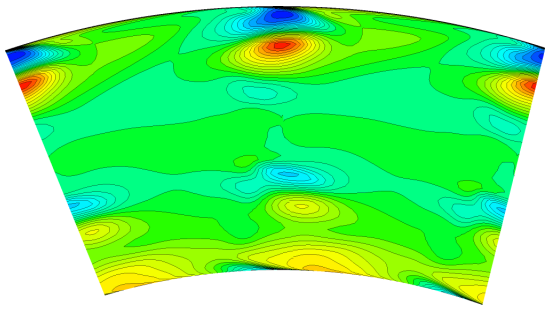

(r)

Fig. 7.11: Relative flow angle (β_3) at rotor exit (X3) (cont)

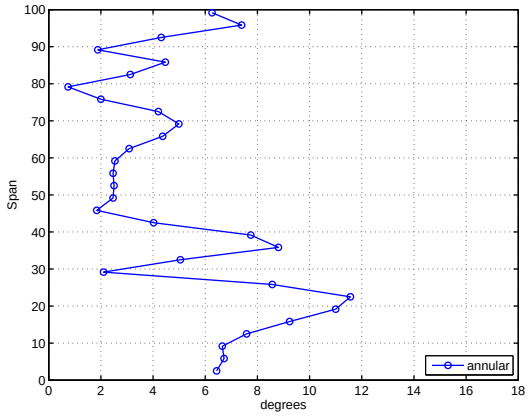

(a) annular

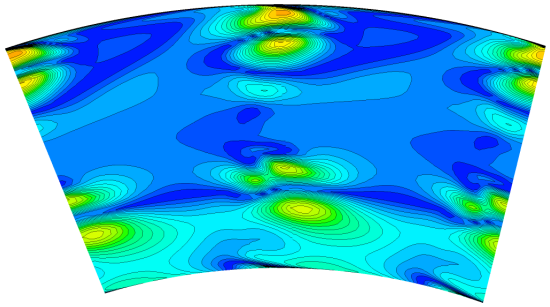

(b)

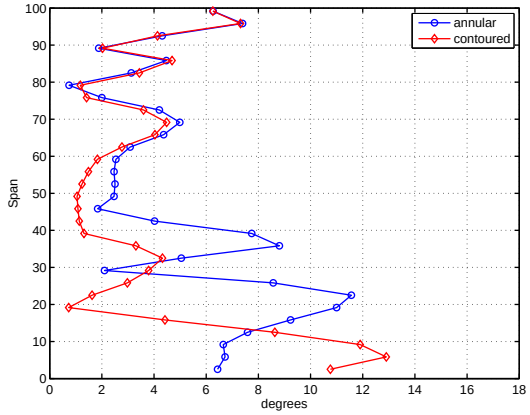

(c) $\eta_{tt} - based$

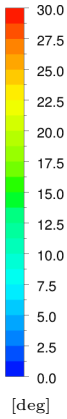

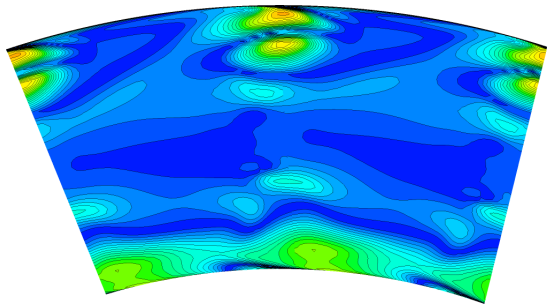

(d)

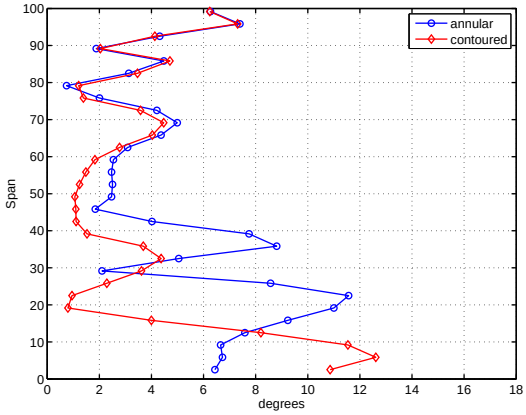

(e) $C_{ske} - based$

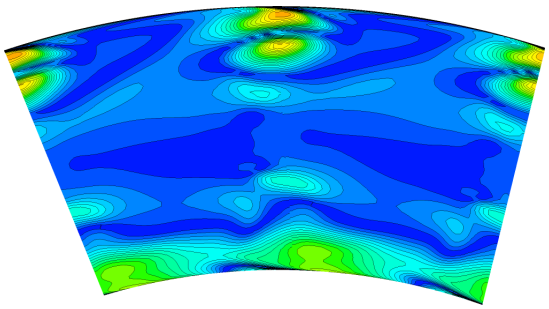

(f)

Fig. 7.12: Relative flow angle deviation ($\beta_{dev,3}$) at rotor exit (X3)

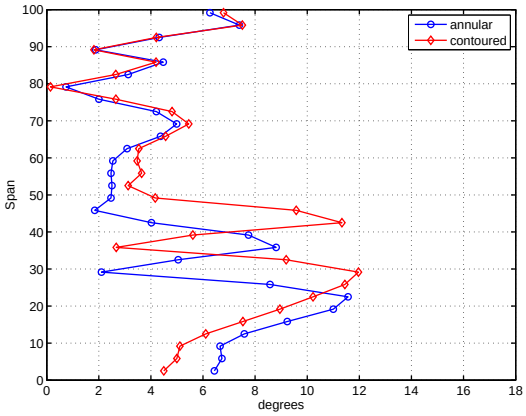

(g) $C_{p0,rel} - based$

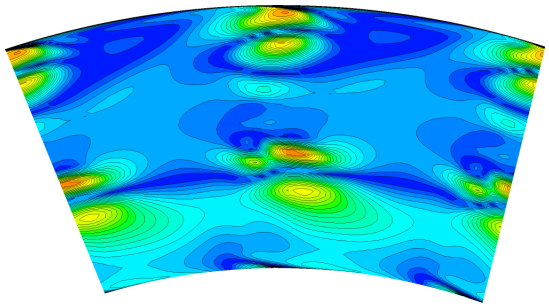

(h)

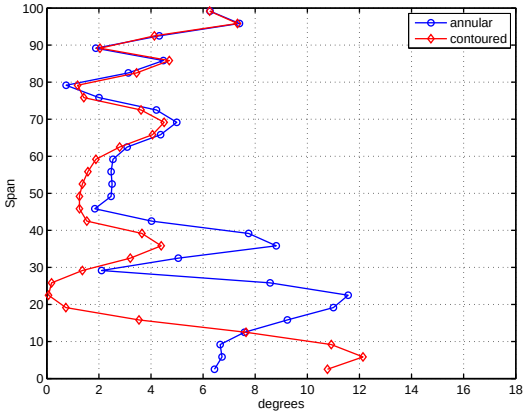

(i) $\beta_{dev} - based$

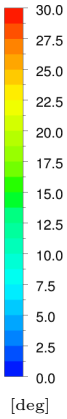

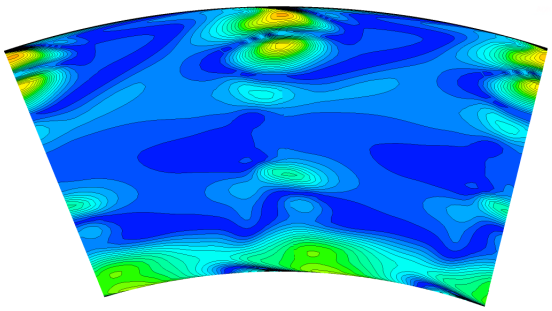

(j)

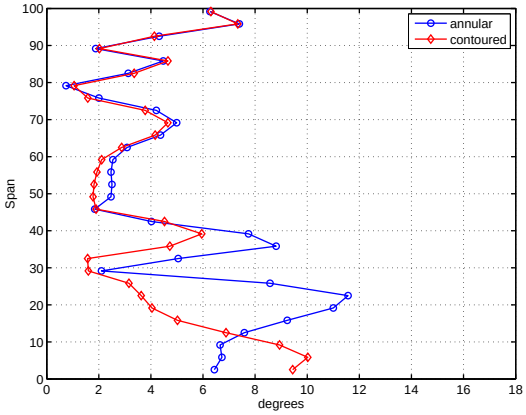

(k) $SKEH - based$

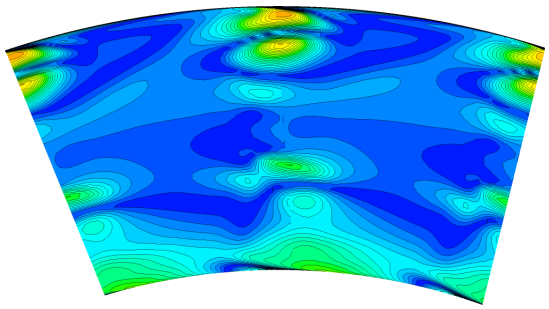

(l)

Fig. 7.12: Relative flow angle deviation ($\beta_{dev,3}$) at rotor exit (X3) (cont)

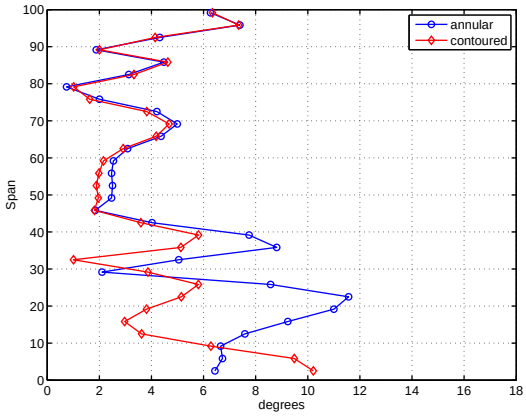

(m) $\eta_{de} - based$

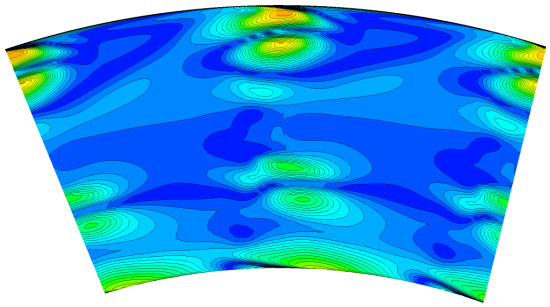

(n)

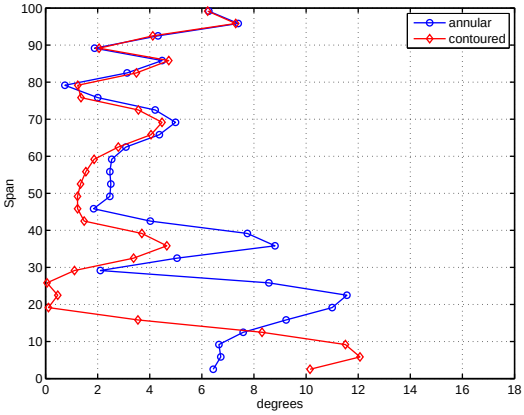

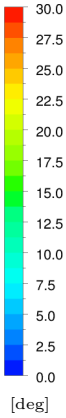

(o) $C_{ske,1} + \beta_{dev,0.7} - based$

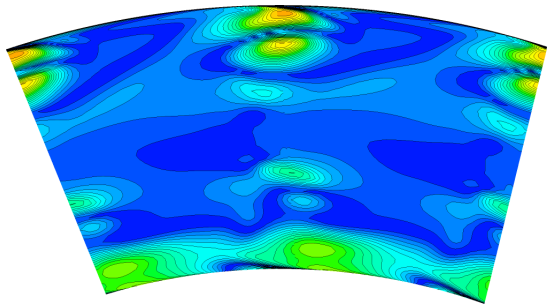

(p)

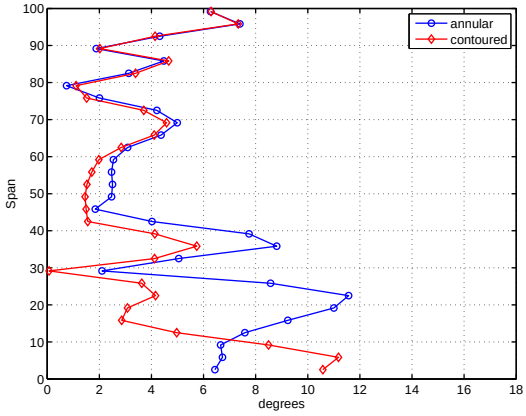

(q) $C_{p0,rel} + \beta_{dev,0.7} - based$

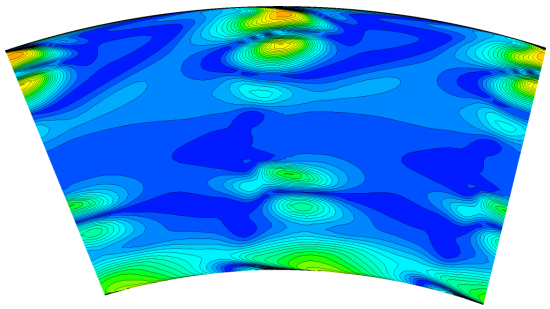

(r)

Fig. 7.12: Relative flow angle deviation ($\beta_{dev,3}$) at rotor exit (X3) (cont)

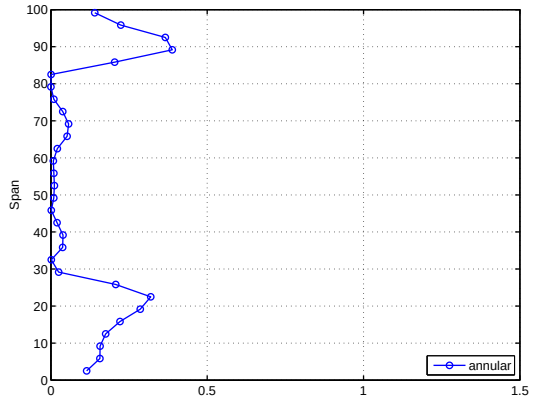

(a) annular

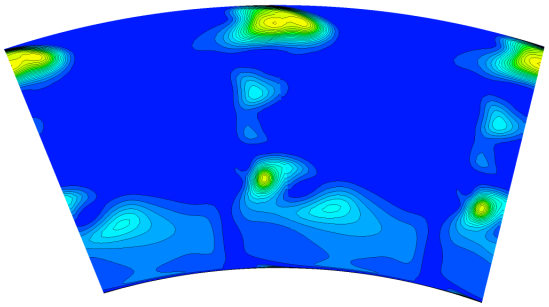

(b)

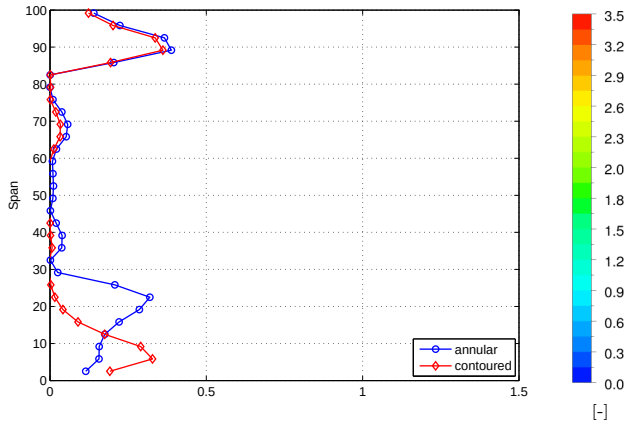

(c) $\eta_{tt} - based$

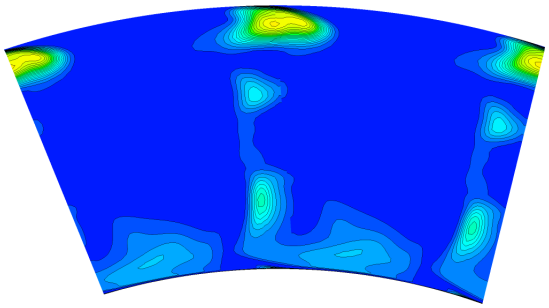

(d)

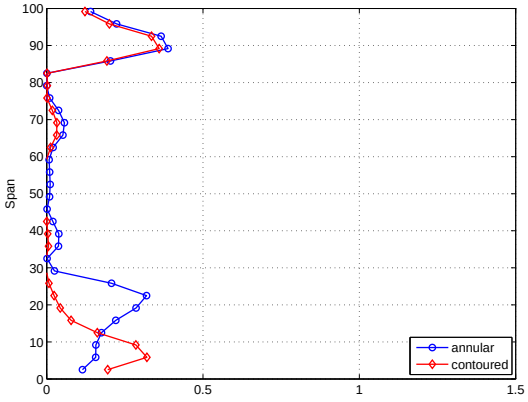

(e) $C_{ske} - based$

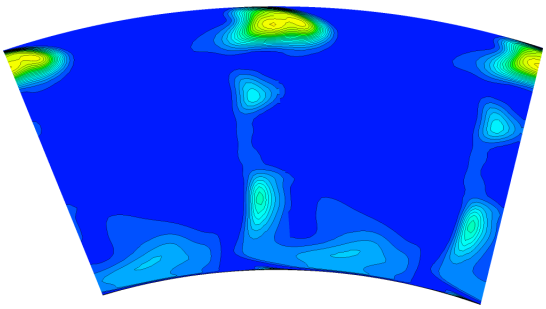

(f)

Fig. 7.13: Coefficient of secondary kinetic energy ($C_{ske,3}$) at rotor exit (X3)

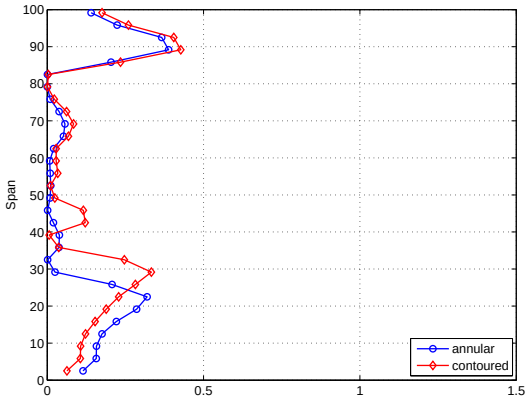

(g) $C_{p0,rel} - based$

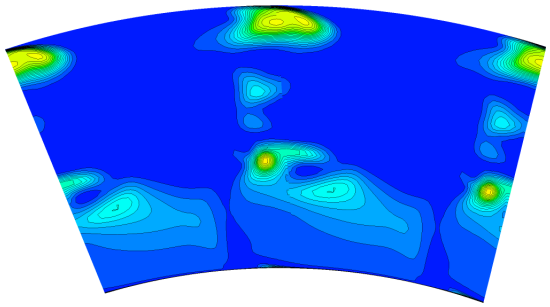

(h)

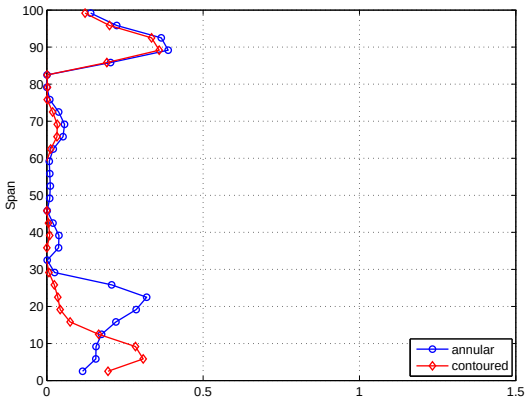

(i) $\beta_{dev} - based$

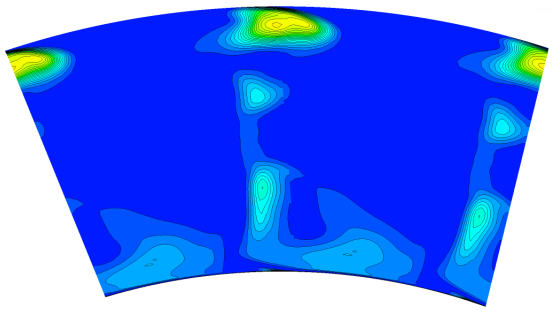

(j)

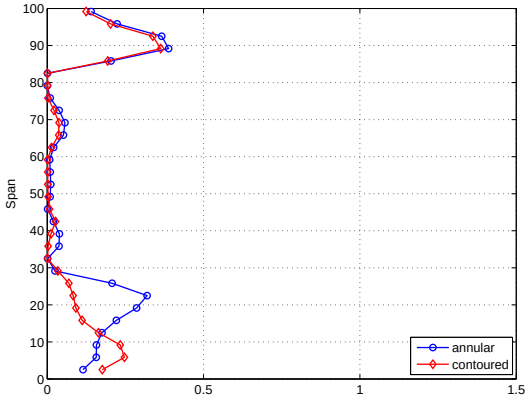

(k) $SKEH - based$

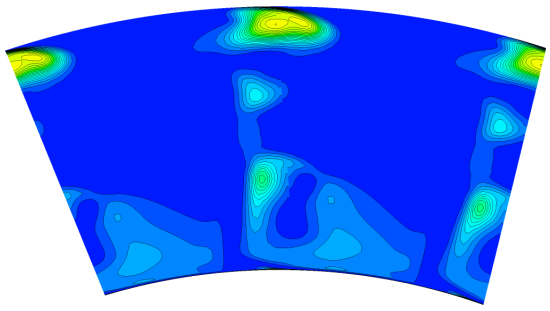

(l)

Fig. 7.13: Coefficient of secondary kinetic energy ($C_{ske,3}$) at rotor exit (X3) (cont)

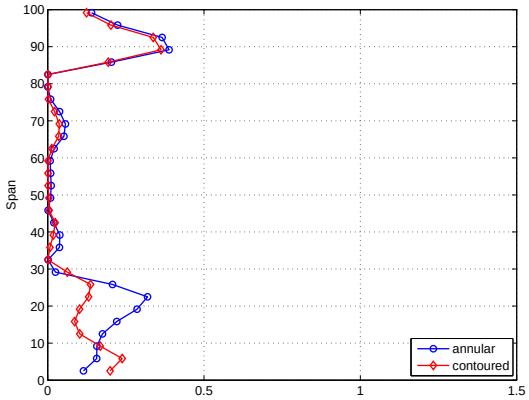

(m) $\eta_{de} - based$

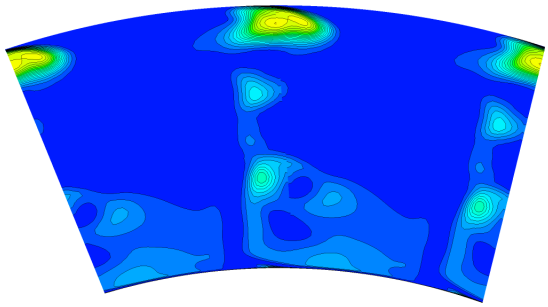

(n)

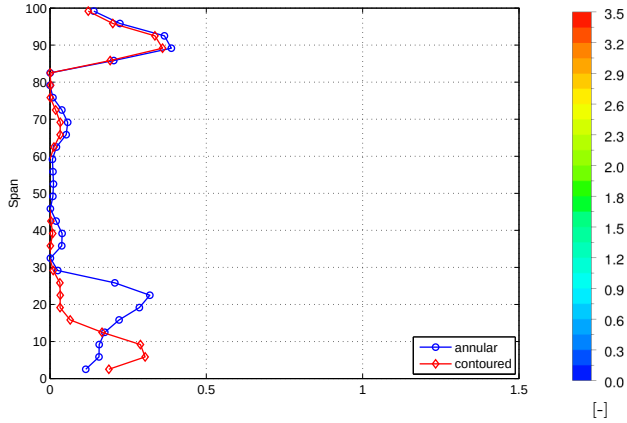

(o) $C_{ske,1} + \beta_{dev,0.7} - based$

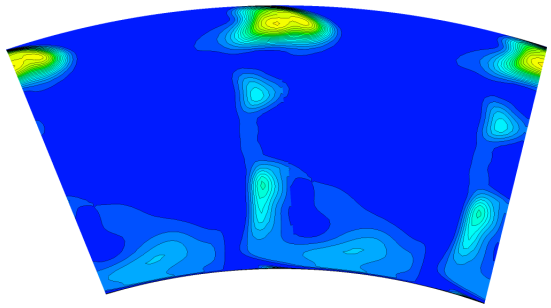

(p)

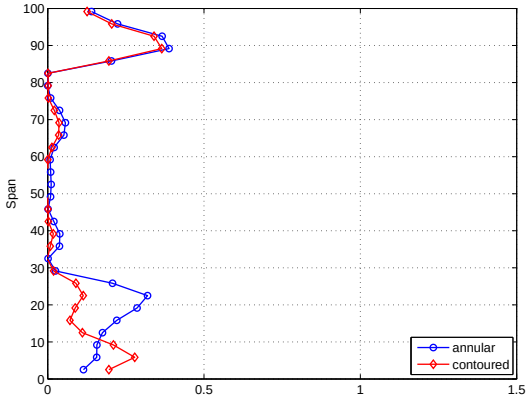

(q) $C_{p0,rel} + \beta_{dev,0.7} - based$

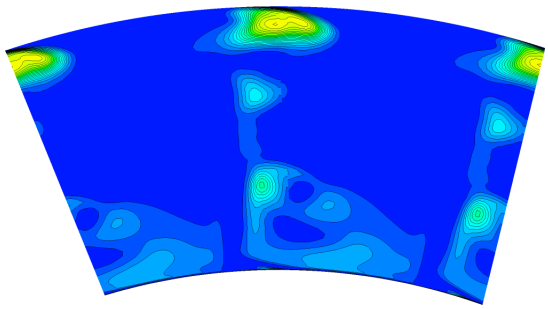

(r)

Fig. 7.13: Coefficient of secondary kinetic energy ($C_{ske,3}$) at rotor exit (X3) (cont)

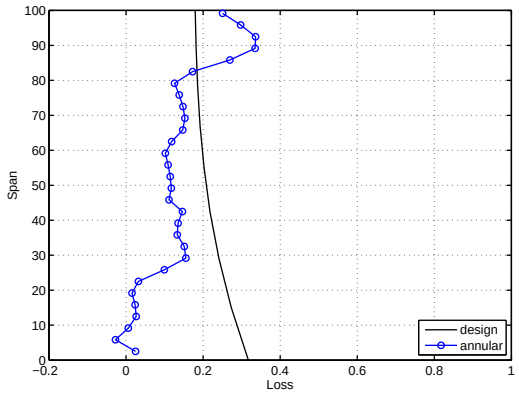

(a) annular

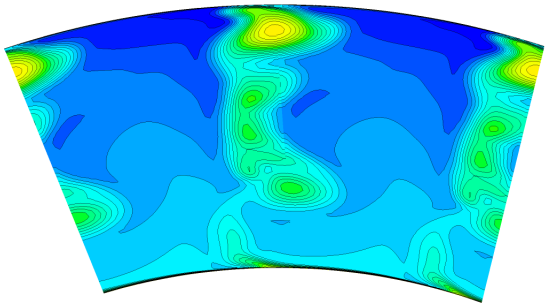

(b)

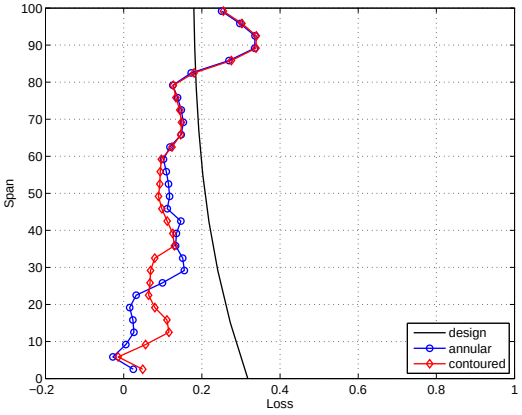

(c) $\eta_{tt} - based$

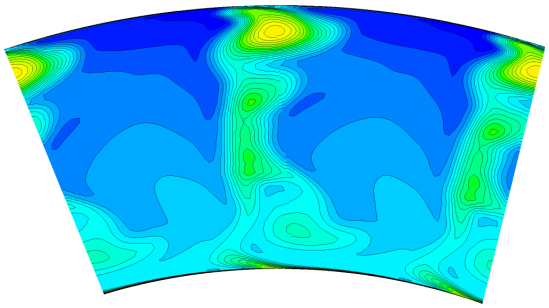

(d)

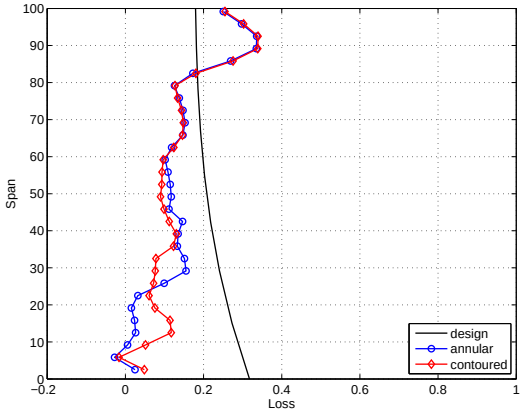

(e) $C_{ske} - based$

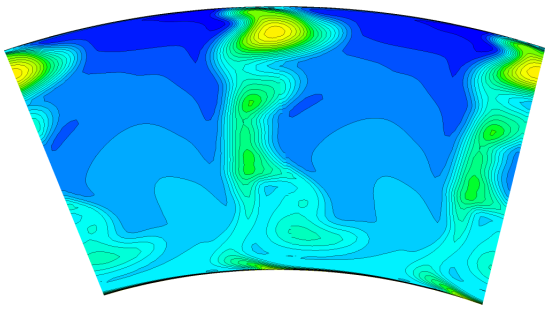

(f)

Fig. 7.14: Relative total pressure loss coefficient ($C_{p0,rel,3}$) at rotor exit (X3)

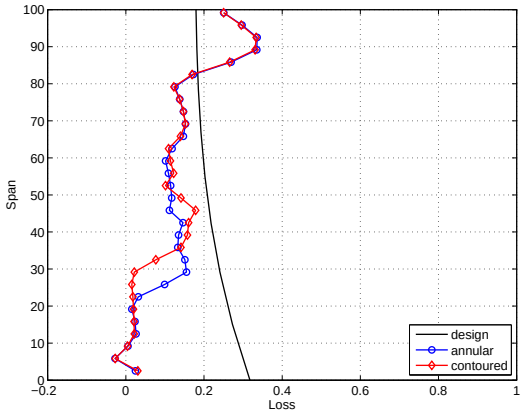

(g) $C_{p0,rel} - based$

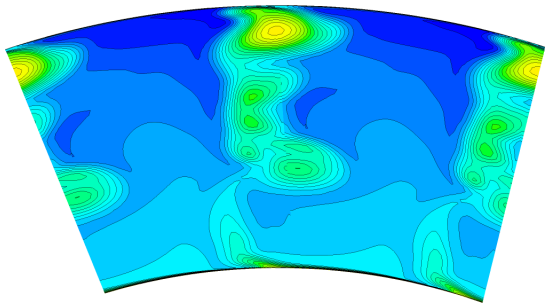

(h)

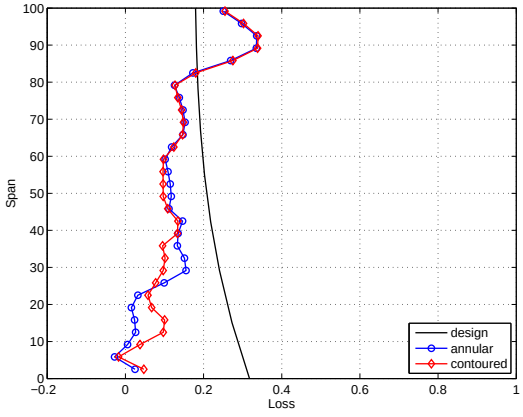

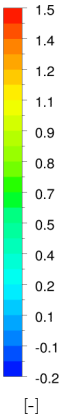

(i) $\beta_{dev} - based$

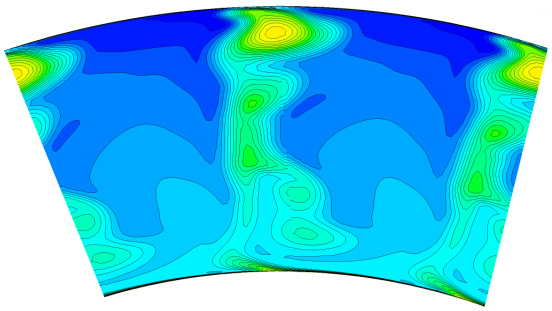

(j)

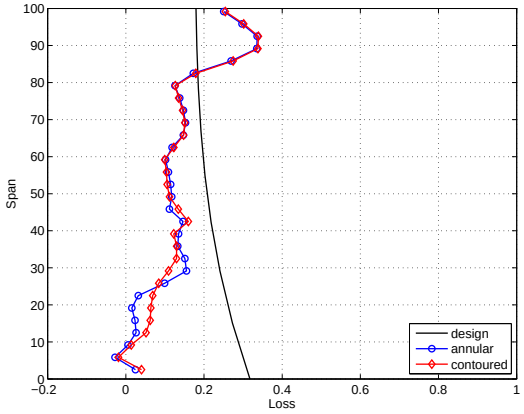

(k) $SKEH - based$

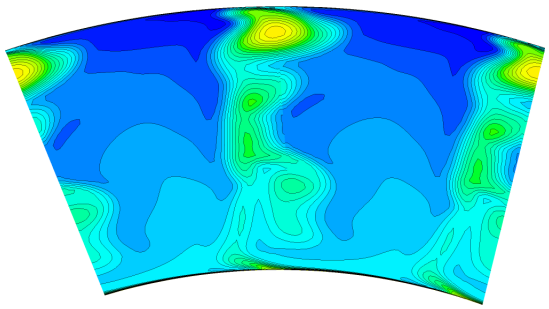

(l)

Fig. 7.14: Relative total pressure loss coefficient ($C_{p0,rel,3}$) at rotor exit (X3) (cont)

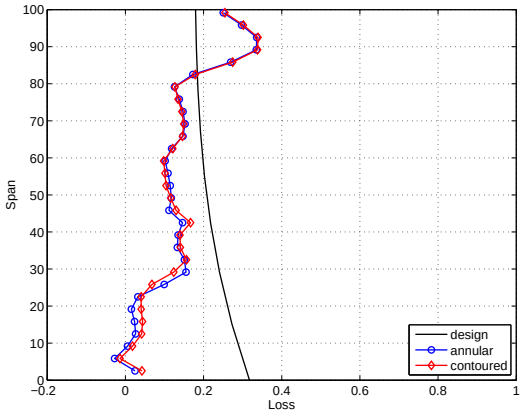

(m) $\eta_{de} - based$

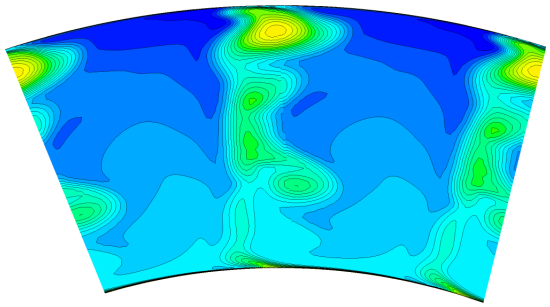

(n)

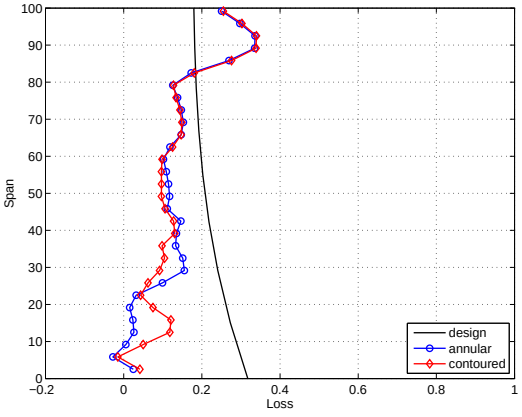

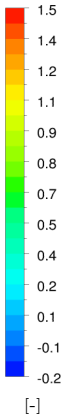

(o) $C_{ske,1} + \beta_{dev,0.7} - based$

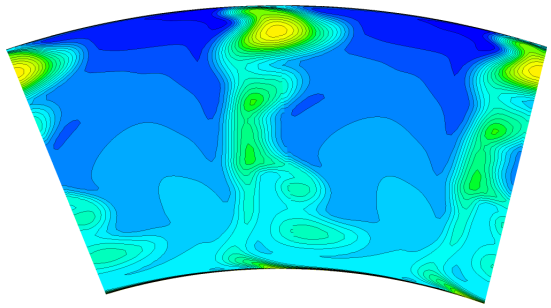

(p)

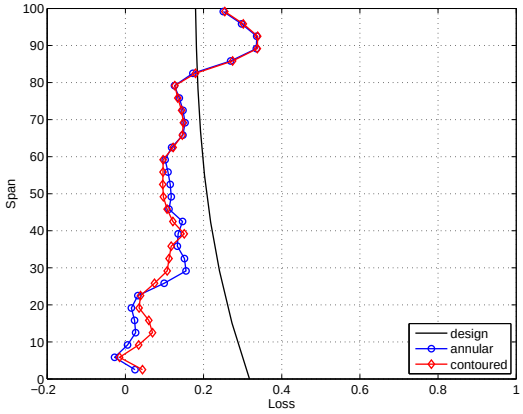

(q) $C_{p0,rel} + \beta_{dev,0.7} - based$

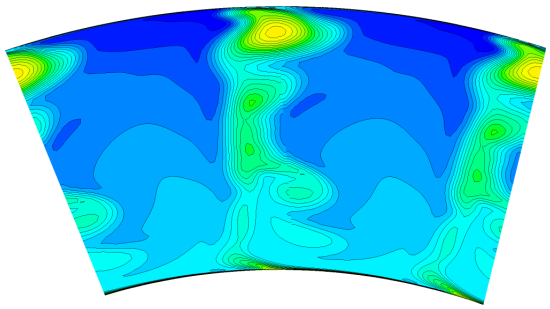

(r)

Fig. 7.14: Relative total pressure loss coefficient ($C_{p0,rel,3}$) at rotor exit (X3) (cont)

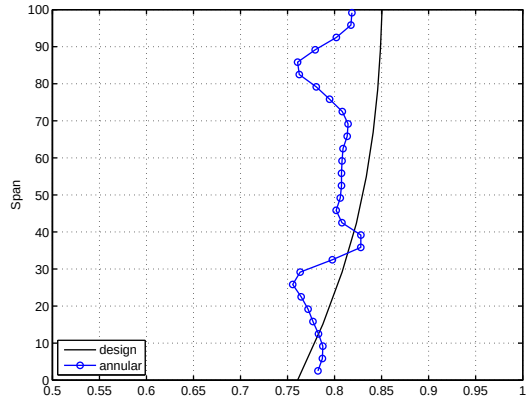

(a) annular

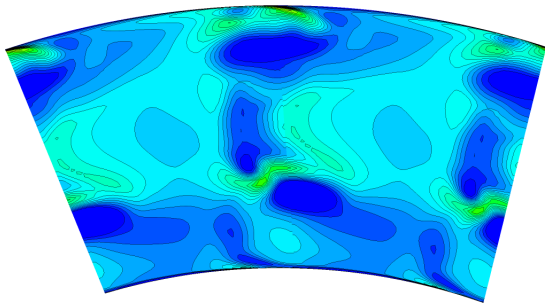

(b)

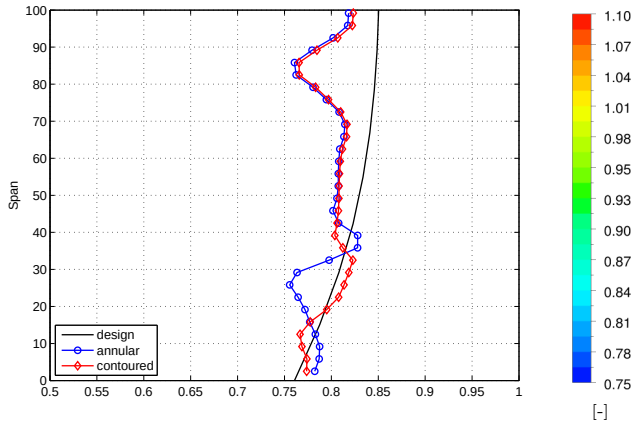

(c) η_{tt}-based

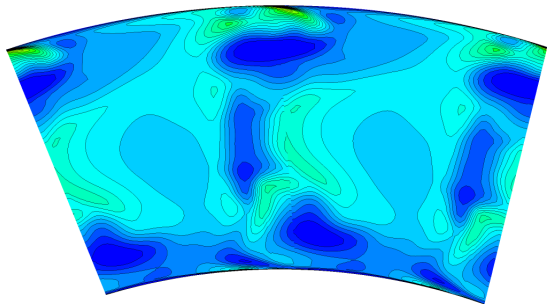

(d)

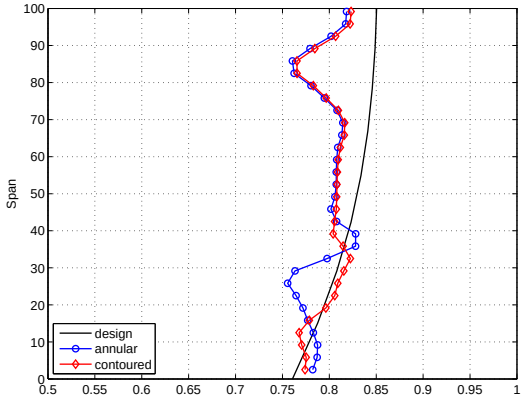

(e) $C_{ske} - based$

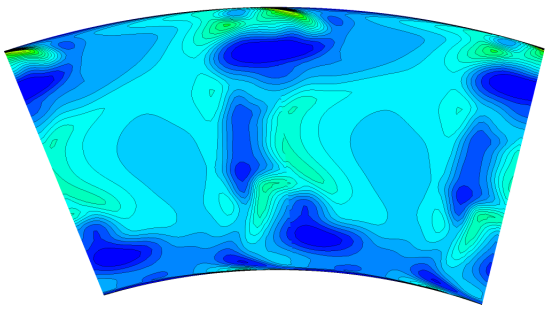

(f)

Fig. 7.15: Rotor total-total efficiency ($\eta_{tt,3}$) at rotor exit (X3)

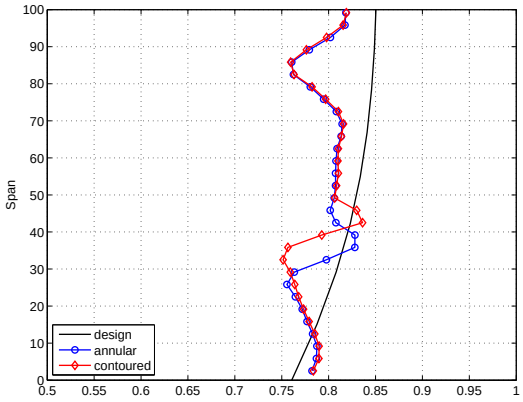

(g) $C_{p0,rel} - based$

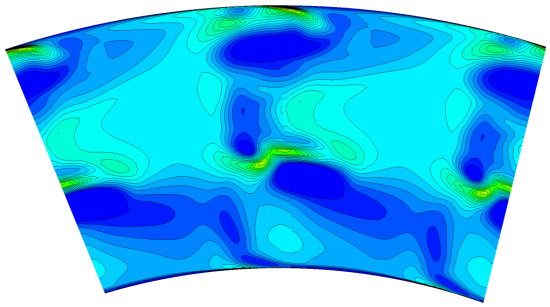

(h)

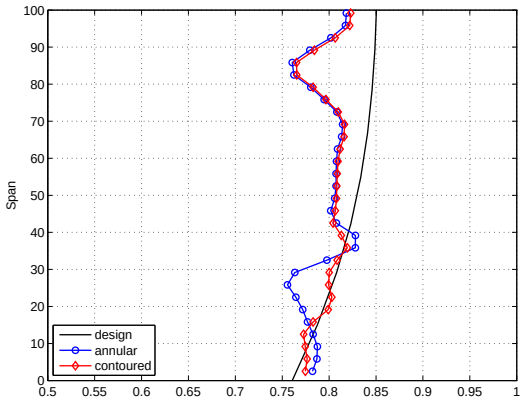

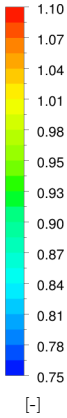

(i) $\beta_{dev} - based$

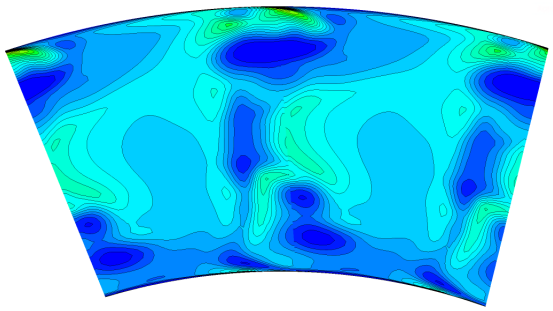

(j)

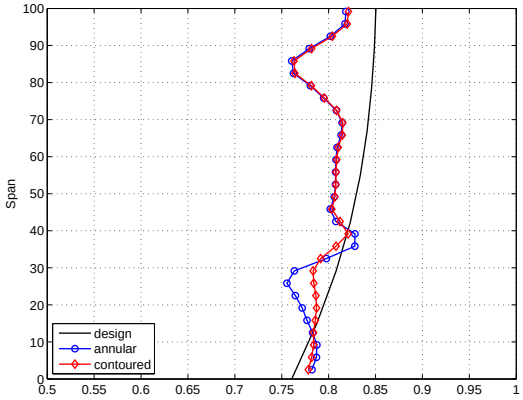

(k) $SKEH - based$

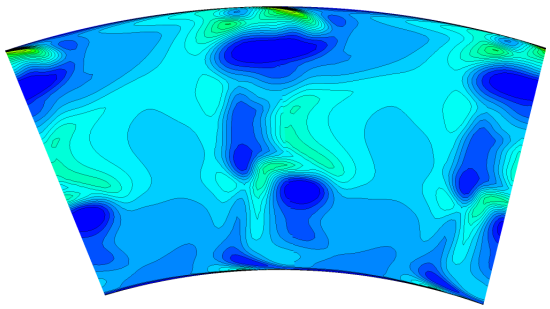

(l)

Fig. 7.15: Rotor total-total efficiency ($\eta_{tt,3}$) at rotor exit (X3) (cont)

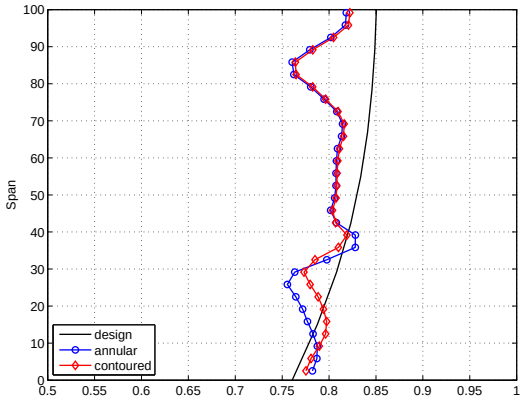

(m) $\eta_{de} - based$

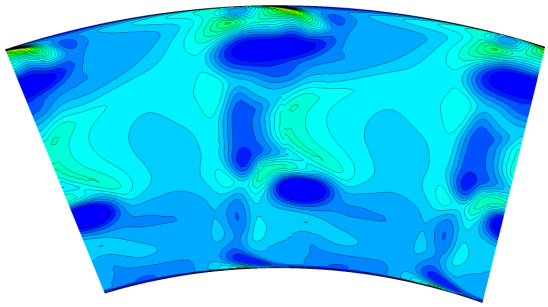

(n)

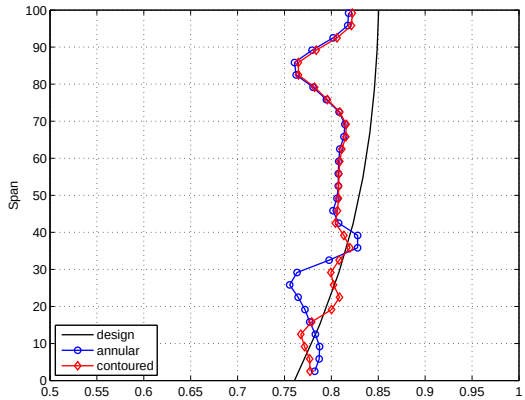

(o) $C_{ske,1} + \beta_{dev,0.7} - based$

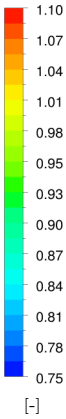

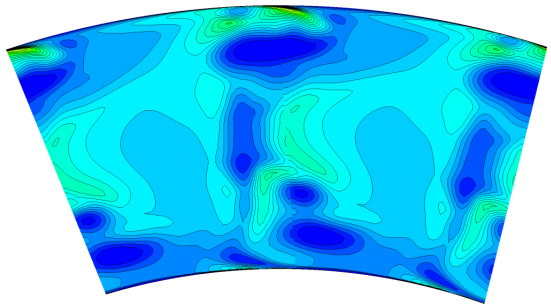

(p)

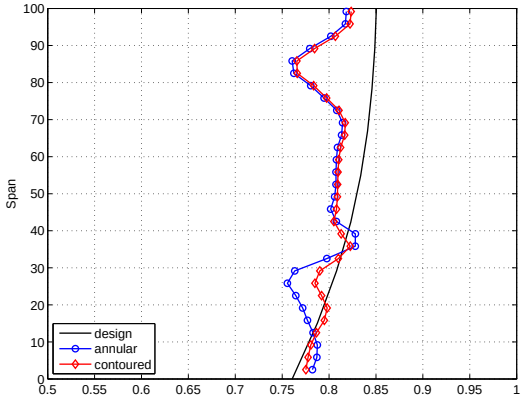

(q) $C_{p0,rel} + \beta_{dev,0.7} - based$

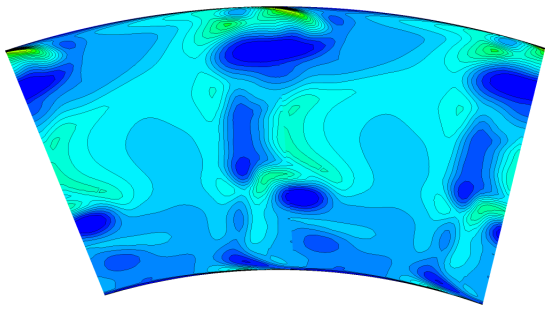

(r)

Fig. 7.15: Rotor total-total efficiency ($\eta_{tt,3}$) at rotor exit (X3) (cont)

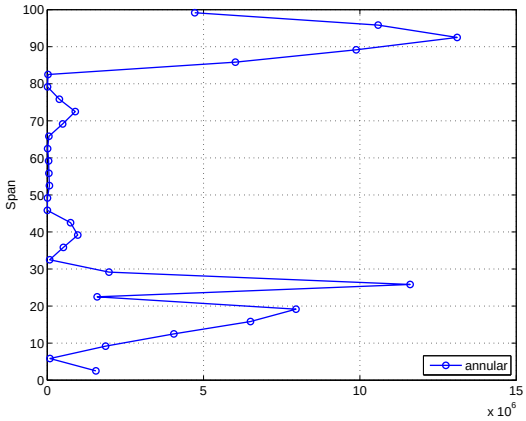

(a) annular

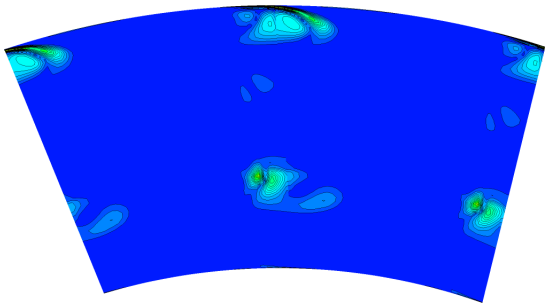

(b)

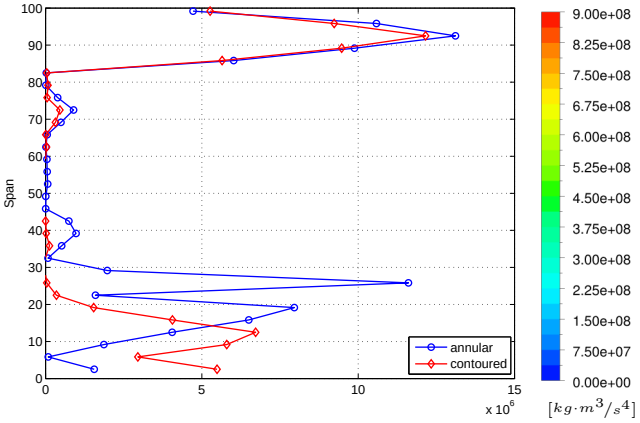

(c) $\eta_{tt} - based$

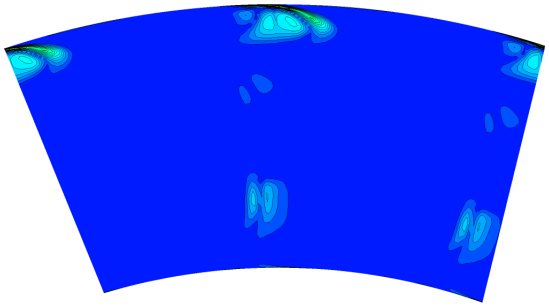

(d)

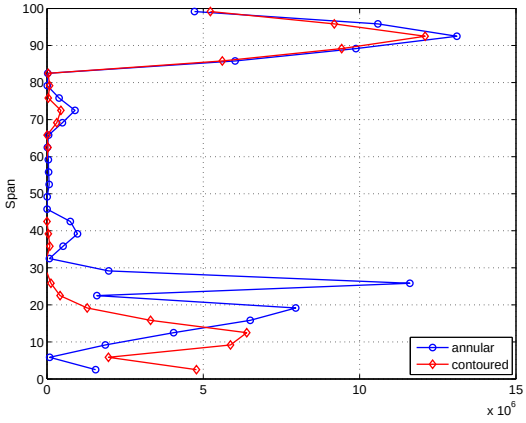

(e) $C_{ske} - based$

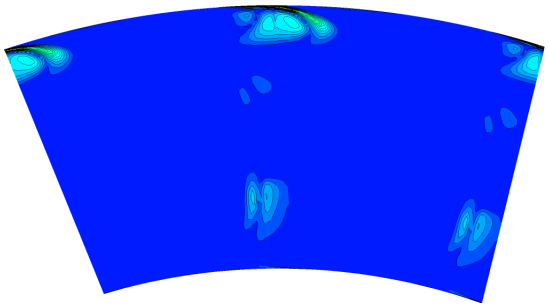

(f)

Fig. 7.16: Secondary kinetic energy helicity ($SKEH_3$) at rotor exit (X3)

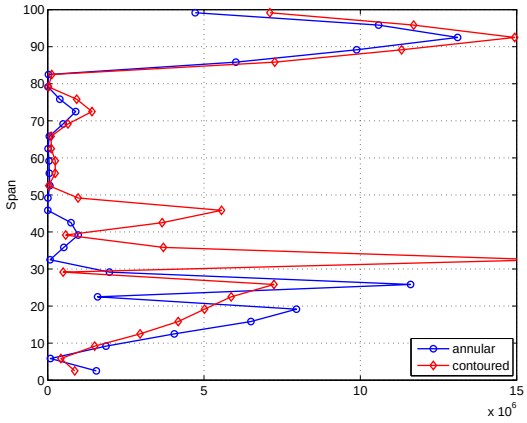

(g) $C_{p0,rel} - based$

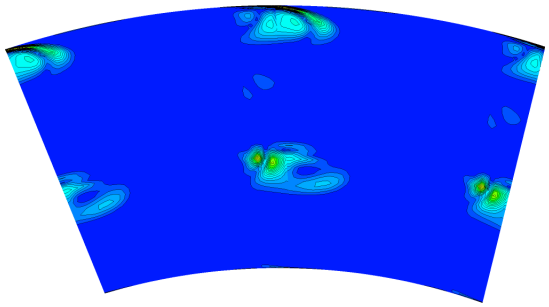

(h)

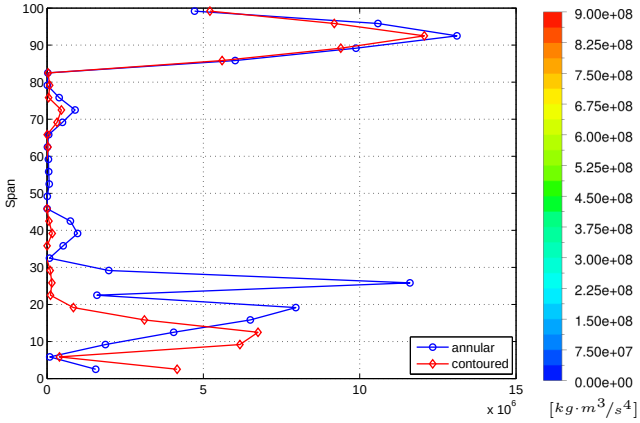

(i) $\beta_{dev} - based$

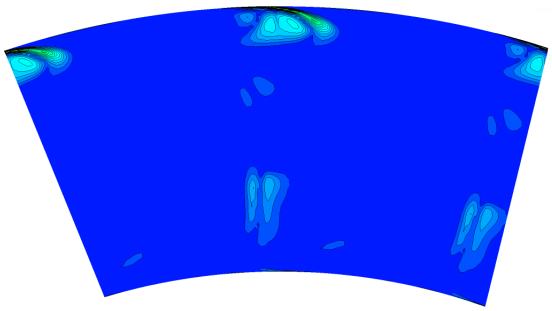

(j)

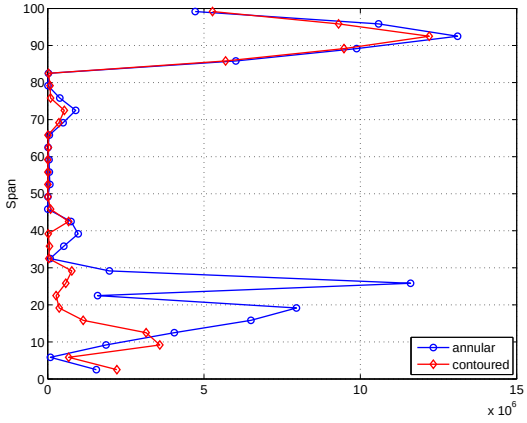

(k) $SKEH - based$

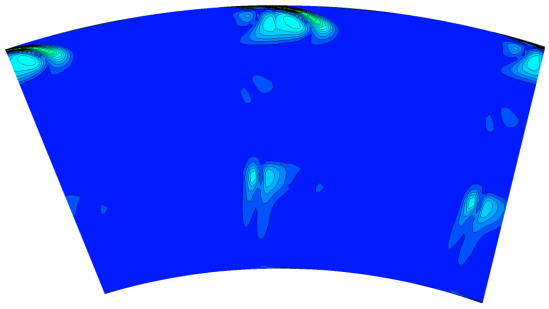

(l)

Fig. 7.16: Secondary kinetic energy helicity ($SKEH_3$) at rotor exit (X3) (cont)

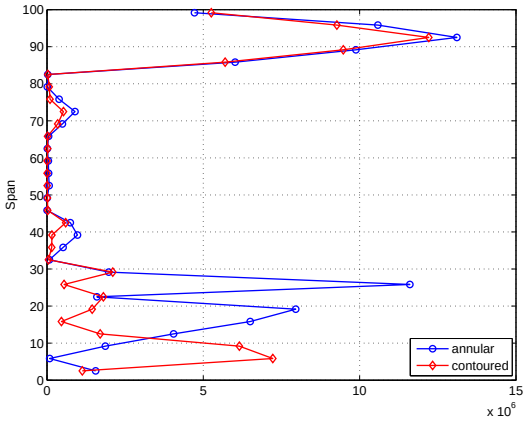

(m) $\eta_{de} - based$

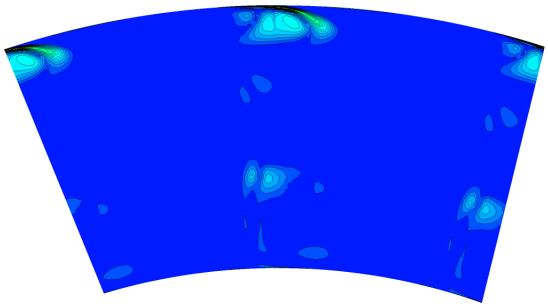

(n)

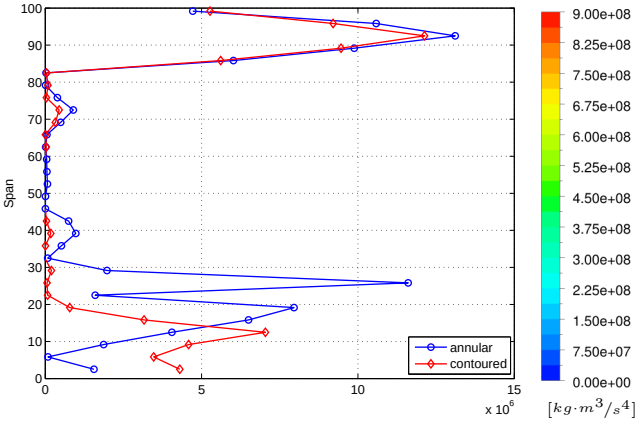

(o) $C_{ske,1} + \beta_{dev,0.7} - based$

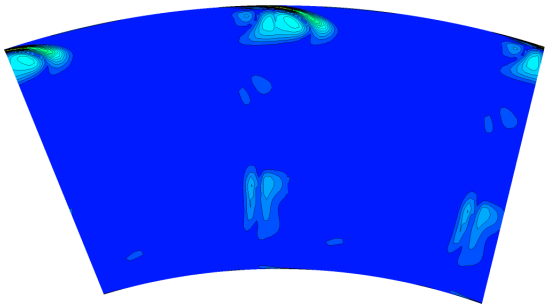

(p)

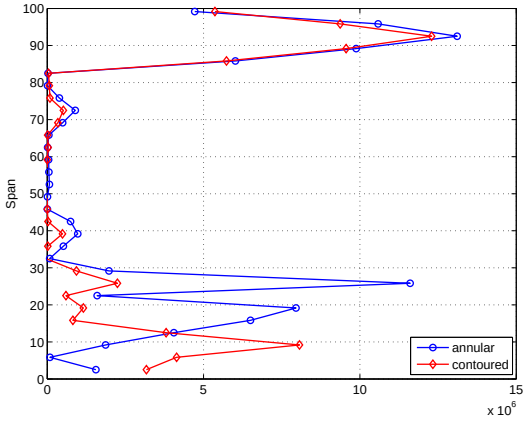

(q) $C_{p0,rel} + \beta_{dev,0.7} - based$

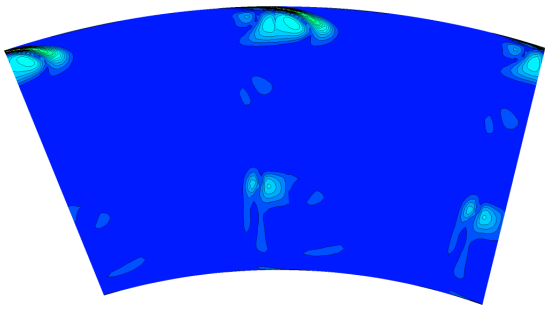

(r)

Fig. 7.16: Secondary kinetic energy helicity ($SKEH_3$) at rotor exit (X3) (cont)

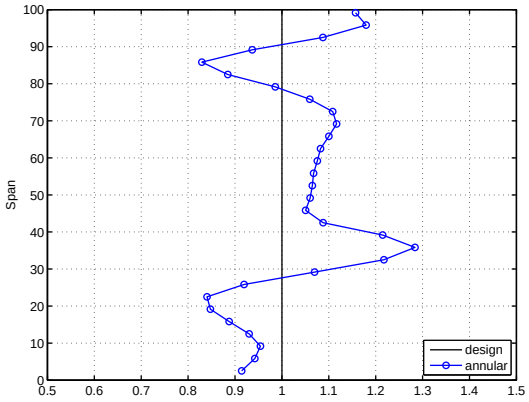

(a) annular

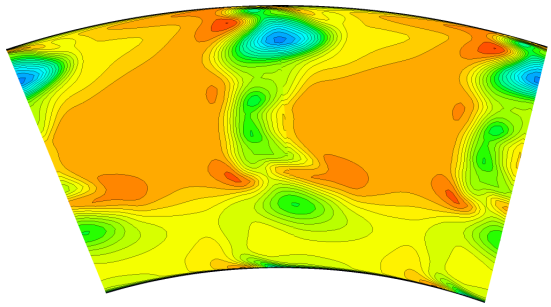

(b)

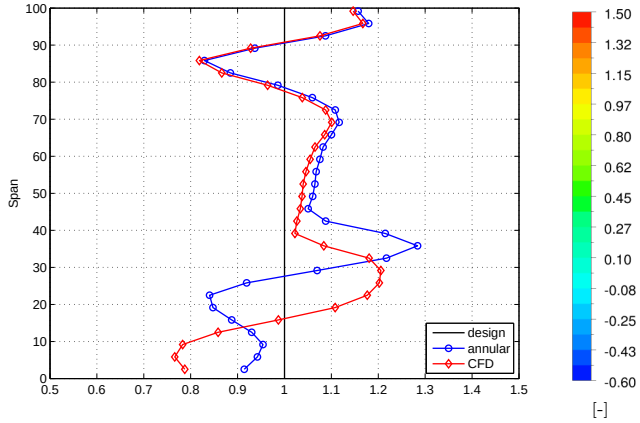

(c) $\eta_{tt} - based$

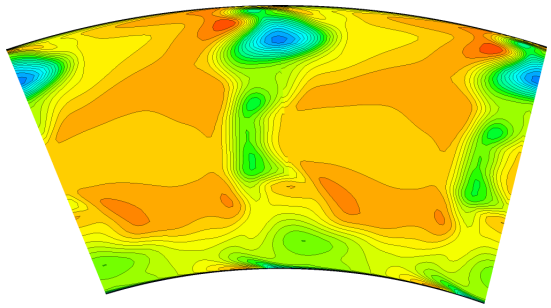

(d)

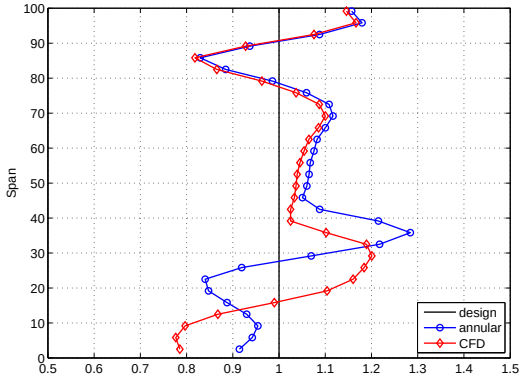

(e) $C_{ske} - based$

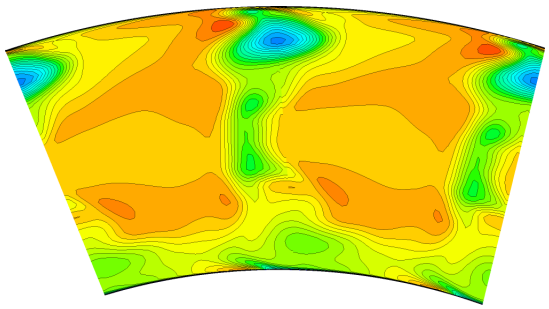

(f)

Fig. 7.17: Design efficacy ($\eta_{3de,}$) at rotor exit (X3)

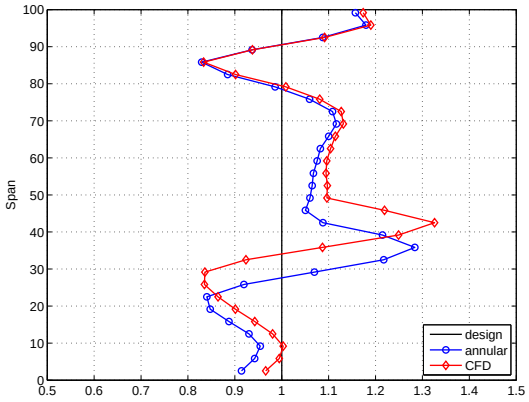

(g) $C_{p0,rel} - based$

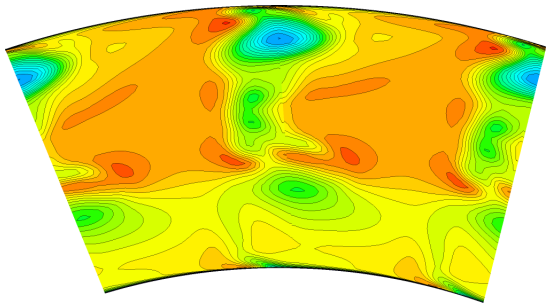

(h)

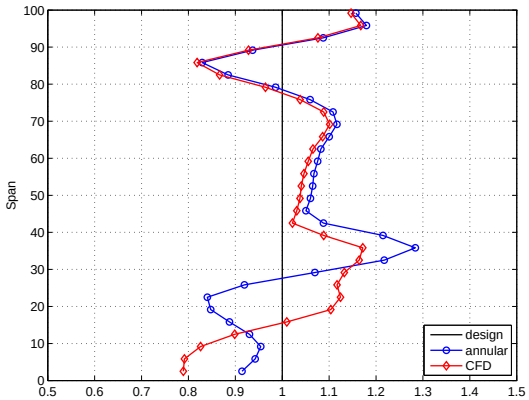

(i) $\beta_{dev} - based$

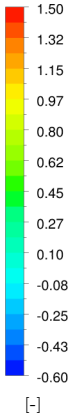

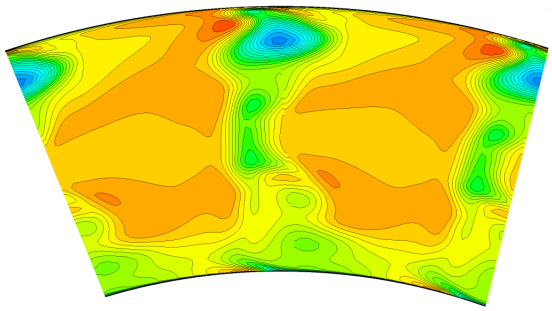

(j)

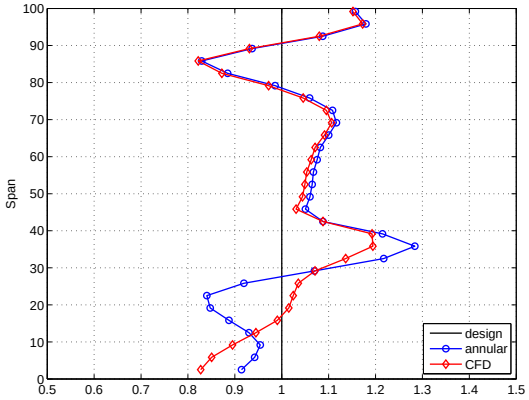

(k) $SKEH - based$

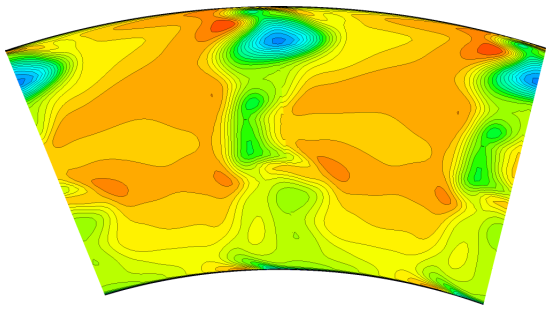

(l)

Fig. 7.17: Design efficacy ($\eta_{de,3}$) at rotor exit (X3) (cont)

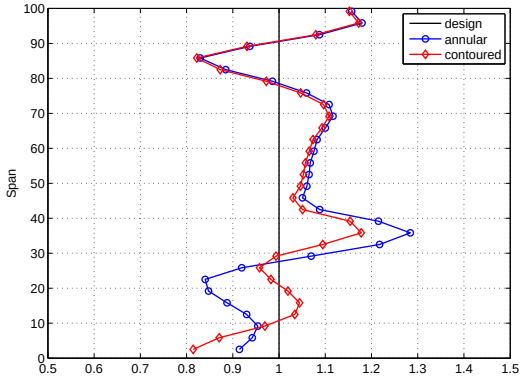

(m) $\eta_{de} - based$

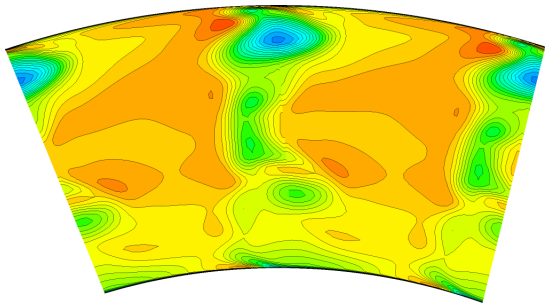

(n)

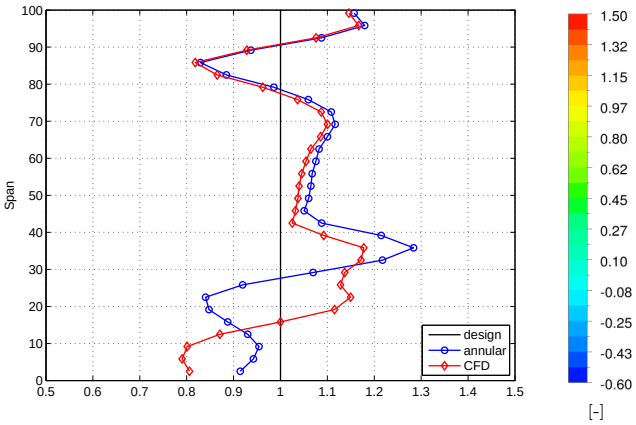

(o) $C_{ske,1} + \beta_{dev,0.7} - based$

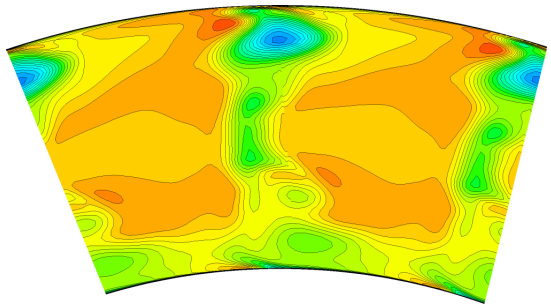

(p)

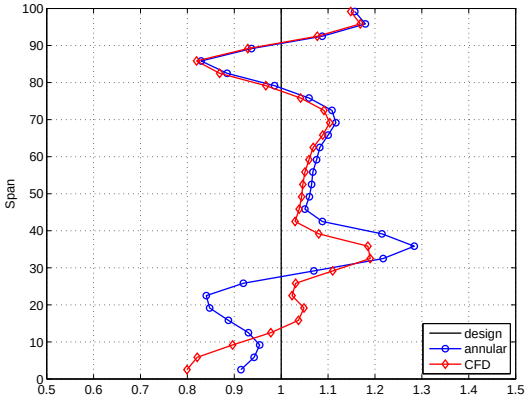

(q) $C_{p0,rel} + \beta_{dev,0.7} - based$

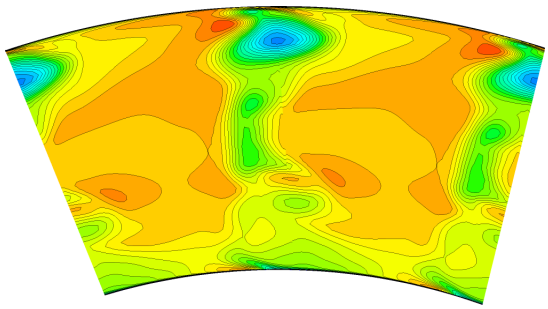

(r)

Fig. 7.17: Design efficacy ($\eta_{de,3}$) at rotor exit (X3) (cont)

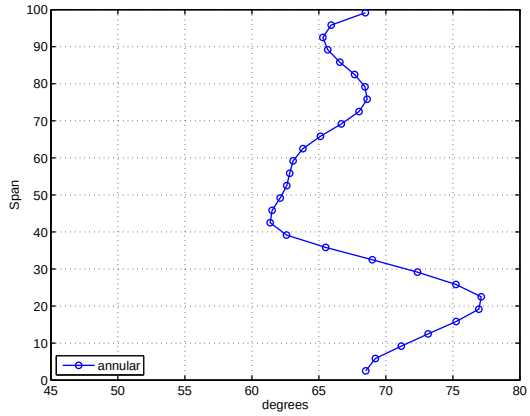

(a) annular

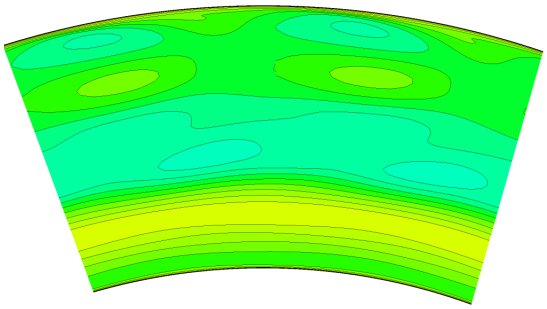

(b)

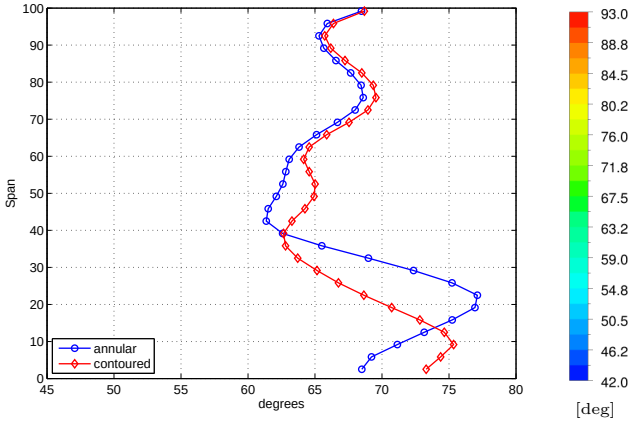

(c) $\eta_{tt} - based$

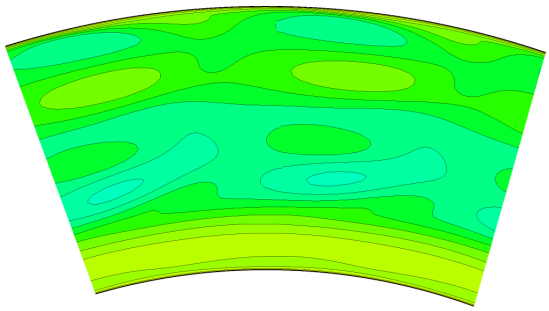

(d)

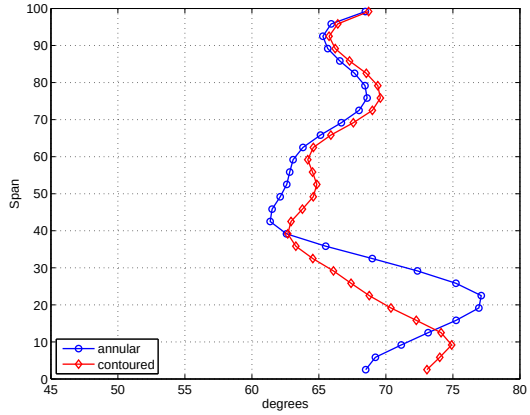

(e) $C_{ske} - based$

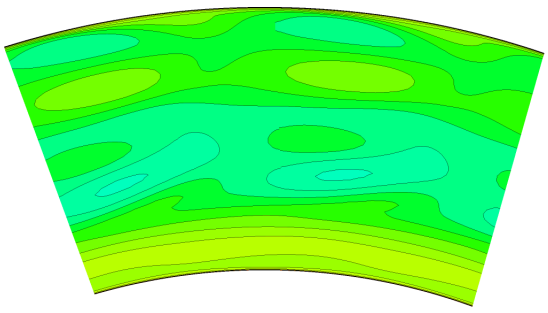

(f)

Fig. 7.18: Relative flow angle (β_4) at downstream plane (X4)

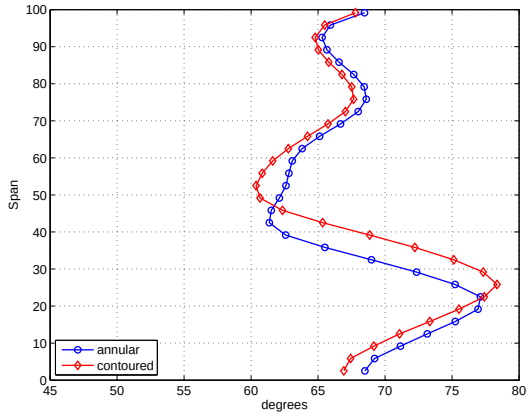

(g) $C_{p0,rel} - based$

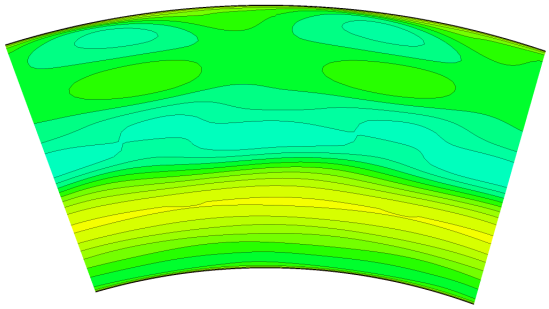

(h)

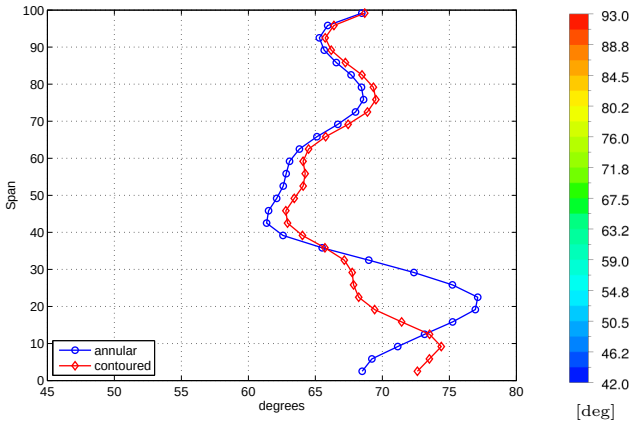

(i) $\beta_{dev} - based$

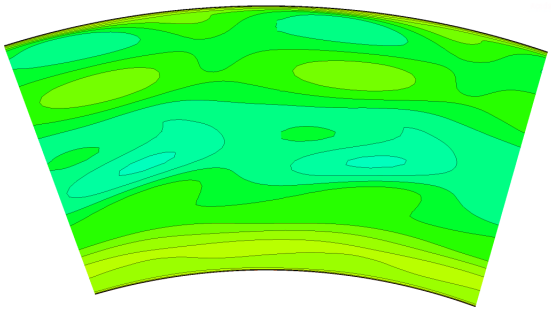

(j)

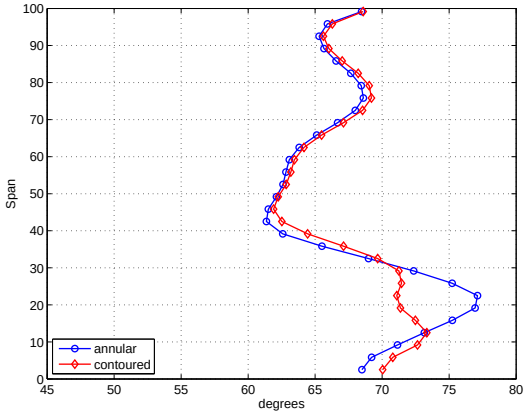

(k) $SKEH - based$

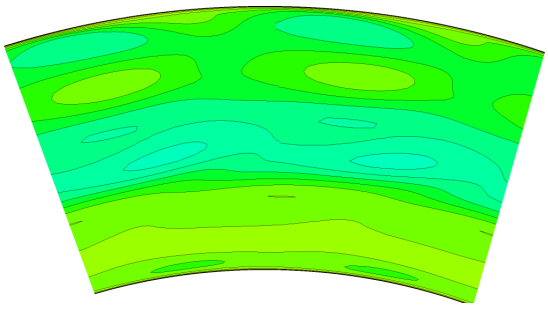

(l)

Fig. 7.18: Relative flow angle (β_4) at downstream plane (X4) (cont)

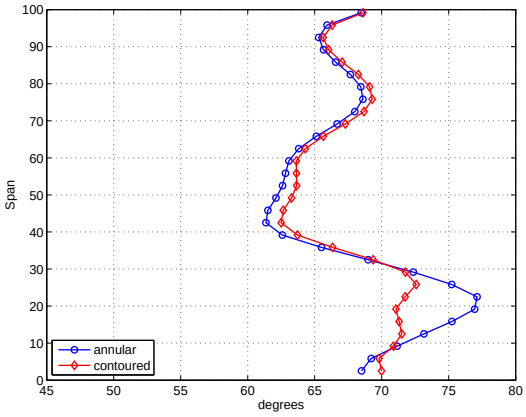

(m) $\eta_{de} - based$

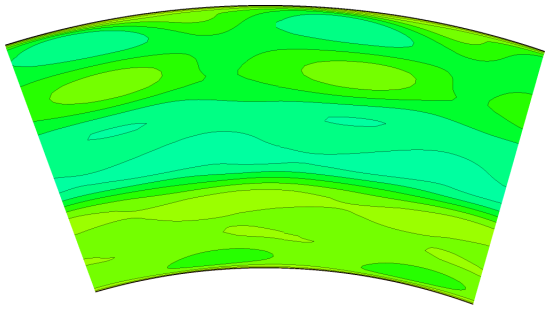

(n)

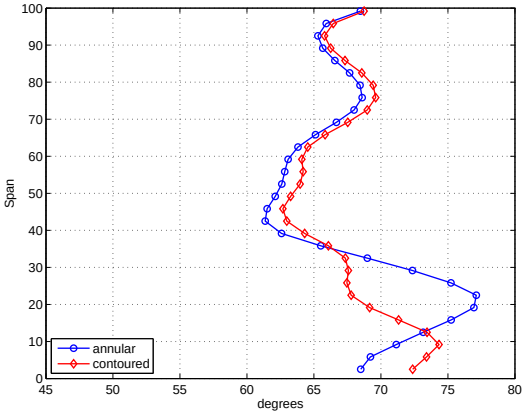

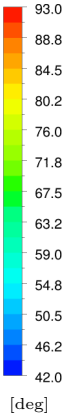

(o) $C_{ske,1} + \beta_{dev,0.7} - based$

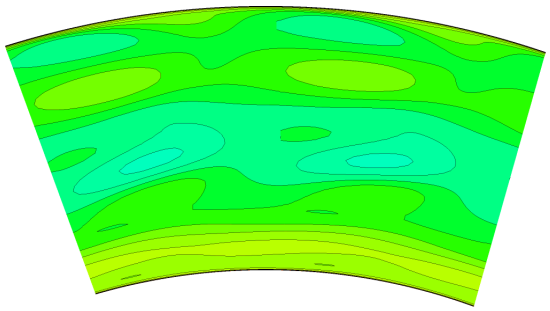

(p)

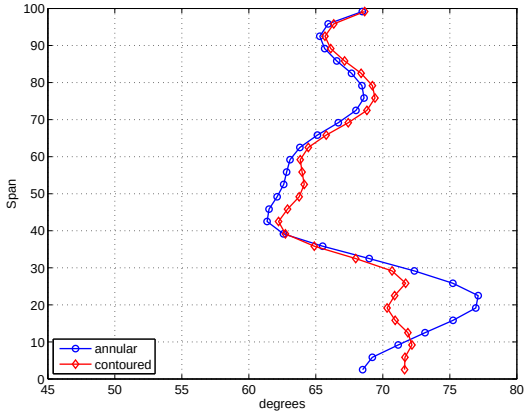

(q) $C_{p0,rel} + \beta_{dev,0.7} - based$

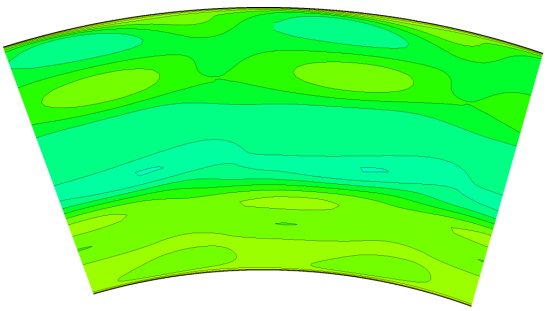

(r)

Fig. 7.18: Relative flow angle (β_4) at downstream plane (X4) (cont)

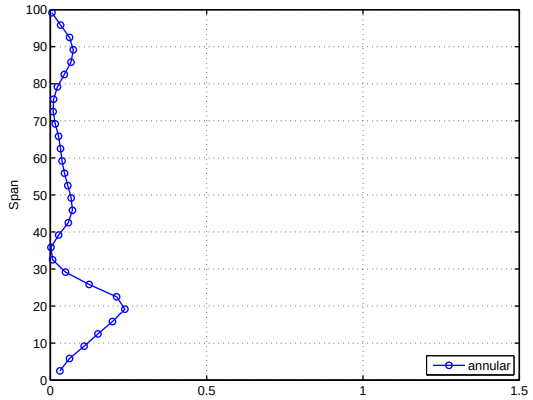

(a) annular

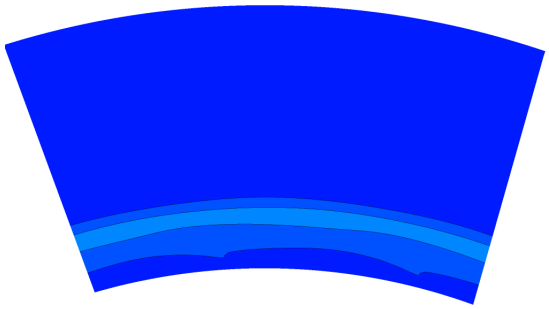

(b)

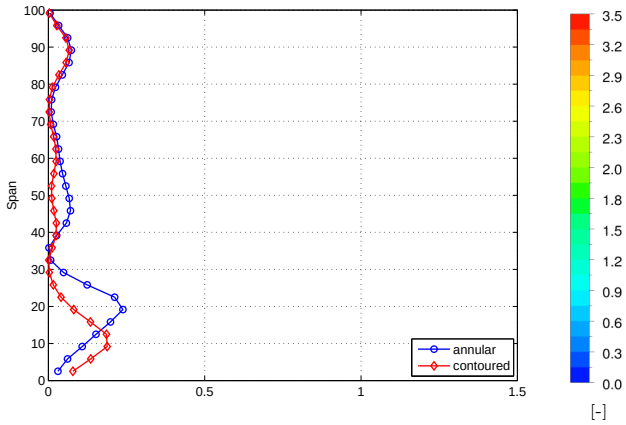

(c) $\eta_{tt} - based$

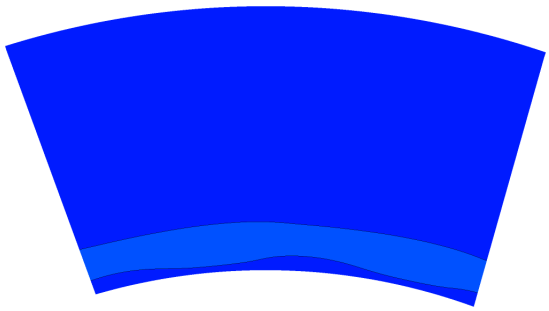

(d)

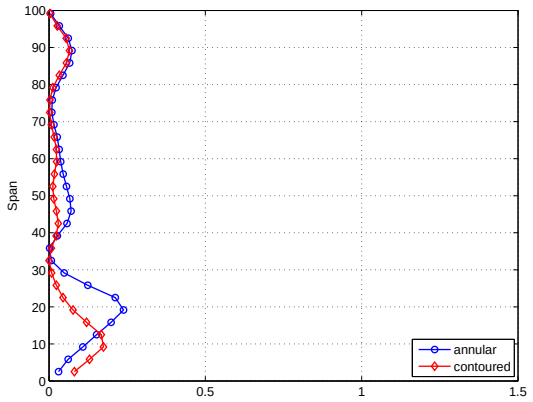

(e) $C_{ske} - based$

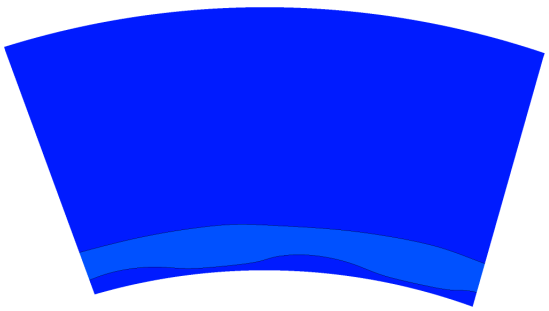

(f)

Fig. 7.19: Coefficient of secondary kinetic energy ($C_{ske,4}$) at downstream plane (X4)

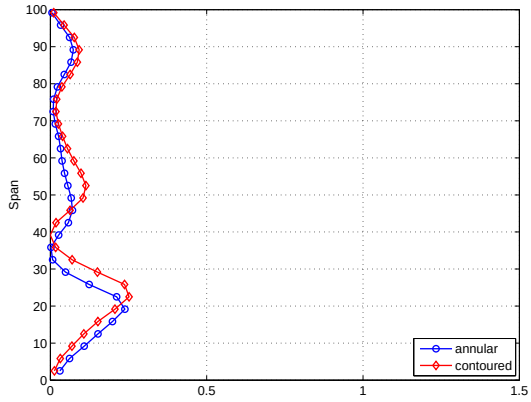

(g) $C_{p0,rel} - based$

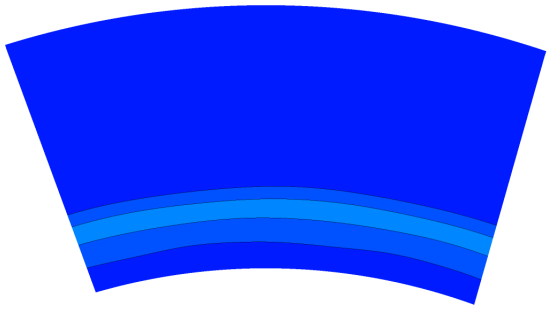

(h)

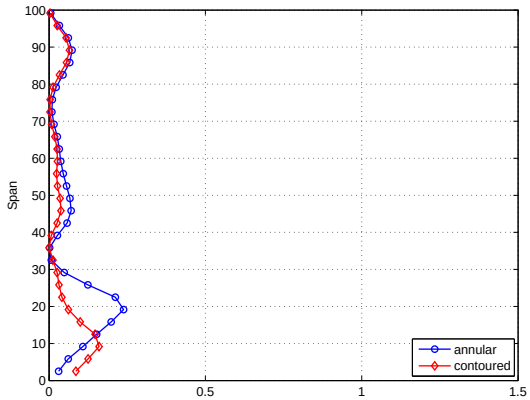

(i) $\beta_{dev} - based$

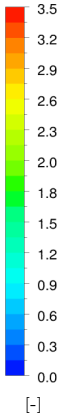

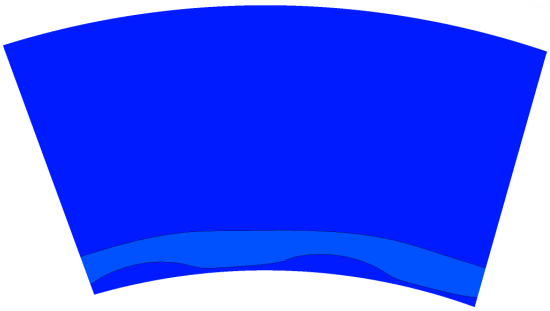

(j)

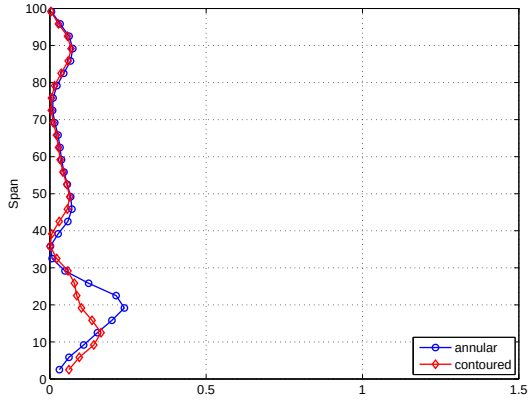

(k) $SKEH - based$

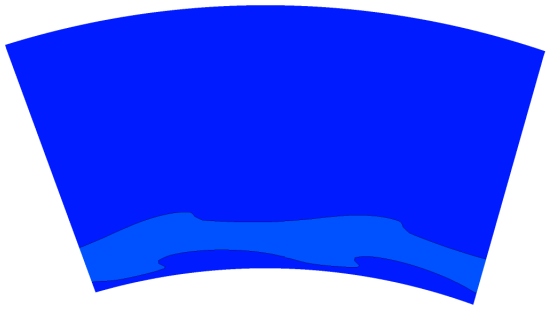

(l)

Fig. 7.19: Coefficient of secondary kinetic energy ($C_{ske,4}$) at downstream plane (X4) (cont)

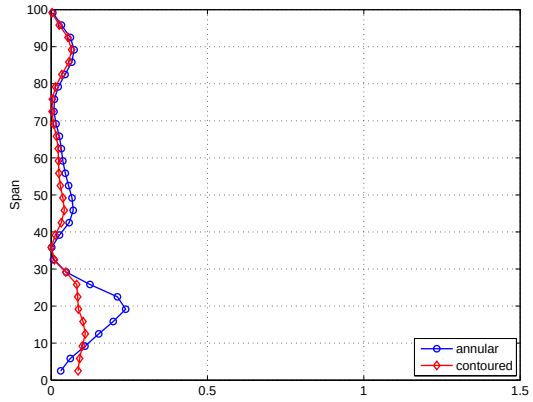

(m) $\eta_{de} - based$

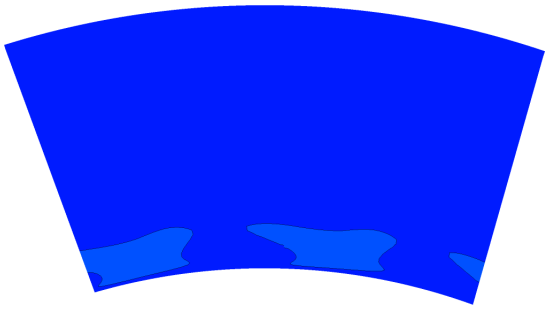

(n)

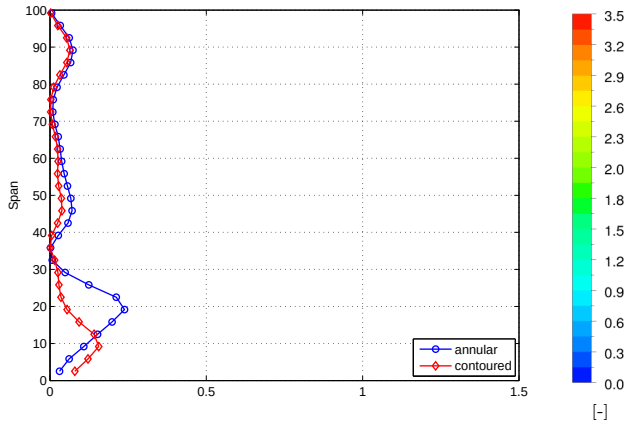

(o) $C_{ske,1} + \beta_{dev,0.7} - based$

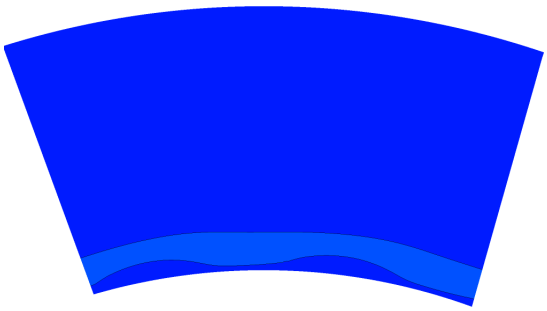

(p)

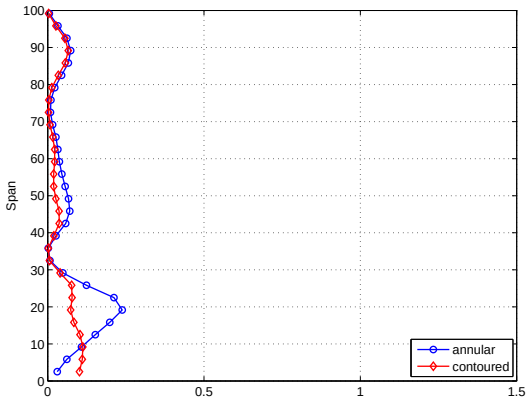

(q) $C_{p0,rel} + \beta_{dev,0.7} - based$

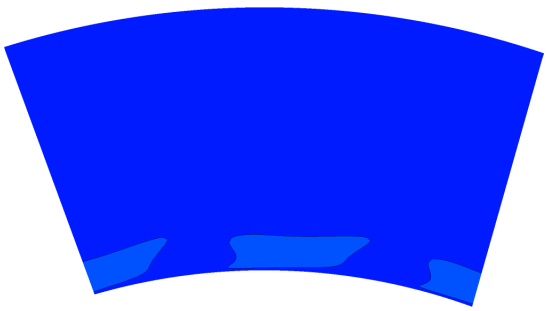

(r)

Fig. 7.19: Coefficient of secondary kinetic energy ($C_{ske,4}$) at downstream plane (X4) (cont)

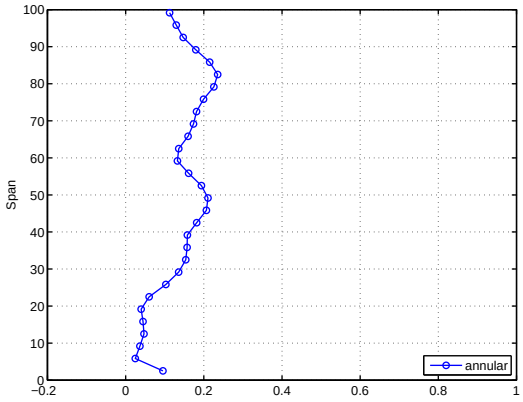

(a) annular

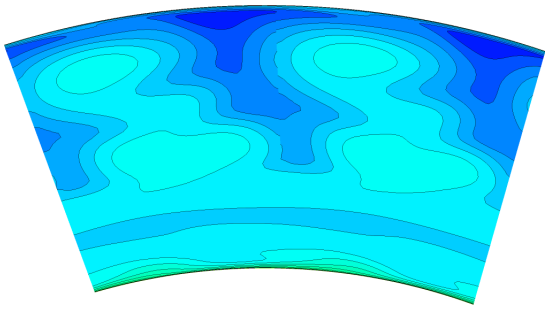

(b)

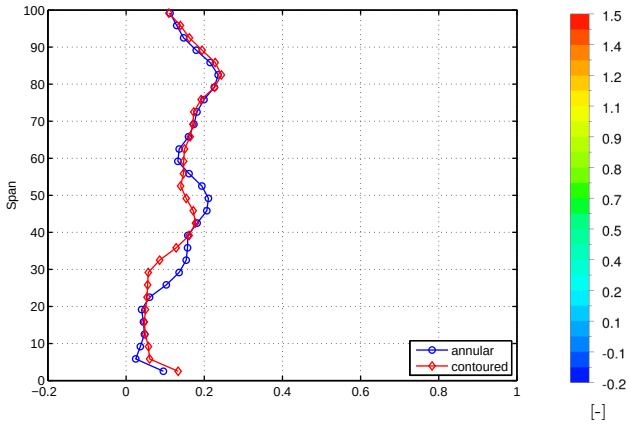

(c) $\eta_{tt} - based$

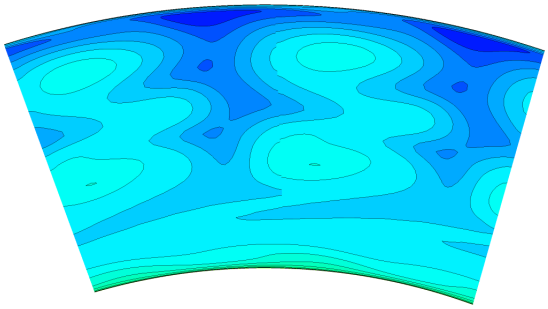

(d)

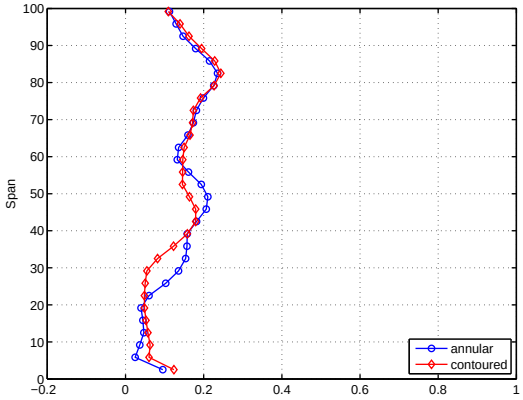

(e) $C_{ske} - based$

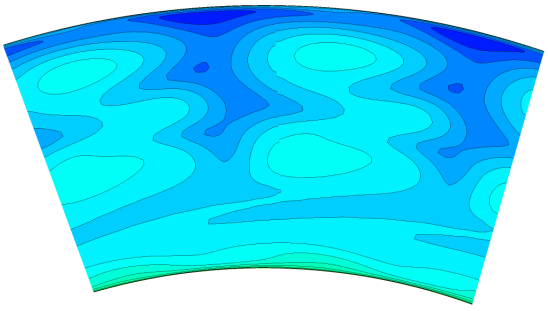

(f)

Fig. 7.20: Relative total pressure loss coefficient ($C_{p0,rel,4}$) at downstream plane (X4)

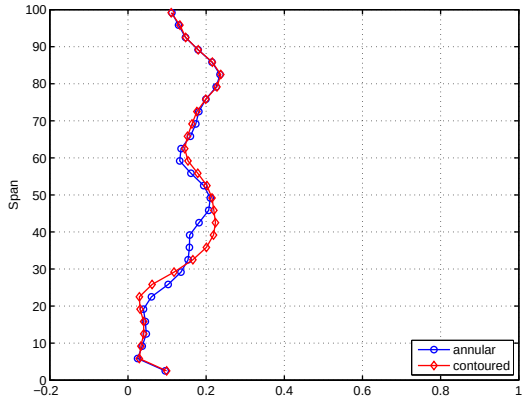

(g) $C_{p0,rel} - based$

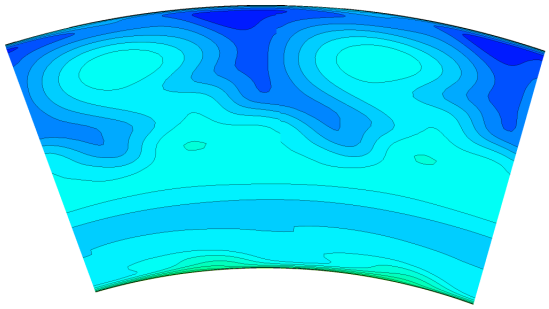

(h)

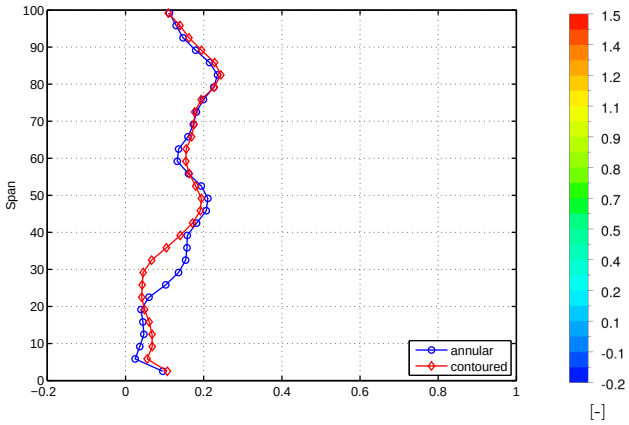

(i) $\beta_{dev} - based$

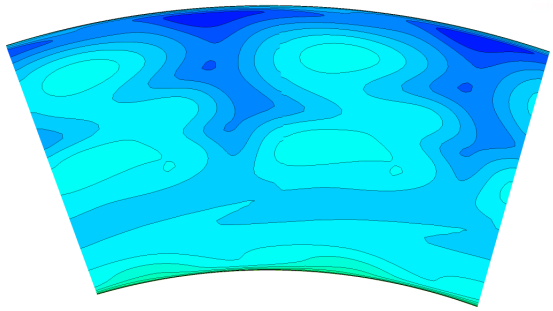

(j)

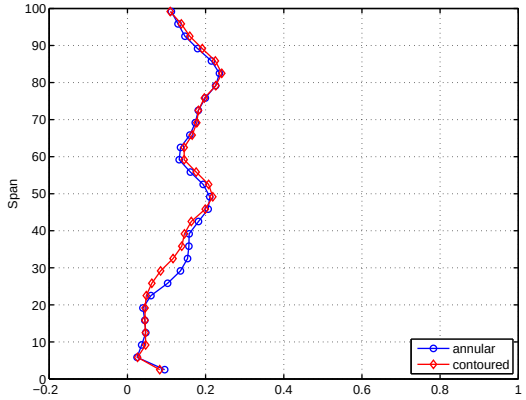

(k) $SKEH - based$

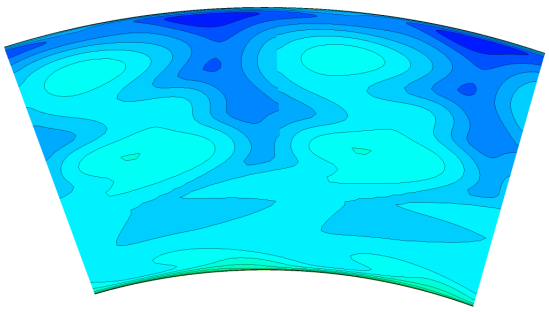

(l)

Fig. 7.20: Relative total pressure loss coefficient ($C_{p0,rel,4}$) at downstream plane (X4) (cont)

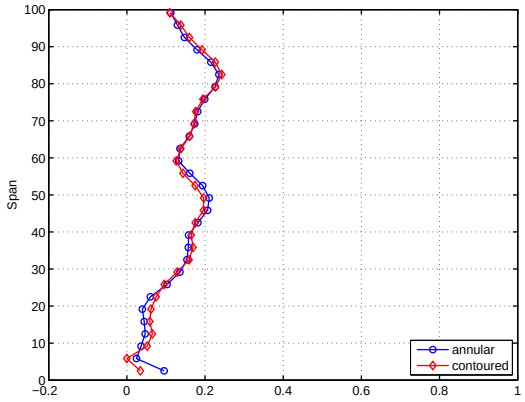

(m) $\eta_{de} - based$

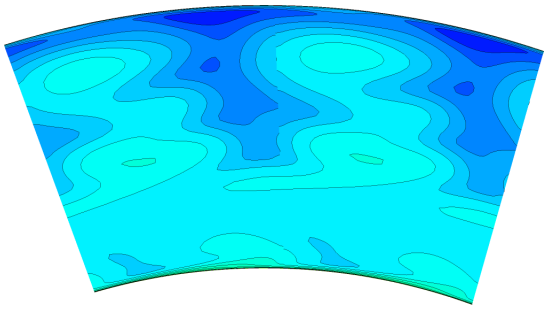

(n)

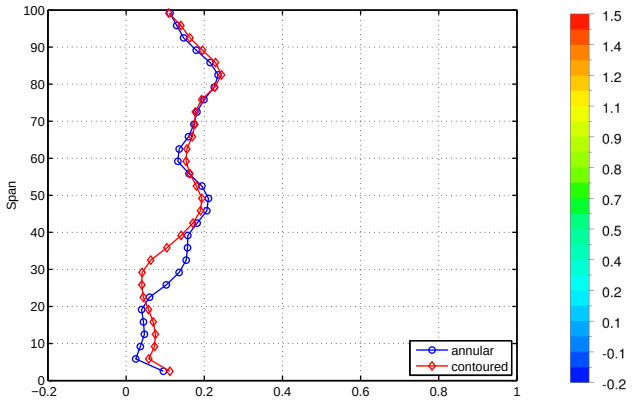

(o) $C_{ske,1} + \beta_{dev,0.7} - based$

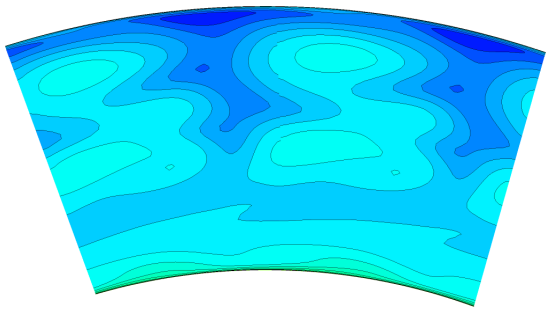

(p)

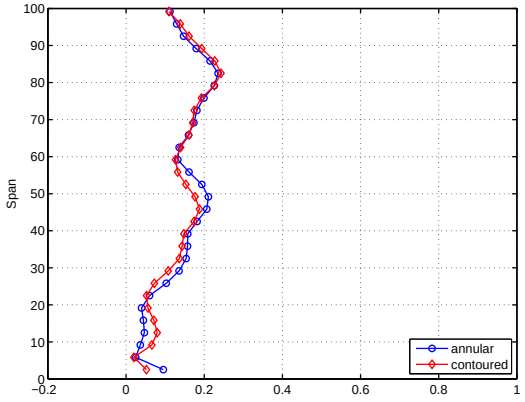

(q) $C_{p0,rel} + \beta_{dev,0.7} - based$

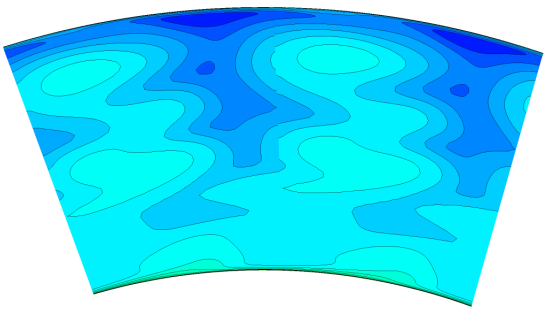

(r)

Fig. 7.20: Relative total pressure loss coefficient ($C_{p0,rel,4}$) at downstream plane (X4) (cont)

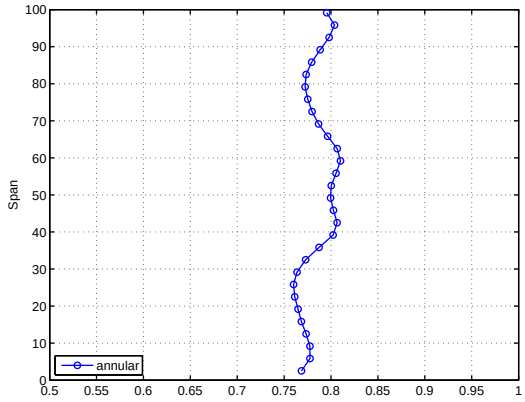

(a) annular

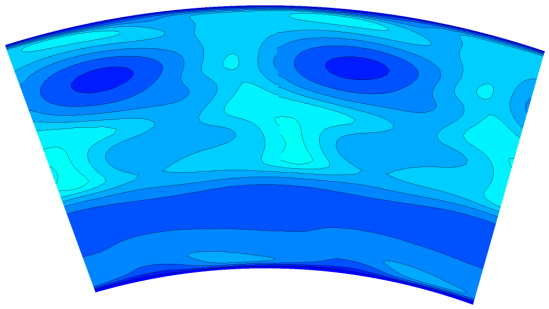

(b)

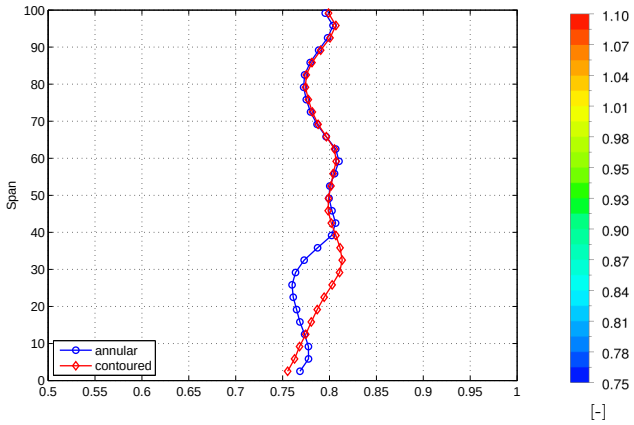

(c) $\eta_{tt} - based$

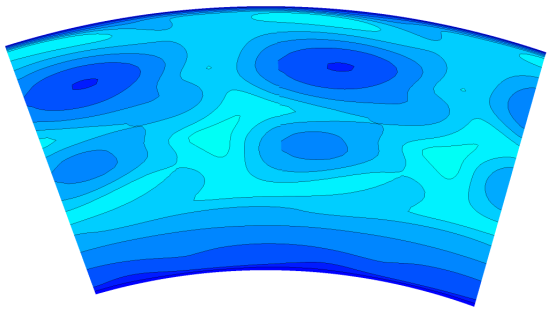

(d)

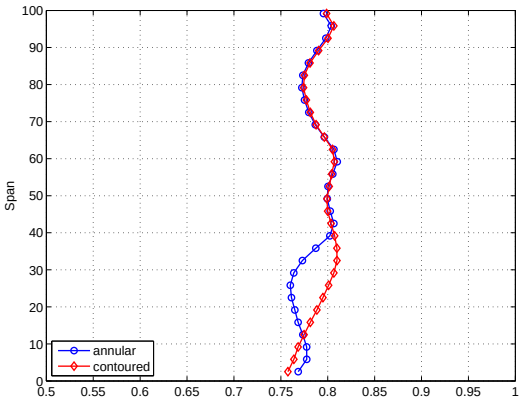

(e) $C_{ske} - based$

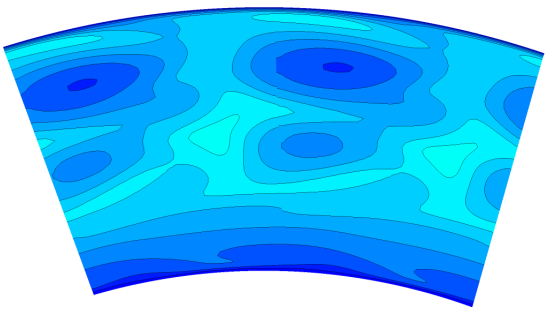

(f)

Fig. 7.21: Rotor total-total efficiency ($\eta_{tt,4}$) at downstream plane (X4)

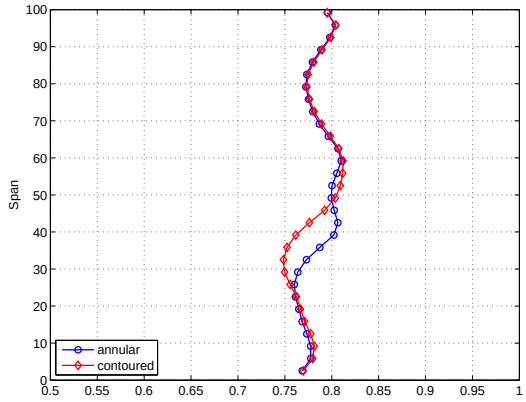

(g) $C_{p0,rel} - based$

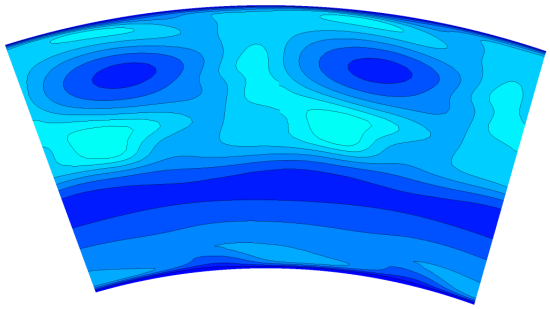

(h)

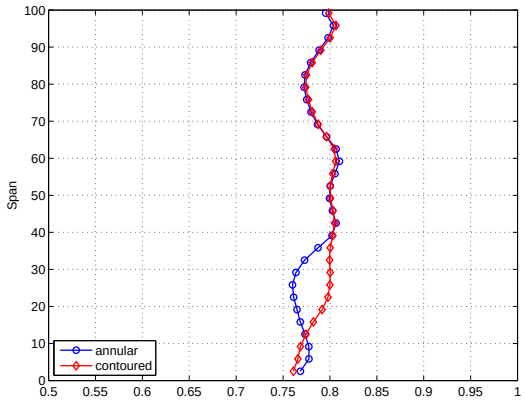

(i) $\beta_{dev} - based$

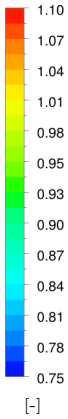

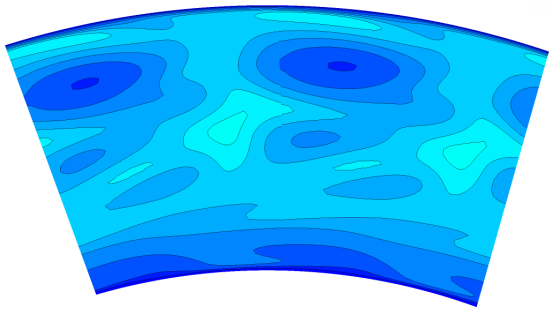

(j)

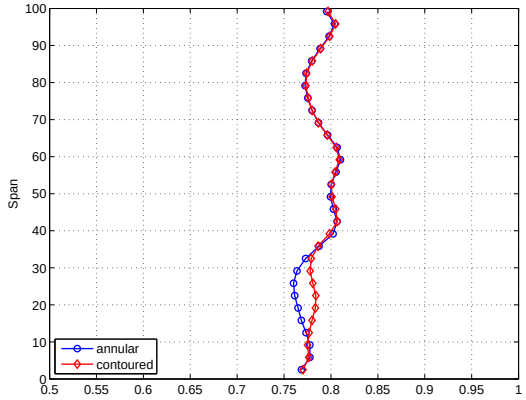

(k) $SKEH - based$

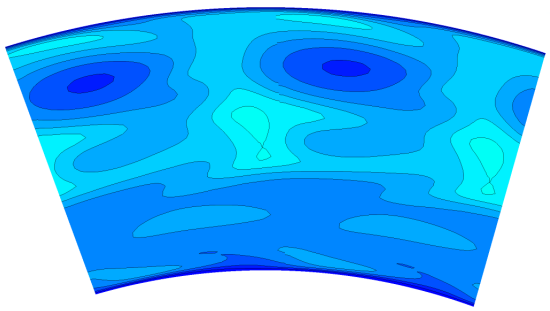

(l)

Fig. 7.21: Rotor total-total efficiency ($\eta_{tt,4}$) at downstream plane (X4) (cont)

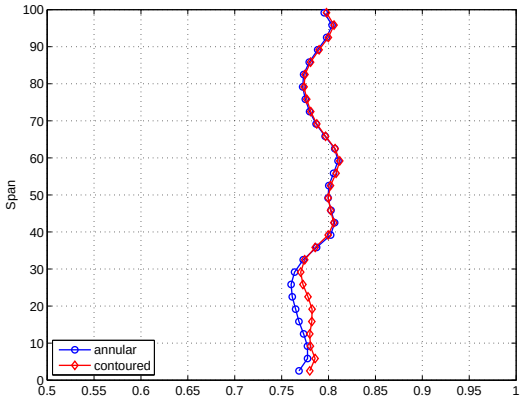

(m) $\eta_{de} - based$

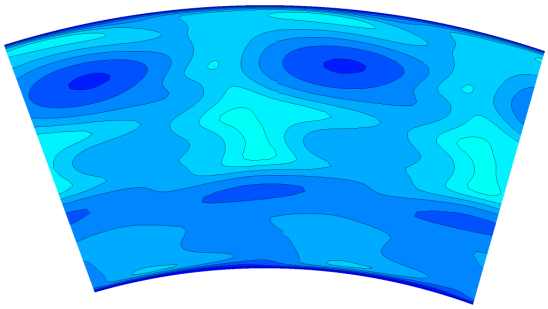

(n)

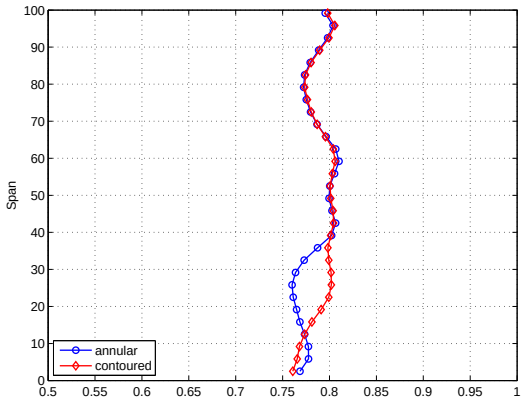

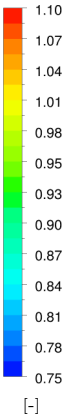

(o) $C_{ske,1} + \beta_{dev,0.7} - based$

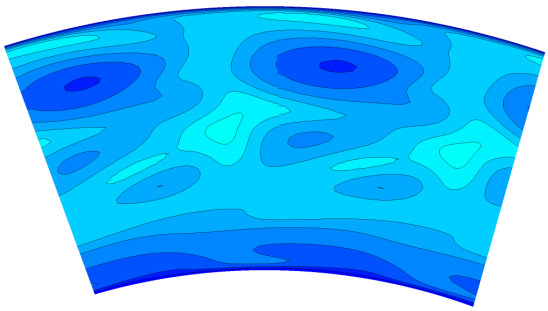

(p)

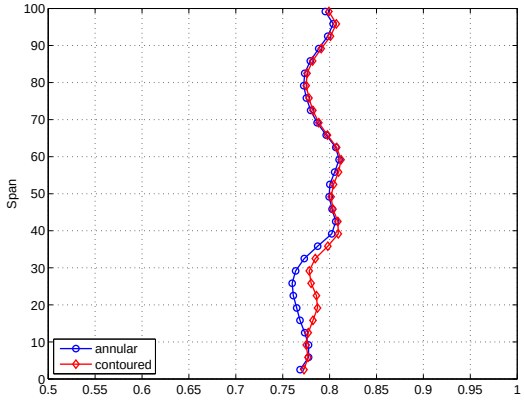

(q) $C_{p0,rel} + \beta_{dev,0.7} - based$

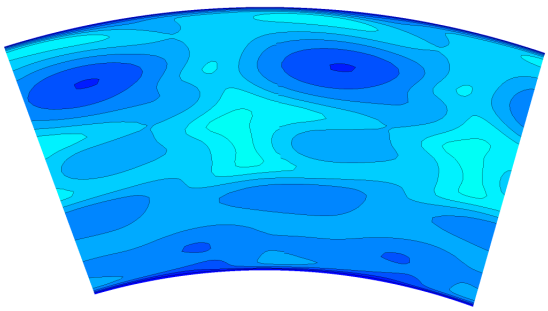

(r)

Fig. 7.21: Rotor total-total efficiency ($\eta_{tt,4}$) at downstream plane (X4) (cont)

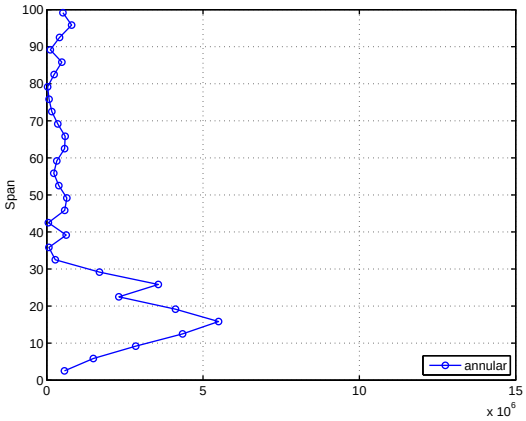

(a) annular

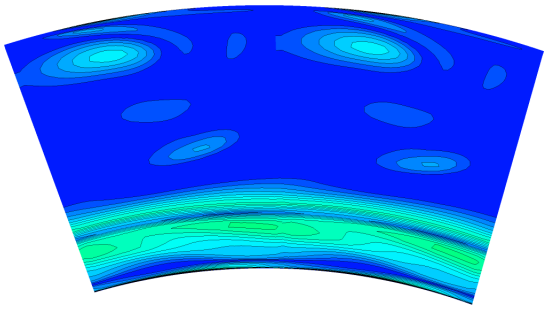

(b)

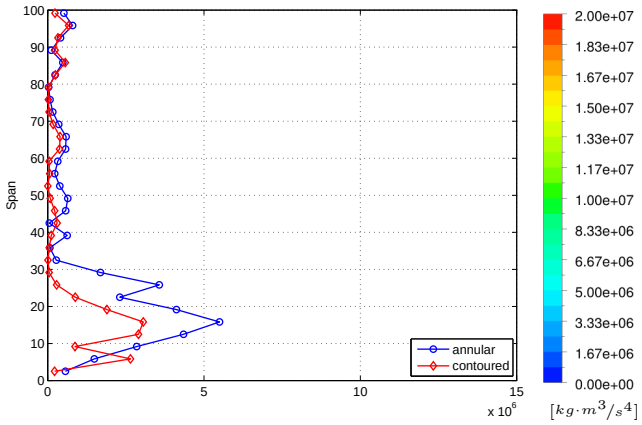

(c) $\eta_{tt} - based$

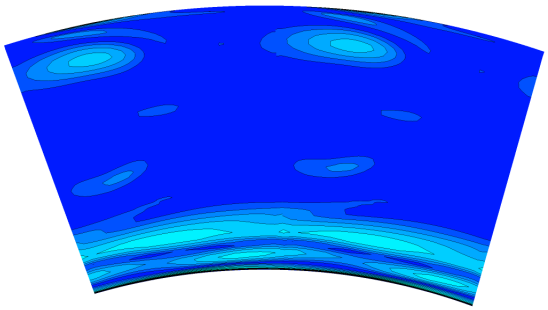

(d)

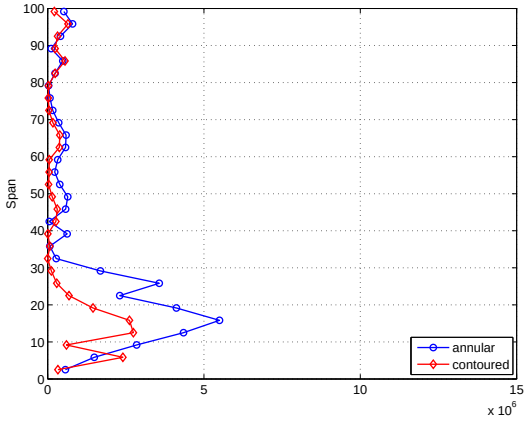

(e) $C_{ske} - based$

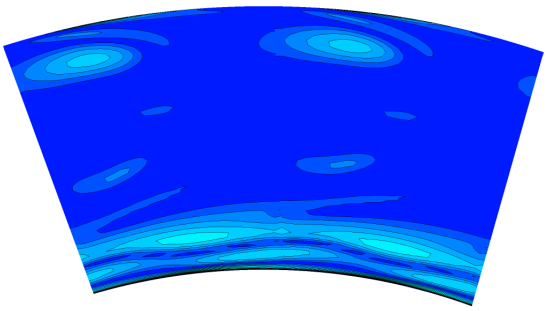

(f)

Fig. 7.22: Secondary kinetic energy helicity ($SKEH_4$) at downstream plane (X4)

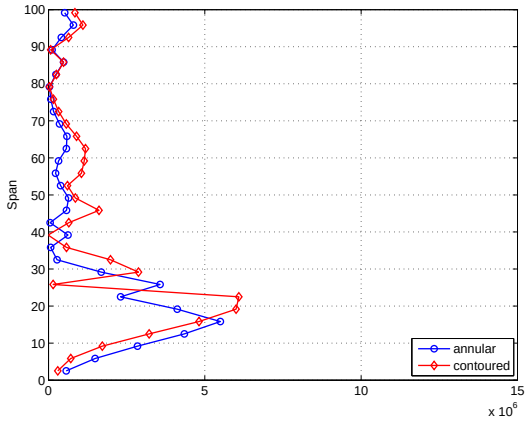

(g) $C_{p0,rel} - based$

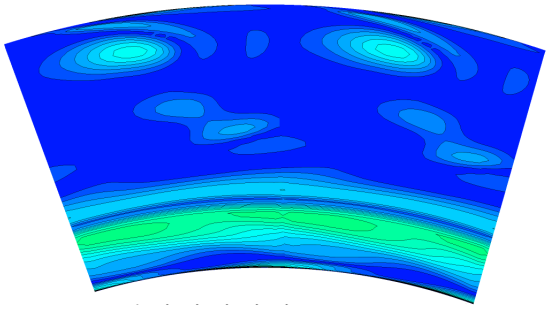

(h)

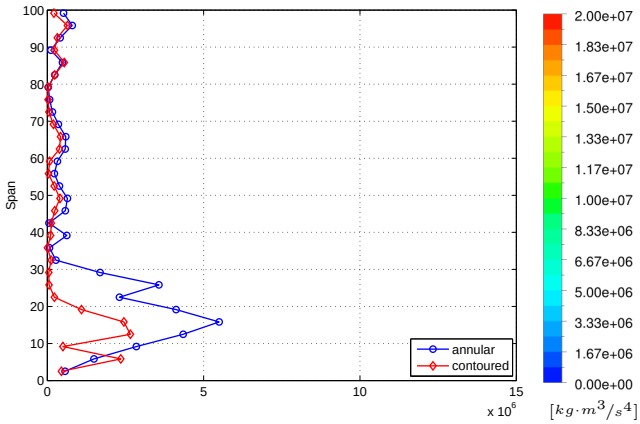

(i) $\beta_{dev} - based$

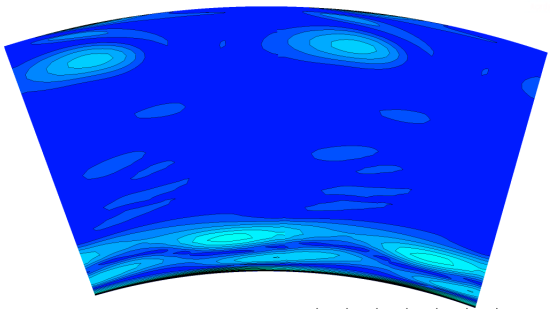

(j)

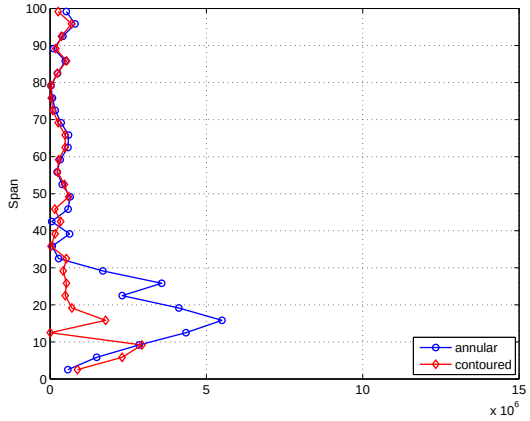

(k) $SKEH - based$

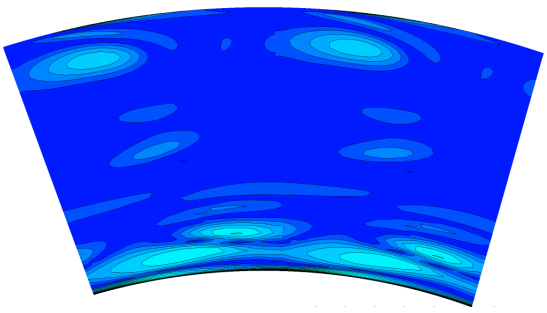

(l)

Fig. 7.22: Secondary kinetic energy helicity ($SKEH_4$) at downstream plane (X4) (cont)

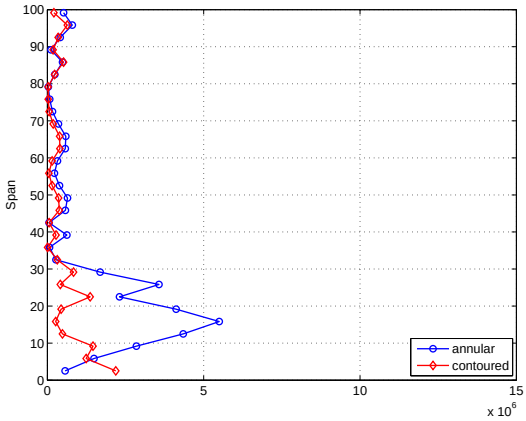

(m) $\eta_{de} - based$

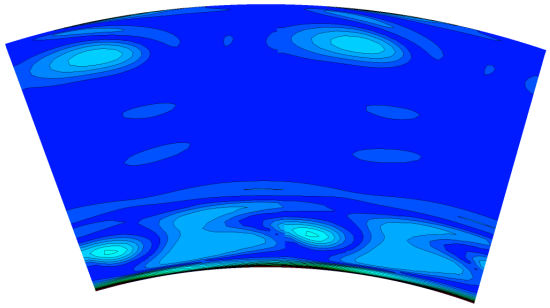

(n)

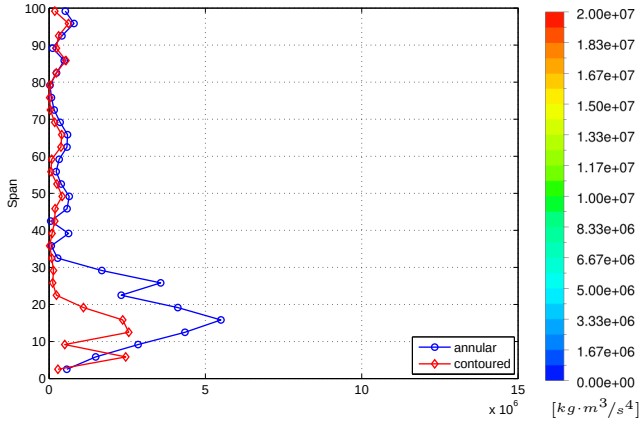

(o) $C_{ske,1} + \beta_{dev,0.7} - based$

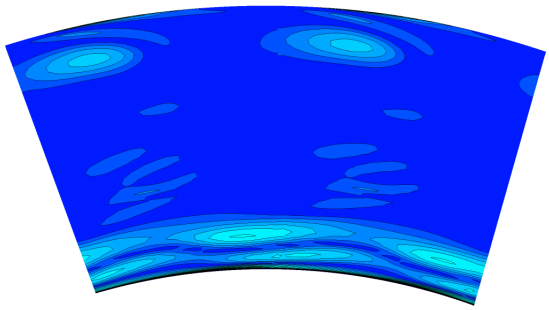

(p)

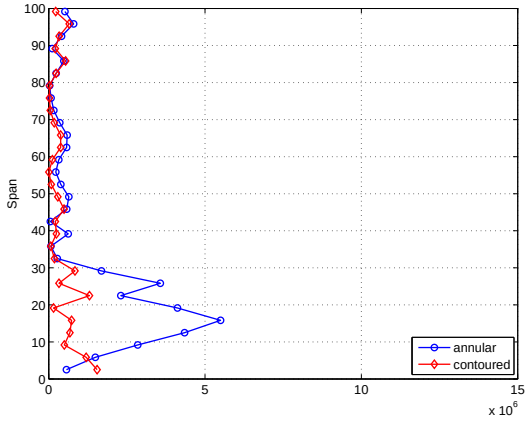

(q) $C_{p0,rel} + \beta_{dev,0.7} - based$

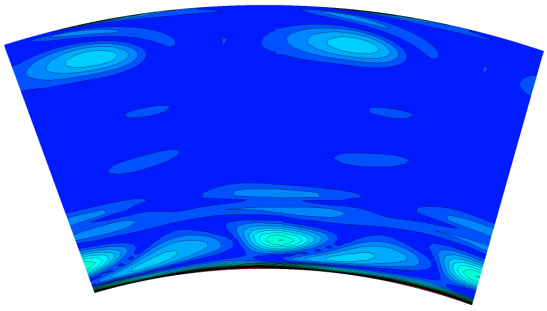

(r)

Fig. 7.22: Secondary kinetic energy helicity ($SKEH_4$) at downstream plane (X4) (cont)

7.5 Mass-averaged experimental results

This section contains a comparison between the mass-averaged CFD and experimental results for a subset of the designs designs presented in the previous section. As was done for the CFD results, for each endwall the measurements are presented as mass-averaged changes from the annular case at both the rotor exit (X3) as well as at the downstream (X4) measurement planes.

In contrast to the CFD results however, in this section the mass-averages of $SKEH$ are not presented since the calculation of the helicity for a rotating blade was not possible in the test rig. In addition, as was the done for the CFD-only results, neither the flow deviation from design (β_{dev}) nor design efficacy (η_{de}) is reported at the downstream plane due to the lack of an appropriate design flow angle at this measurement location.

Selection of experimental subset

As indicated above, only a subset of the original set of designs produced during the endwall design & optimization phase of this work were tested experimentally. Due to the costs associated with manufacturing each blade set, a total of 5 sets of blades could be manufactured. The designs included in the experimental subset were selected based on the following rationale:-

1. the **annular** endwall was selected to assess the baseline performance of the rig to allow for comparisons with the contoured designs.
2. the $\boldsymbol{\eta_{tt} - \textbf{based}}$ endwall was selected as this represented the design which was predicted to perform best out of all those designed (in terms of the overall predicted increase in rotor efficiency) and therefore was expected to serve as a natural benchmark against which the remaining contoured designs could be compared.
3. the $\boldsymbol{C_{ske} - \textbf{based}}$ endwall was selected as this represented the design which was predicted to perform most similarly to the η_{tt}-based endwall and therefore presented an opportunity to investigate the relative performance of the two designs, but also because this endwall represented the best performing design of all those produced using a proxy quantity rather than the rotor efficiency itself. In addition, as indicated by Table 2.2, to date, the coefficient of secondary kinetic energy has formed the basis of the vast majority of objective functions (either alone or in a compound setting) used to date for the design of non-axisymmetric endwalls and therefore its performance relative to the η_{tt}-based design discussed above, was felt to be of considerable interest.
4. the $\boldsymbol{C_{ske,1} + \beta_{dev,0.7} - \textbf{based}}$ endwall was selected because despite the β_{dev}-based design being predicted to produce a larger improvement in the rotor efficiency, testing of this design would result in an opportunity to investigate the performance of a design produced using a so-called 'compound' objective function, but also one for which non-trivial improvements in the rotor efficiency as well as the mass-averaged rotor exit C_{ske} and flow deviations from design were predicted.
5. finally, the $\boldsymbol{C_{p0,rel,1} + \beta_{dev,0.7} - \textbf{based}}$ design was selected for two principal reasons:-
   - the use of 'loss' as predicted using CFD has proven to be a contentious choice among researchers with a number of investigators concluding the quantity was *not* able to be predicted accurately enough by CFD for it to be used reliably, *and*

- despite the poor predicted performance of the rotor exit loss coefficient ($C_{p0,rel}$) reported previously, the addition of the β_{dev} term appears to have corrected the difficulties associated with the quantity and in turn resulted in the 3^{rd} most efficient rotor (after the η_{tt}- & C_{ske}-based endwalls respectively).

The remainder of the endwalls not selected for inclusion in the experimental subset were not included due to a number of reasons, including:-

- in the case of the $\mathbf{C_{p0,rel}-based}$ design, despite being predicted to reduce the rotor exit loss coefficient, this endwall was in fact predicted to *increase* the amount of secondary flow as well as result in a decrease in the overall efficiency of the rotor,
- further, in the cases of the $\mathbf{SKEH-}$ & $\boldsymbol{\eta_{de}-based}$ endwalls, although these endwalls were predicted to result in an increase in the overall rotor efficiency, as well as reductions in their corresponding target metrics, the final endwall shapes were considered too complex for consideration as practical designs, and finally,
- since the $\boldsymbol{\beta_{dev}}$ flow metric was included in the $C_{ske,1}+\beta_{dev,0.7}$- & $C_{p0,rel,1}+\beta_{dev,0.7}$-based objective functions - both of which were included in the experimental testing subset above - this endwall was *not* included in the experimental subset.

As was the case for the CFD results, a summary of the overall mass-averaged magnitudes, as well as percent changes from the annular case, at both the rotor exit (X3) and 'mixed-out' measurement planes (X4) planes, are included in Figs. 7.23 & 7.24.

Line	Description
	Experimental (change from annular)
	CFD (change from annular)

Table 7.5: Plot legend - Experimental vs CFD mass-averaged results

7.5.1 Rotor exit (X3)

η_{tt} − based

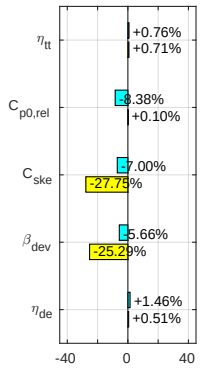

The results of the experimental testing corroborated the numerical predictions of the rotor total-total efficiency for the η_{tt}-based endwall very well, with the difference between the predicted and measured result being only approximately $\sim$ 0.05%. In terms of the relative total pressure loss coefficient, while the results of the endwall design procedure predicted a small increase in the coefficient, in contrast, the results of the experiment showed a relatively large decrease in the rotor exit loss (−8.38%). Of the remaining quantities, all three measured results corroborated the trends in the changes from the annular case, although in all cases except the the design efficacy (η_{de}), the measured reductions in each quantity from the datum case were significantly smaller than originally predicted (−27.75% c.f. −7.00% and −25.29% c.f. −5.66%). In the case of the design efficacy (η_{de}), the overall measured mass-averaged improvement at X3 in comparison to the annular case was +1.46% compared to the predicted improvement of +0.51%.

C_{ske} − based

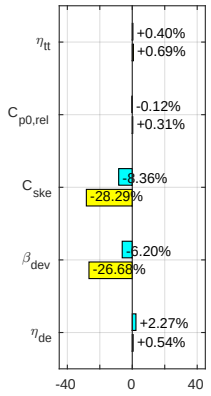

For the C_{ske}-based design, as was the case for the η_{tt}-based endwall, when compared to the measured result over the full blade span, the predicted changes in the overall rotor total-total efficiency from the datum case were relatively similar, although in this instance, the increase in efficiency as a result of the endwall contouring was *over*-predicted (+0.29%). Again similar to the previous case, while a small increase (+0.31%) in the overall mass-averaged rotor exit relative total pressure loss coefficient was predicted as a result of the introduction of the C_{ske}-based endwall contours. The experimental characterisation of the contoured rotor showed a small decrease in the overall relative total pressure loss coefficient (−0.12%). Once again, as was the case for the η_{tt}-based endwall, for the remainder of the quantities assessed at the rotor exit, the measured changes in each of these quantities were significantly smaller than those predicted during the optimization procedure, apart from once again the design efficacy, whose actual improvement was significantly larger than that predicted for the design (+2.27% c.f. +0.54%).

$C_{ske,1} + \beta_{dev,0.7} - based$

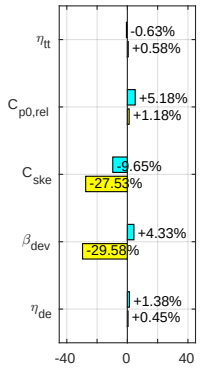

In contrast to the η_{tt}- and C_{ske}-based designs as well as the predicted results of the design routine, when calculated at the rotor exit plane, the $C_{ske,1} + \beta_{dev,0.7}$-based design resulted in a relatively significant decrease in the rotor total-total efficiency (-0.63%) rather than the increase ($+0.58\%$) which was predicted by the CFD. Again, in contrast to the previous cases, for the $C_{ske,1} + \beta_{dev,0.7}$-based endwall, the predicted increase in the rotor exit relative total pressure loss coefficient was corroborated by the experimental results, although for the present case the measured increase in the loss coefficient was significantly larger than was predicted by the design procedure ($+5.18\%$ vs $+1.18\%$). Similar to the η_{tt}- and C_{ske}-based designs, for the present case, the actual reductions in the mass-averaged coefficient of secondary kinetic energy were somewhat smaller than those predicted by the design routine (-9.65% c.f. -27.53%) and in contrast to the CFD predictions, the measured results actually resulted in an increase in the mass-averaged rotor exit flow angle deviation as opposed to the predicted decrease ($+4.33\%$ c.f. -29.58%). Finally, the rotor exit design efficacy (η_{de}) was relatively well predicted with both the experimental and numerical results indicating a improvement in the overall mass-averaged quantity, although consistent with the previous cases, the actual improvements were again larger than those predicted by the optimization routine.

$C_{p0,rel,1} + \beta_{dev,0.7} - based$

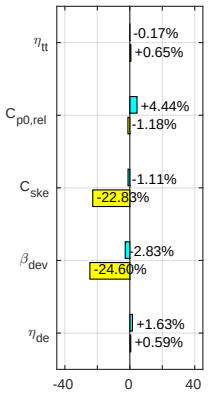

Apart from the rotor relative total pressure loss coefficient ($C_{p0,rel}$), testing of the $C_{p0,rel,1} + \beta_{dev,0.7}$-based endwall resulted in similar trends to the changes from the datum case noted for the $C_{ske,1} + \beta_{dev,0.7}$-based design. More specifically, as for the previous case, while the results of the numerical analysis for this endwall predicted an *increase* in the overall rotor total-total efficiency ($+0.65\%$), the flow traverses at the rotor exit showed a definite *decrease* in the overall rotor efficiency (-0.17%) as a result of these contours. Similar to the preceding designs, the predicted reductions of the mass-averaged coefficient of secondary kinetic energy, rotor exit relative flow angle from deviation and design efficacy were all confirmed by the experimental results, although once again, the actual reductions in each quantity were significantly smaller than their predicted counterparts (-22.83% c.f. -1.11% and -24.60% c.f. -2.83%) and the measured increase in the design efficacy, was again larger than the predicted result ($+1.63\%$ c.f. $+0.59\%$).

7.5.2 Downstream (X4)

η_{tt} − based

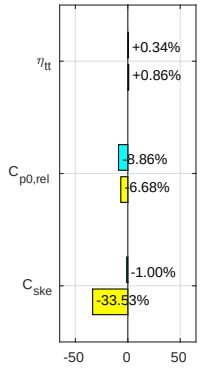

At the downstream plane, the predicted increase in the rotor total-total efficiency was corroborated by the experimental results, although the actual increase was significantly smaller than that predicted (+0.34% c.f. +0.86%). In contrast to the upstream result, at the mixed-out plane, the reductions in the rotor relative total pressure loss coefficient were well predicted, with the actual reductions compared to the datum case being slightly larger than the predicted result (−8.86% c.f. −6.68%). Finally, similar to the upstream result, the reductions in the mass-averaged coefficient of secondary kinetic energy as a result of the rotor endwall contouring (−33.53%) were significantly larger than those measured in the experimental test case (−1.00%).

C_{ske} − based

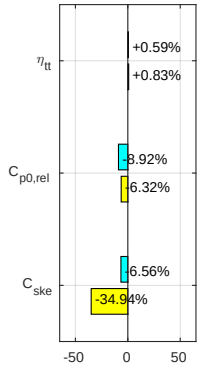

Again, as for the η_{tt}-based design, at the mixed-out measurement plane, the changes in the rotor total-total efficiency, and mass-averaged coefficient of relative total pressure loss were relatively well predicted by the numerical optimization scheme. Significantly, again, the reduction in the downstream loss coefficient was most reliably predicted (−8.92% c.f. −6.32%), followed by the predicted increase in rotor total-total efficiency (+0.59% c.f. 0.83%). Again, as for the previous design, although the correct trend in the change in the downstream coefficient of secondary kinetic energy was predicted, the overall magnitude of the change was poorly predicted (−6.56% c.f. −34.94%).

$C_{ske,1} + \beta_{dev,0.7} - based$

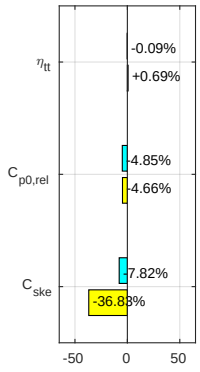

An analysis of the mass-averaged changes in the $C_{ske,1} + \beta_{dev,0.7}$-based design at the downstream measurement plane, showed that overall a small decrease in the rotor total-total efficiency was measured contrary to the moderate increase predicted by the CFD (+0.34% c.f. −0.09%). In contrast however, the measured results for both the relative total pressure loss coefficient and coefficient of secondary kinetic energy for this design were shown to be in direct agreement with the CFD predictions, similar to those results discussed already for the η_{tt}- and C_{ske}-based designs, with changes to the downstream relative total pressure loss coefficient ($C_{p0,rel}$) being extremely well predicted (−4.85% c.f. −4.66%), while - as was the case for the preceding cases - the reduction mass-averaged mixed-out coefficient of secondary kinetic energy (C_{ske}) were significantly over-predicted by the CFD (although an overall reduction in the quantity was measured) (−36.88% c.f. −7.82%).

$C_{p0,rel,1} + \beta_{dev,0.7} - based$

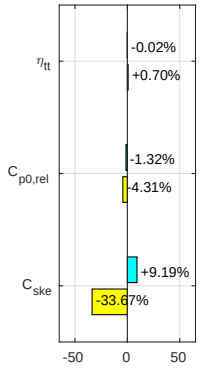

Finally, for the $C_{p0,rel,1} + \beta_{dev,0.7}$-based design, in terms of the rotor efficiency, while a significant increase in the efficiency was predicted for this design, as was the case for the rotor exit, overall, a small decrease in the actual efficiency was measured (+0.70% c.f. −0.02%). Further to this, while again both the CFD as well as experimental results indicated decreases in the mass-averaged loss coefficient at the downstream plane, the measured reductions in the present case were smaller than those predicted and the agreement between the predicted and actual results were not as similar as found for the preceding cases (−4.31% c.f. −1.32%). Finally, while the agreement between the predicted and measured results for the coefficient of secondary kinetic energy at the mixed-out plane for all of the previous designs was not particularly good, agreement in the trends associated with the coefficient was achieved. In the present case however, while similar to all the previous cases, a large reduction in the mass-averaged coefficient of secondary kinetic energy was predicted (−33.67%), the physical testing of the endwall indicated a fairly substantial *increase* in the overall secondary kinetic energy coefficient (+9.19%) in comparison to the annular case.

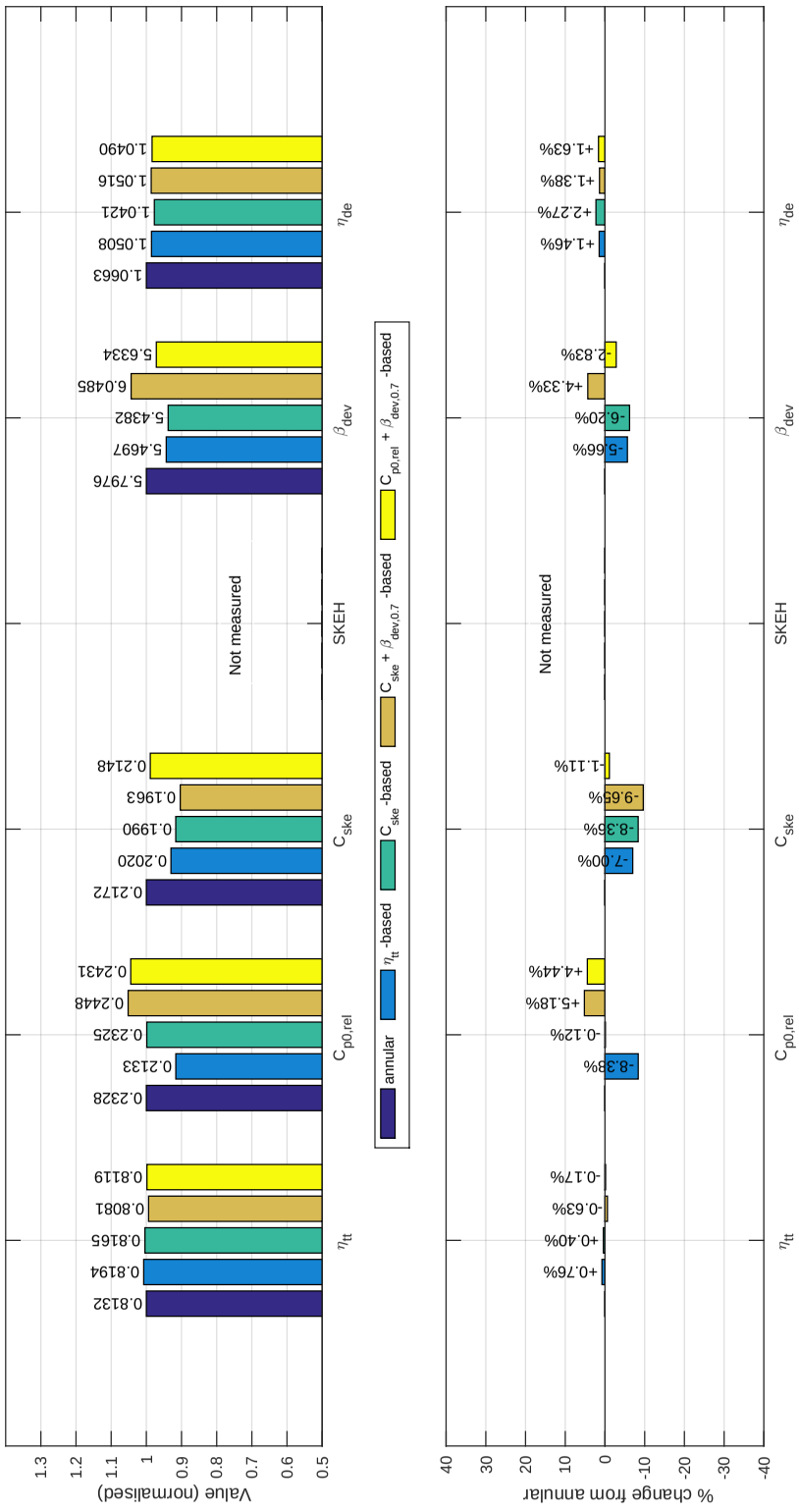

Fig. 7.23: Summary of mass-averaged experimental results at the rotor exit (X3) measurement plane

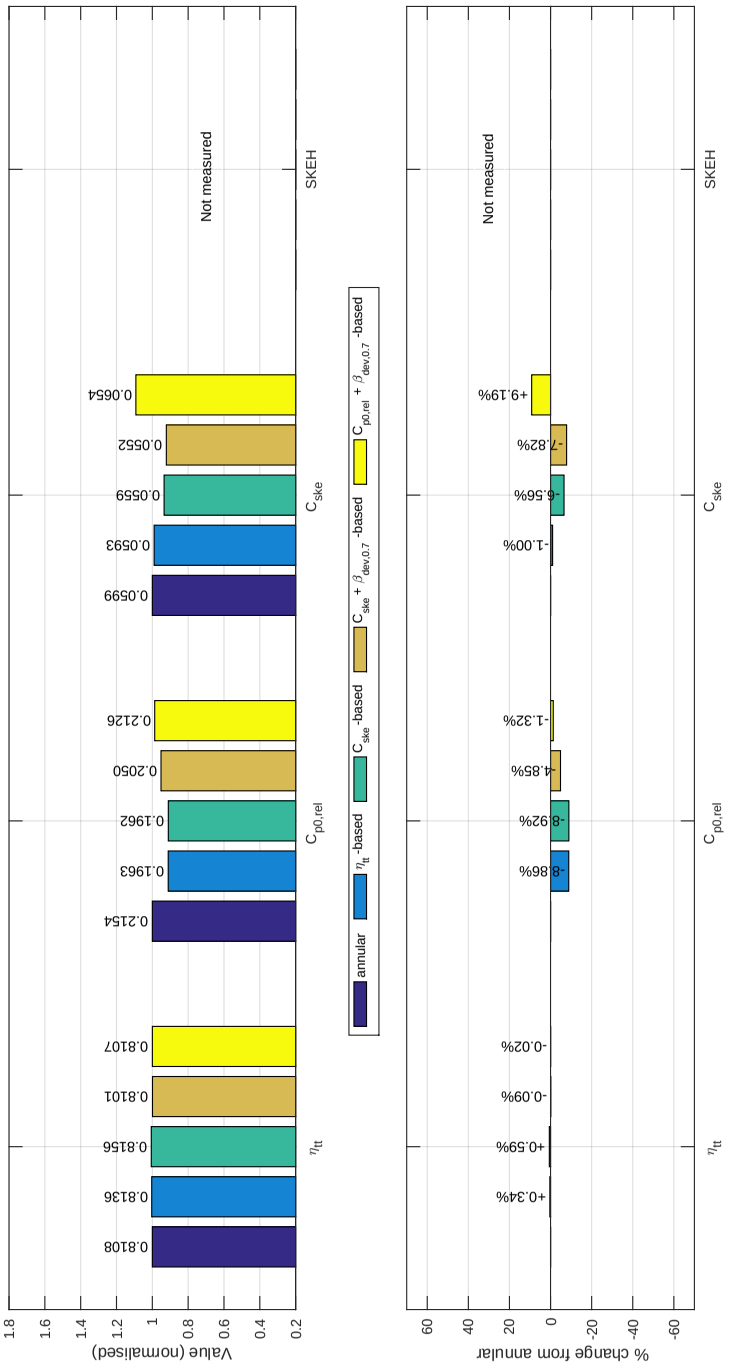

Fig. 7.24: Summary of mass-averaged experimental results at the downstream (X4) measurement plane

7.6 Circumferentially-averaged experimental results

As was done for the CFD results, the circumferentially-averaged experimental results for each quantity at the rotor exit (X3) and downstream (X4) measurement planes are now presented. In each case, and where applicable, the design as well as corresponding CFD profiles are included.

Line	Marker	Description
———	none	Design
———	○	Experimental
———	◇	CFD

Table 7.6: Plot legend - Experimental vs CFD circumferentially-averaged results

7.6.1 Rotor exit (X3)

The spanwise profiles of each of the rotor exit quantities are shown in Figs. 7.25 to 7.30. For each case and metric, the experimental results are presented alongside their corresponding CFD predictions for comparative purposes. However, unlike the computational results, because 2-dimensional data was not available behind the rotor, only the spanwise profiles are presented.

Relative flow (β) / flow deviation (β_{dev}) angles

In the interests of brevity, the rotor exit experimental profiles of relative flow and flow deviation from design angles are discussed together and presented in Figs. 7.25a - 7.26e. In general, the CFD predictions complemented the experimental results reasonably well, although the following overall characteristics were noticeable:-

- The largest discrepancies were noted in the tip region, where the underturning was consistently underpredicted by the CFD. In contrast, the smaller overturning peak (located at $\sim 85\%$ span), was considerably better predicted, with the results for the annular and η_{tt}-based cases noted to be particularly accurate.
- Below this and through the midspan, a number of recurrent features were noticeable:-
  - the secondary underturning peak predicted for all the cases by the CFD (at $\sim 70\%$) span was consistently overpredicted in magnitude, while the location of this feature was located consistently closer to the midspan (at approximately $\sim 60\%$ span) in all the experimental cases. Further, as a result of the above, the region of constant turning predicted between $\sim 40 - 60\%$ span for all cases was considerably reduced in length for all the experimental results, with the exception of the annular case, for which this region appeared to be particularly well predicted.
- Below the midspan and for the annular case, both the under- as well as overturning magnitudes immediately adjacent to the endwall, were well predicted by the CFD, although the magnitude of the overturning peak at $\sim 22\%$ span was again overpredicted by the CFD.

- Further to this and for the same region, for the contoured cases, the reductions in the underturning induced by the passage vortex (as a result of the endwall contouring), were again overpredicted while for most cases, although the locations of this peak were reasonable well predicted. Finally, for all cases except the $C_{p0,rel,1} + \beta_{dev,0.7}$-based design, the maximum overturning close to the endwall (at $\sim 5\%$ span) was over estimated.

In terms of the specific endwall results then, for the η_{tt}- & C_{ske}-based designs (Figs. 7.25b, 7.25c), both the CFD as well as the experimental results, showed a high degree of similarity to one another, with the only noticeable differences between the profiles noted at approximately $\sim 10\%$ span, where a small inflection point in the relative flow angle was noticeable for the η_{tt}-based case and was not for the C_{ske}-based design. Further, in both cases, the magnitude of the overturning immediately adjacent to the endwall surface was overpredicted ($\sim 4.5°$) by the CFD in comparison to the measured results.

For the $C_{ske,1} + \beta_{dev,0.7}$- & $C_{p0,rel,1} + \beta_{dev,0.7}$-based cases (Figs. 7.25d, 7.25e), while for both cases a clear point of inflection was predicted in the rotor exit flow angle profiles by the CFD (at approximately $\sim 20\%$ span), this feature was considerably less discernible in the experimental results for the $C_{p0,rel,1} + \beta_{dev,0.7}$-based case, and absent for the $C_{ske,1} + \beta_{dev,0.7}$-based results . Finally, in contrast to the η_{tt}- & C_{ske}-based results, for both compound designs, immediately adjacent to the endwall, the flow angles were much more accurately reproduced.

Coefficient of secondary kinetic energy (C_{ske})

The experimental rotor exit profiles of C_{ske} are shown in Figs. 7.27a - 7.27e. Once again:-

- The largest discrepancies between the predicted and measured rotor exit C_{ske} profiles occurred in the tip region, with the CFD results noted to be significantly smaller in magnitude in comparison to the measured results, while the local C_{ske} peak (corresponding to the previously discussed underturning peak (located at $\sim 70\%$ span)) was again not obvious in the experimental C_{ske} profiles.
- Below the midspan, the local C_{ske} peak predicted by the CFD and associated with the underturning of the passage vortex ($\sim 37\%$ span), was again seen to feature less prominently in the experimental profiles, although below this, the region of elevated C_{ske}, resulting from the overturning associated with the secondary flow was well captured.

Further to the above, while for all cases, the circumferentially-averaged magnitude of the C_{ske} in the vicinity of the endwall was reduced as a result of the endwall contouring, the degree to which this quantity was confined to the endwall adjacent region was significantly overpredicted by the CFD. Finally, as was the case for the previous quantities, while the inflection point predicted by the CFD for the $C_{ske,1} + \beta_{dev,0.7}$-based design was barely discernible in the experimental results, this feature was again significantly more distinguishable in the $C_{p0,rel,1} + \beta_{dev,0.7}$-based experimental profile.

Loss ($C_{p0,rel}$)

The rotor exit loss profiles for the experimental subset are shown in Figs. 7.28a - 7.28e. In general, the experimental profiles of the loss coefficient showed a great deal more variation between each design, than was the case for the metrics discussed thus far.

In general:-

- The predictions of the rotor exit loss for the annular case was reasonably good (especially below $\sim 60\%$ span), although once again, as was the case for the previous metrics, agreement in the immediate vicinity of the endwall, as well as in the tip region, was poor.
- Once again, overall the profiles for the η_{tt}- & C_{ske}-based designs (Figs. 7.28b, 7.28c) were largely identical to one another, although some differences between the designs were noticeable between $20-30\%$ span, where although the peak loss magnitudes were similar, the overall spanwise extent of the region of elevated loss was increased for the C_{ske}-based case. As indicated, above and below this region, the loss profiles for each design were effectively identical.
- Similarly, while above the midspan as well as immediately adjacent to the endwall surface, the $C_{ske,1} + \beta_{dev,0.7}$- & $C_{p0,rel,1} + \beta_{dev,0.7}$-based designs (Figs. 7.28d, 7.28e) showed a great deal of similarity to one another, the details of the loss profiles between $\sim 10-40\%$ again showed some differences. In particular:-
  - For the $C_{ske,1} + \beta_{dev,0.7}$-based design, in contrast to the CFD predictions in which a general reduction of the loss was predicted in this region, as well as the formation of a local loss core close to the endwall, the experimental results show a single large core (with a peak magnitude of ~ 0.2) located at approximately $\sim 25\%$ span.
  - Similarly, for the $C_{p0,rel,1} + \beta_{dev,0.7}$-based design, while again in contrast to the CFD predictions, in which a general abatement of the loss between $\sim 10-40\%$ span was predicted, instead a reasonably prominent (but more localised in comparison to the $C_{ske,1} + \beta_{dev,0.7}$ case) loss peak was noted.

Efficiency (η_{tt})

The rotor exit experimental efficiency profiles (Figs. 7.29a - 7.29e) showed similar trends to those discussed for the rotor exit loss profiles above, with a similar degree of accuracy when compared to the predicted results:-

- For the annular case (Fig. 7.29a), the general form of the experimental profile matched that predicted by the design routine, although while the efficiency magnitudes in the tip region were overpredicted, for the remainder of the span, the efficiencies were consistently underpredicted. Further to this, as was the case for the rotor exit loss, immediately adjacent to the casing and endwall surfaces, the predicted trend in the efficiencies were reversed to those measured.
- Again, while both the experimental and CFD results for the η_{tt} & C_{ske}-based (Fig. 7.29b - 7.29c) cases were similar to one another, the large increase in spanwise efficiency predicted for both cases in the region affected by the passage vortex were not evident in the measured results. Further to this :-

  - While the efficiency improvements in the vicinity of the passage vortex (i.e. $\sim 20\%$ span) were similar for both designs, immediately adjacent to the endwall, the C_{ske}-based design resulted in an appreciable reduction in the efficiency.

- Further to this, and consistent with the changes to the rotor exit loss profiles for the same endwall reported above, the region of reduced efficiency for the $C_{ske,1} + \beta_{dev,0.7}$-based design (Fig. 7.29d) between $\sim 10 - 40\%$ span was increased in its peak intensity, as well as spanwise extent.
- Similarly, in the same region, the rotor exit efficiency profile for the $C_{p0,rel,1} + \beta_{dev,0.7}$-based endwall (Fig. 7.29e) was seen to display a slight decrease in the circumferentially-averaged efficiency magnitudes but over a smaller spanwise locality. This was consistent with the smaller spanwise extent of increased loss for the same design discussed above.

Finally, for both of the latter designs, no significant changes to the circumferentially-averaged efficiencies were noted over the remainder of the span.

Design efficacy (η_{de})

Finally, the rotor exit circumferentially-averaged design efficacy (η_{de}) profiles for the experimental subset are shown in Figs. 7.30a - 7.30e.

As expected, the spanwise profiles of η_{de} displayed a similar degree of accuracy to those already discussed for the relative flow (β) and flow deviation angle (β_{dev}). As such, in the blade tip region, the discrepancies between the predicted and measured η_{de} profiles were large, while through the midspan, a reasonable degree of agreement was acheived. More specifically then, for each endwall:-

- For the annular case (Fig. 7.30a), apart from the tip gap, the overall η_{de} was predicted well, including (as was for the rotor exit β and β_{dev}) within the region between the endwall and midspan.
- Once again, for the η_{tt}- & C_{ske}-based designs (Figs. 7.30b, 7.30c), the experimental profiles showed a high degree of similarity to one another, although the inflection point at approximately $\sim 10\%$ span was more pronounced for the η_{tt}-based design. In comparison to the predicted profiles:-
  - The local η_{de} peaks located at $\sim 30\%$ span were reduced both in spanwise location, as well as magnitude. Below this point and closer to the endwall, for both cases, the agreement was poorer.
- Similary, for the $C_{ske,1} + \beta_{dev,0.7}$- & $C_{p0,rel,1} + \beta_{dev,0.7}$ cases, while in the tip gap, the CFD failed to predict the correct magnitudes of η_{de}, above $\sim 40\%$ span, the overal profile shapes were reasonably well predicted.
- Further to this, below the midspan, and for both designs, although the overall profile shapes were reasonably faithfully reproduced by the CFD, the peak η_{de} magnitudes at $\sim 35\%$ span were both underpredicted, while the additional secondary η_{de} peak predicted for the $C_{ske,1} + \beta_{dev,0.7}$-based design was not found in the experimental results.

- Once again, as was the case for the flow and deviation angles, while the inflection point predicted for the $C_{p0,rel,1} + \beta_{dev,0.7}$-based case at $\sim 20\%$ span was present, this feature was somewhat less well-defined in the experimental result.

7.6.2 Downstream (X4)

The circumferentially-averaged experimental profiles for each of the aforementioned quantities at the downstream (X4) measurement plane are shown in Figs. 7.31 to 7.34[3].

Relative flow angle (β)

Once again, overall, the relative flow angle (β) (Figs. 7.31a - 7.31e) at the 'mixed-out' measurement plane was generally well predicted by the CFD, although as was the case at the rotor exit, in general, the magnitudes of the various over- and underturning peaks were overpredicted. Further, as was predicted, while the peak mixed-out magnitudes flow angles were smaller than those at the rotor exit, in general, the actual reductions were somewhat smaller than predicted by the CFD. Again, and as was predicted, the location for the underturning peak associated with the secondary flow was seen to migrate closer to the midspan, although in contrast to the CFD predictions, the peak of overturned fluid close to the endwall was actually seen to migrate closer to the endwall surface in comparison to its rotor exit position.

Coefficient of secondary kinetic energy (C_{ske})

The overall characteristic profiles of the 'mixed-out' coefficient of secondary kinetic energy (C_{ske}) at the downstream measurement plane (Figs. 7.32a - 7.32e) were once again generally well predicted by the CFD with the overall increases in C_{ske} through the midspan as well as the migration of the circumferentially-averaged peak value away from the endwall surface (as predicted by the CFD) and reductions in the tip gap faithfully validated. However, because of the greater radial extent of the region of elevated C_{ske} adjacent to the endwall surface measured at the rotor exit (in comparison to that predicted by the CFD), the actual spanwise migration of the measured wall-adjacent C_{ske} peak was somewhat less distinct than was originally predicted. Finally, as was the case for the 'mixed-out' relative flow angle above, for the $C_{p0,rel,1} + \beta_{dev,0.7}$-based design, the detailed structure of the downstream C_{ske} profile was not well captured.

Loss ($C_{p0,rel}$)

The mixed-out rotor loss profiles are shown in Figs. 7.33a - 7.33e. Again, as was the case at the rotor exit, the agreement between the predicted and measured loss profiles in the tip gap region were poor, although this did improve to some degree closer to the midspan. Close to the endwall, the agreement was again seen to be poorer than expected, where for the majority of the

[3] Once again, as was done for the mass-averaged results (and for the same reasons), at the downstream plane (X4), the β_{dev} and η_{de} plots are not shown

cases, the CFD was generally found to underpredict the loss. This was particularly noticeable for the η_{tt}-, C_{ske}-based & $C_{ske,1} + \beta_{dev,0.7}$-based cases, with the actual loss for the latter case considerably larger than was predicted by the CFD. In contrast however, this was not the case for the $C_{p0,rel,1} + \beta_{dev,0.7}$-based design, where the predicted magnitudes of the circumferentially-averaged loss coefficient was substantially better.

Efficiency (η_{tt})

Finally, the comparisons between the mixed-out predicted and experimental efficiencies are shown in Figs. 7.34a - 7.34e. In comparison to the remainder of the designs, the mixed-out predictions of the rotor efficiency for the η_{tt}- & C_{ske}-based cases were significantly better. Although above the midspan, the remaining cases (i.e. the annular, $C_{ske,1} + \beta_{dev,0.7}$- & $C_{p0,rel,1} + \beta_{dev,0.7}$-based designs) did show a reasonable degree of similarity with their experimental counterparts, in general, below $\sim$ 40% span, the agreement was poor. More specifically, although in all cases, the predicted efficiencies were consistently lower than those actually measured, for the annular case, this discrepancy was significantly larger. Further while for the $C_{ske,1} + \beta_{dev,0.7}$-based design, while the CFD was seen to predict and overall increase in the efficiency, the experiment showed a clear decrease in the rotor performance in this region. Although less obvious, a similar situation was noted for the $C_{p0,rel,1} + \beta_{dev,0.7}$-based design, with the CFD predicting a small but distinct improvement in the efficiency (centred at $\sim$ 20% span), while the measured profile showed the small but clear decrease in the efficiency in this region.

7.7 Summary: Experimental results

Once again, similar to what was done for the various endwall designs, the predictions for each of the metrics included in the experimental subset could also be aggregated into various groups, however in this case, the results were once again considered on a *per metric* basis rather than *per design* basis.

In general, the overall mass-averaged, as well as spanwise trends for each of the metrics were well predicted. In particular, this included both the secondary kinetic energy (C_{ske}) as well as flow deviation (β_{dev}) metrics, although for both cases, the changes to these metrics were overpredicted both in terms of the mass- as well as circumferentially-averaged results. In addition, at the rotor exit, the changes to the design efficacies (η_{de}) of each rotor were again well predicted by the CFD, although, in contrast to the previous metrics, these changes were generally seen to be underpredicted in both the overall as well as spanwise change in comparison to the experimental results.

Further, the mass-averaged rotor efficiencies (η_{tt}) were again generally well predicted, although at the rotor exit specifically, the accuracy of these results were seen to depend heavily on the accurate prediction of the local loss coefficient, which in general was not well predicted. This situation was illustrated clearly by the poor predictions of rotor efficiency for both the $C_{ske,1} + \beta_{dev,0.7}$- & $C_{p0,rel,1} + \beta_{dev,0.7}$-cases at the rotor exit, for which the actual mass-averaged loss coefficients were not well predicted. At the downstream measurement plane however, the agreement between the predicted and measured 'mixed-out' losses was significantly better, leading to significantly better predictions of the rotor efficiency at this measurement location as well.

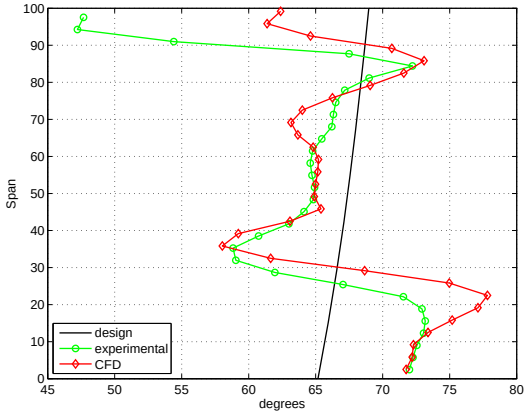

(a) annular

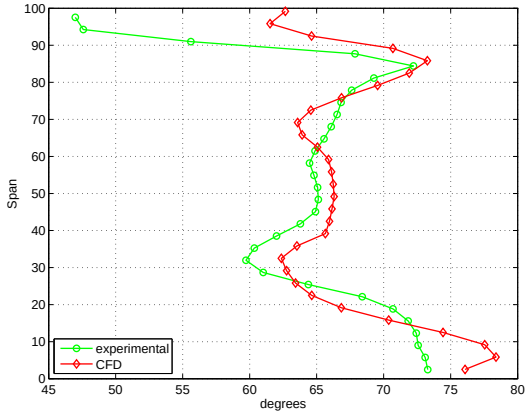

(b) $\eta_{tt} - based$

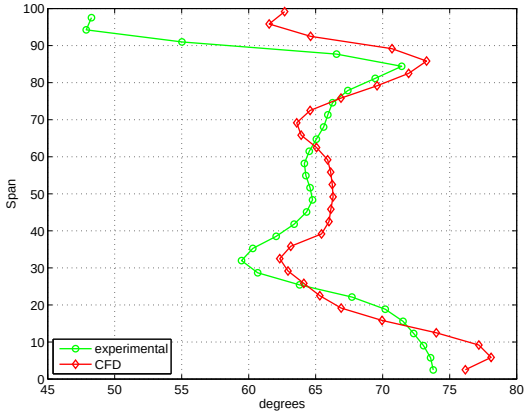

(c) $C_{ske-based}$

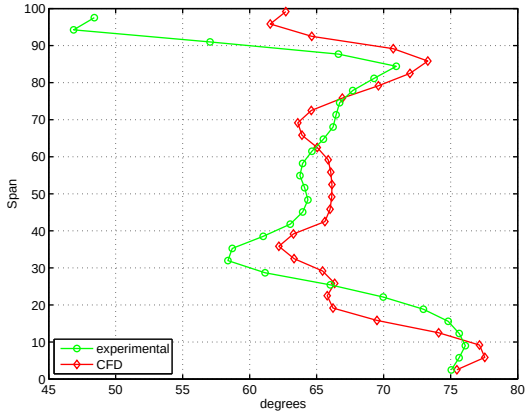

(d) $C_{ske,1} + \beta_{dev,0.7} - based$

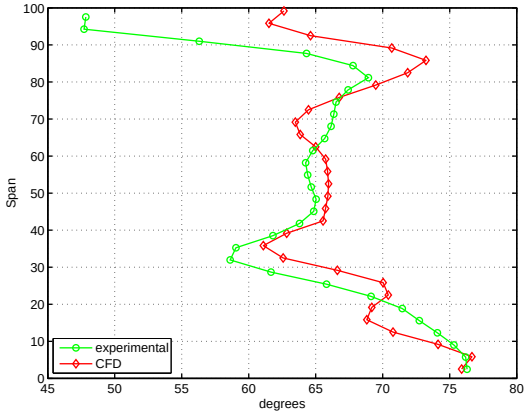

(e) $C_{p0,rel} + \beta_{dev,0.7} - based$

Fig. 7.25: Experimental relative flow angle (β_3) at rotor exit (X3)

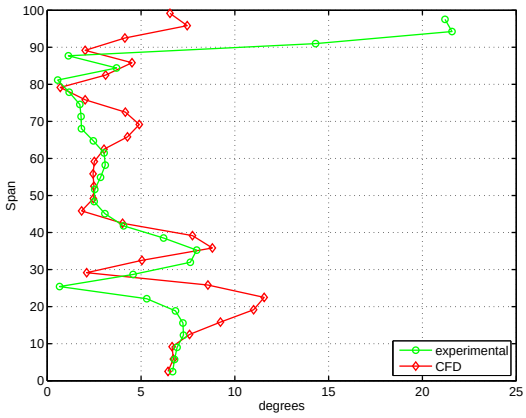

(a) annular

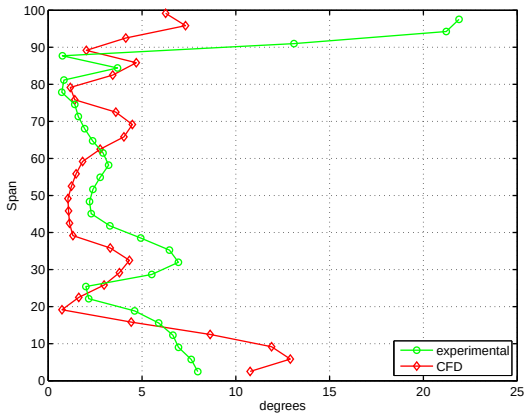

(b) $\eta_{tt} - based$

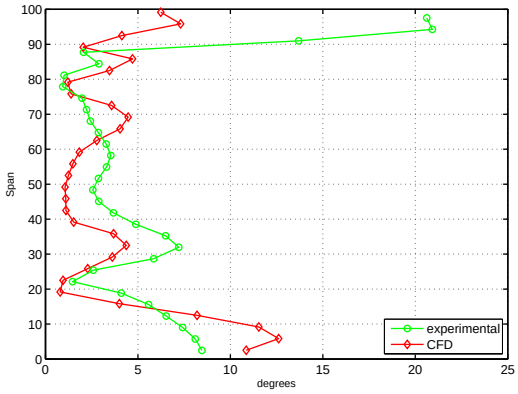

(c) $C_{ske-based}$

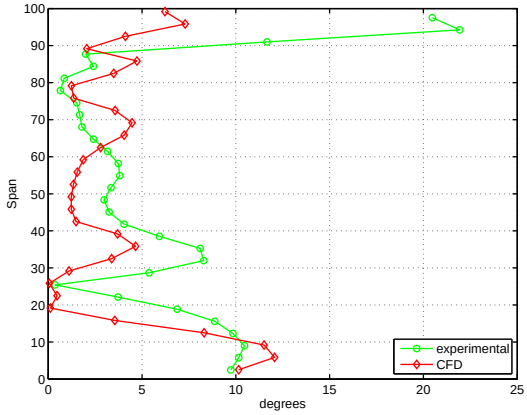

(d) $C_{ske,1} + \beta_{dev,0.7} - based$

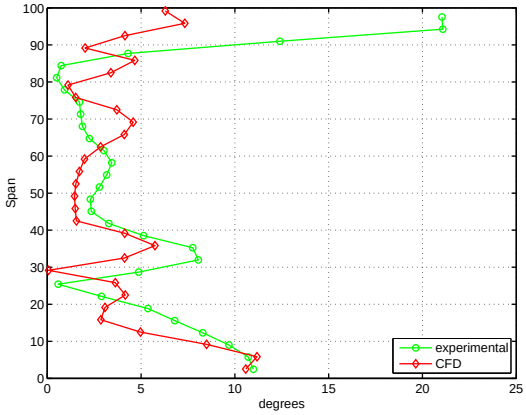

(e) $C_{p0,rel} + \beta_{dev,0.7} - based$

Fig. 7.26: Experimental relative flow angle deviation from design ($\beta_{dev,3}$) at rotor exit (X3)

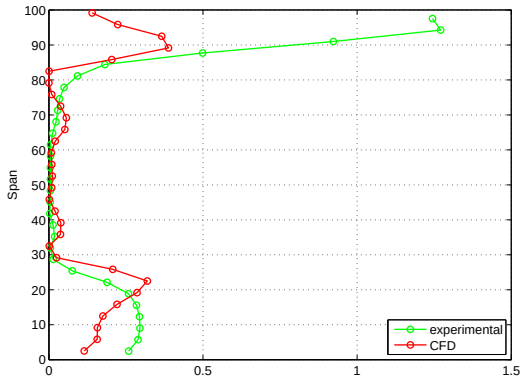

(a) annular

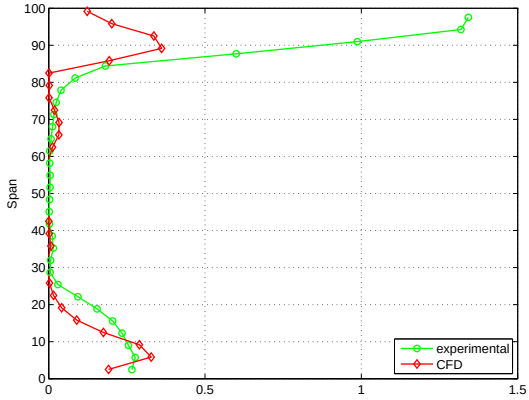

(b) $\eta_{tt} - based$

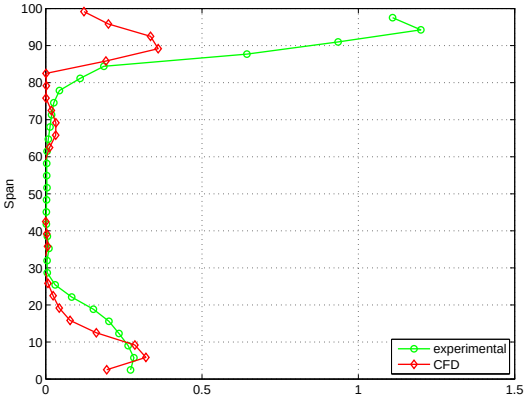

(c) $C_{ske-based}$

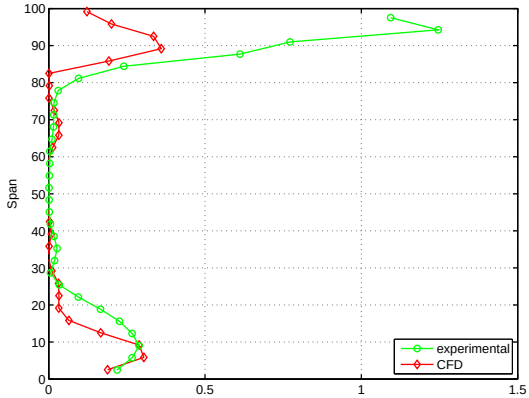

(d) $C_{ske,1} + \beta_{dev,0.7} - based$

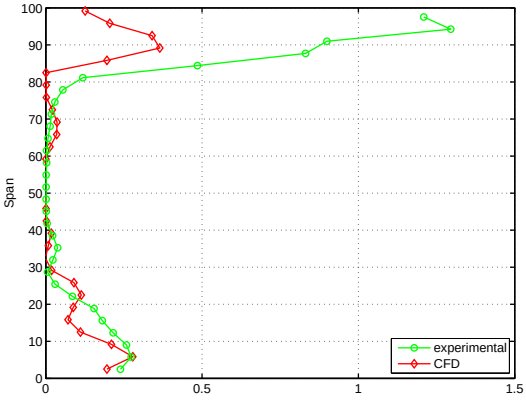

(e) $C_{p0,rel} + \beta_{dev,0.7} - based$

Fig. 7.27: Experimental coefficient of secondary kinetic energy ($C_{ske,3}$) at rotor exit (X3)

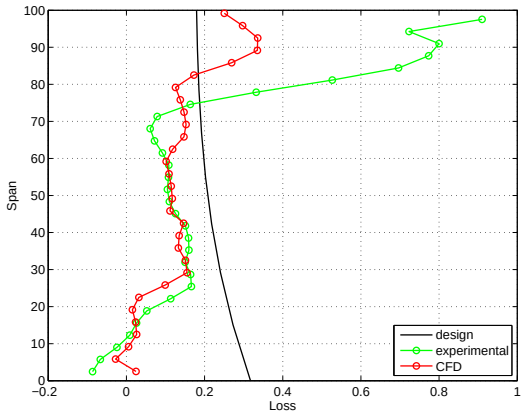

(a) annular

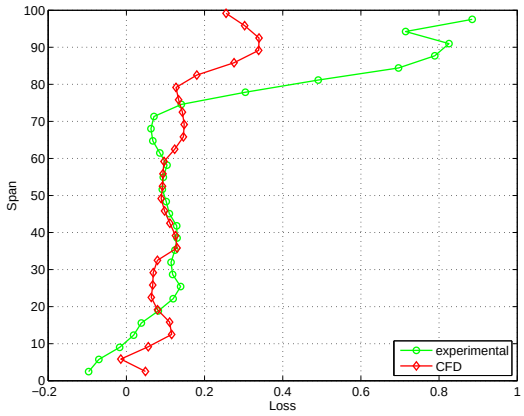

(b) $\eta_{tt} - based$

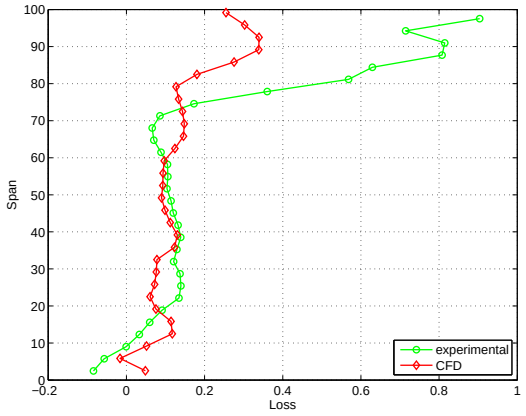

(c) $C_{ske-based}$

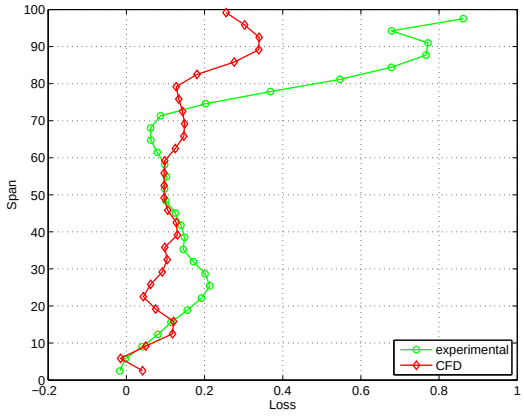

(d) $C_{ske,1} + \beta_{dev,0.7} - based$

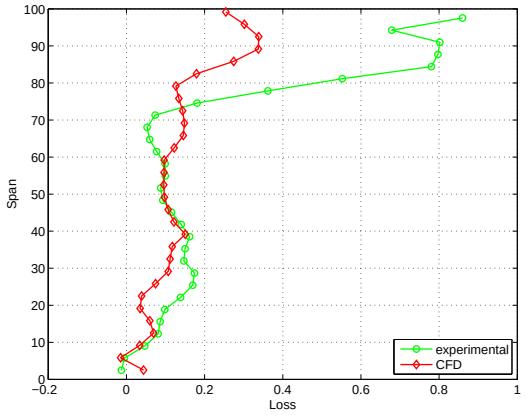

(e) $C_{p0,rel} + \beta_{dev,0.7} - based$

Fig. 7.28: Experimental coefficient of total relative pressure loss ($C_{p0,rel,3}$) at rotor exit (X3)

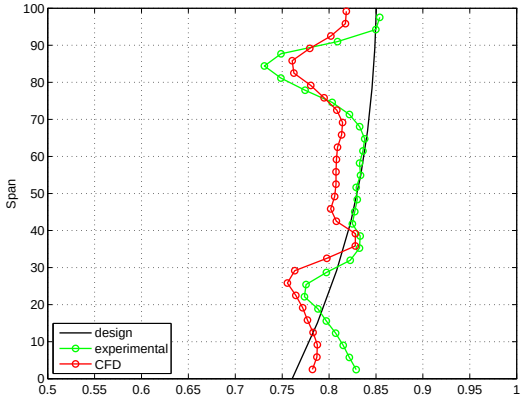

(a) annular

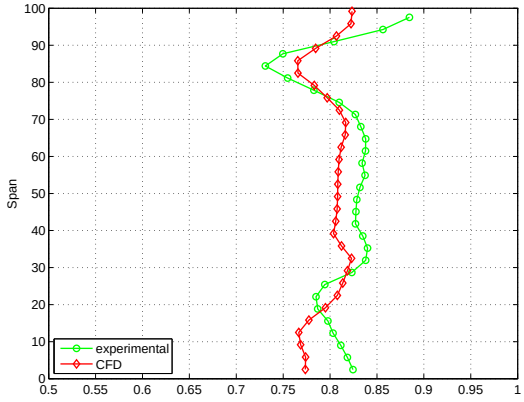

(b) $\eta_{tt} - based$

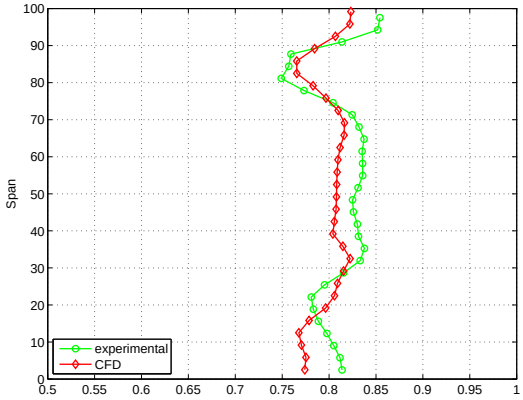

(c) $C_{ske-based}$

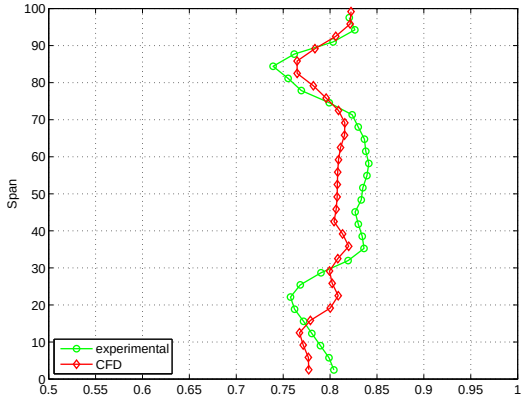

(d) $C_{ske,1} + \beta_{dev,0.7} - based$

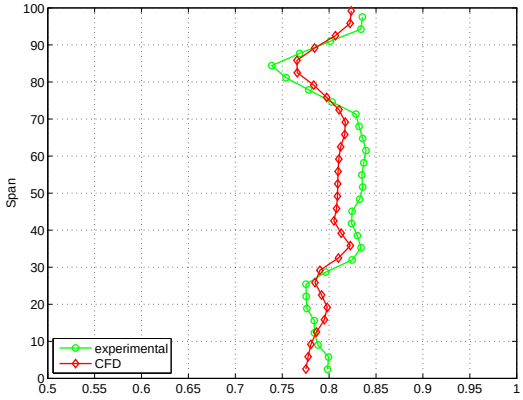

(e) $C_{p0,rel} + \beta_{dev,0.7} - based$

Fig. 7.29: Experimental rotor total-total efficiency ($\eta_{tt,3}$) at rotor exit (X3)

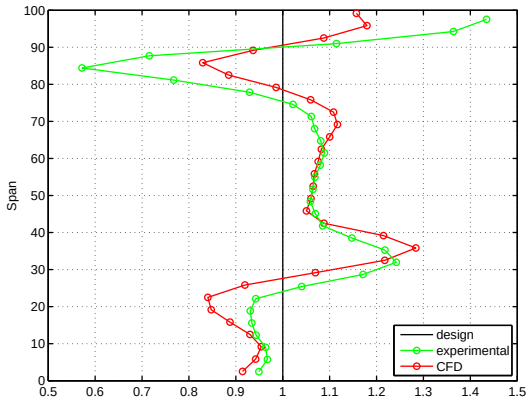

(a) annular

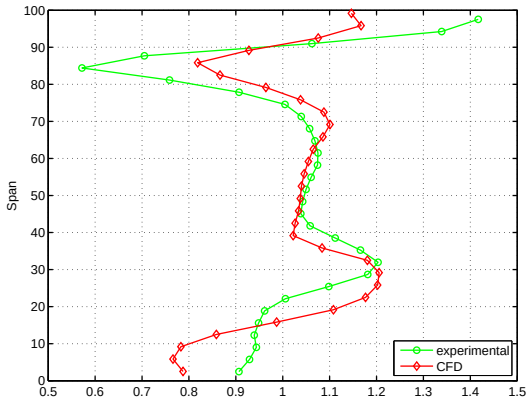

(b) $\eta_{tt} - based$

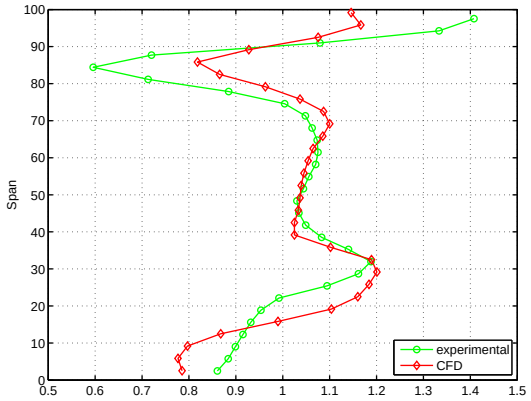

(c) $C_{ske-based}$

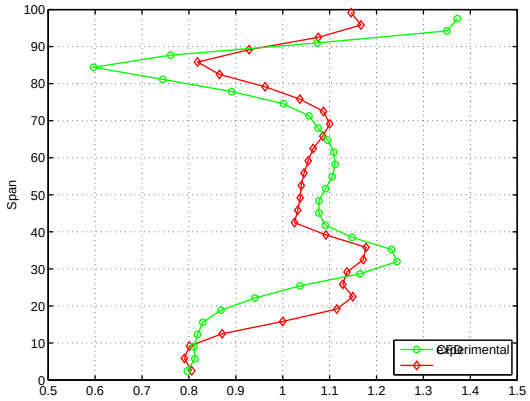

(d) $C_{ske,1} + \beta_{dev,0.7} - based$

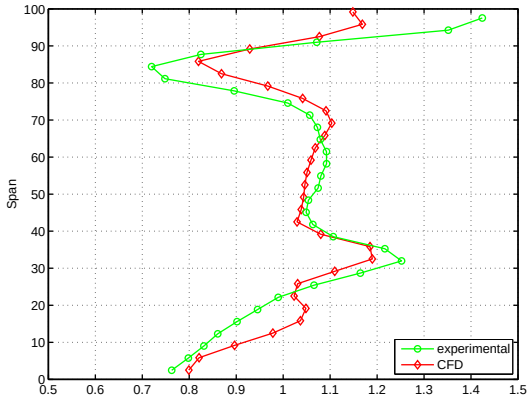

(e) $C_{p0,rel} + \beta_{dev,0.7} - based$

Fig. 7.30: Experimental design efficacy ($\eta_{de,3}$) at rotor exit (X3)

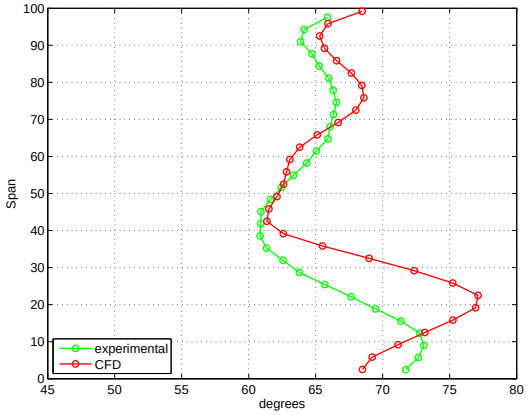

(a) annular

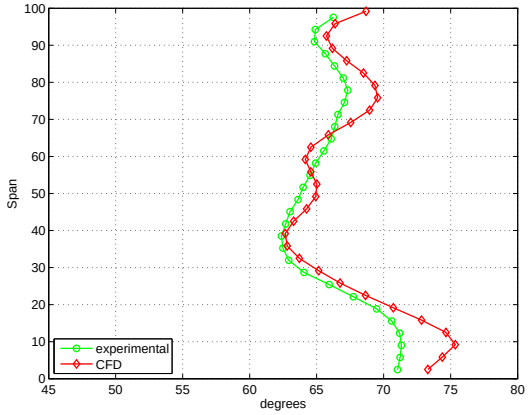

(b) $\eta_{tt} - based$

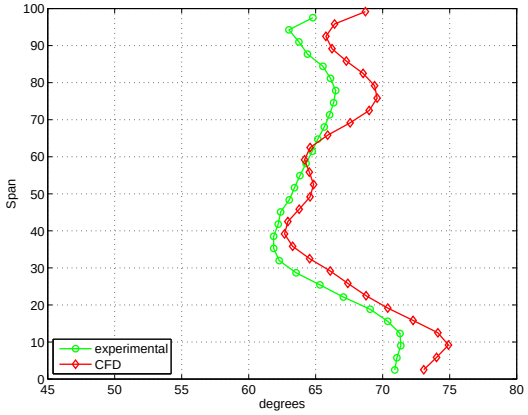

(c) $C_{ske-based}$

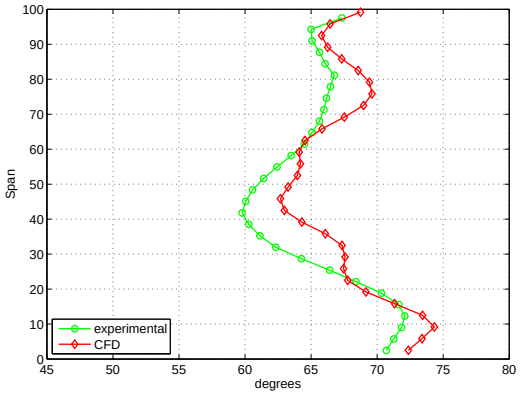

(d) $C_{ske,1} + \beta_{dev,0.7} - based$

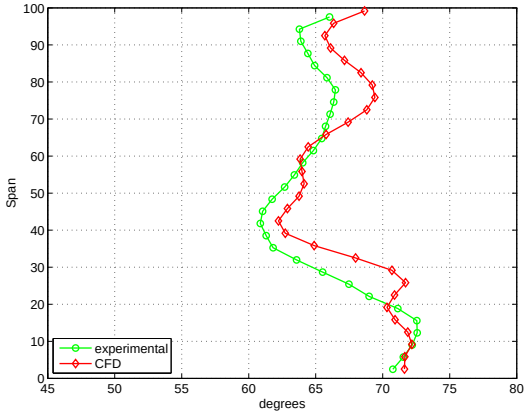

(e) $C_{p0,rel} + \beta_{dev,0.7} - based$

Fig. 7.31: Experimental relative flow angle (β_4) at downstream plane (X4)

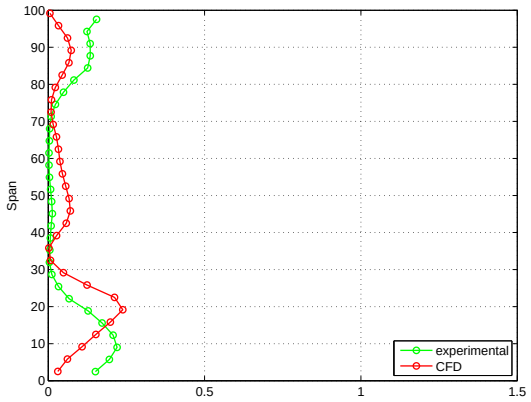

(a) annular

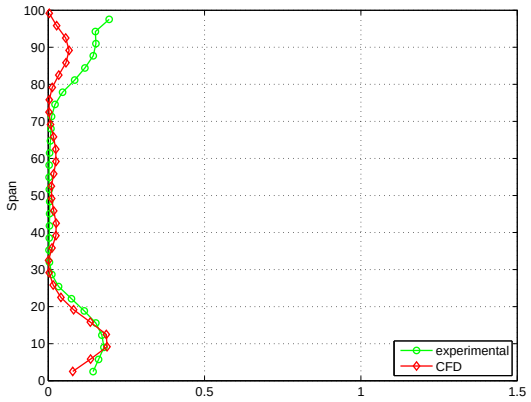

(b) $\eta_{tt} - based$

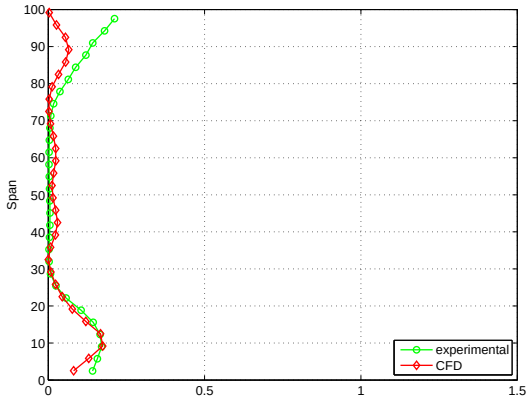

(c) $C_{ske-based}$

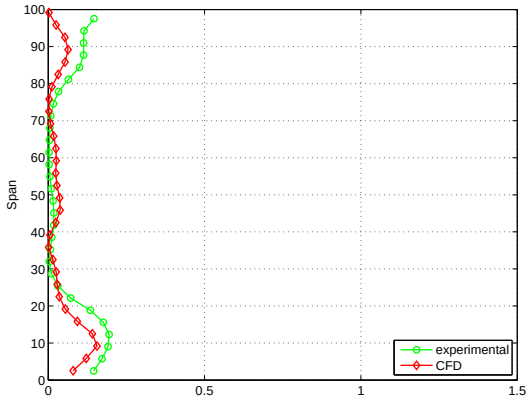

(d) $C_{ske,1} + \beta_{dev,0.7} - based$

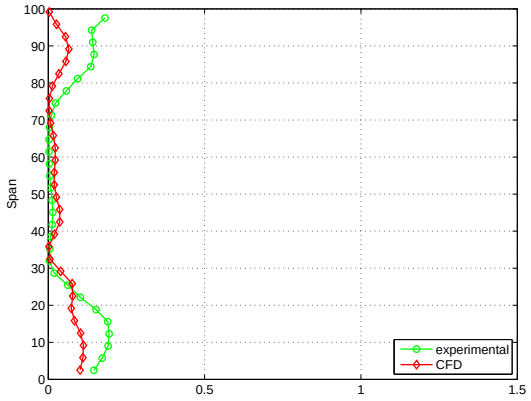

(e) $C_{p0,rel} + \beta_{dev,0.7} - based$

Fig. 7.32: Experimental coefficient of secondary kinetic energy ($C_{ske,4}$) at downstream plane (X4)

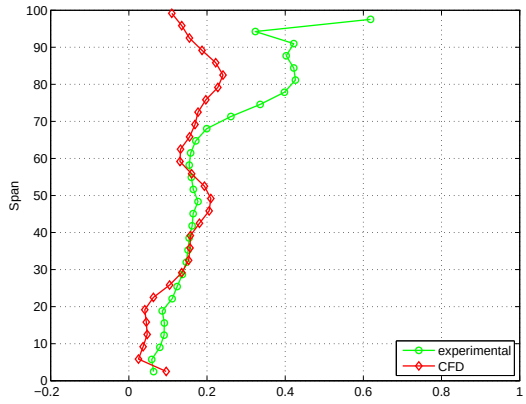

(a) annular

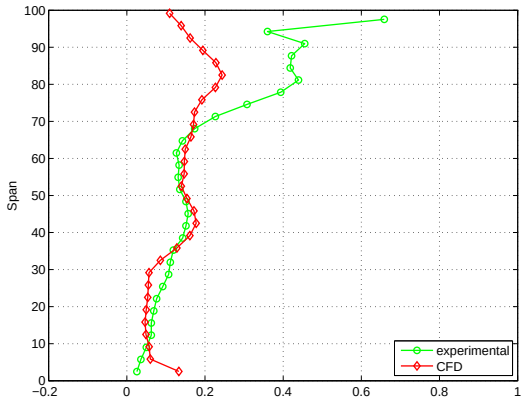

(b) $\eta_{tt} - based$

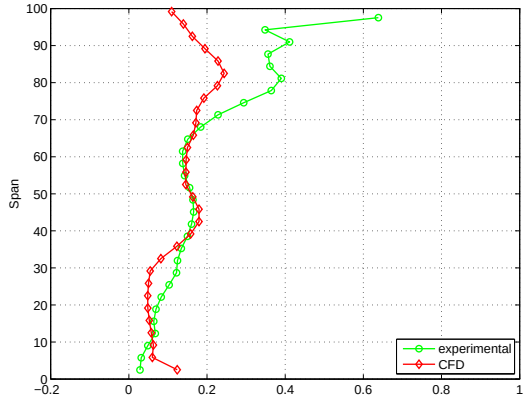

(c) $C_{ske-based}$

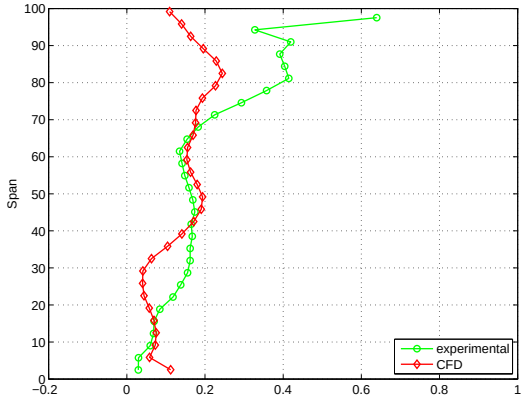

(d) $C_{ske,1} + \beta_{dev,0.7} - based$

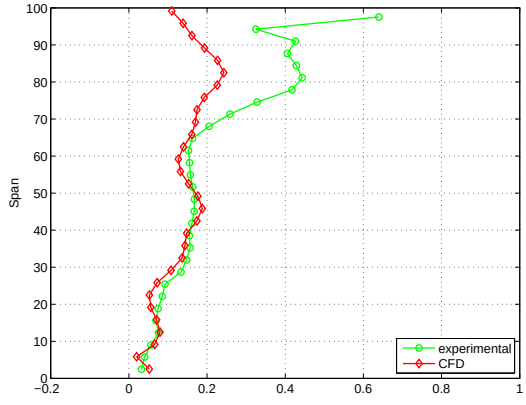

(e) $C_{p0,rel} + \beta_{dev,0.7} - based$

Fig. 7.33: Experimental coefficient of relative total pressure loss ($C_{p0,rel,4}$) at downstream plane (X4)

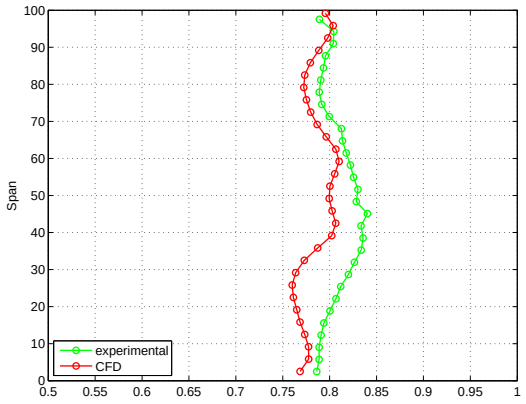

(a) annular

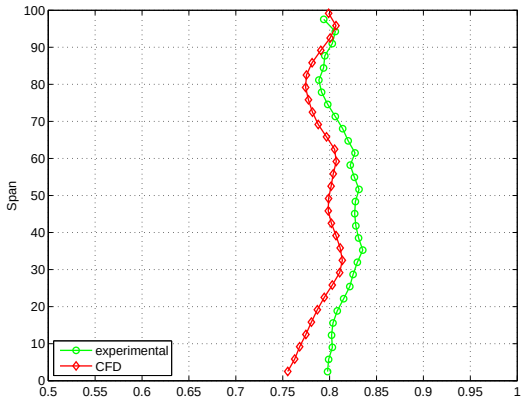

(b) $\eta_{tt} - based$

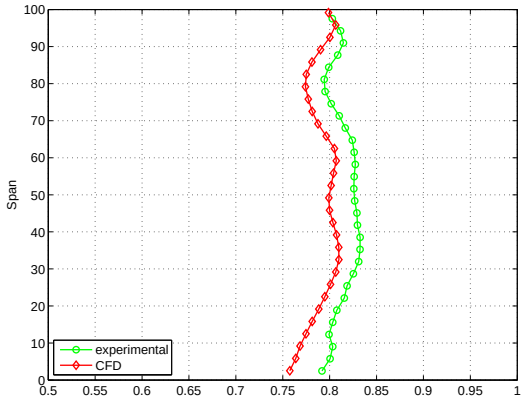

(c) $C_{ske-based}$

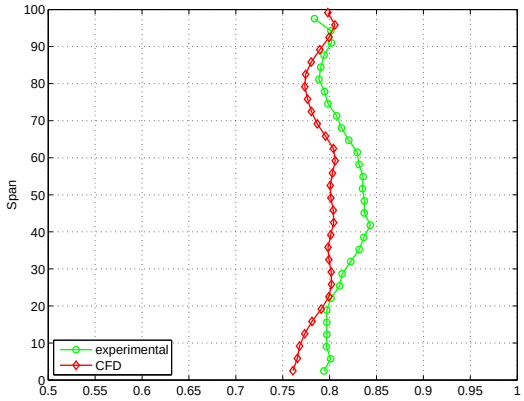

(d) $C_{ske,1} + \beta_{dev,0.7} - based$

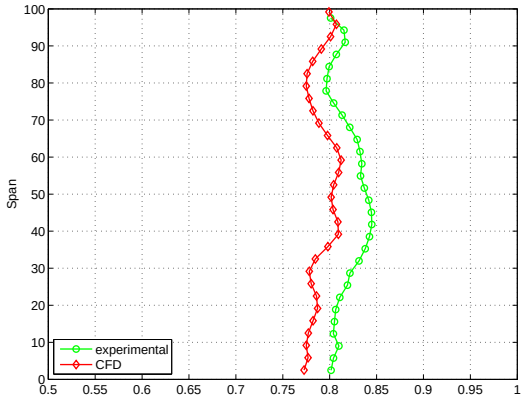

(e) $C_{p0,rel} + \beta_{dev,0.7} - based$

Fig. 7.34: Experimental rotor total-total efficiency ($\eta_{tt,4}$) at downstream plane (X4))

8

Discussion of Flow Results

In this Chapter, the results of the previous one are discussed in an attempt to provide qualitative explanations for the changes in the various flow metrics observed as a result of the introduction of each of the contoured endwall designs produced.

Firstly, the calculated and experimental torque output for the various designs, as well as changes in area as well as contributions to the overall rotor torque from the blade and endwall surfaces are discussed. Thereafter, the calculated static pressure distributions (presented as a static pressure coefficient, C_p) on the endwall (Fig. 8.3) and blade loading plots (Figs. 8.4 - 8.9) for each design are presented, whereafter the computed surface (oilflow) and 3-dimensional streamlines for each endwall (including the annular case) are presented (Figs. 8.13 - 8.19).

Finally, the evolution of the loss within and downstream of the blade passage (computed as the local entropy generation rate) as well as the mass-averaged rotor efficiencies, normalized rotor work output and isentropic pressure drop through the blade passage (which were used to calculated the rotor efficiencies), are presented.

8.1 Torque

8.1.1 Overall predicted and measured changes

The predicted and measured total rotor torque magnitudes for each endwall design are presented in Fig. 8.1.

The changes to the rotor torque output predicted by the CFD as a result of the introduction of the various endwall designs were small (~ 0.02 Nm), with only the $C_{p0,rel}$-, $SKEH$-, η_{de}- & $C_{p0,rel,1} + \beta_{dev,0.7}$-based cases predicted to result in non-negligible changes in the output. In each case, the rotor torque was predicted to increase as a result of the introduction of the endwall contours, with the greatest of these predicted for the $C_{p0,rel}$-based design.

In contrast, the experimental results for all of the endwalls included in the experimental subset showed reductions in the actual torque produced by the rotor, and although these were larger than the changes predicted by the CFD, these reductions were moderate, with the largest reduction measured for the C_{ske}-based design (-2.18%), and the smallest recorded for the η_{tt}-based (-0.89%) endwall. Of the two 'compound' designs included in the test set, the $C_{p0,rel,1} + \beta_{dev,0.7}$-based design resulted in the

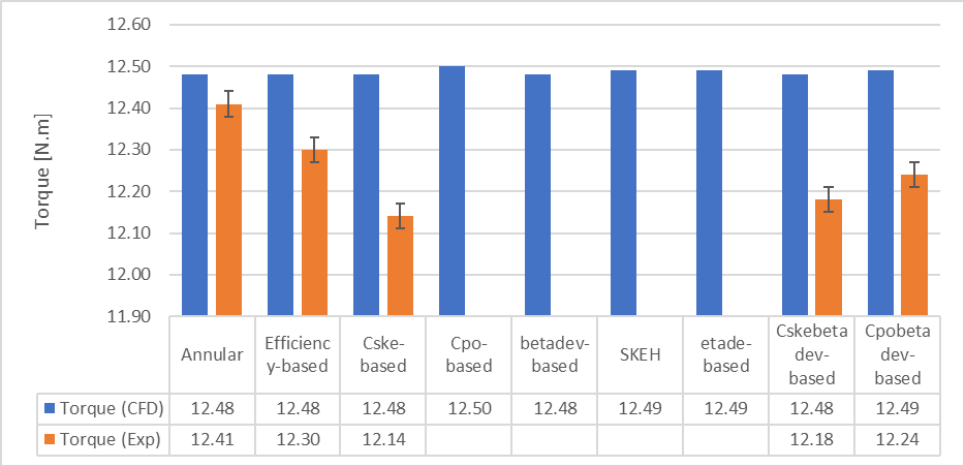

	Annular	Efficiency-based	Cske-based	Cpo-based	betadev-based	SKEH	etade-based	Cskebetadev-based	Cpobetadev-based
Torque (CFD)	12.48	12.48	12.48	12.50	12.48	12.49	12.49	12.48	12.49
Torque (Exp)	12.41	12.30	12.14					12.18	12.24

Fig. 8.1: Total predicted (CFD) & experimental rotor torque magnitudes ($error = \pm 0.03Nm$)

smaller reduction (-1.37%) than in its C_{ske}-based equivalent, which was slightly larger but still less than that measured for the C_{ske}-only based endwall (-1.85%).

8.1.2 Changes to blade / endwall areas and torque contributions

The individual contributions (as a result of both the pressure and viscous forces) to the overall rotor torque by the endwall and rotor suction surface, as well as the net torque generated per blade passage, are shown in Figs. 8.2a, 8.2b & 8.2c respectively. In addition, the total surface areas, as well as percentage changes in surface area of the suction, pressure and endwall surfaces are shown in Table 8.1.

While the measured changes in the rotor torque for those designs included in the experimental test set were considerably larger than predicted by the CFD, the origin of the predicted increases in torque predicted for the $C_{p0,rel}$-, $SKEH$-, η_{de}- & $C_{p0,rel,1} + \beta_{dev,0.7}$-based designs are further explained by Fig. 8.2. In particular, while for all the designs (with the exception of the $C_{p0,rel}$-based design), the net contribution to the overall torque output from the rotor blade was predicted to be increased, the introduction of the endwall contouring in the η_{tt}-, C_{ske}- & β_{dev}-based designs resulted in similarly large negative contributions to the overall rotor moment, while in the cases of the $SKEH$-, η_{de} and $C_{p0,rel,1} + \beta_{dev,0.7}$-based designs, these contributions were smaller.

In contrast however, while the torque predicted to be generated by the blade (suction) surface for the $C_{p0,rel}$-based design was in fact less than that of the baseline case, in this case, a positive contribution to the overall torque by the endwall was predicted, resulting in a reasonably large predicted increase in the rotor output discussed previously. In all cases, the net effects of the fluid viscosity were negligible.

While the changes to the blade loading for each design are discussed in Section 8.2.2, the predicted net contribution to the overall rotor torque by the endwall surface for the $C_{p0,rel}$-based design deserves some mention here. As shown in Fig. A.1c (Appendix A), the 'inverted' nature of the contours for this design resulted in a stacking of the endwall against (particularly) the pressure surface of the blade, resulting not only in the net increase and decreases in the endwall and blade surface areas reported in

Table 8.1: Suction, pressure and endwall surface area changes

Endwall	*Area* (mm^2)		
	Suction surface	*Pressure surface*	*Endwall*
annular	4939	4362	2939
η_{tt}-based	4971 (+0.65%)	4329 (−0.76%)	2965 (+0.88%)
C_{ske}-based	4973 (+0.69%)	4328 (−0.78%)	2979 (+1.36%)
$C_{p0,rel}$-based	4906 (−0.67%)	4352 (−0.23%)	3022 (+2.82%)
β_{dev}-based	4974 (+0.71%)	4339 (−0.53%)	2979 (+1.36%)
$SKEH$-based	4972 (+0.67%)	4350 (−0.28%)	3018 (+2.69%)
η_{de}-based	4952 (+0.26%)	4336 (−0.60%)	2963 (+0.82%)
$C_{ske,1} + \beta_{dev,0.7}$-based	4940 (+0.02%)	4340 (−0.50%)	2986 (+1.60%)
$C_{p0,rel,1} + \beta_{dev,0.7}$-based	4963 (+0.49%)	4329 (−0.76%)	2965 (+0.88%)

Table 8.1 but also in the larger pressure-based contribution to the overall rotor torque by the endwall itself.

8.2 Endwall pressures and blade loading

8.2.1 Endwall pressures

In this Section, the calculated static pressure contours on the endwall surface for the annular as well as each of the contoured rotors are presented. As an aid to understanding, contour plots of the physical endwall layouts are included as insets above each pressure plot in addition to being included in the Appendix A once again. As indicated previously, in each case, the data is presented as a pressure coefficient (C_p) non-dimensionalised using the downstream static pressure at the exit of the turbine which was a prescribed boundary value for each of the CFD simulations.

Overview

For the majority of endwalls[1], the effect of the endwall contouring on the rotor hub pressure distribution was clear:-

- a reduction in the extent of the high pressure region in the vicinity of the blade pressure surface predominantly in the tangential direction, as well as,
- an adjustment of the isobars within the forward portion of each contoured region to be more aligned with the axis of rotation of the turbine (i.e. more axially aligned) rather than at an inclined angle of approx. $\sim 45^\circ$ between the pressure and suction surfaces as was the case for the annular case.

In addition to this, in the vicinity of the leading edge, for the majority of the designs, the endwall pressure contours were seen to reorientate themselves into a configuration more perpendicular to the

[1] Excluding the $C_{p0,rel}$- & $SKEH$-based endwalls

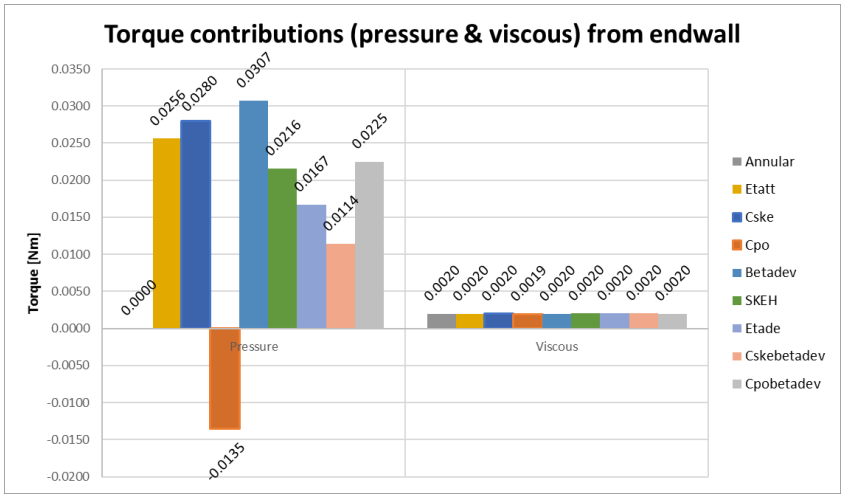

(a)

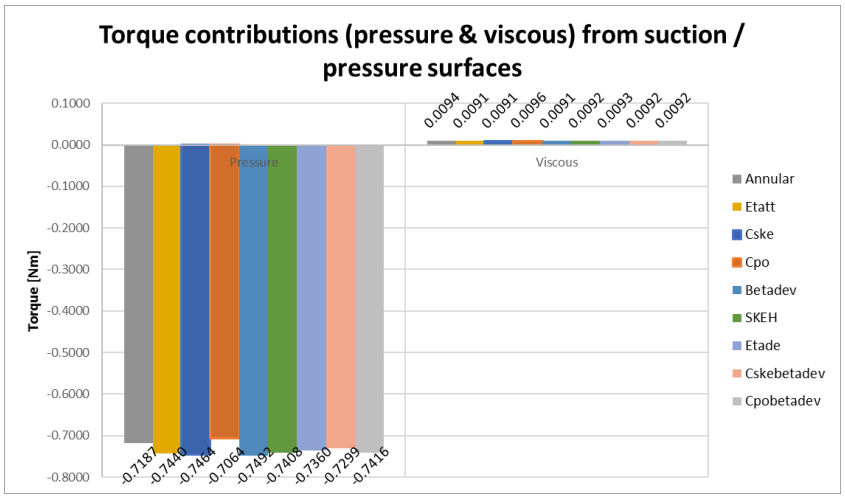

(b)

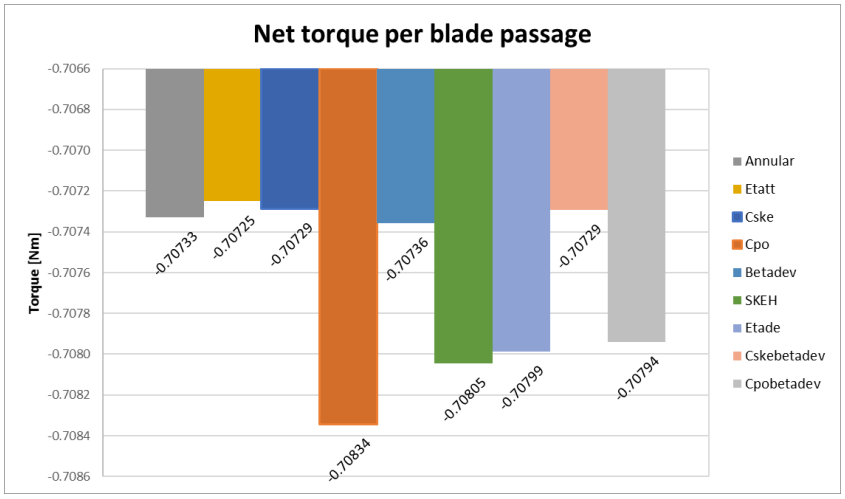

(c)

Fig. 8.2: Computed contributions to the overall rotor torque from the (a) endwall, (b) blade (pressure & suction surfaces) as well as (c) overall net torque per blade passage

axis of rotation of the rotor, and in so doing, extended the region of high pressure in the vicinity of the pressure surface forward of its original limits, leading to the disruption of the channel of low pressure which was seen to cross the blade passage from the leading edge of the rotor to the $\sim 40\%$ C_{ax} position on the suction surface of the adjacent blade in the annular case.

In the vicinity of the suction surface leading edge, the plots showed a reversal in the direction of the pressure gradient around the suction side of the leading edge leading to one in which the local static pressure was seen to decrease in magnitude in this direction, while for the annular case this pressure was seen to increase with increasing axial position. Further to this, the above-mentioned channel of low pressure which, for the annular case, was calculated to form within the blade passage, was seen to reorientate itself more closely with the curvature of the adjacent blade's suction surface (especially for the η_{tt}-based design), while the region of low pressure which was formerly present only immediately adjacent to the blade's suction surface at approx. $\sim 20\%$ C_{ax}, was seen to grow in size and extend in direction towards the blade leading edge.

η_{tt}-based

For the most part, the η_{tt}-based endwall (Fig. 8.3b) showed the majority of the artefacts discussed above, although the channel of low pressure which was formed adjacent to the suction surface was particularly well defined for this case, as was the low pressure region which formed closely adjacent to the blade suction surface near the leading edge.

C_{ske}-based

The results for the C_{ske}-based design (Fig. 8.3c) were largely similar to those of the η_{tt}-based design, although the minimum pressure within the low pressure region which formed immediately adjacent to the suction surface, was predicted to be slightly lower for this endwall than was the case for the η_{tt}-based design. Further to this, the region of low pressure discussed to extend towards the leading edge of the blade suction surface, was again prominent for this endwall, as was the case for the previous design.

$C_{p0,rel}$-based

In contrast to the above, the endwall pressure contours for the $C_{p0,rel}$-based case (Fig. 8.3d) showed characteristics considerably more similar to those of the annular endwall. More specifically, the formation of the channel of low pressure, which for both previous designs was seen not seen to form, appeared to be encouraged to form for the present design, while in addition, the local static pressure immediately ahead of the rotor leading edge was seen to be increased, in stark contrast to the decreases noted in the same region for the two previous designs. Finally, the region of low pressure in the vicinity of the suction side leading edge (which for the majority of endwalls was seen to grow in size as well as extend towards the leading edge), was seen to reduce in size slightly as well as to migrate further aft towards the trailing edge rather than extend towards the leading edge.

β_{dev}-based

The predicted endwall pressure contours for the β_{dev}-based case (Fig. 8.3e) showed a great deal of similarity to those already presented for the C_{ske}-based design, although the peak pressure in the low pressure channel was predicted to be slightly lower than that of the C_{ske}-based design as was the case with the low pressure region predicted to form immediately adjacent to the suction surface. One further difference for the current design in comparison to those predicted for the C_{ske}-based design, was the enhancement of the existing low pressure zone immediately adjacent to the blade suction surface as well as to the formation of two additional low pressure 'bubbles' within this region. These features were noted to form immediately before and aft of the 3^{rd} (i.e. *curve* 4) circumferential endwall control line, which itself was seen to extend considerably closer to the blade suction surface than was the case for the same control line within the C_{ske}-based design.

$SKEH$-based

Despite the physical complexity of the optimized contours for this endwall, the $SKEH$-based design (Fig. 8.3f) did present some elements in common with the majority of the previously discussed design, including:- 1) a disruption of the cross-passage low pressure channel as well as, 2) the development of an enlarged region of low static pressure near to the suction side leading edge. However, for the present design, the contours within the profiled portion of the blade passage did not display the same degree of uniformity predicted for the previous designs, with the high pressure zone immediately adjacent to the pressure surface seen to be separated into two distinct regions while a number of 'bubbles' of very low pressure were seen to form within the passage, with the most noticeable of these forming once again immediately adjacent to the suction surface of the adjacent blade.

η_{de}-based

The endwall pressures for the η_{de}-based case (Fig. 8.3g) showed a return to an overall pattern noted already for the majority of the previous design, although a few small differences were noted. In particular, in the midpassage region, the isobars for the current design tended to take on a slightly 'convex' shape with the high pressure region within the blade passage predicted to expand in the circumferential direction towards the adjacent suction surface. In addition, a channel of low pressure close to the adjacent suction surface was seen to form and follow the curvature of the blade suction surface. The increase in prominence of the low pressure region on the suction side leading edge was reduced in intensity in comparison to the majority of the previous designs, although the region of very low pressure immediately adjacent to the suction surface, was enlarged with the magnitude of the pressure at its centre considerably reduced. Finally, a small but very low 'bubble' of pressure close to the point at which the 1^{st} circumferential control line was seen cross the blade passage, was also noted.

$C_{ske,1} + \beta_{dev,0.7}$-based

The endwall pressure plots for the $C_{ske,1} + \beta_{dev,0.7}$-based design (Fig. 8.3h) showed a reasonable degree of similarity to the η_{tt}- & C_{ske}-based endwalls, although the isobars located approximately in the centre of the contoured region for this design were (as was the case for the η_{de}-based case), noted to take on a slightly convex shape and extend towards the suction surface of the adjacent blade. Aft of this position, the isobars were seen to take on a moderately concave character, and recede towards the pressure surface of the blade.

Finally, similar to what was noted for the β_{dev}-based case, two small but significant regions of low and high local pressure immediately fore and aft of the final (i.e. 4^{th}) endwall control line were seen, which for the current case, was seen to extend across the entire blade passage, and intersect with the adjacent blades suction surface.

$C_{p0,rel,1} + \beta_{dev,0.7}$-based

Finally, the static pressure contours for the $C_{p0,rel,1} + \beta_{dev,0.7}$-based design are shown in Fig. 8.3i, and were again seen to share many similarities with the η_{tt}, C_{ske}- & $C_{ske,1} + \beta_{dev,0.7}$-based endwalls. Most conspicuously, within the contoured region, the isobars for the current design were seen to orient themselves in a predominantly axial direction with the channel of low pressure described for the annular case once again absent. In addition, as well as a strengthening of the low pressure region towards the leading edge of the blade suction surface, a small region of convex contours extending towards the adjacent blades suction surface, similar to that noted for the $C_{ske,1} + \beta_{dev,0.7}$ endwall was noted, although for the current case, this feature was significantly more subtle.

Summary

In general, the changes in the endwall pressures reflected those expected as a result of the changes introduced by the endwall contouring, with convex curvature resulting in lower endwall pressures and vice versa.

More specifically however:-

- For the majority of cases, the increase and decrease in the endwall heights adjacent to the pressure and suction surfaces of each blade resulted in the decreases in the local static pressure close to the pressure surface and an increase close to the corresponding suction surfaces.
- Further to this, the channel of low pressure which was seen to cross the passage for the annular case (and which corresponded to the trajectory of the pressure side horseshoe and later passage vortices) was seen to be disrupted for all the designs, with the express exception of the $C_{p0,rel}$-based design.
  - These effects, combined with the migration of the midspan isobars forward of their original position and the formation of the low pressure region near the suction side leading of the blades indicated that, in most cases, the endwall contouring at least in the early part of the blade

passage, functioned in part by obstructing the formation of the pressure side horseshoe vortex and in so doing considerably reduced the formation of the passage vortex downstream.

- This was in contrast to the traditional explanation used to describe the functioning of non-axisymmetric endwall contouring, in which the reduction in the strength of the passage vortex was explained almost exclusively through a reduction of migration of the low momentum endwall boundary layer fluid across the blade passage only, which itself was as a result of a reduction in the cross-passage static pressure gradient.

- Although present in almost all the designs investigated in this thesis, in addition to the aerodynamic blocking of the pressure side horseshoe vortex, the endwall contours of the $\boldsymbol{\eta_{tt}-}$ & **Cske − based** designs were also understood to function by including the traditional mechanism of reducing the cross-passage endwall pressure gradient and this was evidenced by the introduction of the 'hump-and-dip' profile throughout the contoured region, through which the local endwall static pressure gradient was then influenced.
- This was not the case for the $\mathbf{C_{p0,rel}}$ **− based** design, which instead was seen to result in largely the opposite trend. In particular, for this endwall, the endwall contours resulted in:-

  - an increase in the pressure on the suction side of the blade leading edge, suggesting a decrease in the flow around to this side of the blade as well as,
  - the re-emergence of the 'channel' of low pressure which was seen to traverse the blade passage for the datum case (suggesting an encouragement of formation of the pressure side horseshoe and later the passage vortex), within the blade passage as well as their traversal through the passage with almost the exact trajectory of that noted for the annular case.

- The results of the endwall contouring for the $\boldsymbol{\beta_{dev}}$ **− based** case were similar to that already noted for the η_{tt}- & C_{ske}-based cases, with the exception of the very low 'spot' pressures which were seen to form close to the suction surface of the adjacent blade in the aft portion of the contoured region. These isolated regions of low pressure were noted to coincide closely with the extension of the 3^{rd} (i.e. *curve* 4) circumferential driving curve almost completely across the blade passage and the consequences of this feature is discussed later in this Chapter.
- The seemingly discordant nature, as well as patches of low and high pressure seen close to the suction surface for the **SKEH − based** design, were as a direct result of the complex nature of the endwall contours produced by the optimizer for this objective function.

  - In particular, while the disruption of the cross-passage channel noted for the majority of the preceding endwalls was again noted for this endwall, the island of higher pressure located adjacent to the pressure surface in the forward portion of the contoured region was formed by the uncharacteristic region of low endwall height in this area, while the isolated spots of low pressure close to the suction surface were understood to be as a result of the undulatory characteristics of the profiling in this region.

- The pressure distribution for the $\boldsymbol{\eta_{de}}$ **− based** design showed a return to the more characteristic nature of the earlier designs with the disruption of the cross-passage low pressure channel and the strengthening of the flow around the suction side leading edge of the blade, however:-

- distinct from the previous designs was the slight enlargement of the low pressure bubble adjacent to the suction surface at a position of approximately $\sim 20\%\ C_{ax}$ which although was not as severe as those noted for designs such as the $C_{ske,1} + \beta_{dev,0.7}$- & $SKEH$-based endwalls, could be understood as a consequence of the proximity of the most forward contour of the design to the suction surface for this case.

- In addition to the general comments above, specifically for the $\mathbf{C_{ske,1} + \beta_{dev,0.7} - based}$ case, the slightly concave inflection of the endwall pressure contours in the vicinity of the blade midspan corresponded to the slight hollow in the endwall shape which was seen to form in the middle of the contoured region, while the concave region in the pressure contours aft of this were understood to be as a product of the large, cross-passage 'deflector' contour which was seen to form at the exit of the contoured region. Finally, the bubble of low pressure immediately adjacent to the suction surface at approximately $\sim 50\%\ C_{ax}$ was noted to correspond to point at which the aforementioned 'deflector' contour intersected with the suction surface.
- Finally, for the $\mathbf{C_{p0,rel,1} + \beta_{dev,0.7} - based}$ design, the convex portion of the isobars in the centre of the contoured region were again understood to relate to that portion of the physical contours, where the radial amplitude of the contours was reduced in comparison to those forward and aft of that position. Similarly, the concave portion of the final pressure contour immediately adjacent to the pressure surface, were understood to be as a result of the peak in the profiling height immediately adjacent to the blade pressure surface.

8.2.2 Blade loading

Figs. 8.4 - 8.9 show the blade loading at various heights above the nominal (annular) endwall surface position as percentages of the total span. In addition, alongside each set of graphs, contour plots of the static pressure coefficient on the endwall as well as the blade suction surfaces for both the annular and each contoured case are included.

In general:-

- **5% span** - Close to the endwall, the loading for the majority of the endwalls was predicted to increase as a result of the introduction of the endwall contours. As has been discussed by various authors (e.g. Snedden et al. (2010b), Snedden (2011)), the contouring was noted to have a larger impact on the suction side pressure distribution because of the higher dynamic pressures present there, although some small reductions in the pressure side static pressure distribution were visible
- **10% span** - Above this region, in general, the effect of the endwall contouring was to increase the blade loading forward of the $\sim 40\%\ C_{ax}$ position, but also on the latter part of the blade (from $\sim 65 - 100\%\ C_{ax}$). Moreover, at this spanwise location and again for the majority of endwalls, between these two regions (i.e. $40 - 65\%\ C_{ax}$) the effect of the endwall contouring was to increase the local static pressure of the blades effectively unloading the suction surface of the blade
- **20% span** - At the 20% spanwise position, on the forward portion of the blade, the effects of the endwall contouring were seen to be largely negligible, with the pressure distribution on the suction surface of each blade seen to be almost identical to that of the datum case. In contrast however,

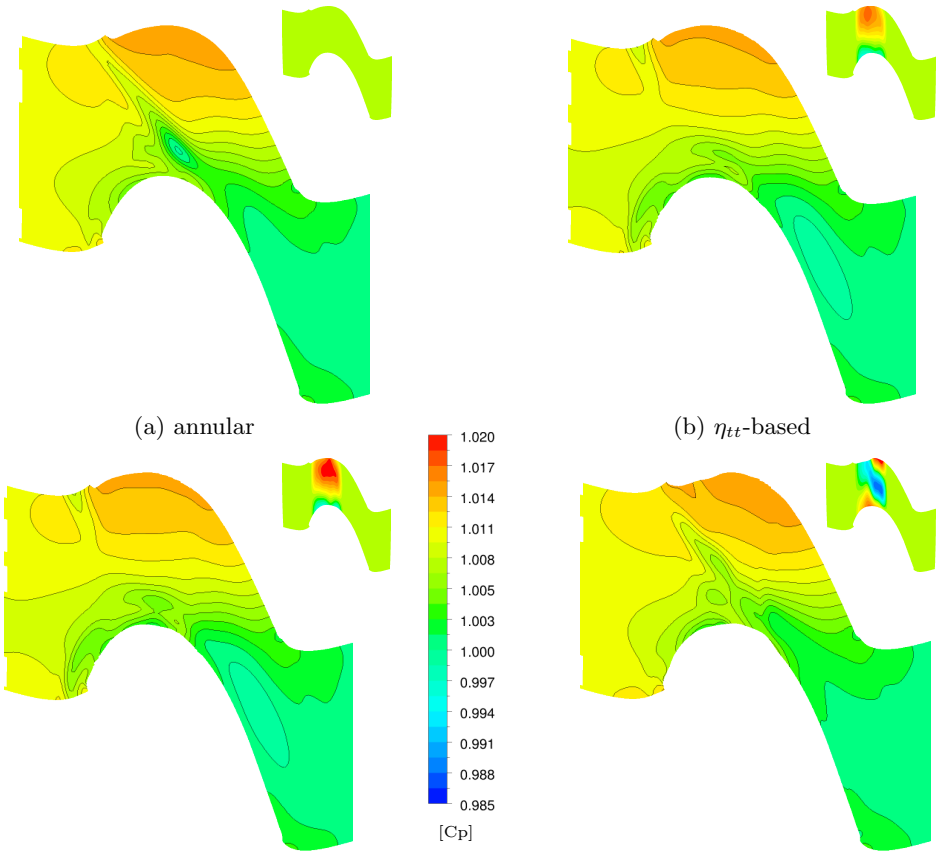

(a) annular (b) η_{tt}-based

(c) C_{ske}-based (d) $C_{p0,rel}$-based

(e) β_{dev}-based (f) $SKEH$-based

aft of the midchord once again, the action of the endwall contouring in the majority of cases was to reduce the loading

- **50% span** - Finally at the midspan, for all cases, the effect of the endwall contouring was again seen to be negligible, with the pressure distributions for both the suction and pressure sides predicted to match those of the datum case almost identically

More specifically then, in terms of each endwall:-

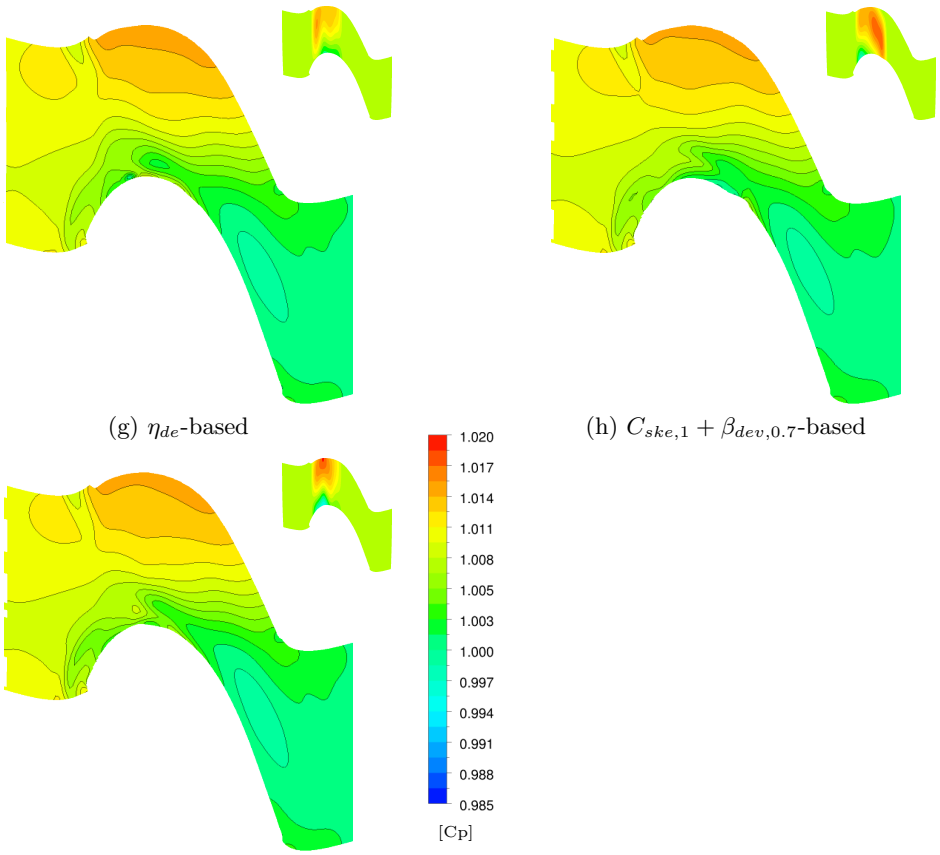

(g) η_{de}-based

(h) $C_{ske,1} + \beta_{dev,0.7}$-based

(i) $C_{p0,rel,1} + \beta_{dev,0.7}$-based

Fig. 8.3: Endwall pressure contours for each endwall with height contours (inset)

η_{tt}-based

In general, the blade loadings computed for the η_{tt}-based (Fig. 8.4) design were similar to those discussed above, although the predicted increase in the loading at the 5% span height was calculated to be largely uniform across the entire blade chord as a result of the uniform reduction in the endwall height adjacent to the suction surface for the design. The net effect of this was, a reduction in the spanwise pressure gradient on the blade suction surface, with the lower static pressure present higher up the span then persisting through to the 5% spanwise position. The effects of this situation were still evident on the forward portion of the blade at the 10% span position, although the increased loading towards the rear portion of the chord at both the 10% & 20% spanwise heights could be understood to be as a result of an reduction in the intensity of the passage vortex (see Section 8.3) and the corresponding increase in magnitude of the core static pressure of the passage vortex and consequently the static pressure where the vortex impinged on the suction surface.

C_{ske}-based

The results for C_{ske}-based design (Fig. 8.5) were very similar to those noted for the η_{tt}-based design, although the increase in loading across the chord at the 5% span was predicted to be

slightly larger for the current case than the previous one. This was most likely to be as a result of the slightly more aggressive contouring (and therefore lower endwall height) adjacent to the suction surface which was produced using the C_{ske}-based objective function. As indicated, above the 5% spanwise position, the loadings were largely identical to those predicted for the η_{tt}-based case.

$C_{p0,rel}$-based

Once again, the $C_{p0,rel}$-based design (Fig. 8.6) represented a significant departure from the general observations made for the previous endwalls. In particular, at most of the spanwise positions, the blade loading for the $C_{p0,rel}$-based design matched those of the annular case reasonably closely with the exception of distinct departures from the baseline at various positions on the chord. More specifically, at 5% span and at approximately 35% C_{ax}, a large decrease in the local chordwise loading was noted, while at 10% span, the effects of the relatively complex geometry of the endwall were seen to persist with a series of local peaks and troughs in the suction surface static pressure ($\sim 25-45\%\ C_{ax}$), before a further increase followed by an immediate subsequent decrease in the loading was noted. A similar trend to this was noted at the 20% spanwise position, although the double peaked portion of the suction surface loading was not present at this height.

A study of the suction surface static pressure contours in combination with the streamlines (discussed in Section 8.3) showed the major reason for these effects were:-

- the impingement of an increased amount of endwall boundary layer fluid against the suction surface at the intersection of the endwall and suction surface resulting in increased local pressure and decreased blade loading at the 5% span, and
- an increase in the intensity and therefore a lower core vortex pressure and therefore subsequently lower local static pressures and increased blade loading at the chordwise locations at which the vortex was seen to impinge on the suction surface itself

Finally, as was the case with the η_{tt}- & C_{ske}-based designs, at the midspan, the effects of the endwall contouring on the blade loading were predicted to be largely negligible.

β_{dev}-based

The blade loading and contour plots for the β_{dev}-based design (Fig. 8.7) were somewhat similar to those noted for the η_{tt}- & C_{ske}-based designs, although this endwall shared some similarities with those features noted for the $C_{ske,1} + \beta_{dev,0.7}$-based case discussed below. More specifically, at the 5% spanwise position, the loading over the entire blade surface was increased, with a particularly prominent decrease in the suction surface pressure close to the midchord. Further away from the endwall (at 10% span), once again an increase in the loading over the forward portion of the chord was noted, followed by a decrease in the vicinity of the midchord and finally an increase in the loading once again over the aft portion of the blade. Further, the local decrease in the suction surface pressure which was noted closer to the endwall, was still evident at this height. Finally, as was the case for a number of the previous endwalls, at 20% span the endwall

contouring of the current design resulted in a slight increase in the blade loading over the forward portion of the chord as well as an unloading of the chord over the aft portion of the blade. Once again, at 50% span, no influence of the contouring was evident.

$SKEH$-based

In contrast to the majority of previous designs, the blade loadings for the $SKEH$-based endwall (Fig. 8.8) showed considerably more similarity to the $C_{p0,rel}$-based design in that overall, the pressure and suction surface pressure distributions followed those calculated for the datum case more closely than the η_{tt}-, C_{ske}, β_{dev} & 'compound' designs. In contrast to the $C_{p0,rel}$-based endwall however, at the 5% span and at 40% C_{ax}, the local blade loading was seen to increase dramatically rather than decrease. The contour plot of the suction surface indicated that this isolated increase in the blade loading was as a result of a core of low pressure seen to form close to the suction surface immediately aft of the first of the two endwall contours which were seen to extend across the majority of the blade passage. The streamline plots of Section 8.3 showed that this low pressure channel was formed as a result of a small but intense vortex seen to split from a larger structure formed in the hollow on the opposite side of the passage adjacent to the pressure surface.

At the 10% spanwise location, the effects of the endwall contouring were still present, with a smaller increase in the loading visible as a result of the aforementioned vortex, as well as a slight increase in the loading aft of the midchord as a result of the increased portion of the blade exposed to the more diffused passage vortex (see Section 8.3).

Once again, at the 20% & 50% spanwise positions, the blade loadings for this endwall were largely identical to those noted for the previous designs with the exception of the $C_{p0,rel}$-based design.

η_{de}-based

The blade loadings and endwall and suction surface pressure contours for the η_{de}-based design are shown in Fig. 8.9. As was the case for the $C_{p0,rel}$- & $SKEH$-based endwalls, the blade loadings for the η_{de}-based design were somewhat distinct from those of the η_{tt}-, C_{ske}-, β_{dev}- & 'compound' designs. At the 5% spanwise position, the blade loading was seen to increase in a relatively isolated range of $30 - 50\%$ C_{ax}. Inspection of the suction surface contour plot showed that this was as a result of the migration of the impingement position of the passage vortex forward from its datum position to closer to the start of the contoured region of the passage, and more specifically to a position almost directly aft the endwall contour positioned at the entrance to the blade passage. The effects of the repositioning of the passage vortex were still evident at a radial position of 10% span, while at 20% span, the effect of this forward migration of the passage vortex was a shift in the position of the peak suction pressure on the suction surface to a chordwise position of 65% C_{ax} from its datum position at approximately 78% C_{ax}.

$C_{ske,1} + \beta_{dev,0.7}$-based

The loading plots for the $C_{ske,1} + \beta_{dev,0.7}$-based design (Fig. 8.10) showed a return to the general characteristics of those noted for the majority of the endwalls, with a overall increase in the loading at 5% span (although this was noted to be somewhat less significant in the forward portion of the chord than in previous cases but significantly more prominent in the midchord region). Inspection of the endwall and suction surface pressure contours showed this was as a direct result of the adaptation of the flow to the blockage presented by the large cross-passage 'deflector' contour located at the exit of the contoured region and the rapid increase in flow velocity (and corresponding decrease in the local static pressure) as the flow approached the contraction. Immediately behind this point, the increase in the flow area corresponded to an relatively abrupt increase in the local static pressure (and decrease in the blade loading) to a magnitude similar to that of the datum case.

At 10% span, the increase in the blade loading over the forward portion of the chord as a result of the 'deflector' contour was still noticeable, although the repositioning of the passage vortex and its impingement on the suction surface as a result of the contouring, resulted in lower local static pressures and a subsequent increase in the local blade loading over the rear portion of the chord. At the 20% span, the endwall once again showed increased similarity to the η_{tt}- & C_{ske}-based designs, with a slight increase in the loading between $\sim 25-50\%$ C_{ax} and a decrease in the loading towards the rear of the blade surface. Once again, at 50% span, the differences between the datum and current design were negligible.

$C_{p0,rel,1} + \beta_{dev,0.7}$-based

Finally, the blade loading and endwall / suction surface contour plots for the $C_{p0,rel,1} + \beta_{dev,0.7}$-based design are shown in Fig. 8.11. Once again, a general increase in the blade loading was noted at the 5% span corresponding to a more docile change in the static pressure on the suction surface as the endwall is approached, while similar results to those of η_{tt}- & C_{ske}-based designs were noted at the 10% & 20% spanwise location. In general, the changes in the blade loading for the current case were less prominent than those reported for the η_{tt}- & C_{ske}-based designs, but this was determined to be as a result of the more subtle nature of the contours produced for this objective function.

Summary

In summary then:-

- In general and particularly for the $\boldsymbol{\eta_{tt}-}$ & $\mathbf{C_{ske}-based}$ designs,
  - Close to the hub (i.e. $\sim 5\%$ span), the effect of the contouring was to *increase* the overall blade loading. For the majority of the endwalls, this was achieved by a decrease in the local static pressure on the suction side near the leading edge of the blade (and was consistent with the strengthening of the suction side horseshoe vortices for most designs, as discussed in Section8.3)

and over the aft section of the chord, as a result of the impingement of the more diffuse passage vortex on the blade suction surface

- Further away from the endwall (i.e. $\sim$ 10% span), the contouring was seen to result in a slight increase in the blade loading over the forward portion of the blade accompanied by a decrease in the loading near the midchord. Aft of the midchord, for the majority of the endwalls, an increase in the blade loading in comparison to the annular case was noted
- Closer to the midspan (i.e. $\sim$ 20% span), the general effects of the contouring were limited to the aft portion of the blade, with the pressures over the forward portion of the blade seen to be largely unchanged from the annular case. The change in loading over the aft portion of the blade was again noted to be as a result of the impingement of the more diffuse passage vortex on the blade suction surface, resulting in higher pressures and therefore reduced loading over this portion of the blade
- Finally, at the midspan itself (i.e. $\sim$ 50% span), for all endwalls, the effects of the endwall contouring were seen to be effectively negligible

- Once again, this was not the case for the $\mathbf{C_{p0,rel} - based}$ case, whose predicted blade loadings were considerably more similar to those of the the annular case, although in some regions the local blade loading was dominated by flow features introduced into the flow by the specific details of the endwall geometry.
- The $\boldsymbol{\beta_{dev} - based}$ case was again similar to the η_{tt}- & C_{ske}-based cases, although again the local perturbations of the endwall geometry resulted in a few highly localised departures from the general case, including most obviously, a local increase in the blade loading near the midchord as a result of a local contraction presented to the flow formed by a cross-passage contour located midway through the contoured region.
- For the $\mathbf{SKEH - based}$ design, the local blade loading was somewhat similar to that of the baseline case, although close to the endwall (i.e. $>$ 10% span), isolated increases in the local blade loading in the vicinity of the midchord were predicted. As discussed in Section 8.3, these were determined to be primarily as a result of the introduction of a local 3-dimensional flow feature rather than a general decrease in the suction surface pressure. This change was seen to diminish at a radial position of $\sim$ 20% span, although aft of the midchord at this spanwise location, the local loading was decreased, once again as a result of the impingement of a more diffuse passage vortex on the blade's surface.
- The $\boldsymbol{\eta_{de} - based}$ design once again showed a general increasing of the loading close to the endwall surface and near to the blade midchord. This was found to be as a result of the re-positioning of the passage vortex and its impingement on the suction surface further forward on the blade suction surface. Slightly further from the endwall (i.e. $\sim$ 10% span), this increased loading was sustained and was accompanied by a small increase in the blade loading towards the trailing edge of the blade, which was also noted to occur as a result of the re-positioning of the passage vortex described above. Finally, at 20% span, a similar scenario was noted although at this increased height above the hub, the increased loading peak was shifted aft towards the trailing edge and thereafter accompanied by a reasonably substantial decrease in the local blade loading.

- The blade loading for the $\mathbf{C_{ske,1} + \beta_{dev,0.7} - based}$ design showed a high dependency on the details of the endwall geometry, most noticeably the local 'blockage' effect of the 'deflector' contour at the exit of the contoured region. The net effect of this feature was to cause a sharp pressure rise aft of the contour and which was well reflected in the decreasing loading aft of the midchord at the 5% & 10% spanwise locations. Above this height, the changes to the passage vortex as discussed previously resulted in slight unloading of the aft portion of the chord, although forward of the midchord, a slight increase in the loading was also noted.
- Finally, although the results for the $\mathbf{C_{p0,rel,1} + \beta_{dev,0.7} - based}$ design were similar to those reported for the majority of the previous designs, the changes to the loading profiles were more muted than noted for the η_{tt}-, C_{ske} & $C_{ske,1} + \beta_{dev,0.7}$-based designs. For instance, at the 10% spanwise position, the chord was noted to have slightly increased loading over the forward and aft portions of the blade, as well as a slight reduction in the loading near the midspan. Again, at 20% span, while the forward portion of the blade remained similarly loaded to the datum case, aft of the midchord, the more diffuse nature and higher core pressures of the passage vortex resulted in a decrease in the local blade loading. Once again, at the midspan, the effects of the contouring where negligible.

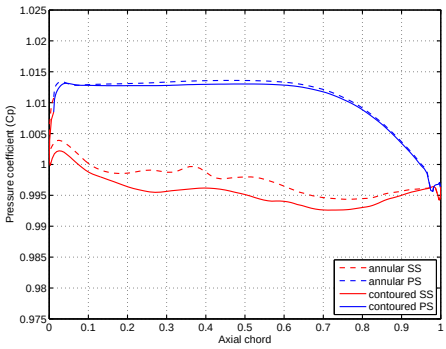

(a) 5% span

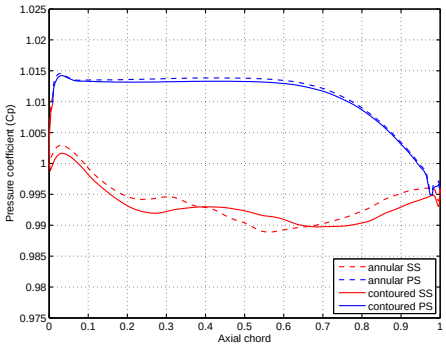

(b) 10% span

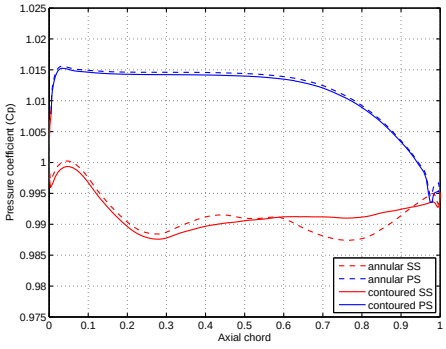

(c) 20% span

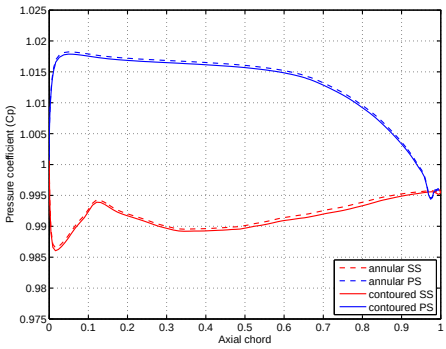

(d) 50% span

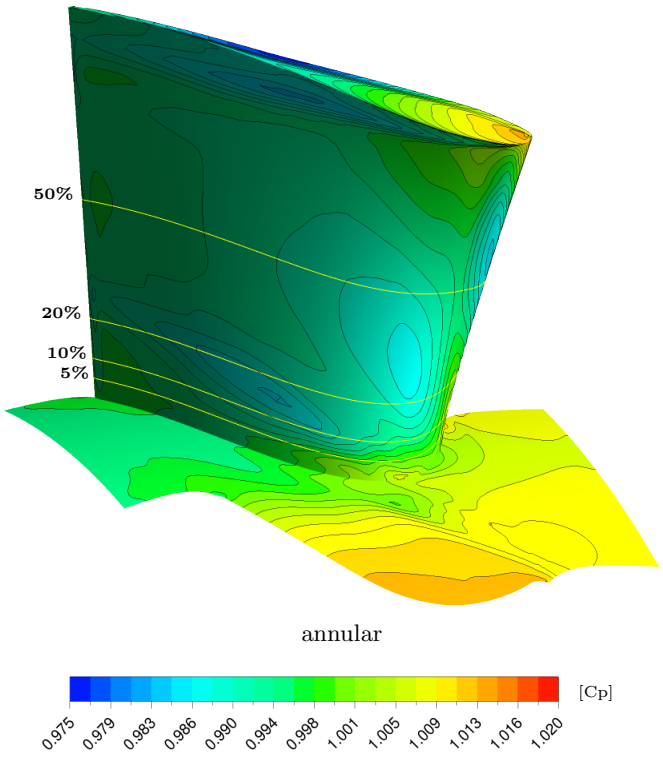

annular

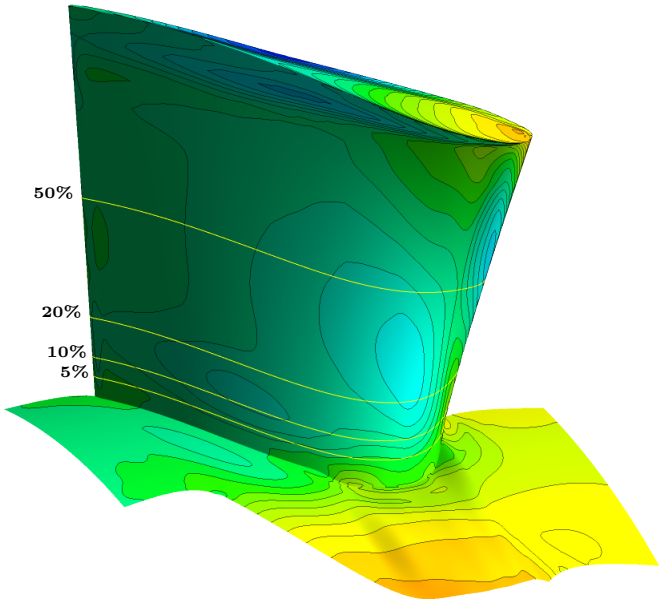

η_{tt}-based

Fig. 8.4: Blade loading profiles for the η_{tt}-based endwall

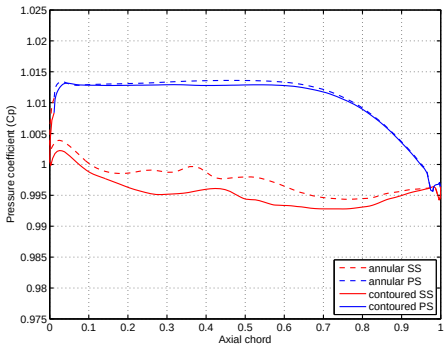

(a) 5% span

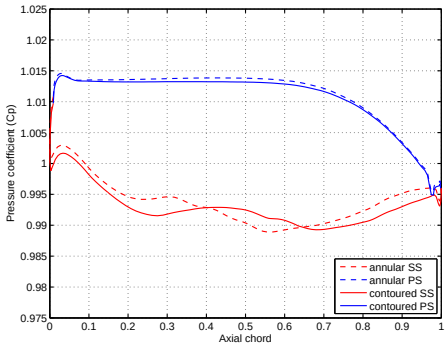

(b) 10% span

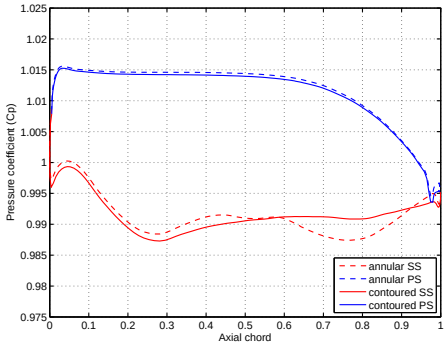

(c) 20% span

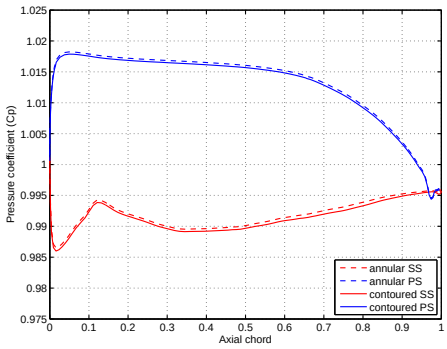

(d) 50% span

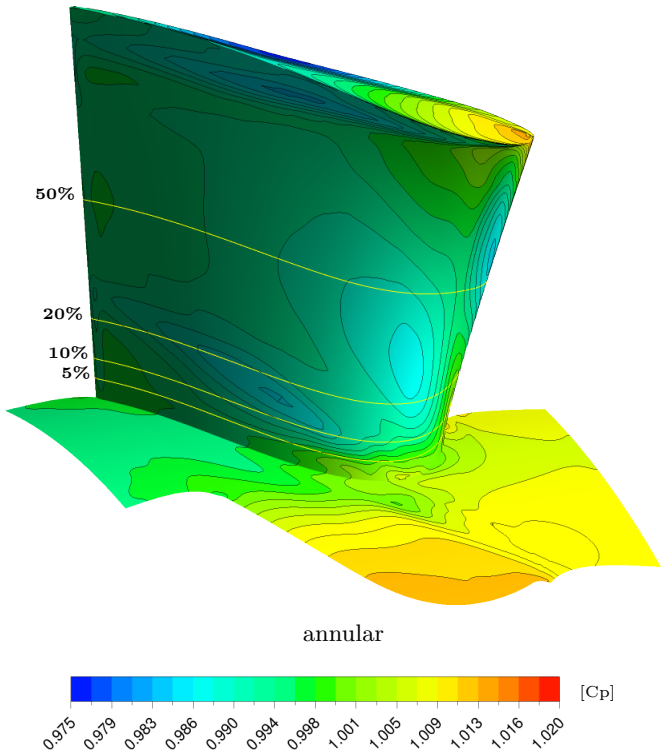

annular

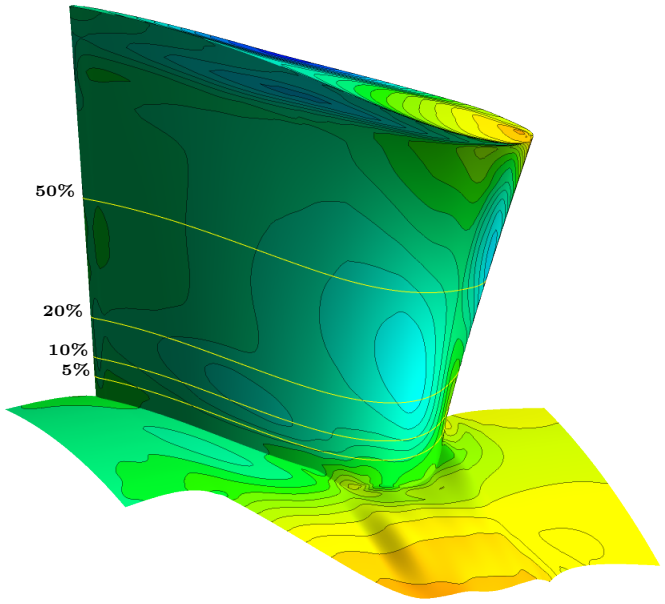

C_{ske}-based

Fig. 8.5: Blade loading profiles for the C_{ske}-based endwall

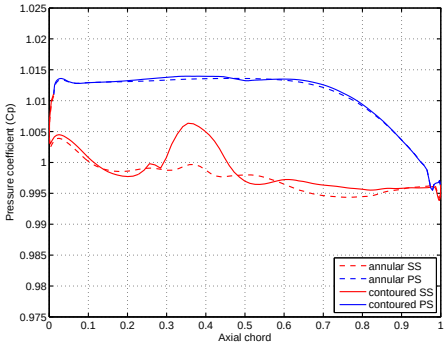

(a) 5% span

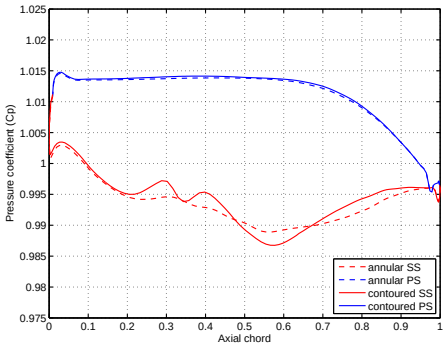

(b) 10% span

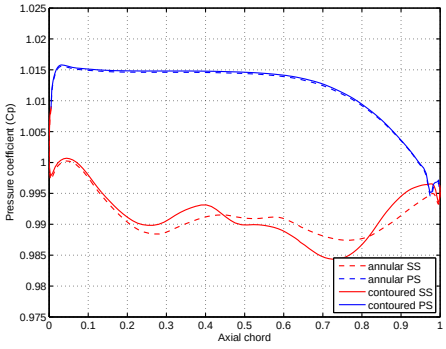

(c) 20% span

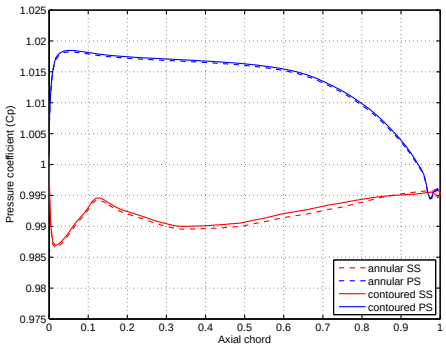

(d) 50% span

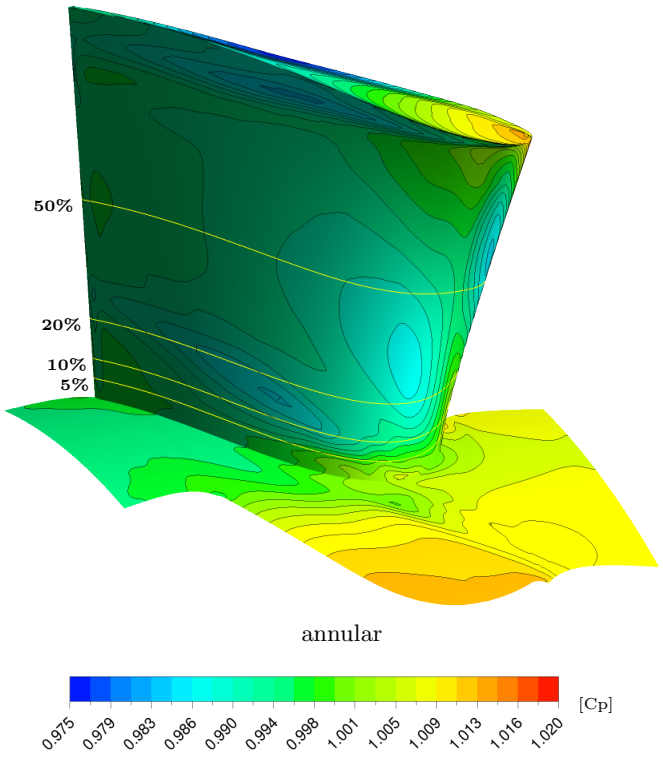

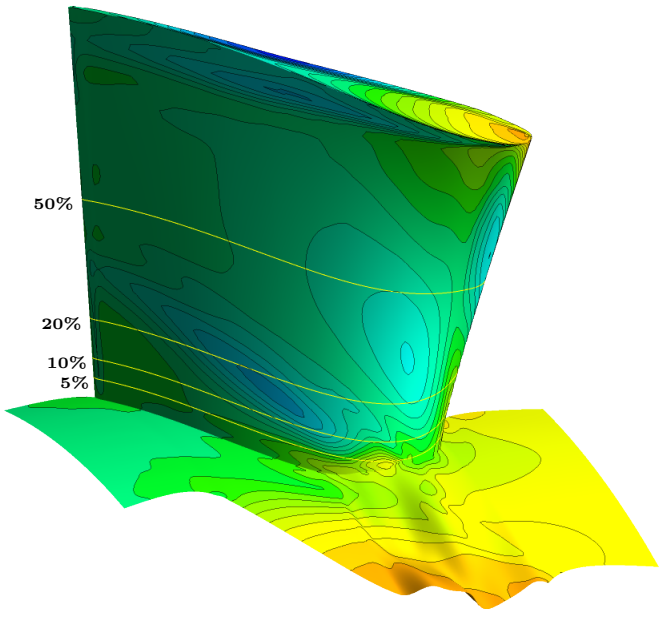

$C_{p0,rel}$-based

Fig. 8.6: Blade loading profiles for the $C_{p0,rel}$-based endwall

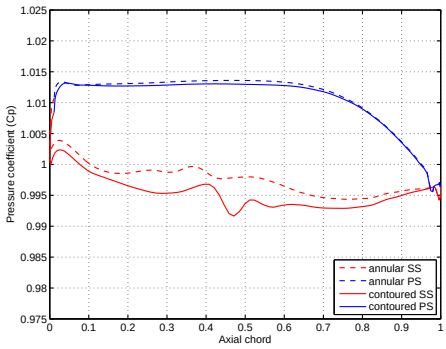

(a) 5% span

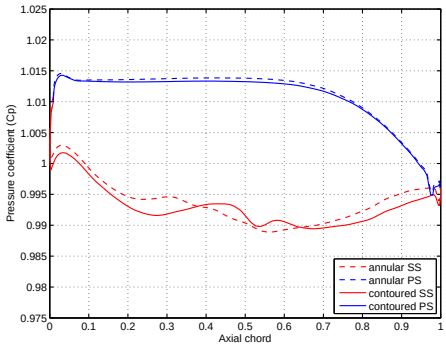

(b) 10% span

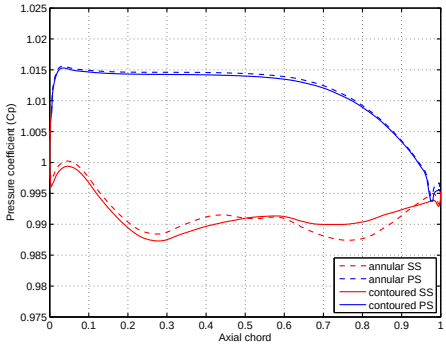

(c) 20% span

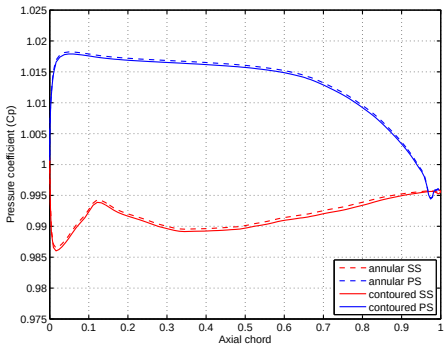

(d) 50% span

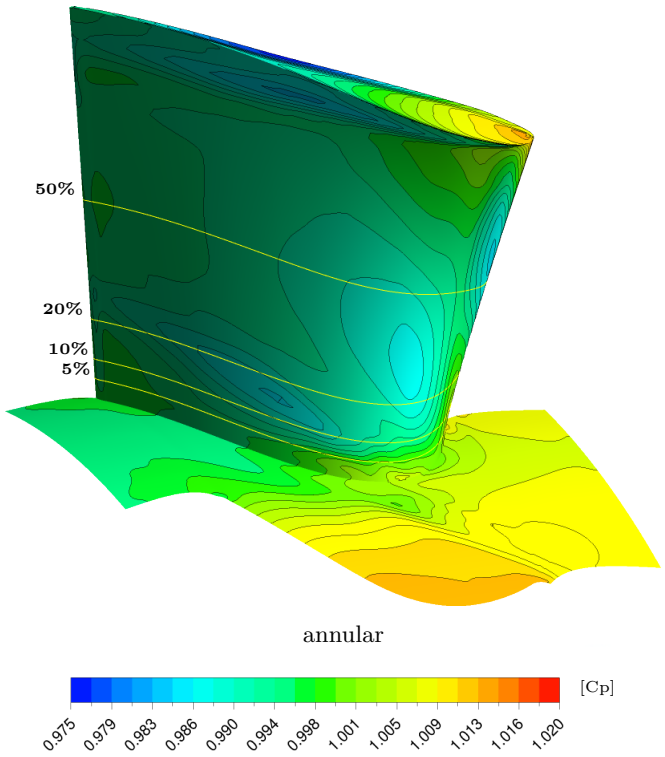

annular

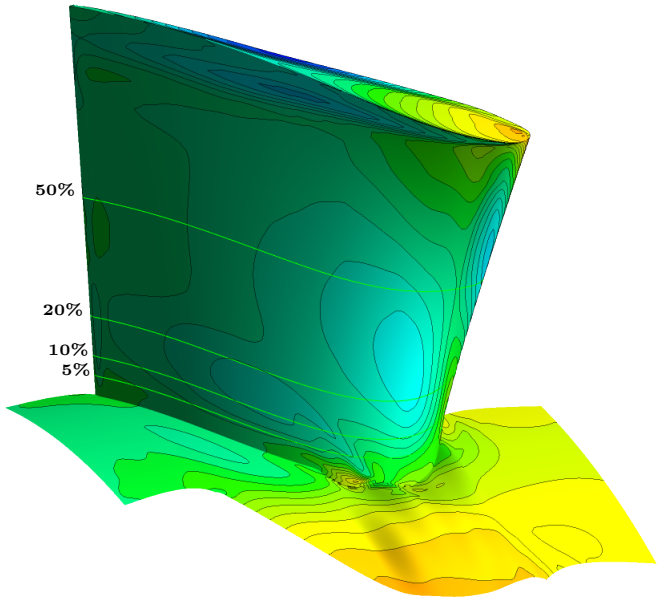

β_{dev}-based

Fig. 8.7: Blade loading profiles for the β_{dev}-based endwall

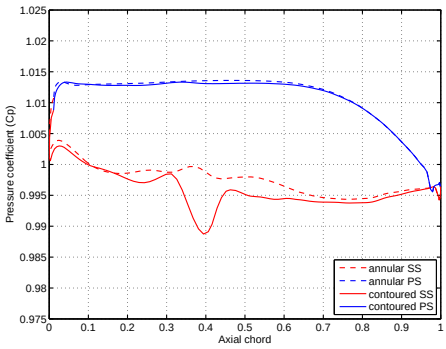

(a) 5% span

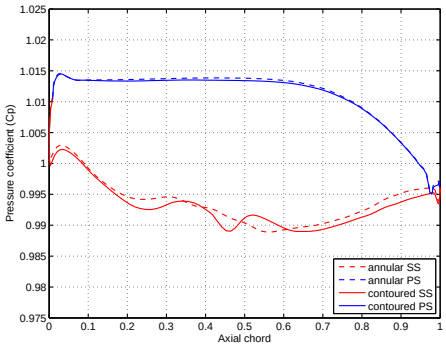

(b) 10% span

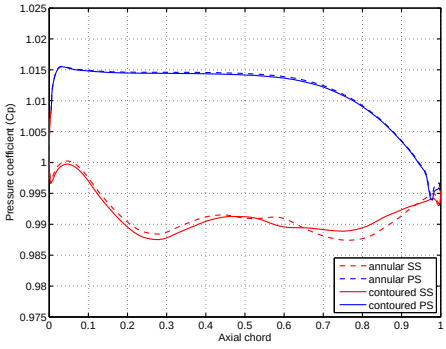

(c) 20% span

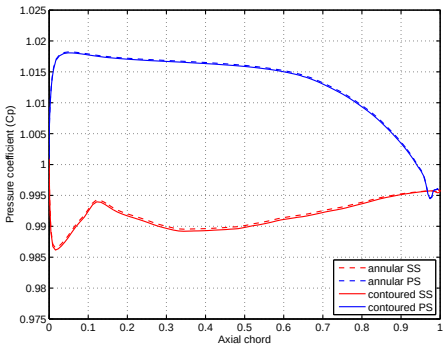

(d) 50% span

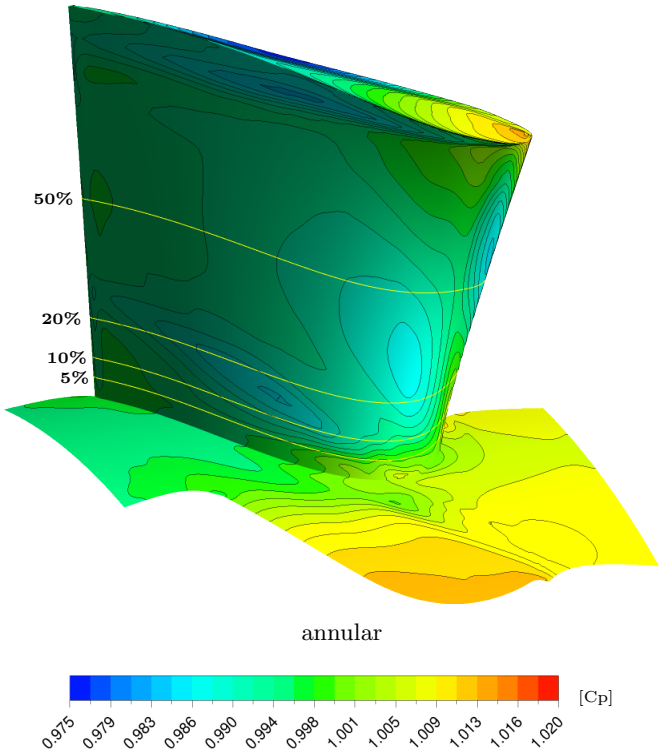

annular

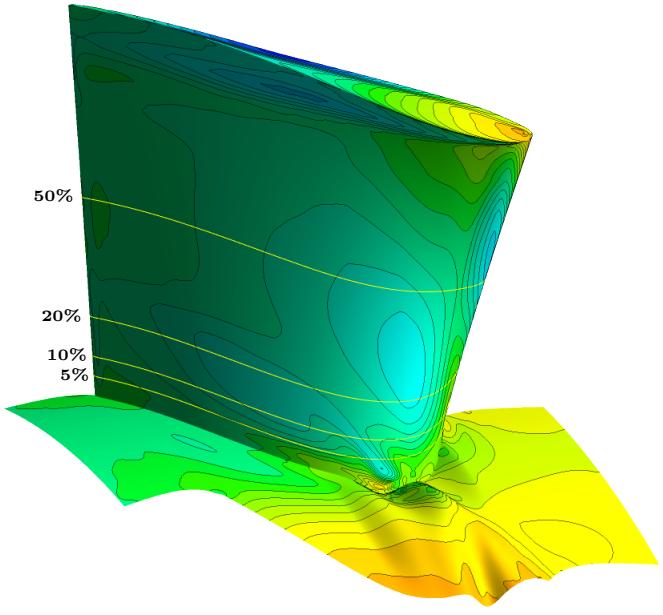

$SKEH$-based

Fig. 8.8: Blade loading profiles for the $SKEH$-based endwall

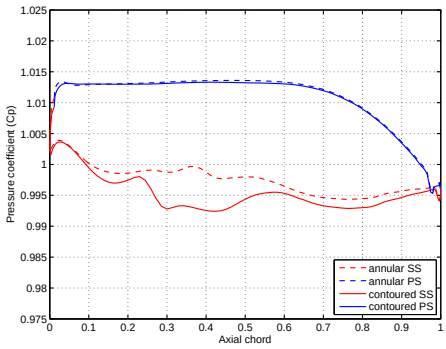

(a) 5% span

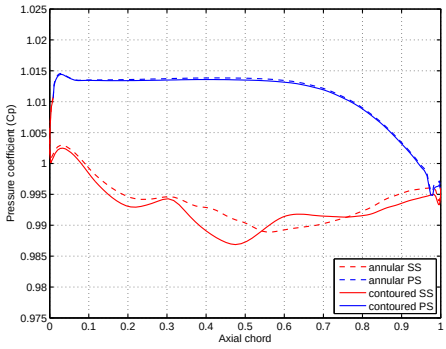

(b) 10% span

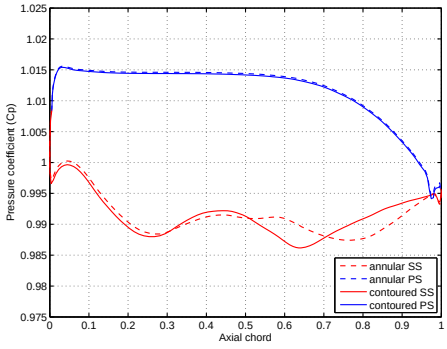

(c) 20% span

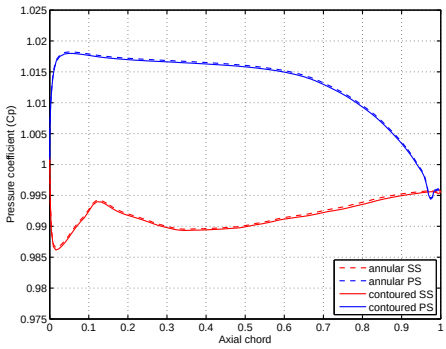

(d) 50% span

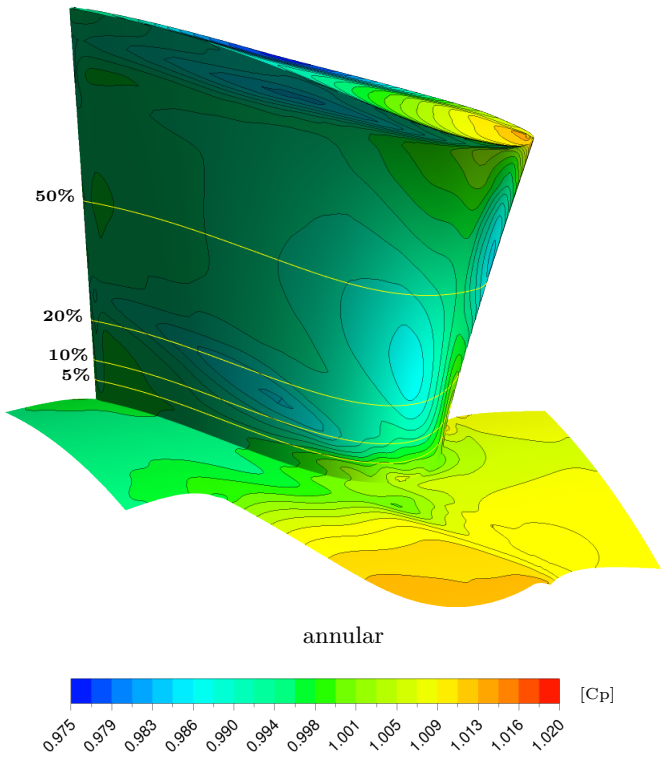

annular

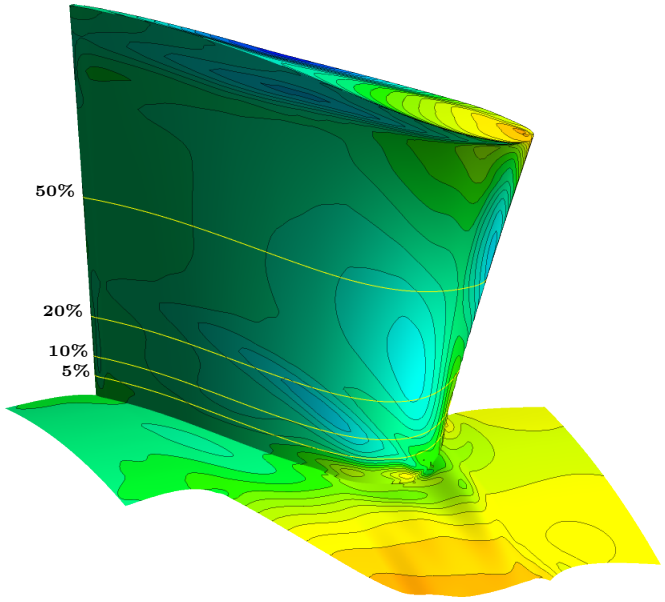

η_{de}-based

Fig. 8.9: Blade loading profiles for the η_{de}-based endwall

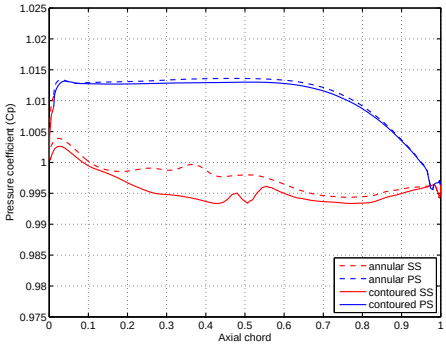

(a) 5% span

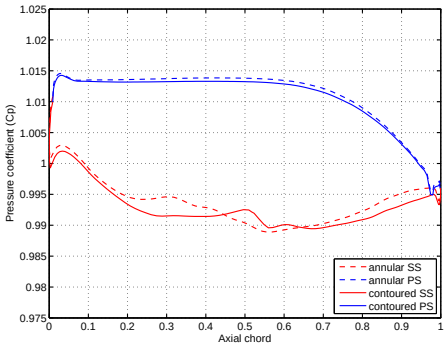

(b) 10% span

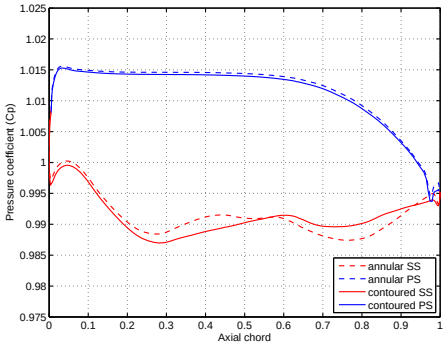

(c) 20% span

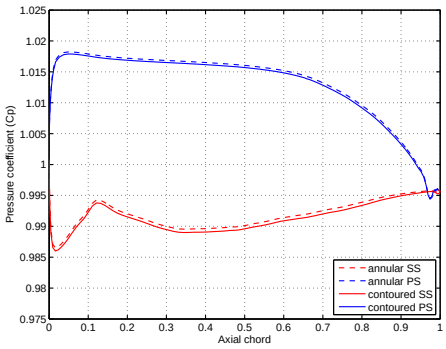

(d) 50% span

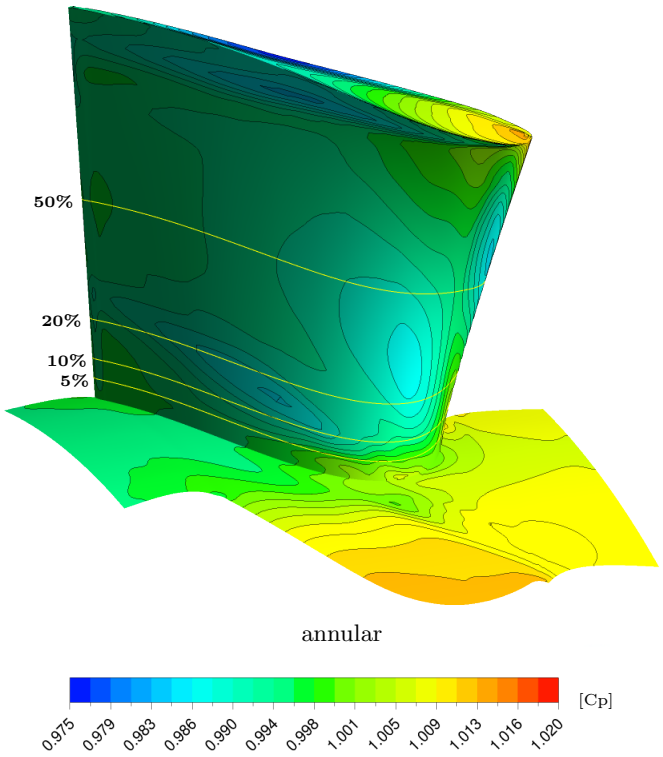

annular

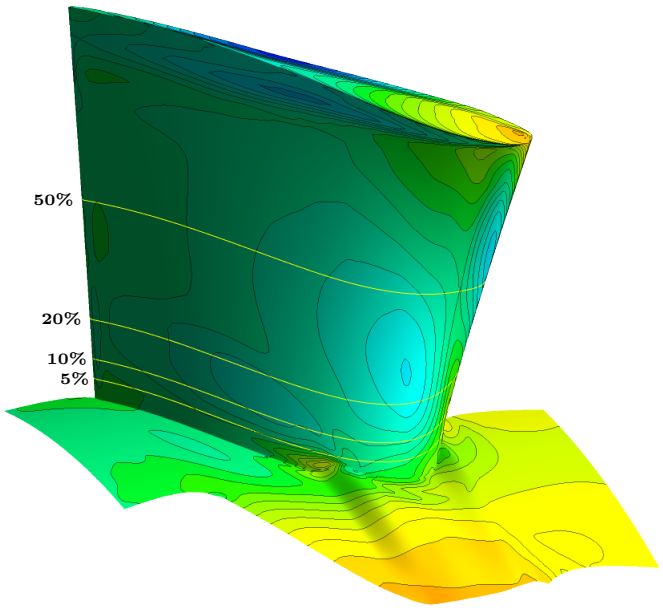

$C_{ske,1} + \beta_{dev,0.7}$-based

Fig. 8.10: Blade loading profiles for the $C_{ske,1} + \beta_{dev,0.7}$-based endwall

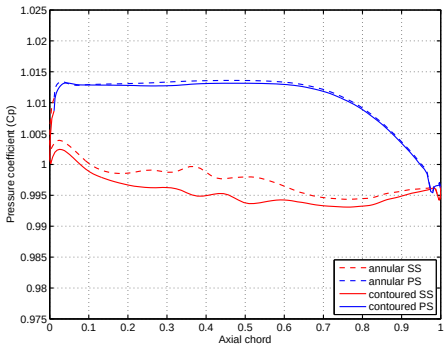

(a) 5% span

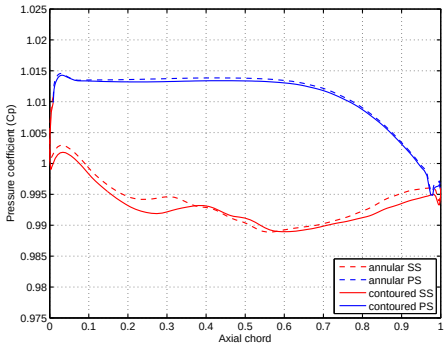

(b) 10% span

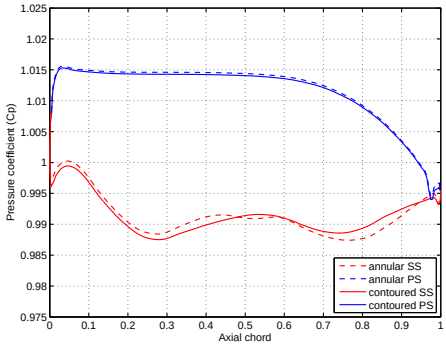

(c) 20% span

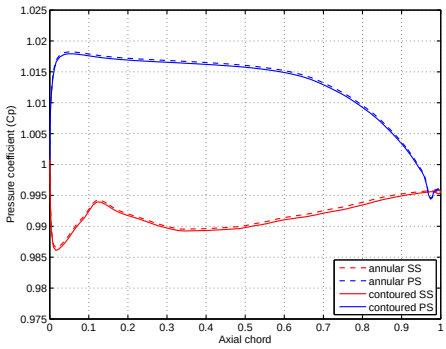

(d) 50% span

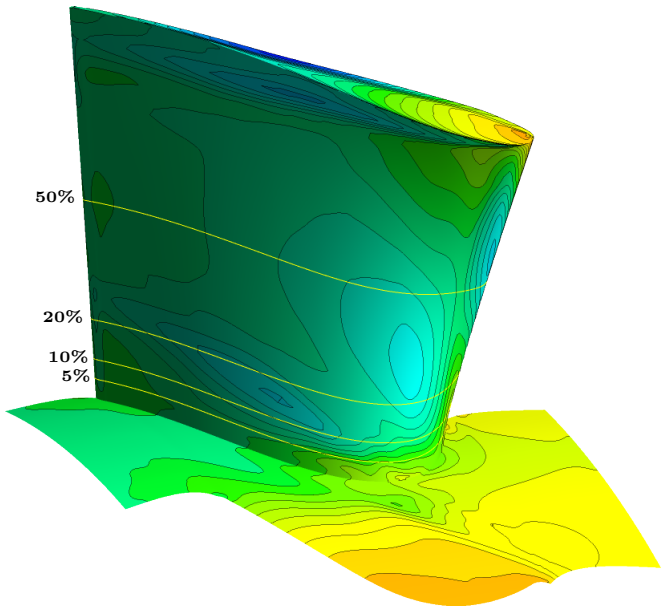

annular

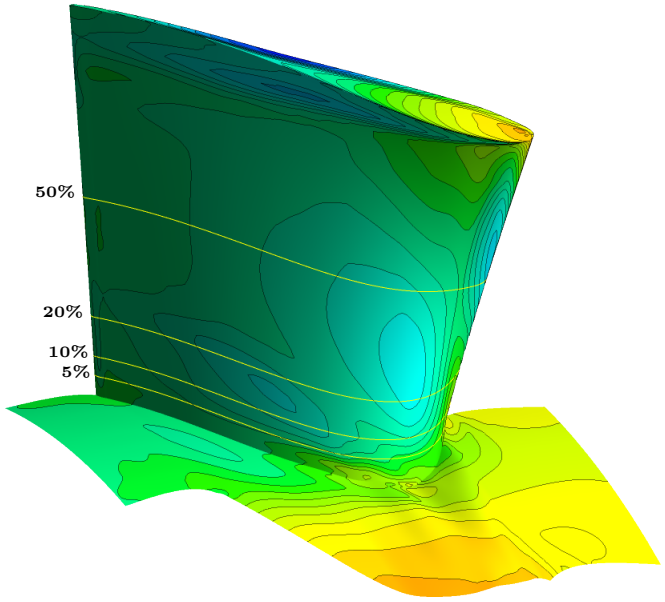

$C_{p0,rel,1} + \beta_{dev,0.7}$-based

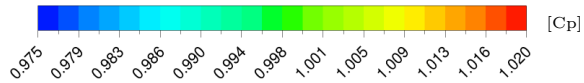

Fig. 8.11: Blade loading profiles for the $C_{p0,rel,1} + \beta_{dev,0.7}$-based endwall

8.3 Structure of the secondary flows

In this Section, the computed streamlines for the annular and contoured endwalls are presented (Figs. 8.13 - 8.19). For each case, both the surface limiting (i.e. oilflow) as well as the 3-dimensional streamlines are shown. Further, in each figure, the streamlines were coloured according to their approximate origin, including:-

- **black** - the limiting surface streamlines, released from the endwall surface and calculated using the endwall surface shear stress (τ_{wall}),
- **red** - the endwall boundary layer flow, released from within the blade passage adjacent to the blade pressure surface,
- **gold** / **blue** - the suction / pressure side *HSV*'s, released from ahead of the blade leading edge and rotor inlet respectively.

Finally, the **green** coloured streamtubes seen in various of the plots, corresponded to the fluid released from the inner $\sim 1/5$ ($\sim$ 0.4mm) of the inlet boundary layer. Inspection of the streamlines calculated for each endwall design showed that the final locality of this fluid at the exit of the blade row depended on the details of the endwall contours and so this fluid was identified separately from the remainder of the inlet boundary layer fluid.

Annular

The limiting streamlines (Fig. 8.13a) for the annular case showed the familiar migrations of the endwall boundary layer fluid on the endwall surface well and in particular, the saddle point as well as detail of the separation line associated with the pressure side horseshoe. In addition, a further separation line closer to the inlet was also visible and was determined to be the so-called secondary horseshoe vortex discussed by Sabatino and Smith (2007) (see Fig. 2.8). After the migration of the boundary layer fluid across the blade passage, the point at which this fluid finally separated from the endwall surface is also clear.

The 3-dimensional streamlines associated with the above mentioned endwall flow are shown in Fig. 8.13b. In addition to the cross-passage flow, the separation of this fluid from the endwall and its subsequent migration up the suction surface of the adjacent blade was clear. In addition, in the figure, that a portion of the endwall flow which was actively convected into the passage vortex was also clear, where it was seen not to form part of the *core* of the passage vortex, but locate primarily on the outer periphery of the vortex.

The formation of the pressure and suction side horseshoe vortices was also clear (Fig. 8.13c), where it was immediately clear that the pressure side horseshoe vortex was formed primarily by fluid from the outer portion of the inlet boundary layer, and which was also seen to convect some of the inner boundary layer fluid into the passage vortex. For this case, the passage of the suction side horseshoe vortex around the blade leading edge and its subsequent 'orbiting' (as discussed by Sieverding and Van den Bosch (1983)) around the passage vortex structure was also visible. Finally, the last notable aspect of this flow was the convection of some of the inner boundary layer fluid *under* the passage vortex structure, a portion of which was then convected

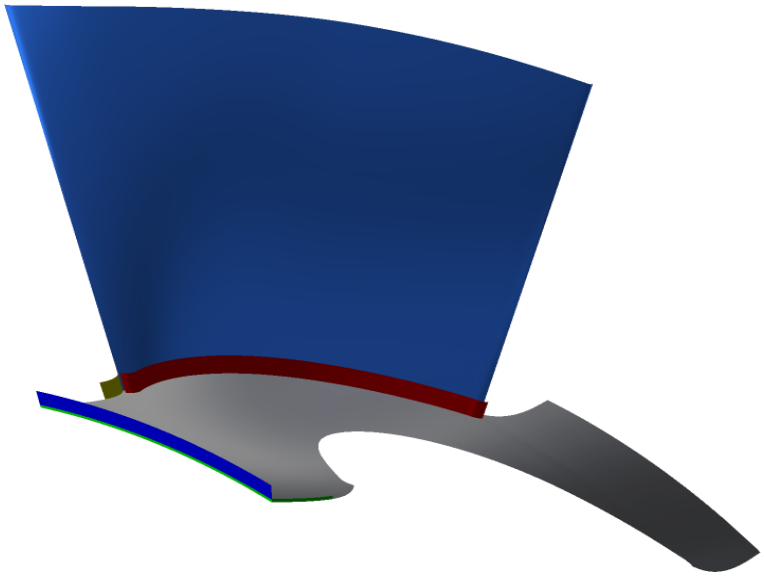

Fig. 8.12: Schematic showing approximate locations of streamline release surfaces (**red** - passage / pressure side endwall boundary layer fluid, **gold** - suction side horseshoe vortex, **blue** - inlet boundary layer fluid, **green** - inner inlet boundary layer fluid)

into the main passage vortex structure while the remainder was seen to be driven up the suction surface eventually exiting the passage near to the midspan and distinct from the passage vortex.

η_{tt}-based

When compared to the annular case, the effect of the endwall contouring in the η_{tt}-based design on the computed surface streamlines (Fig. 8.14a) was immediately clear. Most obviously, no evidence of the pressure side horseshoe vortex separation line is visible and instead, the majority of the boundary layer fluid from the vicinity of the leading edge was seen to migrate forward down the face of first contour, where it was then seen to join the suction side horseshoe vortex and flow around the leading edge to the suction side of the blade. Despite this, some of this leading edge fluid was also seen to migrate towards the blade pressure surface, where after an initial separation, it was seen to re-attach to the endwall surface and then migrate towards the adjacent blade's suction surface following a similar trajectory to the fluid of the passage boundary layer flow.

Within the blade passage, the majority of the endwall flow was seen to cross the passage in the usual way although this fluid was seen to separate from the endwall significantly earlier than what was predicted for the annular case. This separation persisted forward to a position approximately $\sim 20\%$ C_{ax} aft of the leading edge, where again unlike the annular case, it was seen to occur at an increased distance from the suction surface.

The 3-dimensional streamlines (Fig. 8.14b) told a similar story:-

- While the formation of the suction side horseshoe vortex was clear, on the pressure side of the blade, the fluid from the vicinity of the leading edge was seen to flow across the passage in an apparently attached fashion.

- Further to this, the separation of this flow some distance from the adjacent blades suction surface as well as its convection up the blade suction surface was also clear.
- Finally, the absence of any flow forward towards the blade row inlet within the passage (as was predicted in the vicinity of the pressure side *HSV* for the annular) was also clear.

The 3-dimensional streamlines of Fig. 8.14c for this case further compliment the results presented in Fig. 8.14a, as well as the discussion on the endwall static pressure distribution (discussed in Section 8.2.1):-

- In the immediate vicinity of the leading edge, the increased intensity of the suction side horseshoe vortex is evident, while on the pressure side, the pressure side flow is seen to be predominantly attached.
- Further, as a result of the increased strength of the suction side vortex, in this case the fluid of the inner inlet inner boundary layer was seen to convected almost completely *into* the suction side horseshoe vortex, rather than being convected up the suction suction external to the main vortex structure (as was the case for the annular design).
- Finally, further downstream in the passage, as a result of the absence of a well-formed pressure side horseshoe vortex, the entire resulting secondary flow system downstream of the midchord was predicted to be considerably more diffuse in nature in comparison to the annular case.

C_{ske}-based

Once again, the oilflow lines for the C_{ske}-based case (Fig. 8.15a) were largely identical to those discussed for the η_{tt}-based design, including:- a clear migration of the fluid near the blade leading edge towards the suction surface as well as the remaining pressure side flow staying attached to the endwall surface. However for the present case, the endwall flow within the contoured region appeared to be directed slightly further aft than was the case for the η_{tt}-based design.

In corroboration of the above, within the blade passage, the predicted 3-dimensional streamlines for the C_{ske}-based design (Fig. 8.15b) showed a more obviously aftwards orientated trajectory than was predicted for the η_{tt}-based case, as well as the clear development of a strengthened suction side horseshoe vortex near the blade leading edge as well as a distinct absence of the pressure side leg of the same vortex. The separation of the endwall flow as well as its subsequent migration up the suction surface of the adjacent blade was also clearly evident, although consistent with the increased aftwards orientation of the endwall flow, this was seen to occur further downstream than was noted for the η_{tt}-based case.

Finally, with respect to the horseshoe vortices (Fig. 8.15c) and overall secondary flow system (Fig. 8.15d), the increased strength of the suction side horseshoe vortex as well as predicted absence of the pressure side leg was clear, resulting in a significantly less intense set of secondary flow structures with a distinct absence of a well-formed passage vortex structure.

$C_{p0,rel}$-based

The computed oiflow streamlines for the $C_{p0,rel}$-based case are shown in Fig. 8.16a, and - as was the case for the computed endwall pressures - these showed a great deal of similarity to those already discussed for the annular case. More specifically, as was the case for the annular endwall and in contrast to the results discussed for the η_{tt}- & C_{ske}-based designs, the computed streamlines in the early part of the blade passage showed the clear migration of the fluid close to the blade pressure surface forward and towards the region in which the pressure side leg of the horseshoe vortex was seen to form for the annular case. In addition upon reaching the opposite side of the passage, the computed oilflow lines showed that this fluid was seen to separate from the endwall surface much closer to the adjacent blade's surface than was the case for either of the previous design (as was the case the annular endwall).

The 3-dimensional streamlines released from within the blade passage are shown in Fig. 8.16b, and these showed all the structures already noted for the annular case, although for the current case, in addition to the above, a small but well-defined corner vortex formed at intersection of the blade suction and endwall surfaces close to the ~ 50 C_{ax} chord position was also predicted. Finally, as a result of the increased strength of the pressure side horseshoe (and therefore subsequently the passage vortex), for the current case, the amount of endwall fluid originating from the endwall surface which was predicted to impinge upon and then migrate up the adjacent blade's suction surface, was considerably less than that noted for not only the two previous cases but also the annular case.

Fainlly, the streamlines of Fig. 8.16b showed a return to a suction side horseshoe vortex of reduced intensity, as well as the development of a pressure side horseshoe vortex of *increased* strength. As discussed above, while a significant portion of the inner inlet boundary layer was seen to be drawn into the passage vortex (as noted by the surface streamlines), some of this fluid was decoupled from the overall secondary flow system and driven up the suction surface of the adjacent blade. However, as a result of the increased intensity of the passage vortex, unlike the annular case, even this fluid was eventually drawn into the passage vortex structure and seen to exit the blade row as part of this vortex.

β_{dev}-based

The predicted oiflow and 3-dimensional streamlines for the β_{dev}-based design (Fig. 8.17) showed a large degree of similarity to the both the η_{tt}- & C_{ske}-based designs and therefore are not discussed in their entirety here. However, one distinct feature of this flow worthy of discussion was the deflection of a portion of the endwall migratory flow much closer to the suction surface of the adjacent blade. This feature was shown clearly by both the oilflow lines of Fig. 8.17a, where in contrast to the η_{tt}- & C_{ske}-based designs, in the aft portion of the passage, the endwall boundary layer flow was seen to migrate almost completely across the blade passage before impinging upon the adjacent blade's suction surface and separating from the endwall.

In addition to the above, the 3-dimensional streamlines of Fig. 8.17b also showed this feature clearly, where the fluid of the endwall boundary layer flow was clearly seen to impinge upon the suction surface of the adjacent blade and thereafter seen to form a small, but visible vortex

(which was then seen to migrate radially towards the midspan before leaving the passage at a radial height of $\sim 20 - 30\%$ span).

Finally, the computed streamlines of the inner and outer inlet boundary layer, as well as the suction side horseshoe vortex (Fig. 8.17c & 8.17d) showed that, although the bulk of the flow was similar to that already discussed for the η_{tt}- & C_{ske}-based designs, at the passage exit, the additional vortex discussed above remained noticeably more distinct from the remainder of the flow, resulting in a more complex secondary flow structure consisting of a more diffuse structure consisting predominantly of the fluid from the suction side horseshoe vortex (and inner inlet boundary layer) as well as the above mentioned additional vortex located above this fluid and closer to the midspan.

SKEH-based

The computed surface and 3-dimensional streamlines for the $SKEH$-based case are shown in Fig. 8.18. The complexity of the endwall makes the interpretation of the surface streamlines of Fig. 8.18a somewhat difficult, although the following details were clear:-

- The formation of a separation line in the vicinity of the suction side of the blade leading edge, corresponding to the formation of the suction side leg of the horseshoe vortex as well as the presence of an attached flow across the initial region of the entrance to the contoured region (in the vicinity of the usual pressure side leg of the horseshoe vortex).
- The flow of endwall fluid from each of the successive endwall 'humps' into the shared 'valley' (formed by *curve* 2) adjacent to the blade pressure surface, as well as a vortex separation line at the centre of this valley alluding to the formation of a strong clockwise rotating vortex within this valley. The surface streamlines associated with this vortical flow were seen to separate from the endwall surface some distance from the suction surface of the neighbouring blade.
- Aft of this region, the surface streamlines showed the migration of additional endwall fluid from the pressure side of the passage towards the neighbouring suction surface in the usual fashion, where this fluid was again seen to separate from the endwall surface itself.

The 3-dimensional streamlines initiated from within the blade passage (Fig. 8.18b) showed a similar picture, with the formation of the strengthened suction side horseshoe vortex ahead of the blade leading edge, as well as a high intensity vortex structure immediately adjacent to the blade pressure surface. Over the remainder of the passage endwall surface, the endwall boundary layer fluid was seen to migrate across the blade passage under the action of the cross-passage pressure gradient, whereupon it was seen to separate from the endwall surface and was convected into the aforementioned vortex. Finally, aft of the contoured region and consistent with the endwall oilflow lines for this region, the remainder of the endwall fluid was seen to be convected across the passage, separate and be convected up the adjacent blades suction surface.

The 3-dimensional streamlines associated with the suction side horseshoe vortex as well as the inlet boundary layer (Fig. 8.18c) again showed a strengthening of the suction side leg of the horseshoe vortex, but also a convection of a great deal of the inlet boundary layer fluid under

the suction side horseshoe vortex structure and into the vortex structure seen to originate close to the pressure surface discussed above. Finally, that portion of the the inlet boundary layer fluid which was not convected into the main vortex structure, was assimilated into the suction side horseshoe vortex, which was then seen to locate below the main vortex structure already discussed.

η_{de}-based

The surface streamlines for this case (Fig. 8.19a) showed a return to a less chaotic flow structure than was seen for the $SKEH$-based design and in addition to exhibiting a number of the elements of the majority of designs already discussed (such as the blocking of the pressure side horseshoe vortex, and enhancement of the suction side component), a number of elements specific to the this design only.

In particular, for the current design, over the majority of the blade passage, the endwall boundary layer flow was found to be more tangentially orientated than was for the majority of previous contoured cases, and this fluid was also seen to migrate significantly closer to the adjacent blade's suction surface before finally separating from the endwall surface. In addition and specific to only this design, in the early portion of the contoured region, the endwall flow aft of the 1^{st} endwall contour (i.e. *curve* 2) was seen to migrate not only across the blade passage, but also *towards* the rotor inlet, before finally separating from the endwall surface.

The forward migration of the endwall fluid discussed above was well illustrated by the 3-dimensional streamlines of Fig. 8.19b, where, after having crossed the blade passage, this fluid was seen to separate from the endwall and form a small, but intense vortex structure. Further to this, the remainder of the endwall fluid which was not drawn into this vortex, was seen to migrate across the blade passage in a predominantly tangential direction, before separating from the endwall and being convected up the suction surface of the adjacent blade.

As was the case for a number of the previous designs, the strengthening of the suction side horseshoe vortex was again clear from the streamlines of Fig. 8.19c although specific to this design only, this figure also showed the convection of the majority of the inlet (inner and outer) boundary layer fluid towards the suction surface of the adjacent blade, where it was seen to be entrained into larger vortex structure, the core of which was seen to be formed by the high intensity vortex core mention above.

$C_{ske,1} + \beta_{dev,0.7}$-based

The endwall surface streamlines of the $C_{ske,1} + \beta_{dev,0.7}$-based case (Fig. 8.15a) once again shared some of the similarities with those designs already discussed, including the increased flow around the leading edge of the blade and as well as the absence of the separation line associated with the formation and separation of the pressure side horseshoe vortex within the blade passage. In addition however, the predicted surface streamlines for the current design also showed a number of features specific to this design only, the most obvious of which was noted close to the exit of the contoured region.

In this area, a migration of a portion of the endwall flow almost completely across the endwall surface and with a slightly forward trajectory (in a fashion similar to that already described for the η_{de}-based design) was noted, although in this case, the flow was noted aft of the final (i.e. 4^{th}, *curve* 5) endwall control line rather than the first. As was noted for the η_{de}-based design, this feature corresponded to the presence of a large cross passage 'deflector' contour which was noted to extend completely across the blade passage and discussed previously in terms of the predicted endwall surface pressures and blade loadings (in Section 8.2.1 & 8.2.2). Finally, aft of this feature, the calculated oilflow lines for this endwall showed a return to the flow dynamics noted ahead of the so-called 'deflector' contour as well as aft of the contoured region for all of the designs discussed to date[2], with the separation of the endwall boundary layer fluid from the endwall surface at the junction of the endwall and suction surfaces some distance from the adjacent blade's suction surface, made clear by the reappearance of the separation line downstream of the contoured region.

An inspection of the 3-dimensional streamlines for this design (Fig. 8.20b) provided a great deal of addition context to the 2-dimensional plots, confirming the analysis provided above, and showing that this flow was associated with a portion of the endwall boundary layer fluid in the latter portion of the contoured region which was directed across the blade passage aft of the 'deflector' contour, and up the suction surface, separating only immediately adjacent to the suction surface itself. The formation of a corner vortex although small, was also confirmed immediately aft of this separation, consistent with the re-emergence of the endwall-suction surface separation line downstream of the contoured region.

The similarity of the current design to the majority of previous ones was once again demonstrated by the computed streamlines of the suction and pressure side horseshoe vortices (Fig. 8.20c) (which showed the strengthened of the suction side horseshoe vortex component and weakening of the pressure side component), however, distinct from the previous designs, the fluid of the suction side horseshoe vortex and outer inlet boundary layer seen to remain largely separate from one another, with the fluid of the inlet boundary layer seen to pass underneath that of the suction side leg before exiting the blade passage as two distinct flow features. Finally, as a result of the strengthened suction side leg of the horseshoe vortex, the majority of the inner inlet boundary layer was noted to be convected into the suction side leg of the horseshoe vortex and exit the blade passage with this feature.

$C_{p0,rel,1} + \beta_{dev,0.7}$-based

The computed surface and 3-dimensional streamlines for the $C_{p0,rel,1} + \beta_{dev,0.7}$-based design was somewhat more complex than was seen for the previous designs. The surface streamlines for the $C_{p0,rel,1} + \beta_{dev,0.7}$-based case (Fig. 8.21a) showed an increased degree of similarity to those of the η_{tt}- & C_{ske}-based endwalls than was noted for the previous (i.e. $C_{ske,1} + \beta_{dev,0.7}$-based) design. Once again, these streamlines suggested an enhanced flow of fluid around the blade leading edge towards the suction surface (suggesting a strengthened suction side leg of the horseshoe vortex) as well as an attached flow over the initial portion of the contoured region, corresponding to the location of the pressure side leg of the horseshoe vortex for the annular case. In contrast to the

[2] With the exception of the $C_{p0,rel}$-based design

detailed dynamics of the η_{tt}-, C_{ske}- as well as the $C_{ske,1} + \beta_{dev,0.7}$-based endwalls however, for the current design the fluid of the inner inlet boundary layer was seen to be divided between the suction side leg of the horseshoe vortex, as well as a portion which was seen to be driven underneath the main secondary flow structures and up the early part of the blade suction surface. In this way then, this design showed some similarity to aspects of both the annular as well as the $C_{p0,rel}$-based endwall which was not apparent at all in the η_{tt}-, C_{ske}- & $C_{ske,1} + \beta_{dev,0.7}$-based designs.

The 3-dimensional streamlines of Fig. 8.21b and 8.21c confirmed this view:- a general absence of the pressure side leg of the horseshoe vortex and a strengthening of the suction side leg of the vortex was clear, as was the case for the η_{tt}-, C_{ske} & $C_{ske,1} + \beta_{dev,0.7}$-based designs, while as was the case only for the $C_{ske,1} + \beta_{dev,0.7}$-based design, the components of the overall secondary flow system appeared to be decoupled from one another resulting in two distinct structures at the exit of the blade passage, with the fluid of the inlet boundary layer shared between both of these groups.

Summary

In summary, the following general points were noted in relation to the detailed structure of the flow within each blade passage for each design:-

- For **all** the contoured designs (with the exception of the $C_{p0,rel}$-based case), among the primary effects of the endwall contouring, was an enhancement of the flow towards the suction side of the blade surface and a corresponding increase in the intensity of the suction side leg of the horseshoe vortex, as well as a disruption in the formation of the pressure side leg of the vortex.
  - Further, for these endwalls, the increased suction side vortex resulted in the earlier separation of the inner inlet boundary layer in the vicinity of the blade leading edge, and its convection into the suction side horseshoe vortex structure.
- For the $\boldsymbol{\eta_{tt}-}$ & $\mathbf{C_{ske}-based}$ designs, the endwall migratory flow in the early part of the blade passage was directed further aft as a result of the endwall contouring, while further aft in the passage, the flow remained largely unchanged from the annular case, resulting in a overall secondary flow system of reduced intensity and with a more diffuse character.
- In contrast, once again, the $\mathbf{C_{p0,rel}-based}$ design showed considerable similarities to the annular design including:- a decrease in the flow of the suction side horseshoe vortex around the blade leading edge; a clear enhancement of the formation of the pressure side leg of the horseshoe vortex; a clear increase in the strength in the impingement of the fluid of the inner inlet boundary layer against the suction surface, as well as the separation and migration of this fluid up the blade. Together, these effects resulted in an overall strengthening of the secondary flow system, to the point where even the additional inner inlet boundary layer fluid, which for the annular case was seen to migrate up the blade suction surface, was seen to be convected into the passage vortex structure.
- While the predicted streamlines for the $\boldsymbol{\beta_{dev}-based}$ design showed a considerable degree of similarity not only to the η_{tt}- & C_{ske}-based designs, specifically for this design, a portion of the

endwall migratory flow was noted to be directed underneath the main secondary flow structures and thereafter against the blade suction surface, resulting in a decoupling of these flow structures and the emergence of two distinct flow structures from the blade passage at the rotor exit. While this effect did not appear to be as distinct as that recorded for the $C_{ske,1} + \beta_{dev,0.7}$-based case, the decoupling between the vortices is clear both in the streamlines as well as the inflection points noted in the rotor exit flow angles reported previously.

- Although the predicted streamlines for the $\mathbf{SKEH - based}$ design were noted to be extremely complex, the following details were clearly discernible from the surface as well as the 3-dimensional streamlines, including:-
  - the strengthening of suction side horseshoe vortex, and
  - the formation of a large 'bespoke' vortex within the blade passage, originating from within the 'valley' structure close to the blade pressure surface.
- Once again, the $\boldsymbol{\eta_{de} - based}$ flow showed a return to a less chaotic flow structure within the blade passage, where in addition to a strengthened suction side horseshoe vortex flow, the endwall boundary layer fluid in the early portion of the contoured region was seen to migrate across the blade passage behind the first endwall contour and in the general direction of the adjacent blade's leading edge. At the suction surface, this fluid was seen to separate from the endwall, forming a small but intense vortex, which was then seen to form the core of a custom vortex structure. This vortex was then later seen to draw in a relatively large portion of the inlet boundary layer fluid from both the inner and outlet portions of the boundary layer, before exiting the blade row.
- In addition to the flow elements noted for the η_{tt} & C_{ske}-based designs, the streamlines for the $\mathbf{C_{ske,1} + \beta_{dev,0.7} - based}$ design also showed some similarity to the β_{dev}-based design, with the diversion of a portion of the endwall migratory flow towards the suction surface of the adjacent blade at the exit of the contoured region. As was the case for the β_{dev}-based design, the net result of this diversion was the deflection of the majority of the deflected endwall fluid underneath the suction side horseshoe vortex leg, decoupling the endwall flow from that of the remaining secondary flow components, and resulting in the emergence of a pair of vortices from the blade passage at the passage exit.
- Finally, the streamlines for the $\mathbf{C_{p0,rel,1} + \beta_{dev,0.7} - based}$ design showed a distinct departure from those of the original $C_{p0,rel}$-based design, with the predicted streamlines indicating a clear return to the flow structures noted for the η_{tt} & C_{ske}-based designs. This included an enhanced flow around the leading of the blade towards the suction surface, as well as a reduction in the formation of the pressure side horseshoe vortex. For the present case however, unlike the previous designs, the incoming fluid was again divided between two main flow structures:- the first comprised primarily of the suction side horseshoe vortex, and the second comprising of fluid from the former pressure side horseshoe vortex and the fluid of the endwall migratory flow. Unlike the $C_{ske,1} + \beta_{dev,0.7}$-based case, the fluid of the inner inlet boundary layer was divided between the two main flow structures.

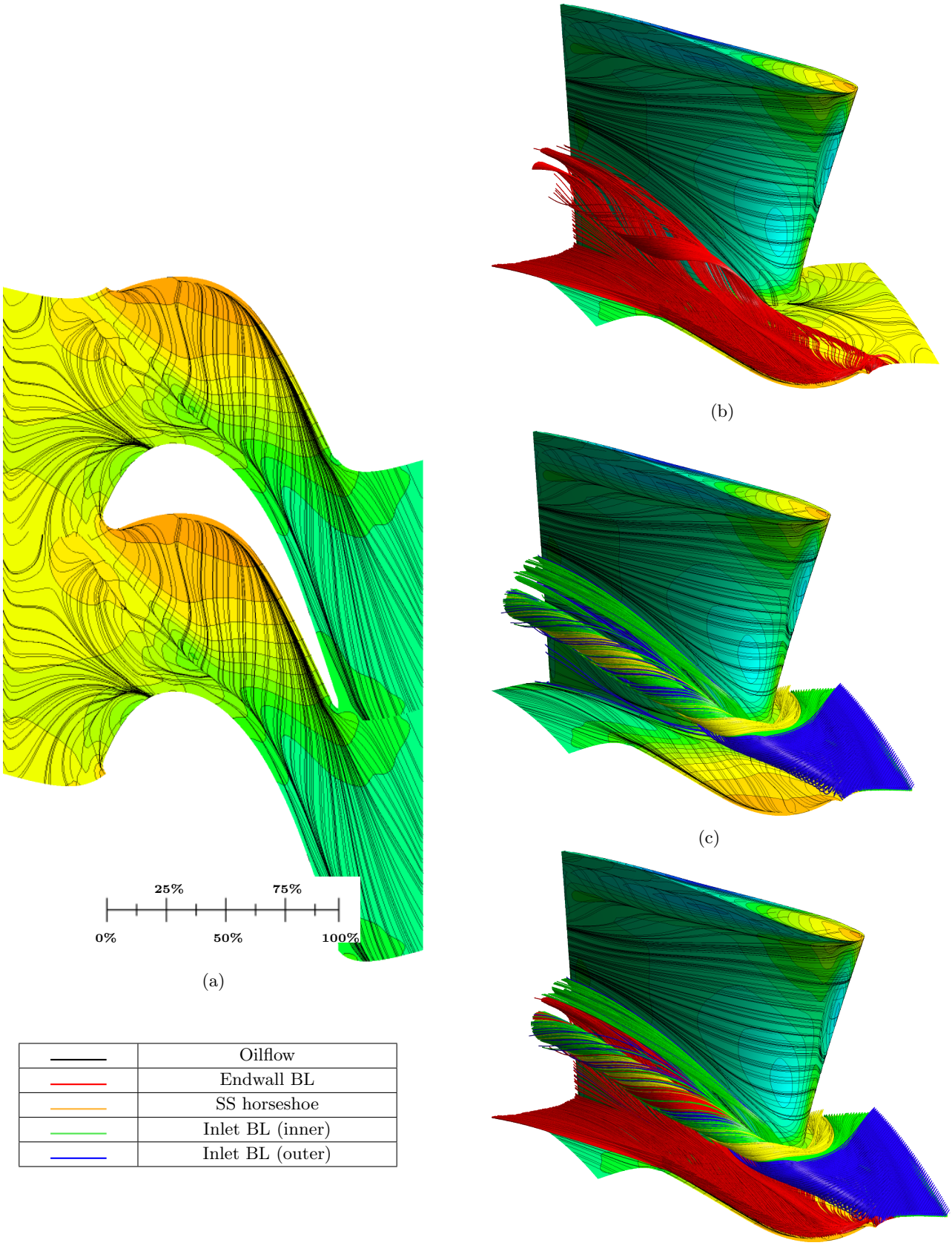

Fig. 8.13: Calculated (a) oilflow, (b) endwall boundary layer flow, (c) suction / pressure side horseshoe vortices and (d) complete secondary flow streamlines for annular design

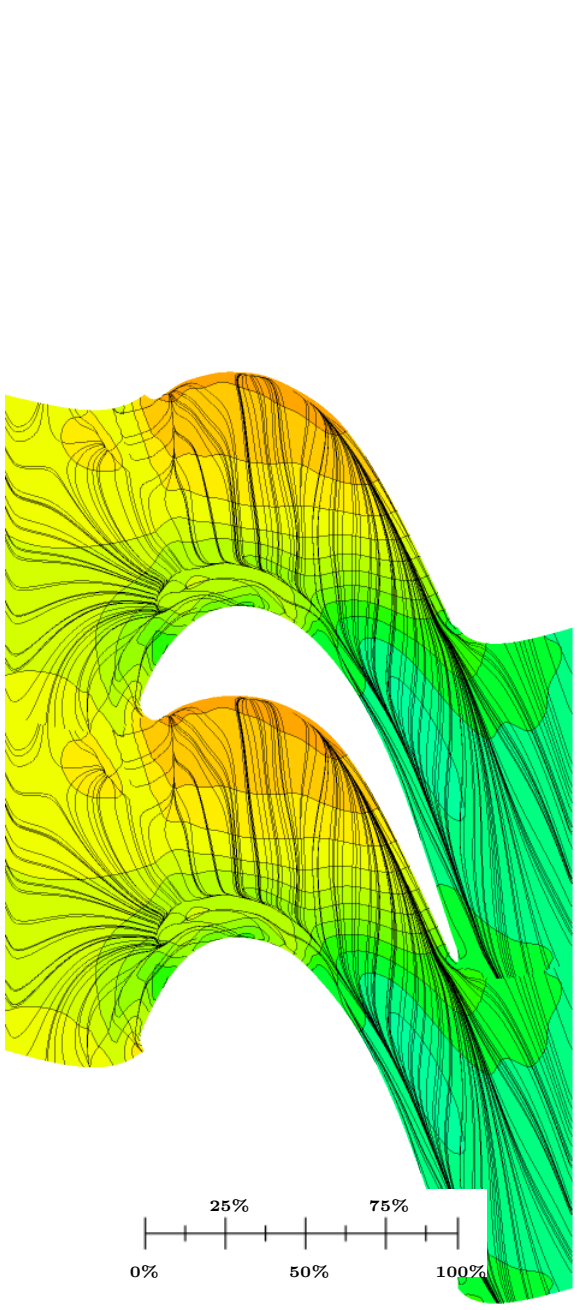

(a)

	Oilflow
	Endwall BL
	SS horseshoe
	Inlet BL (inner)
	Inlet BL (outer)

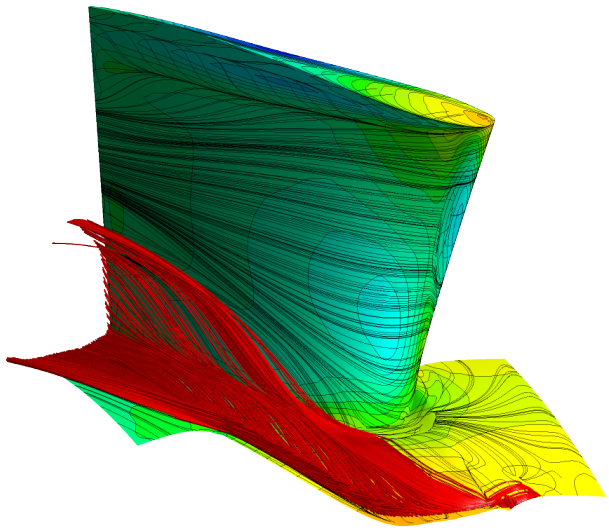

(b)

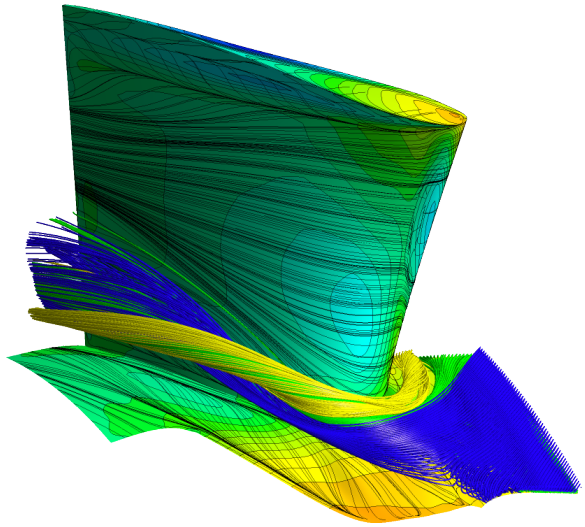

(c)

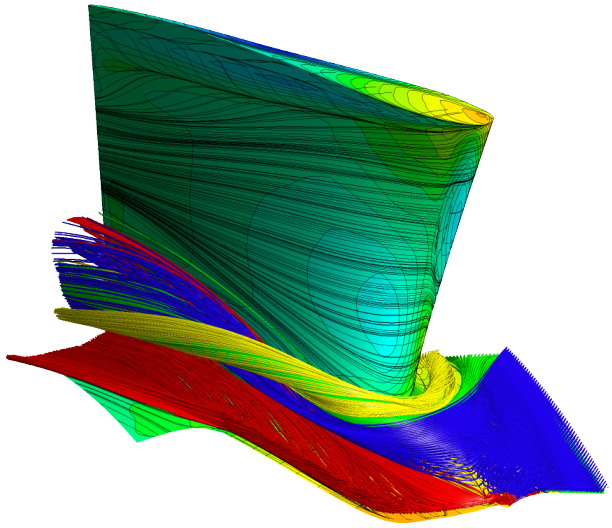

(d)

Fig. 8.14: Calculated (a) oilflow, (b) endwall boundary layer flow, (c) suction / pressure side horseshoe vortices and (d) complete secondary flow streamlines for η_{tt}-based design

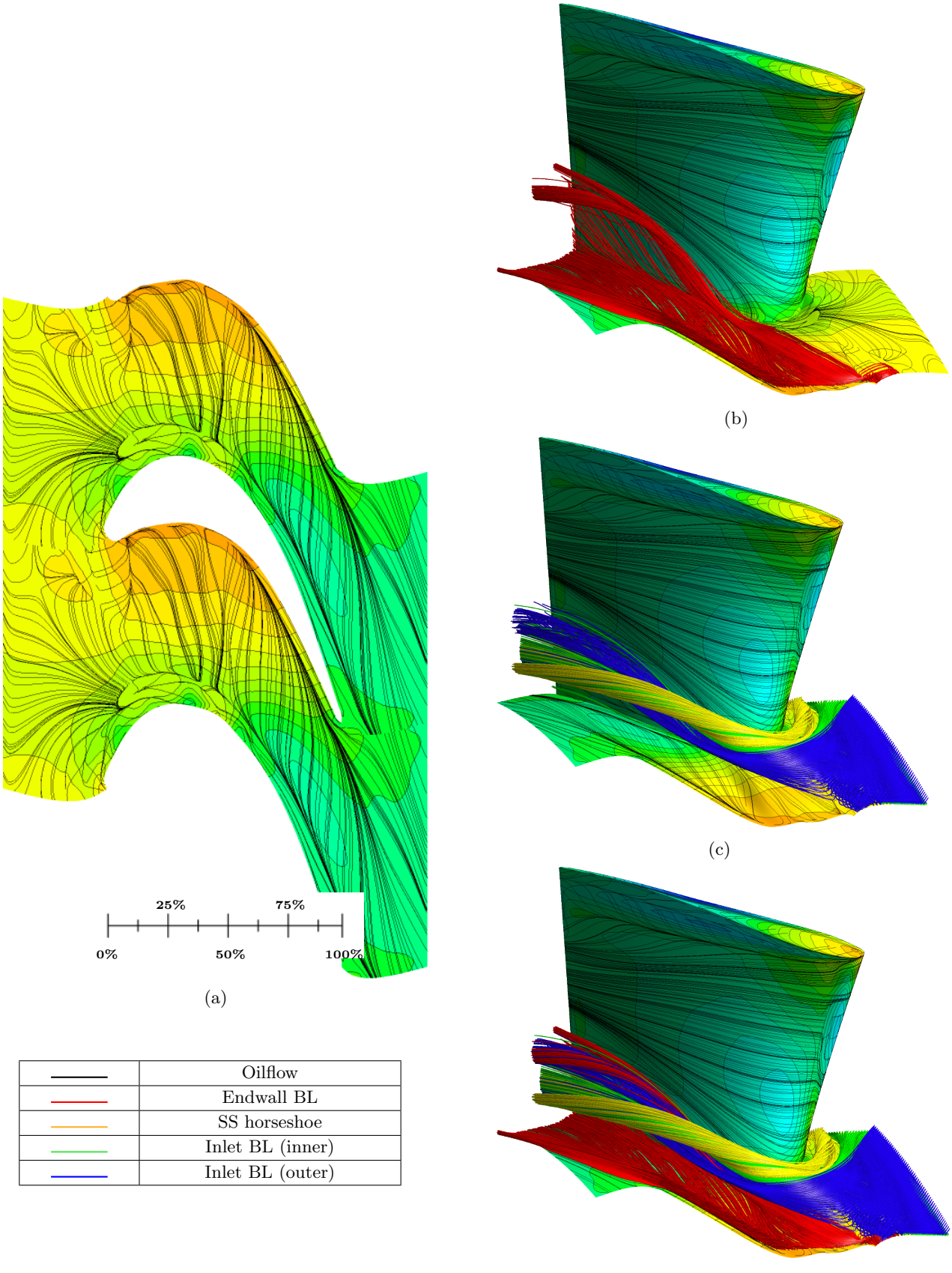

Fig. 8.15: Calculated (a) oilflow, (b) endwall boundary layer flow, (c) suction / pressure side horseshoe vortices and (d) complete secondary flow streamlines for C_{ske}-based design

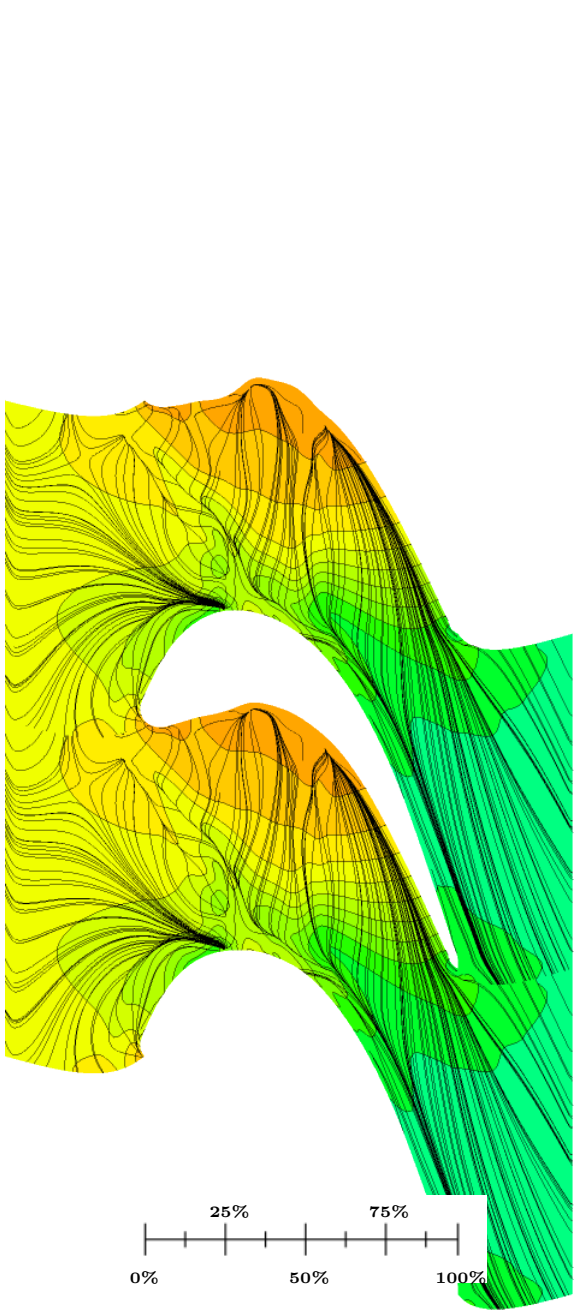

(a)

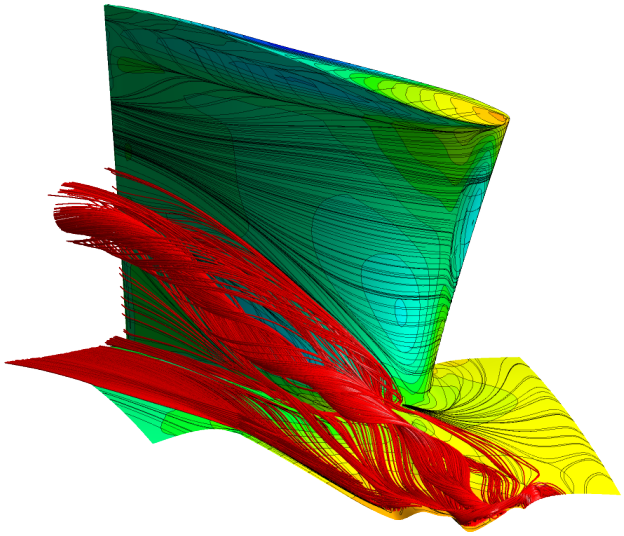

(b)

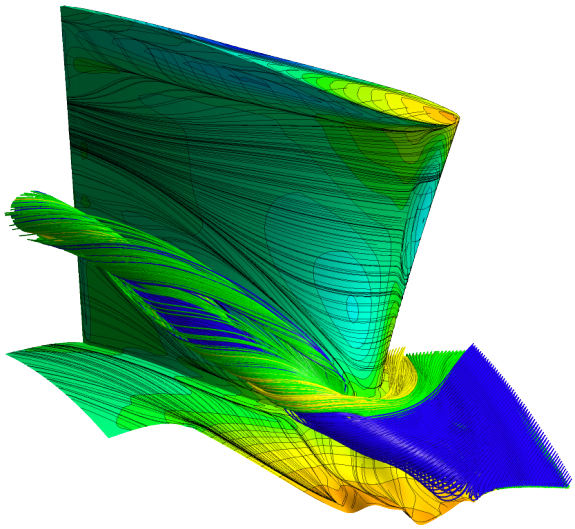

(c)

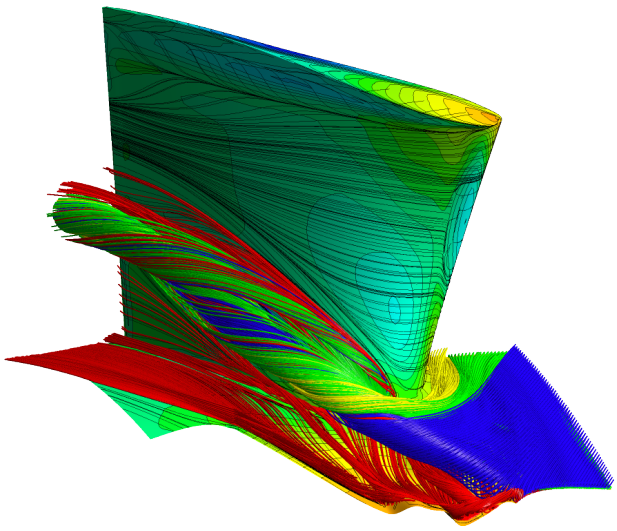

(d)

	Oilflow
	Endwall BL
	SS horseshoe
	Inlet BL (inner)
	Inlet BL (outer)

Fig. 8.16: Calculated (a) oilflow, (b) endwall boundary layer flow, (c) suction / pressure side horseshoe vortices and (d) complete secondary flow streamlines for $C_{p0,rel}$-based design

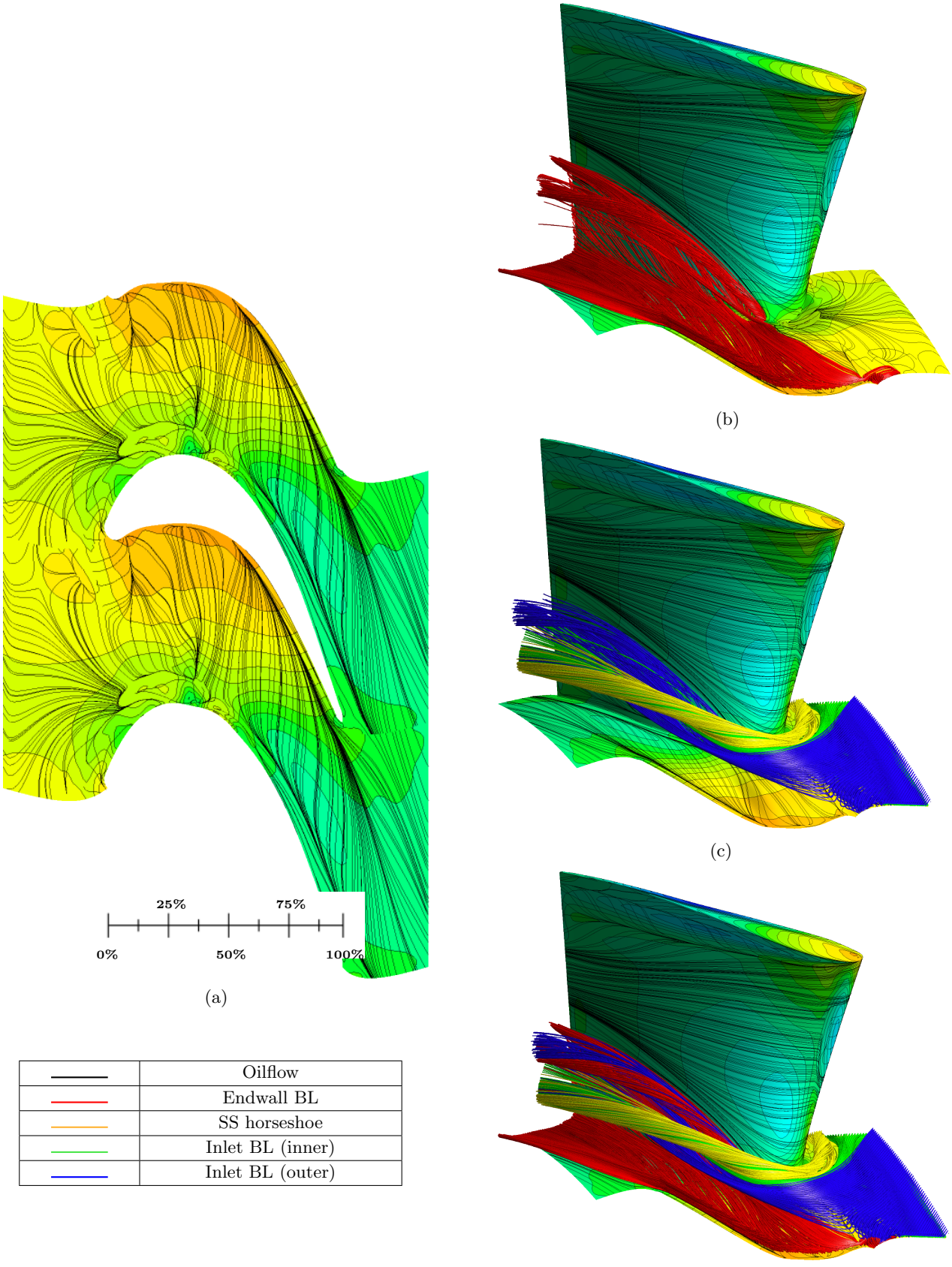

Fig. 8.17: Calculated (a) oilflow, (b) endwall boundary layer flow, (c) suction / pressure side horseshoe vortices and (d) complete secondary flow streamlines for β_{dev}-based design

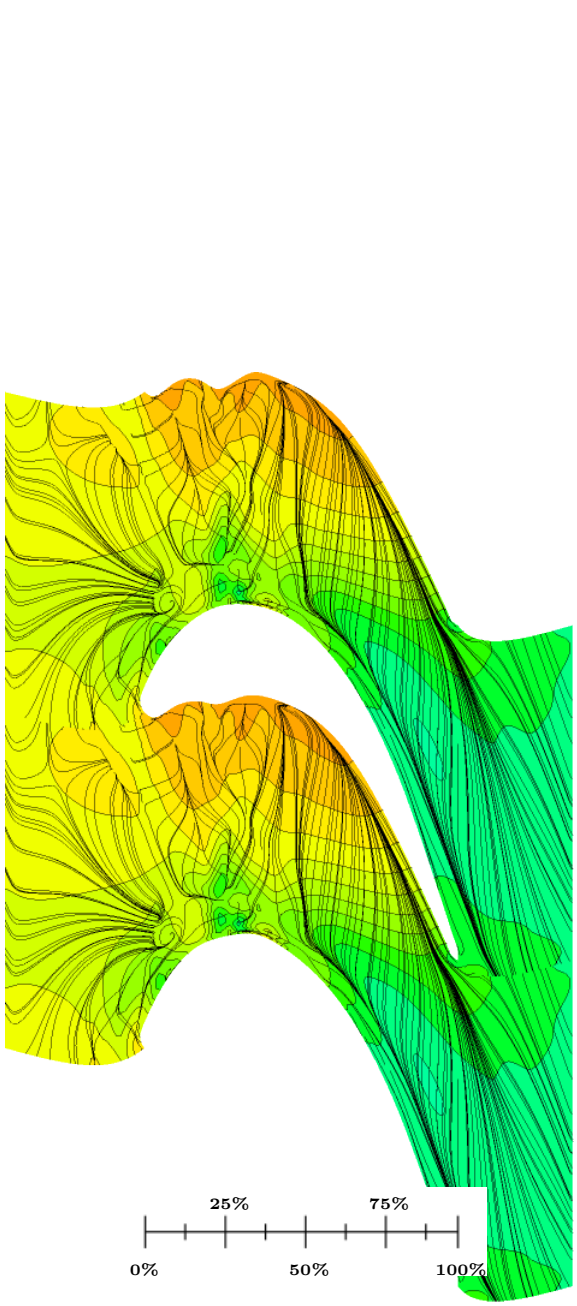

(a)

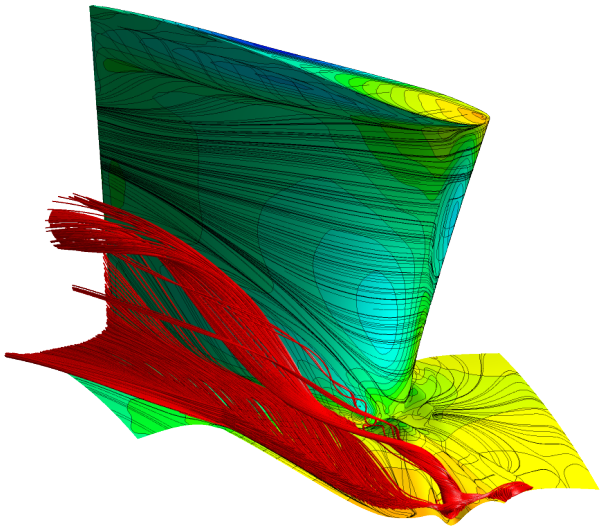

(b)

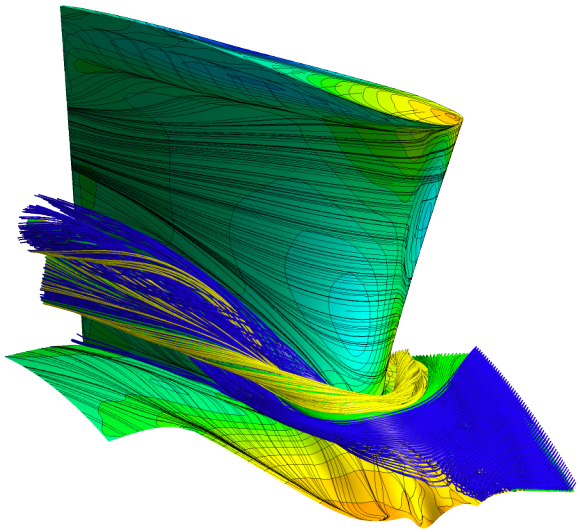

(c)

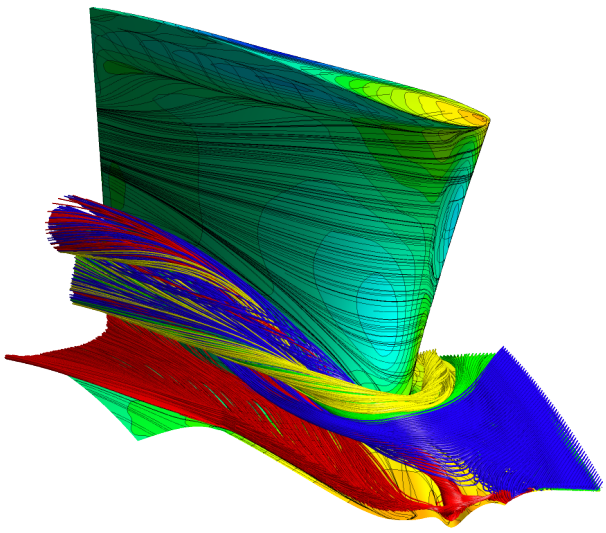

(d)

	Oilflow
	Endwall BL
	SS horseshoe
	Inlet BL (inner)
	Inlet BL (outer)

Fig. 8.18: Calculated (a) oilflow, (b) endwall boundary layer flow, (c) suction / pressure side horseshoe vortices and (d) complete secondary flow streamlines for $SKEH$-based design

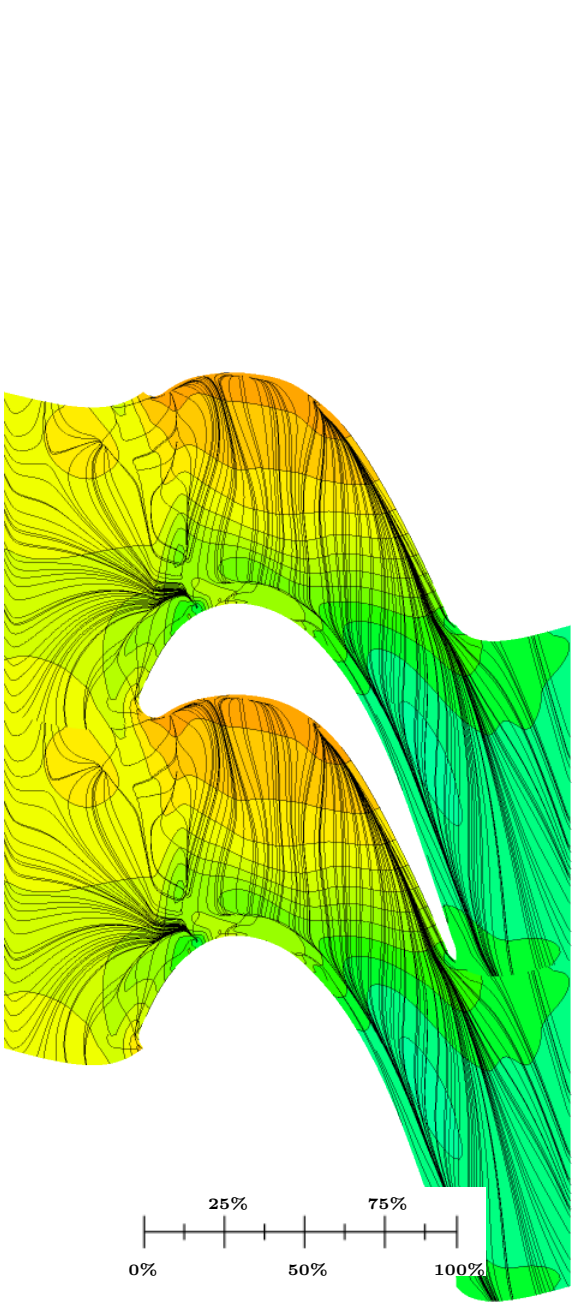

(a)

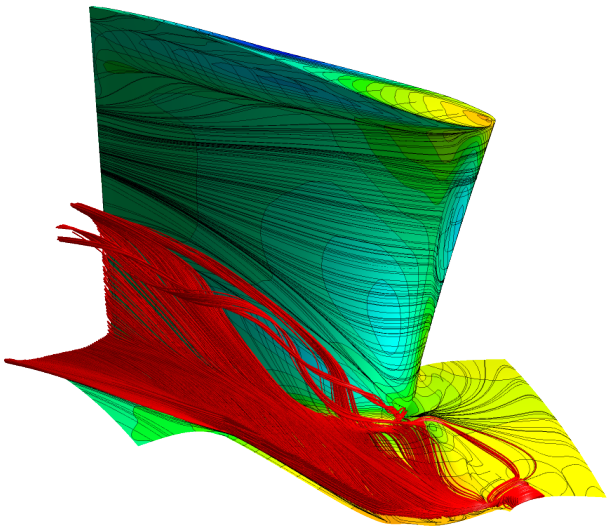

(b)

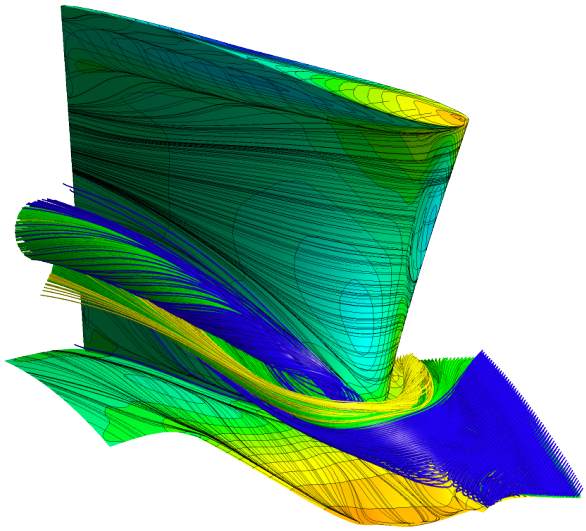

(c)

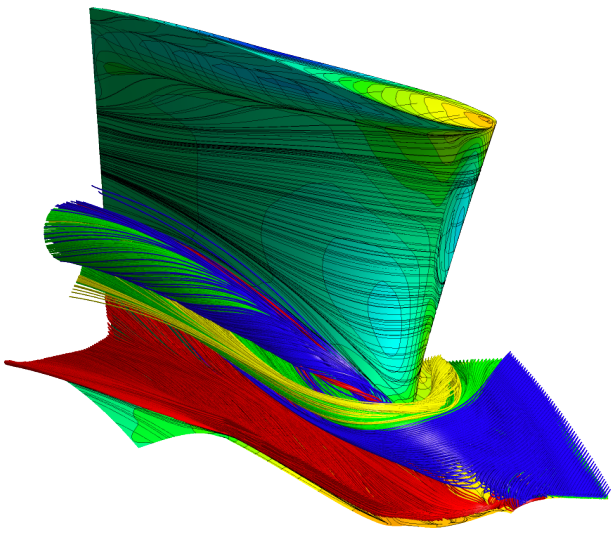

(d)

	Oilflow
	Endwall BL
	SS horseshoe
	Inlet BL (inner)
	Inlet BL (outer)

Fig. 8.19: Calculated (a) oilflow, (b) endwall boundary layer flow, (c) suction / pressure side horseshoe vortices and (d) complete secondary flow streamlines for η_{de}-based design

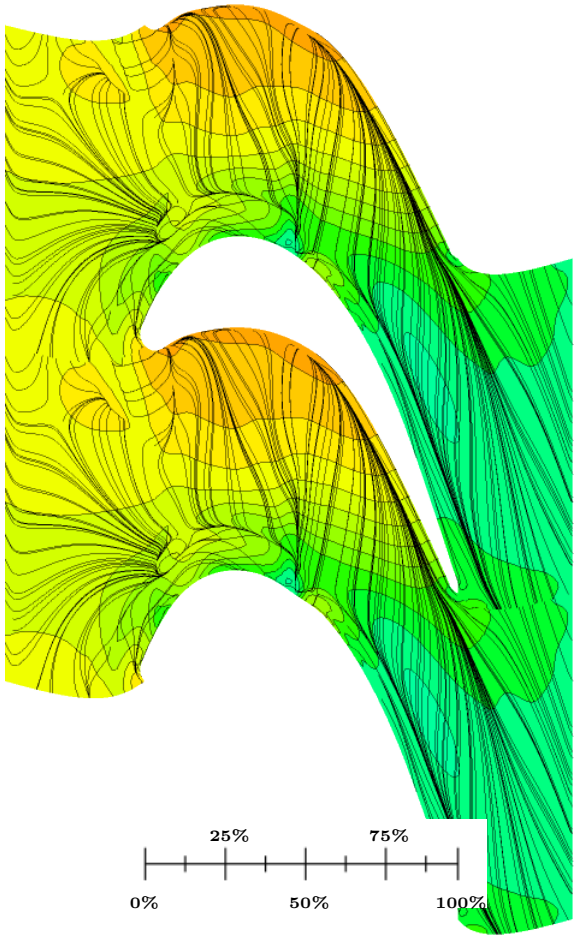

(a)

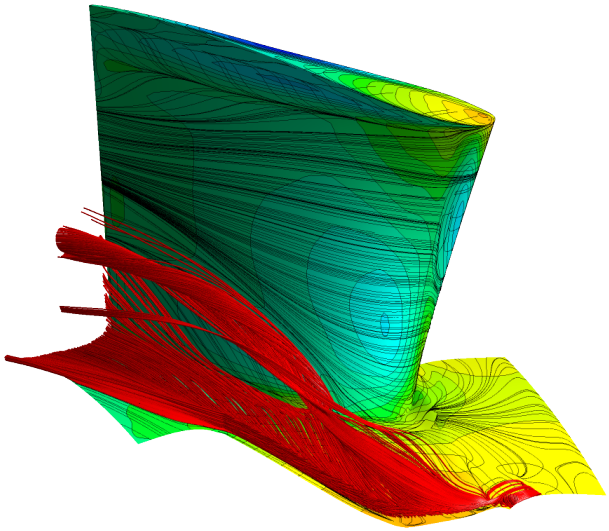

(b)

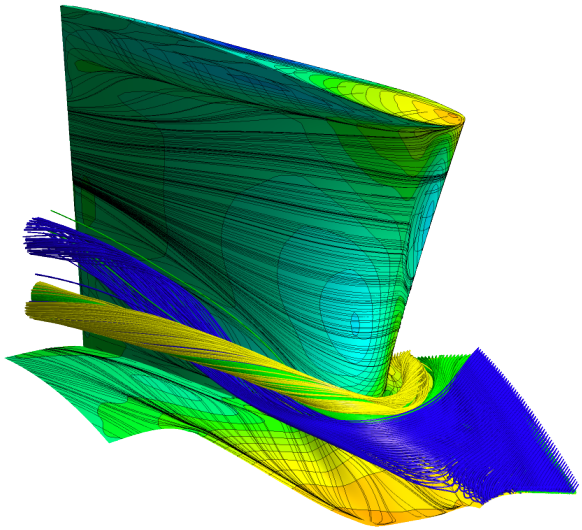

(c)

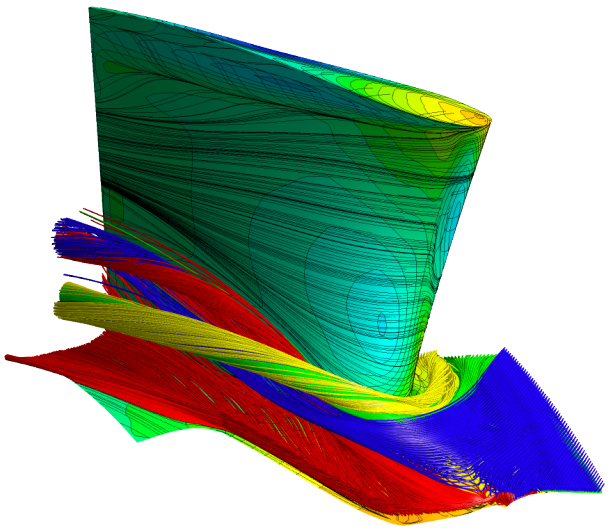

(d)

	Oilflow
	Endwall BL
	SS horseshoe
	Inlet BL (inner)
	Inlet BL (outer)

Fig. 8.20: Calculated (a) oilflow, (b) endwall boundary layer flow, (c) suction / pressure side horseshoe vortices and (d) complete secondary flow streamlines for $C_{ske,1} + \beta_{dev,0.7}$-based design

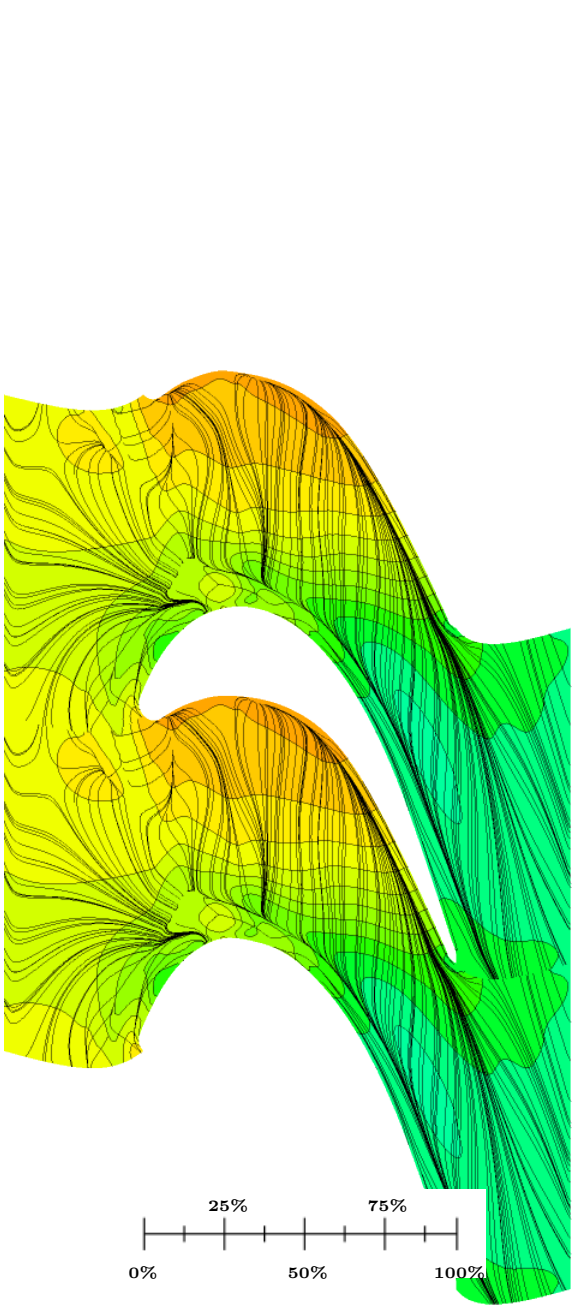

(a)

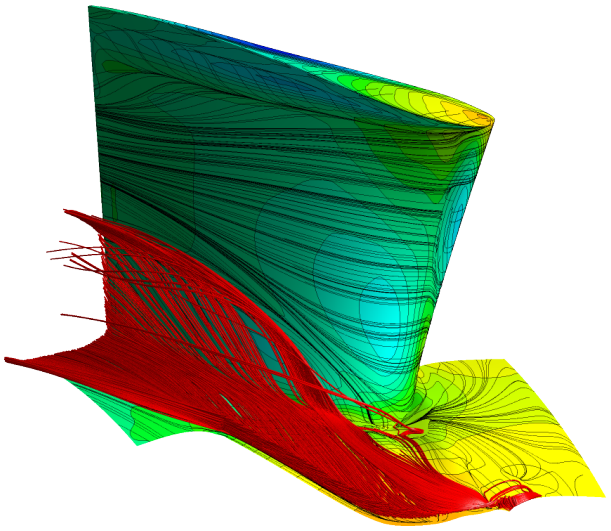

(b)

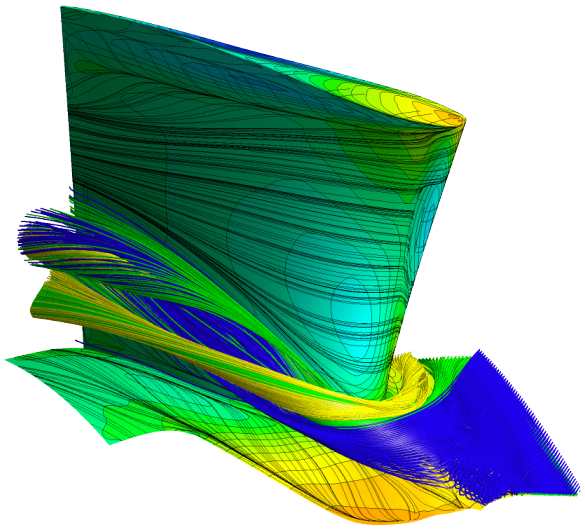

(c)

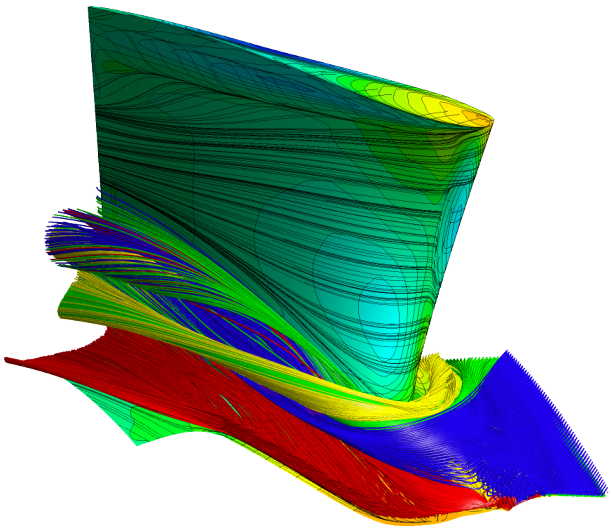

(d)

	Oilflow
	Endwall BL
	SS horseshoe
	Inlet BL (inner)
	Inlet BL (outer)

Fig. 8.21: Calculated (a) oilflow, (b) endwall boundary layer flow, (c) suction / pressure side horseshoe vortices and (d) complete secondary flow streamlines for $C_{p0,rel,1} + \beta_{dev,0.7}$-based design

8.4 Loss generation

As discussed by Denton (1993), the only real sources of loss within a turbine flow are the irreversibilities within the fluid itself, primarily because of the relatively short residence time of the fluid within the turbine and the resulting adiabatic nature of the flow.

Figs. 8.23 - 8.29 show the calculated entropy (loss) generation rates ($\dot{s}_{gen}$) and wall shear stresses (τ_{wall}) for the rotor blade passage of each endwall design. In addition, Fig. 8.22a show the mass-averaged entropy generation rates at the rotor inlet, within the blade row (corresponding to the planes on which the contours are plotted in Figs. 8.23 - 8.29 respectively), while Fig. 8.22b shows the mass-averaged changes in the calculated entropy generation rates from the annular case for each endwall. The entropy generation rates for each figure were calculated using an equivalent approach to that of Denton and Pullan (2012) (although were not presented here in their non-dimensionalised form) using a user defined function (written in the 'C'-programming language) and computed by running an additional 50 iterations of the CFD solver on the converged solution for each final endwall at the conclusion of each optimization run. As indicated by Denton and Pullan (2012), although in low speed flows, the entropy generation is dominated by the viscous ($\dot{s}_v$) component, in the results presented, contributions from both terms (i.e. the viscous ($\dot{s}_v$) as well as thermal dissipation ($\dot{s}_t$)) from the entropy generation equation were included.

Overview and annular case

Although, given the documented difficulties in the prediction of loss by CFD, it was not expected that the entropy generation rates calculated and presented in this section were not expected to the without error, it *was* felt some insight into the dynamics of each endwall could be gained from this analysis, and so it is included for that reason and should be viewed from a qualitative viewpoint.

- **X2** (**inlet**) - at the rotor inlet, the loss generation rates for **all** of the endwalls was largely identical. This is expected since it investigations of the endwall contouring on the downstream (rotor) row, showed the potential effects on the upstream flow were small, if not negligible
- **X2a** ($\mathbf{-3\%C_{ax}}$) - slightly ahead of the blade leading edge, the loss generation plot for the annular case shows 3 clear regions of high entropy generation: 1) the first close to the suction side leading edge, corresponding to the suction side leg of the horseshoe vortex, and 2) the second in the vicinity of the leading edge on the blade pressure side. Careful inspection of this second region shows that it is comprised of two combined loss generation cores, which were understood to relate to the primary and secondary legs of the pressure side leg of the horseshoe vortex. Finally, the third region found covering the majority of the middle portion of the passage entrances, was found to correspond to the 2-dimensional shearing of the inner inlet boundary which, as discussed previously, was seen to be driven across the passage entrance towards the suction surface of the adjacent blade before finally separating from the endwall and being convected up the suction surface. For both the suction and pressure side side legs of the horseshoe vortex, the contours for the endwall shear stresses show distinct regions of increased τ_{wall} confirming the positions of the secondary structures through the initial part of the passage

- **X2b** (**37%C_{ax}**) - aft of the leading edge and closer to the midchord, further effects of above flows may be seen. Firstly, close to the suction surface, the formation and growth of a distinct loss generation core associated with the suction side horseshoe vortex is clear, as well as the interaction of this vortex with the blade suction surface boundary layer, resulting in a region of slightly elevated entropy generation on the suction surface. Secondly and similarly, the entropy generation core associated with the pressure side leg of the horseshoe vortex was also seen to grow in size and intensity, although probably most importantly, the interaction of this vortex with the endwall boundary layer was seen to result in a region of intense loss production where interaction of the comparatively high velocity fluid of the vortex sheared past that of the low momentum endwall boundary layer flow. In terms of overall loss production intensity, it was the suction side horseshoe vortex and the interaction of the pressure side leg of the horseshoe vortex with the endwall boundary flow rather than the vortex itself, which are predicted to be the major sources of the loss
- **X2c** (**78%C_{ax}**) - aft of the midchord, due to the increased complexity of the actual flow field (due in part to the interaction of the secondary flow vortices not only with each other, but also with the blade suction surface), the loss generation contours also show an enhanced degree of complexity:
  - firstly, the localised but very high entropy production due to the thickening of the endwall boundary layer, its separation and impingement on the blade suction surface under the action of the cross-passage pressure gradient as well as the passage vortex, is clear
  - in addition, inspection of the large region of moderate intensity loss generation within the bulk flow showed this loss was associated with the shearing of the fluid of the now well formed passage vortex, with the primary flow, but also as a result of shearing within the vortex itself
  - above this region, inspection of the streamlines showed the inverted 'teardrop' region of increased loss production immediately adjacent to the suction surface corresponded once again to the convection and separation of the fluid of the endwall boundary layer[3] away from the suction surface by the passage vortex
  - further above this region still, the enclosed region of low entropy production closer to the midspan was found to be associated with the inlet inner boundary layer fluid which was previously noted to be driven up the suction surface and which formed a slowly rotating vortex above the main passage vortex
  - the significant increase in loss production as a result of the deceleration and thickening of the suction side boundary layer on the aft portion of the suction surface is clear
- **X2d** (**99%C_{ax}**) - finally, immediately forward of the trailing edge, sustained action of the cross-passage pressure gradient and migration and separation of the endwall boundary layer remained clear. The local increase in loss production on the lower aft portion of the blade suction surface as a result of the convection of the endwall fluid up the blade suction surface also remained clear as did the 'teardrop' associated with the eventual separation of this fluid under the action of the passage vortex from the blade surface. Further away from the blade surface, the large region of moderate intensity loss generation once again was noted to correspond to the shearing of the passage vortex fluid with that of the primary flow

[3] similar to that which occurs on the endwall itself

η_{tt}-based

The calculated entropy generation rates at various locations upstream, downstream and within the blade passage for the η_{tt}-based design are shown in Fig. 8.24 and Fig. 8.22a.

As was the case for all the endwalls, upstream of the blade passage (i.e. at the rotor inlet), the mass-averaged entropy generation rate was identical to that of the datum case. Inspection of the mass-averaged loss generation rate for the η_{tt}-based design immediately ahead of the blade passage (X2a) however showed a slight increase in the production of loss. An inspection of the associated contour plots (Fig. 8.24a) suggested this was was a result of an increase in the loss generation associated with the strengthened suction side horseshoe vortex, as well as a slight increase in the loss generated by the same vortex adjacent to the pressure side leading edge, due to the stagnation of the pressure side vortex ahead of the first endwall contour.

Within the passage (X2b), the significant reduction in entropy generation due to the reduced strength of the pressure side horseshoe vortex is again clear, along with a reduction in the entropy produced by the scraping of the pressure side leg of the horseshoe vortex against the endwall surface. Above this loss generation core, despite the strengthening of the suction side flow, the intensity of the loss generation associated with the suction side horseshoe vortex is also seen to be reduced, and this was attributed to two main factors:-

- a reduction in the shearing between the counter rotating pressure and suction side legs of the horseshoe vortex (due to the reduced overall strength of the pressure side horseshoe vortex) as well as
- a reduction in the shearing between the inner inlet boundary layer fluid which, for the annular case, was seen to travel underneath the suction side horseshoe vortex and then up the blade suction surface. The result of this effect was also noted on the suction surface shear stress contours, by the absence of region of high shear stress originating near the centre of the contoured region

Aft of the midchord (X2c), the effect of the endwall contouring was evident primarily in the loss generation contours within the bulk flow, as well as immediately adjacent to the blade suction surface, where:-

- the reduced intensity of the passage vortex resulted in a decrease overall loss generation within the bulk flow, *and*
- while some increased loss generation within the suction surface boundary layer as a result of the migration of the endwall fluid up the suction surface was remained, the reduced intensity of the passage vortex resulted in a reduction in the scraping of this fluid off of the suction surface
- finally, there is a complete absence of the additional loss generating structure noted above this region for the annular endwall which was found to originate as a result of the migration of the inner inlet boundary layer fluid up the suction surface

At the exit of the passage (X2d), once again, a reduction in the loss generation within the bulk flow as a result of the more diffuse nature of the passage vortex was noted, while effects

of the migration of fluid of the endwall boundary layer onto and up the blade suction surface remained.

C_{ske}-based

The entropy generation rates within the blade passage for the C_{ske}-based design (Fig. 8.25) were largely identical to those already discussed for the η_{tt}-based case. However, although the overall loss generating structures remained largely unchanged between this case and the previous (η_{tt}-based) design, Fig. 8.22a showed that with the exception of the rotor inlet as discussed previously as well as at the rotor exit (X3) plane where the overall mass-averaged entropy generation rate was lower, the loss production rates at each axial station through the blade passage were higher than those calculated for the η_{tt}-based design.

$C_{p0,rel}$-based

The entropy generation rates for the $C_{p0,rel}$-based case are shown in Fig. 8.26. In contrast to the previous cases, at the blade leading edge, the local mass-averaged rate of loss generation was lower than that of the datum case, and substantially lower than the previous contoured cases. Analysis of Fig. 8.26 (X2a) showed this was as a result of a decrease in the loss generation associated with the suction side leg of the horseshoe vortex as well as decrease in the overall loss produced by the pressure side leg of the vortex. The reduction in loss production associated with the suction side horseshoe vortex was likely to be as a result of a reduction in the flow around the suction side leading edge, while the decreased loss generation within the pressure side leg seen for the annular and η_{tt}- / C_{ske}-based cases, was understood to be as a result of a reduced obstruction presented to the formation of the pressure side leg vortex particularly in comparison to the contoured cases, where the loss production associated with the blockage effects on the pressure side of the leading edge were large.

Downstream of the leading edge (X2b), the loss generation rate remained lower than that of the annular case but also lower than that of the previous contoured cases. This was noted to be as a result of the decreased interaction of the suction side horseshoe vortex and the endwall fluid and what appeared to be reduced interaction between the each of the legs of the horseshoe vortex which are shown distinctly separate from one another in the figure.

Aft of the midchord, the loss production from the current case was now seen to increase above that of the annular and previous cases and this was established to be as a result of the increased interaction of the more intense passage vortex and the boundary layer of the suction surface as well as increased shearing within the passage vortex itself and with the primary flow around it.

Finally, at the trailing edge, while the calculated production of entropy remained higher than that of the annular case at the same location, the overall rate of loss production remained effectively constant between the midchord and the passage exit.

β_{dev}-based

In the early part of the passage (X2a, X2b), the entropy generation contours for the β_{dev}-based design (Fig. 8.27) showed a great deal of similarity to the η_{tt}-, C_{ske}, $C_{ske,1} + \beta_{dev,0.7}$- & $C_{p0,rel,1} + \beta_{dev,0.7}$-based endwalls, with increase loss creation noted on the suction side of the blade leading edge, as well as slight increase in the loss generation on the pressure side as well, both resulting in an increase in the entropy generated at the leading edge in comparison to the annular case. Aft of the leading edge, the entropy generation contours matched those of the η_{tt}- & C_{ske}-based designs suggesting that similar mechanisms to those described for the those endwalls were present for the current case. However, for both the $C_{ske,1} + \beta_{dev,0.7}$ & current design (β_{dev}-based), a region of very high shear wall shear stress ($> 50^{N}/_{m}$) was noticed adjacent to the endwall on the suction surface. In both cases, this high stress region was present aft of the contours which were described to deflect the endwall boundary layer flow across the blade passage and under the suction side leg of the horseshoe vortex, decoupling the components of the secondary flow.

Aft of the midchord (X2c & X2d), the entropy generation contours again matched those of the $C_{ske,1} + \beta_{dev,0.7}$-based design most closely, although overall, the mass-averaged intensity of the loss generation was lower than that of the $C_{ske,1} + \beta_{dev,0.7}$-based endwall and matched the values of the C_{ske}-only based design more closely.

$SKEH$-based

At the entrance to the blade passage (X2a), once again the entropy generation rates of the $SKEH$-based design was similar to those of the majority of the previous designs (with the exception of the $C_{p0,rel}$-based design), although the mass-averaged loss generation rate for this endwall was in fact the highest of all the endwalls designed. This was once again attributed to the influences on the suction / pressure side horseshoe vortices already presented, although for this design, and this increase appeared to come predominantly from an increase in the loss creation intensity within the pressure side horseshoe vortex.

Aft of the passage entrance (X2b) however, the loss generation rate for the current design was significantly higher than all the previous contoured endwalls, as well as the annular case. This was clearly visible in the corresponding contour plot where the 'valley' created by the local reduction in the endwall height resulted in extremely loss generation rates within the fluid, as well as large shear shear stresses on the suction surface as well. Inspection of the flow streamlines in this region showed that these high local loss generation rates were generated predominantly by extremely 'confused' fluid from the inner inlet and endwall boundary layers.

Aft of the midchord (X2c), the overall loss generation rate for the current endwall remained reasonably high, although not as high as the $C_{p0,rel}$-based design. With reference to the entropy generation contours, the generation of the loss within the bulk flow was produced predominantly by the flow structures comprising of inlet and endwall boundary layer fluid, with the lower 'lobe' of the contours noted to be generated by a high level of shearing within the endwall flow which was driven up the suction surface, and the central portion associated with the usual passage vortex structure.

Finally, at the exit of the blade row (X2d), the loss generation contours for the current design showed some similarity to a number of the previous endwalls (although not the η_{tt} & C_{ske}-based designs) including the annular case, although, for the current design, although the loss generation contours covered a spatially larger portion of the passage, the lower intensity of these contours in comparison to the annular case, resulted in a lower overall loss generation rate at this plane.

η_{de}-based

The loss generation for the η_{de}-based design (Fig. 8.29) near the blade leading edge, was similar to those of all the previous designs (with the exception of the $C_{p0,rel}$-based design) and so calculated to be slightly higher than the datum design.

Further, closer to the midchord (X2b), as was the case for the $SKEH$-based design, the mass-averaged loss generation was higher than the remainder of the endwalls (although not as high as that of the $SKEH$-based design), and the structure of the contours was somewhat more complex. More specifically, high loss generation associated with the suction side horseshoe vortex, as well as distinct interaction between the fluid of the endwall boundary layer, which was previously described to migrate *forward* and towards the suction surface leading edge and then separate and travel up the suction surface. A reasonably strong interaction between the remnants of the much reduced pressure side leg of the horseshoe vortex and the endwall boundary layer fluid, which combined with the local reduction in endwall height, resulted in a relatively strong separation and ensuing entropy generation immediately adjacent to the endwall surface. The intensity of this vortex was also noted by the region of very high wall shear stress located in the region where this vortex was described to have formed.

Aft of the midchord (X2c), the loss generation contours were once again complex, although the main contributors to the intensity of the these contours within the bulk flow was the small, but high intensity vortex which was described (above and previously) to separate from the endwall surface close to the passage entrance, and then grow in size by attracting a large portion of the inlet boundary layer and endwall fluid into it.

At the exit of the blade passage (X2d), the loss generation contours mirrored those of the annular case (in terms of characteristic shape), although the intensity as well as size of the loss generation region was reduced in comparison to that case.

$C_{ske,1} + \beta_{dev,0.7}$-based

The loss production rates for the $C_{ske,1} + \beta_{dev,0.7}$-based design are shown in Fig. 8.30, where at the leading edge (X2a), the overall loss generation rate was estimated to be similar to the η_{tt}- & C_{ske}-based cases and for similar reasons. Similarly, aft of the leading edge (X2b), the overall loss generation characteristics appeared similar but fractionally higher to the η_{tt}- & C_{ske}-based cases and this was as a result of slightly higher loss creation levels associated with the pressure side horseshoe vortex than noted for the previous cases.

Aft of the midchord (X2c), the two fold nature of the endwall was clear:-

- Within the bulk flow, the reduced loss generation due to the smaller passage vortex (which was primarily affected by the C_{ske} component of the objective function) was clear, while
- The increase in loss generation immediately adjacent to the suction surface associated with the increased impingement and interaction of the endwall boundary layer fluid with that of the suction surface as a result of the increased deflection of the endwall fluid by the 'deflector' contour was also clear

At the trailing edge (X2d) although while the effects of the secondary C_{ske} in the bulk flow were clear, a slight increase in the loss production on the suction surface resulted in a slightly increase level of loss creation in comparison to the previous 'successful' (i.e. η_{tt}-, C_{ske}-based) contours.

$C_{p0,rel,1} + \beta_{dev,0.7}$-based

Finally, plots of the loss production rates through the blade passage for the $C_{p0,rel,1} + \beta_{dev,0.7}$-based case are shown in Fig. 8.31. While once again, at the inlet to the rotor row (X2), the loss generation rates were equivalent to the both the annular, as well as all the contoured cases, at the blade leading edge (X2a), were similar to those of the η_{tt}-based design. This was once again attributed to the increased loss creation associated with the stronger suction side horseshoe vortex, as well as an increase in loss generation associated with the pressure side vortex in the vicinity of the leading edge.

Similarly, forward of the midchord (X2b), once again, for this endwall, the loss generation rates were similar, but slightly higher than those of the η_{tt}-based design, although structurally, the contours of the entropy generation were rather different from those of the η_{tt}- & C_{ske}-based design, and this was in line with the more complex flow described previously for this endwall in this region.

Aft of the midchord (X2c), the overall loss generation rates for the current endwall returned to values more similar to those calculated of the $C_{ske,1} + \beta_{dev,0.7}$-based design and the contour plots at this location in the passage appeared to take on an overall shape more similar by slightly reduced version as those already described for the $C_{p0,rel}$-based design.

Finally, at the exit of the blade passage (X2d), the overall loss production rate returned to a mass-averaged value similar to that originally calculated for the η_{tt}-based design, although the characteristics (plot) of the entropy generation contours again resembled those of the annular and $C_{p0,rel}$-based endwalls rather than those of any of the previous contoured designs.

Downstream

Downstream of the blade row (Fig. 8.22a, X3 - X4), in general:-

- the overall trend for each endwall (including the annular case), was to produce less loss than was generated within the blade row. This was expected, since downstream of the blade passage, there is no driving force for the generation of loss producing structures.

- in addition, since, for the majority of endwalls, the strength of the secondary kinetic energy at the blade row exit was less than that of the annular case, the entropy generation rates downstream of the passage were lower than that of the annular case.
- further, as would also be expected, the differences in the loss generation rates between each of the contoured endwalls as well as the annular case, was seen to decrease due to the incremental 'mixing-out' of the secondary flow structures

In contrast to this however, inspection of Figs. 8.22a & 8.22b showed that despite the reduced entropy generation *within* the blade passage, for the $C_{p0,rel}$-based design, aft of the blade passage the loss generation is consistently greater than that of the annular case, with a final rate approximately $\sim 30\%$ greater than that of the baseline case at the final 'mixed-out' measurement plane.

Summary

In general, the following observations were able to be made regarding the calculated loss generation rates within and downstream of blade passage for each endwall design:-

- With the exception of the $C_{p0,rel}$-based design, consistent with the observations made in terms of the endwall static pressures and 2 / 3-dimensional streamlines, the aerodynamic blocking of the pressure side horseshoe vortex resulted in an overall increase in the mass-averaged entropy generation rates in the vicinity of the blade leading edge, with the most significant increase relative to the annular case noted for the $SKEH$-based ($\sim +4.4\%$) design and an average increase of approximately ($\sim +3\%$). As indicated, in contrast to this, a reduction in the mass-averaged entropy generation rate of approximately $\sim -2\%$ was noted for the $C_{p0,rel}$-based design.
- Aft of this position, while for the majority of designs, the reduced strength of the passage vortex resulted in a reduction in the entropy generation rates in comparison to the datum case, for the $C_{p0,rel}$-based design, despite the encouragement of the formation of the pressure side horseshoe vortex, the reduced interaction between this leg of the vortex with the endwall boundary layer as well as with the suction side leg of the same vortex, resulted in overall reductions in the predicted loss generation rates of almost $\sim -5\%$ in comparison to the annular design. Finally, consistent with the formation of the pair of bespoke vortices close to the suction surface leading edge and endwall-pressure surface junction for the η_{de}- & $SKEH$-based designs respectively, the loss generation rates for these designs were considerably higher than for the remainder of the cases, with the $\dot{s}_{gen}$ rates for the $SKEH$-based design in fact predicted to exceed those of the annular case quite substantially ($\sim +5.4\%$).
- Aft of the midchord, for all cases with the continued exception of the $C_{p0,rel}$-based case (for which substantial increases of approximately $\sim +4.7 - 5.1\%$ in comparison to the annular case were predicted) , the reduced strength of the passage vortex as well as its interaction with the adjacent blade's suction surface, resulted in overall decreases in the mass-averaged entropy generation rates.
- Finally, downstream of the blade row, all the contoured designs (with the exception of the $C_{p0,rel}$-based case for which substantial increases in the loss generation rates were noted), continued to exhibit decreased loss generation rates as a result of the reduced secondary kinetic energy leaving the blade rows, with the η_{tt}-, C_{ske}- & β_{dev}-based designs exhibiting the greatest reductions in

comparison to the annular case while the η_{de}- & $SKEH$-based were noted to result calculated loss generation rates consistently higher than the previous designs but still less than the annular case.

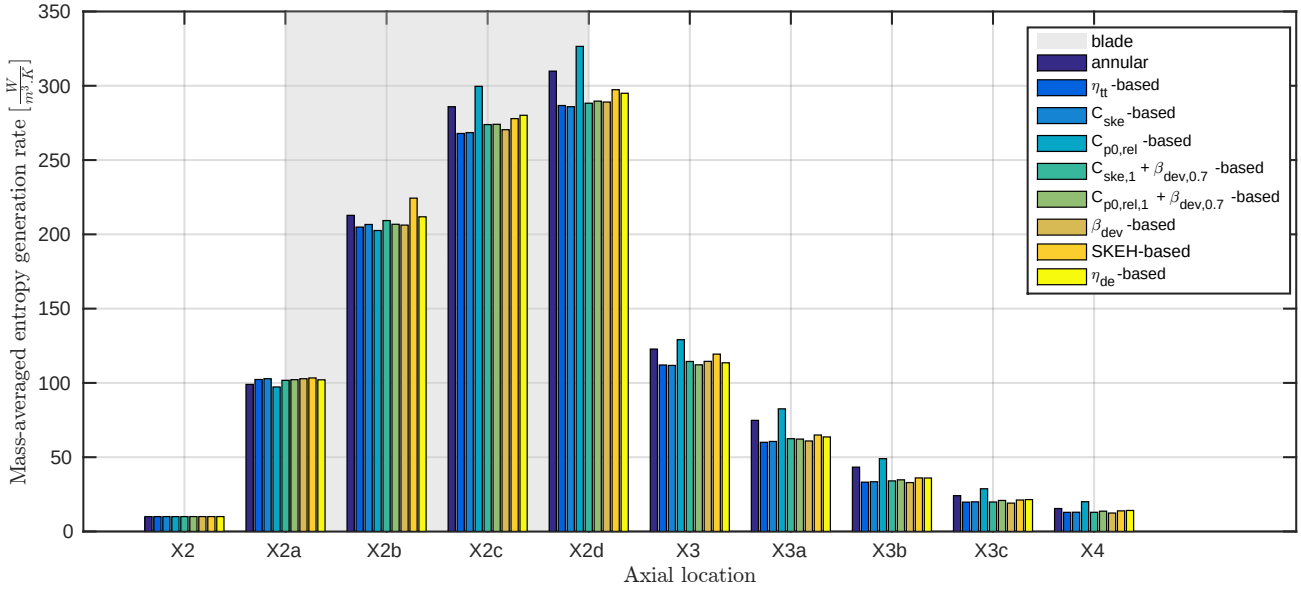

(a) Predicted mass-averaged entropy generation rates ($\dot{s}_{gen}$) for the annular as well as contoured designs

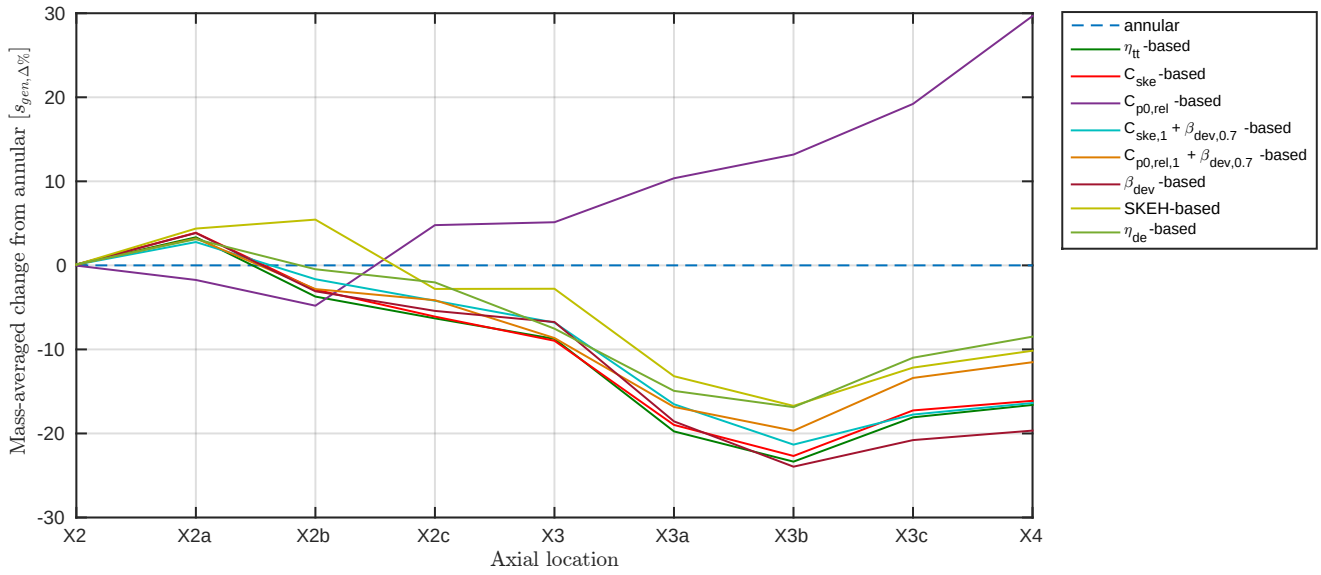

(b) Predicted mass-averaged changes in entropy generation rates ($\Delta\dot{s}_{gen}\%$) from the annular case

Fig. 8.22: Calculated mass-averaged entropy generation rates and changes from the annular case for the annular and contoured endwalls

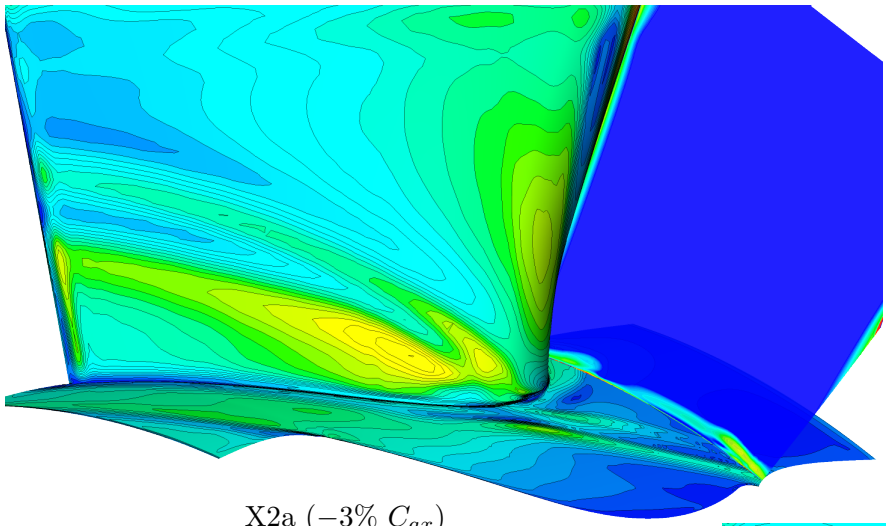

X2a ($-3\%\ C_{ax}$)

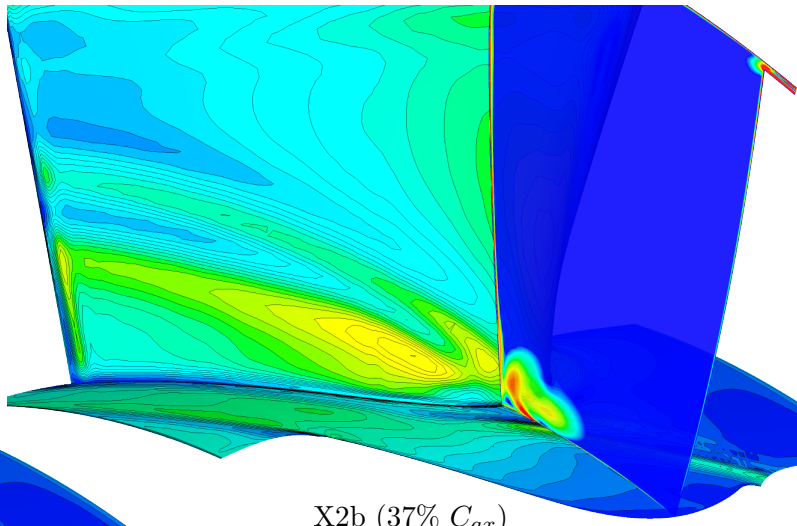

X2b ($37\%\ C_{ax}$)

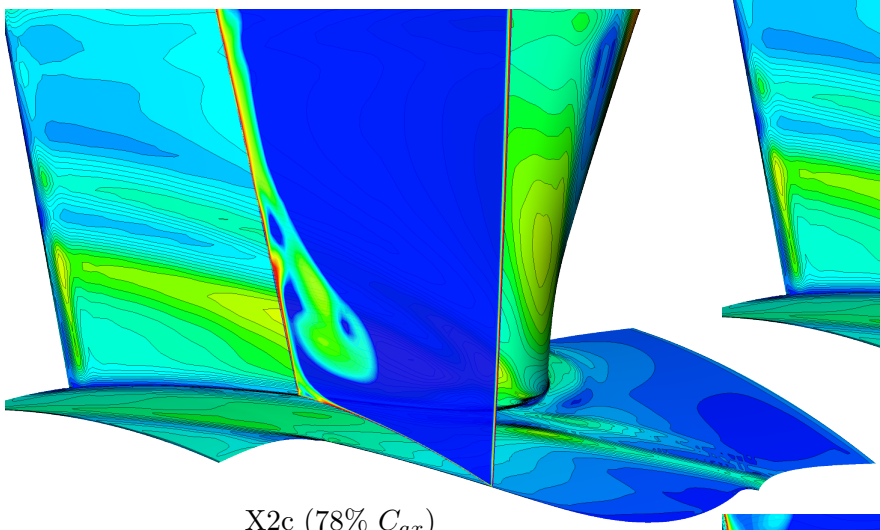

X2c ($78\%\ C_{ax}$)

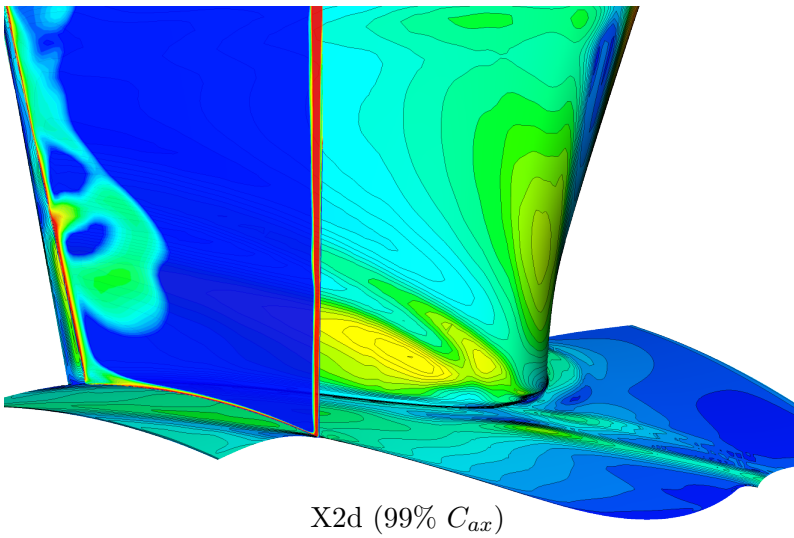

X2d ($99\%\ C_{ax}$)

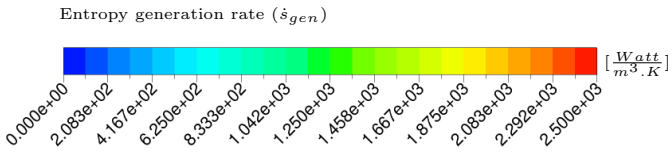

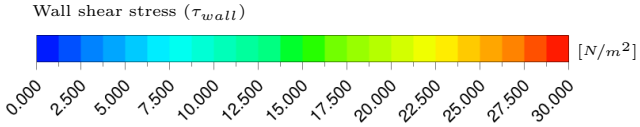

Fig. 8.23: Calculated wall shear stress (endwall, suction surface) & entropy generation rate (passage) for the annular design

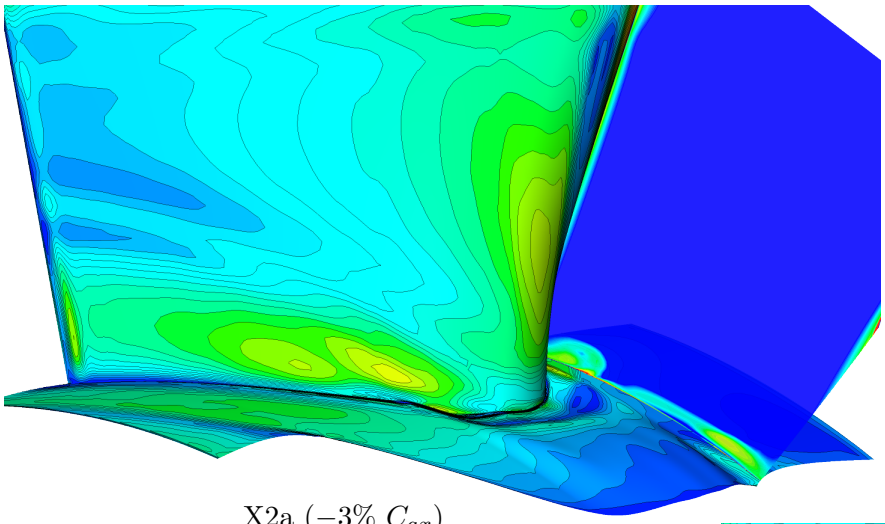

X2a ($-3\%\ C_{ax}$)

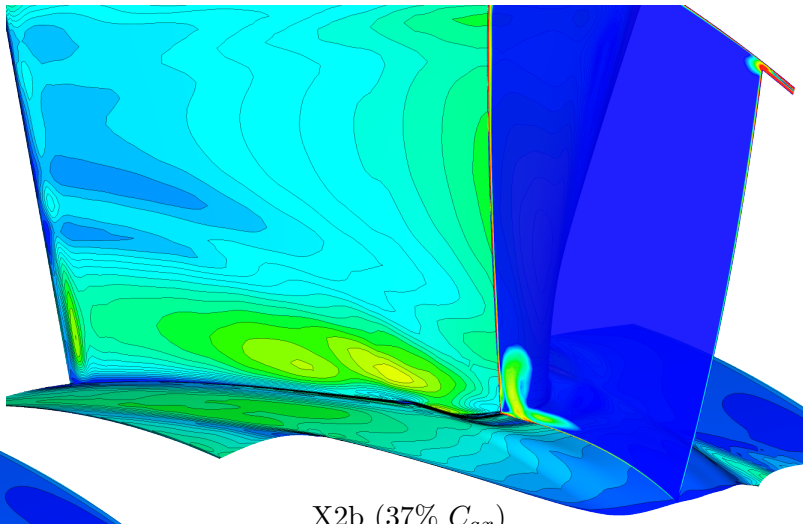

X2b ($37\%\ C_{ax}$)

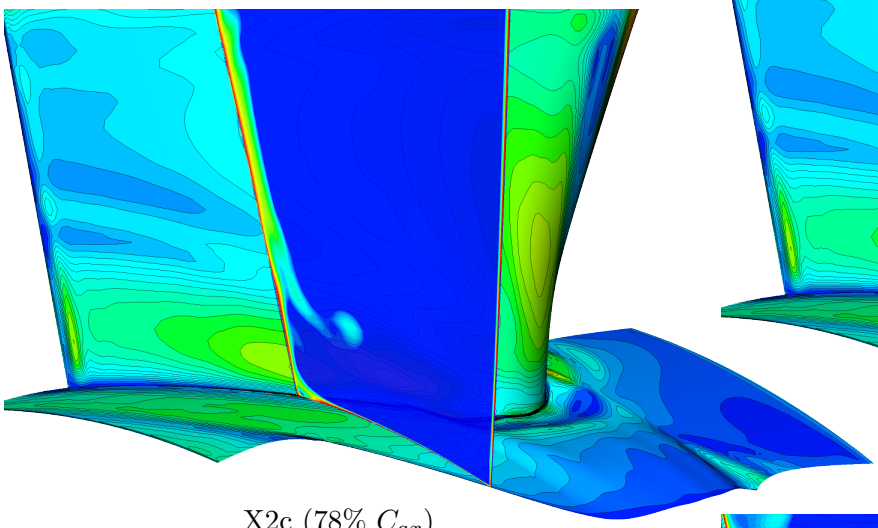

X2c ($78\%\ C_{ax}$)

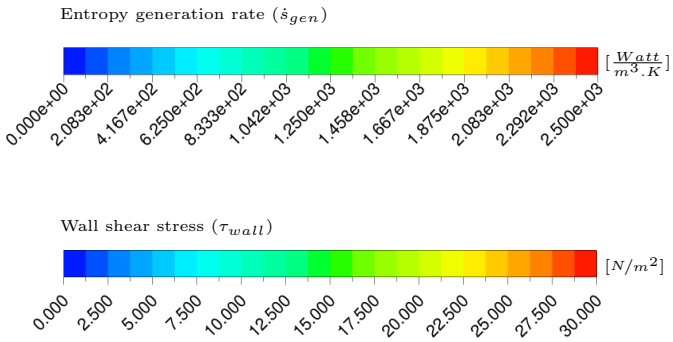

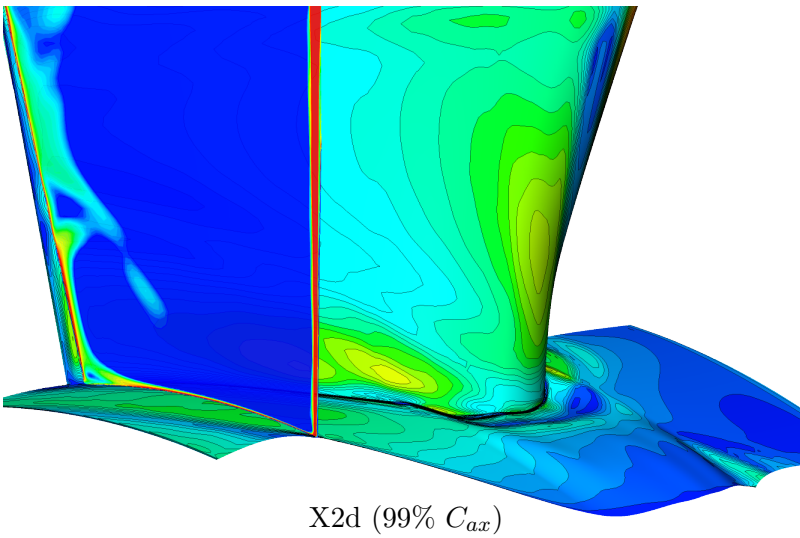

X2d ($99\%\ C_{ax}$)

Fig. 8.24: Calculated wall shear stress (endwall, suction surface) & entropy generation rate (passage) for the η_{tt}-based design

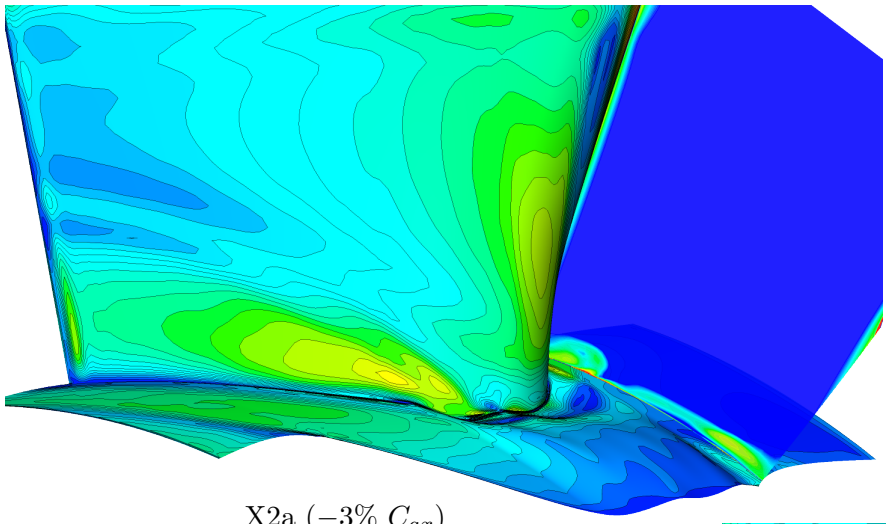

X2a ($-3\%\ C_{ax}$)

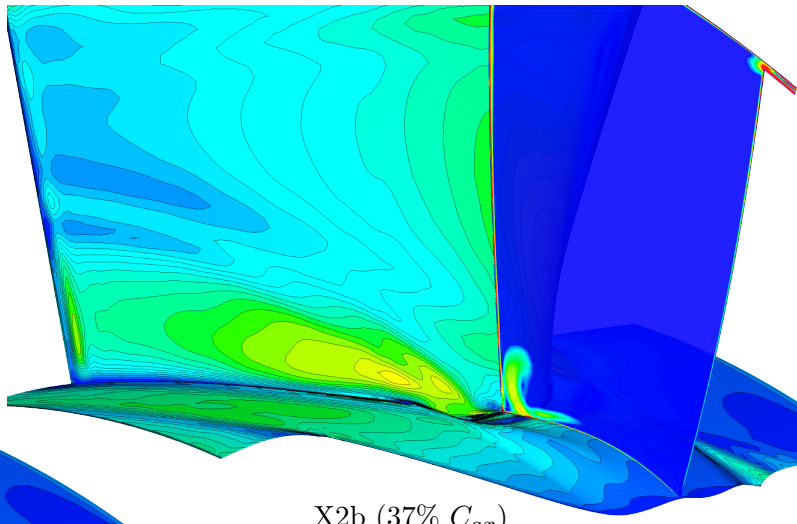

X2b ($37\%\ C_{ax}$)

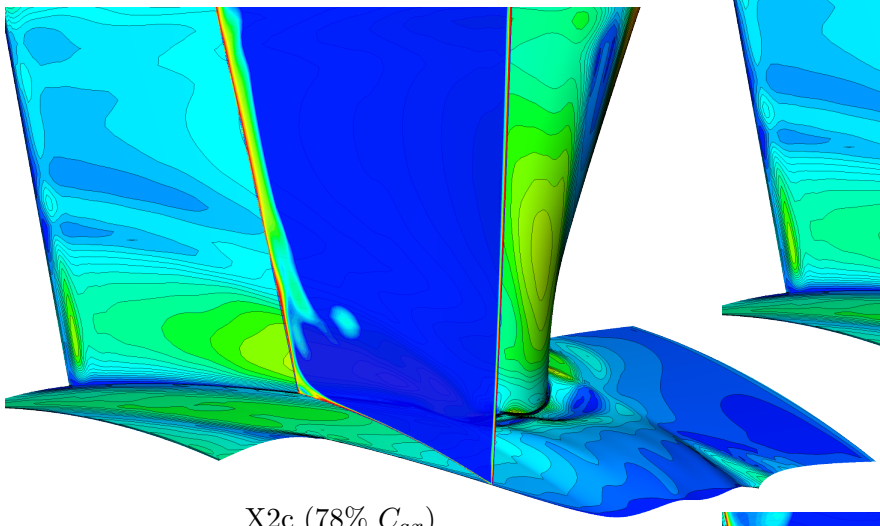

X2c ($78\%\ C_{ax}$)

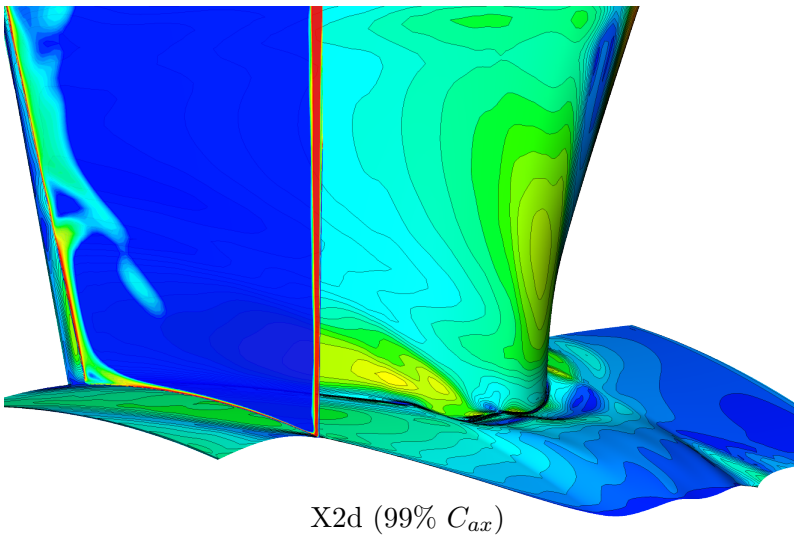

X2d ($99\%\ C_{ax}$)

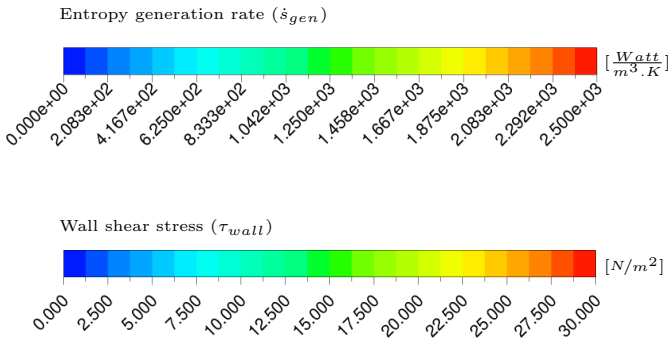

Fig. 8.25: Calculated wall shear stress (endwall, suction surface) & entropy generation rate (passage) for the C_{ske}-based design

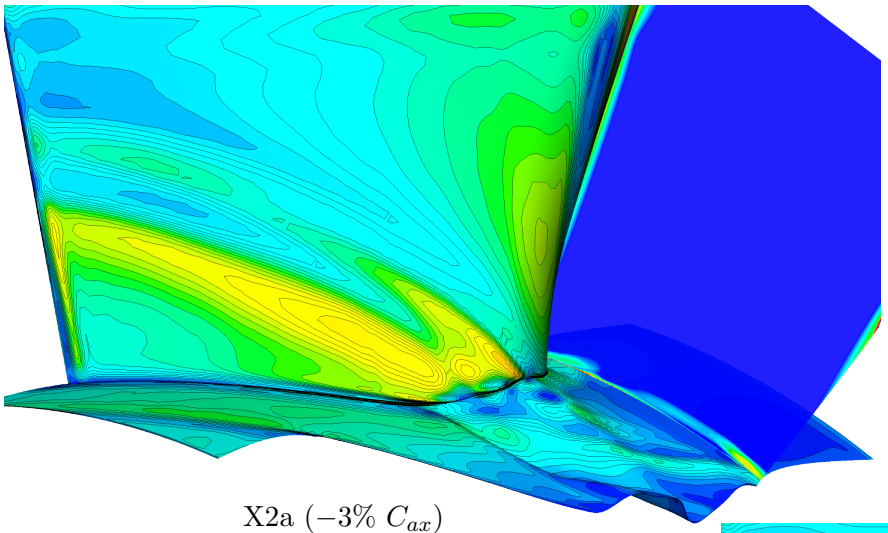

X2a ($-3\%\ C_{ax}$)

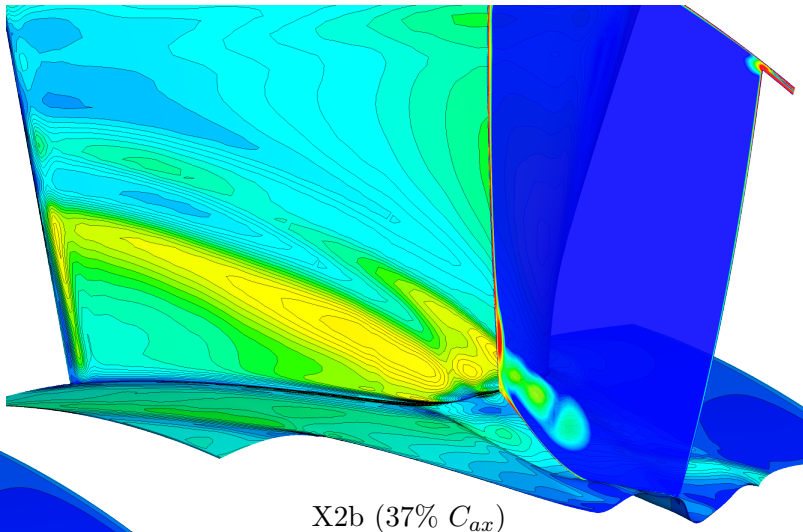

X2b ($37\%\ C_{ax}$)

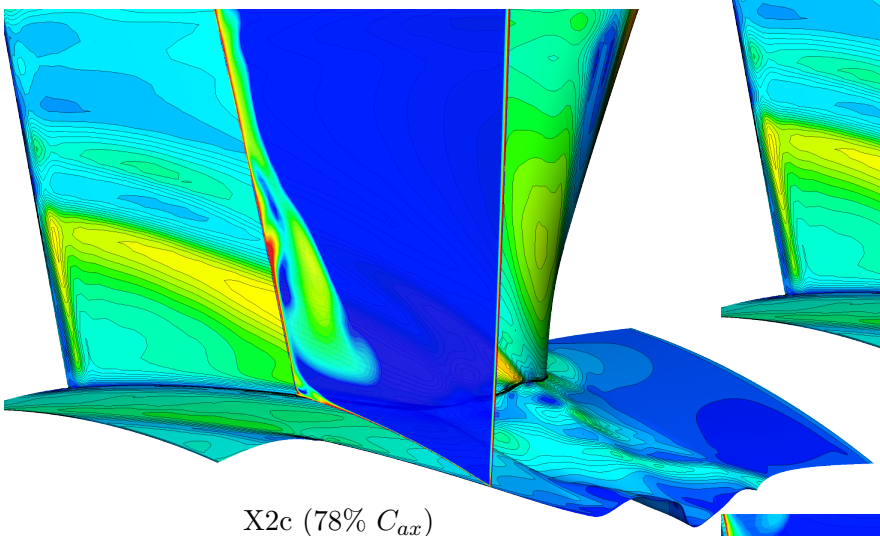

X2c ($78\%\ C_{ax}$)

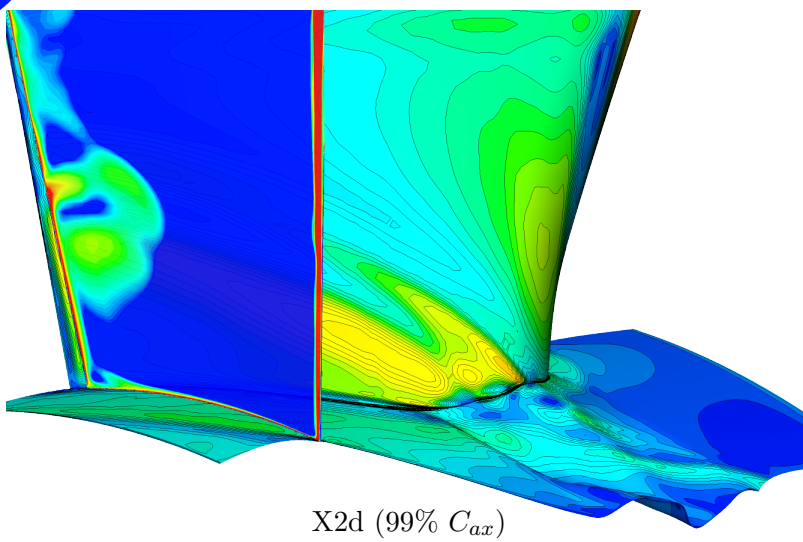

X2d ($99\%\ C_{ax}$)

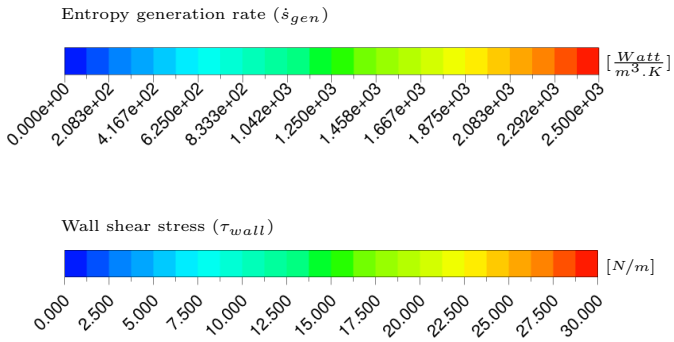

Fig. 8.26: Calculated wall shear stress (endwall, suction surface) & entropy generation rate (passage) for the $C_{p0,rel}$-based design

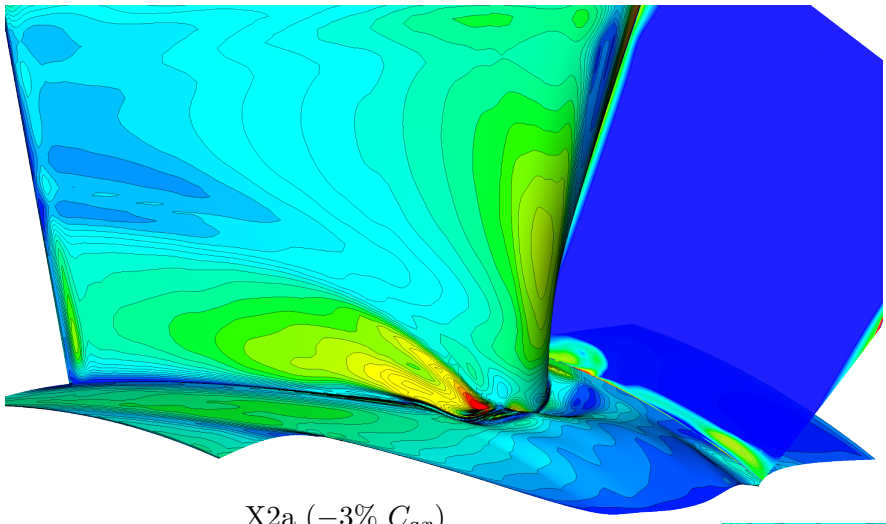

X2a ($-3\%\ C_{ax}$)

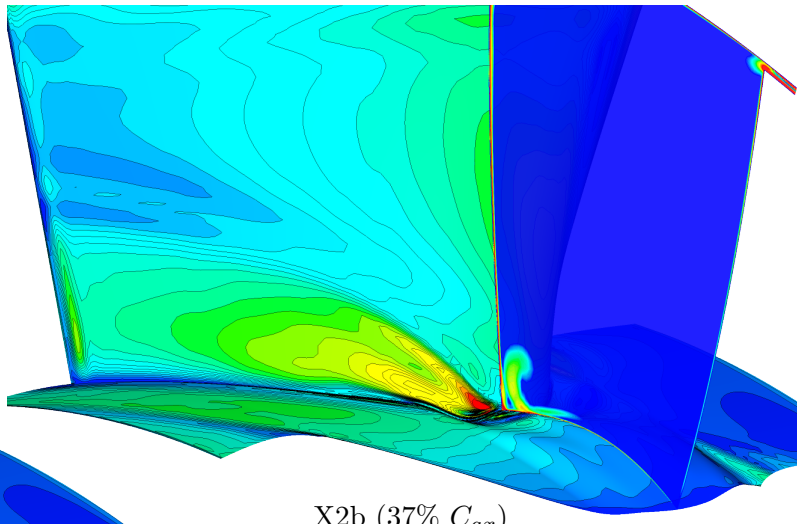

X2b ($37\%\ C_{ax}$)

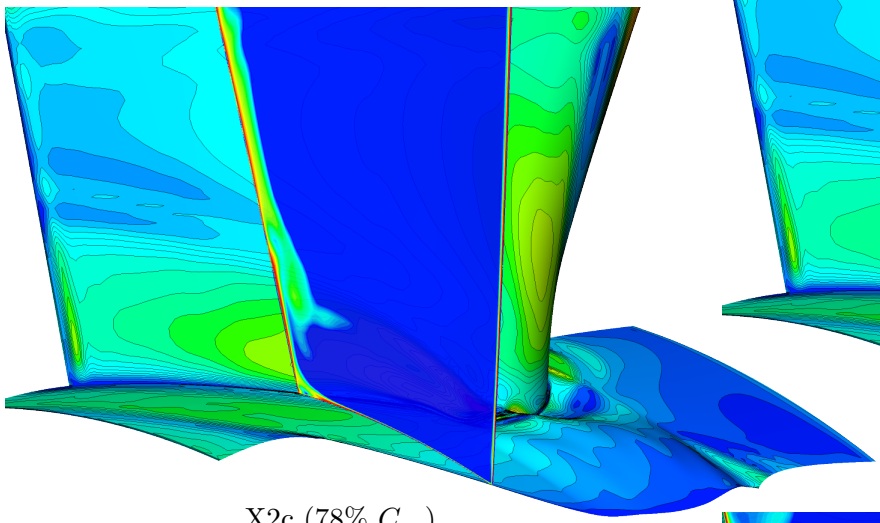

X2c ($78\%\ C_{ax}$)

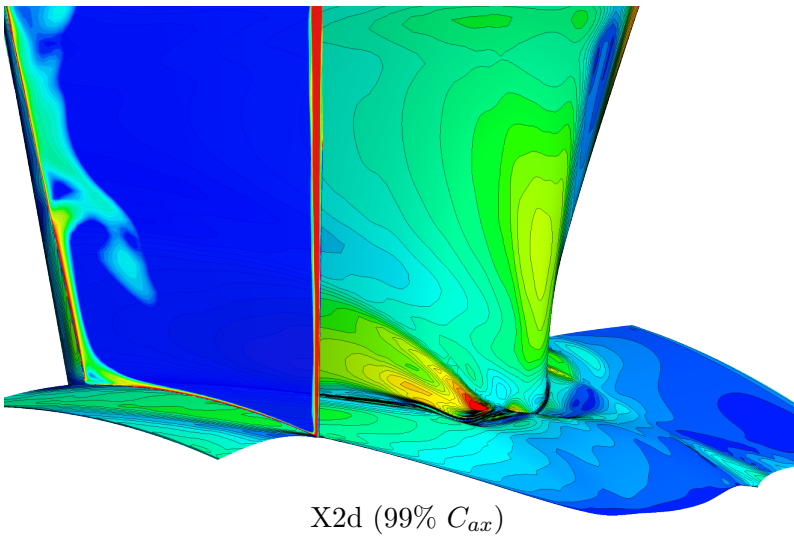

X2d ($99\%\ C_{ax}$)

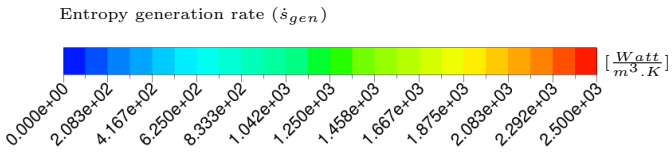

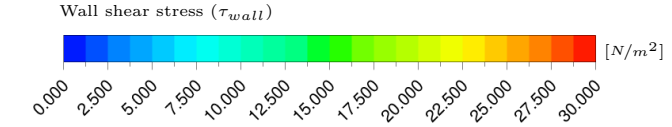

Fig. 8.27: Calculated wall shear stress (endwall, suction surface) & entropy generation rate (passage) for the β_{dev}-based design

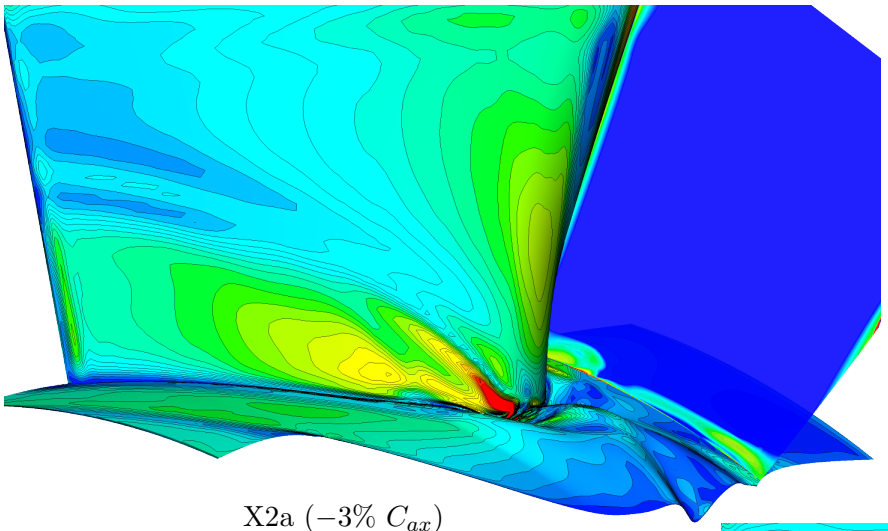

X2a ($-3\%\ C_{ax}$)

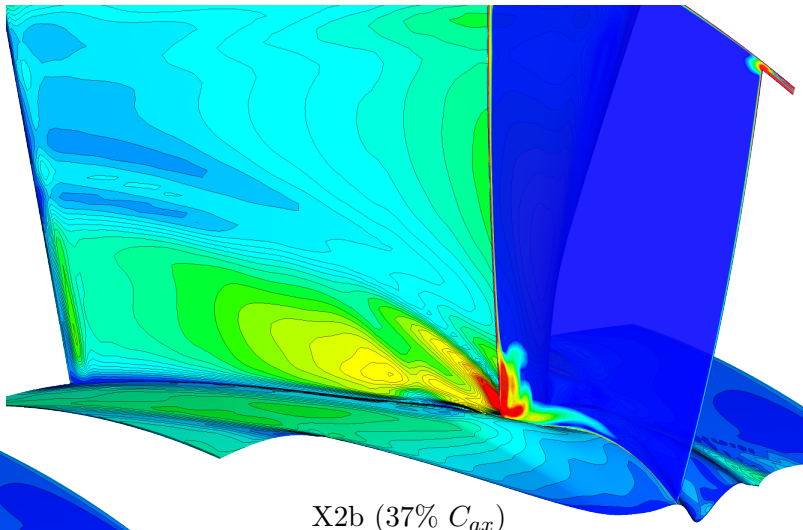

X2b ($37\%\ C_{ax}$)

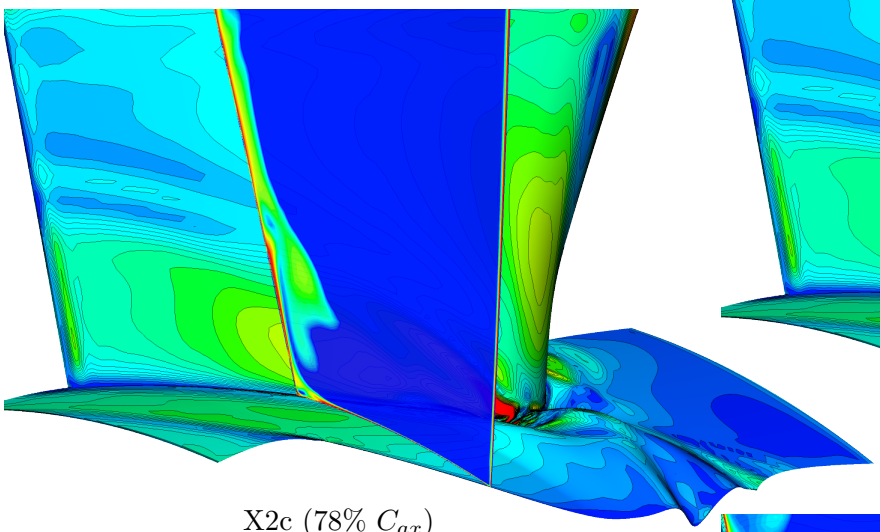

X2c ($78\%\ C_{ax}$)

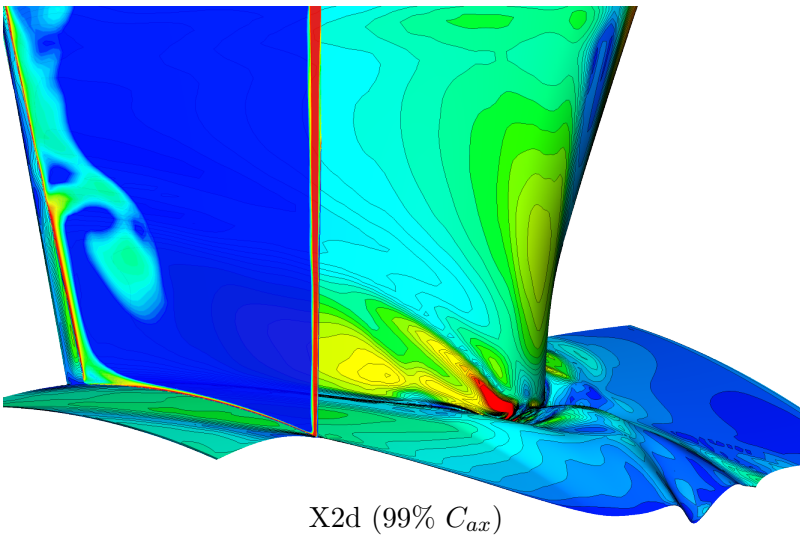

X2d ($99\%\ C_{ax}$)

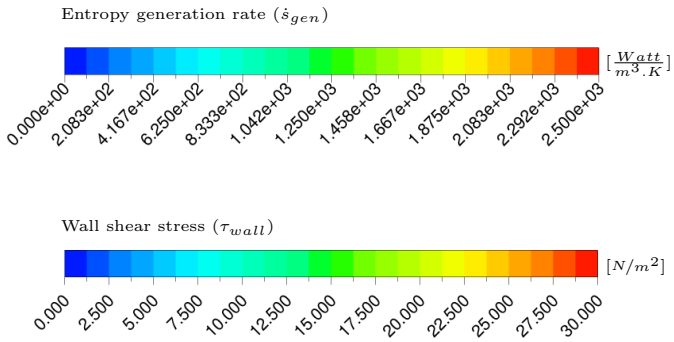

Fig. 8.28: Calculated wall shear stress (endwall, suction surface) & entropy generation rate (passage) for the $SKEH$-based design

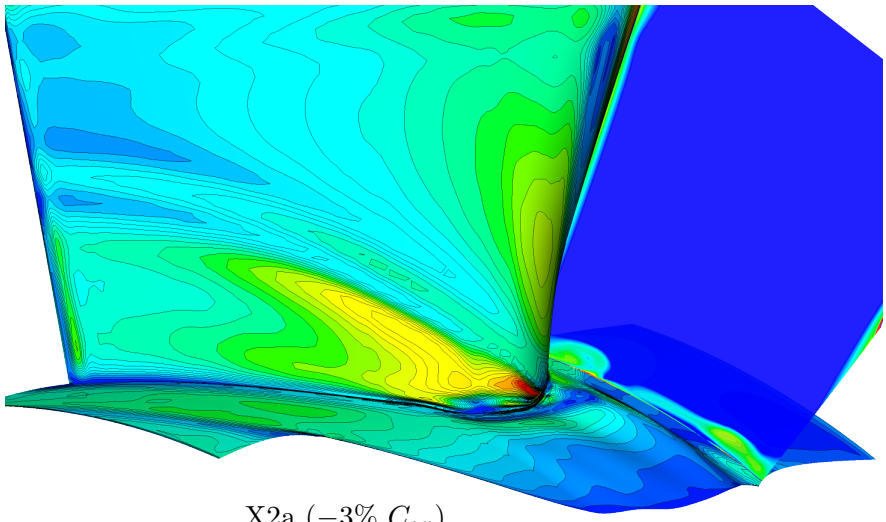

X2a ($-3\%\ C_{ax}$)

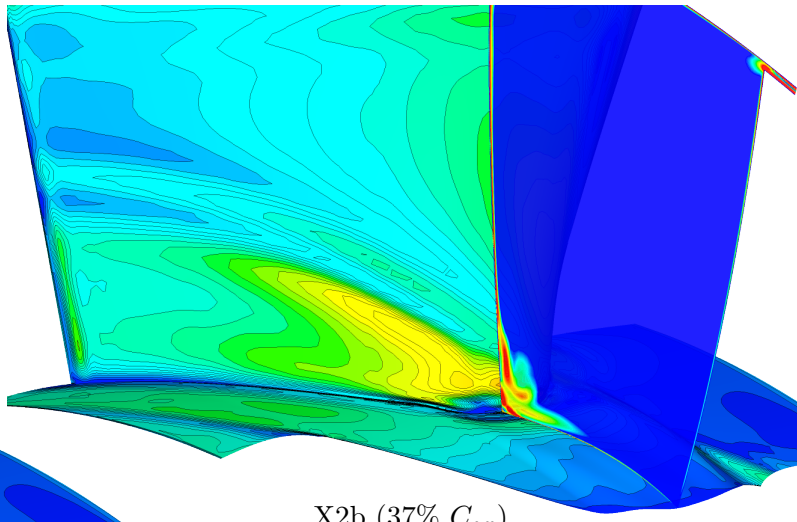

X2b ($37\%\ C_{ax}$)

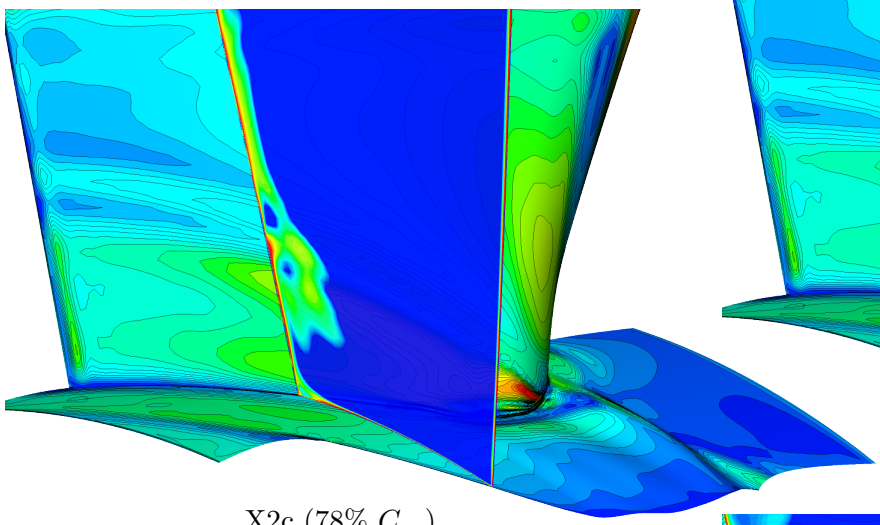

X2c ($78\%\ C_{ax}$)

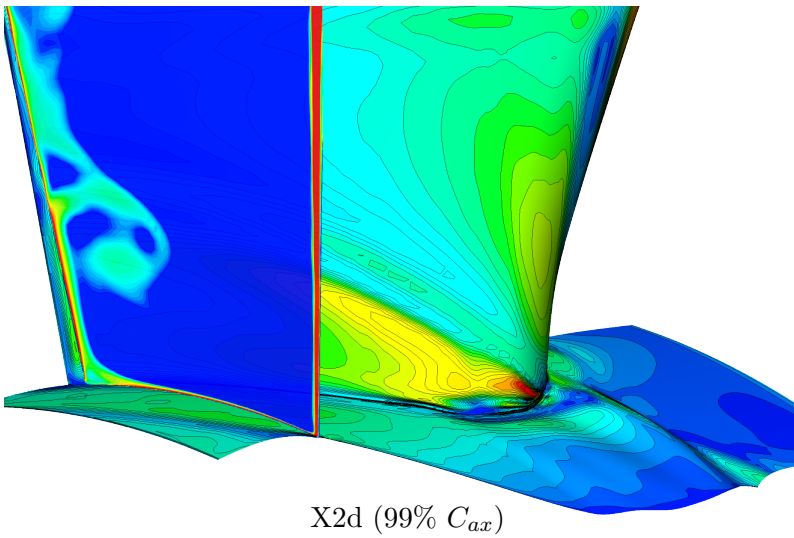

X2d ($99\%\ C_{ax}$)

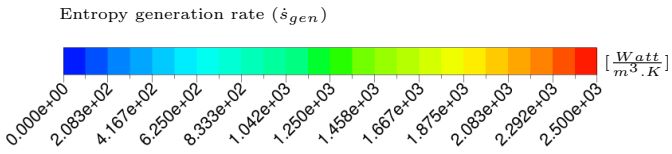

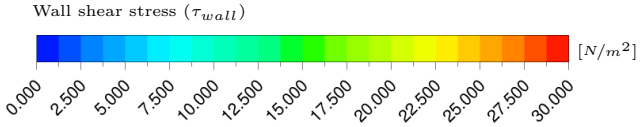

Fig. 8.29: Calculated wall shear stress (endwall, suction surface) & entropy generation rate (passage) for the η_{de}-based design

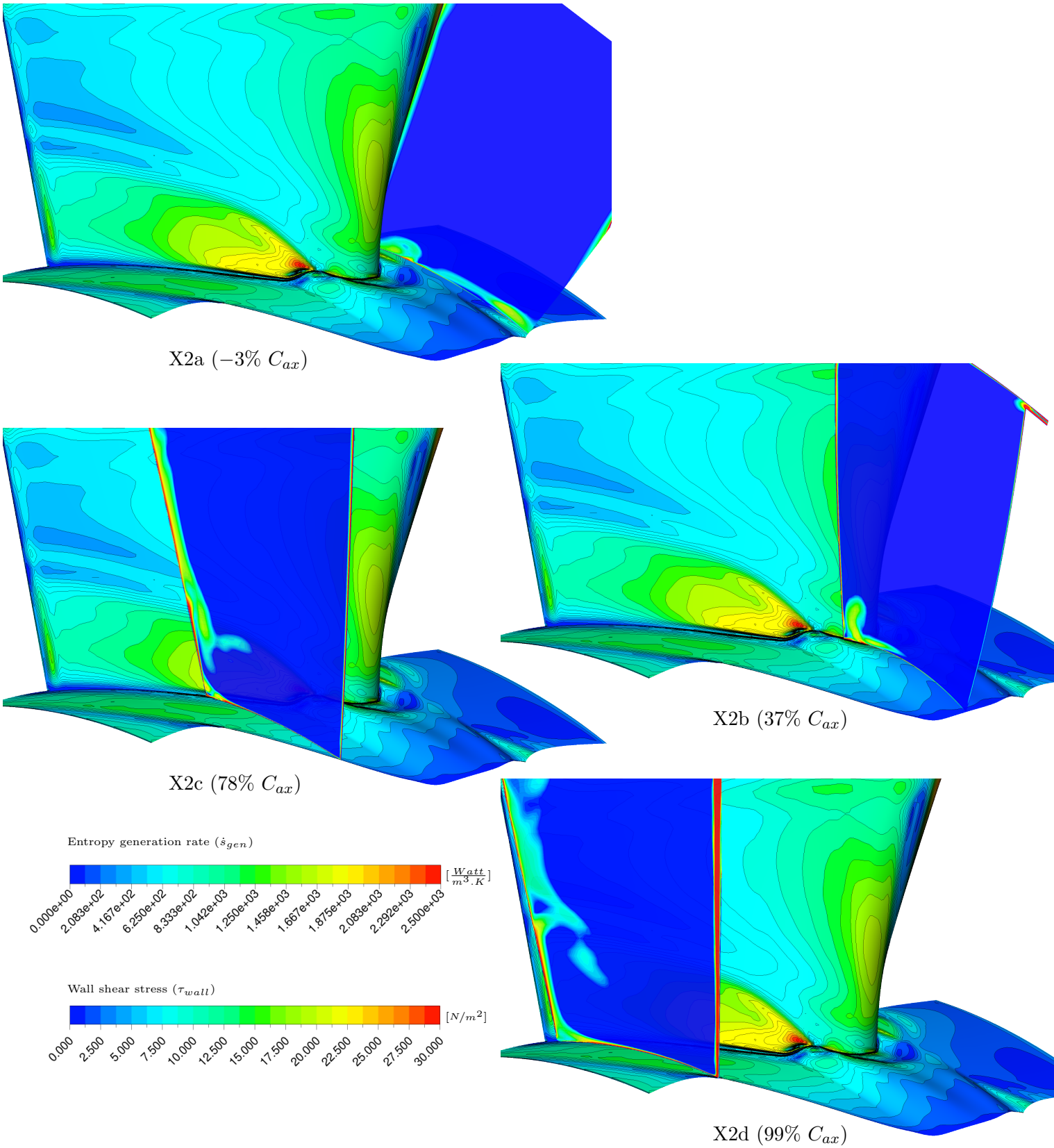

Fig. 8.30: Calculated wall shear stress (endwall, suction surface) & entropy generation rate (passage) for the $C_{ske,1} + \beta_{dev,0.7}$-based design

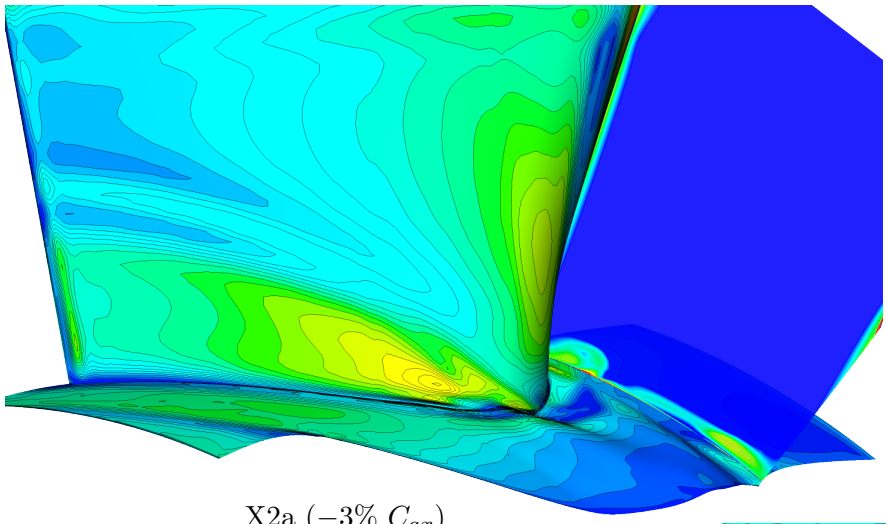

X2a ($-3\%\ C_{ax}$)

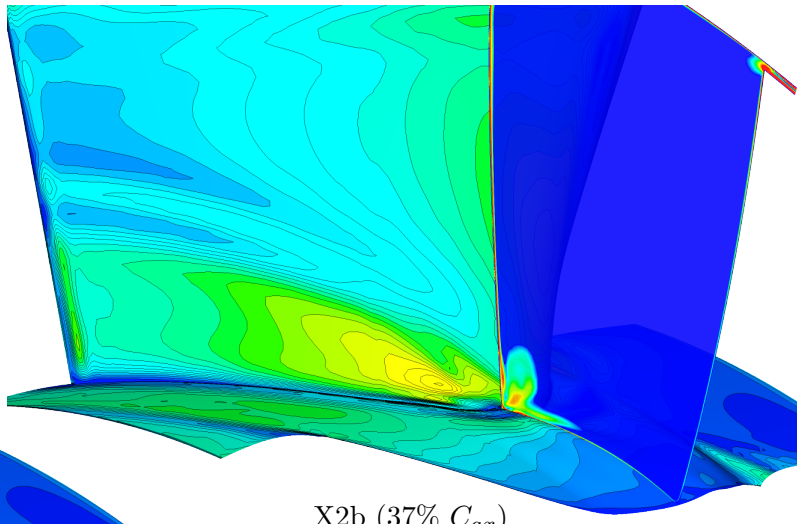

X2b ($37\%\ C_{ax}$)

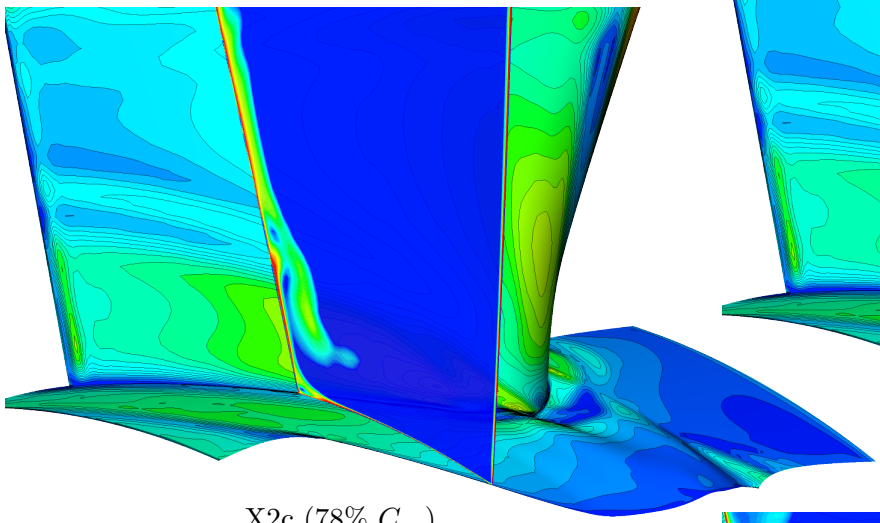

X2c ($78\%\ C_{ax}$)

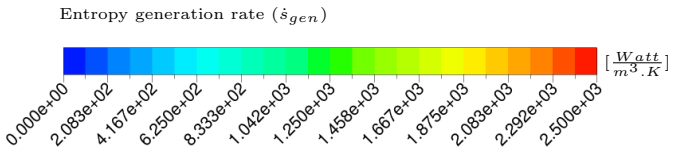

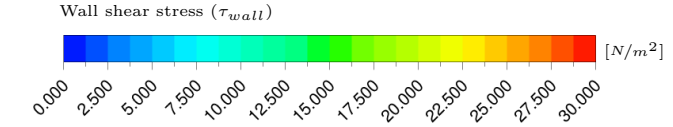

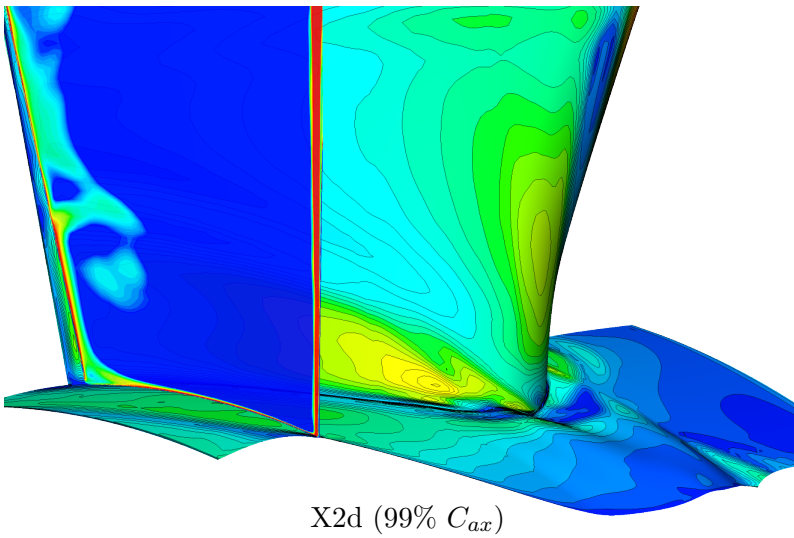

X2d ($99\%\ C_{ax}$)

Fig. 8.31: Calculated wall shear stress (endwall, suction surface) & entropy generation rate (passage) for the $C_{p0,rel,1} + \beta_{dev,0.7}$-based design

8.5 Efficiencies

In this Section, the efficiencies for both the numerical as well as the experimental cases are discussed. As discussed previously, because of the low characteristic speeds associated with the test rig, the flow through the turbine was assumed to be both isothermal and incompressible. Further to this, in both the numerical and experimental setups, the quantities measured as part of the efficiency calculation for each design included the upstream total pressure, rotor torque, RPM and rotor exit velocities and static pressures. From these quantities, the rotor total isentropic pressure drop, work output and finally efficiency could then be calculated as described in Section 3.3.1. In addition, as described in Chapter 4, in both the numerical and experimental configurations, the inlet velocity to the turbine is set (rather than the pressure drop through the turbine) and therefore a pressure boundary condition at the exit of the CFD model was required, and this was set to a value representative of the pressure at the exit of the rig.

The predicted and measured rotor efficiencies calculated at the X3 and X4 measurement planes, are shown in Table 8.2. In addition, the rotor work output, total isentropic pressure drop and velocities for both the numerical and experimental sets are shown Fig. 8.32.

At the rotor exit (X3), from the CFD results (Fig. 8.32a), it is clear that in all cases where an improvement in the efficiency of the rotor was predicted, this was achieved by at least maintaining, if not improving the rotor work output in comparison to the datum case, while at the same time reducing the total isentropic pressure drop through the blade passage. In contrast, in the case of the $C_{p0,rel}$-based design, while a substantial increase in the pressure drop through the rotor was predicted, as a result of the only moderately larger work output predicted for that design, an overall decrease in the efficiency was predicted.

As was the case for the CFD results, the measured results of the designs included in the experimental subset are shown in in Fig. 8.32b. While for the η_{tt}- & C_{ske}-based designs, the measured rotor work output was smaller than that of the datum case, the corresponding reductions in the blade row total isentropic pressure drop predicted by the CFD were validated, resulting in the overall measured increases in the rotor efficiency as predicted. In contrast however, for both the $C_{ske,1} + \beta_{dev,0.7}$- & $C_{p0,rel,1} + \beta_{dev,0.7}$-based designs, the predicted increases in rotor efficiency were not validated, and this was shown to be as a result of the larger pressure drop through the blade row in comparison to the total work output of the rotor. The slightly higher rotor exit velocities of the $C_{ske,1} + \beta_{dev,0.7}$- & $C_{p0,rel,1} + \beta_{dev,0.7}$-based designs in comparison to the η_{tt}- & C_{ske}-based cases as predicted by the CFD were validated however.

At the downstream measurement (X4) plane, the CFD results were largely identical to those already presented at the rotor exit and this is reflected in the very similar relative magnitudes of as well as changes in the magnitudes of the efficiencies between designs. Because of the similarity in the results, they are not shown as was done for the rotor exit data. For the downstream experimental data (Fig. 8.32c) however, while the results for the η_{tt}- & C_{ske}-based designs were again reasonably similar to the rotor exit results, the change in results for both of the compound designs in terms of efficiency, were seen to be as a result of the smaller total pressure drop with respect to the annular case for these designs.

Table 8.2: Summary of predicted (and experimental) mass-averaged rotor efficiencies at the rotor exit (X3) and downstream (X4) measurement planes

Endwall	*Total-total efficiency (η_{tt})*	
	Total	$\Delta_{\%,annular}$
	Rotor exit (X3)	
annular	79.52 (81.32) %	-
η_{tt}-based	80.08 (81.94) %	+0.71% (+0.76%)
C_{ske}-based	80.06 (81.65) %	+0.69% (+0.40%)
$C_{p0,rel}$-based	79.30 %	-0.27%
β_{dev}-based	80.00 %	+0.61%
$SKEH$-based	79.75 %	+0.30%
η_{de}-based	79.83 %	+0.39%
$C_{ske,1} + \beta_{dev,0.7}$-based	79.97 (80.81) %	+0.58% (-0.63%)
$C_{p0,rel,1} + \beta_{dev,0.7}$-based	80.03 (81.19) %	+0.65% (-0.17%)
	Downstream (X4)	
annular	78.62 (81.08) %	-
η_{tt}-based	79.29 (81.36) %	+0.86% (+0.34%)
C_{ske}-based	79.28 (81.56) %	+0.83% (+0.59%)
$C_{p0,rel}$-based	78.31 %	-0.39%
β_{dev}-based	79.20 %	+0.74%
$SKEH$-based	78.91 %	+0.36%
η_{de}-based	78.97 %	+0.45%
$C_{ske,1} + \beta_{dev,0.7}$-based	79.17 (81.01) %	+0.69% (-0.09%)
$C_{p0,rel,1} + \beta_{dev,0.7}$-based	79.18 (81.07) %	+0.70% (-0.02%)

It should be noted that, in all cases (with the exception of the $C_{p0,rel}$-based case), both for the CFD as well as experimental results, although the normalized rotor exit and downstream velocities were noted to be consistently lower than those of the annular case, since the velocities mentioned above were the averages of all the velocity magnitudes (including the primary and secondary flow components) and *not* the average of the normal component of the velocity, the mass flow through the blade row was not affected, with this parameter being set as part of the CFD as well as the experimental setups.

Finally, the rotor efficiency measured at the rotor exit (X3) for the $C_{ske,1} + \beta_{dev,0.7}$-based design was noted to be somewhat lower than that measured at the downstream (X4) measurement plane. Although the trend (i.e. a reduction in the efficiency) was considered correct, the magnitude of this reduction was considered anomalous (i.e. too low) and due to an unexpected separation in the flow resulting in lower estimates of the static pressure and therefore efficiency for this design in this location. This separation is described in more detail in Section 9.3.7.

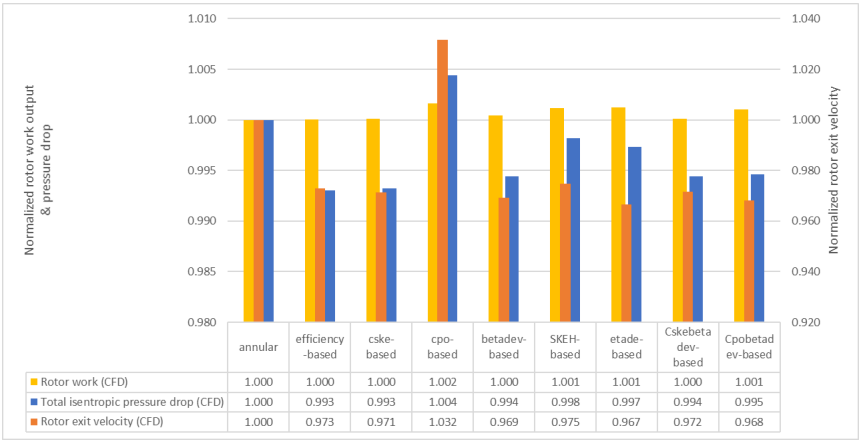

	annular	efficiency -based	cske-based	cpo-based	betadev-based	SKEH-based	etade-based	Cskebeta dev-based	Cpobetad ev-based
Rotor work (CFD)	1.000	1.000	1.000	1.002	1.000	1.001	1.001	1.000	1.001
Total isentropic pressure drop (CFD)	1.000	0.993	0.993	1.004	0.994	0.998	0.997	0.994	0.995
Rotor exit velocity (CFD)	1.000	0.973	0.971	1.032	0.969	0.975	0.967	0.972	0.968

(a) CFD (X3)

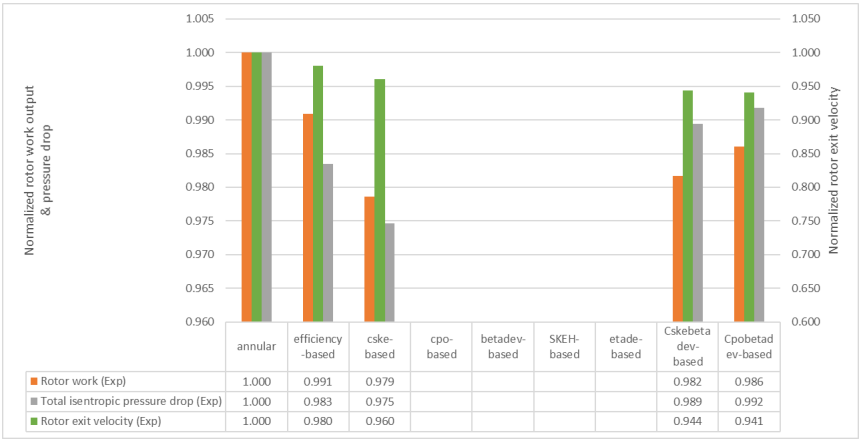

	annular	efficiency -based	cske-based	cpo-based	betadev-based	SKEH-based	etade-based	Cskebeta dev-based	Cpobetad ev-based
Rotor work (Exp)	1.000	0.991	0.979					0.982	0.986
Total isentropic pressure drop (Exp)	1.000	0.983	0.975					0.989	0.992
Rotor exit velocity (Exp)	1.000	0.980	0.960					0.944	0.941

(b) Experimental (X3)

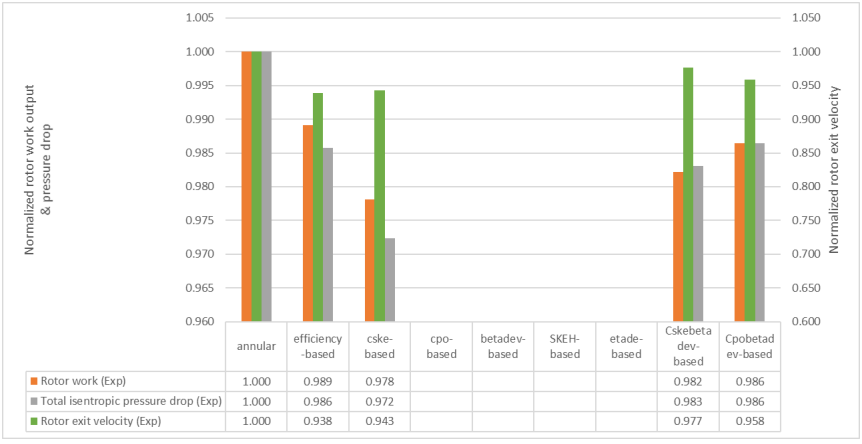

	annular	efficiency -based	cske-based	cpo-based	betadev-based	SKEH-based	etade-based	Cskebeta dev-based	Cpobetad ev-based
Rotor work (Exp)	1.000	0.989	0.978					0.982	0.986
Total isentropic pressure drop (Exp)	1.000	0.986	0.972					0.983	0.986
Rotor exit velocity (Exp)	1.000	0.938	0.943					0.977	0.958

(c) Experimental (X4)

Fig. 8.32: Normalized CFD and experimental rotor work output, isentropic total pressure drop and exit velocities at the rotor exit (X3) and downstream (X4) measurement planes

9

Observations on the selection metrics for the design of non-axisymmetric endwalls

In this Chapter, the results of previous chapters are discussed with the intention of presenting a series of observations on the usefulness of each of the metrics investigated in this work for the design of non-axisymmetric endwall contours.

Firstly, the reductions in each objective function and convergence of the endwall design routine are discussed. The reductions are discussed in terms of the overall decrease in the normalized cost functions, while the convergence of the routine is discussed in terms of various metrics designed to quantify the overall reduction in the variability in the cost function evaluations with progression of the design algorithm. Thereafter, the overall predictability of each of the metrics considered in this thesis was explored by investigating the correlations between the changes in each metric for each of the endwalls (including the annular case) included in the experimental subset as a result of the introduction of the various endwall designs. After this, experimental and original CFD mass- and circumferentially-averaged results for one of the designs (the C_{ske}-based design) are compared with predictions made using a different simulation in order to given an idea of the robustness of the predictions for each of the metrics to changes in the CFD setup.

Finally, the chapter is concluded with a series of observations and summary of the use of each of the previously discussed metrics investigated in this thesis for reliable and effective design of non-axisymmetric rotor endwall contours.

9.1 Optimization

9.1.1 Overall reduction in normalized cost function

A final convergence plot for each endwall optimization, normalized by the initial objective function value (i.e. at iteration 1), is shown in Fig. 9.1. Despite the excellent performance of this endwall, Fig. 9.1 showed that the η_{tt}-based design actually resulted in the smallest overall reduction in the final objective function when compared to the starting value. This was followed by the $C_{p0,rel}$-, $C_{p0,rel,1}+\beta_{dev,0.7}$- and C_{ske}-based endwalls, and then the β_{dev}-, $C_{ske,1}+\beta_{dev,0.7}$-, $SKEH$- and η_{de}-based endwalls, for whom the greatest overall normalized reductions were noted. Further analysis showed an additional interesting feature, and this was that the ranking of the endwalls in terms of their greatest overall reductions generally followed a natural ordering in those metrics whose calculation relied more indi-

rectly on the primary flow variables (such as $C_{p0,rel}$, η_{tt} and C_{ske}). These generally showed smaller reduction ratios and significantly more 'docile' convergence profiles compared to those metrics based more directly on the primary flow quantities (such as the flow angles and velocities).

In addition, with the exception of the $SKEH$-based result, a second grouping could be established, with those metrics generally concerned with the direct or indirect prediction of loss or loss proxy (i.e. the $C_{p0,rel}$-, η_{tt}- and C_{ske}-based endwalls) also tending to show smaller overall reductions in the normalized cost function, while those metrics generally concerned with 'flow quality', tended to show significantly greater reductions. Further, the effect of the combination of the total relative pressure loss coefficient ($C_{p0,rel}$) with the β_{dev} metric in the compound $C_{p0,rel,1} + \beta_{dev,0.7}$-based objective function was clear, with this metric showing a considerably more tempered reduction in the overall objective function than was the case for the β_{dev}-based objective function alone.

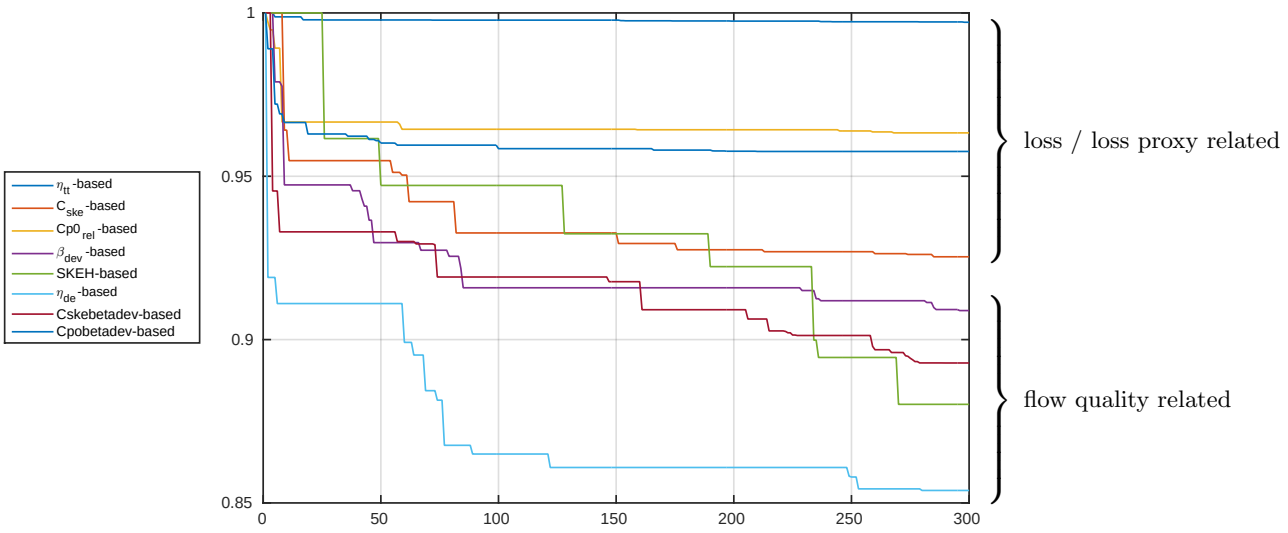

Fig. 9.1: Normalized cumulative minimum objective function values for iterations 1 - 300 ($EI_1 = 1 - 150$, $WB_1 = 150 - 300$)

9.1.2 Convergence

Fig. 9.2 shows the changes in the mean and standard deviations of the objective function values for each phase of the optimization individually, as well as on a cumulative basis. These included the data points in the initial DACE model databases for each objective function, the ISC points evaluated during the balanced (EI_1) search phase of the endwall optimization routine, and finally the ISC points from the (WB_1) (i.e. local) search phase of the optimization procedure which were intended to refine each design. For the 'per phase' plots, the results were normalized using the appropriate objective function values from the initial database data, and for the 'cumulative' plots, the results were normalized using corresponding values calculated over the cumulative data sets.

The different datasets used in the calculations (i.e. the individual and cumulative datasets), as well as the metrics used (i.e. the mean and standard deviations) were devised for the following reasons:-

- **per phase** - this was intended to allow for comparison of the convergence behaviour of each metric between the different phases of the optimization
- **cumulative**[1] - this was intended to allow for the comparison of the convergence behaviour of each metric during each of the optimization phases in terms of the global / overall optimization context
- **mean**[2] - intended to provide an indication of the overall general decrease in objective function magnitude as the algorithm proceeded
- **std dev** (σ) - intended to provide an indication of convergence of each objective function to a final, single value as the algorithm proceeded or equivalently, the overall reduction in the variability of the objective functions as the optimization proceeded.

As expected, despite the inclusion of the additional non-minimum points in the metric, the *mean* objective function metric (Figs. 9.2a - 9.2b) showed similar overall characteristics to those presented already for the reductions in the overall minimum / optimal objective function value (Fig. 9.1). However, for the current metric, the higher percentage of larger objective function values even during the later stages of the endwall optimizations for the $SKEH$- and η_{de}-based endwalls, resulted in a change in the overall ordering, with the $C_{ske,1} + \beta_{dev,0.7}$-, β_{dev}- & C_{ske}-based metrics now showing the greatest overall average reductions in the cost functions.

This is significant because, despite the superior performance of the $SKEH$- and η_{de}-based metrics in terms of the improvement in the minimum objective function value above, this metric showed that even at the conclusion of the design optimization, these objective functions did not reflect the best reductions in the objective function *on average*, and rather larger overall average reductions were achieved by the C_{ske}- and β_{dev}-based metrics, while the η_{tt}-, $C_{p0,rel}$ and $C_{p0,rel,1} + \beta_{dev,0.7}$-based metrics still resulted in relatively small reductions in the overall cost function.

When considered on a 'per optimization phase' basis (Fig. 9.2c), the best performing objective functions were found to be the η_{tt}- and C_{ske}-based metrics. The performance of these metrics were followed by the $C_{ske,1} + \beta_{dev,0.7}$-, β_{dev}-, $SKEH$-, η_{de}-based, and finally the $C_{p0,rel,1} + \beta_{dev,0.7}$- and $C_{p0,rel}$-based metrics. Inspection of the raw data confirmed the excellent reductions in the overall variability of the η_{tt}- and C_{ske}-based objective functions, where at the conclusion of the endwall optimization run, both these metrics showed very little variation in the final objective function values. Again, the poorer-than-expected performance of the $C_{p0,rel}$- & $C_{p0,rel,1} + \beta_{dev,0.7}$-based design metrics in comparison to the $SKEH$- & η_{de}-based metrics was unexpected, and analysis of the raw data showed that this was because of the significantly smaller range of objective function magnitudes present in

[1] Cumulative in this instance meant the statistics were calculated initially over the *entire* dataset ($DB - WB_1$), reduced $EI_1 - WB_1$ dataset, and finally the WB_1 data only

[2] It should be noted that convergence metrics based on the **min** (minimum) objective function values were not included as, for some cases, some objective function values contained in the database dataset were *lower* than those contained calculated later in the EI_1 / WB_1 optimization phases, but were were located in invalid portions of the parameter space (as defined by the parameter constraints in Section 5.6.5) and it was felt these comparisons would skew the overall results. Further, although these points *were* included in the *mean* & *std dev* calculations, because overall only a small number of points were found to violate the parameter constraints, these would have only a small effect on the calculation of these metrics.

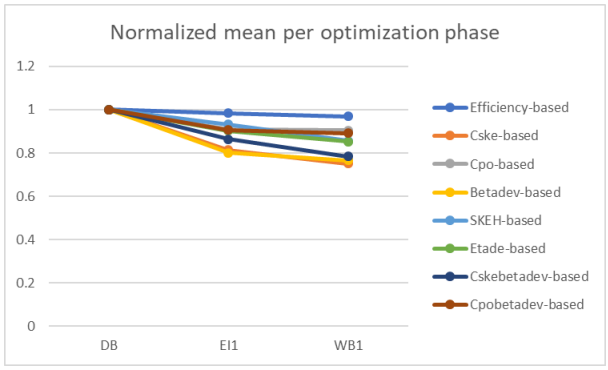

(a) Normalized mean (per optimization phase)

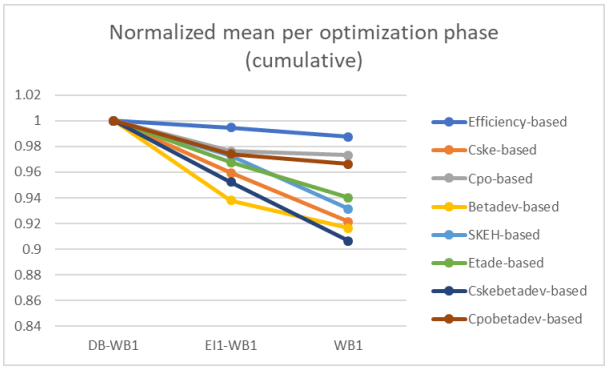

(b) Normalized mean (cumulative)

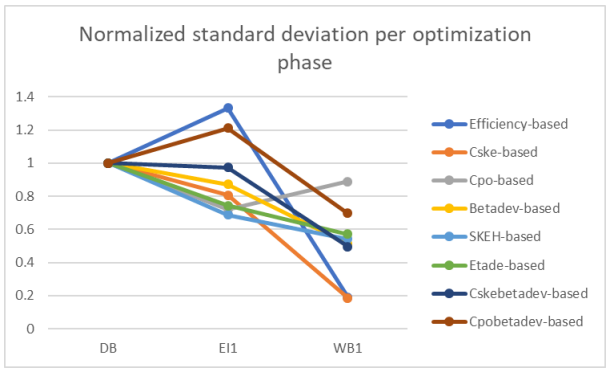

(c) Normalized std dev (σ) (per optimization phase)

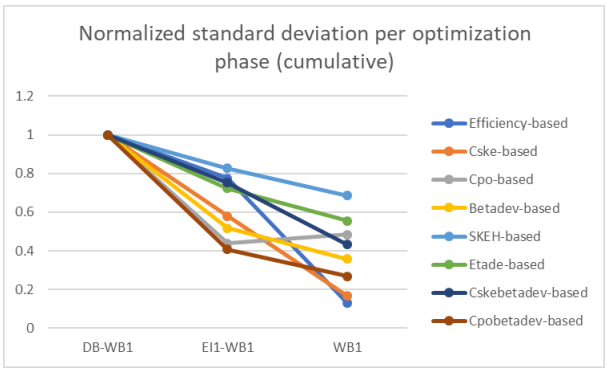

(d) Normalized std dev (σ) (cumulative)

Fig. 9.2: Changes in normalized mean and standard deviation for each endwall calculated per optimization phase (left) and cumulatively (right)

the initial $C_{p0,rel}$ and $C_{p0,rel,1} + \beta_{dev,0.7}$ *DACE* model databases. Recomputing the standard deviation metric over the entire dataset in a cumulative sense resulted in re-ranking of the reductions in the overall cost function standard deviation magnitudes which was more inline with what was expected. The large residual variability in the $SKEH$- & η_{de}-based metrics was once again captured.

The complete objective function evaluation histories for each endwall are shown in Figs. 9.3, coloured by magnitude, as well as the trace of the current lowest feasible objective function magnitude at each iteration.

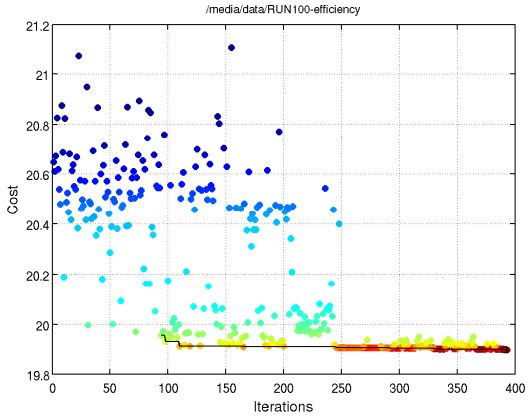

(a) η_{tt}-based

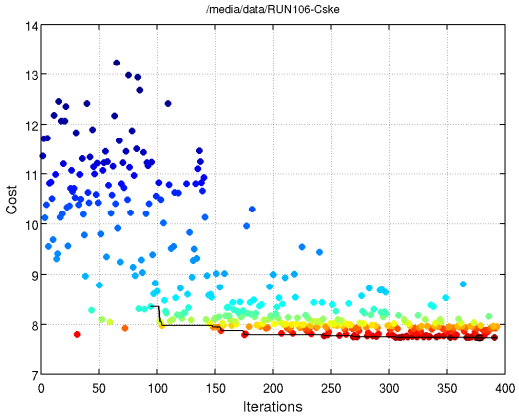

(b) C_{ske}-based

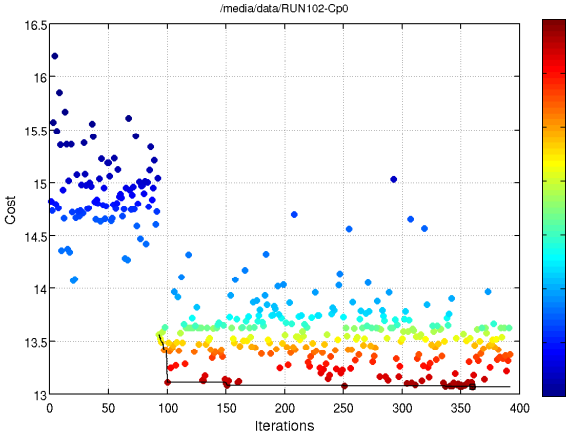

(c) $C_{p0,rel}$-based

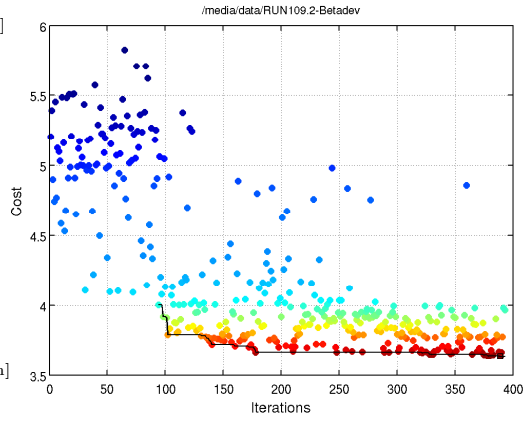

(d) β_{dev}-based

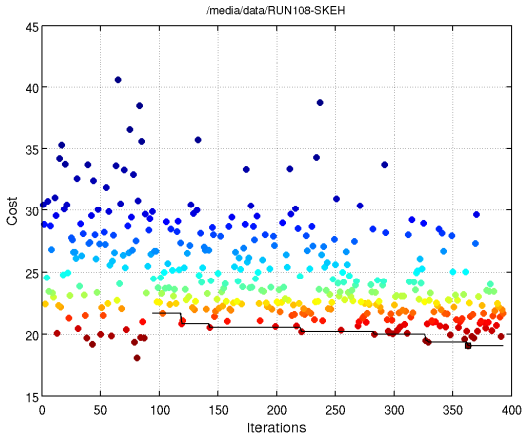

(e) $SKEH$-based

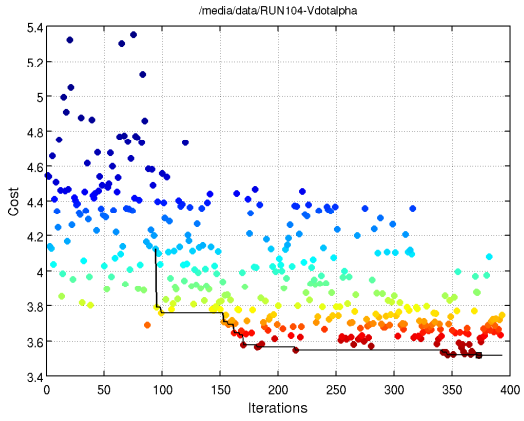

(f) η_{de}-based

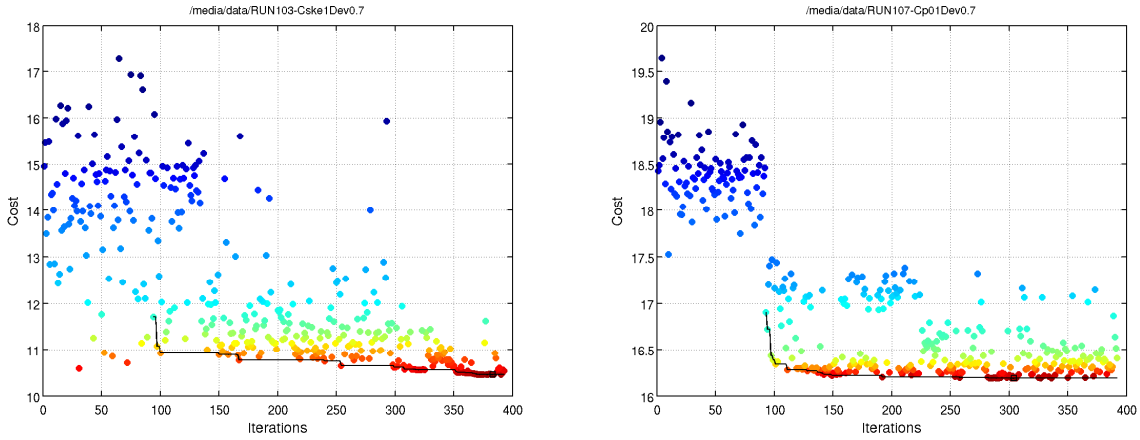

(g) $C_{ske,1} + \beta_{dev,0.7}$-based (h) $C_{p0,rel,1} + \beta_{dev,0.7}$-based

Fig. 9.3: Objective function evaluation histories for each optimized design (including the initial objective function evaluations used to generated the initial *DACE* model database, Iterations 1 - 92/93)

Line	Description
●	high OF value point
●	low OF value point
———	current best OF value
□	final (optimum) OF value

Table 9.1: Plot legend - Objective function magnitudes

9.1.3 Summary

Analysis of the final optimization data produced during each endwall optimization resulted in the discovery of a number of interesting details:-

- In terms of the overall reduction in the mass-averaged objective function magnitudes, the 'flow quality' orientated metrics resulted in significantly greater reductions in the final objective function value when compared to the 'loss' and 'loss proxy' metrics (including the efficiency).
  - Further, the loss type metrics (including the loss proxy metrics, with the exception of the $SKEH$), showed considerably more 'docile' characteristics as the final objective function value was approached, with reasonably evenly spaced small reductions in the current minimum objective function value in comparison to the 'flow quality' type metrics, which continued to show reasonably significant stepwise reductions in the objective function magnitude even relatively close to the end of the endwall optimization run.
  - Finally, when the normalized reductions in the objective function values were plotted together (excluding the $SKEH$-based metric), the C_{ske}-based metric was found to form the partition between the 'loss' and the 'flow quality' type functions.

- The overall change in the range of the objective function magnitudes (i.e. variability) was quantified by calculating the reductions in the normalized mean and standard deviations of the objective function magnitudes per optimization phase, as well as cumulatively over the entire optimization run.
  - Whether considered per optimization phase, or cumulatively, the η_{tt}- & C_{ske}-based both showed the best decreases in objective function variability, suggesting that these metrics had converged satisfactorily to a reasonably well-defined optimum point.
  - In contrast, both the η_{de}- & $SKEH$-based metrics both continued to show a great deal of variability in objective function magnitudes even within the final optimization phase, suggesting that for these cost functions, the convergence to a well-defined / single optimum had not necessarily been achieved. This corroborated the findings discussed in the presentation of the optimization results in Chapter 7 (Section 7.1 and Figs. B.17 - B.24).
  - In addition, although when considered only per optimization phase, the $C_{p0,rel}$ & $C_{p0,rel,1} + \beta_{dev,0.7}$-based metrics showed poorer performance than expected, when considered over the entire optimization dataset, the above average reductions in objective function variability magnitudes were noted, again suggesting that these metrics had converged reasonably well to a well-defined optimum.

9.2 Predictability

9.2.1 Correlation with experiments

Because each of the flow metrics (with the exception of the $SKEH$) investigated in this study were measured for each of the four contoured (as well as the annular) designs included in the experimental subset, some comment can be made regarding the predictability of each of these metrics and therefore their potential usefulness in the design of endwall contours. This was done by comparing the predicted changes of each quantity as a result of the changes made to the endwall surfaces, to those measured for each endwall design. Although the overall magnitudes predicted for each quantity were important, in the discussion below, more emphasis was placed on the predictability of the *relative* magnitudes of each quantity between designs. This is because, in design optimization, one is usually more interested in maximising (or minimizing) a particular quantity relative to a baseline case rather than optimizing design with the express intent of achieving a particular predetermined value for that quantity.

Line	Description
	Experimental
	CFD
	Polynomial fit (Exp)
	Polynomial fit (CFD)

Table 9.2: Plot legend - Comparison between experimental & CFD mass-averaged total quantities at rotor exit (X3) and downstream (X4) measurement planes

Table 9.3: Summary of Pearson correlation coefficients for each metric[a] at rotor exit (X3) and downstream (X4) measurement planes including and excluding the 'compound' endwall designs

Endwall	*Rotor exit (X3)*		*Downstream (X4)*	
	All	*Excluding 'compounds'*	*All*	*Excluding 'compounds'*
η_{tt}	0.24	0.89	0.49	0.90
C_{ske}	0.61	0.99	0.16	0.65
$C_{p0,rel}$	-0.01	0.18	0.88	0.99
β_{dev}	0.14	0.99	-	-
η_{de}	0.92	0.94	-	-

[a] excluding $SKEH$

In the figures below (Figs. 9.4a - 9.5h), both the predicted as well as experimental magnitudes of each of the flow metrics investigated in this thesis were plotted, with the former including data from the entire experimental subset, and the latter including only the results for the annular, η_{tt}- & C_{ske}-based designs. In each case, the experimental and CFD results were plotted on different vertical axes because for some metrics, large differences between the predicted and experimental absolute magnitudes of the metric existed. This also allowed for the visual comparison of the changes in each metric for the different endwalls relative to one another. In addition, for each of the metrics, a 4^{th}-order polynomial trendline, was computed. These are also plotted on each figure as an additional means to qualitatively compare the correlation between the two sets of results.

In addition, the correlations between the predicted and experimental mass-averaged magnitudes of each design metric for each design included in the experimental subset are reported in Table 9.3. For these comparisons, the correlations were calculated as the well-known Pearson correlation coefficient (r), which gives an indication of the degree of linear correlation between two variables. For this analysis therefore, strong positive correlations (i.e $r = +1$) would indicate a robust positive correlation between the predicted and experimental magnitudes of each metric for different endwall designs and vice versa.

As indicated, the correlations are reported twice, initially for the simple (i.e. annular and η_{tt}- & C_{ske}-based) cases only, and secondly including the results from the remaining two endwalls (i.e. the 'compound' designs). Finally, the reasons for the exclusion of the compound designs are discussed as part of the observations made for these endwalls in Section 9.3.

Efficiency (η_{tt})

Although in general, both at the rotor exit (X3) (Fig. 9.4a) and downstream (X4) (Fig. 9.4b), the rotor efficiencies appeared to be well predicted by the CFD, inspection of Table 9.3 showed that when calculated over the entire experimental subset, the actual correlation between the changes to the endwall surface and the predicted efficiencies, were relatively poor (+0.24 & +0.49 respectively). Review of Figs. 9.5a & 9.5b in the light of the above showed that, at both measurement locations, the poor correlations were as a result of the $C_{ske,1} + \beta_{dev,0.7}$- & $C_{p0,rel,1} + \beta_{dev,0.7}$ efficiency predictions, which were both overpredicted at the rotor exit, while at the downstream location, were both overpredicted. Re-calculation of the correlations, including

only the 'simple' designs, resulted in considerably better correlations between the changes to the endwalls and the predicted efficiencies (+0.89 & +0.90) at both measurement planes.

Secondary kinetic energy (C_{ske})

Table 9.3 and Fig. 9.4c showed that, at the rotor exit (X3), the prediction of the coefficient of secondary kinetic energy, was reasonably good (+0.61), even when the results of the 'compound' endwalls were included. As was the case with the efficiency results, when the $C_{ske,1} + \beta_{dev,0.7}$- & $C_{p0,rel,1} + \beta_{dev,0.7}$-based results were excluded, a near perfect linear correlation between the predicted and experimental results for each endwall geometry was shown. Downstream of the rotor exit, the predictability of the secondary kinetic energy was poor (+0.16), however once again, this was improved when the results of the compound designs were removed (+0.65).

Loss ($C_{p0,rel}$)

At the rotor exit (X3), the correlation between the relative magnitudes of the predicted and measured loss coefficients for each endwall was poor, both including and excluding the 'compound' designs. This was clearly illustrated in Fig. 9.5e where the reasonably large reduction in loss measured for the η_{tt}-based design, was not reflected in the CFD results. Similarly, the predicted reduction in the loss coefficient at the rotor exit for the $C_{p0,rel,1} + \beta_{dev,0.7}$-based design was not seen to manifest during the experimental testing of that endwall. Further downstream however (Fig. 9.4f), the correlations between the predicted and experimental loss coefficients for each design were very good (+0.88), and this was seen to be even better with the 'compound' designs excluded from the calculation (+0.99) (Fig. 9.5f).

Flow deviation (β_{dev})

As was the case for all the results presented to date, results for the flow deviation from design (β_{dev}) were only presented at the rotor exit, since design flow angles were not available at the downstream (X4) measurement plane. When calculated over the entire dataset (Fig. 9.4g), the correlations for the mass-averaged flow deviations were poor (+0.14), and this was once again as a result of the poor agreement between the predicted and measured results for the so-called 'compound' designs. As was the case for both the rotor efficiency as well as the coefficient of secondary kinetic energy, this correlation was found to improve dramatically when excluding the 'compound' designs (+0.99) (Fig. 9.5g).

Design efficacy (η_{de})

Once again, results for the design efficacy (η_{de}) are only presented at the rotor exit (X3) (Figs. 9.4h & 9.5h). At this location, the correlation between the predicted and experimental design efficacies for those endwalls included in the experimental subset, were extremely good (+0.92), resulting in fact in the best correlations of all those results for which the entire set of experimental

results were included. Further to this, and as was the case for the majority of the endwalls, when the so-called 'compound' designs were omitted from the calculations, the overall degree of correlation was seen to increase further (+0.94). As was the case for the rotor exit flow deviation angles, apart from the relative overprediction of the design efficacy of the $C_{p0,rel,1}+\beta_{dev,0.7}$-based design, the CFD was also noted to overestimate the mass-averaged magnitude of the η_{tt}-based rotor exit design efficacy, which when measured, was significantly closer to that measured for the C_{ske}-based design.

Summary

Analysis of the predicted and experimental magnitudes of each of the metrics above in a fashion similar to that done for the *DACE* model predictions of the CFD simulations during the endwall optimizations (i.e. Fig. 5.3a), showed that in almost all cases, it was the poor prediction of the various metrics for the two compound endwalls which resulted in the poor correlations reported in Table 9.3. As a result of this visual inspection of the data, the coefficients were recomputed excluding the predictions for the 'compound' endwalls, and reported in the table with the generally improved values for r discussed above.

Notwithstanding the above, the excellent predictability of the coefficient of secondary kinetic energy (C_{ske}), flow deviation (β_{dev}) and design efficacy (η_{de}) at the rotor exit were noted. These results, in addition to the comparatively poor predictability of the rotor exit loss coefficient, corroborate the views of a number of previous researchers, who have long held that the flow velocity and angles were among those metrics which could be expected to be most reliably predicted by CFD, while the opposite was true of the loss. However, in addition to this, one of the most significant findings of this analysis, was the excellent prediction of the rotor efficiency, both at the rotor exit, as well as at the downstream ('mixed-out') measurement plane, which now provides a further potentially excellent metric to future researchers for the design of endwall contours. In addition, while neither the complete dataset, nor the exclusion of the so-called 'compound' metrics from the data resulted in correlations of note between the CFD and experiment for the total relative loss coefficient at the rotor exit, at the downstream plane, the predictions for this quantity correlated well with the experimental measurements, with a near perfect linear correlation between the data when the 'compound' metrics were excluded.

Further, the reversal in fortunes between predictions of the coefficient of secondary kinetic energy and loss coefficient at the 'mixed-out' plane was most certainly (in the absence of the issues related to the compound designs mentioned above) a result of inaccuracies in the calculation of the mixing out of the flow by the turbulence model used in the investigation.

Finally, while the sample sizes used in the calculation of the correlations reported above were small, especially with the exclusion of the so-called compound designs, they did provide at least some quantitative measure of the predictability of the metrics examined in this investigation especially since the results did appear to corroborate a number of previously held positions on the predictability of various quantities and also confirm some of the findings related to the excellent performance and validation of the rotor efficiency in this investigation.

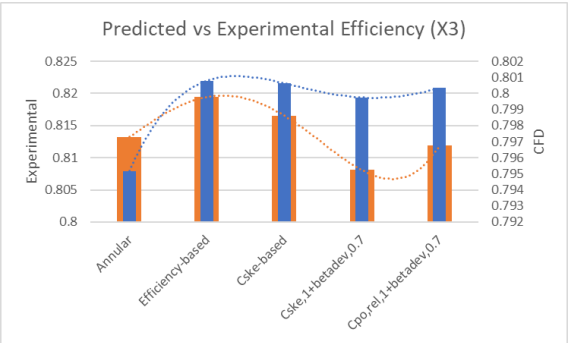

(a) η_{tt} (X3)

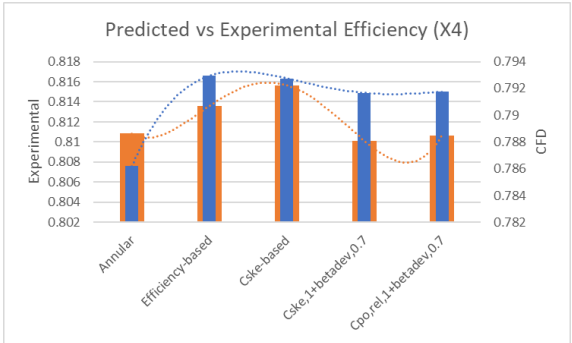

(b) η_{tt} (X4)

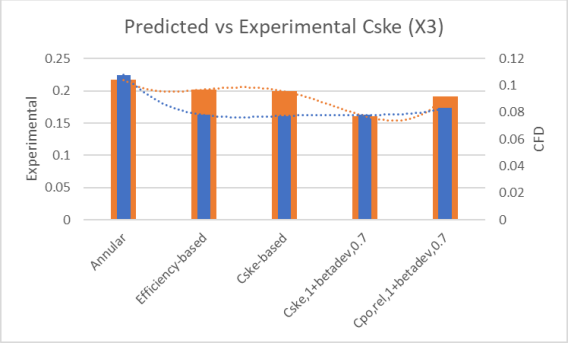

(c) C_{ske} (X3)

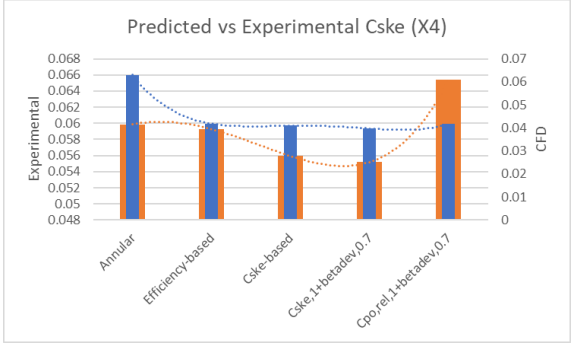

(d) C_{ske} (X4)

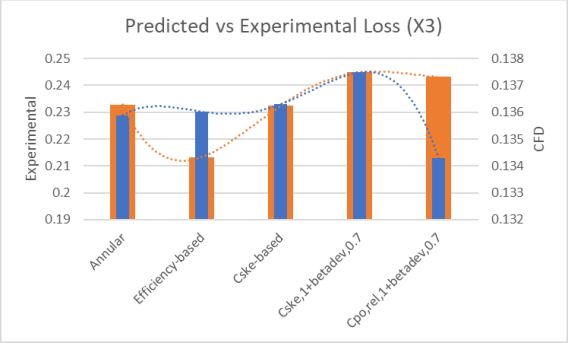

(e) $C_{p0,rel}$ (X3)

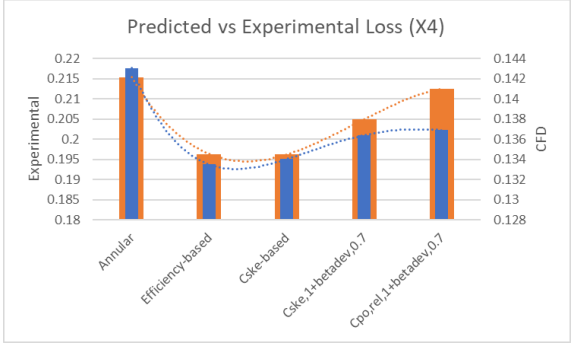

(f) $C_{p0,rel}$ (X4)

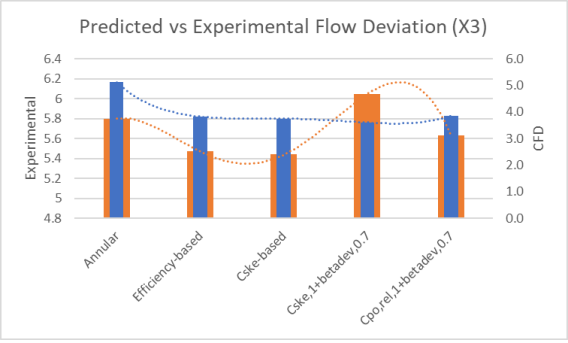

(g) β_{dev} (X3)

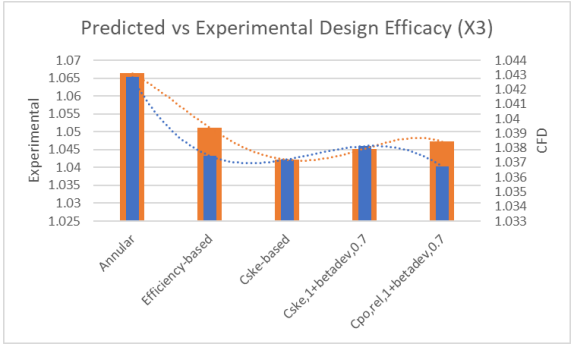

(h) η_{de} (X3)

Fig. 9.4: Predictability of the various flow metrics at the rotor exit (X3) and downstream ('mixed-out') measurement (X4) planes based on the full experimental data set

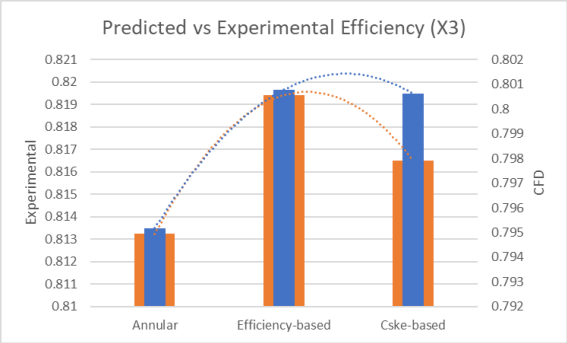

(a) η_{tt} (X3)

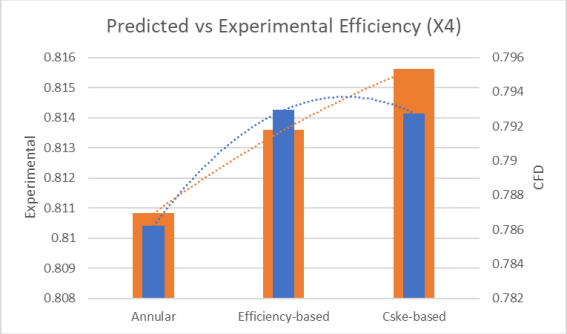

(b) η_{tt} (X4)

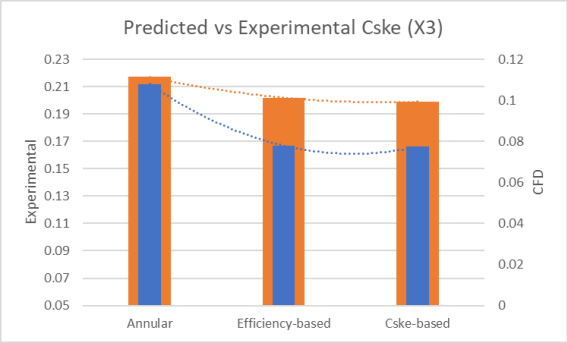

(c) C_{ske} (X3)

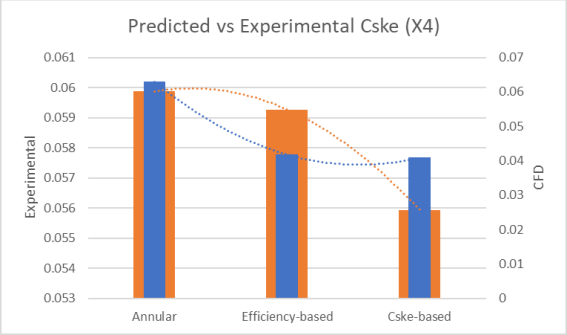

(d) C_{ske} (X4)

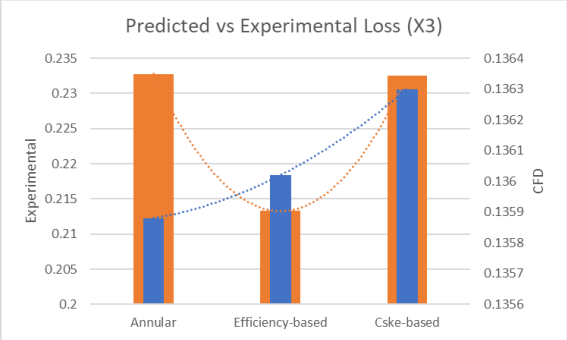

(e) $C_{p0,rel}$ (X3)

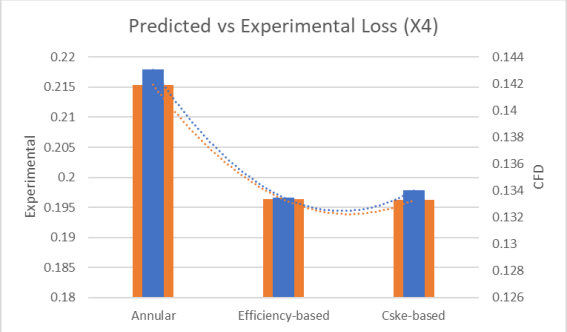

(f) $C_{p0,rel}$ (X4)

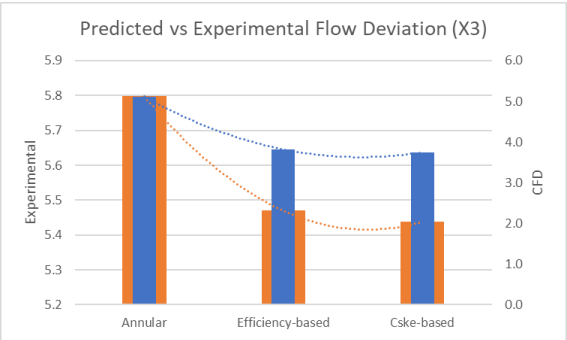

(g) β_{dev} (X3)

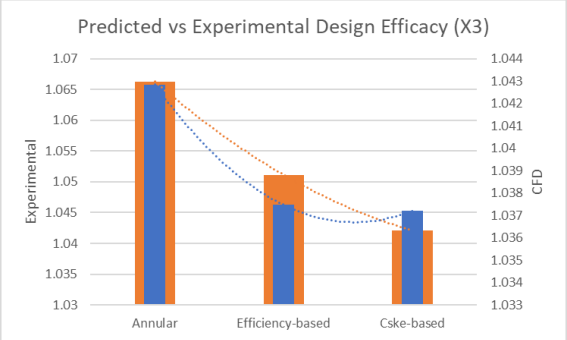

(h) η_{de} (X3)

Fig. 9.5: Predictability of the various flow metrics at the rotor exit (X3) and downstream ('mixed-out') measurement (X4) planes based on the reduced experimental data set

9.2.2 Comparison with Spalart-Allmaras turbulence model

In this Section, the robustness of each metric's predictability is examined by comparing the original experimental and CFD results with a further set of computational results produced using a slightly modified CFD routine. For this part, changes to the CFD were limited to the turbulence closure used, because differences in turbulence model selection were considered most likely to be among the largest differences between different design investigations.

The Spalart-Allmaras model was chosen for this comparison because - although it is a comparatively simple model - it has seen increasing use within the turbomachinery community for the prediction of turbine flows (Dunn et al. (2009), Denton and Pullan (2012)).

As was done previously, the comparisons in this section are made on both mass-averaged as well as circumferentially-averaged bases for each quantity.

Line	Description
	Experimental
	$k-\omega\ SST$
	Spalart-Allmaras

Table 9.4: Plot legend - Experimental vs CFD mass-averaged results for different turbulence models

Mass-averaged results

Overall and in terms of the the mass-averaged predictions, the two sets of CFD predictions showed a reasonable degree of consistency to one another.

More specifically, at the rotor exit (X3) measurement plane:-

- Both turbulence models predicted the same trends for all of the flow quantities, with the exception of the rotor exit loss coefficient ($C_{p0,rel}$), which for the original simulation, was predicted to increase while for the Spalart-Allmaras predictions, was predicted to decrease in magnitude (consistent with the measured results of the experiment).
- Further and with the exception of the rotor exit (X3) η_{de} results, although as was the case for the $k-\omega\ SST$ model, the Spalart-Allmaras model tended to overpredict the overall changes of each metric from the baseline design, although specific to the Spalart-Allmaras case, the magnitude of these overpredictions were generally smaller, indicating that while the overall prediction of trends for each metric was robust, the magnitude of the changes was highly dependent on the turbulence model used, corroborating the observations relating to turbulence model selection discussed in Section 6.3.5.
- Finally, the absolute magnitude of the mass-averages for all quantities were consistently underpredicted for both turbulence models.

At the downstream (X4) measurement plane, again, both turbulence models were seen to predict the correct trends in terms of the changes from the baseline case with reasonable accuracy. However, in contrast to the rotor exit results, at this location, this included the 'mixed-out' loss.

In addition to the above, the following observations were noteworthy:-

- In general, the mass-averaged reductions in the downstream secondary kinetic energy (i.e. C_{ske}) were again overpredicted by both turbulence models (and once again, especially by the $k-\omega$ SST model), while the reduction in mass-averaged 'mixed-out' loss was underpredicted by both models.
- At the downstream measurement plane, the Spalart-Allmaras model was seen to predict the improvement in the rotor efficiency considerably more accurately than the more complex model, although as was the case at the rotor exit, in both cases the actual efficiencies were again underpredicted in magnitude.

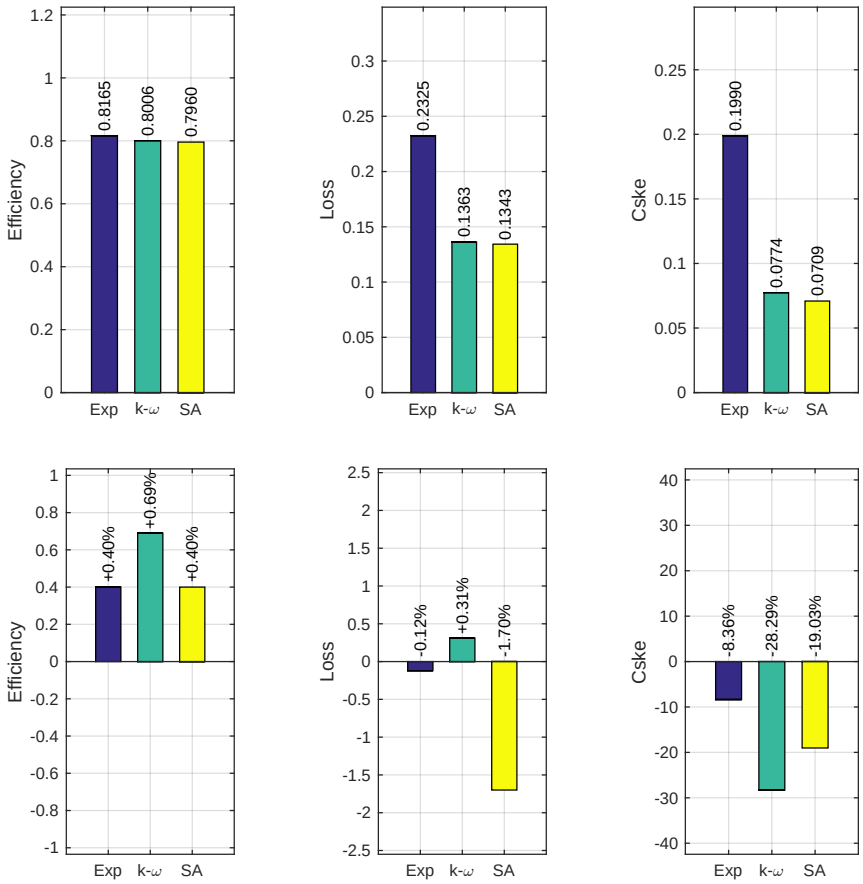

Fig. 9.6: Mass-averaged (top) & percentage change from annular (bottom) at the rotor exit (X3) for the experimental, $k-\omega$ SST and Spalart-Allmaras-based simulations

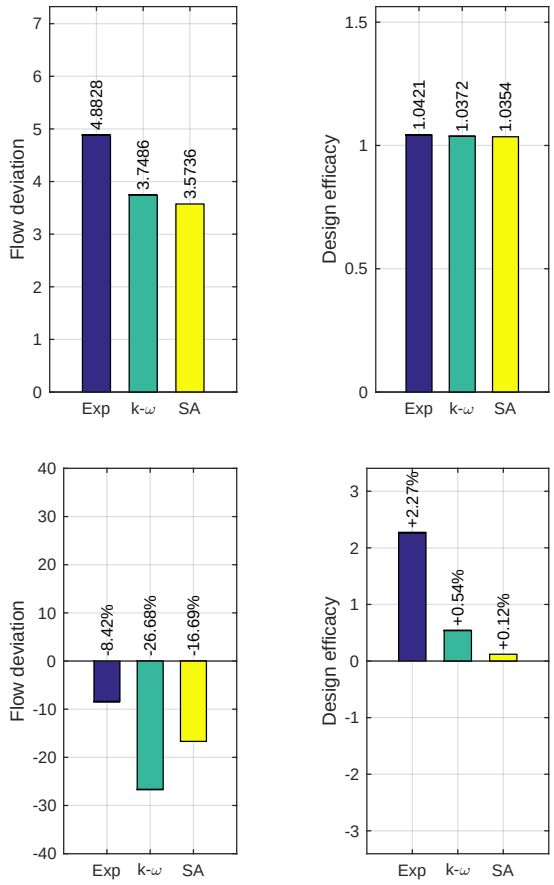

Fig. 9.6: Mass-averaged (top) & percentage change from annular (bottom) at the rotor exit (X3) for the experimental, $k-\omega$ SST and Spalart-Allmaras-based simulations (cont)

Circumferentially-averaged results

Figs. 9.8 to 9.9 show the comparisons between the circumferentially-averaged experimental and CFD predictions produced using the $k-\omega$ SST and Spalart-Allmaras turbulence models at the rotor exit (X3) and downstream (X4) measurement planes respectively. In addition to those quantities presented previously for each design, for the current set, the rotor relative flow velocity (W) at both locations is also presented.

Line	Marker	Description
———	none	Design
———	○	Experimental
———	◇	$k-\omega$ SST
———	◇	Spalart-Allmaras

Table 9.5: Plot legend - Experimental vs CFD (different turbulence models) circumferentially-averaged results

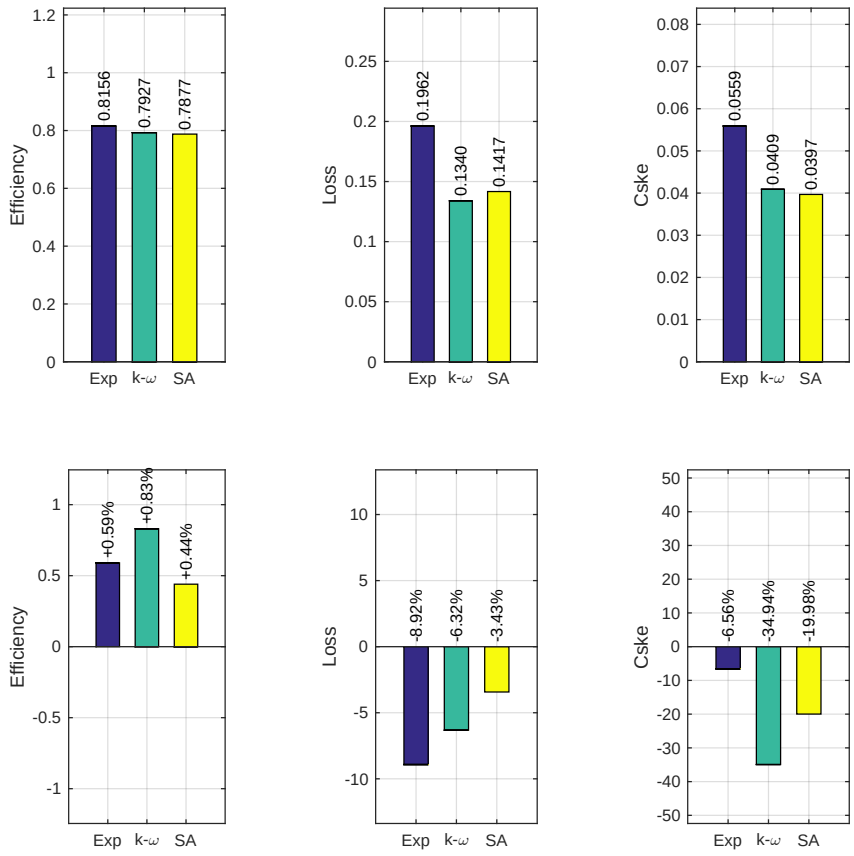

Fig. 9.7: Mass-averaged (top) & percentage change from annular (bottom) at the downstream (X4) measurement plane for the experimental, $k-\omega$ SST and Spalart-Allmaras runs

At the rotor exit (X3), in general, the overall characteristic forms of the spanwise profiles computed using the simpler Spalart-Allmaras (Figs. 9.8a-9.8f) model matched those produced using the more complex model confirming the general robustness of the CFD to predict each of the quantities with reasonable confidence, with the most important observations being:-

- As indicated, for all quantities (with the express exception of the rotor exit relative velocity (W) and loss ($C_{p0,rel}$)), the overall characteristic shapes of the spanwise profiles for both turbulence models matched one another with a reasonably high degree of similarity with the locations of the various peaks noted to be largely identical in their spanwise positions.
- Further to the above, while the spanwise locations of the various peaks were noted to correspond well to one another for both turbulence models (as well as - generally - the experimental results), the most notable difference between the predictions were restricted to the magnitude of these peaks, with these differences (although reasonably small), noted to be most prevalent in the tip and endwall adjacent regions.
- Finally, as indicated above, in contrast to the majority of the metrics, the spanwise profiles of the rotor exit relative flow velocity (W) (Fig. 9.8b) and relative total pressure loss coefficient ($C_{p0,rel}$)

(Fig. 9.8d) showed that, the change in the turbulence models used for each simulation resulted in non-trivial changes to the spanwise profiles for each quantity, particularly in the secondary flow region.

- In particular, in terms of the rotor relative flow velocity (W), the differences between the predictions of each turbulence model were particularly clear between $\sim 0-40\%$ span, where although the average magnitudes were overpredicted, the velocity profile for the Spalart-Allmaras simulation was noticeably better than that of the more complex model.
- Similarly and consistent with the better prediction of the relative flow velocities, the prediction of the rotor relative loss coefficient for the same region was noted to be significantly better for the Spalart-Allmaras result.

Finally, at the downstream (X4) measurement plane, the comments related to robustness of the different turbulence models for the prediction of the major flow variables at the rotor exit (X3) remained valid, with the results both CFD simulations predicting the same spanwise locations for the various local circumferentially-averaged peaks for the majority of the quantities as well as similar overall characteristic shapes for each profile.

Once again however, as was the case at the rotor exit, at the downstream plane, the predictions of the 'mixed-out' relative velocities in the secondary flow region were noticeably better for the simpler (Spalart-Allmaras) model than for the $k-\omega$ SST case, with the former reproducing the characteristic shape of the velocity profile with considerable more accuracy. Once again, this result was accompanied by a correspondingly better prediction of the 'mixed-out' loss coefficient whose spanwise profile was noted to match that of the experiment below the midspan with near perfect accuracy.

Summary

The general robustness of the majority of the parameters investigated in this thesis quantified by the correlation coefficients presented in the previous section, appeared to be confirmed *and extended* by the results presented in this section, including the general robustness of the majority of the metrics investigated in this thesis (at both measurement planes), including the coefficient of secondary kinetic energy (C_{ske}), flow angles (β) (and therefore the flow deviation angle (β_{dev}) as well) and design efficacy (η_{de}), but also the rotor efficiency (η_{tt}).

In addition, the lack of robustness in terms of the predictability of the rotor relative total pressure loss coefficient ($C_{p0,rel}$) - particularly at the rotor exit - was shown, with the change to the simpler turbulence model resulting in a change to the previous trend predicted by the CFD, to one which matched the experiment for this endwall. The discrepancies between the two predictions of the rotor exit loss coefficient was easily noted to be as a result of the much better prediction of the relative flow velocity at the rotor exit (which although were overpredicted for both cases), was significantly more reliably reproduced by the Spalart-Allmaras model. A similar result was noted at the downstream measurement plane, although, in this case, despite the better prediction of the relative velocity profile, the effect was less evident, with both CFD results predicting the correct trends in terms of the changes in loss from the annular endwall. This then provided additional corroboration of the better correlations of the loss changes between endwalls at the downstream measurement plane discussed in the preceding section.

9.2.3 Conclusions

The results of this section tell an interesting story. In general, when considering the correlations between the changes to the rotor endwall geometry and the various flow metrics investigated in this study, and when the so-called 'compound' designs were excluded, the following conclusions can be made:-

- In terms of the correlations between predicted and observed changes to each of the flow metrics with changes to the endwall geometry, the most reliably predicted metric, both at the rotor exit as well as at the downstream measurement plane, was the rotor total-total efficiency (η_{tt}).
- Similarly, the coefficient of secondary kinetic energy (C_{ske}) was also generally well predicted, although this metric showed a clear advantage even over the rotor efficiency when considered immediately behind the rotor, while it was also noted that the selection of the turbulence model was important in determining its predictability downstream.
- The results for rotor loss coefficient ($C_{p0,rel}$) showed that, close to the rotor exit, the predictability of the metric was poor, although further downstream at the 'mixed-out' measurement plane, the correlations between the predicted and experimental loss coefficient were very good.
- Finally, although the flow deviation (β_{dev}) and design efficacy (η_{de}) were only measured at the rotor exit, the correlations between the predicted mass-averaged magnitudes of each metric and the changes to the endwall geometry, were found to be very good - with the correlations for the design efficacy noted to be nearly perfectly linear.

Making changes to the CFD simulation parameters (and more specifically, changing the turbulence closure), allowed for an investigation into the sensitivity of each metric to variations in the numerical setup. For this comparison, the reasonably simple 1-equation Spalart-Allmaras model was selected primarily because of its increasing popularity within the turbomachinery community.

Despite the changes to the turbulence model, in general, the CFD was still able to predict the correct trends for the majority of the design metrics, with only the loss at the at the rotor exit proving difficult. Further to this:-

- While the general trends for each of the metrics remained robust with the turbulence model change, the overall magnitudes of each metric predicted by the CFD in most cases remained largely unaffected by the changes to the CFD setup, in both cases, these magnitudes were well below the actual experimental values, with the rotor exit efficiency (η_{tt}) and design efficacy (η_{de}) appearing to be the most significantly affected quantities.
- Further to this, and again while the overall trends for each metric remained unchanged, the percentage change in each metric from the baseline case *was* found to be dependent on the selection of the turbulence model, with the more complex $k-\omega$ SST model found to predict consistently larger changes than the simpler Spalart-Allmaras model.
- Finally, while the simpler model was found to generally predict smaller changes from the baseline case, the magnitude of these changes were, in general, much closer in size to those measured during the experiments.

When the spanwise profiles for each metric were compared, in general, it was found that although both simulations produced reasonably similar predictions, those metrics which were found to be most dependent on the relative flow velocity (W) (i.e. the relative total pressure loss coefficient ($C_{p0,rel}$) and design efficacy (η_{de})), displayed the greatest differences.

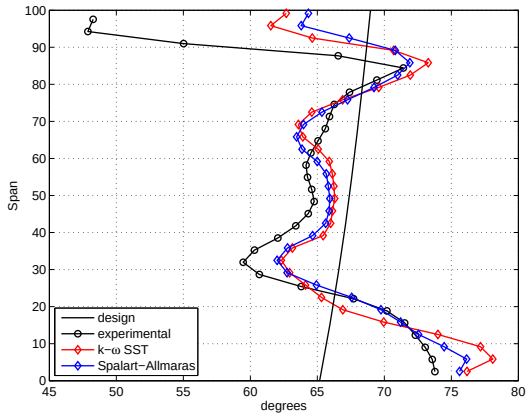

(a) β_3

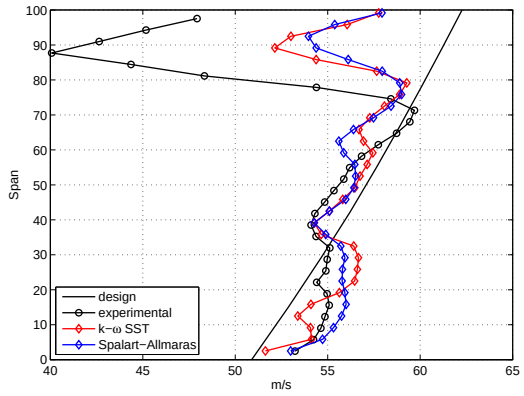

(b) W_3

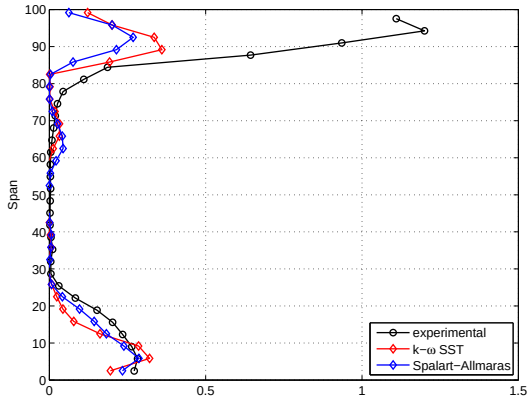

(c) $C_{ske,3}$

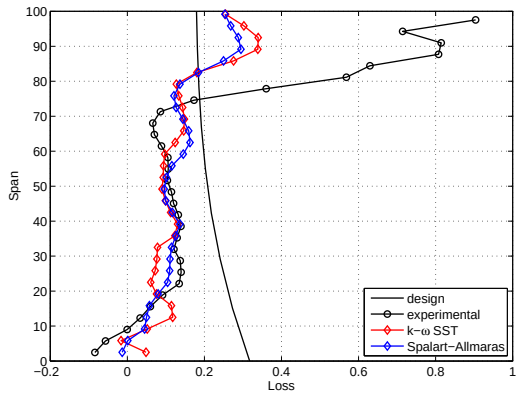

(d) $C_{p0,rel,3}$

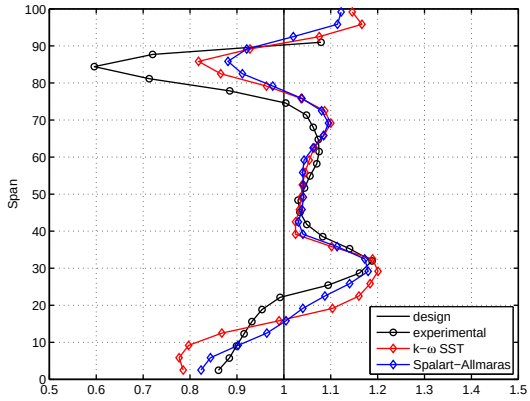

(e) $\eta_{de,3}$

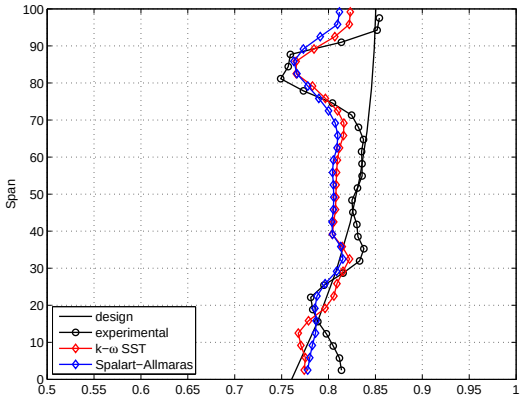

(f) $\eta_{tt,3}$

Fig. 9.8: Comparison of predicted & experimental results for the C_{ske}-based endwall using the $k-\omega$ *SST* & Spalart-Allmaras turbulence models at the rotor exit measurement plane (X3)

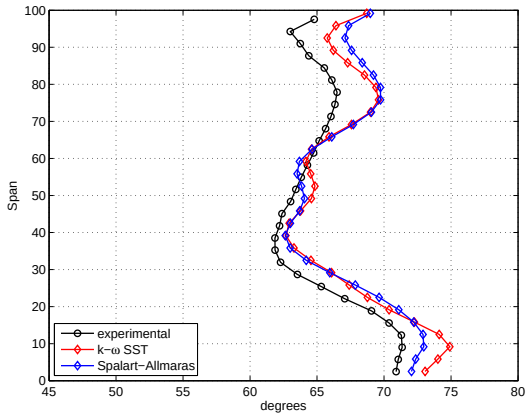

(a) β_4

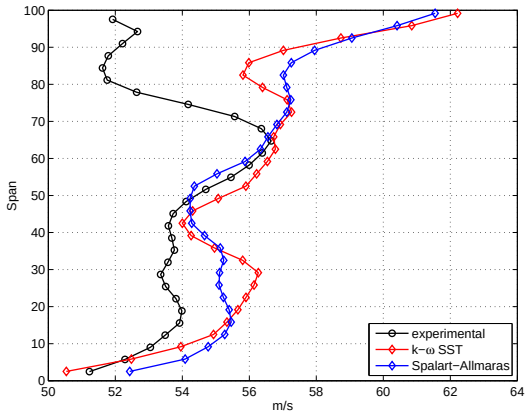

(b) W_4

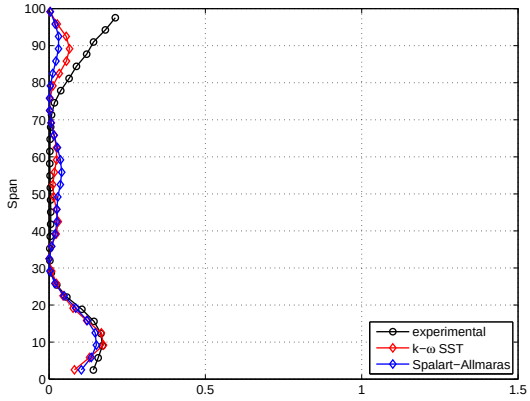

(c) $C_{ske,4}$

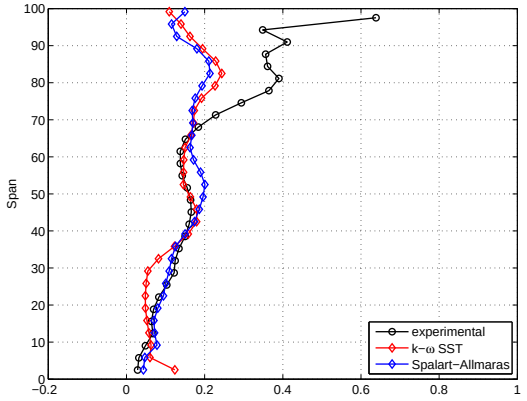

(d) $C_{p0,rel,4}$

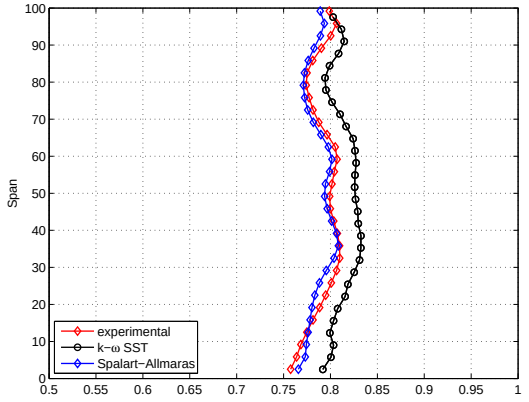

(e) $\eta_{tt,4}$

Fig. 9.9: Comparison of predicted & measured results for the C_{ske}-based endwall using the $k-\omega$ *SST* & Spalart-Allmaras at the 'mixed-out' measurement plant (X4)

9.3 Observations on objective function selection

9.3.1 Efficiency (η_{tt})

In this investigation, the best performing endwall - both predicted as well as when tested experimentally - was the η_{tt}-based design, which resulted in a predicted increase in the rotor efficiency of +0.71% and a validated increase of approximately +0.76% when measured at the rotor exit (X3). In addition, although a small increase (+0.10%) in the rotor exit loss coefficient was predicted for the design, experimental testing also showed a significant reduction in the final mass-averaged loss magnitude (−8.38%). Further to this, a reasonable reduction in the mass-averaged coefficient of secondary kinetic energy (−7.00%) as well as the flow deviation from design (−5.66%) were also measured.

Analysis of the endwall pressure and streamline plots of Chapters 8 showed that the final η_{tt}-based design functioned in a manner consistent with the descriptions of a number of the earlier investigators to reduce the overall secondary loss and thereby improve the efficiency of the blade row. In short, these could be described as reducing the intensity of the main secondary flow feature - the passage vortex - by:-

1. reducing the cross-passage pressure gradient and therefore the driving force behind the formation of the passage vortex, through the introduction of the familiar 'hump-and-dip' endwall configuration, as well as,
2. interfering with the formation of the pressure side horseshoe vortex (and so the early development of the passage vortex), through the introduction of a physical obstruction to the vortex close to the leading edge of the blade.

While the first mechanism above has been described on numerous occasions with respect to the functioning of non-axisymmetric endwall contouring, the second mechanism was (to the authors knowledge), first described in the context of secondary flow mitigation by endwall contouring by Ingram (2003) - who indicated (as shown in the endwall pressure and streamline plots of Chapter 8) that this mechanism operated by encouraging the flow ahead of the leading edge to flow around the suction side of the leading edge and in so doing, weakened the overall intensity of the pressure side *HSV*. However, in addition to the above, for the present design, analysis of the streamline plots on the pressure side of the leading edge (Fig. 9.10), also showed the propensity of that part of the flow which *was not* forced onto the suction side of the leading edge, to re-attach to the convex (or 'hump') portion of the endwall surface before finally separating from the endwall and being incorporated into the passage vortex.

Although, as discussed above, some of the fluid originally rolled up into the pressure side horseshoe vortex was still seen to enter the blade passage on the pressure side of the leading edge, one consequence of the aerodynamic 'blocking' of the pressure horseshoe vortex described above, was the additional loss generated by the reversal and subsequent shearing of this fluid on itself as it was forced onto the suction side of blade leading edge. This effect was well illustrated in the entropy generation plots of Section 8.4 (Fig. 8.24) for the present case, as well as the C_{ske}-based design, by the increase in the computed entropy generation rates in the early part of the passage in comparison to the annular case - particularly in the vicinity of the blade leading edge. In addition, the effects of the increased intensity of the suction side *HSV* were also illustrated in the same figures, where the loss generation rates (close

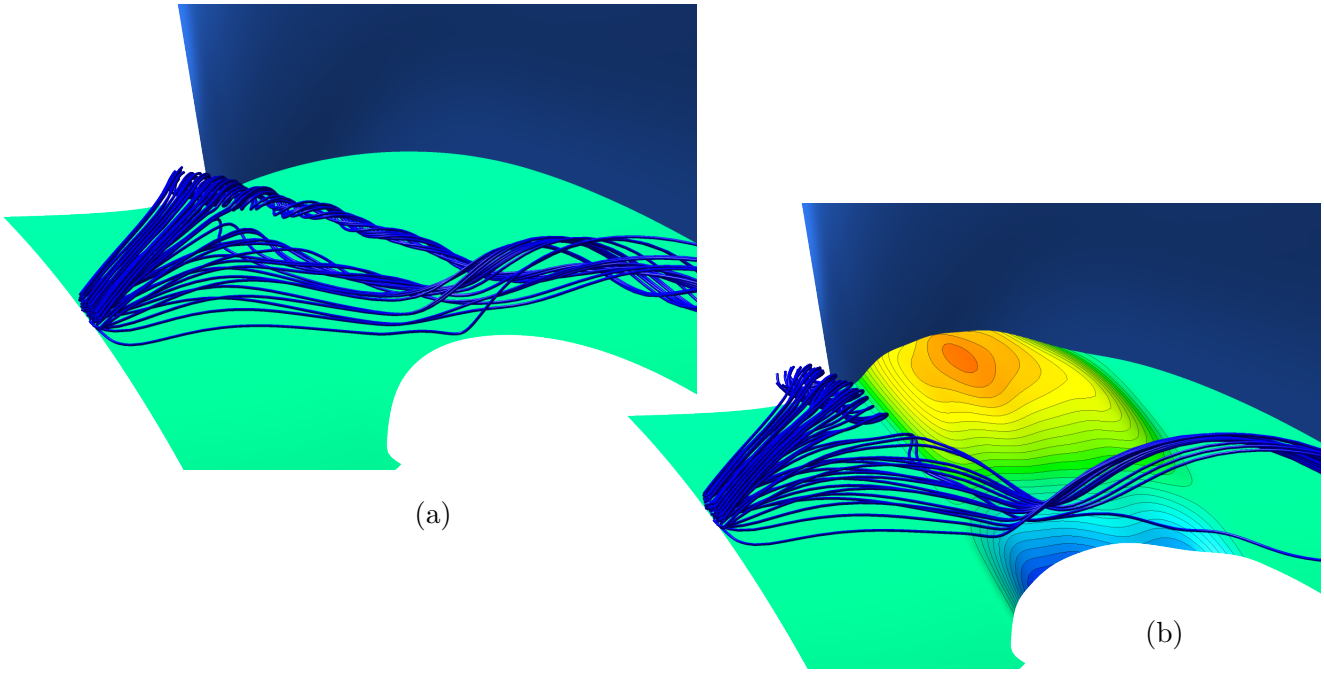

Fig. 9.10: Comparison of pressure side horseshoe and passage vortex formation for the annular (left) and η_{tt}-based (right) designs

to the suction side of the leading edge) were also visibly increased. However, despite these increases in the early part of the passage, the overall reductions in the intensity and increased diffusivity of the passage vortex (as a result of the reduced cross-passage boundary layer flow and blocking of the pressure side *HSV*), were also clearly identifiable and were ultimately evidenced by the net decrease in the overall mass-averaged loss coefficient at the rotor exit.

The improvements in the rotor exit (X3) efficiency and loss coefficient are shown in Fig. 9.11. Although more subtle than predicted by the CFD, the improvements to the experimental rotor efficiency profile are clearly visible (Fig. 9.11a). The accompanying reductions in the the rotor exit loss coefficient for the same spanwise range (Fig. 9.11b) confirmed the general decreasing of the intensity of the passage vortex as well as the secondary loss associated with it. Despite the excellent improvements for the current (i.e. rotor) blade row, analysis of the results for the remaining metrics at the rotor exit showed that the benefits for any downstream row(s) as a result of the η_{tt}-based contouring were likely to be secondary in nature. This was indicated by the more muted predicted (and measured) reductions in the mass-averaged coefficient of secondary kinetic energy (C_{ske}), flow deviation (β_{dev}) and design efficacy (η_{de}) for this endwall. Finally, the benefits of the η_{tt}-based design noted at the rotor exit were seen to extend to the downstream measurement plane, including the validation of the predicted increase in the 'mixed-out' rotor efficiency and decrease in the loss coefficient.

Analysis of all the data presented for this design indicated that the success of this metric for the design of non-axisymmetric endwall contours for the rotor of the test rig, was as a result of the sensitivity of the metric *by design* to all those quantities as well as more importantly, *the ratios between those quantities*, required for the overall improvement of the rotor efficiency. More specifically, while other metrics such as the flow deviation from design *were* sensitive to the overall work output from

the rotor, because these metrics did not take into account the irreversibilities associated with the correction of the flow angles, these objective functions resulted in lower overall predicted increases in the efficiency. Similarly, while metrics such as the relative total pressure loss coefficient ($C_{p0,rel}$) would take into account the irreversibilities generated in the flow, this metric (not being sensitized to the overall total enthalpy drop or ratio between the useful work output and rotor exit velocity produced by the blade row), indicated that sufficient emphasis was not placed on the overall conversion of the total inlet enthalpy to the principal quantity demanded from a rotor blade: the shaft work produced by the rotor. Since the η_{tt}-based objective function was sensitive to all these constituents (i.e the ratio between the rotor work output & total isentropic pressure drop through the blade passage, as well as the degree of irreversibility through which this was obtained), this metric was able to guide the endwall design routine to the optimal balance between these quantities for the design on hand, resulting in the best overall improvement in the rotor efficiency.

Apart from the above, part of the significance of this result was that, to date, this metric has not been commonly used within the literature for the design of non-axisymmetric endwalls and the success of this metric *in this investigation* indicated that it should potentially be considered as a viable option for the design of endwall contours.

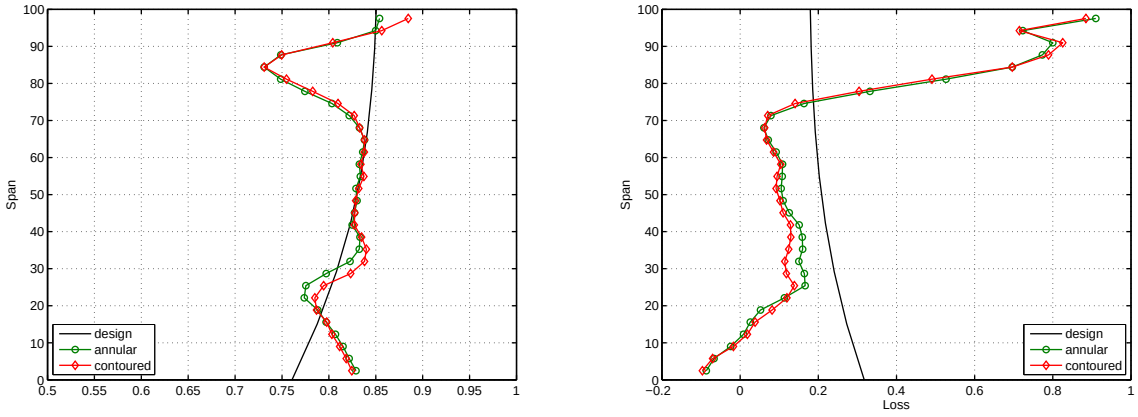

(a) η_{tt} (b) $C_{p0,rel}$

Fig. 9.11: Experimental rotor exit (X3) total-total efficiencies and loss coefficients for the annular and η_{tt}-based endwalls

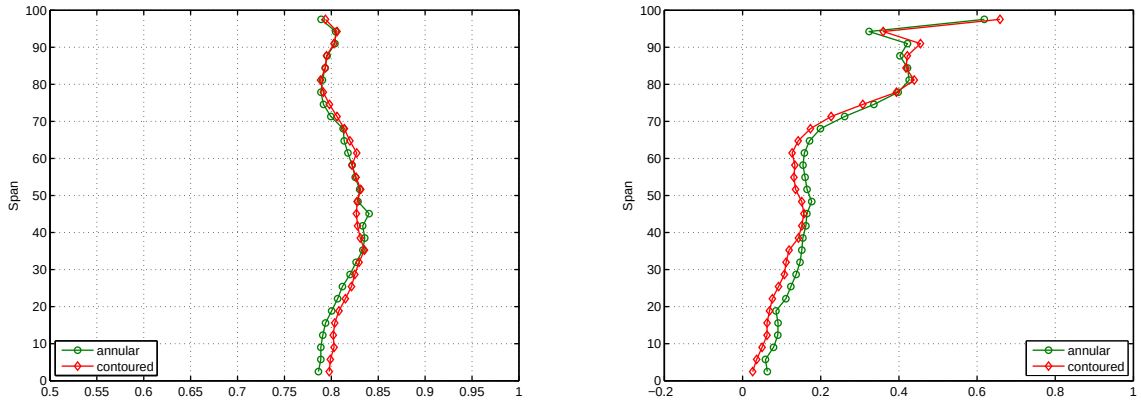

(a) η_{tt} (b) $C_{p0,rel}$

Fig. 9.12: Experimental 'mixed-out' (X4) total-total efficiencies and loss coefficients for the annular and η_{tt}-based endwalls

9.3.2 Secondary kinetic energy (C_{ske})

In terms of overall improvements in the rotor efficiency, the C_{ske}-based design was found to be second only (both predicted as well as when validated), to the design produced using the rotor efficiency as the basis of its objective function. This metric resulted in a final optimized design almost identical to that generated using the η_{tt}-based objective function, although the contours produced using this objective function were found to be more geometrically 'aggressive' than those produced using the η_{tt}-based objective function. Given that this metric was - at best - only a reasonably simple proxy for the secondary loss, this result in itself was considered extremely significant, again notwithstanding the fact that the final endwall geometry for the design was again selected completely autonomously and without any active user intervention during the design procedure.

As would be expected, given the physical similarity of the endwalls, the C_{ske}-based design was predicted to perform almost identically to the η_{tt}-based endwall and this included an increase in the rotor efficiency only slightly smaller than of the previous case (+0.69%) but also with a slight increase in the rotor exit loss coefficient (+0.31%). In addition, as could be expected, the current design was also predicted to achieve a slightly larger reduction in the rotor exit C_{ske} (−28.29%) and corresponding mass-averaged flow deviation from design (β_{dev}) (−6.20%).

The mechanism by which the C_{ske}-based design was understood to work was similar to that of the η_{tt}-based design (i.e. the obstruction of the pressure side horseshoe vortex, as well as mitigation of the development of the passage vortex through a reduction in the cross-passage static pressure gradient), although in this metric, no emphasis was placed on controlling blade row exit loss coefficient as was implicit for the η_{tt}-based case. This situation was exemplified by the slight increase in the rotor exit loss coefficient predicted by the CFD for this design in comparison to the η_{tt}-based endwall and was further confirmed by the experimental results, in which, despite still attaining a reduction in the rotor exit loss coefficient, the reductions measured for the current case were significantly smaller than those achieved by the previous one. Instead, the increased emphasis placed on the reducing the secondary

kinetic energy was clearly illustrated by the predicted (as well as measured) reductions in the mass-averaged coefficient of secondary kinetic energy (C_{ske}) and flow deviation (β_{dev}) as well as the rotor exit design efficacy (η_{de}), all of which were found to be significantly better for the current case than for the previous one.

The greater emphasis on the reduction of the rotor exit C_{ske}, was found to manifest directly in the final geometry of the C_{ske}-based design, which although was found to be very similar in overall characteristic shape to the η_{tt}-based design, was seen to be clearly more 'aggressive' than that produced by the previous metric. More specifically, while the C_{ske}-based design was found to not only reach a greater overall height above the datum, it was also found to incorporate a significantly more rapid return to the nominal endwall height at the downstream limit of the contoured section of the passage. In addition, the penetration of the elevated (i.e. 'hump') portion of the contours across the blade passage towards the suction surface of the adjacent blade was seen to be greater than that noted for the η_{tt}-based design (Fig. 9.14).

The net results of this more aggressive contouring were somewhat predictable, with a decrease in the overall amount of the endwall boundary layer fluid being assimilated into the passage vortex in the early part of the blade passage resulting in a greater volume of overturned fluid being close to the endwall at the exit of the passage. The results of the increased overturning at the endwall, although reasonably small, were noted in both the CFD as well as experimental measurements of the rotor exit relative flow angle (Fig. 9.17).

The more robust interplay between the endwall boundary layer fluid and rotor suction surface is shown in Fig. 9.13, where, in contrast to the more docile η_{tt}-based design, the more distinct separation and re-attachment lines on the hub and suction surfaces of the C_{ske}-based design indicated a significantly more energetic interaction between the endwall boundary layer fluid and the blade suction surface.

The comparatively larger predicted mass-averaged reductions in the C_{ske} for this design were confirmed by the experiment (-8.36%) (Fig. 9.15a). Further to this, despite the reduction in loss close to the midspan as a result of the reduced intensity of the passage vortex (and a corresponding increase in the rotor efficiency in the same spanwise region), the increased overturning as a result of the more aggressive endwall geometry was clearly captured by the reduction in the rotor efficiency between the endwall surface and $\sim 20\%$ span and the increase in the rotor exit loss coefficient in comparison to the annular case in the same region (Figs. 9.16a & 9.16b).

The preceding analysis was able to be extended to the downstream measurement plane, where although the current design was once again predicted to perform similarly to the η_{tt}-based design, the increased emphasis on the reduction of the secondary kinetic energy at the rotor exit was seen to manifest not only through a significant reduction in the mixed-out coefficient of secondary kinetic energy (-6.56%) (Fig. 9.15b), but also through an increased reduction in the 'mixed-out' loss coefficient (-8.92%) (Fig. 9.16d).

Finally, notwithstanding the positive effects associated with the use of the C_{ske}-based objective function for the design of the rotor endwalls discussed above, one residual issue associated with the use of the C_{ske}-based objective function was that this metric did not explicitly emphasize the optimization of the ratio of rotor work output to the total isentropic enthaply drop through the blade row as strictly as was done by the η_{tt}-based objective function.

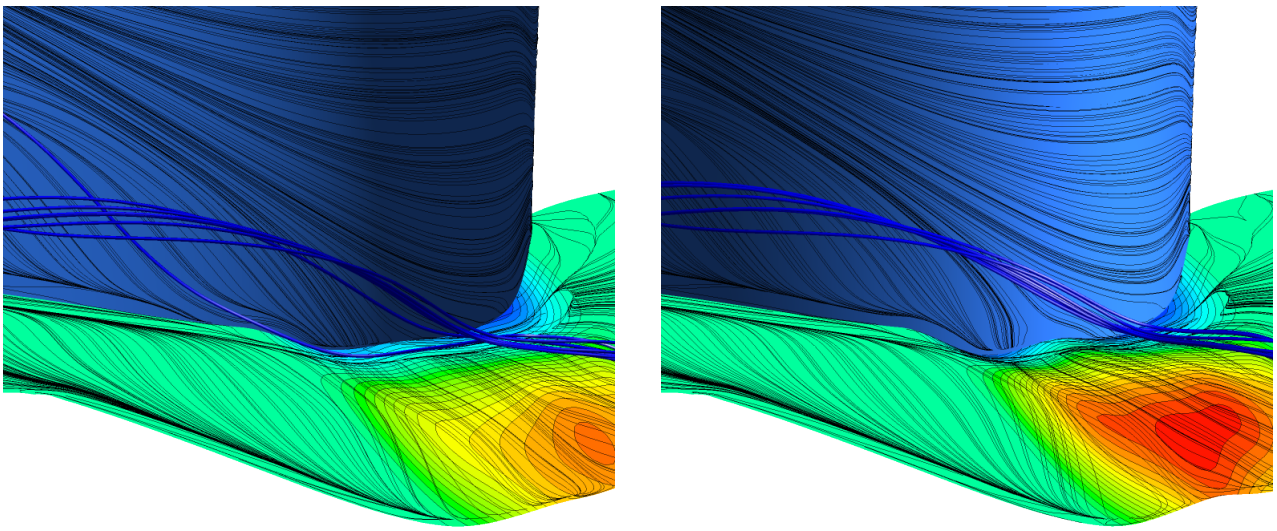

(a) η_{tt}-based (b) C_{ske}-based

Fig. 9.13: Comparison of endwall height contours and oilflow lines at the exit of the contoured region for the η_{tt}- & C_{ske}-based designs

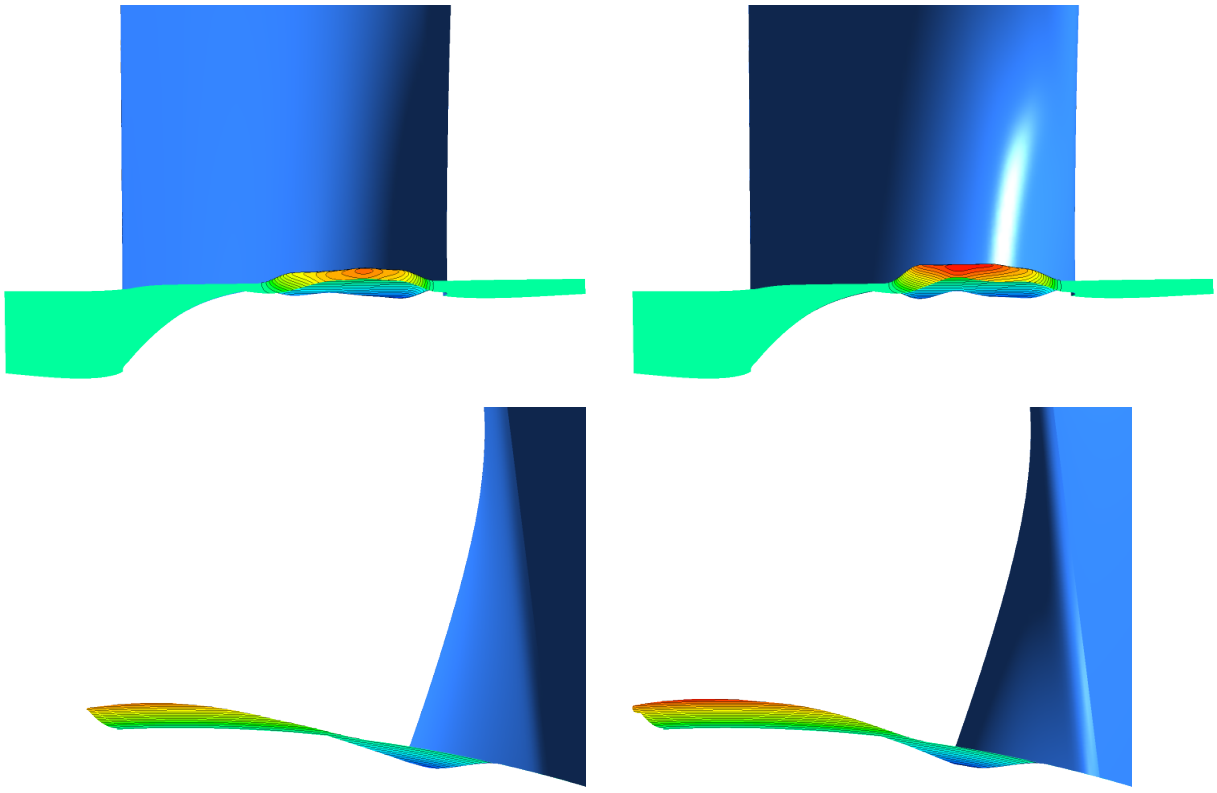

Fig. 9.14: Comparison of contour height (top) and circumferential extent (bottom) of the η_{tt}- (left) & C_{ske}-based (right) cases

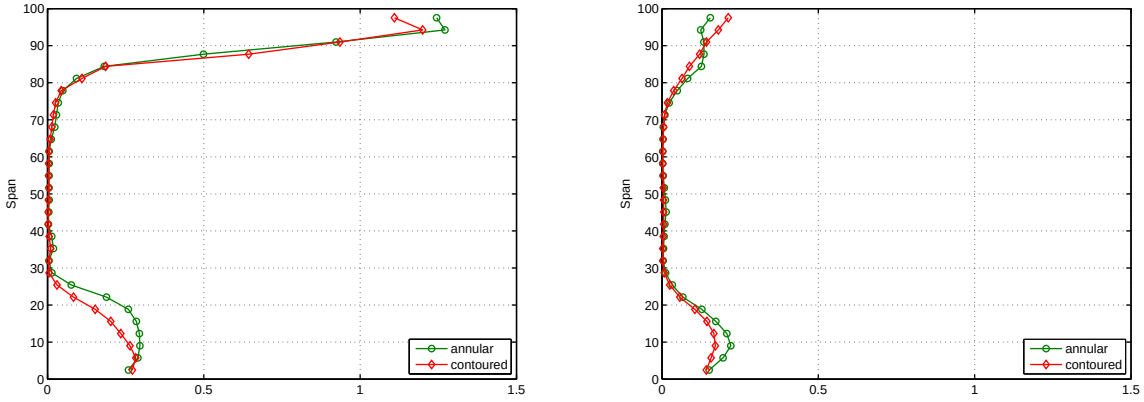

(a) C_{ske} (b) C_{ske}

Fig. 9.15: Experimental rotor exit (X3) (left) and 'mixed-out' (X4) (right) coefficients of secondary kinetic energy for the annular and C_{ske}-based endwalls

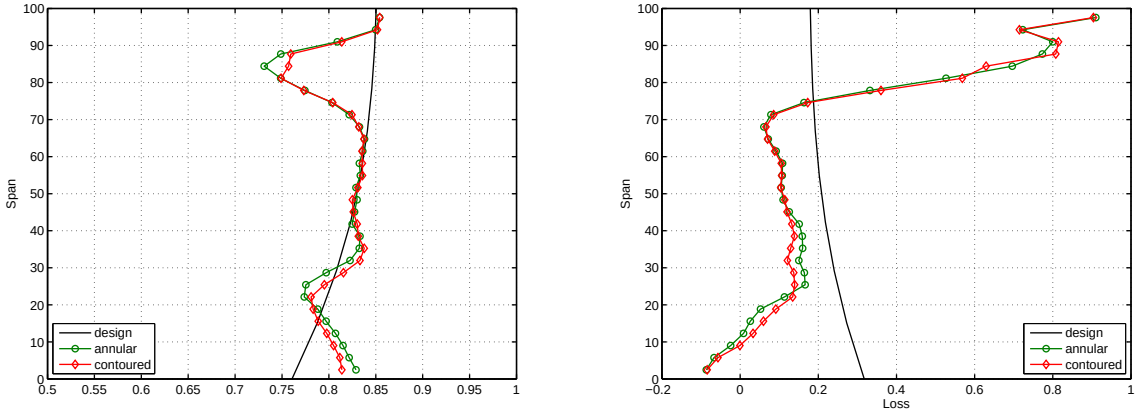

(a) η_{tt} (b) $C_{p0,rel}$

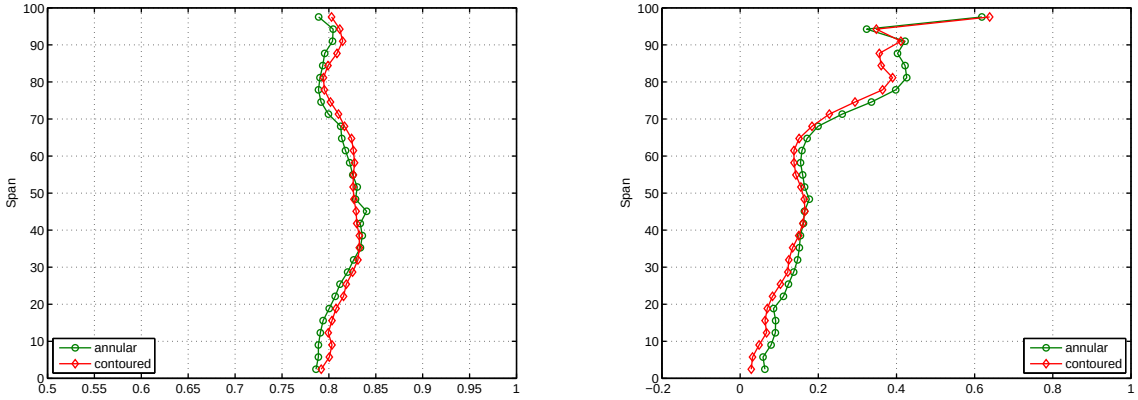

(c) η_{tt} (d) $C_{p0,rel}$

Fig. 9.16: Experimental rotor exit (X3) (top) and 'mixed-out' (X4) (bottom) total-total efficiencies and loss coefficients for the annular and C_{ske}-based endwalls

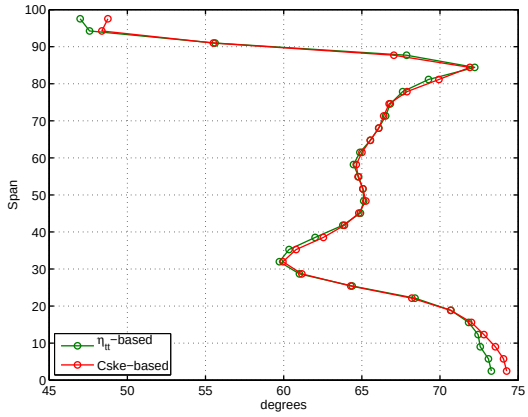

Fig. 9.17: Comparison between experimental rotor exit relative flow angles for the η_{tt}- & C_{ske}-based designs

9.3.3 Loss ($C_{p0,rel}$)

The $C_{p0,rel}$-based objective function presented an interesting case. While as discussed previously, the endwall design routine *did* in fact achieve its goal in reducing the computed mass-averaged loss coefficient at the rotor exit, this was accomplished by the design routine in a somewhat unexpected manner:-

1. Firstly, in contrast to the previous designs, the aerodynamic 'blocking' of the pressure side leading edge flow was not present, with the design of the contours actually reversing the trends of the previous designs and encouraging the flow in the vicinity of the leading edge *towards* the pressure side rather than around the leading edge and towards the suction side of the blade. This was achieved by the replacement of the 'hump' portion of the contours noted for the previous designs with a inverted 'valley' feature which was seen to run across the blade passage with the same approximate trajectory as that noted for the pressure side *HSV* separation line for the annular case.
2. Secondly, the change in geometry above resulted in a change in the interactions (a reduction) between the pressure and suction side horseshoe vortices in the early part of the passage, which resulted in a reduction of the loss generation in the early part of the blade passage, and
3. Finally and also as a result of the particular geometry of the design, the interaction between the pressure side horseshoe (and later passage vortex) and the endwall surface (as well as the high loss endwall boundary layer fluid) was also reduced, resulting in a reduction in the loss usually generated by the shearing between these vortices and the endwall and endwall boundary layer fluid.

Although as mentioned above, the predicted losses within the blade passage were reduced as a result of the above, this geometry resulted in a number of additional unintended and unsatisfactory consequences, including:-

1. A large increase in the intensity of the secondary flow structures within the blade passage, leading to a significant increase in the secondary kinetic energy (as measured by both the C_{ske} & $SKEH$ metrics) as well as flow angle related metrics (i.e. β_{dev}), as well as,
2. Despite the predicted reduction in the rotor exit loss, a slight overall reduction in the mass-averaged rotor efficiency in comparison to the baseline case.

An analysis of the calculated streamlines and endwall pressures for this endwall showed that the increased intensity of the secondary flow structures described above were as a direct consequence of the encouragement of the flow onto the pressure side of the blade leading edge and a subsequent enhancement of pressure side HSV, which was then seen to promote the formation of a significantly more intense passage vortex. In addition, the reduced interaction between the passage secondary flow structures and one another as well as the physical endwall geometry, inevitably resulted in a reduction in the amount of kinetic energy lost as a result of viscous dissipation.

It should be mentioned that, despite this increase in strength of the secondary flow, because the secondary flow itself is (as described by numerous authors, e.g. Sieverding (1985)) largely an inviscid phenomenon, this explanation was consistent with the reduced loss predicted within the blade passage as a result of the reduced interactions between the secondary flow structures in the early part of the blade passage.

Despite the predicted decrease in loss within the blade row for this endwall, the mass-averaged rotor efficiency was predicted to be reduced in comparison to the annular case, and this effect was found to be as a result of several factors which together resulted in the decrease in rotor performance.

1. Firstly, in comparison to both the annular, as well as previous designs, the calculated total pressure (and therefore total enthalpy) drop through the rotor for this design was increased (+0.44%).
2. Secondly, despite this increase in the blade row total pressure drop, the rotor work output was predicted to increase only a relatively small amount (+0.2%), while in contrast the rotor exit velocity was seen to increase significantly (+3.2%).

With reference to the above, once again, despite the increases in the over- and underturning at the rotor exit as a result of the increased intensity of the secondary flows, the rotational nature of this flow meant that the overall increase in the actual mass-averaged flow turning at the rotor exit was comparatively small, resulting in the reasonably small increase in the predicted rotor torque discussed above. In addition, the rotational nature of this flow meant that, despite the increases in the average flow velocity magnitude, the overall mass flow through the blade row was unchanged, and in fact, was set as part of the CFD computations for the simulations to mimic the operation of the test rig. In conclusion then, despite the reduced loss at the rotor exit, as a result of the higher average rotor exit velocities, from an efficiency perspective, the blade row was found to perform more similarly to a nozzle with reduced loss than a rotor with an equivalent improvement in the loss characteristics (and therefore efficiency).

Despite the reductions in loss at the rotor exit (X3) (Fig. 9.18b), at the downstream measurement plane, the mass-averaged loss coefficient (Fig. 9.18d) was seen to be noticeably increased in comparison to the baseline case as a logical consequence of the increased secondary kinetic energy associated with

the flow mixing out downstream of the rotor. The net effect of this was a predicted *increase* in the mixed-out loss coefficient at the X4 measurement plane of nearly +2%.

Notwithstanding the successful reduction in predicted loss at the rotor exit, the use of this metric highlighted a number of important considerations:-

- The use of the loss coefficient on its own, for a rig in which the mass flow rather than pressure (i.e. enthalpy) drop is specified, did not work.
- Although this was an unforeseen outcome at the start of the investigation, this was because of the ability of the endwall design routine to manipulate the operating conditions of the rig by increasing the total pressure drop through the blade passage without concern for the type and quality (in terms of flow angles and velocity) of flow produced by the endwall. Because of the particular circumstances which were exploited by the endwall design routine, it is expected that this issue would only be relevant to a rig of the type used in this investigation.
- While a small increase in the rotor work output was predicted as a result of a small increase in the overall mass-averaged turning of the flow at the rotor exit, the majority of the additional energy supplied to the blade row was converted into a set of enhanced secondary flow structures with increased intensity but with reduced loss.
- Because of the design of the rig, this issue would not affect rotor rows only, although for a stationary blade row, reduced loss would always be expected to translate into increased efficiency, irrespective of the quality of the flow at the blade row outlet.

Finally, the issues experienced with the $C_{p0,rel}$-based metric alone were alleviated through the use of a 'compound' objective function (the $C_{p0,rel,1} + \beta_{dev,0.7}$-based objective function), in which constraints on the flow quality at the blade row exit were enforced and these results are discussed in Section 9.3.7 below.

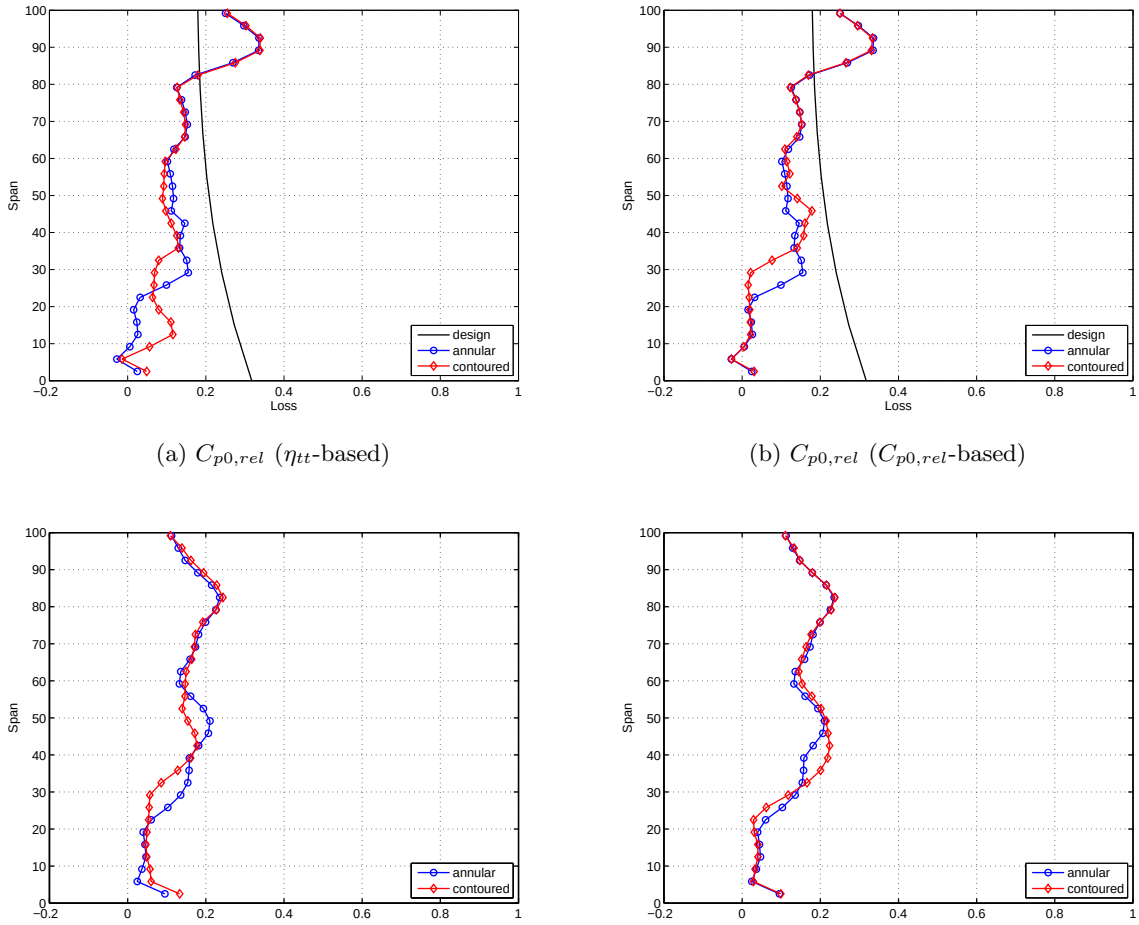

(a) $C_{p0,rel}$ (η_{tt}-based)

(b) $C_{p0,rel}$ ($C_{p0,rel}$-based)

(c) $C_{p0,rel}$ (η_{tt}-based)

(d) $C_{p0,rel}$ ($C_{p0,rel}$-based)

Fig. 9.18: Predicted rotor exit (X3) (top) and downstream (X4) (bottom) loss coefficients for the η_{tt}- & $C_{p0,rel}$-based design

9.3.4 Flow deviation (β_{dev})

As was the case with the C_{ske}-based design and its predecessor (i.e. the η_{tt}-based endwall), the β_{dev}-based endwall was found to share a great deal of similarity with the C_{ske}-based design. To some degree, this was expected because of the natural link between the flow deviation and coefficient of secondary kinetic energy design metrics, where it can be easily appreciated that increased flow deviation will result in increased off-axis flow and a corresponding increase in the coefficient of the secondary kinetic energy.

In fact, a quick inspection of Fig. 9.19 highlights this link, where if the absolute magnitudes for each metric are ignored, the correspondence between the spanwise profiles of the flow deviation angles and C_{ske} is clear. With this in mind, the attractiveness of this metric was, in part, in addition to the potential reduction in the secondary flow by targeting those flow structures which resulted in off-axis

and therefore off-design flow, but also by doing so using a relatively simple metric as well as one which is commonly perceived to be robustly predicted by CFD.

In this investigation, the congruence between the β_{dev}- and C_{ske}-based metrics was well illustrated by the similarity between the final geometries produced by the two metrics as well as by the predicted reductions in each of the investigated quantities at both the rotor exit (X3) and downstream (X4) measurement planes.

Inspection of the final optimized endwalls showed a great deal of geometric similarity between the designs (including the familiar 'hump-and-dip' configuration), similar maximum and minimum endwall heights (both of which were greater than the more moderate η_{tt}-based contours) as well as a single contour located towards the exit of the contoured region which - for both designs - was seen to extend towards the adjacent blade's suction surface[3]. Despite these similarities, some differences between the final designs and flow regimes were apparent. In terms of the endwall geometry, the most notable of these was the enlargement of the above-mentioned contour, which for the β_{dev}-based case, was found to extend considerably more closely to the adjacent suction surface.

The effects of this contour for this endwall were clearly identifiable in the computed streamlines of Fig. 9.21. In particular, while as was the case for the η_{tt}- and C_{ske}-based designs, close to the leading edge, the raised portions of the endwall interacted with, and prevented the full formation of the pressure side *HSV*, the above-mentioned extended contour was seen to operate by directing a portion of the passage endwall fluid across the blade passage and *underneath* the fluid of the inlet boundary layer and suction side horseshoe vortex, where it was then seen to form a smaller secondary vortex and then migrate up the suction surface and exit the blade row. The net effect of this was a decoupling of the endwall boundary layer and inlet / suction side *HSV* vortex fluid and the formation of *two* distinct vortex structures within the blade passage (both of which had the same sense of rotation) rather than the assimilation of all the inlet and endwall boundary layer fluid (as well as the suction suction *HSV*) into a single combined passage vortex structure. The effects of the changes to the secondary flow regime described above on the circumferentially-averaged relative flow angles of the β_{dev}-optimized design (Figs. 9.20) were also clear, with the formation of the point of inflection between $\sim 20-30\%$ span reducing the overall mass-averaged flow deviation as demanded by the β_{dev}-based objective function.

Finally, despite the similarity in predicted performance between the C_{ske}- (and therefore, by extension but to a lesser degree, the η_{tt}-based) & β_{dev}-based designs, a clear trend between the predicted increases in performance (measured by the rotor efficiency and loss coefficient) and the degree of flow correction was noticeable. This is illustrated in Table. 9.6, where the effects of the increased emphasis on flow correction are noted to result in corresponding increases in the rotor exit loss coefficient and similar decreases in the rotor efficiency. Further, while the β_{dev}-based design was not tested as part of the experimental subset in this investigation, the trends predicted by the CFD appear to be confirmed by the mass-averaged experimental results for the remaining 2 designs.

As a result of this, in general despite its excellent predictability as well as congruence with the coefficient of secondary kinetic energy, the use of the β_{dev}-based metric is considered to be more appropriate as part of a compound function, rather than as the basis of a simple metric.

[3] Which although present, was considerably less prominent for the C_{ske}-based design

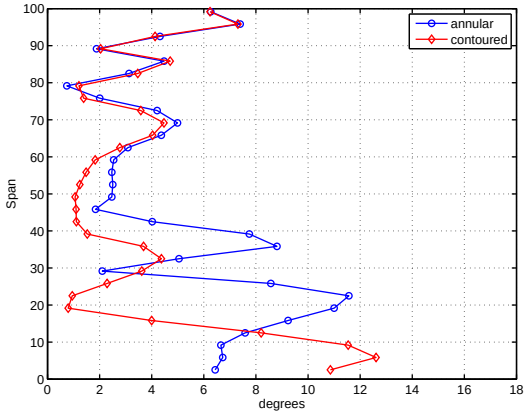

(a) β_{dev} (C_{ske}-based)

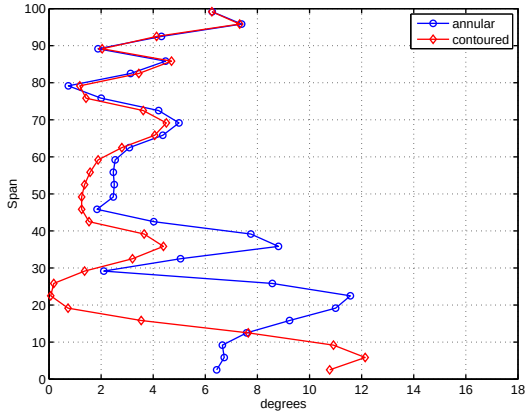

(b) β_{dev} (β_{dev}-based)

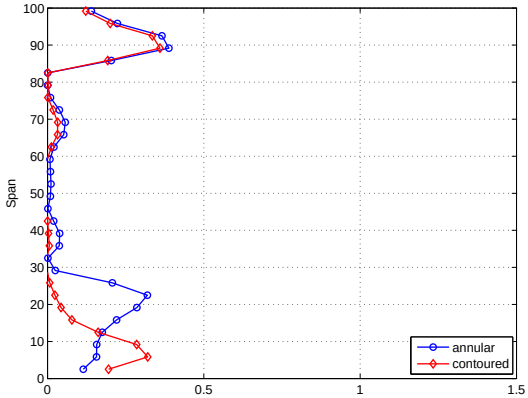

(c) C_{ske} (C_{ske}-based)

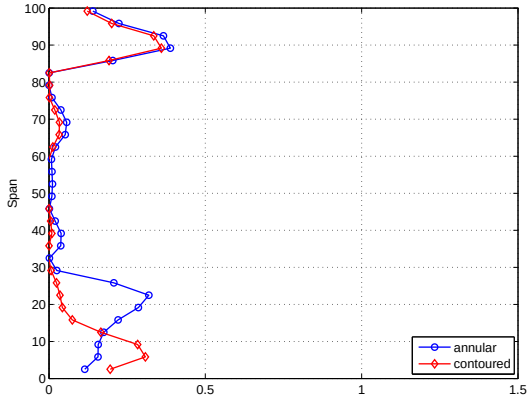

(d) C_{ske} (β_{dev}-based)

Fig. 9.19: Predicted rotor exit (X3) flow deviation angles (top) and coefficients of secondary kinetic energy (bottom) for the C_{ske}- (left) & β_{dev}-based (right) designs

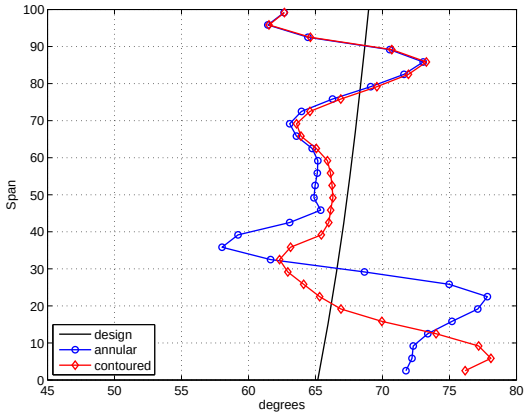

(a) β_3 (C_{ske}-based)

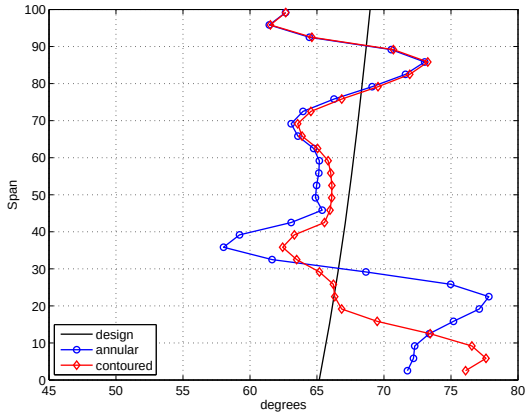

(b) β_3 (β_{dev}-based)

Fig. 9.20: Predicted rotor exit (X3) relative flow angles for the C_{ske}- (left) & β_{dev}-based (right) designs

Table 9.6: Comparison of computed (and experimental) mass-averaged rotor total-total efficiency (η_{tt}), flow deviation from design (β_{dev}) & total relative loss coefficients ($C_{p0,rel}$) for the η_{tt}-, C_{ske}- & β_{dev}-based designs at the rotor exit (X3)

Endwall	Flow deviation (β_{dev})	Loss ($C_{p0,rel}$)	Rotor efficiency (η_{tt})
η_{tt}-based	3.82° (5.47°)	0.1360 (0.2133)	0.8008 (0.8194)
C_{ske}-based	3.75° (5.44°)	0.1363 (0.2325)	0.8006 (0.8165)
β_{dev}-based	3.60°	0.1369	0.8000

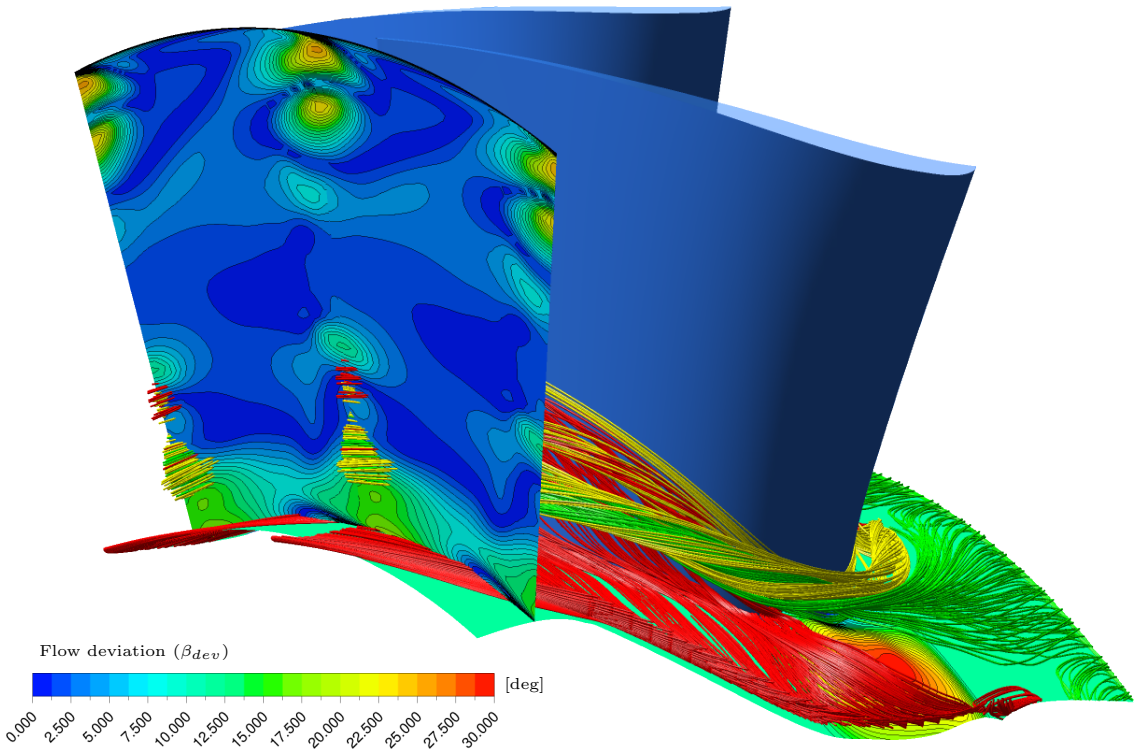

Fig. 9.21: Decoupling of endwall boundary layer (red) and inlet (green) / suction side *HSV* (yellow) fluid (leading to the preservation of the suction side *HSV* and the additional 'secondary' vortex) for the β_{dev}-based design

9.3.5 Secondary kinetic energy helicity ($SKEH$)

The secondary kinetic energy helicity ($SKEH$) is a quantity which has been used successfully by a number of researchers, including Brennan et al. (2001), Harvey et al. (2002) & Bagshaw et al. (2008a,b) but also with mixed and even unsatisfactory results by others (Poehler et al. (2010), Vazquez and Fidalgo (2010)).

One of the principal criticisms made by Germain et al. (2007) of this quantity, was the arbitrary nature of the weighting imposed on the secondary kinetic energy as a result of the inclusion of helicity in the formulation of the metric. In this investigation, a reasonably simple definition of $SKEH$, similar

to that used by Brennan et al. (2001) & Harvey et al. (2002) was used. Although the final endwall design produced using this metric was predicted to reduce the overall mass-averaged secondary kinetic energy helicity, two main issues were encountered which meant that ultimately this metric was found to be unsuitable for the design of the contoured endwalls for this turbine.

The first of these issues was related to the acute sensitivity of the metric to even reasonably small changes to the endwall geometry. This situation itself was related to two sub issues:-

1. The very large relative magnitude of the helicity (H) itself in comparison to the secondary kinetic energy (SKE) component, and secondly,
2. The relative ease with which the optimizer was able to manipulate the predicted helicity field at the rotor exit through the introduction of various geometric features to the endwall surface.

The difficulties encountered by the endwall design routine as a result of these issues were well displayed in the convergence plots of the overall target objective function (Figs. 7.5a & 7.5b), where consecutive reductions in the overall mass-averaged objective function were seen to correspond to large, disparate changes to the overall physical endwall shape and where little or no convergence towards a gradually refined final physical endwall configuration was noticed - even during the extremely local search portion of the optimization. Further evidence of this was found in the analysis of the convergence scatter plots for each set of control line parameters (Figs. B.17 - B.20) where (with the exception of *curve 2*), the plots showed little evidence of well-defined regions in the endwall geometry parameters in which consistently similar objective function values resulted and instead, the parameter space was characterized by a seemingly irregular collection of interspersed objective function values of high and low magnitude.

The second major issue alluded to above was more specifically related to the mathematical definition of the metric itself than the relative magnitudes of the individual H and SKE quantities used in the overall calculation. More specifically, the combination of the secondary kinetic energy (SKE) of the flow with the helicity (H) multiplicatively meant that, despite the original intention of using the helicity as a means only as a means to 'focus' the optimizer on the changes to the SKE associated with the vortical components of the flow, the overall magnitude of the metric could instead be changed by manipulating the magnitude of either of the SKE or H *individually*, rather than the SKE itself as originally intended.

In this investigation, this effect was illustrated in Fig. 9.23 where the predicted reductions in the spanwise profiles of $SKEH$ of the final optimized $SKEH$-based design (Fig. 9.23f) (in comparison to the C_{ske}-based endwall), were shown to be not only as a result of reductions in the secondary kinetic energy of the of the flow (Fig. 9.23b), but also as a result of large reductions in the helicity of the flow (Fig. 9.23d), and in particular close to the endwall ($\sim 15\%$ span). These reductions were seen to decrease the circumferentially-averaged magnitudes of the $SKEH$ significantly in comparison to the C_{ske}-based design.

A further analysis of the predicted results for the η_{tt}- & $SKEH$-based designs showed that, in contrast to the traditional approach of improving the blade row efficiency by reducing the strength of the secondary flows and therefore the overall loss of the blade row (as achieved by the η_{tt}- & C_{ske}-based designs), in the case of the $SKEH$-based design, the endwall design routine was able to exploit the shortcomings of the $SKEH$ metric to produce the results discussed above, and in so doing,

a significantly more complex flow field at the exit of the rotor resulted. More specifically, Fig. 9.24 shows that while for the C_{ske}-based case, the weakening of the passage vortex in the vicinity of the midspan, as well as the confinement of the residual effects of the secondary flow to a region closer to the endwall resulted in a natural decrease in the helicity associated with the passage vortex and a migration of the peak circumferentially-averaged values closer to the endwall, the primary focus of the endwall design routine for the $SKEH$-based case was to distribute the spanwise intensity of the helicity more evenly between the midspan and endwall. For the final optimized $SKEH$-based design, this was achieved by managing the strength of a bespoke vortex relative to the strength of the counter rotating vorticity shed by the blade. This vortex effectively replaced the traditional passage vortex seeded by the pressure side HSV and was instead generated by the complex arrangement of the final endwall contours close to the pressure surface of the blade as shown in Fig. 9.22. Despite the overall reduction in the mass-averaged $SKEH$, the introduction of spurious vortices intended only for the manipulation and management of the rotor exit helicity field rather than an overall reduction in the strength of the secondary flow, showed a clear exploitation of the shortcomings of the design metric as discussed above, and would be likely to result in significant increases in loss, even greater than those predicted by the CFD for this design.

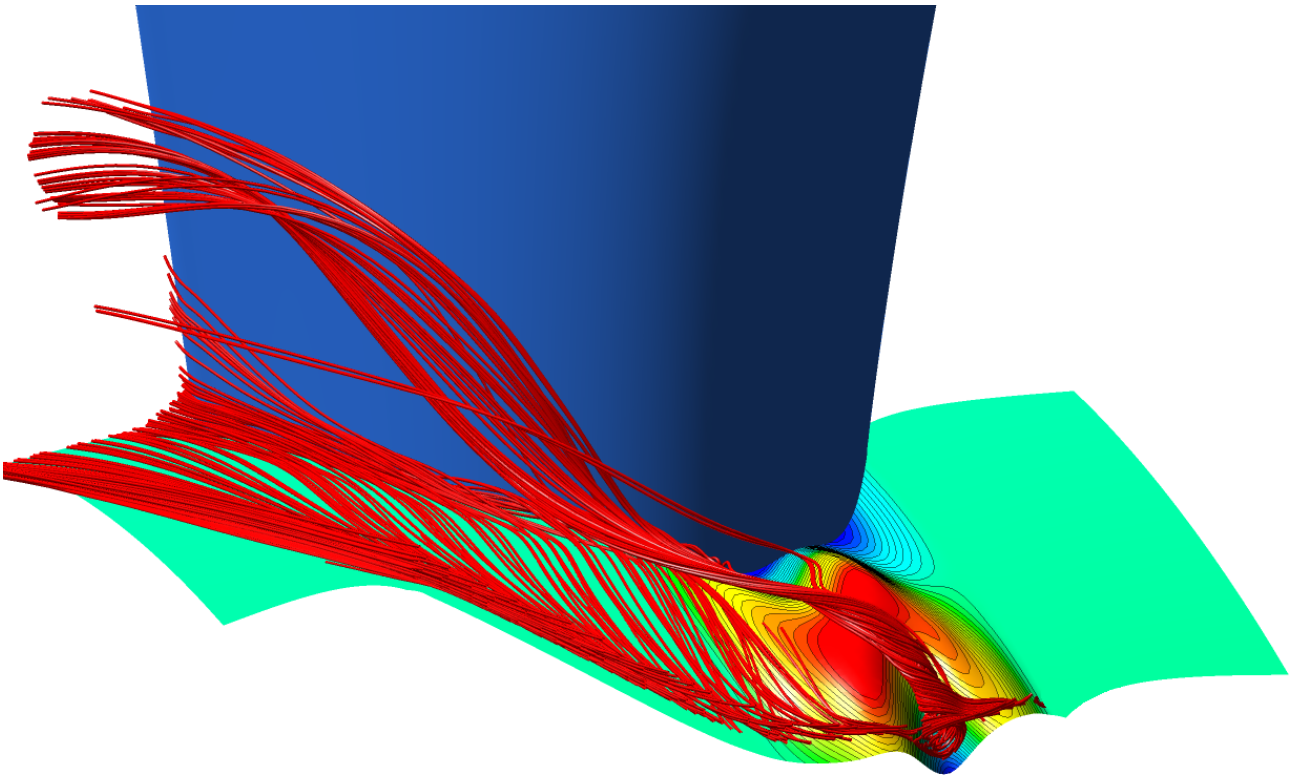

Fig. 9.22: Computed passage streamlines for the $SKEH$-based design showing the contours used for the aerodynamic blocking of the pressure side horseshoe vortex as well as the formation of the 'bespoke' endwall vortex for the manipulation of the rotor exit (X3) helicity

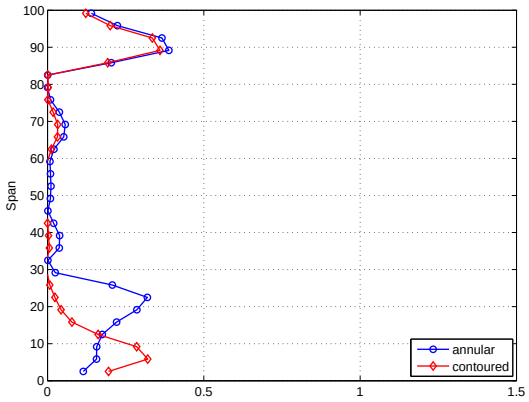

(a) C_{ske} (C_{ske}-based)

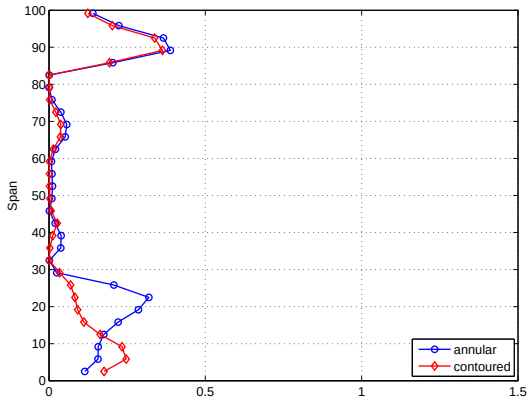

(b) C_{ske} ($SKEH$-based)

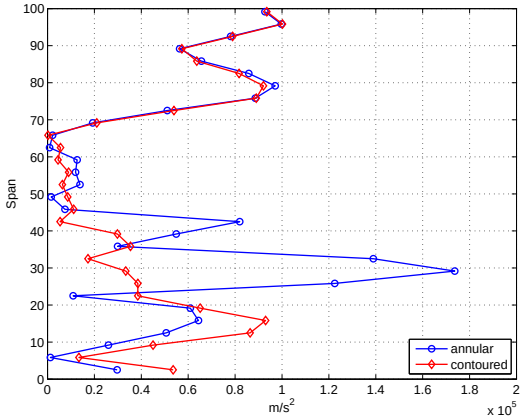

(c) Abs. helicity (C_{ske}-based)

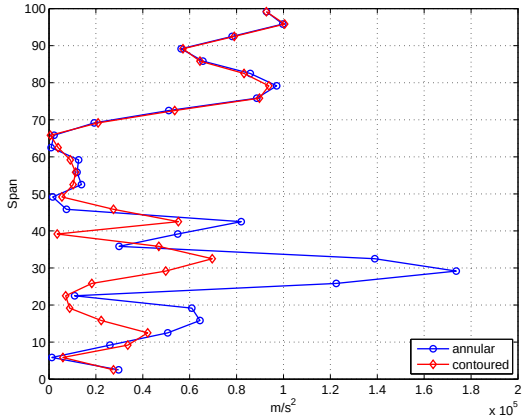

(d) Abs. helicity ($SKEH$-based)

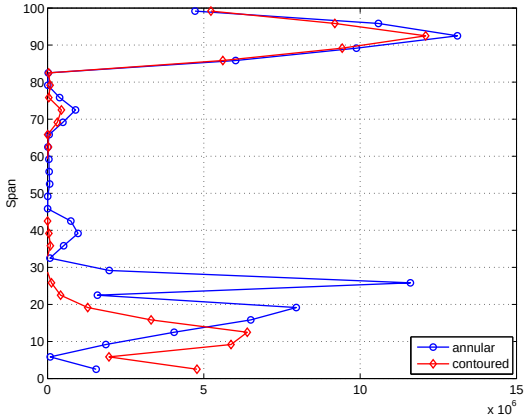

(e) $SKEH$ (C_{ske}-based)

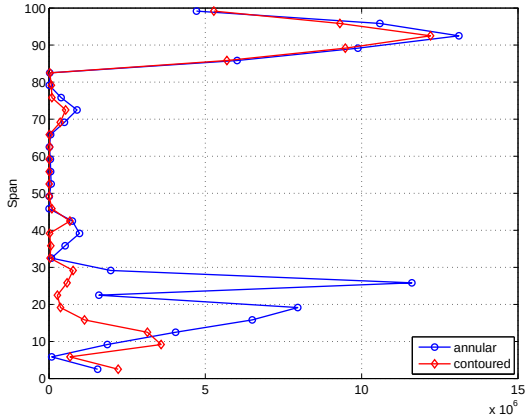

(f) $SKEH$ ($SKEH$-based)

Fig. 9.23: C_{ske}, helicity & $SKEH$ at the rotor exit (X3) measurement plane for the final C_{ske}- (left) & $SKEH$-based (right) designs respectively

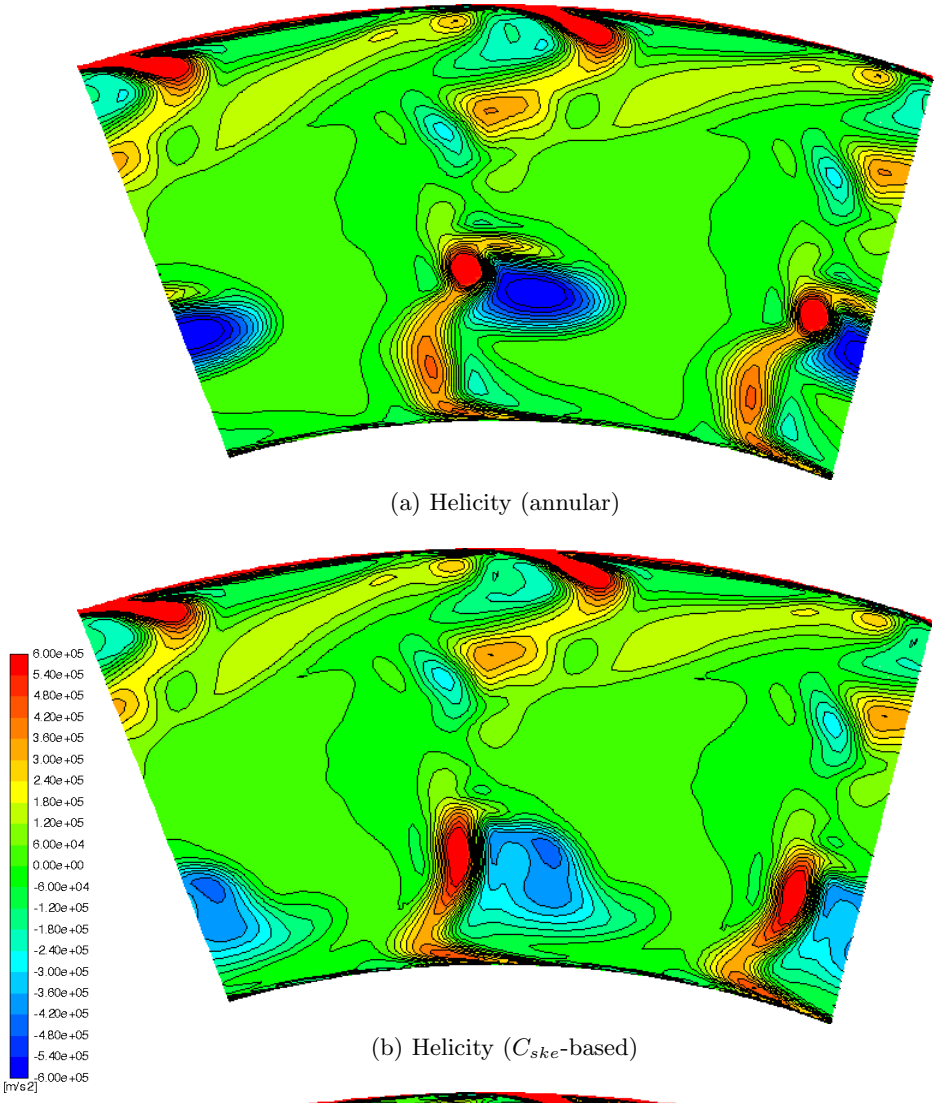

(a) Helicity (annular)

(b) Helicity (C_{ske}-based)

(c) Helicity ($SKEH$-based)

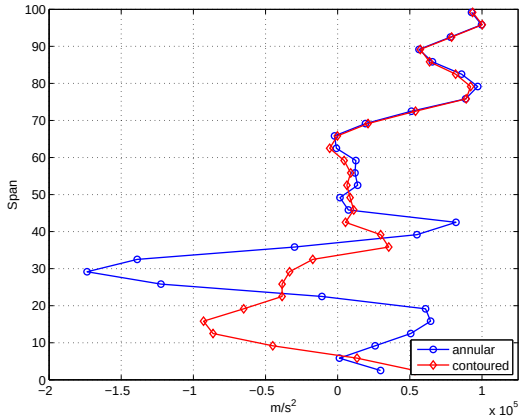

Annular & C_{ske}-based

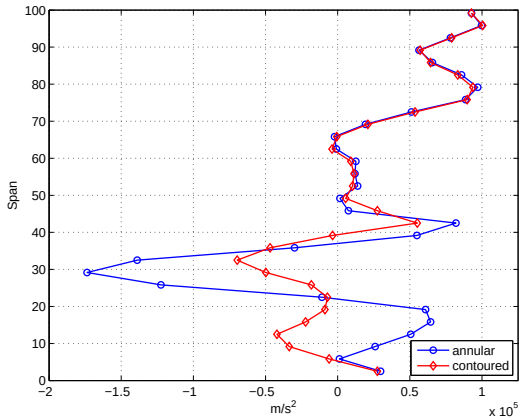

Annular & $SKEH$-based

Fig. 9.24: Predicted helicity contours and spanwise profiles (inset) at the rotor exit (X3) measurement plane for the annular, C_{ske}- & $SKEH$-based designs respectively

9.3.6 Design efficacy (η_{de})

The so-called design efficacy of Dunn (2014) is a new quantity which was proposed by him to aid in the characterisation of turbine performance - much like the aerodynamic efficiency but without the sensitivities to temperature and pressure measurement he noted were present for certain operating conditions. To date, the quantity has been used only in the context of quantifying performance, and never yet as a basis for the actual design of endwall contours. Although the quantity can be formulated using either the stationary or relative reference forms of the relevant quantities, in this investigation, the exact formulation of Dunn, in which stationary quantities were utilised was used. This was done for two reasons:-

1. in the rig, the actual quantities were measured in the stationary frame, and
2. when assessing each formulation, it was noted that when computed using the rotor relative quantities, the overall calculated mass-averaged changes in the design efficacy were somewhat smaller than when formulated in the stationary frame of reference and were therefore considered less useful in the optimization of the final contours.

Fig. 9.25 shows the overall spanwise predictions of design efficacy for the final η_{tt}- as well as η_{de}-based designs, where the η_{tt}-based design was included once again for comparative reasons. Figs. 9.25b & 9.25d show that in its attempt to improve the overall design efficacy at the rotor outlet, both the flow angle as well as velocity in the secondary flow region were adapted by the final endwall design. The most prominent modifications were a reduction in the mass-averaged flow angle and an increase in the overall flow velocity in the secondary flow region for these quantities to more accurately meet the original specifications of the blade row design. Further to this, Fig. 9.26a shows the spanwise weightings applied to the axial and tangential components of the rotor exit velocity (i.e. the **i** & **j** components of $\boldsymbol{\theta}_{\mathbf{D}}$), while Fig. 9.26b shows the weighted axial and tangential velocities for the annular and final optimized case which were used in the calculation of the final design efficacies[4]. In addition to showing the changes to overall velocity magnitude, Figs. 9.26a & 9.26b showed that (consistent with the formulation of the η_{de} in the stationary reference frame), the greatest weighting (and therefore greatest influence on the overall η_{de}) was applied to the axial component of the rotor exit velocity, and that the bulk of the improvements were affected by increasing the magnitude of the axial component of the flow in the region between $\sim 10-25\%$ span, with a small decrease in the tangential component noted in the same region. Comparing the rotor exit axial velocity contour plots for the annular and η_{de}-optimized cases (Fig. 9.28a & 9.28b), the reductions in the primary flow through the midspan for the contoured case and increase in average velocities within the secondary flow region were clear.

Similar to the previous case (i.e the $SKEH$-based design), analysis of the predicted flow streamlines showed that the changes discussed above were achieved through the judicious introduction of a custom vortex, which was seeded close to the suction surface of the adjacent blade by a small but intense additional vortex formed by the migration of a portion of the endwall boundary layer fluid across the blade passage *aft* of the first endwall contour as discussed in Section 8.3. The bulk of the fluid for the main custom vortex was then supplied by the fluid of the inlet boundary layer, which was also seen to 'trip' over the initial endwall contour (which itself was again seen to 'block' the formation of the pressure HSV) and subsequently be entrained into the above mentioned vortex structure.

[4] Before being normalized by the maximum design velocity $V_{d,max}$ as described in Section 3.3.6

Despite the welcome predicted improvement in the rotor efficiency (+0.39%) for this design as well as the *prima facie* potential of the η_{de} metric, the results of the endwall design optimization highlighted a number of concerns associated with the use of this quantity, including:-

1. While improvement of the rotor exit flow profile was beneficial, the required manipulations to the flow *within* the blade row to achieve the current context were severe, and ultimately resulted in the replacement of a number of the existing secondary flow structures of the baseline case with customised replacements, with these replacements having been manipulated to produce flow conditions more consistent with those intended by the design.
2. Further to this, as predicted by the CFD and exemplified by this case, the requirements to produce the improved flow conditions described above at the rotor exit required to the use of a number of somewhat undesirable flow features, including the creation of a new vortex structure as well as the intentional shearing of this vortex against the blade suction surface in order to reduce the local velocities associated with it. Not only would this be likely to result in an overall increase in the overall rotor loss (as predicted by the CFD), but also introduce considerable practical complications such as adverse effects on the local heat transfer characteristics of the blade, as well as present non-trivial flow complexities at off-design conditions.

It should be noted that, in the presentation of the design efficacy in his work, in order to allow for better comparison between the rotor efficiencies and design efficacy, Dunn applied a scaling factor to the divisor of Eqn. 3.29 which resulted in the shifting of the η_{de} curves *left* of the ordinate (i.e. y-axis) and took on spanwise values between 0 - 1. This then allowed for the direct comparison between the changes to the rotor efficiency and the design efficacy. In this investigation however, a scaling factor was *not* applied to Eqn. 3.29, and instead the design efficacy was calculated directly from the flow quantities without modification. This was done because the intended use of the design efficacy in this investigation was the correction of the off-design flow produced by the secondary flow in the vicinity of the endwall, and the objective function used for this design was formulated to reduce this. As a result, while from Fig. 9.25b, it was clear that the bulk of the flow leaving the rotor was *under*turned in terms of the design flow angle, in contrast, when considered in terms of velocity, Fig. 9.25d shows that the majority of the flow through the midspan was above the nominal design velocity. These flow conditions, combined with the use of the unscaled design velocity in Eqn. 3.29, resulted in the majority of the flow through the midspan appearing in Fig. 9.25f as having design efficacies greater than unity.

Due to the complexity of the contours required to modify the rotor exit flow, in this investigation, the design efficacy was not considered appropriate for endwall design. The linkages between the rotor efficiency and the quantity for the majority of the designs did appear sound in that predicted improvements in the efficiency were matched with corresponding improvements in the design efficacy (and vica versa) (Fig. 9.29a). Similar congruence was also noted for those designs included in the experimental subset, although once again this was limited to the η_{tt}- & C_{ske}-based cases (Fig. 9.29b), the reasons for which are discussed in Section 9.3.7.

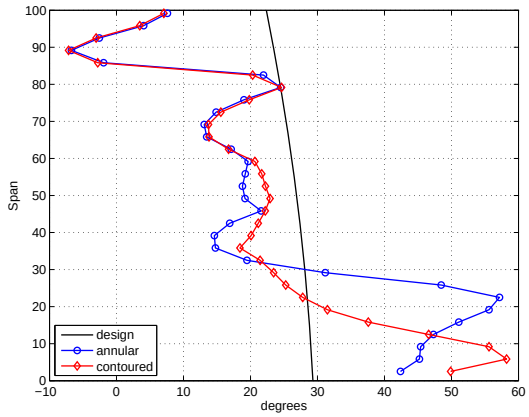

(a) α_3 (η_{tt}-based)

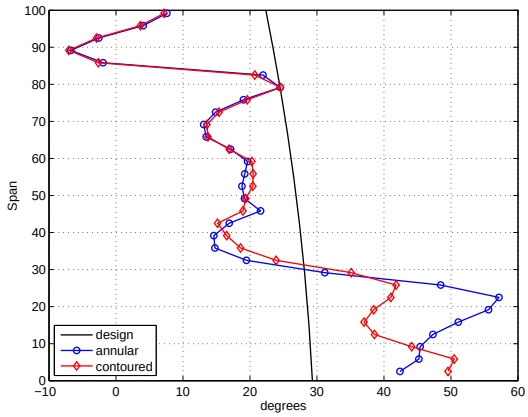

(b) α_3 (η_{de}-based)

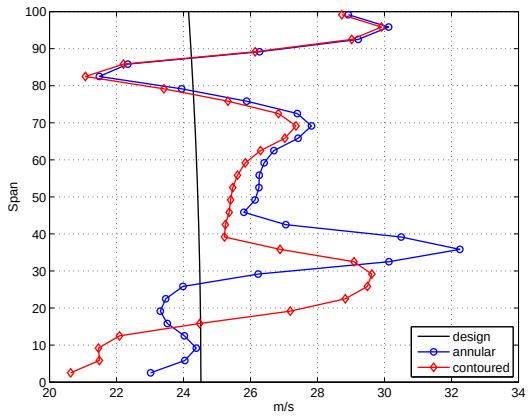

(c) V_3 (η_{tt}-based)

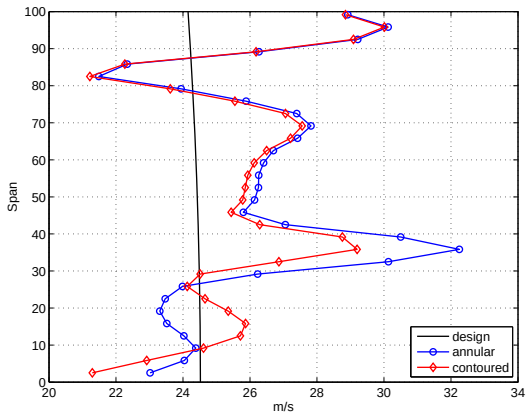

(d) V_3 (η_{de}-based)

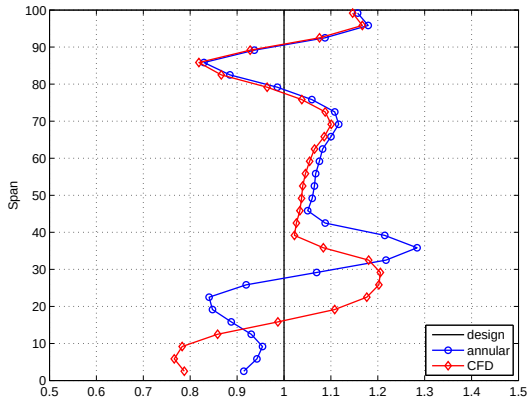

(e) η_{de} (η_{tt}-based)

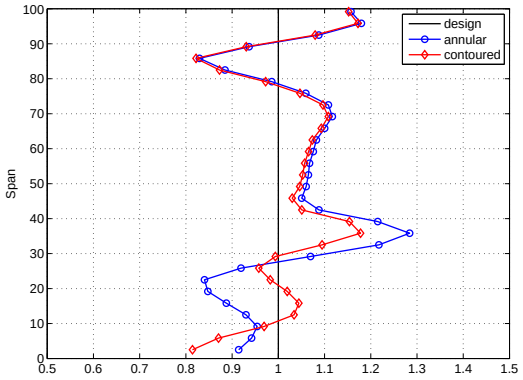

(f) η_{de} (η_{de}-based)

Fig. 9.25: Predicted absolute flow angle (α_3), velocity (V_3) and design efficacy (η_{de}) formulated in the stationary reference frame for the η_{tt}- (left) & η_{de}-based (right) designs

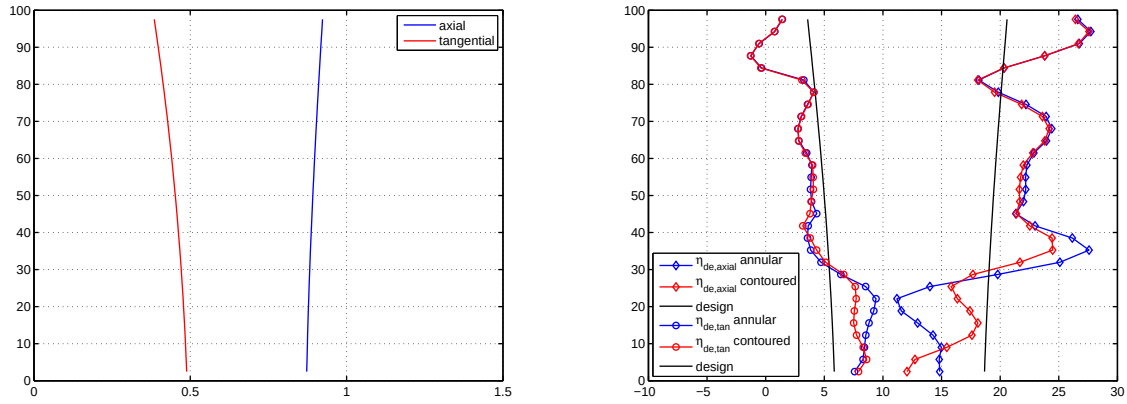

(a) Axial & tangential design vector weightings (b) Axial & tangential η_{de} components (unnormalized)

Fig. 9.26: Design vector weightings and axial and tangential η_{de} components for the annular and η_{de}-based designs

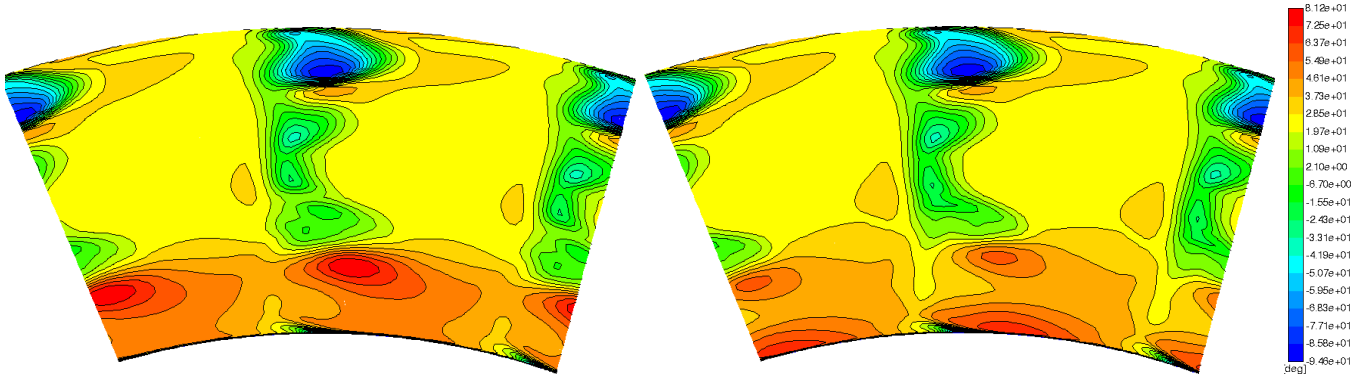

(a) α_3 (annular) (b) α_3 (η_{de}-based)

Fig. 9.27: Predicted absolute flow angle (α_3) at the rotor exit (X3) for the annular & η_{de}-based designs

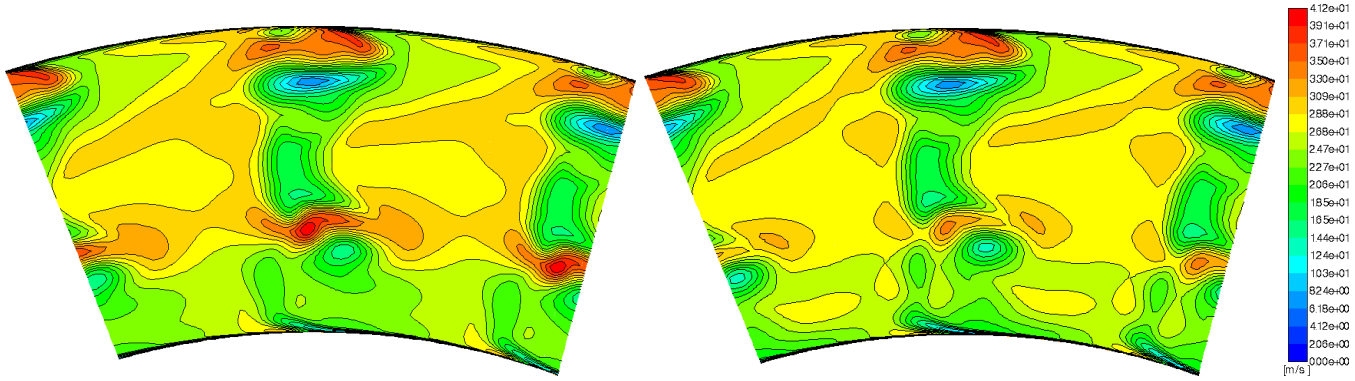

(a) $V_{z,3}$ (annular) (b) $V_{z,3}$ (η_{de}-based)

Fig. 9.28: Predicted axial velocity (V_z) at the rotor exit (X3) for the annular & η_{de}-based designs

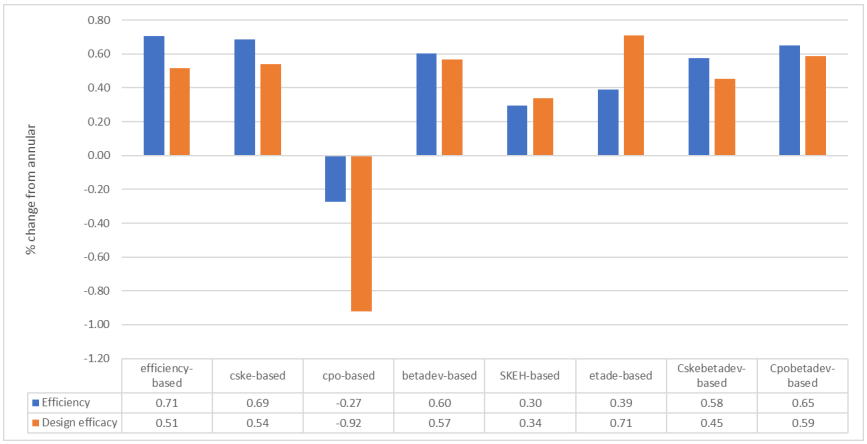

	efficiency-based	cske-based	cpo-based	betadev-based	SKEH-based	etade-based	Cskebetadev-based	Cpobetadev-based
Efficiency	0.71	0.69	-0.27	0.60	0.30	0.39	0.58	0.65
Design efficacy	0.51	0.54	-0.92	0.57	0.34	0.71	0.45	0.59

(a) CFD

	efficiency-based	cske-based	cpo-based	betadev-based	SKEH-based	etade-based	Cskebetadev-based	Cpobetadev-based
Efficiency	0.76	0.40					-0.63	-0.17
Design efficacy	1.46	2.27					1.38	1.63

(b) Experimental

Fig. 9.29: Comparison of predicted (top) and experimental (bottom) changes in rotor efficiencies (η_{tt}) and design efficacies (η_{de})

9.3.7 The 'Compound' designs

Overview

As discussed previously, the so-called 'compound' objective functions were formulated to meet the criteria of Snedden et al. (2010a), who suggested that an effective objective function should:-

1. reduce the strength of the secondary flows *within* the blade row under consideration, *as well as*
2. improve both the quality and consistency of the flow entering any *downstream* blade rows.

In addition, since objective functions based on various combinations of individual flow metrics have been already been used by various researchers within the turbomachinery community, the testing of two reasonably simple such objective functions for a standardized test case would provide an excellent opportunity to investigate the general performance of these types of functions in relation to one another.

In this investigation, the individual metrics used to construct objective functions which met the criteria of Snedden et al. (2010a), were:-

Target row secondary flow mitigation

- $C_{ske,1} + \beta_{dev,0.7}$-based → coefficient secondary kinetic energy (C_{ske})
- $C_{p0,rel,1} + \beta_{dev,0.7}$-based → loss coefficient ($C_{p0,rel}$)

Improve downstream flow quality

- $C_{ske,1} + \beta_{dev,0.7}$-based → flow deviation from design (β_{dev})
- $C_{p0,rel,1} + \beta_{dev,0.7}$-based → flow deviation from design (β_{dev})

As explained in Section 3.1.4, the weightings applied to each term of the overall compound metric determine the bias of the objective function towards reducing either of the metrics included, and hence the relative positioning of the final optimized design on the Pareto Front. For this investigation, the exact biases applied to each of the metrics comprising the final compound objective function were considered somewhat inconsequential, although specifying a pair of grossly unbalanced weightings would clearly bias the compound objective function towards one of the constituent metrics effectively making the use of the compound objective function largely valueless. For this investigation then, the individual weightings were based on those used by MacPherson and Ingram (2010) although for the present cases, the predominant bias was placed on the secondary flow mitigation term.

The CFD simulations predicted similar increases in the overall mass-averaged rotor efficiencies (+0.65% & +0.58%) for the $C_{p0,rel,1} + \beta_{dev,0.7}$- & $C_{ske,1} + \beta_{dev,0.7}$-based designs respectively, as well as might be expected, slightly larger decreases in the mass-averaged rotor exit C_{ske} for the $C_{ske,1} + \beta_{dev,0.7}$-based cases (+27.53% c.f. −22.83%) while similarly, slightly better performance in terms of the rotor exit loss coefficient for the $C_{p0,rel,1} + \beta_{dev,0.7}$-based design (−1.18% c.f. +1.18%) were predicted. The aforementioned link between the C_{ske} and flow deviation, was once again reinforced with the $C_{ske,1} + \beta_{dev,0.7}$-based endwall predicted to achieve somewhat better reductions in the overall mass-averaged flow deviations from design for the $C_{ske,1} + \beta_{dev,0.7}$-based endwall in comparison to the $C_{p0,rel,1} + \beta_{dev,0.7}$-based endwall (−29.58% & −24.60%) while the link between the design efficacy (η_{de}) & efficiency (η_{tt}) was once again reinforced with the same trends and similar relative magnitudes between the metrics predicted for each of the endwalls.

The poorer predicted performance of the $C_{ske,1} + \beta_{dev,0.7}$-based design in comparison to the $C_{p0,rel,1} + \beta_{dev,0.7}$-based endwall in terms of overall mass-averaged loss at the rotor exit, was consistent with the previous predictions for the C_{ske}-based endwall as well as the β_{dev}-based design where the emphasis on improving the flow secondary kinetic energy and / or flow deviations without considering the degree of irreversibility associated with the means by which these improvements were attained, resulted in generally lower predicted performance in comparison to those which included some direct measure of the loss itself.

Further to the above, the CFD results for the compound objective functions also confirmed a number of characteristics which were described previously for the C_{ske}- & $C_{p0,rel}$-based designs respectively. More specifically:-

- As was the case for the C_{ske}-based design, the predicted mass-averaged reductions in the secondary kinetic energy for the $C_{ske,1} + \beta_{dev,0.7}$-based design were seen to extend to the so-called 'mixed-

out' measurement plane, where as expected, these resulted in overall reductions in the calculated mass-averaged loss when compared to the annular design.

- In contrast and consistent with the predictions for the $C_{p0,rel}$-based design, the improved loss characteristics and smaller reductions in secondary kinetic energy at the rotor exit for the $C_{p0,rel,1}+\beta_{dev,0.7}$-based case resulted in an increase in the downstream 'mixed-out' secondary kinetic energy, while finally,
- Consistent with the increased C_{ske} at the downstream plane, the performance of the $C_{p0,rel,1}+\beta_{dev,0.7}$-based design was predicted to perform less well in terms of the mass-averaged loss coefficient in comparison to the $C_{ske,1}+\beta_{dev,0.7}$-based design, although still better than the datum case.

In general then, these predictions appeared to substantiate the idea that those metrics which targeted (and resulted in) reductions in the secondary flow *upstream*, resulted in higher losses at that plane, but thereafter resulted in improved performance in terms of both the secondary kinetic energy as well as loss at the 'mixed-out' plane. Conversely, those metrics which targeted the upstream loss - when achieving this - generally resulted in higher magnitudes of secondary kinetic energy downstream, as well as poorer overall performance in terms of the loss at the downstream plane.

Table 9.7: Comparison of endwall geometries for the C_{ske}- & $C_{ske,1}+\beta_{dev,0.7}$-based cases

Endwall			
C_{ske}-based	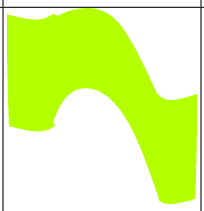	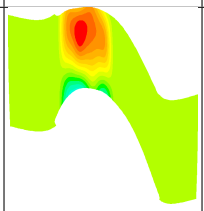	
	Iteration ∼ 0/300	Iteration ∼ 206/300	Iteration ∼ 300/300
$C_{ske,1}+\beta_{dev,0.7}$-based	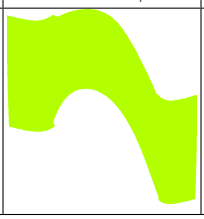	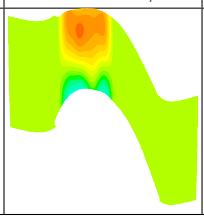	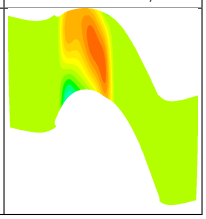

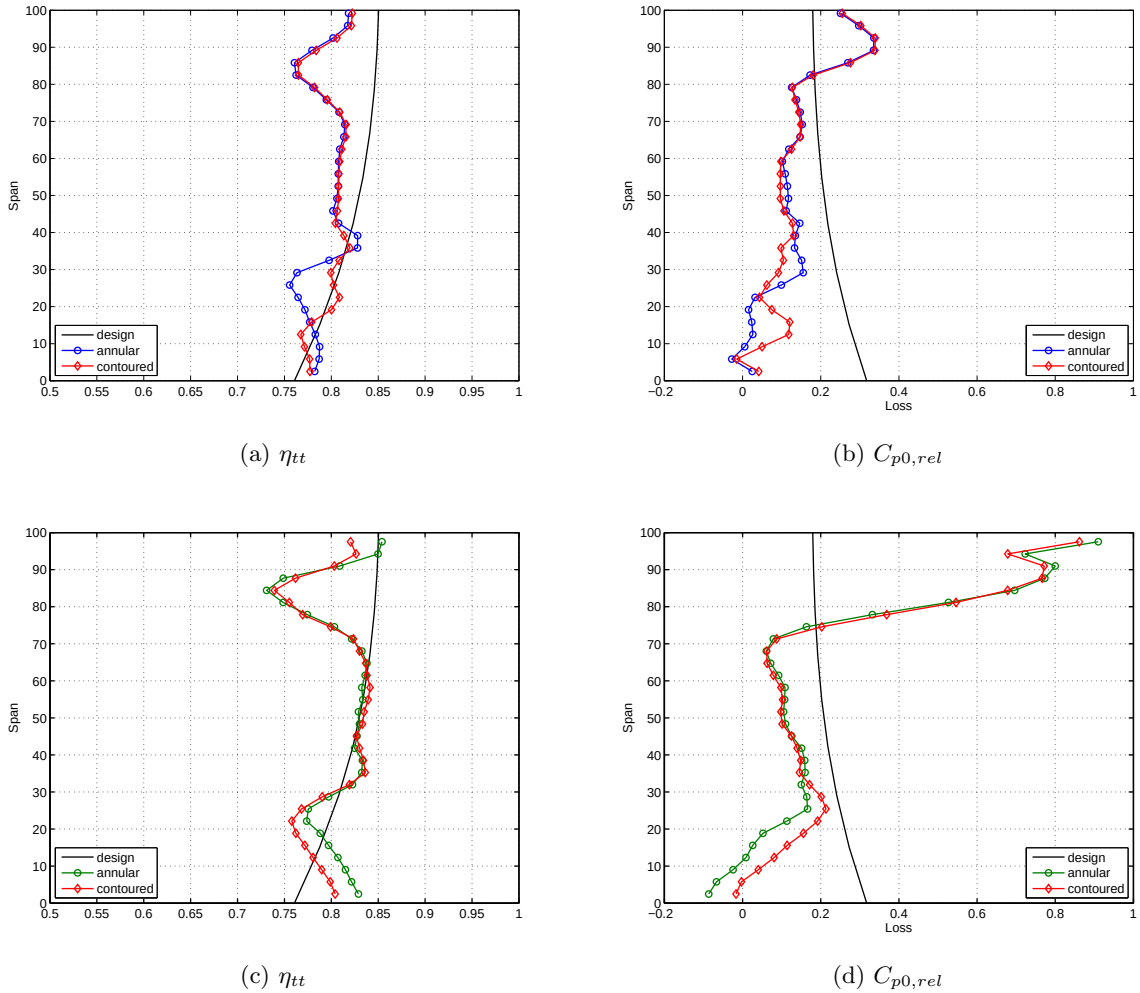

(a) η_{tt} (b) $C_{p0,rel}$

(c) η_{tt} (d) $C_{p0,rel}$

Fig. 9.30: Predicted (top) and experimental (bottom) rotor exit (X3) total-total efficiencies and loss coefficients for the annular and $C_{ske,1} + \beta_{dev,0.7}$-based endwalls

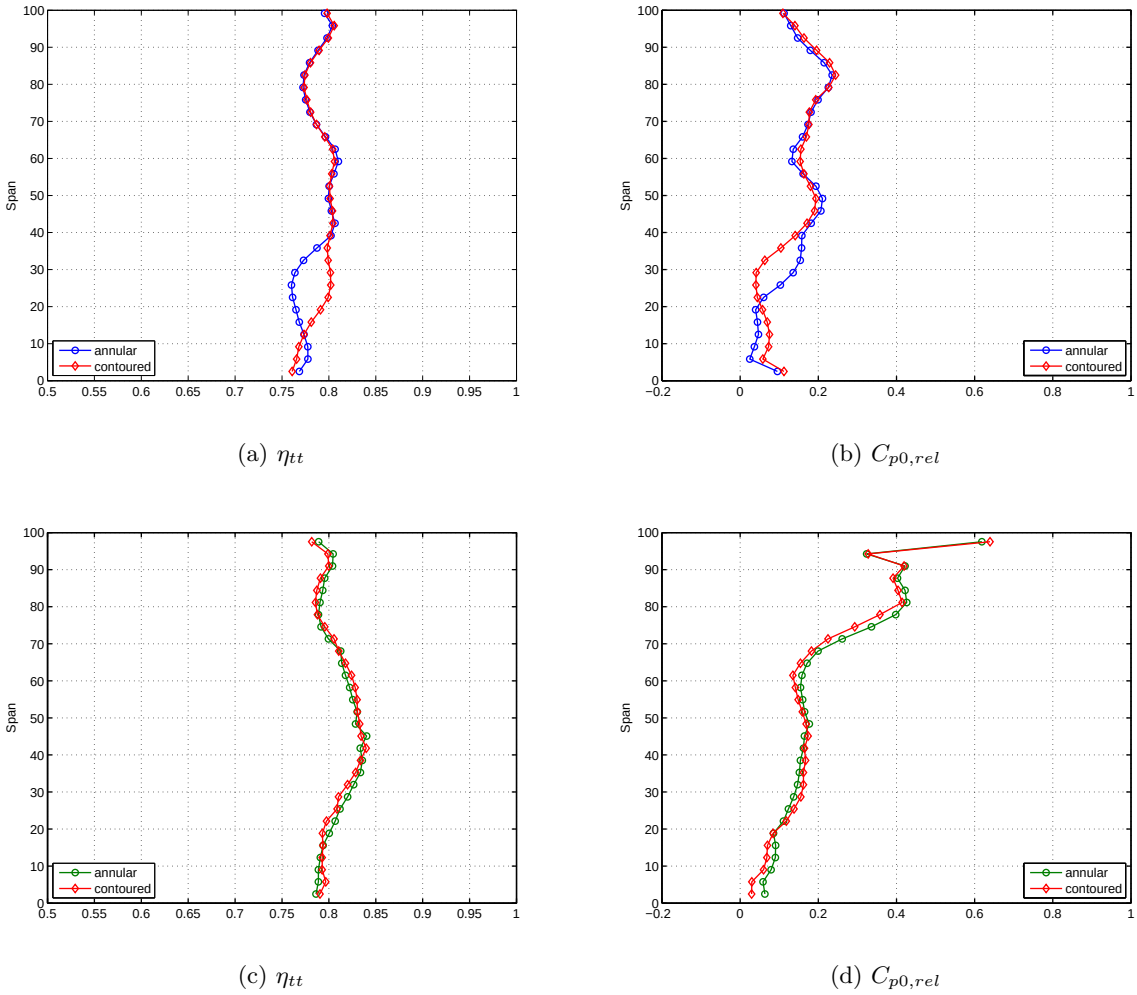

(a) η_{tt} (b) $C_{p0,rel}$

(c) η_{tt} (d) $C_{p0,rel}$

Fig. 9.31: Predicted (top) and experimental (bottom) 'mixed-out' (X4) total-total efficiencies and loss coefficients for the annular and $C_{ske,1} + \beta_{dev,0.7}$-based endwalls

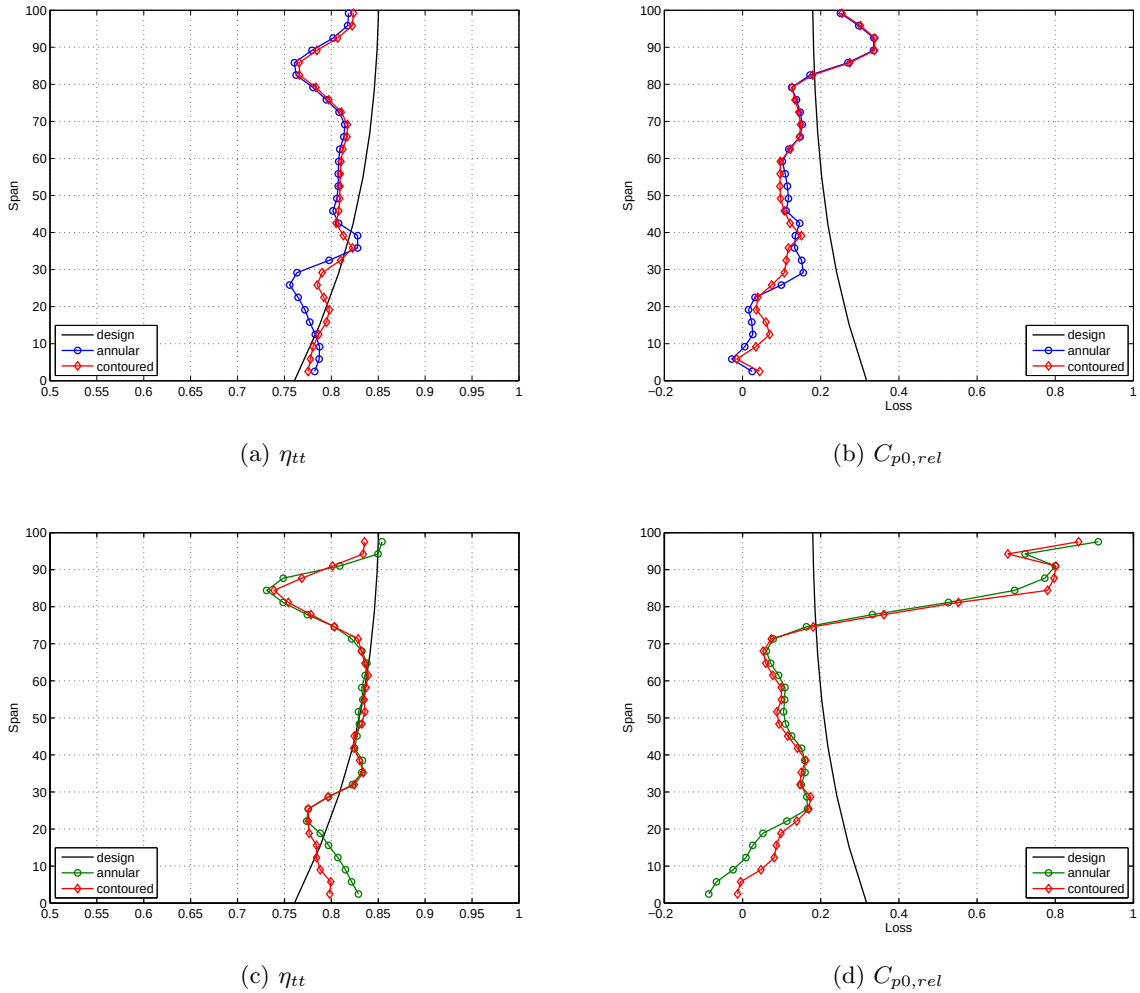

(a) η_{tt} (b) $C_{p0,rel}$

(c) η_{tt} (d) $C_{p0,rel}$

Fig. 9.32: Predicted (top) and experimental (bottom) rotor exit (X3) total-total efficiencies and loss coefficients for the annular and $C_{p0,rel,1} + \beta_{dev,0.7}$-based endwalls

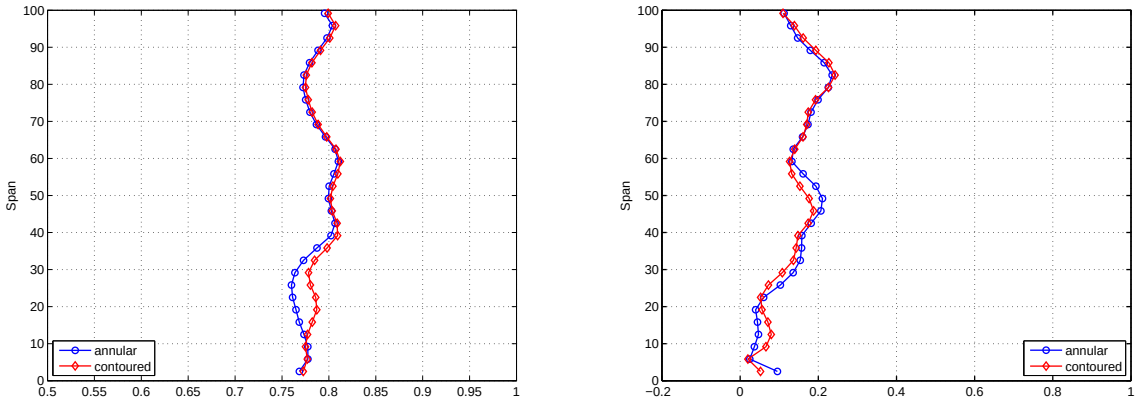

(a) η_{tt} (b) $C_{p0,rel}$

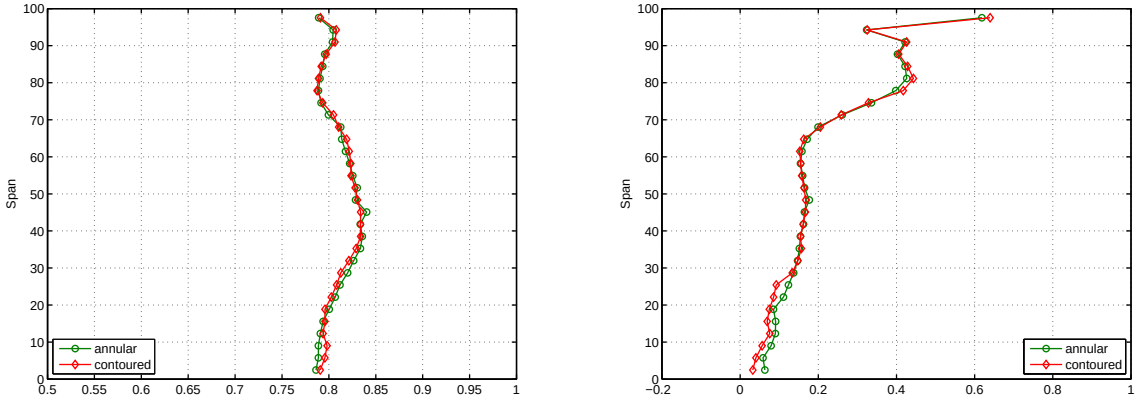

(c) η_{tt} (d) $C_{p0,rel}$

Fig. 9.33: Predicted (top) and experimental (bottom) 'mixed-out' (X4) total-total efficiencies and loss coefficients for the annular and $C_{p0,rel,1} + \beta_{dev,0.7}$-based endwalls

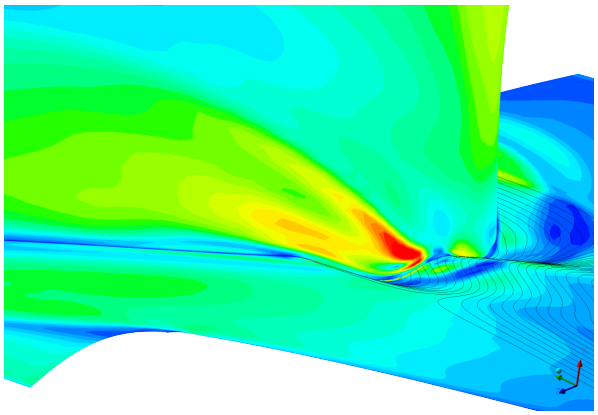

(a) β_{dev}-based

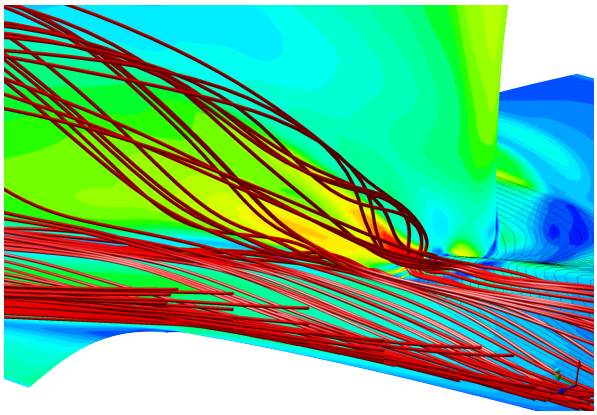

(b) β_{dev}-based (inc. streamlines)

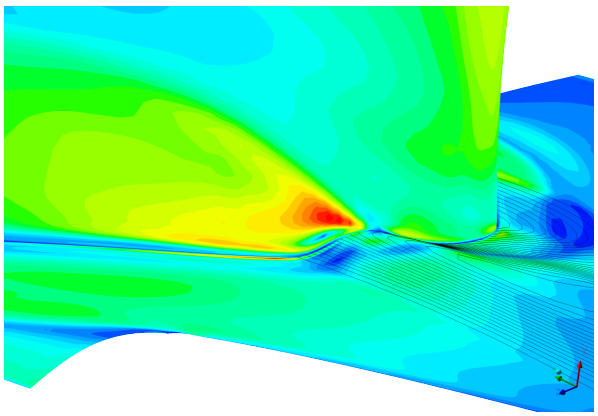

(c) $C_{ske,1} + \beta_{dev,0.7}$-based

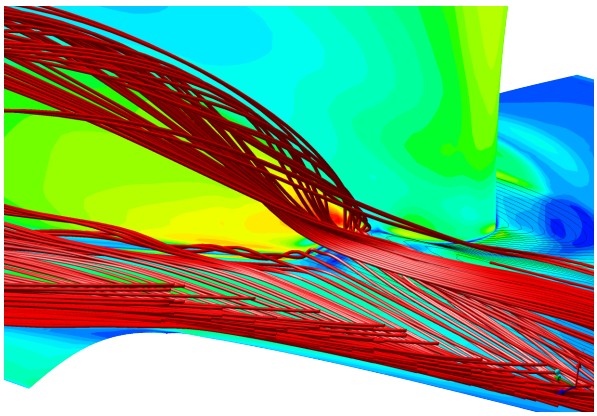

(d) $C_{ske,1} + \beta_{dev,0.7}$-based (inc. streamlines)

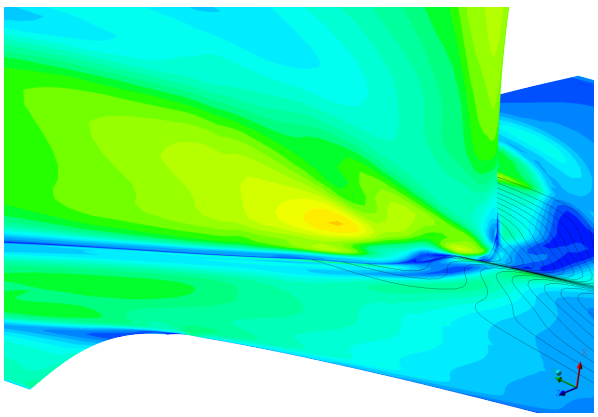

(e) $C_{p0,rel,1} + \beta_{dev,0.7}$-based

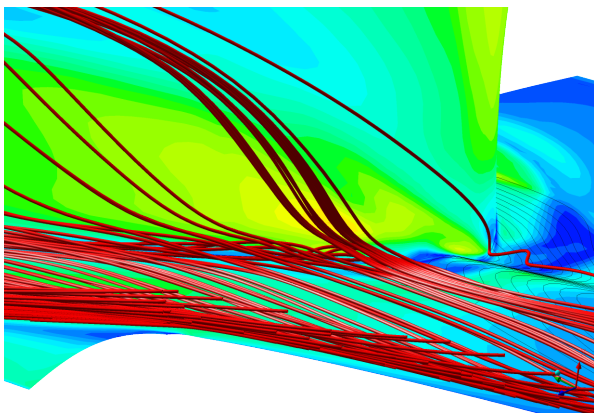

(f) $C_{p0,rel,1} + \beta_{dev,0.7}$-based (inc. streamlines)

Fig. 9.34: Endwall height contours (black), endwall and suction surface shear stress (filled contours) and endwall boundary layer (red) streamlines viewed from the aft of the contoured region for the β_{dev}, $C_{ske,1} + \beta_{dev,0.7}$ & $C_{p0,rel,1} + \beta_{dev,0.7}$-based designs

$C_{ske,1} + \beta_{dev,0.7}$-based

The $C_{ske,1}+\beta_{dev,0.7}$-based objective function was the first of the compound objective functions investigated. As indicated, the intention of this objective function was to attempt to improve the performance of the target blade row by reducing the secondary kinetic energy of the row, while improving the quality of the flow (in terms of flow angles) into a following stage by reducing the overall flow angle deviations from design.

The optimization for this endwall converged well, and after having approximately $^2/_3{}^{rds}$ (i.e. $^{206}/_{300}$ iterations) (Table 9.7) of the total optimization iterations, the endwall closely resembled that of the those produced by the C_{ske}- & β_{dev}-based objective functions, with similar predicted reductions in the rotor exit C_{ske}, flow deviations (β_{dev}) and efficiencies (η_{tt}). However, after a brief period of gradual refinement of this design, the endwall design routine was seen to locate a previously unvisited region of even lower objective function values, and refinement in this new region resulted in the formation of the large cross-passage deflector contour noted in the final design.

The predicted rotor exit (X3) secondary kinetic energy, flow deviation, and compound $C_{ske,1} + \beta_{dev,0.7}$ metric for the $C_{ske,1} + \beta_{dev,0.7}$-based endwall are shown in Fig. 9.36. In addition, the same results for the η_{tt}-based design are included for comparative purposes. In comparison to both the annular, as well as η_{tt}-based designs, the effects of the combined C_{ske} and β_{dev} terms on the predicted rotor exit C_{ske} are clear (Fig. 9.36b) where the additional off-axis flow induced by the upper and lower vortices (formed to correct the flow angle) resulted in a clear increase in the C_{ske} between approximately $\sim 20-30\%$ span. Similarly, the effects of the vortices on the predicted rotor exit flow deviation (Fig. 9.36d) in the same spanwise position was also clear with a considerable decrease in the flow deviation in this region in comparison to the η_{tt}-based case.

Despite the excellent predictions for the $C_{ske,1} + \beta_{dev,0.7}$-based design, the validations (Fig. 9.37) were not as favourable. In particular, for both the rotor exit secondary kinetic energy (C_{ske}) (Fig. 9.37b) as well as the flow deviation (β_{dev}) (Fig. 9.37d), while reductions for both quantities were predicted; the reductions in C_{ske} were not as significant as predicted by the CFD while for the flow deviation, an overall *increase* was in fact measured for this endwall. In addition, while the increase in the flow overturning close to the endwall predicted by the CFD was noted, the degree to which the flow was confined to the endwall region was considerably less than predicted. Further to this, instead of the predicted improvements in efficiency and limited increase in loss (Fig. 9.30a & 9.30b) in the secondary flow region, the experimental profiles (Figs. 9.30c & 9.30d) showed a significant decrease in the circumferentially-averaged efficiencies as well as a substantial increase in the loss spanning from the endwall to a position of approximately $\sim 30\%$ span.

In order to explain the above, an analysis of the computed streamlines close to the endwall was carried out. Fig. 9.34 shows a pair of closeup views of the endwall (from aft of the contoured region) with the endwall height contours plotted (in black, unfilled), calculated wall shear stress (contours, filled) and streamlines released within the endwall boundary layer close to the pressure surface for all those designs which include the β_{dev} flow deviation term. In addition, the predicted and measured rotor relative flow velocities (W_3) for the annular, η_{tt}- and $C_{ske,1}+\beta_{dev,0.7}$-based designs are shown in Figs. 9.35a & 9.35b.

Firstly, Fig. 9.34d shows the endwall adjacent view of the final 'deflector' contour with streamlines for the $C_{ske,1} + \beta_{dev,0.7}$-based design. In comparison to both the β_{dev}-only and $C_{p0,rel,1} + \beta_{dev,0.7}$-based cases, the effect of the significantly larger 'deflector' contour on the endwall flow is clear:- the deflection of almost all the fluid from within the contoured region (as well as some fluid from the annular portion of the endwall aft of the contoured region) onto the suction surface, which resulted in the decoupling, and formation of the additional vortex which was seen to exit the blade passage close to the midspan (shown again in Fig. 9.41a for reference). The effect of impingement of the fluid on the suction surface as described above is also clear where Fig. 9.34c shows a region of extremely high local wall shear stress. In addition, aft of the main deflector contour, a region of low surface shear is predicted. This formed as a result of the separation of the deflected endwall flow immediately ahead of the suction surface.

In addition to the above, Figs. 9.35a & 9.35b show the predicted and measured rotor exit relative flow velocities (W_3) respectively. While not captured by the CFD, the experimental results show a significant reduction in the secondary flow region for the $C_{ske,1} + \beta_{dev,0.7}$-based design (in comparison to both the annular and η_{tt}-based designs) which was also then seen to correspond to the region of increased loss coefficient already discussed for this endwall for the same spanwise region (Fig. 9.30d).

While the endwall parameter constraints of Section 5.6.5 (and specifically the changes in height ($\Delta c_{k,k-1}$), phase (ψ_i) and periodicity ($\Delta n_{k,k-1}$) between consecutive circumferential 'driven' curves) were specifically intended to pre-empt the possibility of separations as a result of the endwall geometry; for the present case, the selected constraint values appear to have not been restrictive enough.

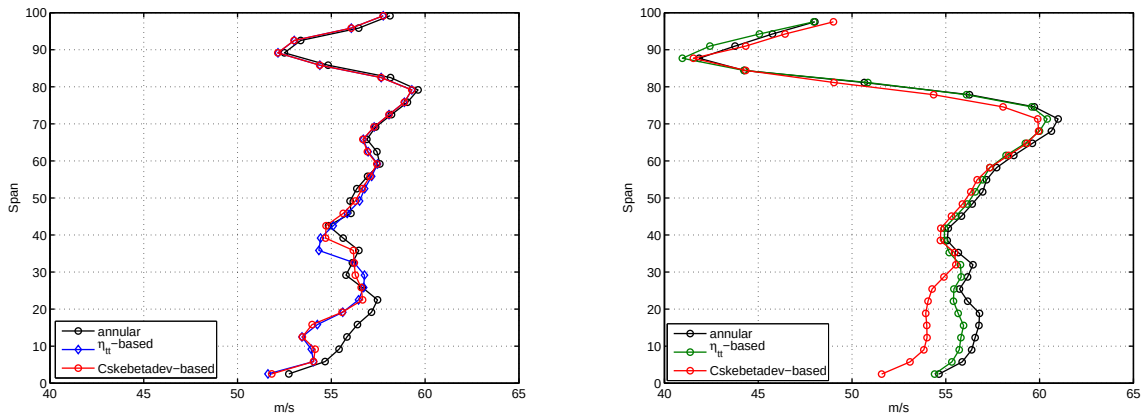

(a) CFD ($W3$) (b) Experimental ($W3$)

Fig. 9.35: Predicted and experimental rotor exit relative flow velocity comparisons for the annular, η_{tt}- & $C_{ske,1} + \beta_{dev,0.7}$-based cases

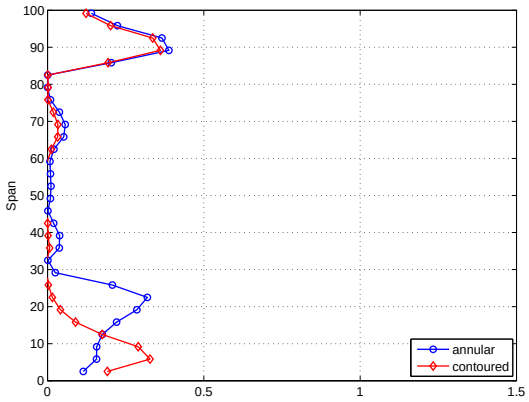

(a) C_{ske} (η_{tt}-based)

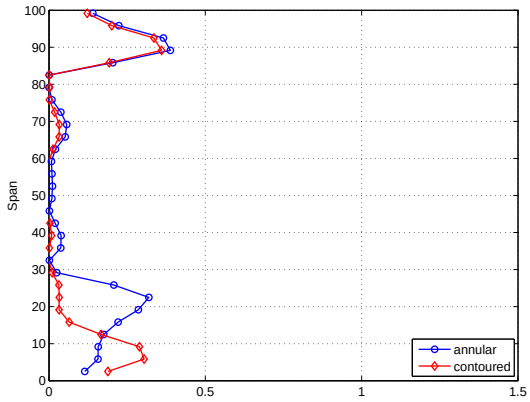

(b) C_{ske} ($C_{ske,1} + \beta_{dev,0.7}$-based)

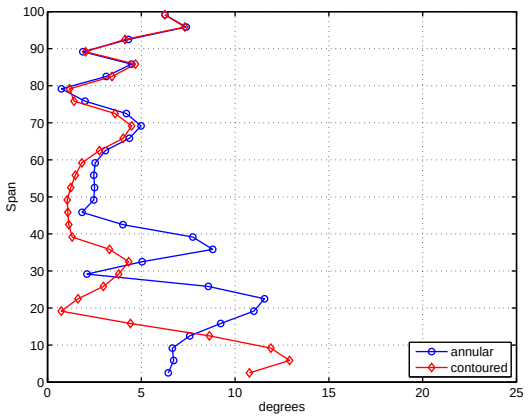

(c) β_{dev} (η_{tt}-based)

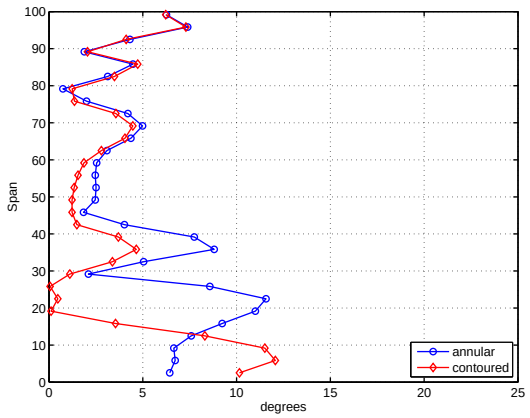

(d) β_{dev} ($C_{ske,1} + \beta_{dev,0.7}$-based)

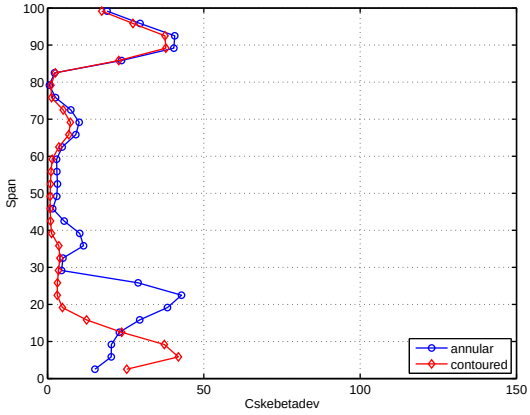

(e) $C_{ske,1} + \beta_{dev,0.7}$ (η_{tt}-based)

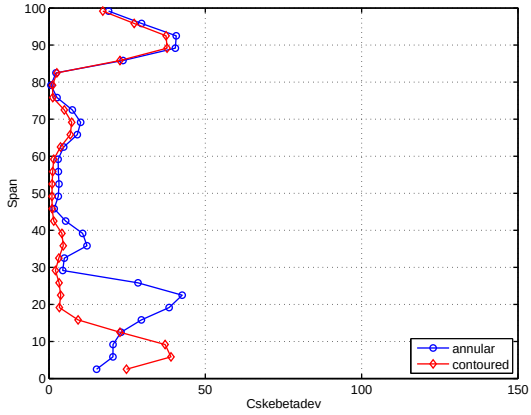

(f) $C_{ske,1} + \beta_{dev,0.7}$ ($C_{ske,1} + \beta_{dev,0.7}$-based)

Fig. 9.36: Predicted C_{ske}, β_{dev} & $C_{ske,1} + \beta_{dev,0.7}$ averages for the η_{tt}- & $C_{ske,1} + \beta_{dev,0.7}$-based designs

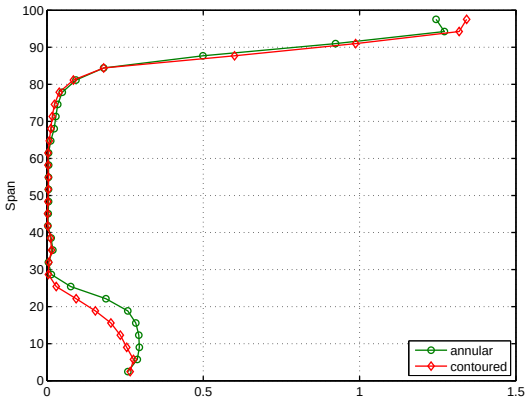

(a) C_{ske} (η_{tt}-based)

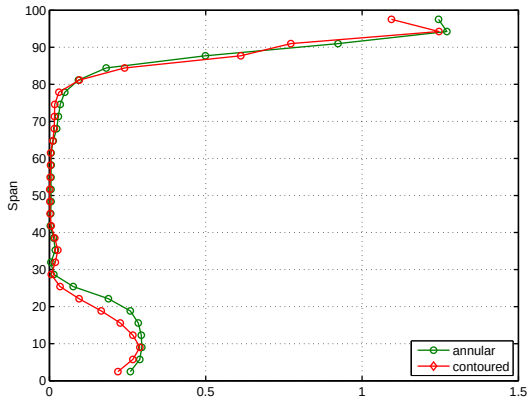

(b) C_{ske} ($C_{ske,1} + \beta_{dev,0.7}$-based)

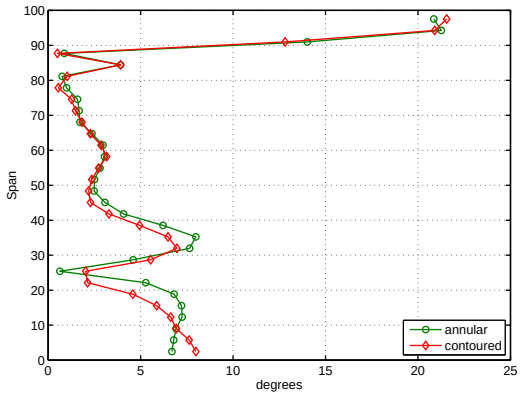

(c) β_{dev} (η_{tt}-based)

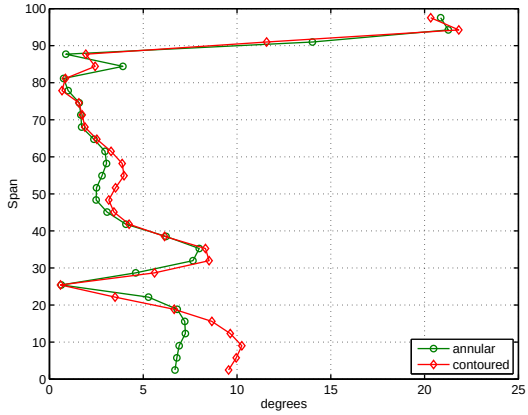

(d) β_{dev} ($C_{ske,1} + \beta_{dev,0.7}$-based)

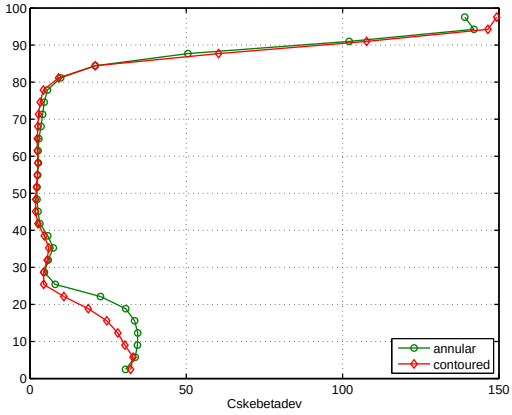

(e) $C_{ske,1} + \beta_{dev,0.7}$ (η_{tt}-based)

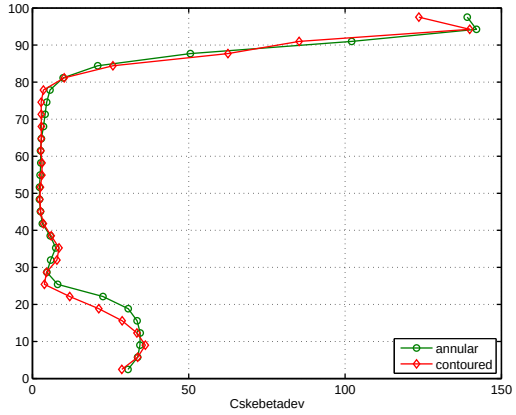

(f) $C_{ske,1} + \beta_{dev,0.7}$ ($C_{ske,1} + \beta_{dev,0.7}$-based)

Fig. 9.37: Experimental C_{ske}, β_{dev} & $C_{ske,1} + \beta_{dev,0.7}$ averages for the η_{tt}- & $C_{ske,1} + \beta_{dev,0.7}$-based designs

$C_{p0,rel,1} + \beta_{dev,0.7}$-based

As with the $C_{ske,1} + \beta_{dev,0.7}$-based objective function, the $C_{p0,rel,1} + \beta_{dev,0.7}$-based metric was designed to use the rotor exit loss coefficient ($C_{p0,rel}$) to reduce the strength of the secondary flows of the target (i.e. current blade row) and the flow deviation (β_{dev}) term to improve the quality of the flow into the following blade row.

As was the case for the $C_{ske,1} + \beta_{dev,0.7}$-based design, this design was also predicted to improve the overall rotor efficiency (at both the rotor exit (X3) as well as at the downstream measurement (X4) planes) (+0.65% & +0.70%). However in contrast to the previous design, the substitution of the rotor exit loss coefficient ($C_{p0,rel}$) for the coefficient of secondary kinetic energy (C_{ske}) as the secondary flow mitigation term was also predicted to result in a decrease in the overall rotor exit loss coefficient (−1.18%). Further to this and as expected, in contrast to the $C_{ske,1} + \beta_{dev,0.7}$-based metric, the reduced emphasis on reducing the off-axis component of the flow as a result of the inclusion of only a single term directly related to this (i.e the β_{dev}-based term) in the objective function, also resulted in smaller overall predicted reductions in the mass-averaged rotor exit secondary kinetic energy (−22.83%) as well as the flow deviation (−24.60%) in comparison to the $C_{ske,1} + \beta_{dev,0.7}$-based objective function. Finally, at the 'mixed-out' measurement plane, as was the case for the previous design, the $C_{p0,rel,1} + \beta_{dev,0.7}$-based design was predicted to have a significant positive effect on the rotor efficiency (+0.70%), as well as a reasonable effect on the loss coefficient (−4.31%).

As alluded to previously, in addition to the above, probably the most significant result for the present objective function, was the resolution of a number of the issues which were noted to be associated with the use of the rotor exit relative total pressure loss coefficient ($C_{p0,rel}$) when used in isolation.

In particular:-

1. despite both metrics predicted to result in a reduction in the predicted mass-averaged rotor exit loss coefficient, unlike for the $C_{p0,rel}$-based case, in the present case, this was achieved in conjunction with a decrease in the rotor exit secondary kinetic energy, flow deviation and $SKEH$, as well as an improvement in the mass-averaged design efficacy, and further,
2. again unlike the $C_{p0,rel}$-only based endwall, for which a raft of adverse effects were predicted for at the downstream measurement plane, in addition to a predicted increase in the mixed-out rotor efficiency, favourable changes in all the remaining metrics were also predicted at the downstream plane for this objective function.

The reasons for the predicted success of the $C_{p0,rel,1}+\beta_{dev,0.7}$-based objective function in comparison to the $C_{p0,rel}$-based metric were understood to be as a result of the the sensitization of the metric to the design rotor exit flow angles which in turn then prevented exploitation of the test rig design by the endwall design routine as was noted for the $C_{p0,rel}$-based case. For this particular test case, this additional constraint once again enforced the proper relationship between the rotor work output and total isentropic enthalpy drop through the blade passage, as evidenced by the results shown for this endwall in Fig 8.32a of Section 8.5.

Despite the promising predictions for this endwall, as was the case for the $C_{ske,1} + \beta_{dev,0.7}$-based design, the validation of the CFD results for this endwall were poor. More specifically, contrary to

the predicted improvements in the rotor exit (X3) efficiency (Fig. 9.30a) and loss coefficient (Fig. 9.30b), this design resulted in an overall reduction in the mass-averaged rotor efficiency (-0.17%) as well as a corresponding increase in the mass-averaged rotor exit loss coefficient ($+4.44\%$). Unlike the $C_{ske,1} + \beta_{dev,0.7}$-based case however, for the present design, the rotor exit relative flow angles (Fig. 9.38a) appeared to suggest that the intended 'decoupling' of the suction side HSV and endwall boundary layer fluid (as illustrated in Fig. 9.41b) was successful, resulting in the validation of the predicted reductions in the mass-averaged flow deviation from design (β_{dev}) (-2.83%), although much smaller than predicted. Although less distinct than predicted by the CFD (Fig. 9.39d), this was clear from the 'kink' in the measured spanwise profile of flow deviation (Fig. 9.40d) at approximately $\sim 20\%$ span.

The reason for the poor correspondence between the predicted and measured rotor exit efficiency and loss was once again understood to be as a result of a smaller but non-negligible flow separation close to the endwall and aft of the final endwall contour. The effects of this feature were once again evidenced through the increase of the circumferentially-averaged loss coefficient between $0 - 20\%$ span (Fig.9.32d). As with the $C_{ske,1} + \beta_{dev,0.7}$-based design, the effect of this increase in the local loss coefficient was once again clear through the noticeable decrease in the measured spanwise profile of the rotor exit efficiency (Fig.9.32c). The origin of this separation was once again explained with reference to Figs. 9.34e & 9.34f, where the region of low surface shear stress on and immediately aft of the final endwall contour for this endwall was clear. Finally, the influence of this separated fluid on the rotor exit (X3) relative flow angle (β_3) and velocity (W_3) is shown in Fig. 9.38a & Fig. 9.38b, where again the 'kink' in both the relative flow angle and velocity profiles at approximately 20% span are also visible.

Finally, as was the case for the $C_{ske,1} + \beta_{dev,0.7}$-based design, while the endwall geometry constraints were specifically selected to minimize the possibility of undesirable flow features (such as the separation discussed above), these constraints appear to have not been restrictive enough, and this was considered unfortunate, based on the seeming promise of this metric.

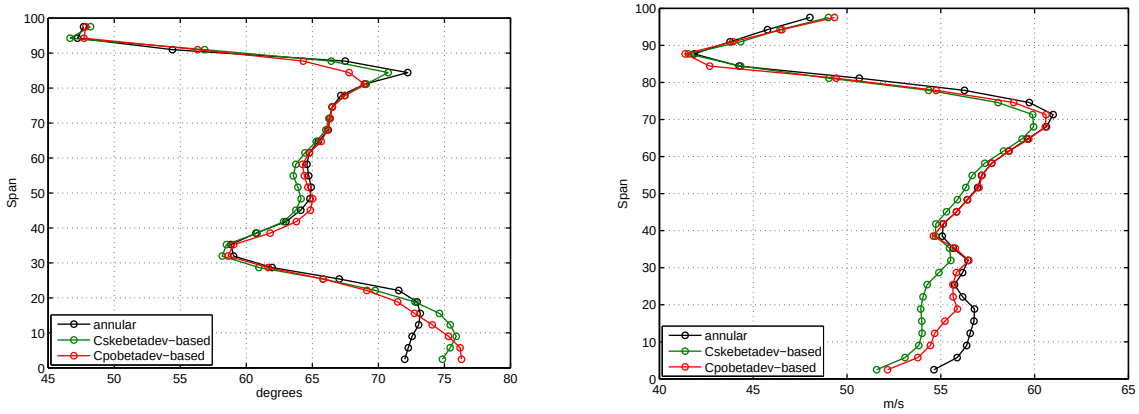

(a) (β_3) (b) ($W3$)

Fig. 9.38: Experimental rotor exit relative flow velocity comparisons for the annular, $C_{ske,1} + \beta_{dev,0.7}$ & $C_{p0,rel,1} + \beta_{dev,0.7}$-based cases

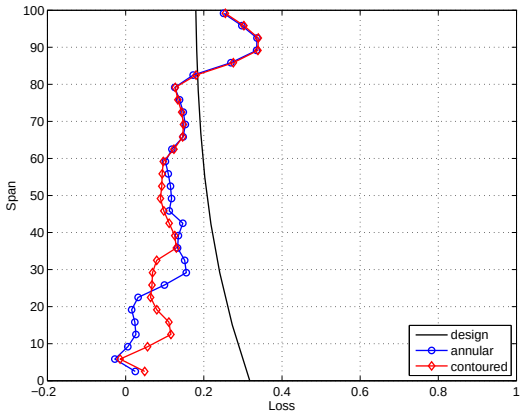

(a) $C_{p0,rel}$ (η_{tt}-based)

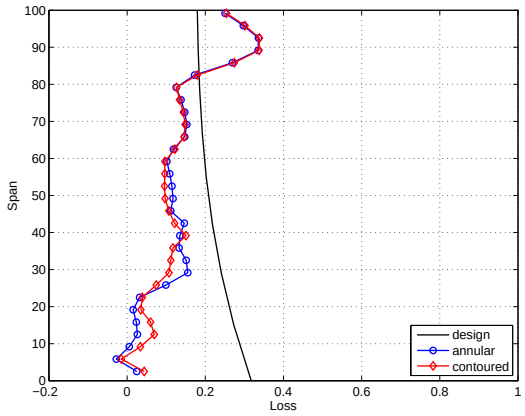

(b) $C_{p0,rel}$ ($C_{p0,rel,1} + \beta_{dev,0.7}$-based)

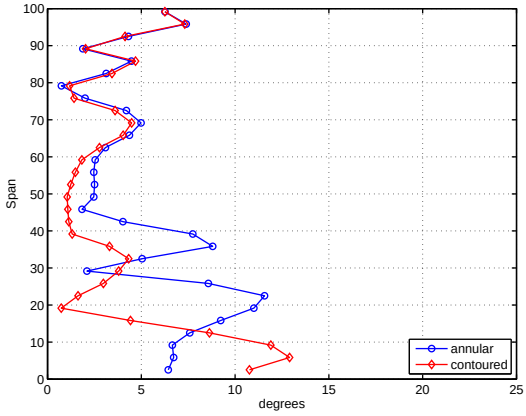

(c) β_{dev} (η_{tt}-based)

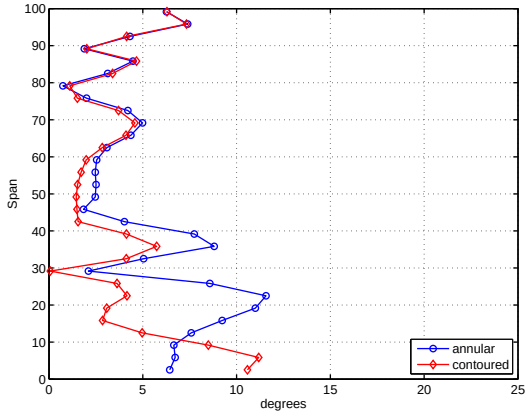

(d) β_{dev} ($C_{p0,rel,1} + \beta_{dev,0.7}$-based)

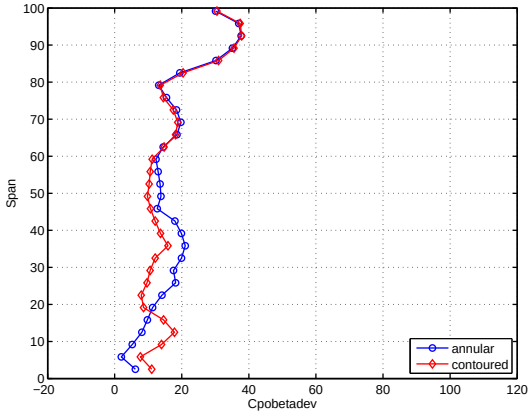

(e) $C_{p0,rel,1} + \beta_{dev,0.7}$ (η_{tt}-based)

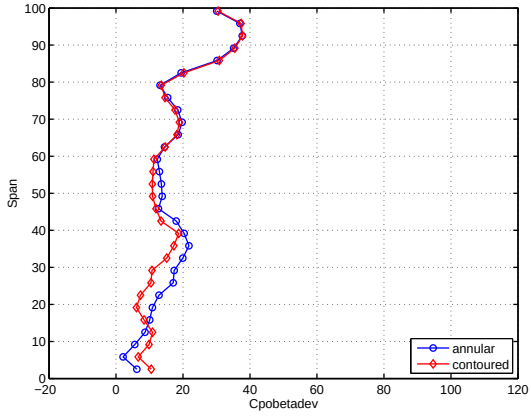

(f) $C_{p0,rel,1} + \beta_{dev,0.7}$ ($C_{p0,rel,1} + \beta_{dev,0.7}$-based)

Fig. 9.39: Predicted $C_{p0,rel}$, β_{dev} & $C_{p0,rel,1} + \beta_{dev,0.7}$ spanwise averages for the η_{tt}- & $C_{p0,rel,1} + \beta_{dev,0.7}$-based designs

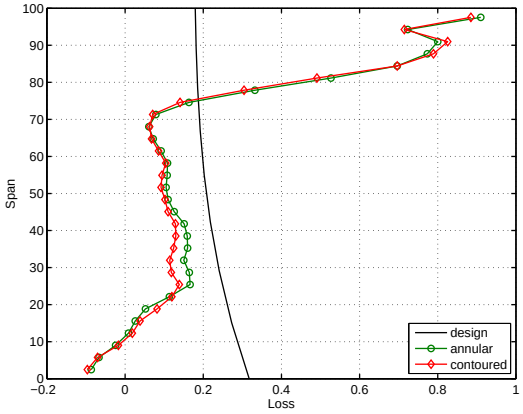

(a) $C_{p0,rel}$ (η_{tt}-based)

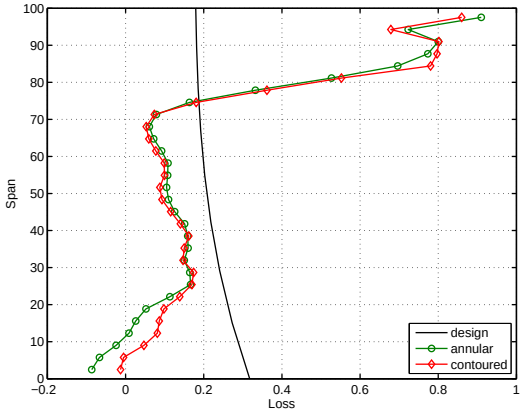

(b) $C_{p0,rel}$ ($C_{p0,rel,1} + \beta_{dev,0.7}$-based)

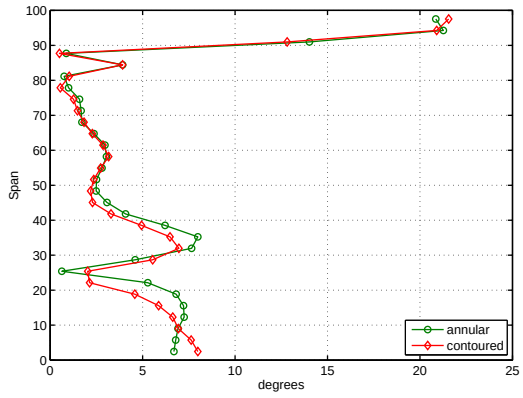

(c) β_{dev} (η_{tt}-based)

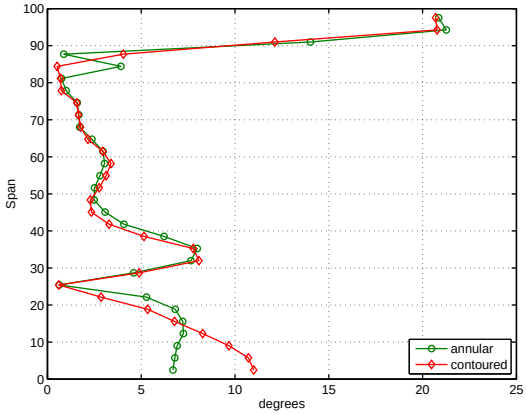

(d) β_{dev} ($C_{p0,rel,1} + \beta_{dev,0.7}$-based)

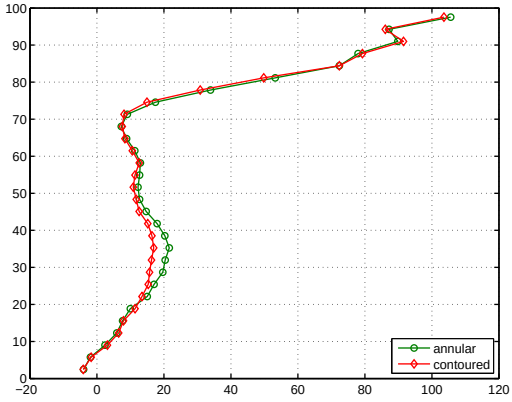

(e) $C_{p0,rel,1} + \beta_{dev,0.7}$ (η_{tt}-based)

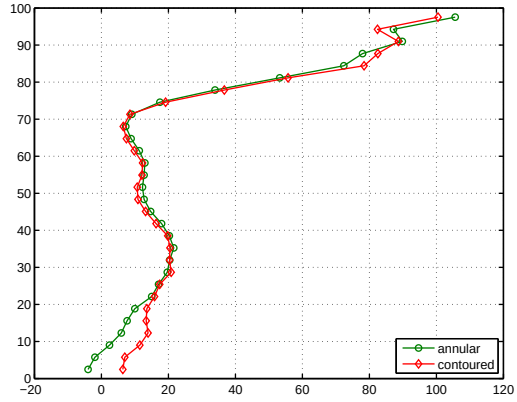

(f) $C_{p0,rel,1} + \beta_{dev,0.7}$ ($C_{p0,rel,1} + \beta_{dev,0.7}$-based)

Fig. 9.40: Experimental $C_{p0,rel}$, β_{dev} & $C_{p0,rel,1} + \beta_{dev,0.7}$ spanwise averages for the η_{tt}- & $C_{p0,rel,1} + \beta_{dev,0.7}$-based designs

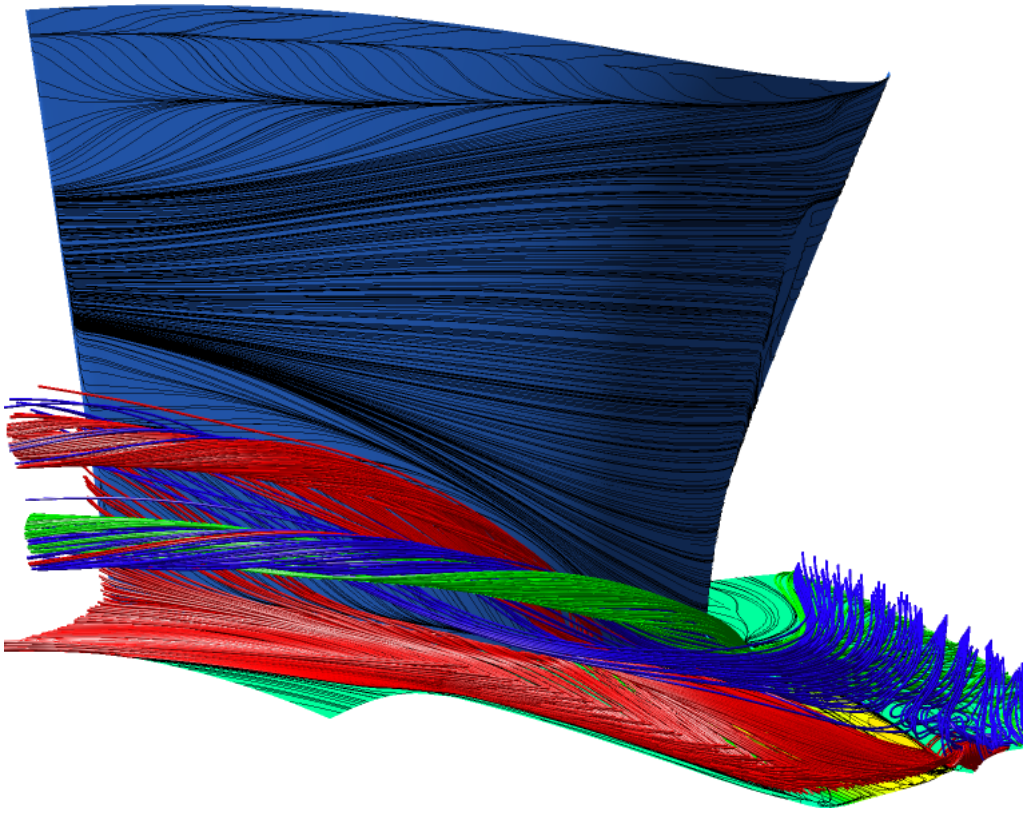

(a) $C_{ske,1} + \beta_{dev,0.7}$-based

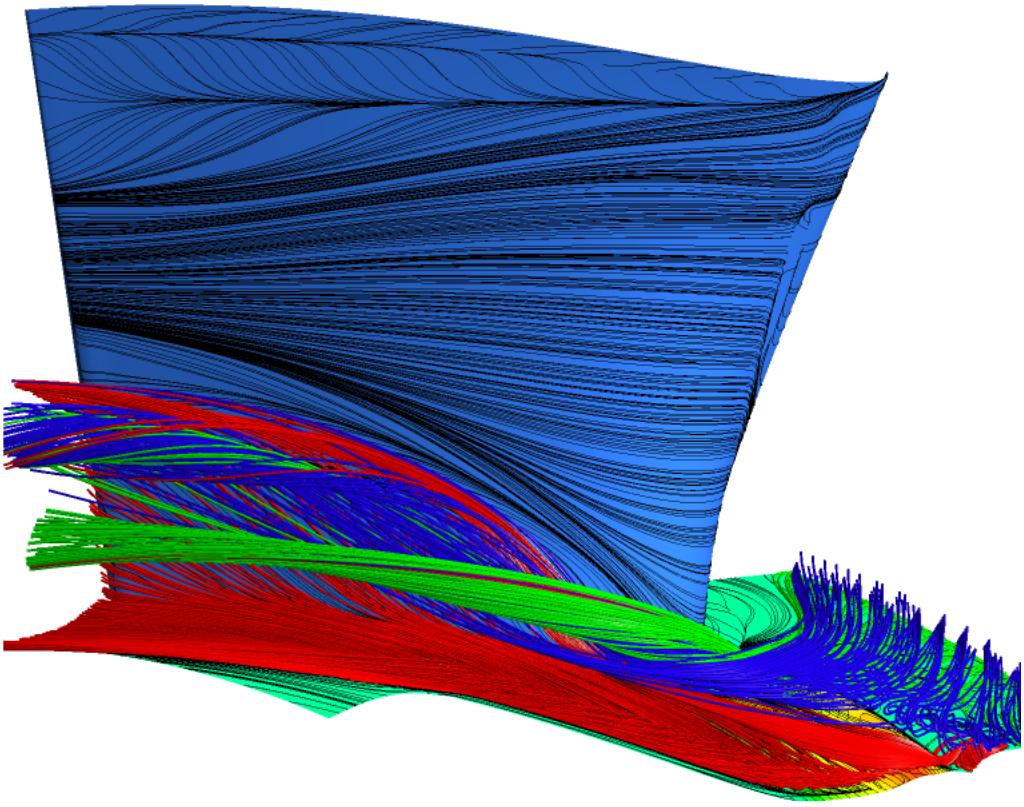

(b) $C_{p0,rel,1} + \beta_{dev,0.7}$-based

Fig. 9.41: Secondary flow vortex structures of the $C_{ske,1} + \beta_{dev,0.7}$- & $C_{p0,rel,1} + \beta_{dev,0.7}$-based endwall designs

9.4 Summary

In this Chapter, the results presented in Chapter's 7 & 8 were reviewed and specific comments applicable to each of the different metrics used in each objective function were made. This included a review of the performance of the endwall optimization routine in terms of overall reduction of the target metric, predictability and convergence characteristics for each metric, as well as performance of each metric in terms of manipulating the secondary flow to improve the efficiency or flow quality produced by the rotor. In addition to being discussed below, a summary of the major findings of this Chapter are included in Table. 9.8 below.

Convergence - In terms of the algorithm convergence, the best performing objective functions were found to be those based on the rotor exit efficiency (η_{tt}), coefficient of secondary kinetic energy (C_{ske}) and loss coefficient ($C_{p0,rel}$, $C_{p0,rel,1} + \beta_{dev,0.7}$), with all of these objective functions showing large decreases in the initial objective function magnitudes followed by a series of small incremental but additional meaningful reductions. This characteristic suggested the overall region of low objective function values were defined and located efficiently by the design routine whereafter the incremental improvements in the cost functions achieved using the local WB_1 search criteria showed the cost function hypersurface appeared to be well-behaved near the optima for these metrics. These assertions were corroborated by the well-defined regions of low cost function magnitudes and clustering of sample points in the so-called scatter plots for these designs.

While not as efficient as the above, the objective functions based on the β_{dev} (including the both β_{dev}- & $C_{ske,1} + \beta_{dev,0.7}$-based objective functions but excluding the $C_{p0,rel,1} + \beta_{dev,0.7}$-based objective function already mentioned) & η_{de} metrics also showed reasonably good overall performance, again indicating reasonably well-defined regions of low cost function magnitudes on the cost function hypersurface which were also well-behaved close to the optimum point.

In contrast, the volatility of the $SKEH$ metric was clear, with $SKEH$-based objective function showing very little evidence of overall convergence, even after 300 EGO iterations and a combination of high and low objective function values interspersed apparently randomly through the parameter space with very little evidence of even a single well defined region of consistently low objective function values.

Endwall geometry - In addition to the excellent convergence characteristics of these metrics, the designs based on the η_{tt} & C_{ske} metrics both produced endwall geometries which were excellent candidates for manufacture and testing, with both designs exhibiting variations of the traditional 'hump-and-dip' configurations. The $C_{p0,rel,1} + \beta_{dev,0.7}$-based design produced a similar configuration although 'concave' nature of this endwall in the center of the contoured region was not shared with the previous designs.

The β_{dev}- & $C_{ske,1} + \beta_{dev,0.7}$-based designs, despite being predicted to be effective in their manipulations of the rotor exit flow deviation angles, as well as C_{ske} and flow deviations respectively, where noted to be somewhat more 'aggressive' than the η_{tt} & C_{ske} based designs (despite the specific intention of the endwall parametrisation to limit the final endwall shapes to reasonably simple configurations), and the the CFD as well as the experimental testing of the $C_{ske,1} + \beta_{dev,0.7}$-based endwall confirmed this was the case.

Finally, despite being successful in reducing their respective target metrics, the final geometries of the $SKEH$-, η_{de}- & $C_{p0,rel}$-based designs were all considered clearly too complex for either experimental testing or to be incorporated in a practical application.

Improvements

Target metric / Other metrics - For all the designs, the endwall design routine produced final designs in which appropriate reductions in each of the base objective function metrics were achieved. Further to this, with the exception of the $C_{p0,rel}$-based objective function (for which the decrease in loss at the rotor exit resulted in increases in all the secondary flow), the impact of the reductions in the target metrics at the X3 measurement plane resulted in corresponding general decreases in the remaining metrics.

Downstream - Once again, the performance gains at the rotor exit were seen to translate into reductions in all the studied metrics at the downstream measurement plane in all cases with the exception of the $C_{p0,rel}$-based case for which a reduction in the rotor efficiency, as well as increases in the loss and secondary flow were predicted.

Validation - A total of 4 of the final optimized endwall designs were tested experimentally. Of these designs, the overall results of both the η_{tt}- & C_{ske}-based designs were found to validate well when tested, with the rotor efficiency predictions for the η_{tt}-based designs noted to be especially accurate. In general however, the predicted (CFD) changes from the datum case were significantly larger than those actually measured by the experiment.

In contrast, the $C_{ske,1} + \beta_{dev,0.7}$- & $C_{p0,rel,1} + \beta_{dev,0.7}$-based designs were found to validate less well, with the losses and efficiencies for both designs at the rotor exit presenting the most obvious differences.

Table 9.8: Summary of final endwall optimization and performance results

Endwall	*Convergence*	*Shape*	*Improvement*			*Experiment*
			Target metric	*Other metrics?*	*Extends to X4?*	*confirms CFD*
η_{tt}-based	GOOD	VERY GOOD	GOOD	VERY GOOD	YES	YES
C_{ske}-based	GOOD	VERY GOOD	GOOD	VERY GOOD	YES	YES
$C_{p0,rel}$-based	VERY GOOD	VERY POOR	GOOD	VERY POOR	NO	n/a[b]
β_{dev}-based	FAIR	FAIR	GOOD	GOOD	n/a[a]	n/a[b]
$SKEH$-based	VERY POOR	VERY POOR	GOOD	FAIR	YES	n/a[b]
η_{de}-based	FAIR	POOR	GOOD	FAIR	n/a[a]	n/a[b]
$C_{ske,1} + \beta_{dev,0.7}$-based	FAIR	FAIR	GOOD	FAIR	YES	NO
$C_{p0,rel,1} + \beta_{dev,0.7}$-based	VERY GOOD	GOOD	GOOD	FAIR	YES	NO

[a] Since no design outlet angle was available at the X4 measurement plane, the performance of this quantity could not be characterised at this location

[b] Not tested experimentally

10

Conclusions and Recommendations for future work

The overall goal of this thesis was to design a series of non-axisymmetric endwall contours using different objective functions based on various common flow metrics drawn from the literature, and thereafter investigate the effectiveness of each design on the performance of the rotor of a low speed research turbine. Of the geometries generated, all the designs were analysed using a validated CFD model, and a further subset of designs (including the annular case) were selected for experimental testing. The reasons for the selection of the endwalls included in the experimental subset were given in Chapter 7.

To produce the required designs, a previously-characterised test case (the CSIR 1½ stage, low speed turbine) which was more representative of a 'real' turbine than a linear cascade was selected as the basis for the investigation and a non-axisymmetric endwall design system. This system comprised a surrogate-based, global optimization routine coupled to fully autonomous geometry generation and flow analysis routine was developed to provide endwall designs refined to as high a degree of optimality as possible for each objective function. In addition, the designs themselves were constructed using a novel geometry parametrisation in which the contouring was intentionally limited to the forward portion of the blade passage as well as to potential shapes which were intended to reduce the secondary flows by restricting the development of the cross passage flows within each blade passage as per the original intention of the early contoured endwall designers. This parametrisation was also designed to provide greater control over the selection of the endwall geometry to the design routine by providing an explicit parameter for each feature of the endwall geometry, rather than as a combination of multiple independent parameters.

A total of 8 geometries were generated using the above-mentioned design system, of which a subset of 5 (including the annular case) were selected for manufacture and experimental testing. Within the experimental subset, both simple and compound functions were tested.

10.1 Conclusions

For the purposes of these conclusions, it is perhaps most instructive to group the endwalls studied in this investigation into three categories, namely:-

1. those endwalls which resulted in not only improved flow, but broadly achieved this in the manner expected (i.e. the $\boldsymbol{\eta_{tt}}-$, $\mathbf{C_{ske}}-$ & $\boldsymbol{\beta_{dev}}$ **− based** designs),

2. those endwalls that did not produce results as expected (i.e. the $\mathbf{C_{p0,rel}-}$, $\mathbf{SKEH-}$ & $\boldsymbol{\eta_{de}}$ $\mathbf{-}$ **based** designs) *and*
3. the 'compound' functions ($\mathbf{C_{ske,1} + \beta_{dev,0.7}-}$ & $\mathbf{C_{p0,rel,1} + \beta_{dev,0.7}}$ $\mathbf{-}$ **based**) which were designed to explore the power of reducing the flow deviation angles in addition to the primary 'loss' metrics which were otherwise limited in their success.

10.1.1 The η_{tt}-, C_{ske}- & β_{dev}-based endwalls

The endwalls of this category represented the best overall performing designs of all those produced, with all three of these designs predicted to increase the overall efficiency of the rotor. The results of the experimental testing largely confirming these predictions, in particular, for the η_{tt}- & C_{ske}-based designs.

Both in the CFD as well as experimental analyses, the $\boldsymbol{\eta_{tt}}$ $\mathbf{-}$ **based design** was shown to be the best performing design, while the metric itself (i.e. the rotor efficiency), was also found to be amongst the most reliably predicted quantity of all those investigated - at both the rotor exit (i.e. at X3), as well as at the downstream measurement plane (X4) when the results of the so-called 'compound' designs (for which unexpected separations in the flow were noted) were excluded. The contours produced using this quantity were also more conventional in nature than the majority of the remaining designs generated (comprising of the well-known 'hump-and-dip' configuration) and were without any additional 'non-standard' features, a number of which were noted for some of the remaining designs. This was significant because it appeared to validate the traditional hump / dip configuration used by many previous researchers as the most efficient for the mitigation of secondary flow and its associated losses, especially since this configuration was selected by the endwall design routine, in a completely autonomous fashion.

The main mechanism by which the η_{tt}-based design was found to function, was through blocking the formation of the pressure side HSV, as well as by reducing the growth of the passage vortex through the reduction of the cross passage pressure gradient and endwall migratory flow, leading to a reduction in the size and intensity of the passage vortex as well as the losses associated with it. In addition however, operating conditions of the η_{tt}-contoured rotor showed that the reductions in the secondary flow (and losses) as accomplished by the methods described above, were not sufficient for improvement in the overall rotor efficiency, and instead, the sensitivity of the η_{tt}-based metric to the ratio between the blade passage isentropic pressure drop and rotor work output was critical to the success of this endwall. Moreover, this meant that the changes to the endwall geometry as produced by the endwall design routine were selected so as to maximize the rotor work output for a given blade row pressure drop. For the η_{tt}-based endwall, this was accomplished by ensuring that that portion of the total inlet enthalpy which was lost to the secondary losses (which represented that part of the total blade row losses which could be influenced by the endwall geometry) were minimized. Overall, the excellent convergence characteristics, predictability as well as superior performance of the η_{tt}-based metric in terms of overall reductions in the secondary flow as well as improvement in the rotor efficiency, made these findings significant because - to date - blade row efficiency has not been extensively used for the design of non-axisymmetric endwall contours. It should be noted however, that the success of the η_{tt}-based objective function in this investigation may have been related to the fact that for the current work, this quantity was pressure-based (and not temperature-based, as is

more common) - and in particular then may have avoided some of the difficulties associated with the prediction and sensitivity of the quantity for the latter variant.

Finally, despite the impressive improvements in the rotor efficiency as well as reduction in the rotor exit loss coefficient, because this design resulted in only moderate improvements in the mass-averaged rotor exit secondary kinetic energy, flow deviation angle and overall design efficacy, it was noted that in a multi-blade row environment, the use of this metric would result in the most beneficial changes to the 'target' blade row rather than any downstream or following blades.

Although the overall configuration of the $\mathbf{C_{ske} - based\ design}$ was very similar to that produced by the η_{tt}-based objective function, the actual effects of the endwall on the rotor performance, as well as the flow, were somewhat different to those by the η_{tt}-based metric. More specifically, while the predicted increase in the rotor efficiency for the design was almost identical to that of the η_{tt}-based design, the actual improvement in the rotor efficiency was somewhat less than what was measured for the η_{tt}-based case, while the reduction in the rotor exit loss coefficient was also significantly smaller. In contrast, for the current endwall, the measured reductions in the rotor exit secondary kinetic energy and flow deviation as well as the improvements in the design efficacy, were all increased for the C_{ske}-based endwall in comparison to the η_{tt}-based design.

Despite the similarity to the η_{tt}-based design, one of the reasons for the poorer relative performance of this endwall (and therefore design metric) in comparison to the η_{tt}-based design, was the indirect sensitivity of the quantity to the aerodynamic loss (as a result of the its constitution as *loss proxy* rather than the *actual* loss), and therefore a lack of sensitivity to the degree of irreversibility implicit in the mechanisms used to reduce the off-axis energy. In this investigation, despite the excellent performance of this metric, this was evident in the slightly poorer performance of this endwall in comparison to the η_{tt}-based design in terms of the rotor exit loss coefficient as well as by the slightly more 'aggressive' nature of the endwall contours produced by the design and which resulted accordingly in slightly larger reductions in the mass-averaged rotor exit coefficient of secondary kinetic energy.

While the performance benefit in terms of increased efficiency was evident at the rotor exit plane, the reductions in the strength of the secondary flow at the same location were also seen to extend downstream where they were noted to manifest themselves in terms of similar reductions to both the downstream secondary kinetic energy and 'mixed-out' loss coefficient. Finally, despite the limited shortcomings discussed for this metric above, the excellent predictability of the C_{ske}, especially at the rotor exit, made this metric an excellent choice for the basis of an endwall optimization, either when used alone or a basis for more complex metrics.

As was the case for the η_{tt}- & C_{ske}-based cases, the overall geometry as well as the predicted results of the $\boldsymbol{\beta_{dev} - based\ endwall}$ were very similar to those of the C_{ske}-based design. This similarity was attributed to the intrinsic link between the flow angle and the coefficient of secondary kinetic energy. Although as indicated, overall this endwall shared a great deal of the same geometric characteristics as the C_{ske}-only based design, the emphasis on the correction of the flow deviation explicitly resulted in the introduction of an additional cross passage contour which was specifically designed to effect larger corrections (through the decoupling of the suction surface and inlet boundary layer fluid from the endwall boundary layer fluid) to the mass-averaged flow deviation angle than was the case for the C_{ske}-only based design. In addition, these corrections were accompanied by a slightly larger predicted

increase in the rotor exit loss coefficient in comparison to the C_{ske}-only based endwall in addition to slightly reduced reductions in the predicted mass-averaged rotor exit C_{ske}.

Once again, as was the case for the C_{ske}-based design, the predicted benefits of the β_{dev}-based endwall were seen to extend unanimously downstream to the so-called 'mixed-out' measurement plane where as was the case for the C_{ske} as well as η_{tt}-based designs, the reduced secondary kinetic energy magnitudes were predicted to result in a significant decrease in the 'mixed-out' loss.

10.1.2 The $C_{p0,rel}$-, $SKEH$- & η_{de}-based endwalls

Despite being based on what appeared to be 'reasonable' metrics, the $C_{p0,rel}$-, $SKEH$- & η_{de}-based objective functions did not result in the improved performance as hoped for these metrics.

The $\mathbf{C_{p0,rel}-based\ design}$ resulted in an interesting case. While the final optimized endwall was in fact predicted to reduce the loss at the rotor exit, the overall efficiency of the rotor was predicted to decrease in comparison to the datum case. Analysis of the detailed structure of the flow within the blade passage showed that the reduction in the loss within the blade passage was accomplished by minimizing the interaction of the secondary flow structures with one another as well as with the endwall surface and fluid itself. More specifically, for this endwall, the results of the endwall design optimization were found to result in an endwall configuration in which the interactions between the pressure side leg of the horseshoe vortex (and later the passage vortex) and the endwall surface (including its boundary layer fluid), as well as between the same vortex and the suction side leg of the horseshoe vortex early in the early portion of the blade passage, were minimized. This resulted in a secondary flow system in which the predicted entropy generation rates within the blade passage were up to 5% lower than those of the annular case. Further, the reductions in the interactions between the secondary flow structures and each other as well as with the endwall as described above, resulted in a significant increase in the mass-averaged secondary flow at the rotor exit, which in turn resulted in increased circumferentially-averaged flow angles and deviations from design. Despite the positive effects on the loss at the rotor exit, the increases in the intensity of the off-axis flow at the rotor exit resulted in a significant increase at the downstream 'mixed-out' measurement plane, as well as higher residual mass-averaged magnitudes of the C_{ske} and $SKEH$.

As indicated, despite the reductions in the overall mass-averaged loss coefficient at the rotor exit, the overall efficiency of this design was predicted to decrease and this was found to be as a result of the exploitation of the endwall design routine of a particular characteristic of the test rig. In particular, it was found that despite the reduction in the mass-averaged rotor exit loss coefficient, the overall isentropic total pressure drop through the rotor was also increased which, although accompanied by an increase in the rotor work output, was significant enough to result in an overall reduction in the rotor efficiency. Further, it was noted that at the rotor exit and in comparison to the remaining designs (including the annular case), the mass-averaged rotor exit velocities were significantly increased indicating that the additional energy provided to the blade row as a result of the above mentioned increase in the blade row total pressure drop, was converted to kinetic energy rather than being extracted by the rotor resulting ultimately in a reduction in the overall rotor efficiency. The above mentioned increase in the total isentropic enthalpy drop was possible because unlike other test rigs, in the CSIR turbine, the target inlet mass flow rate was set rather than the total pressure drop through the blade passage.

Immediately aft of the rotor, the predictability of the loss was poor (even with the exclusion of the 'compound' metrics). However, this was not the case at the downstream plane, where the correlations between the predicted and measured loss results for each endwall were noted to be very good.

Despite the **SKEH − based metric** having been used successfully by various other groups, for this particular investigation, a number of issues were encountered with the use of this metric which resulted in an endwall which was was clearly unsuitable for use. For the current design, a number of issues were noted, including:-

- the large relative magnitude of the helicity (H) component in comparison to the secondary kinetic energy (SKE) component and therefore the large sensitivity of the helicity to even reasonably small changes in the endwall geometry parameters (as evidenced by the large changes in the $SKEH$-based objective function for neighbouring sample points), and
- the inherent decomposability of the metric itself, which meant that the overall value of the metric could be reduced by manipulating only one of the metrics components.

Analysis of the predicted final endwall geometry, computed streamlines and spanwise profiles of C_{ske} and helicity showed that, in the design of this endwall, the endwall design routine had exploited a number of the weaknesses of the metric described above, including manipulating the spanwise distribution of the circumferentially-averaged helicity below the midspan, through the introduction of a new secondary flow vortex which was generated intentionally near the junction of the forwardmost endwall curves and the blade's pressure surface. The reduction of the spanwise helicity close to the endwall for the $SKEH$ in comparison to both the C_{ske} as well as η_{tt}-based designs resulted in an overall reduction in the overall $SKEH$ close to the endwall where the corresponding coefficient of secondary kinetic energy was still reasonably large.

While the design was predicted to result in a small increase in the overall rotor efficiency, the complexity of the endwall geometry meant that it was unlikely that this design would ever be considered a realistic option commercially.

Whereas previously, the basis of the $\boldsymbol{\eta_{de}}$ **− based metric** had only been used by a single investigator as an alternative measure of turbine performance in cases where the uncertainty or errors in experimental measurements or CFD calculations made use of the aerodynamic efficiency difficult, this investigation marked the first time that this metric has been used for the actual design of non-axisymmetric endwall contours.

In this investigation, the design efficacy was formulated using the flow quantities from the absolute frame of reference. An inspection of the numerical results showed that the corrected flow at the rotor exit was more closely aligned with that prescribed by the design, in terms of both the axial and tangential velocity components. As was the case for the $SKEH$-based design, the η_{de}-based objective function also resulted in the introduction of a 'bespoke' vortex into the passage flow which was specifically tailored to bring about changes to the flow as discussed previously. Unfortunately, despite the predicted improvements in the flow, the complexity of the contours required to bring about changes in the flow meant that, as was the case with the $SKEH$-based endwall, this endwall was considered too impractical for actual use.

Despite the failure of the η_{de} metric in this investigation to produce an endwall which could be considered a reasonable candidate for manufacture and testing, a review of the metric in comparison to the calculated rotor efficiencies showed that, in the absence of confounding factors, the changes in this metric correlated well with the changes in the efficiencies predicted for each design. This was significant because, since the metric is dependent only on flow quantities which are expected to be well predicted by the CFD, this metric may be considered a robust replacement for the efficiency.

10.1.3 The 'Compound' designs

Finally, the so-called 'compound'-designs were devised as an attempt to meet the recommendations of Snedden et al. (2009b), who suggested that appropriate endwall design objective functions should promote both reductions in the secondary flow of the target (i.e. current) blade row, as well as the improvement in the quality of the flow into any downstream blade rows.

For the $\mathbf{C_{ske,1} + \beta_{dev,0.7} - based\ metric}$, the coefficient of secondary kinetic energy (C_{ske}) was selected with the intention of reducing the secondary flow strength (and therefore loss) because this metric has been found to be highly successful when used as a standalone metric, while the flow deviation from design (β_{dev}) was used in an attempt to promote an improvement in the flow quality at the rotor exit. While the CFD predictions for this metric were extremely promising, with significant reductions in the secondary flow strength (measured by reductions in both the C_{ske} and $SKEH$) and the flow deviation from design predicted, as well as an increase in the overall rotor total-total efficiency, consistent with the predictions for the β_{dev}-only based design, these improvements were accompanied by a reasonably modest increase in the predicted rotor exit loss coefficient.

During the optimization phase for this endwall, the implicit link between the flow deviation and coefficient of secondary kinetic energy was clearly illustrated by the initial similarities between the endwall geometries of the current design and the C_{ske}-only based design in the early and middle portions of the optimization. However, towards the end of the final portion of the optimization run, it was found that the design was further biased towards reducing the flow deviations from design at the rotor exit. This was evidenced by the introduction of a large cross-passage deflector contour which remained part of the endwall geometry until the conclusion of the final phase of the design optimization.

When tested experimentally, the results of the validations of the $C_{ske,1} + \beta_{dev,0.7}$-based design were mixed with the reductions in the coefficient of secondary kinetic energy, flow deviation as well as improvements in the design efficacy all confirmed by the experiment. However in contrast to the CFD predictions, the measured increases in the rotor exit loss coefficient were significantly larger than originally predicted while overall the the mass-averaged rotor efficiency was seen to decrease reasonably substantially. The reasons for the large increase in rotor exit loss coefficient and corresponding decreases in the rotor efficiency were found to be as a result of a large separation aft of the final 'deflector' contour. Although the potential for a flow separation at this location was alluded to by a distinct decrease in the static pressure and blade loadings close to the endwall ($\sim$ 5% span), the diffusion associated with this decrease in pressure was considered acceptable enough to continue with the manufacture and experimental testing of this endwall.

The failings of this design once again highlighted the issues encountered by a number of previous authors related to the use of loss proxies for the design of non-axisymmetric endwall contours, and that was capacity for the link between the coefficient of secondary kinetic energy and loss to be broken in the presence of unexpected flow features such as an aerodynamic separation.

Despite the failings of this particular design particularly in terms of the rotor efficiency at both measurement planes, at the downstream measurement plane, improvements in all the remaining measured quantities were noted, including a non-trivial reduction in the 'mixed-out' loss and secondary kinetic energy coefficients, as well as an overall increase in the 'mixed-out' efficiency.

Finally, as was the case with the $C_{ske,1} + \beta_{dev,0.7}$-based design, the $\mathbf{C_{p0,rel,1} + \beta_{dev,0.7} - based}$ **metric** was again formulated to meet the requirements of Snedden et al. (2009b), with the distinction that the secondary loss was targeted directly through the use of the rotor exit loss coefficient (i.e. $C_{p0,rel}$), rather than the coefficient of secondary kinetic energy. This was because, although the use of the loss has proven difficult for a number of researchers, the success of the η_{tt}- and *apparent* fidelity of the predictions of the relative total pressure loss coefficient for the $C_{p0,rel}$-only based objective function provided some confidence in this quantity.

In contrast to C_{ske} as used in the previous metric, the inclusion of the $C_{p0,rel}$ term in the $C_{p0,rel,1} + \beta_{dev,0.7}$-based design metric resulted in a predicted reduction in the rotor exit loss coefficient, despite the also being predicted to reduce the mass-averaged C_{ske} and flow deviations from design. Notwithstanding the results of the experimental testing of this endwall, this was considered an important outcome because this result showed that the inclusion of the $C_{p0,rel}$ term did in fact appear to sensitize the overall objective function to the magnitude of the rotor exit loss. This position was further corroborated by the reduced entropy generation rates calculated for this endwall including in particular, in comparison to those predicted for the $C_{ske,1} + \beta_{dev,0.7}$-based design. In light of the difficulties experienced by some researchers in relation to this quantity (i.e. the loss), one explanation for this apparent improvement of the loss predictions in this investigation was the use of a surrogate-based optimization scheme as part of the endwall design procedure, which allowed for the use of as dense as possible computational meshes without rendering the optimization process intractable.

As was the case for the $C_{ske,1} + \beta_{dev,0.7}$-based design, despite the promising predictions for this design, the experimental validations were poor, with the changes in both the rotor exit loss and efficiency found to be worse than the datum case. Despite this, the predicted reductions in C_{ske} and flow deviations were confirmed.

10.2 Recommendations & future work

10.2.1 Recommendations

Based on the findings of this work, in terms of objective function selection, it is recommended that:-

- for a single blade row, or cases in which the performance of only the current row is important, a pressure-based efficiency (η_{tt}) objective function should be used for the optimization of endwall contours, while

- for multi-blade row environments, or cases in which improvements in both the current as well as downstream flow quality is important, a simple C_{ske}-based objective function should be used.

In addition, the results for the $C_{ske,1} + \beta_{dev,0.7}$-based endwall suggested that even though what were thought to be reasonably conservative constraints were placed on the endwall geometry parameters, flow separations are still reasonably easy to achieve. As a result, it is also recommended that:-

- in cases were reasonably 'compact' endwall parametrisations are used (e.g. in this investigation, where the 3-dimensional contouring was intentionally limited to the forward portion of the blade row and a reasonably small interval ($\sim$ 5mm) between each driving endwall curve was used), even greater restrictions on the changes in the endwall parameters (i.e. change in endwall height) should be used in order to prevent the formation of adverse flow features, while
- for less restrictive parametrisations (i.e. in which the full length of the blade passage is contoured or larger intervals between each driving circumferential curve is used), slightly more 'aggressive' geometry parameters may be used.

10.2.2 Future work

This work investigated the performance of customised non-axisymmetric endwall contours for the CSIR 1½ stage turbine in its 1-stage configuration. This was to facilitate investigation of the endwall performance not only at the exit of the rotor itself, but also in terms of its *quasi*-'mixed-out' performance some distance downstream on the rotor.

In this investigation, the performance of each of the customised endwalls were characterised at the 'on-design' (i.e. 0° incidence) condition. As was done by Snedden (2011), one of the most obvious extensions to the current work would be the assessment of each of the successful designs developed in this investigation at the same off-design conditions as those investigated previously.

Further to this, while in the current work, the second stator was (S2) was removed from the rig to allow for the 'mixed-out' measurements, and the potential benefits of each objective function on a downstream row was hypothesized, it is recommended that the change performance of the second stator (S2) be quantified experimentally to confirm or invalidate the projected benefits of each of the successful designs produced in this investigation on the performance of a downstream row. As a direct line to ascertaining the most effective design metrics for multiblade row optimizations for the rig, it is suggested that the endwall design routine developed in this investigation be extended to allow for the contouring of both the upstream (rotor) and downstream (S2) blade rows either in a sequential fashion, in which the target objective function is first evaluated at the rotor exit, and then at the second stator exit or in a 'composite' manner, in which the contours for both blade rows would be optimized simultaneously, with the objective function calculated at the exit of the downstream blade row only.

Finally, as pointed out in Chapter 5, the approach taken in this thesis was different to that taken in many other design scenarios, and that was that the mass flow (rather than the pressure drop) through the blade row was set in both the experiment as well as CFD calculations. One of the pitfalls associated with the design and application of non-axisymmetric endwalls to existing blade designs using the standard approach, is that it is relatively easy to improve the efficiency of a blade row by

simply reducing the mass flow and hence the blade loading and this was pointed out by MacPherson and Ingram (2010). Further, as was also stated, the maintenance of the blade passage cross-sectional flow area and therefore the mass flow was also one of the stated advantages of the so-called sinusoidal Fourier-series endwall parametrisation of Harvey et al. (2000), although more detailed analysis showed that this was not always the case and therefore that the mass flow *could* change. This was also the reason for the inclusion of a mass flow-based penalty term in the work of Sonoda et al. (2009) and Hilfer et al. (2012), although notably of all the literature surveyed, these were the only two examples of the use of such a constraint.

In light of the above, one of the advantages of the current work is that the setting of the mass flow through the turbine, meant that this quantity was then removed as a variable and did not then need to be accounted for during the optimization procedure. In all the cases considered in this thesis (with the exception of the $C_{p0,rel}$-based design), it was not expected that the setting of the mass flow through the turbine would change any of the conclusions of the work, since for these cases, the maintenance of the rotor work output combined with the predicted reductions in pressure drop through the blade row, resulted in an improvement in the overall rotor efficiency. However, for the $C_{p0,rel}$-based design, a restriction on the allowable increase in blade row pressure drop in addition to the specification of the mass flow through the turbine may have resulted in a design for which the overall rotor efficiency was also increased (along with the predicted reduction in rotor loss), and this, in addition to those recommendations already discussed, is felt to be a excellent topic for a future research investigation.

References

Andrianakis, I., Challenor, P., 2012. The effect of the nugget on gaussian process emulators of computer models. Computational Statistics and Data Analysis 56, 4215–4228.

ANSYS, 2014. Webpage. URL: `http://www.ansys.com`.

Aunapu, N., Volino, R., Flack, K., 2000a. Surface flow visualization of a scaled-up turbine blade passage. Measurement Science and Technology 11, 987–991.

Aunapu, N., Volino, R., Flack, K., Stoddard, R., 2000b. Secondary flow measurements in a turbine passage with endwall flow modification, in: Proceedings of ASME Turbo Expo 2000. Munich, Germany, ASME. ASME.

Bagshaw, D., Ingram, G., Gregory-Smith, D., Stokes, M., 2008a. An experimental study of three dimensional turbine blades combined with profiled endwalls. Journal of Power and Energy 222, 103 – 110.

Bagshaw, D., Ingram, G., Gregory-Smith, D., Stokes, M., Harvey, N., 2008b. The design of three-dimensional turbine blades combined with profiled endwalls. Journal of Power and Energy 222, 92 – 102.

Becz, S., Majewski, M., Langston, L., 2004. An experimental investigation of contoured leading edges for secondary flow loss reduction, in: Proceedings of ASME Turbo Expo 2004. Power for Land, Sea and Air, ASME. ASME.

Bergh, J., Snedden, G., Meyer, C., 2012. Optimization of non-axisymmetric end wall contours for the rotor of a low speed, 1 1/2 stage research turbine with unshrouded blades, in: Proceedings of ASME Turbo Expo 2012: GT2012, June 11-15, Copenhagen, Denmark, ASME. ASME.

Bindon, J., 1987. The measurement of tip clearance flow structure on the end-wall and within the clearance gap of an axial turbine cascade, in: Proceedings of the Institute of Mechanical Engineering International Conference on turbomachinery efficiency, prediction and improvement, Institute of Mechanical Engineering, Cambridge. pp. 43–52.

Bindon, J., 1989. The measurement and formation of tip clearance loss. Journal of Turbomachinery 111, 257 – 263.

Van den Braembussche, R., Alsalihi, Z., Verstraete, T., Matsuo, A., Ibraraki, A., Sugimoto, K., Tomita, K., 2012. Multidiscplinary multipoint optimization of a transonic turbocharger compressor, in: Proceedings of ASME Turbo Expo 2012: GT2012, ASME. ASME. pp. 1 – 11.

Brennan, G., Harvey, N., Rose, M., Fomison, N., Taylor, M., 2001. Improving the efficiency of the trent 500 hp turbine using non-axisymmetric end walls: Part 1 turbine design, in: Proceedings of ASME Turbo Expo 2001, New Orleans, USA.

BTS, 2010. Bureau of transportation statistics. airline fuel cost and consumption (US carriers - all) http://www.transtats.bts.gob/fuel.asp?pn=1. Webpage.

Cardwell, N., Sundaram, N., Thole, K., 2005. Effects of mid-passage gap, endwall misalignment and roughness on endwall film-cooling, in: Proceedings of ASME Turbo Expo 2005: Power for Land, Sea and Air, ASME. ASME. pp. 1–11.

Chahine, C., Seume, J., Verstraete, T., 2012. The influence of metamodelling techniques on the multidisciplinary design optimization of a radial compressor impeller, in: Proceedings of ASME Turbo Expo 2012: GT2012, ASME. ASME. pp. 1 – 14.

Cherry, D., Wadia, A., Beacock, R., Subramanian, M., Vitt, P., 2005. Analytical investigation of a low pressure turbine with and without flowpath endwall gaps, seals and clearance features, in: Proceedings of ASME Turbo Expo 2005: Power for Land, Sea and Air, ASME. ASME. pp. 1–7.

Cohen, H., Rogers, G., Saravanmuttoo, H., 1996. Gas Turbine Theory. Fourth ed., Longman Group Ltd, London.

Colban, W., Thole, K., Zess, G., 2003. Combustor turbine interface studies - part1: Endwall effectiveness measurements. Journal of Turbomachinery 125, 193–202.

Cumpsty, N., 1997. Jet Propulsion: A Simple Guide to Aerodynamic and Thermodynamic Design and Performance of Jet Engines. Second ed., Cambridge University Press.

Cumpsty, N., 2009. Igti scholar lecture - preparing for the future: Reducing gas turbine environmental impact, in: Proceedings of ASME Turbo Expo, 2009, Orlando, USA, ASME. ASME. pp. 1–20.

Deng, X., Guo, F., Liu, Y., Han, P., 2013. Aero-mechanical optimization design of a transonic fan blade, in: Proceedings of ASME Turbo Expo 2013: Turbine Technical Conference and Exposition: GT2013, ASME. ASME. pp. 1 – 12.

Denton, J., 1993. Loss mechanisms in turbomachines. Journal of Turbomachinery 115, 621–656.

Denton, J., 2010. Some limitations of turbomachinery cfd, in: ASME Turbo Expo 2010: Power for Land, Sea and Air. Glasgow, UK, ASME. ASME.

Denton, J., Pullan, G., 2012. A numerical investigation into the sources of endwall loss in axial flow turbine, in: Proceedings of ASME Turbo Expo 2012: GT2012.

Denton, J., Xu, L., 1999. The exploitation of three-dimensional flow in turbomachinery design, in: Proceedings of the Institute of Mechanical Engineers: 213 Part C, Institute of Mechanical Engineers.

Dorfner, C., Hergt, A., Nicke, E., Moenig, R., 2011. Advanced nonaxisymmetric endwall contouring for axial compressors by generating an aerodynamic separator - part i: Principal cascade design and compressor application. Journal of Turbomachinery 133, 1–5.

Dunn, D., 2014. The effect of endwall contouring on the unsteady flow through a turbine rotor. Ph.D. thesis. Department of Mechanical Engineering, University of Stellenbosch.

Dunn, D., Snedden, G., von Backstrom, T., 2009. Turbulence model comparisons for a low pressure 1.5 stage test turbine, in: International Society for Air Breathing Engines.

Everitt, B., 1987. Introduction to optimization methods and their application in statistics. St Edmundsbury Press Ltd, London.

Fletcher, R., 1987. Practical Methods of Optimization. Second ed., John Wiley and Sons, Chichester.

Forrester, A., Bressloff, N., Keane, A., 2006. Optimization using surrogate models and partially converged computational fluid dynamics simulations. Proceedings of the Royal Society A: Mathematical, Physical and Engineering Science 462, 2177 – 2204.

Forrester, A., Jones, D., 2008. Global optimization of deceptive functions with sparse sampling, in: Proceedings of 12th AIAA/ISSMO Multidiscplinary Analysis and Optimization Conference, AIAA/ISSMO. pp. 10–12.

Forrester, A., Sobester, A., Keane, A., 2007. Multi-fidelity optimization via surrogate modelling, in: Proceedings of the Royal Society, The Royal Society. pp. 3251 – 3269.

Forrester, A., Sobester, A., Keane, A., 2008. Engineering Design via Surrogate Modelling - A practical guide. 1st ed., John Wiley and Sons, The Atrium, Southern Gate, Chichester, West Sussex, PO19 8SQ, UK.

Fritsche, A., 1955. Stromungsvorgange in schaufelgittern. Techn. Rundschau Sulzer 3.

F.S.F, 2007. Gnu general public license, version 3. http://www.gnu.org/licenses/gpl.html.

Gaugler, R., Russell, L., 1982. Flow visualization study of the horseshoe vortex in a turbine stator cascade. Technical paper 1884. NASA. Lewis Research Centre, Cleveland, Ohio.

Germain, T., Nagel, M., Baier, R.D., 2007. Visualisation and quantification of secondary flow: Application to turbine bladings with 3d-endwalls, in: Proceedings of the 8th International Symposium on Experimental and Computational Aerothermodynamics of Internal Flow.

Germain, T., Nagel, M., Raab, I., Schuepbach, P., Abhari, R., Rose, M., 2008. Improving efficiency of a high work turbine using nonaxisymmetric endwalls - part 1: Endwall design and performance, in: Proceedings of GT2008: ASME Turbo Expo 2008: Power for Land, Sea and Air, ASME. ASME.

Germain, T., Nagel, M., Raab, I., Schupbach, P., Abhari, R., Rose, M., 2010. Improving efficiency of a high work turbine using nonaxisymmetric endwalls - part 1: Endwall design and performance. Journal of Turbomachinery 132, (021007) 1 – 9.

Gier, J., Stubert, B., Brouillet, B., de Vito, L., 2003. Interaction of shroud leakage flow and main flow in a three-stage lp turbine, in: Proceedings of ASME Turbo Expo 2003. Power for Land, Sea and Air. Atlanta, Georgia, USA, ASME. ASME. pp. 1–12.

Goinis, G., Voss, C., Aulich, M., 2013. Automated optimization of an axial-slot type casing treatment for a transonic compressor, in: Proceedings of ASME Turbo Expo 2013: Turbine Technical Conference and Exposition: GT2013, ASME. ASME. pp. 1 – 13.

Goldstein, R., Spores, R., 1988. Turbulent transport on the endwall in the region between adjacent turbine blades. Journal of Heat Transfer 110, 862–869.

Gregory-Smith, D., Bagshaw, D., Ingram, G., Stokes, M., 2008. Using profiled endwalls, blade lean and leading edge extensions to minimise secondary flow, in: ASME Turbo Expo 2008: Power for Land, Sea and Air. June 9-13, 2008. Berlin, Germany, ASME. ASME.

Gregory-Smith, D., Ingram, G., Jayaraman, P., Harvey, N., Rose, M., 2001. Non-axisymmetric turbine end wall profiling, in: Proceedings of 4th European Conference on Turbomachinery. Florence, Italy, pp. 653–664.

Haderlie, J., Crossley, W., 2010. Multiobjective optimization of a supersonic-inlet bypass duct splitter via surrogate modelling, in: Proceedings of 13th AIAA/ISSMO Multidisciplinary Analysis Optimization Conference. Fort Worth, Texas, USA, AIAA. pp. 1 – 10.

Halton, J., 1960. On the efficiency of certain quasi-random sequences of points in evaluating multi-dimensional integrals. Numerische Mathematik 2, 84–90.

Hammersley, J., 1960. Monte carlo methods for solving multivariable problems. Annals of the New York Academy of Sciences 86, 844 – 874.

Harman, R., 1981. Gas Turbine Engineering. The Macmillian Press Ltd, London.

Hartland, J., Gregory-Smith, D., 2002. A design method for the profiling of end walls in turbines, in: Proceedings of ASME Turbo Expo 2002, Amsterdam, The Netherlands.

Hartland, J., Gregory-Smith, D., Harvey, N., Rose, M., 2000. Nonaxisymmetric turbine end wall design: Part ii - experimental validation. Journal of Turbomachinery 122, 286–293.

Hartland, J., Gregory-Smith, D., Rose, M., 1998. Non-axisymmetric endwall profiling in a turbine rotor blade, in: Proceedings of the International Gas Turbine and Aeroengine Congress & Exposition, ASME. ASME. pp. 1–10.

Harvey, N., Brennan, G., Newman, D., Rose, M., 2002. Improving turbine efficiency using non-axisymmetric end walls: Validation in the multi-row environment and with low aspect ratio blading, in: Proceedings of ASME Turbo Expo 2002, Amsterdam, The Netherlands, ASME. ASME. pp. 119 – 126.

Harvey, N., Rose, M., Taylor, M., Shahpar, S., Hartland, J., Gregory-Smith, D., 2000. Nonaxisymmetric turbine end wall design: Part i - three-dimensional linear design system. Journal of Turbomachinery 122, 278–285.

Haupt, R., Haupt, S., 2004. Practical genetic algorithms. second ed., John Wiley and Sons.

Hawthorne, W., 1951. Secondary circulation in fluid flow. Proceedings of the Royal Society of London Series A, Mathematical and Physical Sciences, 374–387.

Hawthorne, W., 1955. Rotational flow through cascades part i. the components of vorticity. Quarterly Journal of Mechanics and Applied Mathematics 8, 266–279.

Hawthorne, W., Armstrong, W., 1955. Rotational flow through cascades part ii. the circulation about the cascade. Quarterly Journal of Mechanics and Applied Mathematics 8, 280–292.

Hilfer, M., Ingram, G., Hogg, S., 2012. Endwall profiling with tip clearance flows, in: Proceedings of ASME Turbo Expo 2012: GT2012, June 11-15, Copenhagen, Denmark, ASME. ASME.

Hoeger, M., Schmidt-Eisenlohr, U., Gomez, S., Sauer, H., Muller, R., 2002. Numerical simulation of the influence of a fillet and a bulb on the secondary flow in a compressor cascade. Task Quarterly 6, 25–37.

Holland, J., 1975. Adaptation in natural and artificial systems: An introductory analysis with applications to biology, control and artificial intelligence. 1st ed., University of Michigan Press.

Ingram, G., 2003. Endwall profiling for the reduction of secondary flow in turbines. Ph.D. thesis. School of Engineering, University of Durham.

Ingram, G., Gregory-Smith, D., 2005. An automated instrumentation system for flow and loss measurements in a cascade. Flow Measurement and Instrumentation 17, 23–28.

Ingram, G., Gregory-Smith, D., Harvey, N., 2005. Investigation of a novel secondary flow feature in a turbine cascade with end wall profiling. Journal of Turbomachinery 127, 209–214.

Ingram, G., Gregory-Smith, D., Rose, M., Harvey, N., Brennan, G., 2002. The effect of end-wall profiling on secondary flow and loss development in a turbine cascade, in: Proceedings of ASME Turbo Expo 2002, Amsterdam, The Netherlands.

Jeong, S., Minemura, Y., Obayashi, S., 2006. Optimization of combustion chamber for diesel engine using kriging model. Journal of Fluid Science and Technology 1, 138 – 146.

Jeong, S., Obayashi, S., 2005. Efficient global optimization (ego) for multi-objective problem and data mining, in: Proceedings of the 2005 IEEE Congress on Evolutionary Computation, IEEE. pp. 2138 – 2145.

Jones, D., Schonlau, M., Welch, W., 1998. Efficient optimization of expensive black-box functions. Journal of Global Optimization 13, 455–492.

Kaiser, I., 1996. The effect of tip clearance and tip gap geometry on the performance of a one and a half stage axial gas turbine. Ph.D. thesis. Department of Mechanical Engineering, University of Natal.

Kawai, T., Adachi, T., 1987. Effects of boundary layer fences on secondary flow and losses in a turbine cascade, in: Proceedings of the 1987 Tokyo International Gas Turbine Congress, p. 115.

Kawai, T., Shinoki, S., Adachi, T., 1989. Secondary flow control and loss reduction in a turbine cascade using endwall fences. JSME International Journal 32, 375–387.

Klein, A., 1966. Investigation of the entry boundary layer on the secondary flows in the blading of axial turbines. BHRA T 1004.

Kok, S., 2012. The asymptotic behaviour of the maximum likelihood function of kriging approximations using the gaussian correlation function, in: EngOpt 2012 - International Conference on Engineering Optimization. Rio de Janeiro, Brazil.

Krige, D., 1951. A statistical approach to some basic mine valuation problems on the witwatersrand. Journal of the Chemical, Metallurgical and Mining Society of South Africa 52, 119–139.

Kumar, K., Goverdhan, M., 2011. Secondary flow loss reduction in a turbine cascade with a linearly varied height streamwise endwall fence. International Journal of Rotating Machinery 2011.

Lampart, P., 2009. Investigation of endwall flows and losses in axial turbines. part i. formation of endwall flows and losses, in: Journal of Theoretical and Applied Mechanics.

Land, A., Doig, A., 1960. An automatic method of solving discrete programming problems. Econometrica 28, 497 – 520.

Launder, B., Spalding, D., 1974. The numerical computation of turbulent flows. Computer Methods in Applied Mechanics and Engineering 3, 269–289.

Lethander, A., 2003. Assessment of a leading edge fillet for decreasing vane endwall temperatures in a gas turbine engine. Ph.D. thesis. Faculty of the Virginia Polytechnic Institute and State University.

Lethander, A., Thole, K., Zess, G., Wagner, J., 2003. Optimizing the vane-endwall junction to reduce adiabatic wall temperatures in a turbine vane passage, in: Proceedings of ASME Turbo Expo 2003. Power for Land, Sea and Air, ASME. ASME.

Lophaven, S., Nielsen, H., Sondergaard, J., 2002. Aspects of the MATLAB Toolbox DACE. Technical Report IMM-REP-2002-13. Technical University of Denmark. DK-2800 Kongens Lyngby, Denmark.

Luke, S., 2009. Essentials of metaheuristics. Online: Lulu.com.

MacPherson, R., Ingram, G., 2010. Endwall profile design for the durham cascade using genetic algorithms, in: Seventh South African Conference on Computational and Applied Mechanics.

Marchal, P., Sieverding, C., 1977. Secondary flows within turbomachinery bladings, in: Agard-CP-24 Secondary Flows in Turbomachines, Von Karman Institute for Fluid Dynamics.

Martin, J., Simpson, T., 2004. On the use of kriging models to approximate deterministic computer models, in: ASME 2004 International Design Engineering Technical Conferences and Computers and Information in Engineering Conference. Salt Lake City, Utah. USA. September 28 - October 2, 2004, ASME.

McIntosh, J., MacPherson, R., Ingram, G., Hogg, S., 2011. Profiled endwall design using genetic algorithms with different objective functions, in: ASME Turbo Expo Vancouver, Canada, June 6-11, ASME. ASME.

McKay, M., Beckman, R., Conover, W., 1979. A comparison of three methods for selecting values of input variables in the analysis of output from a computer code. Technometrics 21, 239 – 245.

Menter, F., 1994. Two-equation eddy-viscosity turbulence models for engineering applications. American Institute of Aeronautics and Astronomics Journal 32, 1598 – 1605.

Menter, F., Kuntz, M., Langtry, R., 2003. Ten years of industrial experience with the sst turbulence model, in: Hanjalic, K., Nagano, Y., Tummers, M. (Eds.), Proceedings of the Fourth International Symposium on Turbulence, Heat and Mass Transfer, Begell House, Redding, CT.

Menter, F., Langtry, R., Likki, S., Suzen, Y., Huang, P., Volker, S., 2006. A correlation-based transition model using local variables - part 1: Model formulation. Journal of Turbomachinery 128, 413 – 422.

Menter, F., Smirnov, P., Liu, T., Avancha, R., 2015. A one-equation local correlation-based transition model. Flow, Turbulence and Combustion , 1–37.

Miyoshi, I., Higuchi, S., 2013. Improving the performance of a high pressure gas turbine stage using a profiled endwall, in: Proceedings of ASME Turbo Expo 2013: Turbine Technical Conference and Exposition, ASME. ASME.

Moon, Y., Koh, S., 2001. Counter-rotating streamwise vortex formation in the turbine cascade with endwall fence. Computers & Fluids 30, 473–490.

Moore, H., 1995. Experiments in a turbine cascade for the validation of turbulence and transition models. Ph.D. thesis. School of Engineering and Computer Sciences, University of Durham. UK.

Moore, H., Gregory-Smith, D., 1996. Transition effects on secondary flows in a turbine cascade, in: International Gas Turbine & Aeroengine Congress & Exhibition, Birmingham, UK, ASME. ASME.

Morphis, G., 1993. The performance of a one and a half stage axial turbine including various tip clearance effects. Ph.D. thesis. Department of Mechanical Engineering, University of Natal.

Morphis, G., Bindon, J., 1988. The effects of relative motion, blade edge radius and gap size on the blade tip pressure distribution in an annular turbine cascade with clearance, in: Proceedings of Gas Turbine and Aeroengine Congress. Amsterdam, The Netherlands., ASME. ASME.

Morphis, G., Bindon, J., 1994a. The flow in a second stage nozzle of a low speed axial turbine and its effect on tip clearance loss development, in: Proceedings of the International Gas Turbine and Aerospace Congress and Exposition. The Hague, Netherlands. June 13-16, ASME. ASME.

Morphis, G., Bindon, J., 1994b. The performance of a low speed one and a half-stage axial turbine with varying rotor tip clearance and tip gap geometry, in: Proceedings of the International Gas Turbine and Aerospace Congress and Exposition, ASME. ASME, New York.

Moustapha, S., Okapuu, U., Williamson, R., 1986. Influence of rotor blade aerodynamic loading on the performance of a highly loaded turbine stage, in: 31st International Gas Turbine Conference and Exhibit. Dusseldorf, Germany, ASME. ASME.

Muller, R., Sauer, H., Vogeler, K., Hoeger, M., 2002. Influencing the secondary losses in compressor cascades by a leading edge bulb modification at the endwall, in: Proceedings of ASME Turbo Expo 2002, Amsterdam, The Netherlands, ASME. ASME. pp. 1–9.

Nagel, M., Baier, R.D., 2005. Experimentally verified numerical optimization of a three-dimensional parameterized turbine vane with non-axisymmetric end walls. Journal of Turbomachinery 127, 380–387.

Nagel, M., Fottner, L., Baier, R.D., 2001. Optimization of three dimensionally designed turbine blades and side walls, in: Proceedings of ISABE 2001, International Society of Air Breathing Engines.

Ong, J., Miller, R., Uchida, S., 2006. The effect of coolant injection on the endwall flow of a high pressure turbine, in: Proceedings of ASME Turbo Expo 2006: Power for Land, Sea and Air. Barcelona, Spain, ASME. ASME. pp. 1–10.

Piggush, J., Simon, T., 2005. Flow measurements in a first stage nozzle cascade having endwall contouring, leakage and assembly features, in: Proceedings of ASME Turbo Expo 2005: Power for Land, Sea and Air. Reno-Tahoe, Nevada, USA, ASME. ASME. pp. 1–13.

Poehler, T., Gier, J., Jeschke, P., 2010. Numerical and experimental analysis of the effects of non-axisymmetric contoured stator endwalls in an axial turbine, in: ASME Turbo Expo 2010: Power for Land, Sea and Air. Glasgow, UK.

Praisner, T., Allen-Bradley, E., Grover, E., Knezevici, D., Sjolander, S., 2007. Application of non-axisymmetric endwall contouring to conventional and high-lift turbine airfoils, in: AMSE Turbo Expo 2007: Power for Land, Sea and Air. May 14-17, 2007, Montreal, Canada, ASME.

Praisner, T., Grover, E., Knezevici, D., Popovic, I., Sjolander, S., 2008. Towards the expansion of low-pressure-turbine airfoil design space, in: Proceedings of GT2008: ASME Turbo Expo 2008: Power for Land, Sea and Air, ASME.

Price, K., Storn, R., Lampinen, J., 2005. Differential evolution: A practical approach to global optimization. Natural Computing Series, Springer-Verlag, Berlin, Germany.

Prumper, H., 1972. Application of boundary layer fences in turbomachinery. Technical Report 164. AGARD.

Queipo, N., Verde, A., Pintos, S., Haftka, R., 2009. Assessing the value of another cycle in gaussian process surrogate-based optimization. Struct. Multidisc. Optim 39, 459 – 475.

de la Rosa Blanco, E., Hodson, H., Vazquez, R., 2005. Effect of upstream platform geometry on the endwall flows of a turbine cascade, in: Proceedings of GT2005: ASME Turbo Expo 2005: Power for Land, Sea and Air, ASME. ASME. pp. 1–11.

Rose, M., 1994. Non-axisymmetric endwall profiling in the hp ngv's of an axial flow gas turbine, in: Proceedings of the International Gas Turbine and Aerospace Congress and Exposition. The Hague, Netherlands. June 13-16, ASME.

Rose, M., Harvey, N., Seaman, P., Newman, D., McManus, D., 2001. Improving the efficiency of the trent 500 hp turbine using non-axisymmetric end walls. part ii: Experimental validation, in: Proceedings of ASME Turbo Expo 2001, New Orleans, USA.

Rosenbrock, H., 1960. An automatic method for finding the greatest or least value of a function. The Computer Journal 3, 175 – 184.

Sabatino, D., Smith, C., 2007. Boundary layer influence on the unsteady horseshoe vortex flow and surface heat transfer, in: Proceedings of ASME Turbo Expo 2007: Power for Land, Sea and Air. Montreal, Canada, ASME. ASME.

Sacks, J., Welch, W., Mitchell, T., Wynn, H., 1989. Design and analysis of computer experiments. Statistical Science 4, 409–435.

Sasena, M., 2002. Flexibility and Efficiency Enhancements for Constrained Global Design Optimization with Kriging Approximations. Ph.D. thesis. University of Michigan. Ann Arbor, Michigan, USA.

Sasena, M., Papalambros, P., Gooverts, P., 2000. Metamodeling sampling criteria in a global optimization framework, in: 8th AIAA/USAF/NASA/ISSMO Symposium on Multidiscplinary Analysis and Optimization, AIAA, Long Beach, CA.

Sasena, M., Papalambros, P., Gooverts, P., 2002. Exploration of metamodelling sampling criteria for constrained global optimization. Eng. Opt 34, 263–278.

Sauer, H., Muller, R., Vogeler, K., 2001. Reduction of secondary flow losses in turbine cascades by leading edge modifications at the endwall. Journal of Turbomachinery 123, 207–213.

Schuepbach, P., Abhari, R., Rose, M., Germain, T., Raab, I., Gier, J., 2008. Improving efficiency of a high work turbine using nonaxisymmetric endwalls - part 2: Time-resolved flow physics, in: Proceedings of ASME Turbo Expo 2008: Power for Land, Sea and Air: GT2008, ASME. ASME. pp. 1 – 13.

Schuepbach, P., Rose, M., Gier, J., Raab, I., Germain, T., Abhari, R., 2009. Non-axisymmetric end wall profiles including fillet radii in a 1.5 stage axial flow turbine, in: Proceedings of the 8th European Conference on Turbomachinery Fluid Dynamics and Thermodynamics (ETC '09), Graz, Austria.

Shahpar, S., Lapworth, B., 1998. A forward and inverse three-dimensional linear design system for turbomachinery applications, in: 4th ECCOMAS Computational Fluid Dynamics Conference, European Community on Computational Methods in Applied Sciences. pp. 377–382.

Sharma, O., Butler, T., 1987. Predictions of endwall losses and secondary flow in axial flow turbine cascades. Journal of Turbomachinery 109, 229–236.

Shih, T., Lin, Y.L., 2003. Controlling secondary-flow structure by leading-edge airfoil fillet and inlet swirl to reduce aerodynamic loss and surface heat transfer. Journal of Turbomachinery 125, 49–56.

Sieverding, C., 1985. Recent progress in the understanding of basic aspects of secondary flows in turbine blade passages. Journal of Engineering for Gas Turbines and Power 107, 248–257.

Sieverding, C., Van den Bosch, P., 1983. The use of coloured smoke to visualize secondary flows in a turbine cascade. Journal of Fluid Mechanics 134.

Simpson, T., Lin, D., Chen, W., 2001. Sampling strategies for computer experiments: Design and analysis. International Journal of Reliability and Applications 2, 209 – 240.

Snedden, G., 2011. The application of non-axisymmetric endwall contouring in a 1 1/2 stage, rotating turbine. Ph.D. thesis. School of Engineering, University of Durham.

Snedden, G., 2015. Private communications.

Snedden, G., Dunn, D., von Backstrom, T., Ingram, G., 2010a. Observations on the selection of objective function for the optimisation of turbine endwalls using computational fluid dynamics, in: Seventh South African Conference on Computational and Applied Mechanics.

Snedden, G., Dunn, D., Ingram, G., Gregory-Smith, D., 2009a. The application of non-axisymmetric endwall contouring in a single stage, rotating turbine, in: Proceedings of ASME Turbo Expo, 2009, Orlando, USA.

Snedden, G., Dunn, D., Ingram, G., Gregory-Smith, D., 2010b. The performance of a generic non-axisymmetric end wall in a single stage, rotating turbine at on and off-design conditions, in: Proceedings of ASME Turbo Expo 2010: Power for Land, Sea and Air, Glasgow, UK.

Snedden, G., Dunn, D., Zwane, N., 2009b. Deliverable D6.2.10B - Experimental Results Report. Technical Report EU FP6 VITAL Report.

Snedden, G., Roos, T., Dunn, D., Mathebula, R., Gregory-Smith, D., 2007. Characterisation of a refurbished 1 1/2 stage turbine test rig for flowfield mapping behind blading with non-axisymmetric contoured endwalls, in: Internation Society for Air Breathing Engines.

Song, H., Choi, K., Lamb, D., 2013. A study on improving the accuracy of kriging models by using correlation model / mean structure selection and penalized log-likelihood function, in: 10th World Congress on Structural and Multidisciplinary Optimization. Orlando, Florida. USA, ASME / AIAA. pp. 1 – 10.

Sonoda, T., Hasenjager, M., Arima, T., Sendhoff, B., 2009. Effect of end wall contouring on performance of ultra-low aspect ratio transonic turbine inlet guide vanes. Journal of Turbomachinery 131, 011020.

Spalart, P., Allmaras, S., 1992. A one-equation turbulence model for aerodynamic flows, in: 30th Aerospace Sciences Meeting & Exhibit, American Institute of Aeronautics and Astronautics, Washington D.C.

Squire, H., Winter, K., 1949. The secondary flow in a cascade of aerofoils in a non-uniform stream. Technical Report No. Aero-2317. Royal Aircraft Establishment, Farnborough.

Storn, R., Price, K., 1995. Differential Evolution - a simple and effective adaptive scheme for global optimization over continuous spaces. Technical Report TR-95-012. ICSI.

Torre, D., de la Rosa Blanco, E., Vazquez, R., Hodson, H., 2006. A new alternative for reduction of secondary flows in low pressure turbines, in: ASME Turbo Expo 2006: Power for Land, Sea and Air. May 8-11, 2006. Barcelona, Spain, ASME.

Tusar, T., Filipic, B., 2007. Differential evolution versus genetic algorithms in multiobjective optimization, in: EMO'07 Proceedings of the 4th International Conference on Evolutionary Multicriterion optimization, pp. 257–271.

Vazquez, R., Fidalgo, V., 2010. The effect of reynolds and mach number on end-wall profiling performance, in: Proceedings of ASME Turbo Expo 2010: Power for Land, Sea and Air, Glasgow, UK, ASME. ASME.

Verstraete, T., 2008. Multidisciplinary turbomachinery component optimization considering performance, stress and internal heat transfer. Ph.D. thesis. Universiteit Ghent. Ghent, Belgium.

Verstraete, T., He, L., Shahpar, S., 2012. Introduction to optimization methods and tools for multidisciplinary design in turbomachinery workshop. lecture notes.

Viana, F., 2013. Things you wanted to know about the latin hypercube design and were afraid to ask, in: Proceedings of the 10th World Congress on Structural and Multidisciplinary Optimization, pp. 1 – 9.

Walsh, J., 1987. Secondary flows and inlet skew in axial flow turbine cascades. Ph.D. thesis. School of Engineering and Applied Science, University of Durham. UK.

Walsh, J., Gregory-Smith, D., 1989. Inlet skew and the growth of secondary losses and vorticity in a turbine cascade, in: Proceedings of Gas Turbine and Aeroengine Congress and Exposition. Toronto, Ontario, Canada., ASME. ASME. pp. 1–11.

Wang, H., Olson, S., Goldstein, R., Eckert, E., 1997. Flow visualization in a linear turbine cascade of high performance turbine blades. Journal of Turbomachinery 119, 1–8.

Warnes, J., Ripley, B., 1987. Problems with likelihood estimation of covariance functions of spatial gaussian processes. Biometrika 74, 640 – 642.

Watanabe, H., Harada, H., 1999. Suppresion of secondary flows in a turbine nozzle with controlled stacking shape and exit circulation by 3d inverse design method, in: Proceedings of International Gas Turbine & Aeroengine Congress & Exhibition. Indianapolis, Indiana, USA, ASME. ASME. pp. 1–12.

Watson, A., Barnes, R., 1995. Infill sampling criteria to locate extremes. Mathematical Geology 27, 589–608.

Wilcox, D., 1994a. Simulation of transition with a two-equation turbulence model. American Institute of Aeronautics and Astronomics Journal 32, 247–255.

Wilcox, D., 1994b. Turbulence modeling for CFD. 2nd ed., DCW Industries Inc.

Yakhot, V., Thangam, S., Gatski, T., Orszag, S., Speziale, C., 1992. Development of turbulence models for shear flows by a double expansion technique. ICASE report 91-65. Institute for Computer Applications in Science and Engineering, NASA Langley Research Center. Virginia.

Zess, G., Thole, K., 2002. Computational design and experimental validation of using a leading edge fillet on a gas turbine vane. Journal of Turbomachinery 124, 167–175.

Zimmerman, R., 2015. On the condition number anomaly of gaussian correlation matrices. Linear Algebra and its Applications 466, 512–526.

A

Endwall geometries

A Single metric designs

(a) η_{tt}-based

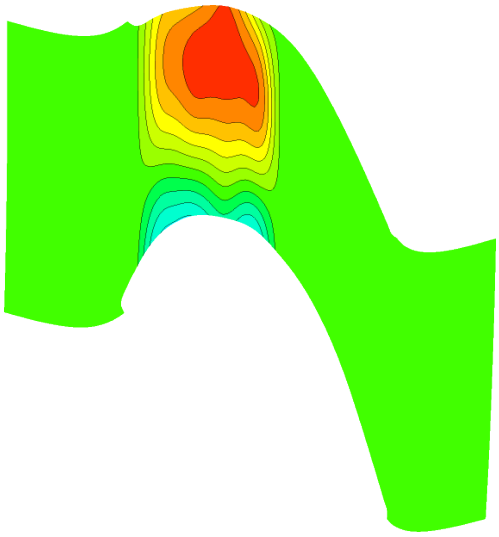

(b) C_{ske}-based

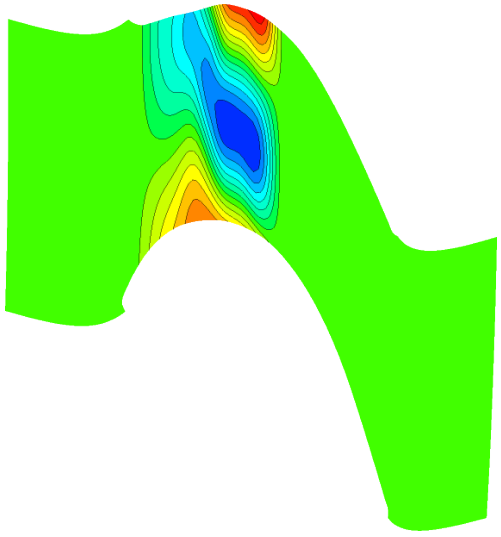

(c) $C_{p0,rel}$-based

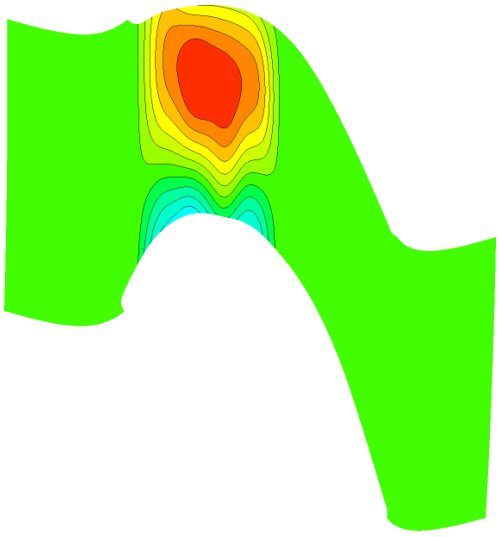

(d) β_{dev}-based

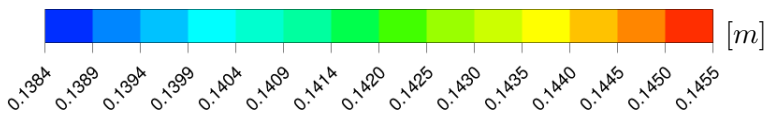

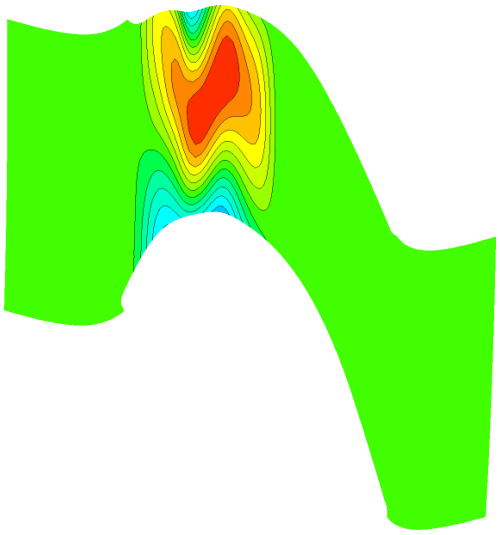

(e) $SKEH$-based

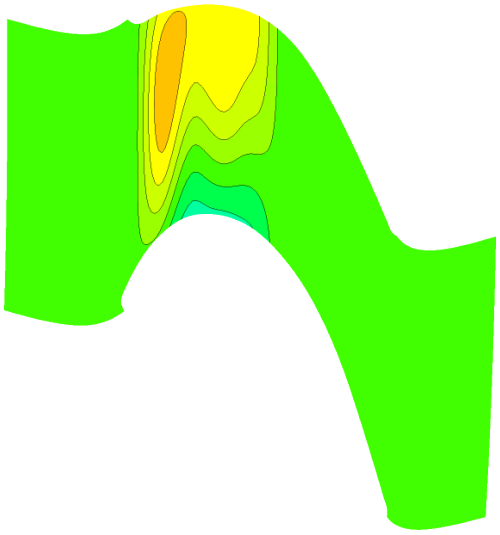

(f) η_{de}-based

B 'Compound' designs

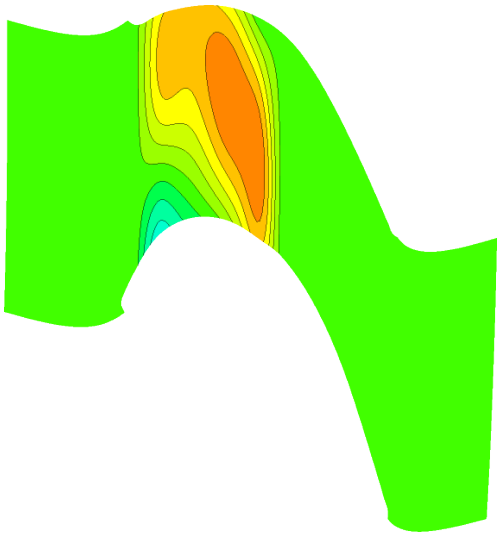

(a) $C_{ske,1} + \beta_{dev,0.7}$-based

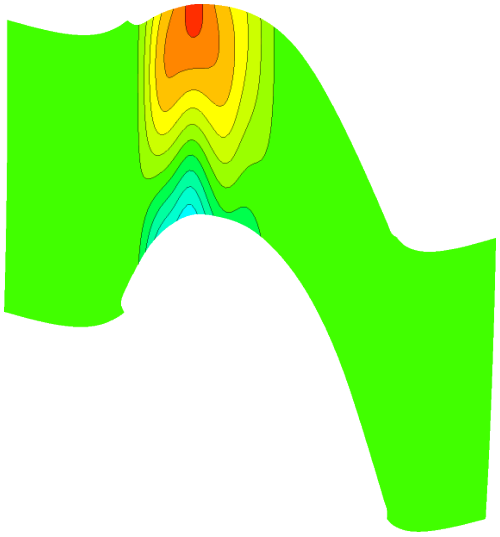

(b) $C_{p0,rel,1} + \beta_{dev,0.7}$-based

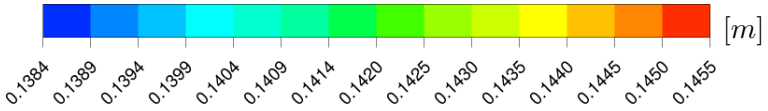

C Endwall coefficients

Table A.1: Summary of final endwall design vector components for the single metric designs

Endwall	c_1	n_1	Ψ_1	c_2	n_2	ψ_1	c_3	n_3	ψ_3	c_4	n_4	ψ_4
150 (72)	2.00	0.66	-1.65	2.55	0.57	0.44	1.79	0.61	0.24	1.34	0.86	-0.79
η_{tt}-based												
300 (298)	2.00	0.67	-1.64	2.65	0.59	0.41	2.16	0.55	0.24	1.53	0.80	-0.56
150 (82)	1.99	0.66	-1.55	3.01	0.71	0.30	2.48	0.51	0.71	2.02	0.76	-0.69
C_{ske}-based												
300 (285)	2.00	0.68	-1.60	2.83	0.68	0.28	2.94	0.53	0.58	2.50	0.78	-0.61
150 (59)	1.33	0.60	1.54	2.43	0.82	-0.43	3.50	0.98	0.79	3.50	1.00	0.14
$C_{p0,rel}$-based												
300 (268)	1.35	0.61	1.54	2.42	0.74	-0.43	3.50	0.98	0.78	3.50	0.97	0.37
150 (85)	2.00	0.70	-1.56	3.40	0.70	0.09	3.00	0.74	0.16	2.64	0.81	-0.78
β_{dev}-based												
300 (296)	2.00	0.67	-1.57	3.15	0.78	0.10	2.91	0.67	0.70	2.07	0.81	-0.78
150 (128)	1.99	0.65	-1.36	2.00	0.75	0.63	2.00	0.50	0.27	3.49	0.50	-0.78
$SKEH$-based												
300 (270)	1.99	0.69	-1.88	3.40	0.94	0.59	3.48	0.75	-0.13	2.10	0.64	0.78
150 (122)	2.00	0.50	-0.38	1.97	0.51	-0.78	1.46	0.76	-0.01	1.46	0.51	-0.44
η_{de}-based												
300 (280)	2.00	0.54	-0.76	2.21	0.51	-0.78	2.10	0.75	-0.78	0.31	0.50	0.00

Table A.2: Summary of final endwall design vector components for the 'compound' designs

Endwall	c_1	n_1	Ψ_1	c_2	n_2	ψ_1	c_3	n_3	ψ_3	c_4	n_4	ψ_4
150 (147)	2.00	0.65	-1.81	1.50	0.68	0.50	1.50	0.53	0.36	1.50	0.63	-0.22
$C_{ske,1} + \beta_{dev,0.7}$-based												
300 (290)	1.85	0.65	-1.54	1.85	0.50	0.79	2.56	0.54	0.45	2.45	0.50	0.78
150 (100)	2.00	0.66	-1.24	2.76	0.50	0.79	1.90	0.56	-0.24	1.61	0.60	-0.13
$C_{p0,rel,1} + \beta_{dev,0.7}$-based												
300 (212)	1.96	0.63	-1.34	2.70	0.53	0.00	1.87	0.50	0.68	0.76	0.50	-0.26

B

Convergence scatter plots

.

A η_{tt}-based endwall

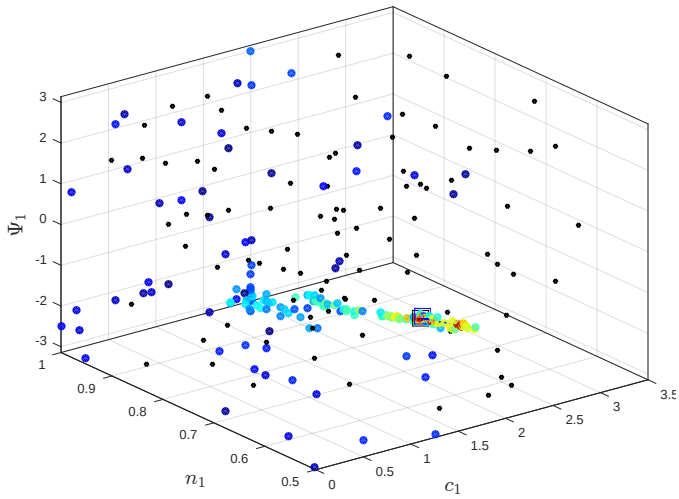

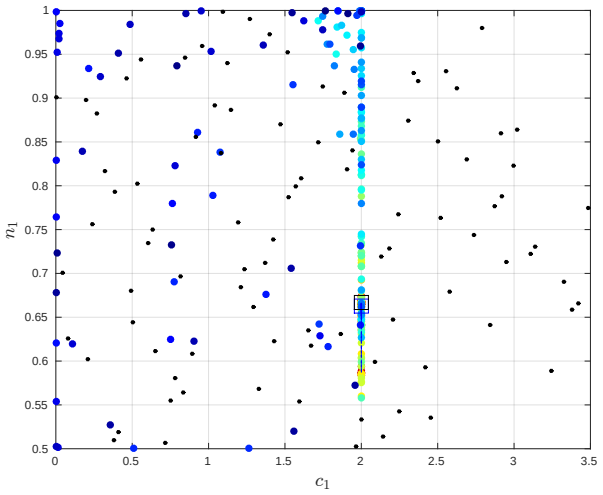

$c_1 - n_1$ plane

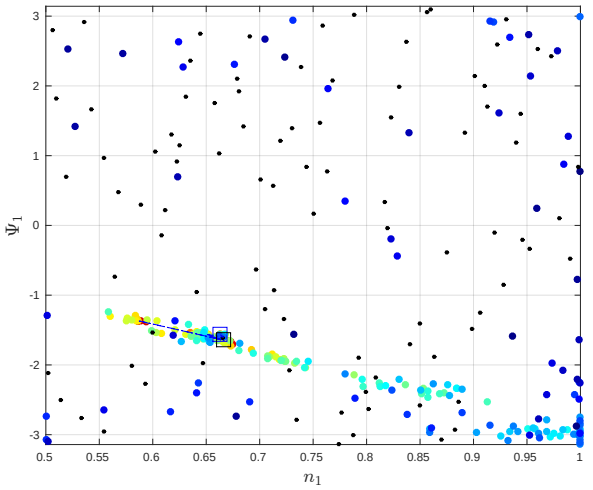

$n_1 - \Psi_1$ plane

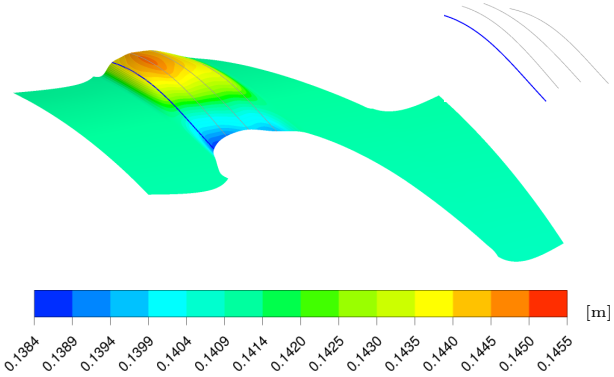

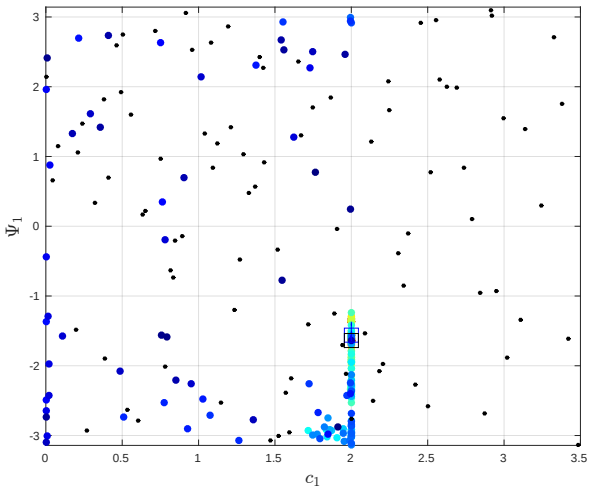

$c_1 - \Psi_1$ plane

Fig. B.1: Infill history for circumferential curve 2 (η_{tt}-based endwall)

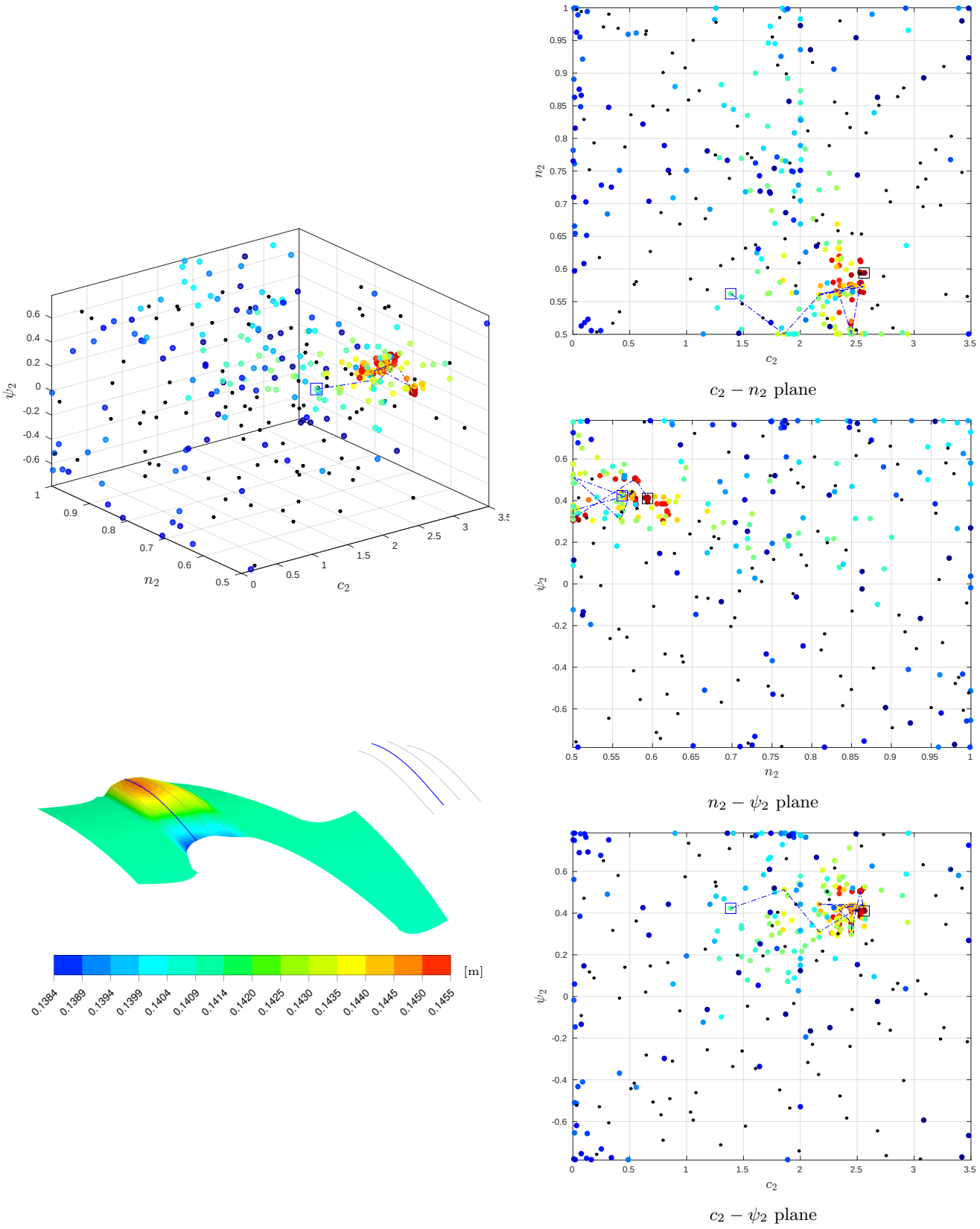

Fig. B.2: Infill history for circumferential curve 3 (η_{tt}-based endwall)

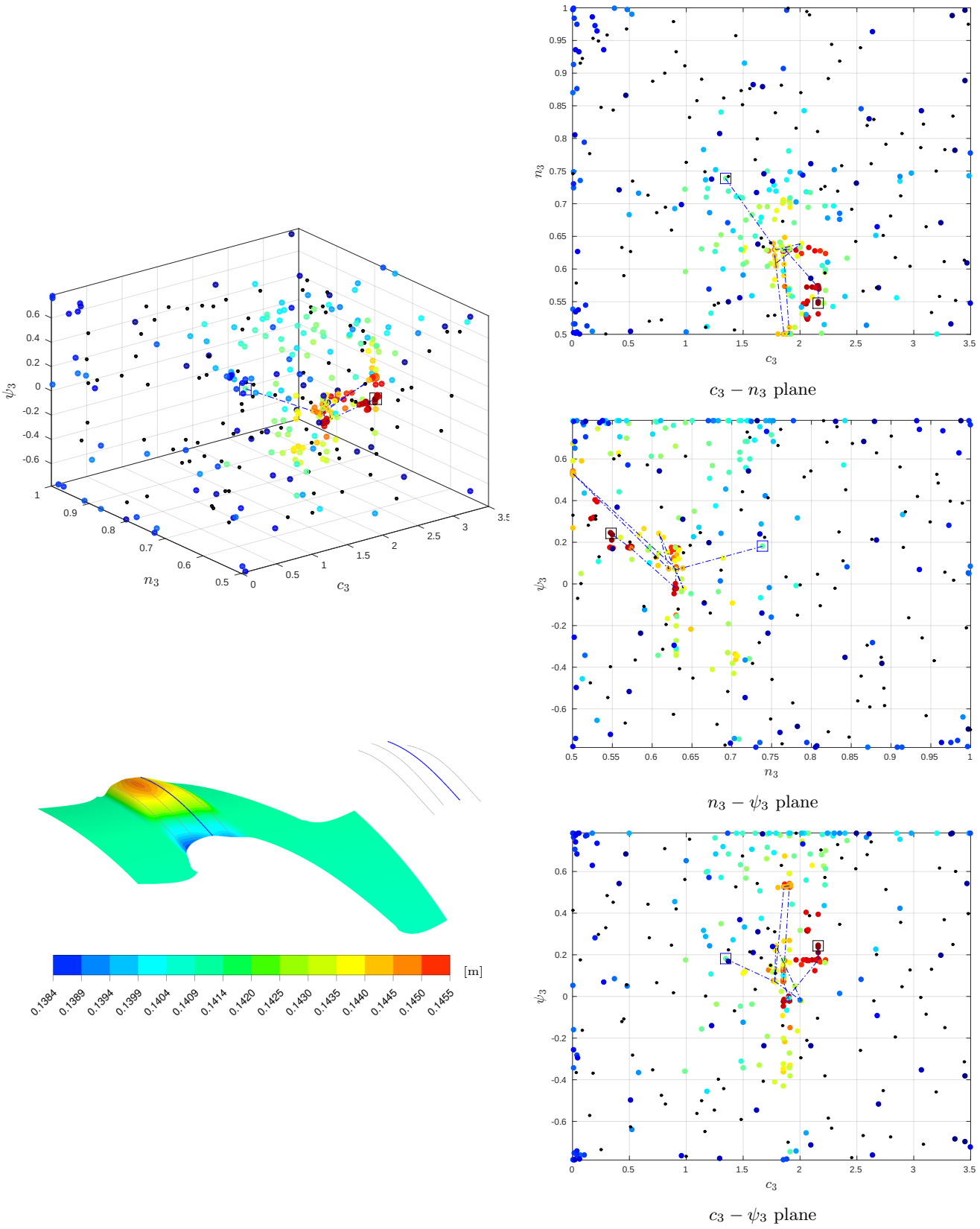

Fig. B.3: Infill history for circumferential curve 4 (η_{tt}-based endwall)

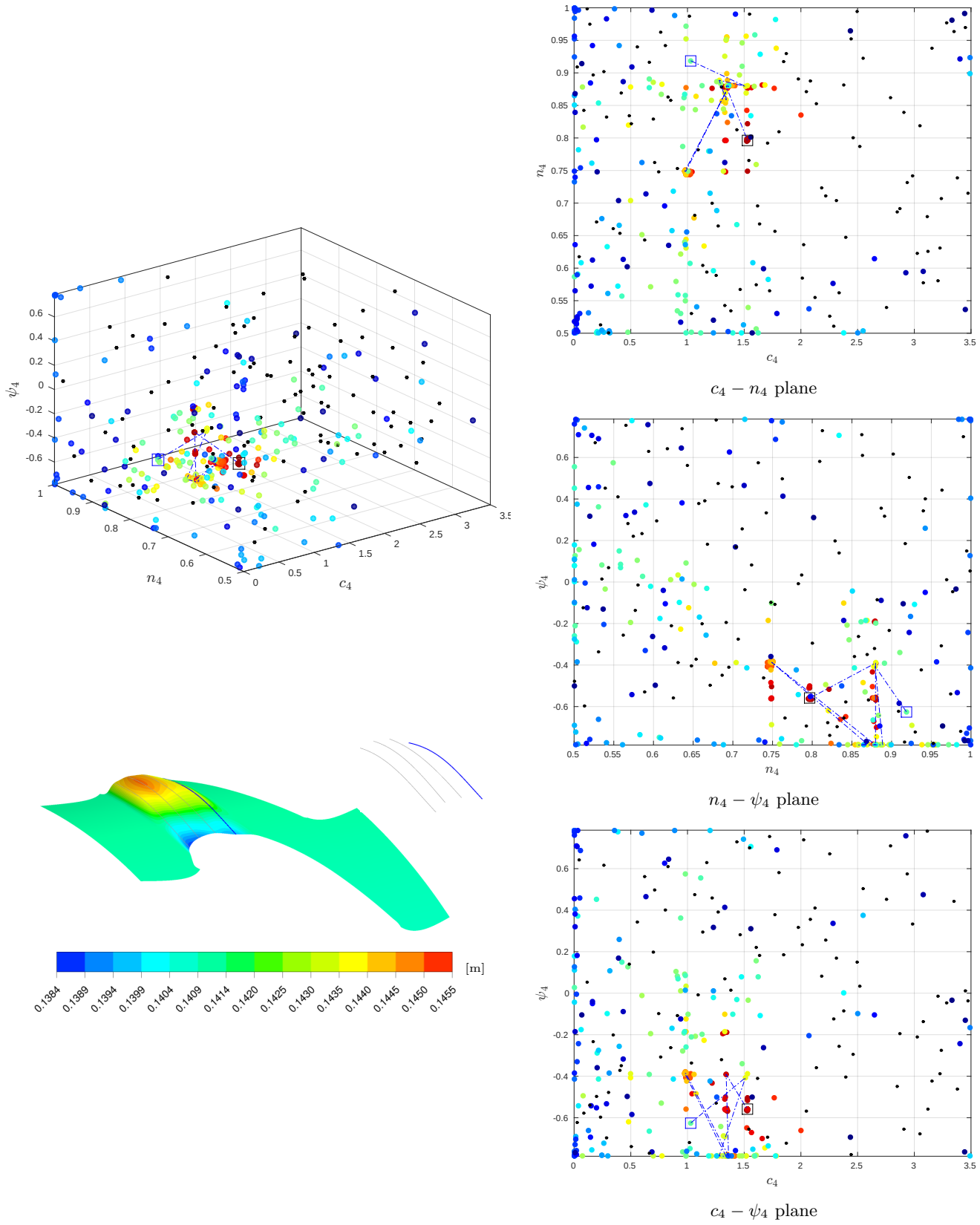

Fig. B.4: Infill history for circumferential curve 5 (η_{tt}-based endwall)

B C_{ske}-based endwall

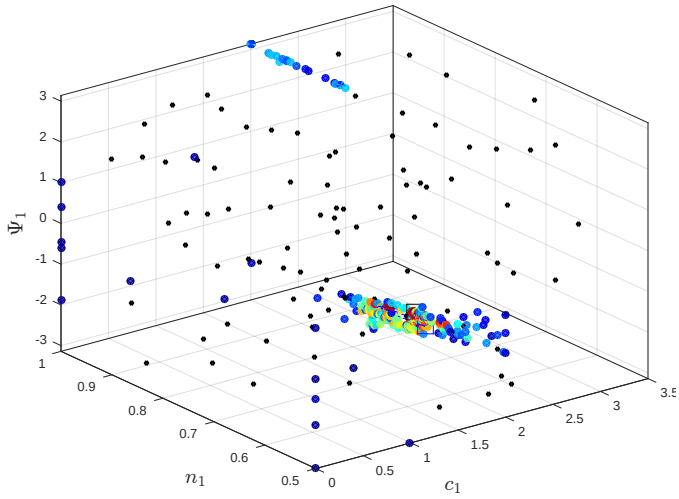

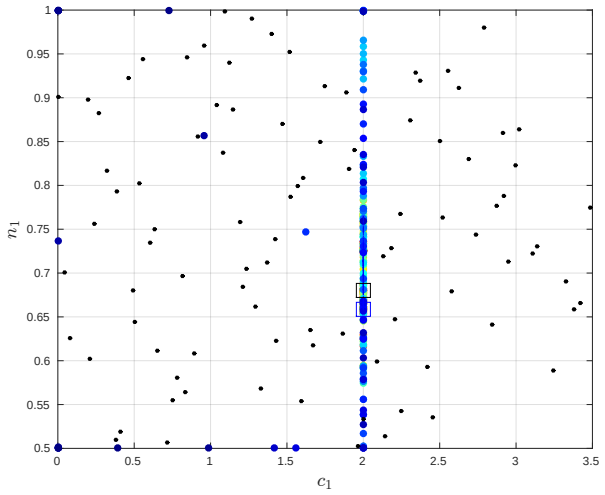

$c_1 - n_1$ plane

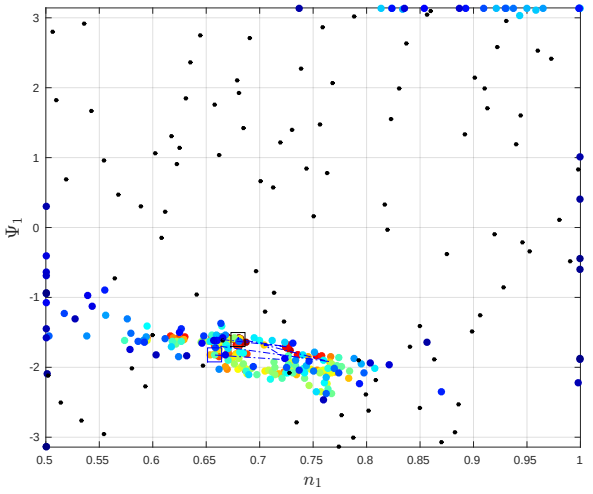

$n_1 - \Psi_1$ plane

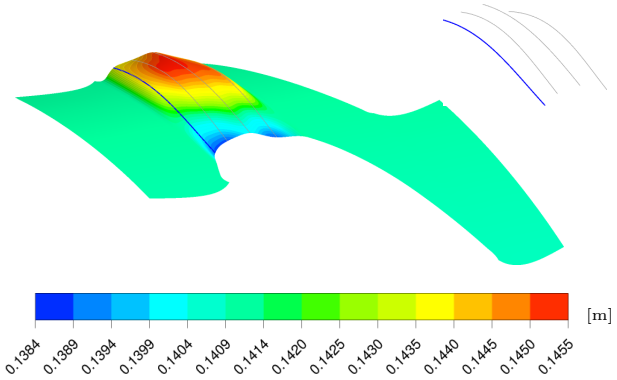

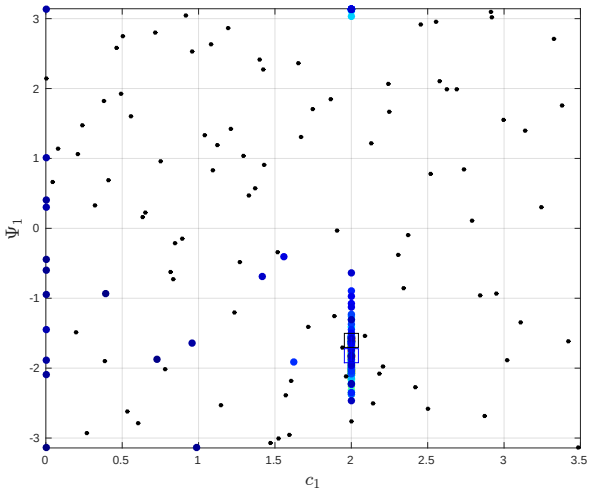

$c_1 - \Psi_1$ plane

Fig. B.5: Infill history for circumferential curve 2 (C_{ske}-based endwall)

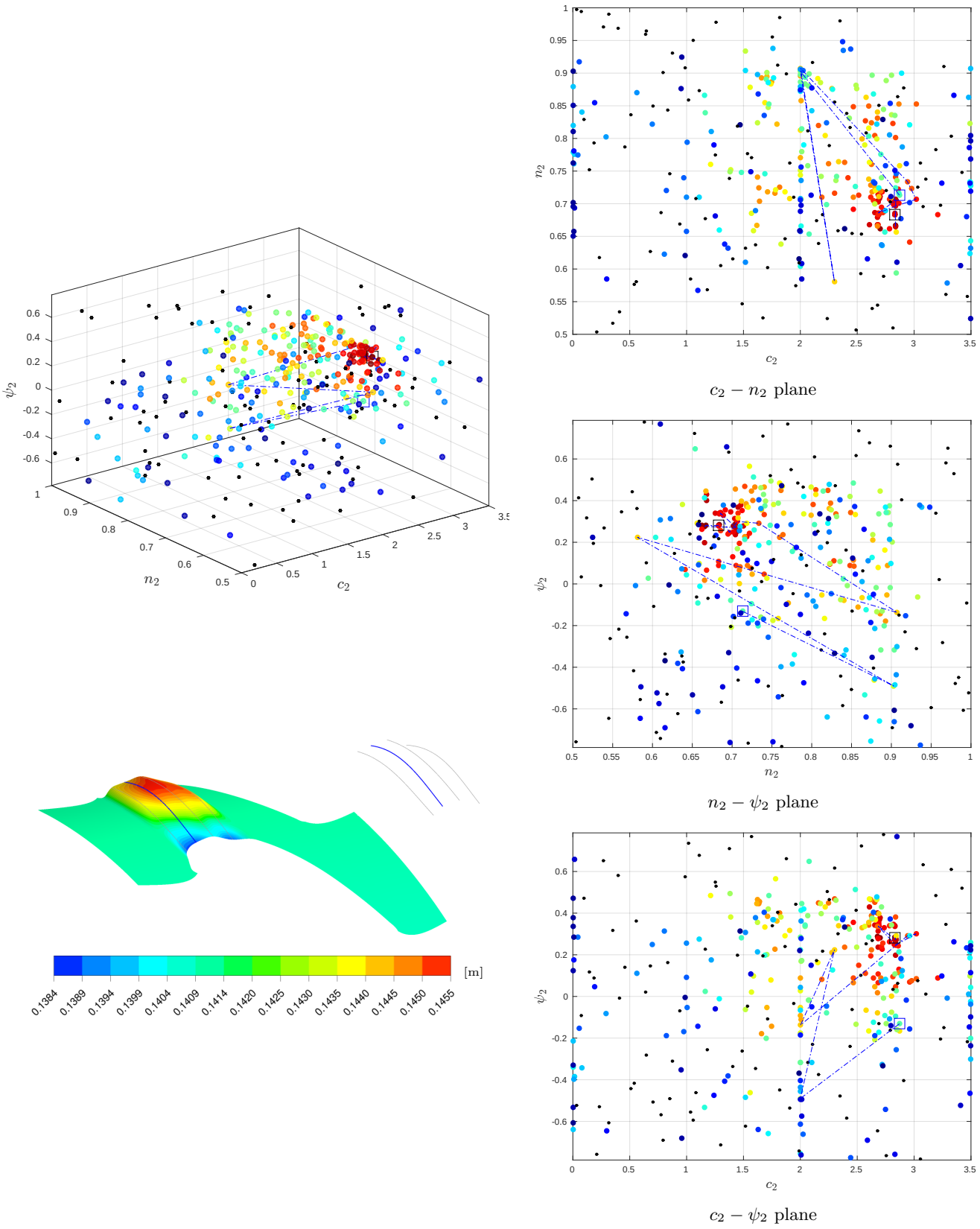

Fig. B.6: Infill history for circumferential curve 3 (C_{ske}-based endwall)

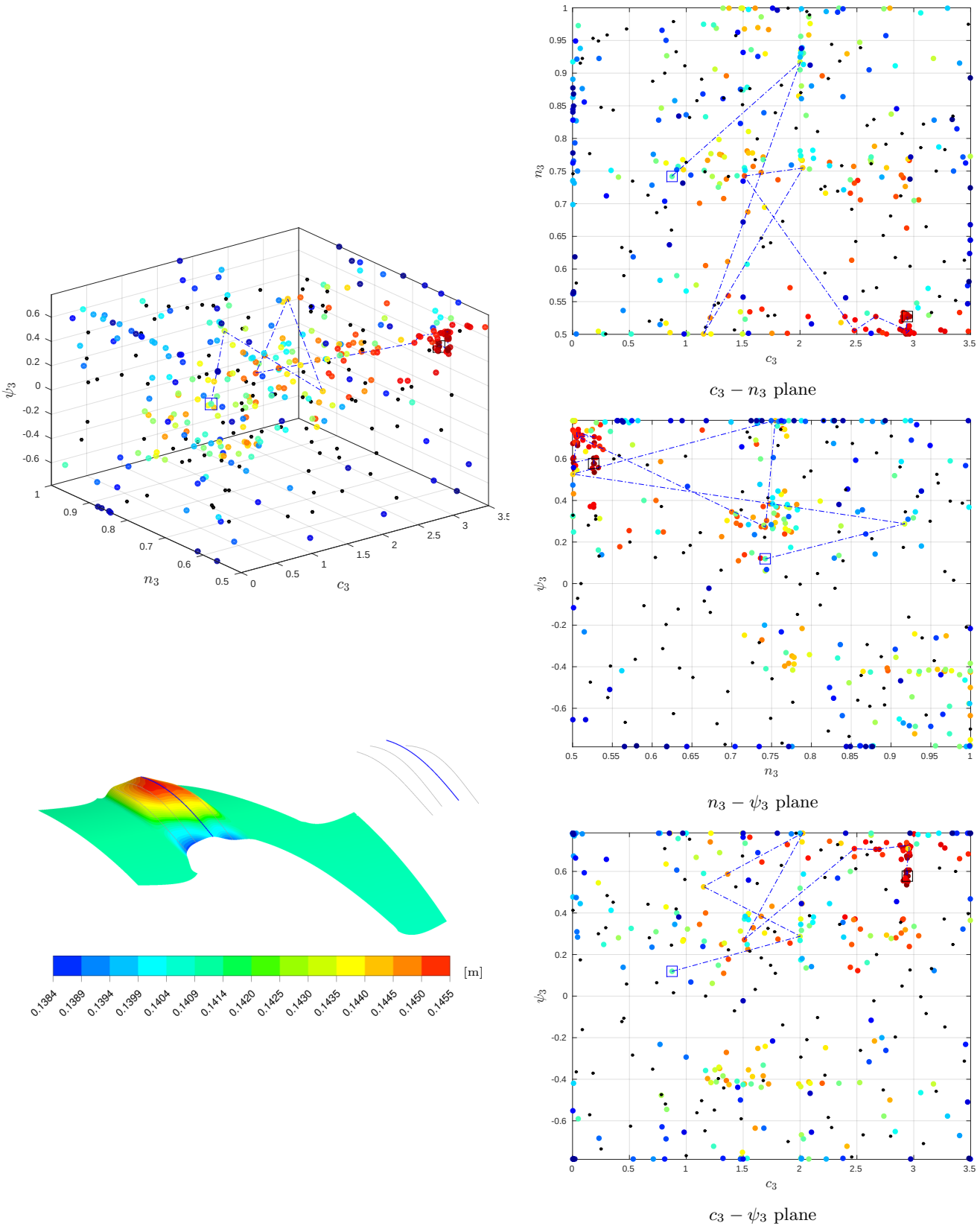

Fig. B.7: Infill history for circumferential curve 4 (C_{ske}-based endwall)

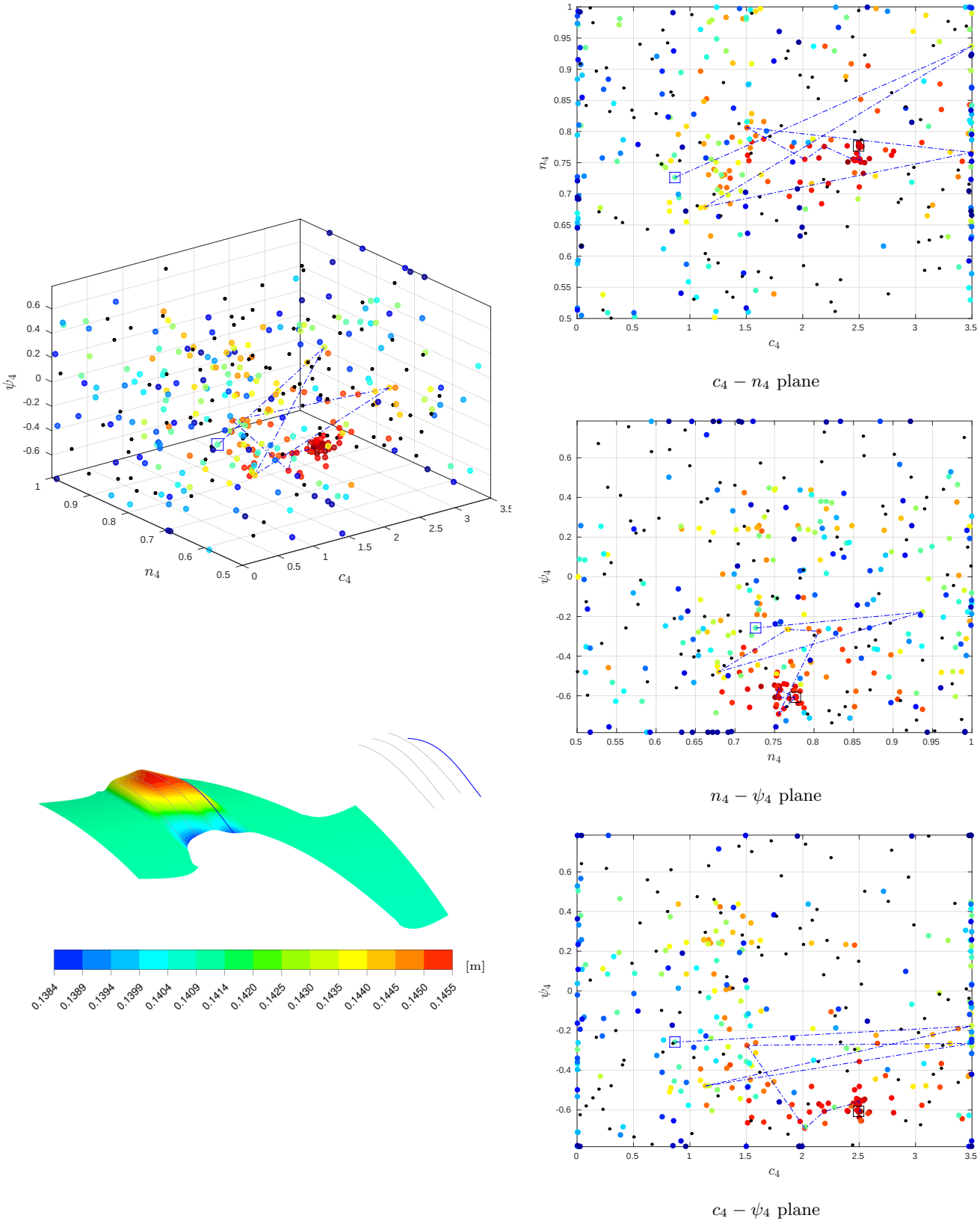

Fig. B.8: Infill history for circumferential curve 5 (C_{ske}-based endwall)

C $C_{p0,rel}$-based endwall

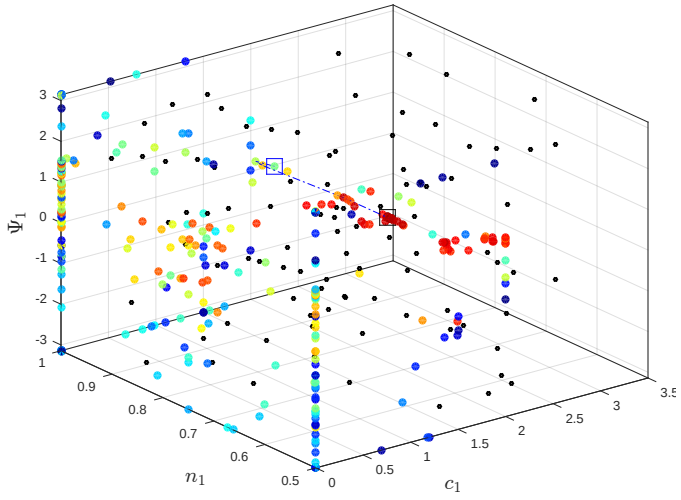

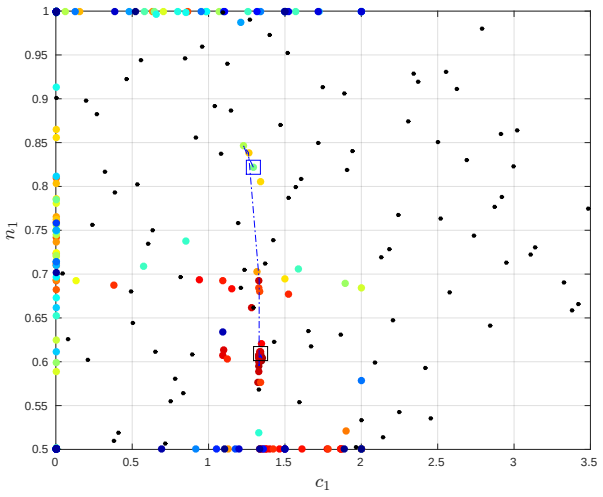

$c_1 - n_1$ plane

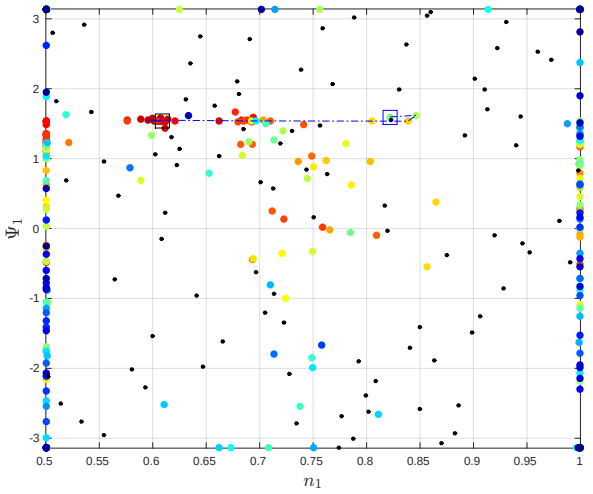

$n_1 - \Psi_1$ plane

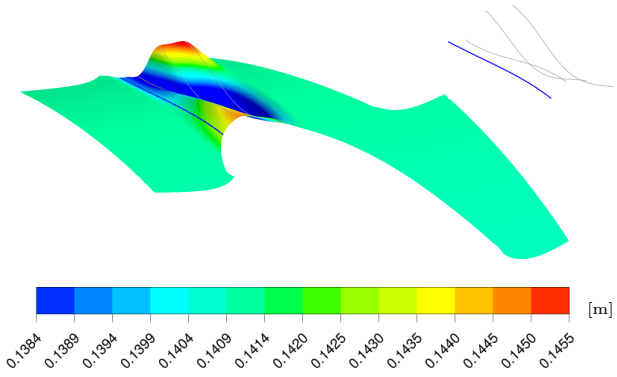

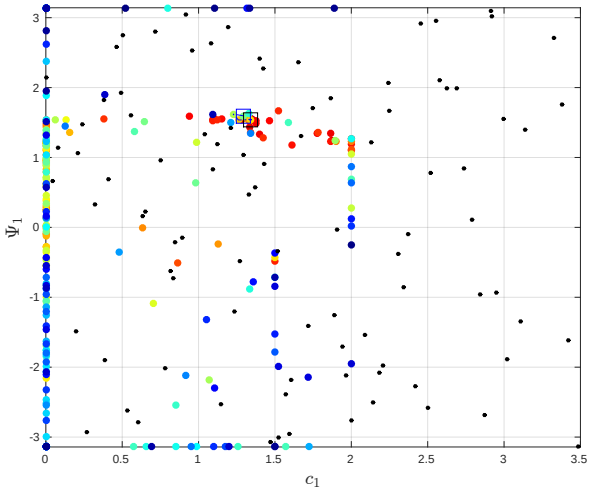

$c_1 - \Psi_1$ plane

Fig. B.9: Infill history for circumferential curve 2 ($C_{p0,rel}$-based endwall)

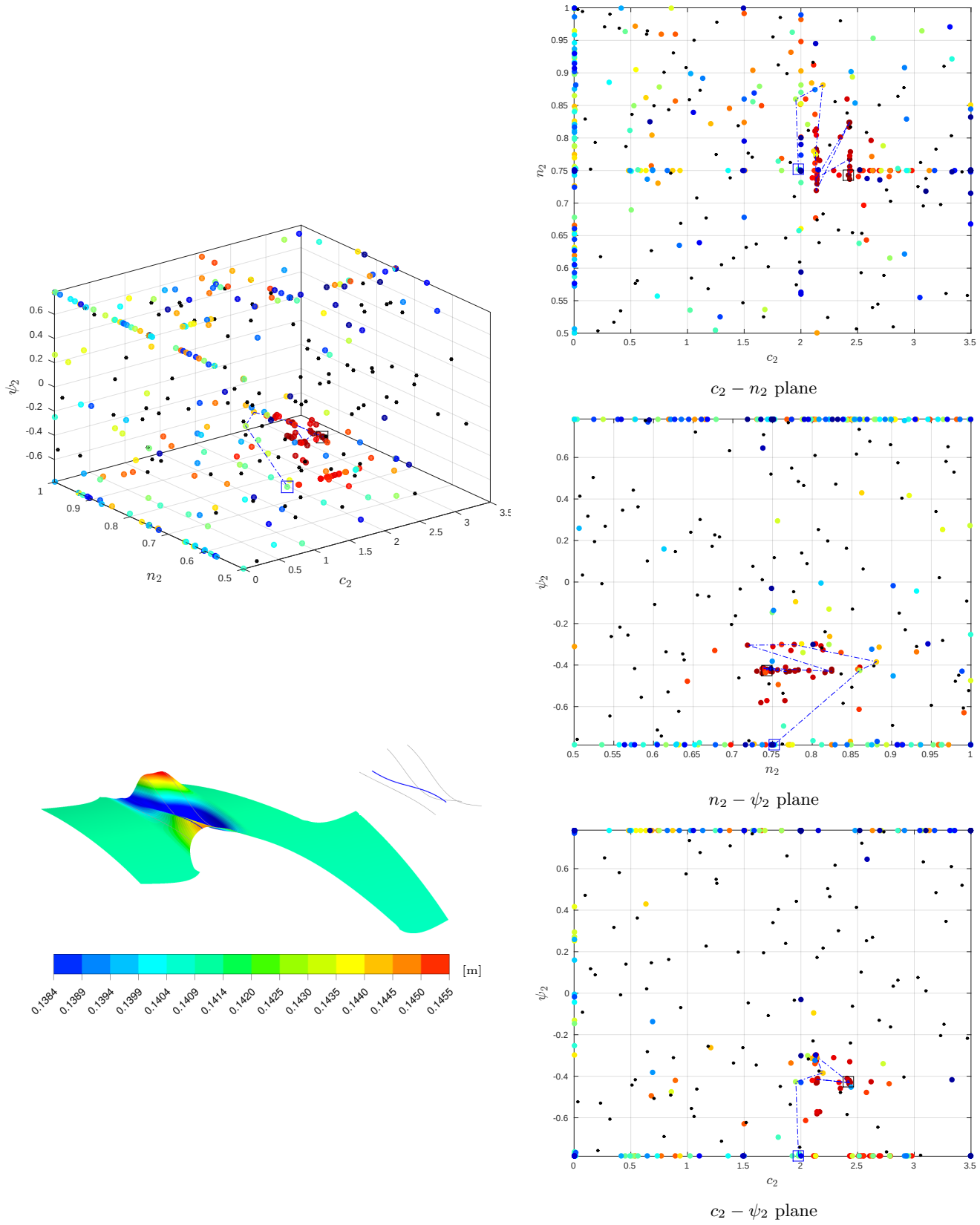

Fig. B.10: Infill history for circumferential curve 3 ($C_{p0,rel}$-based endwall)

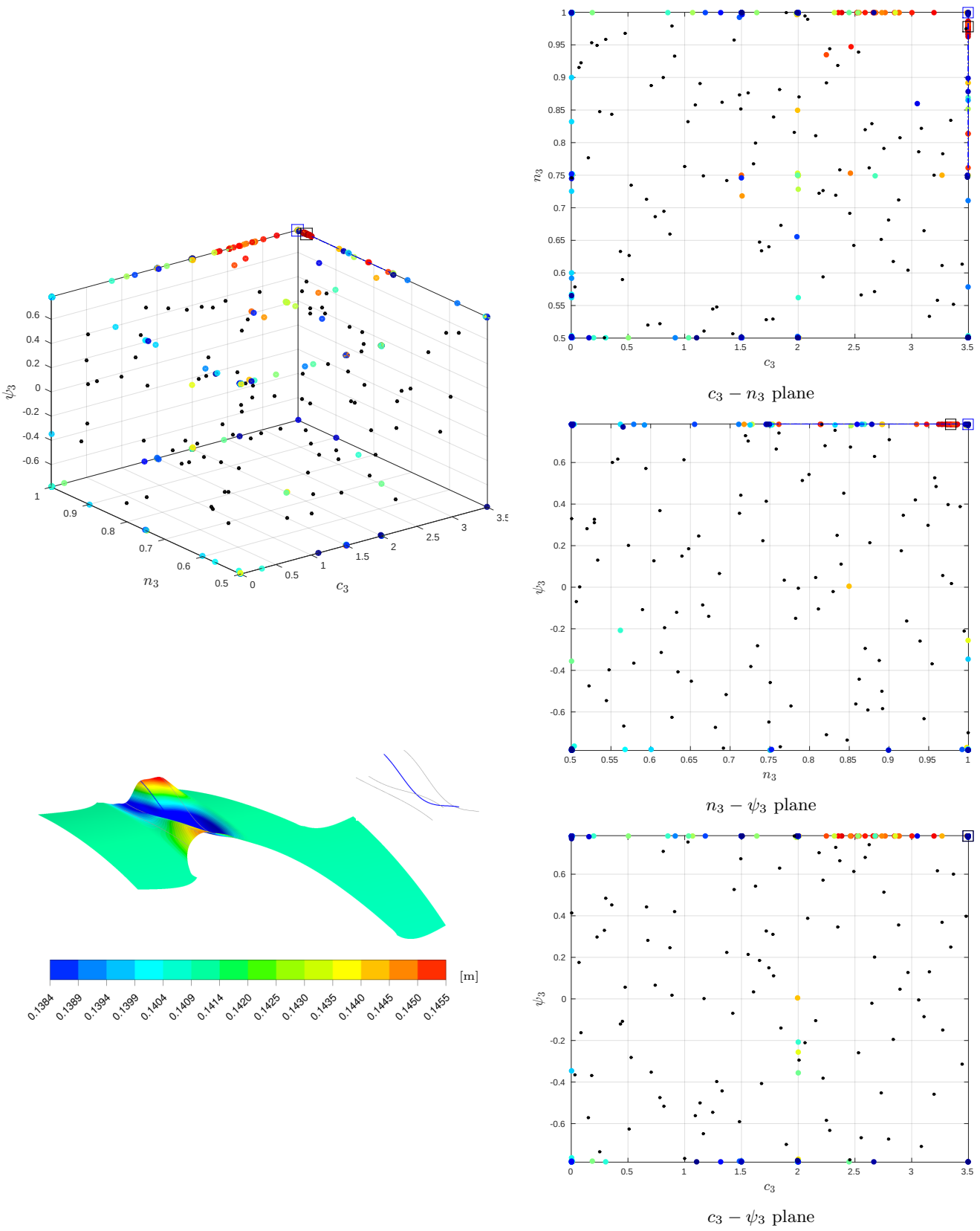

Fig. B.11: Infill history for circumferential curve 4 ($C_{p0,rel}$-based endwall)

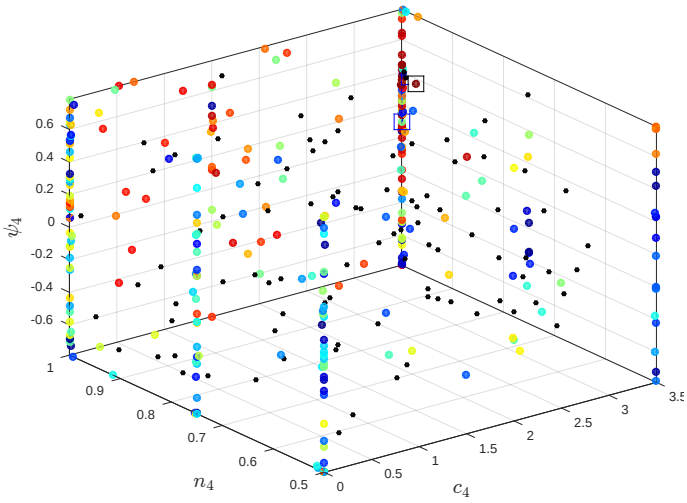

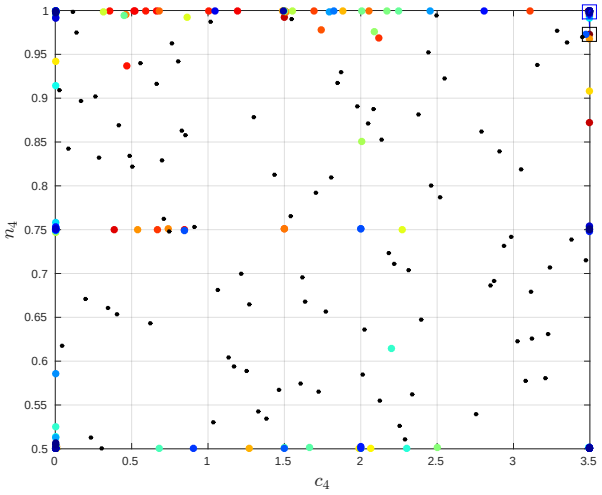

$c_4 - n_4$ plane

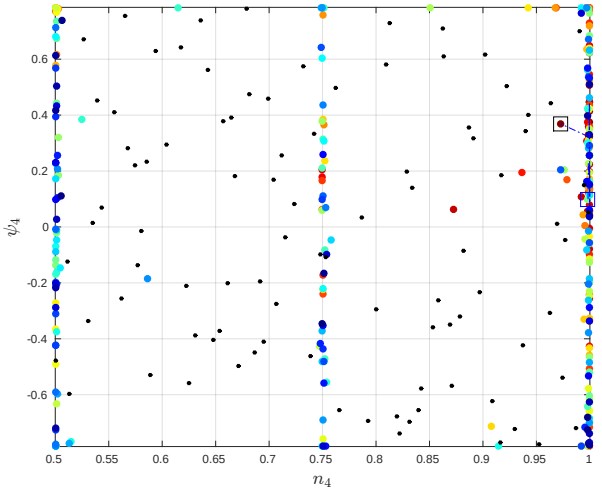

$n_4 - \psi_4$ plane

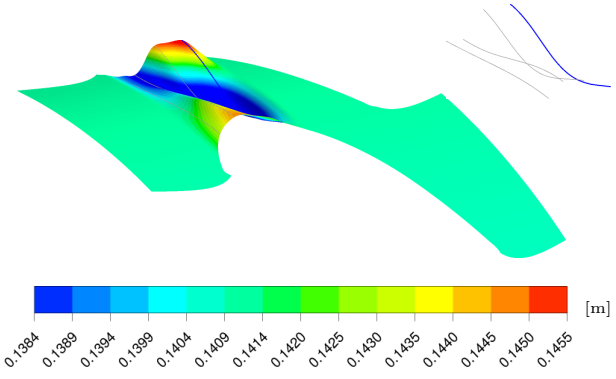

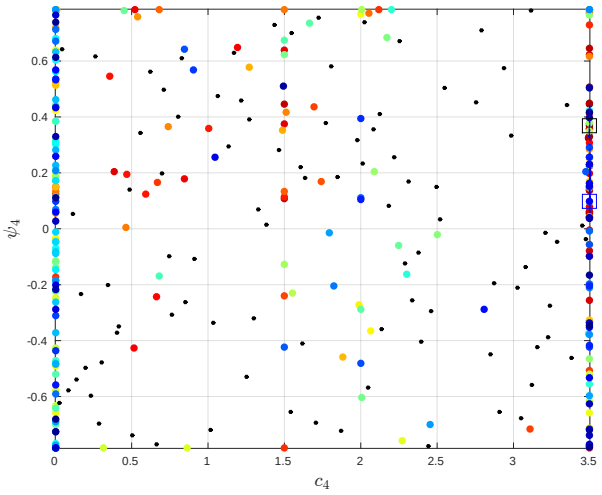

$c_4 - \psi_4$ plane

Fig. B.12: Infill history for circumferential curve 5 ($C_{p0,rel}$-based endwall)

D β_{dev}-based endwall

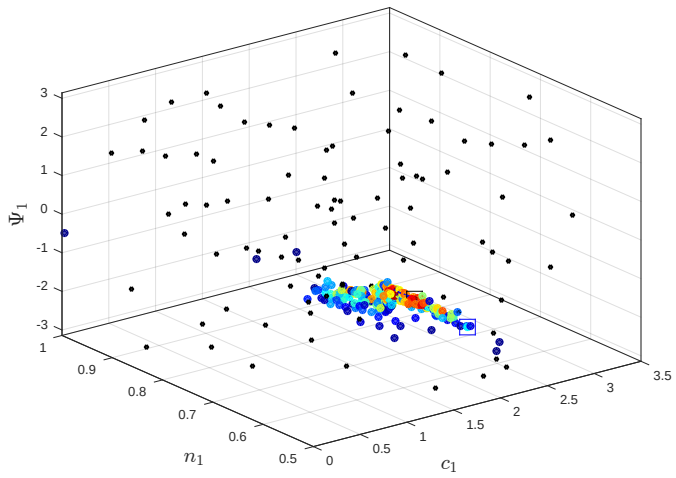

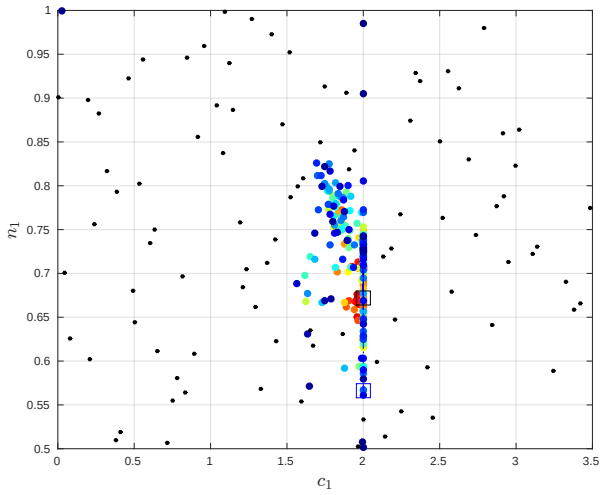

$c_1 - n_1$ plane

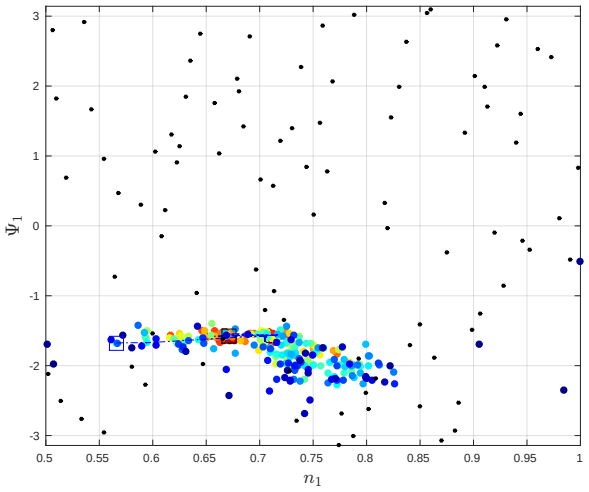

$n_1 - \Psi_1$ plane

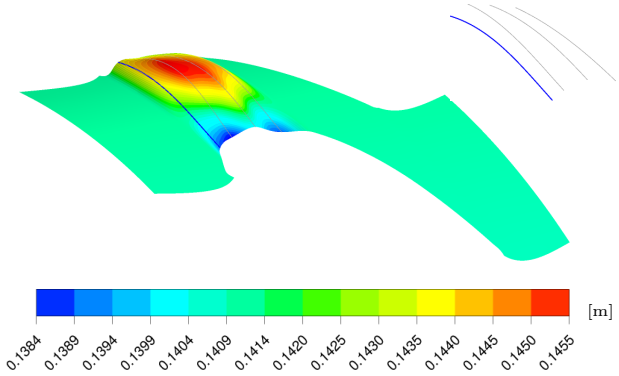

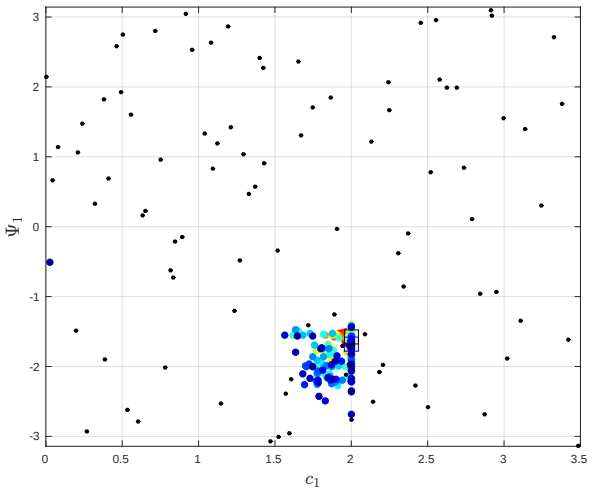

$c_1 - \Psi_1$ plane

Fig. B.13: Infill history for circumferential curve 2 (β_{dev}-based endwall)

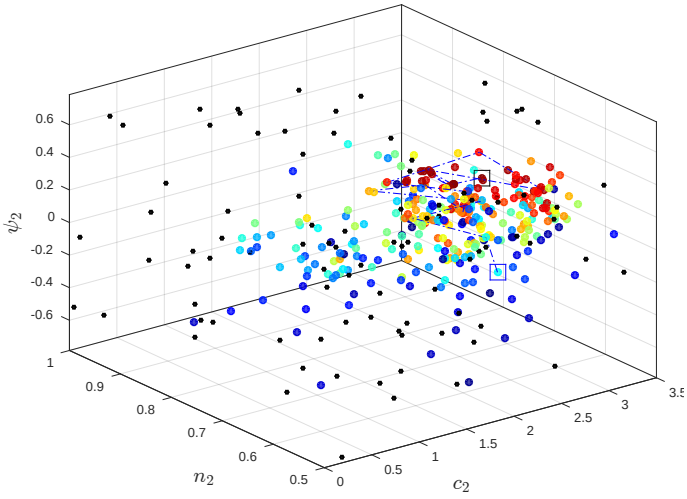

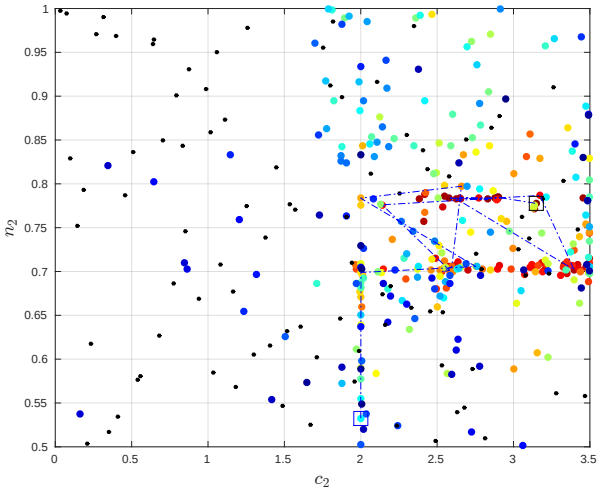

$c_2 - n_2$ plane

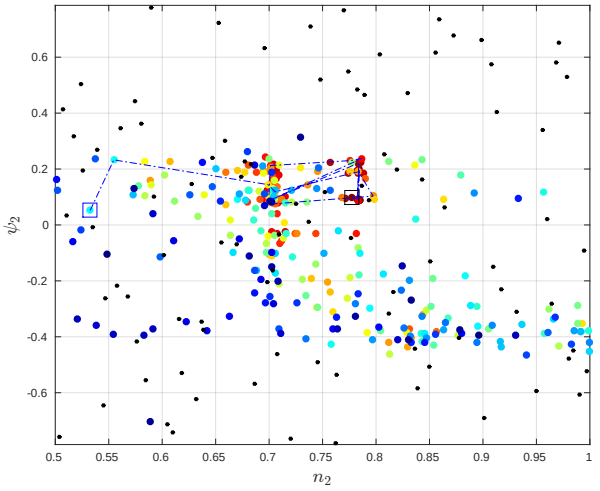

$n_2 - \psi_2$ plane

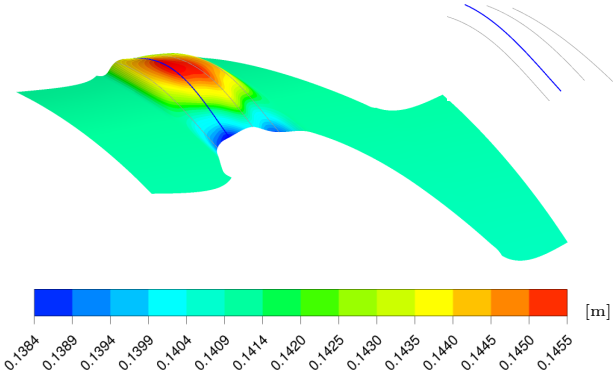

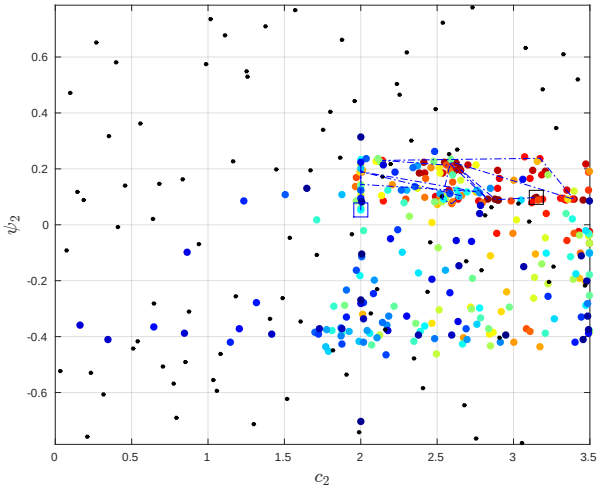

$c_2 - \psi_2$ plane

Fig. B.14: Infill history for circumferential curve 3 (β_{dev}-based endwall)

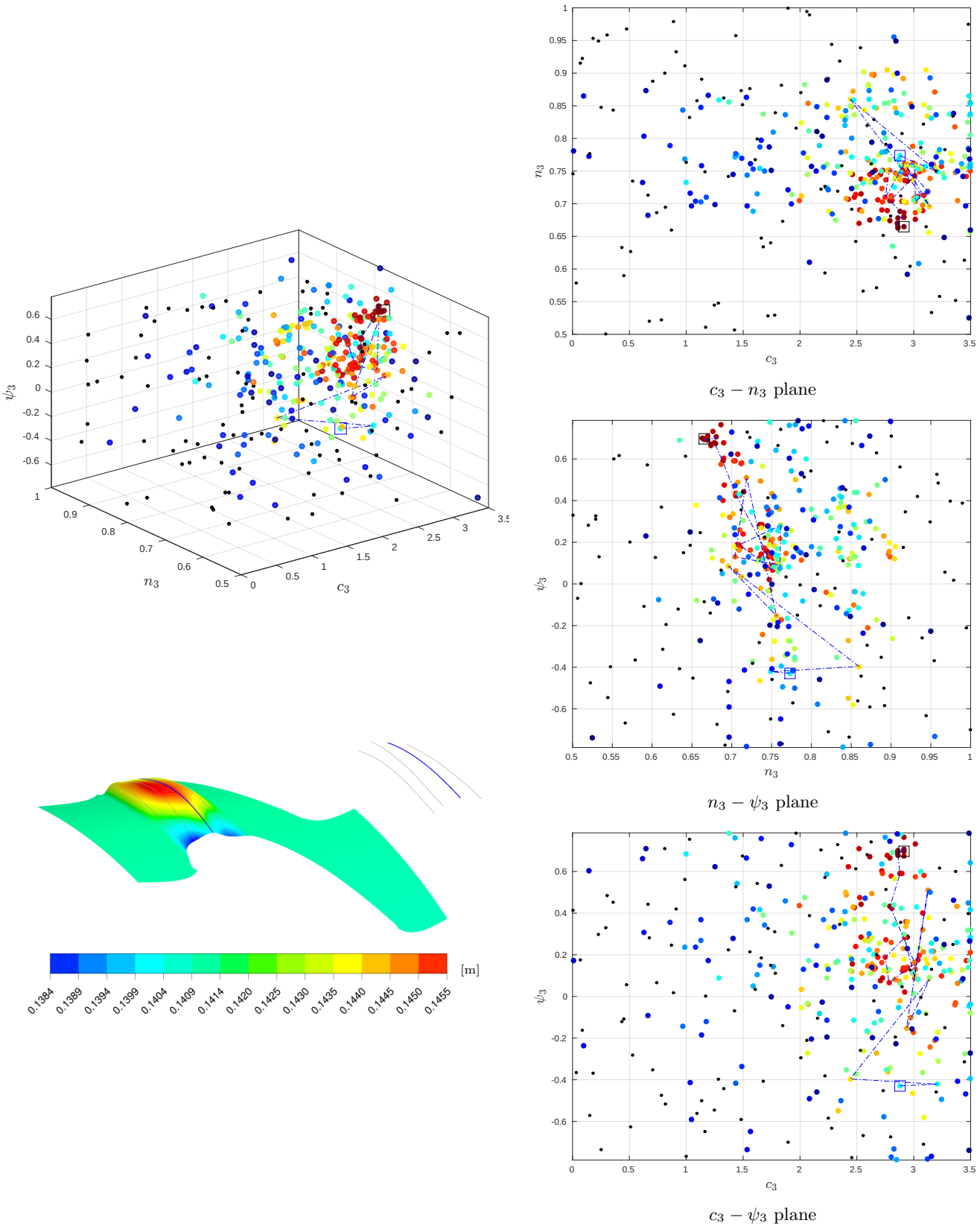

Fig. B.15: Infill history for circumferential curve 4 (β_{dev}-based endwall)

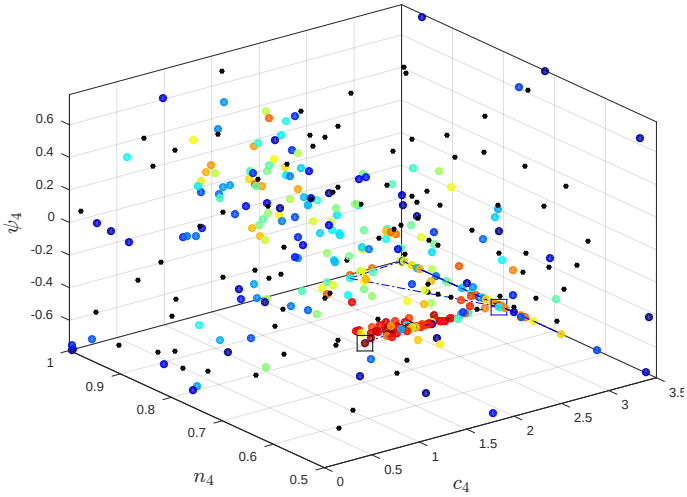

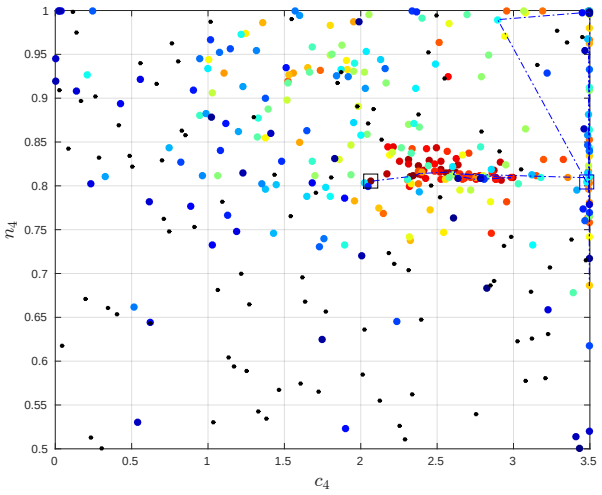

$c_4 - n_4$ plane

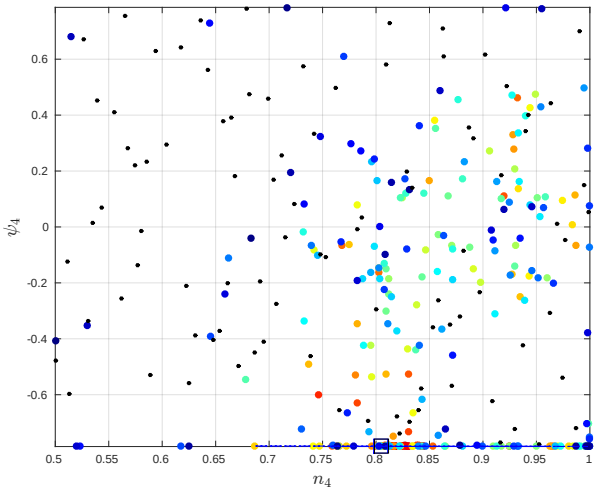

$n_4 - \psi_4$ plane

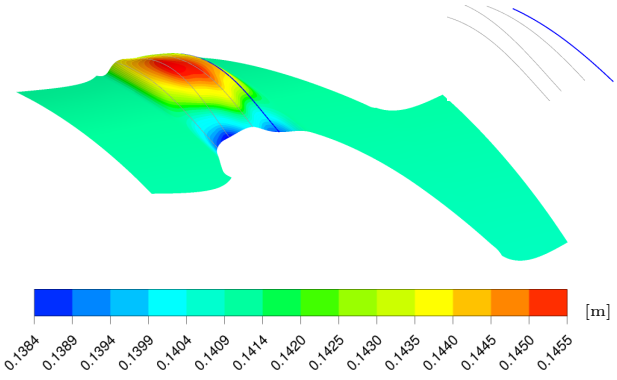

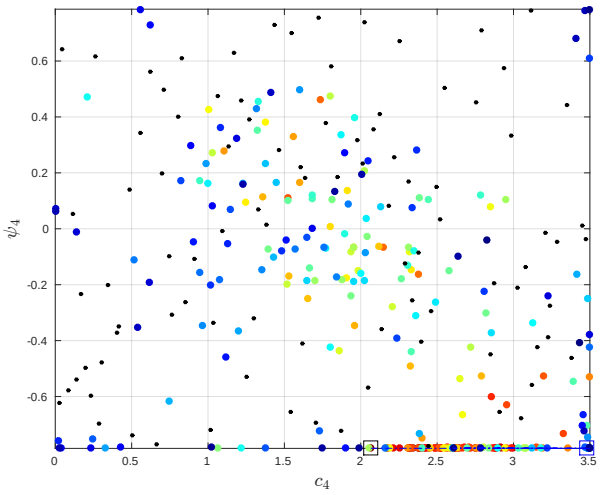

$c_4 - \psi_4$ plane

Fig. B.16: Infill history for circumferential curve 5 (β_{dev}-based endwall)

E *SKEH*-based endwall

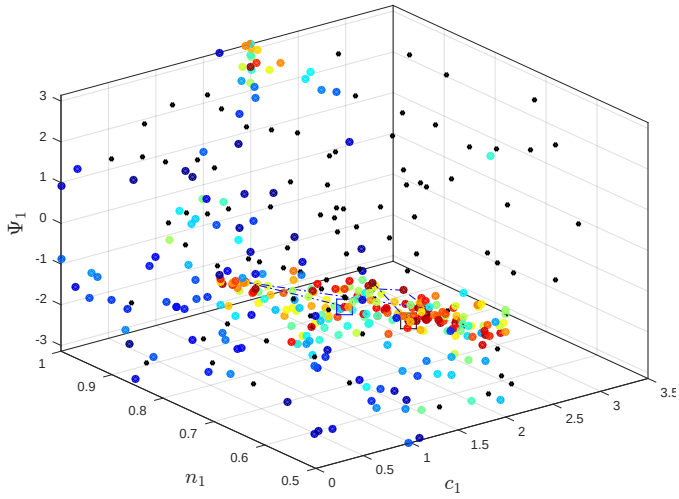

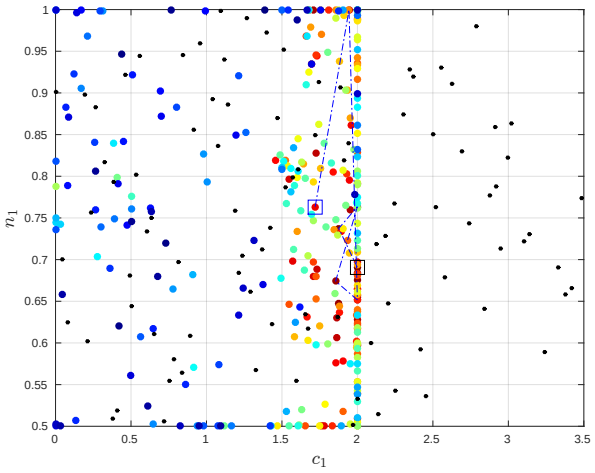

$c_1 - n_1$ plane

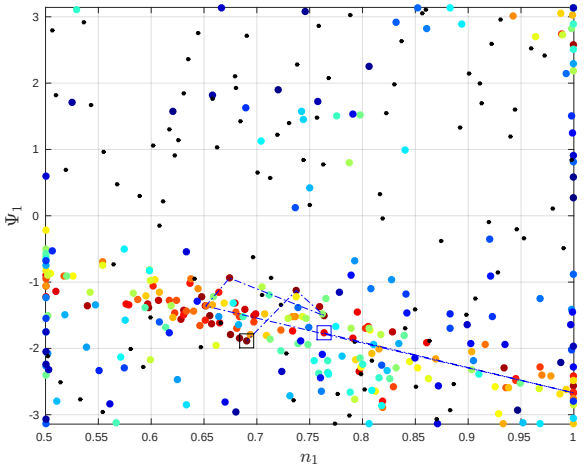

$n_1 - \Psi_1$ plane

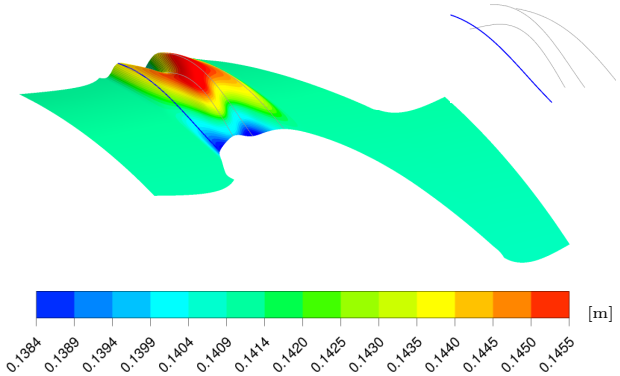

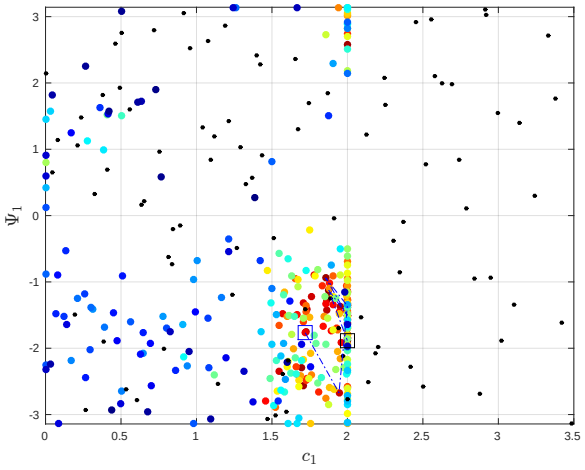

$c_1 - \Psi_1$ plane

Fig. B.17: Infill history for circumferential curve 2 (*SKEH*-based endwall)

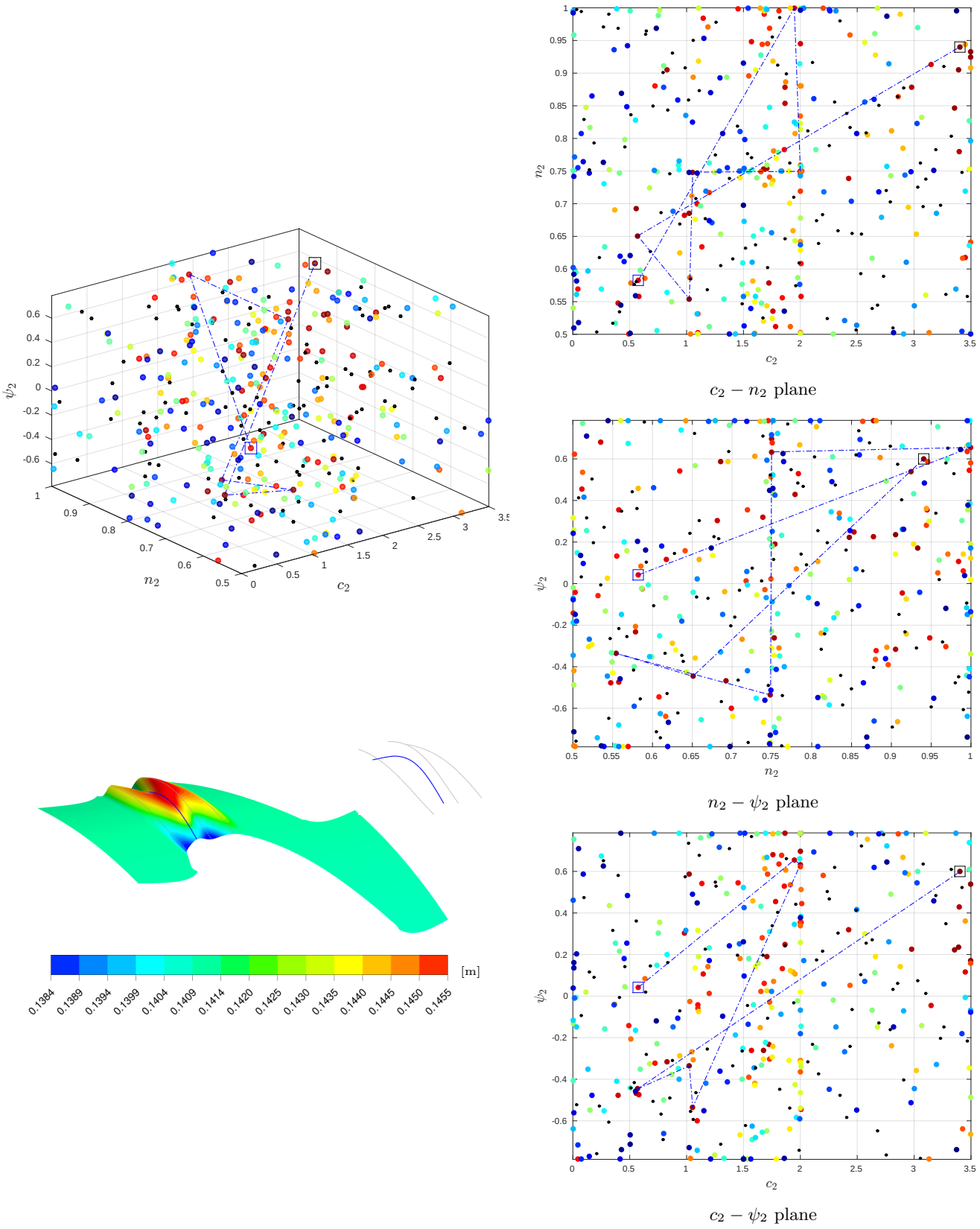

Fig. B.18: Infill history for circumferential curve 3 ($SKEH$-based endwall)

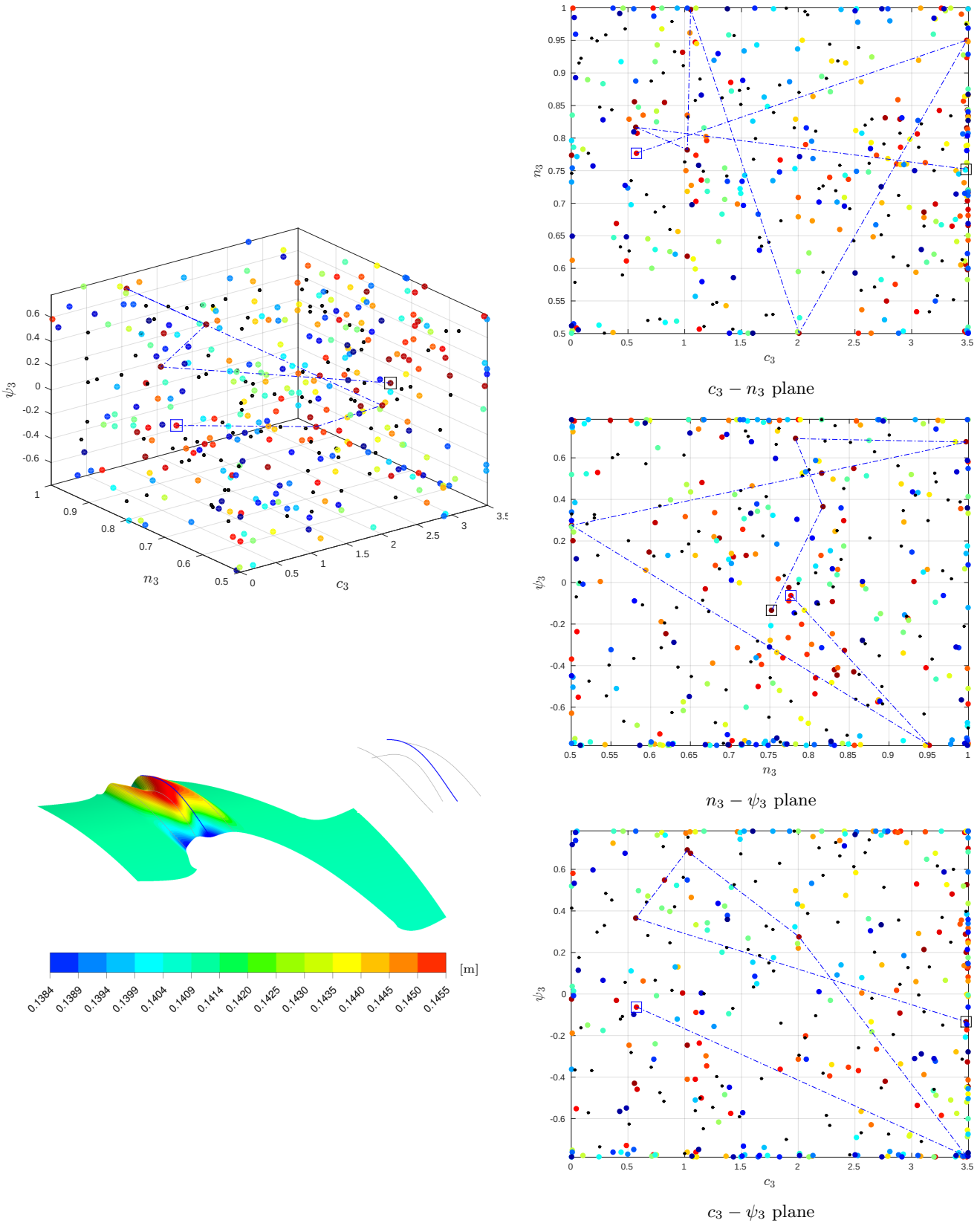

Fig. B.19: Infill history for circumferential curve 4 ($SKEH$-based endwall)

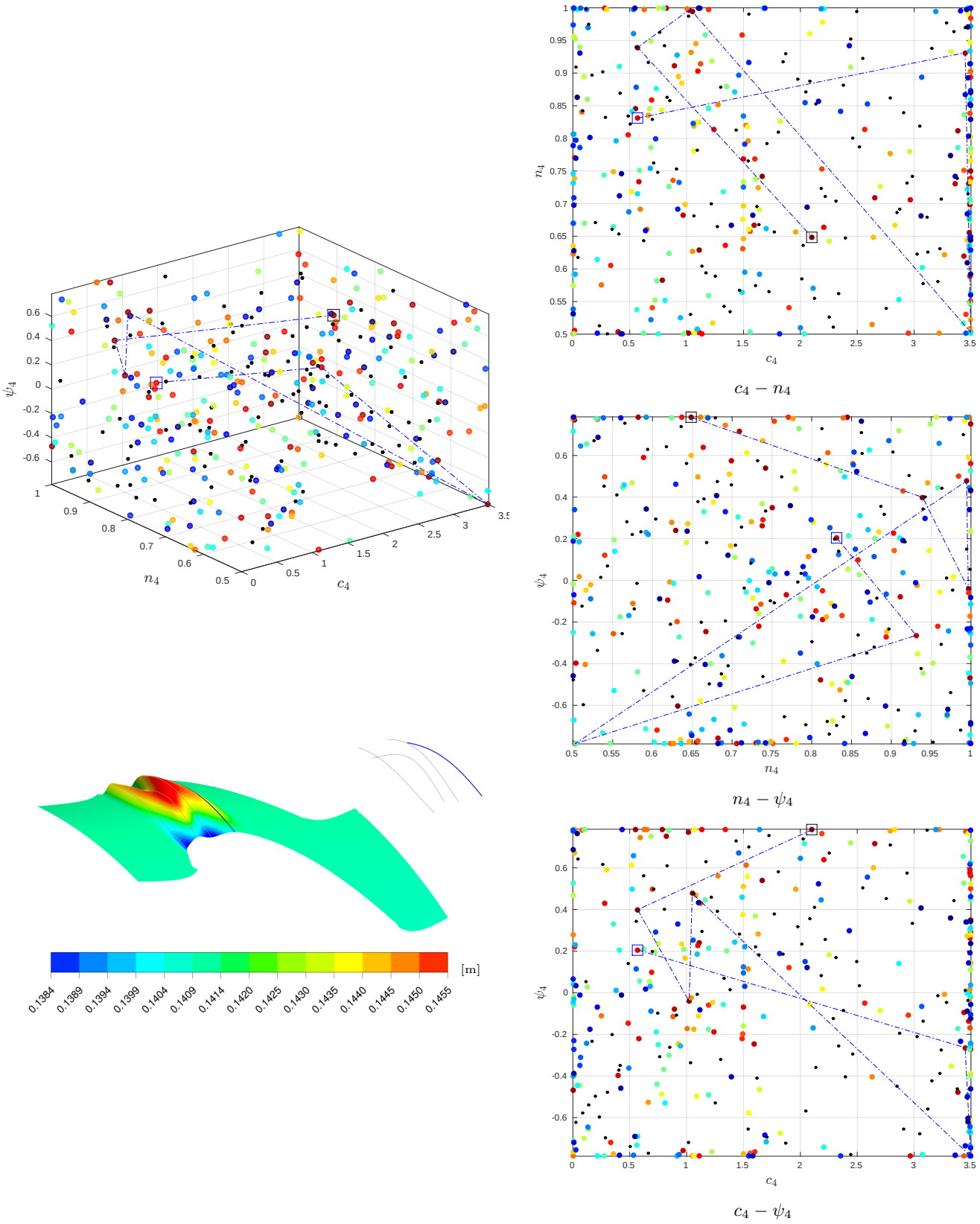

Fig. B.20: Infill history for circumferential curve 5 ($SKEH$-based endwall)

F η_{de}-based endwall

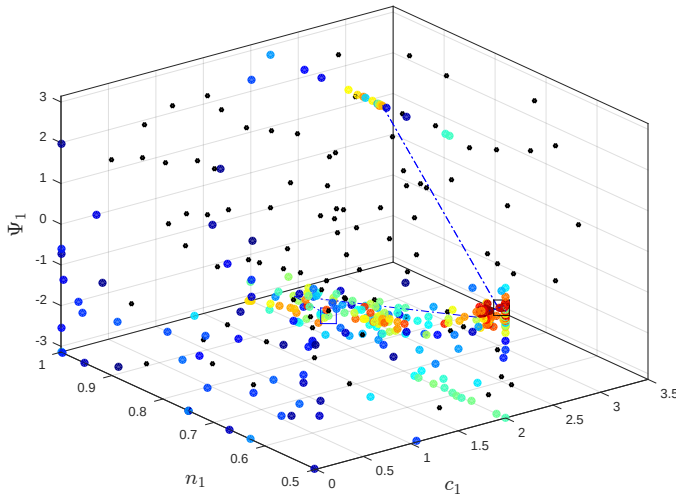

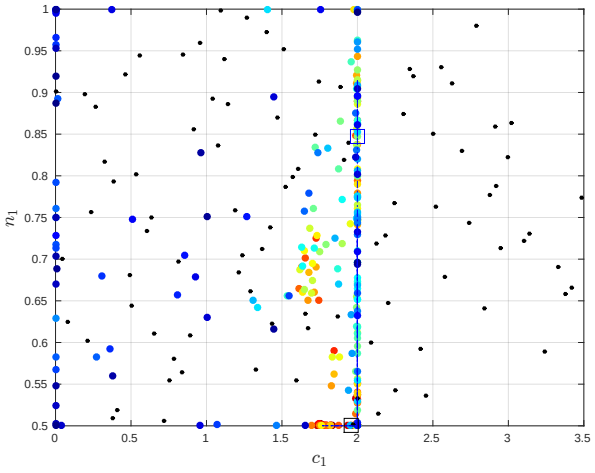

$c_1 - n_1$ plane

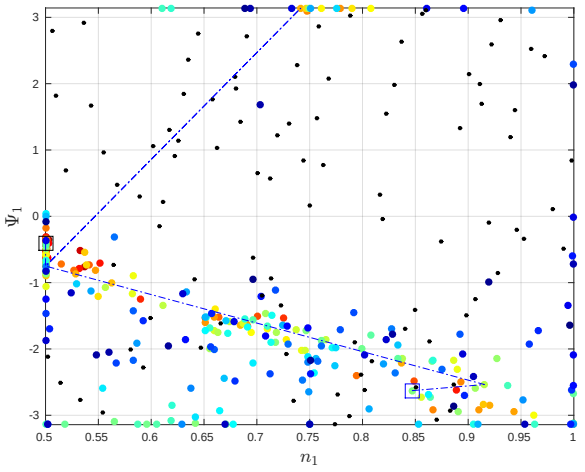

$n_1 - \Psi_1$ plane

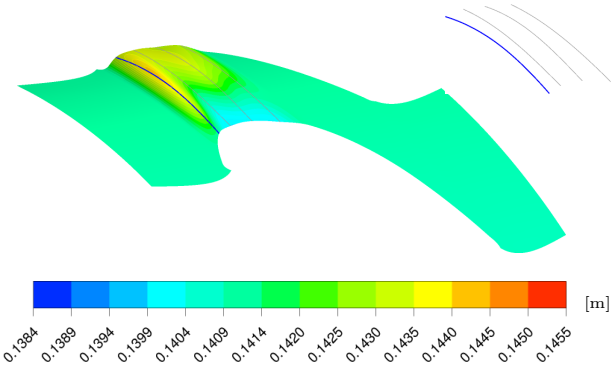

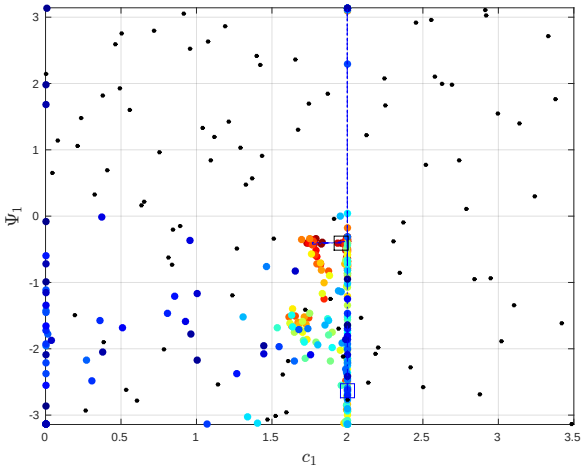

$c_1 - \Psi_1$ plane

Fig. B.21: Infill history for circumferential curve 2 (η_{de}-based endwall)

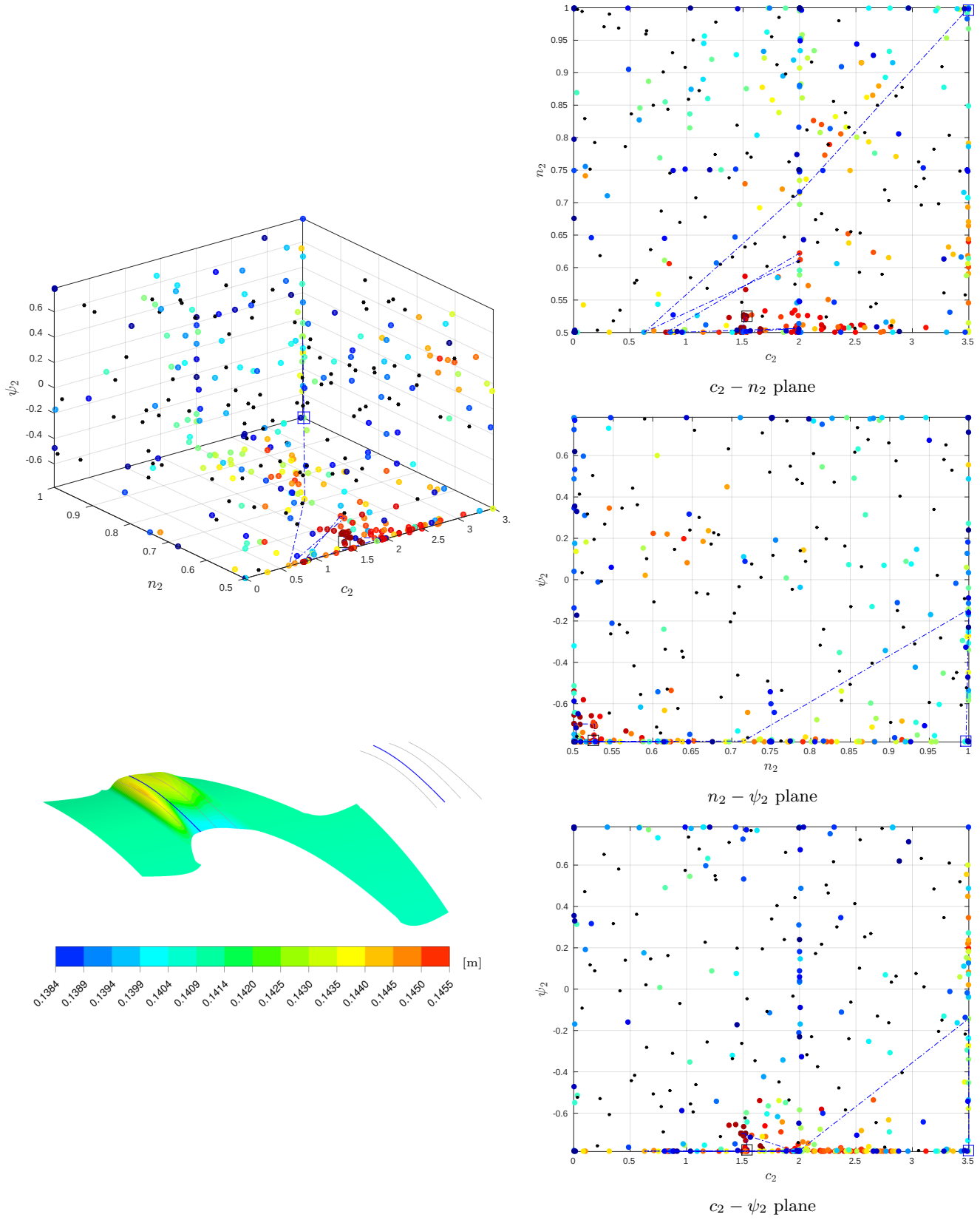

Fig. B.22: Infill history for circumferential curve 3 (η_{de}-based endwall)

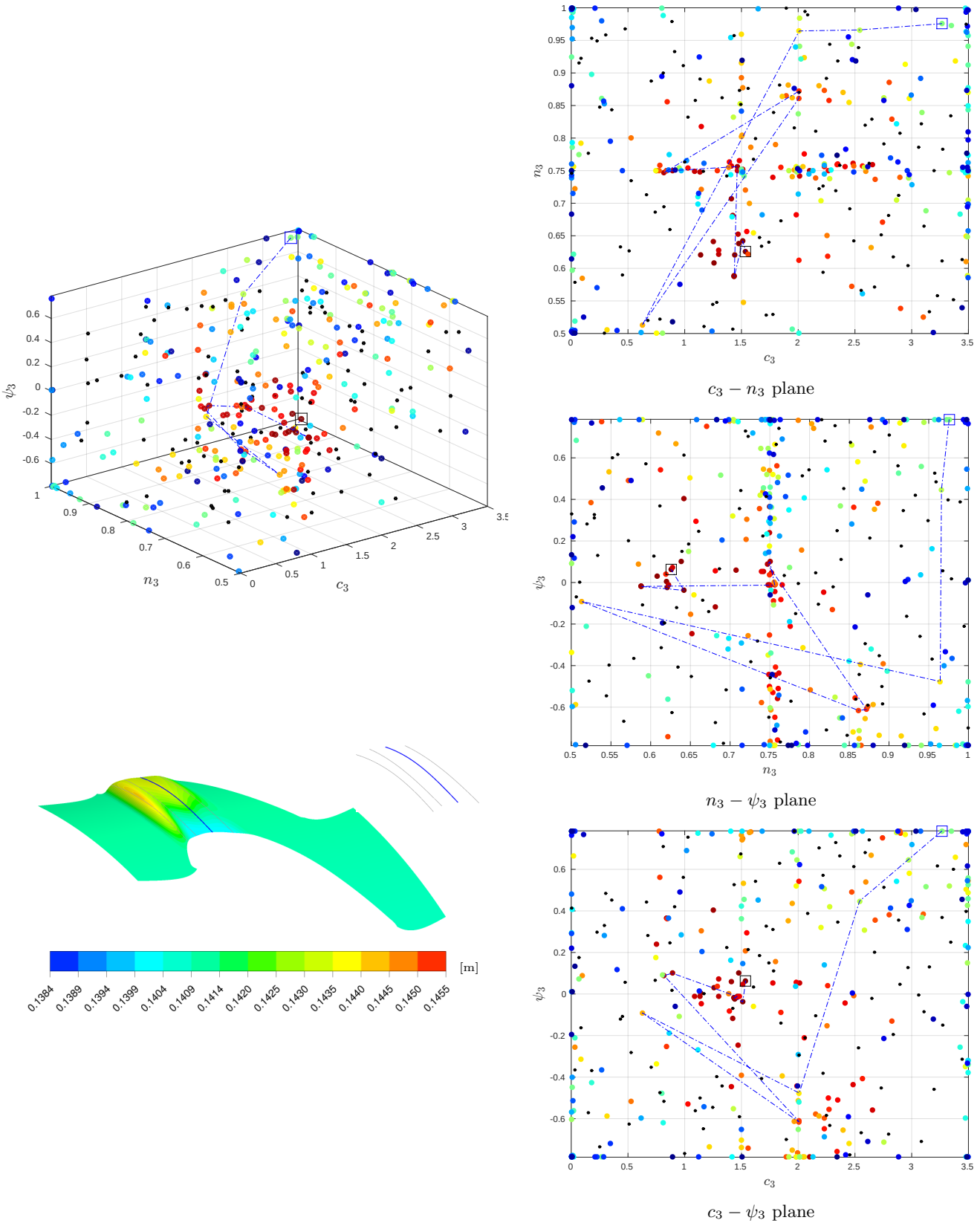

Fig. B.23: Infill history for circumferential curve 4 (η_{de}-based endwall)

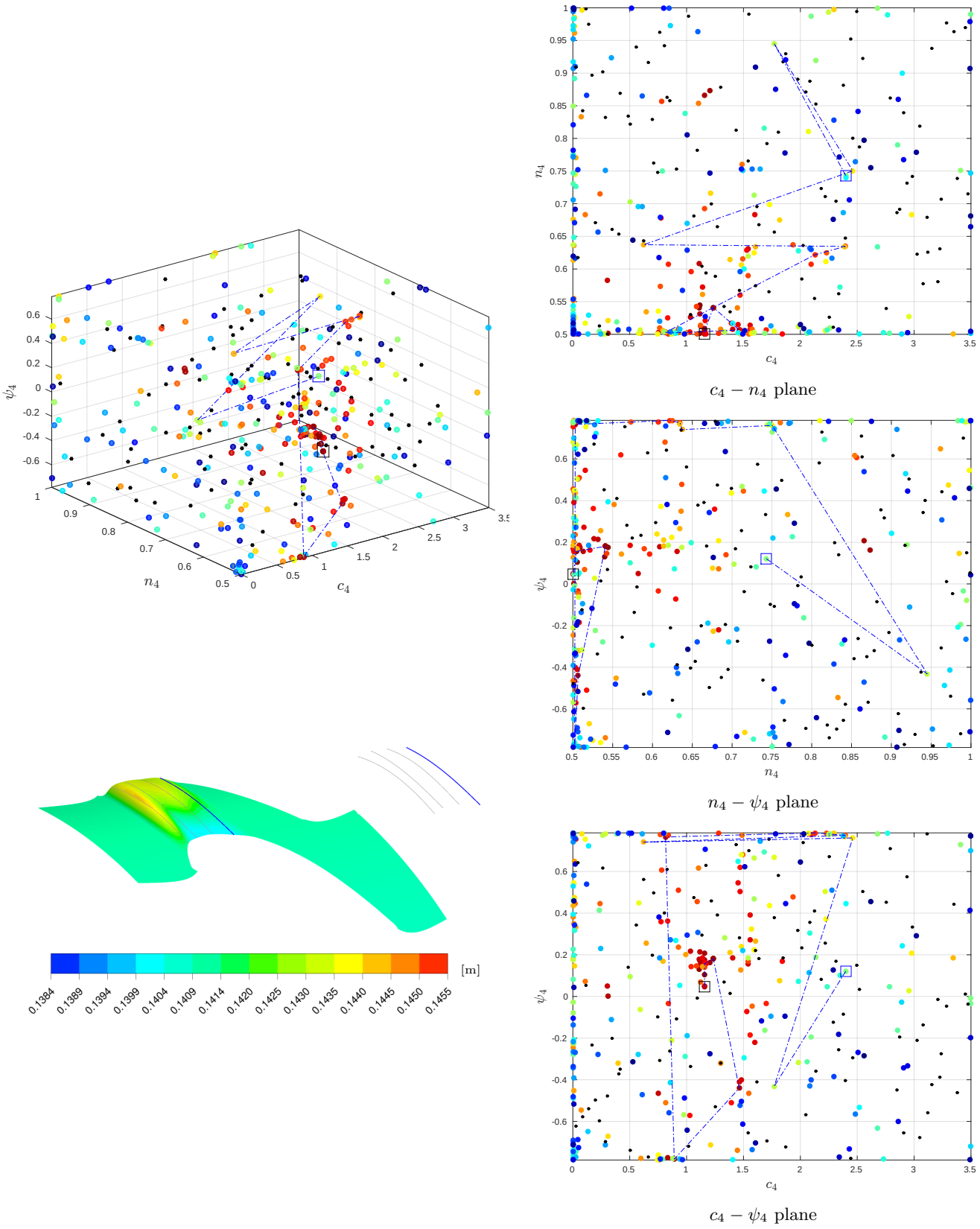

Fig. B.24: Infill history for circumferential curve 5 (η_{de}-based endwall)

G $C_{ske,1} + \beta_{dev,0.7}$-based endwall

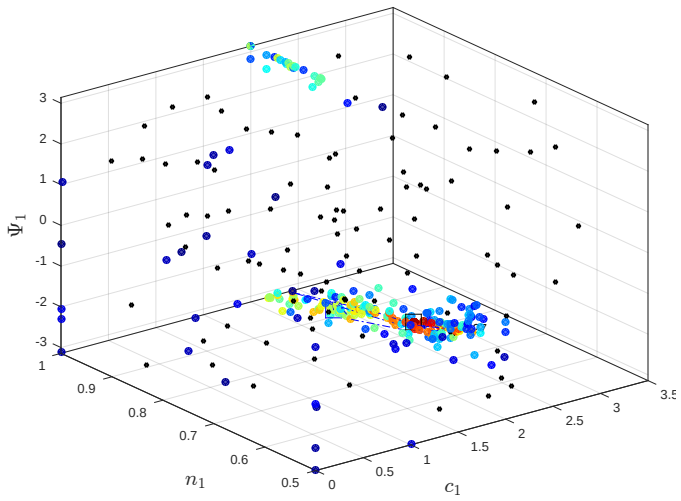

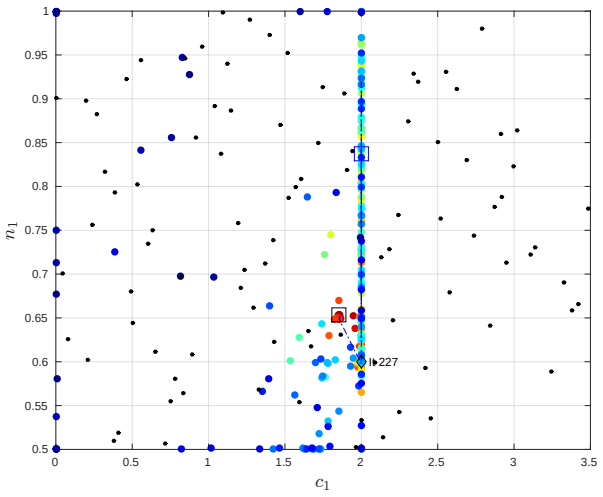

$c_1 - n_1$ plane

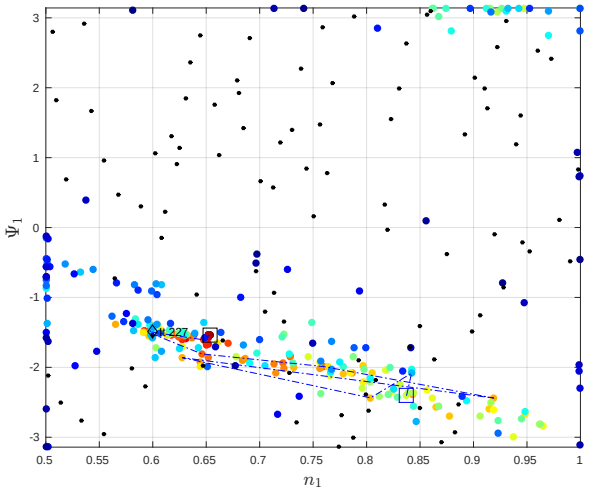

$n_1 - \Psi_1$ plane

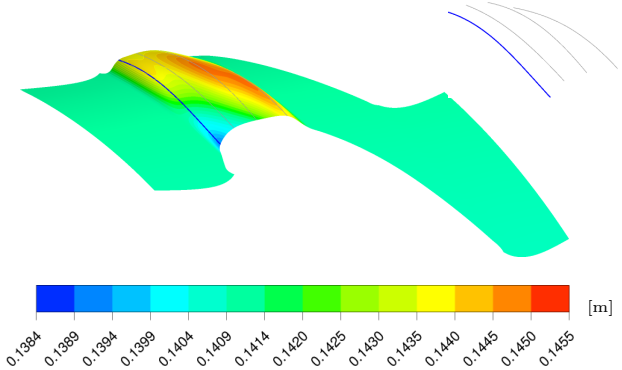

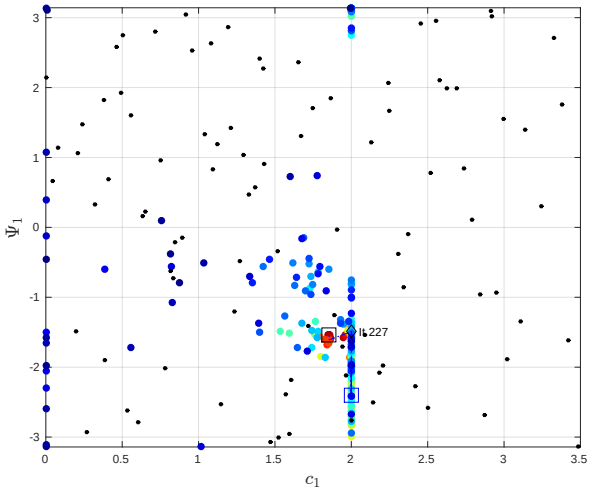

$c_1 - \Psi_1$ plane

Fig. B.25: Infill history for circumferential curve 2 ($C_{ske,1} + \beta_{dev,0.7}$-based endwall)

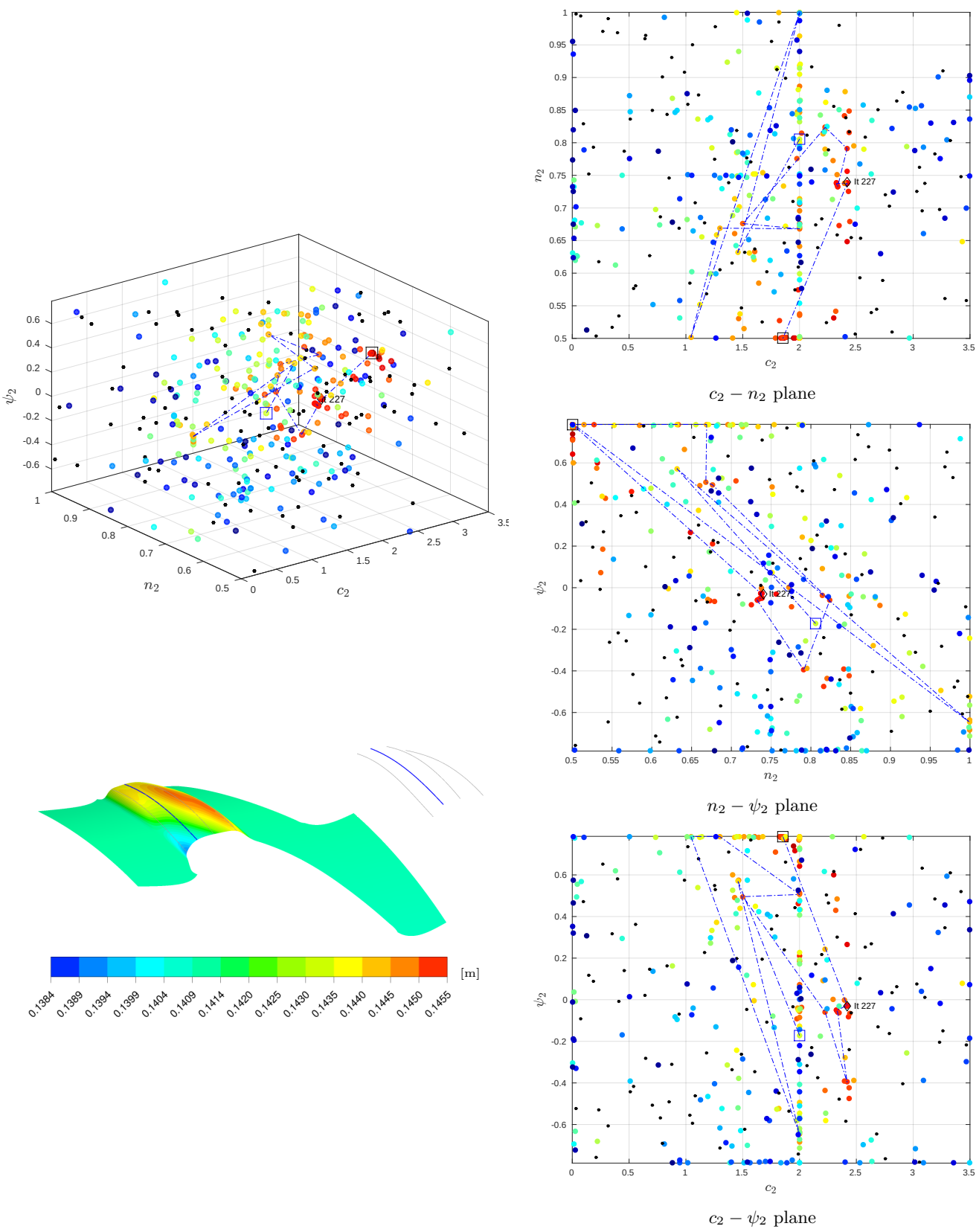

Fig. B.26: Infill history for circumferential curve 3 ($C_{ske,1} + \beta_{dev,0.7}$-based endwall)

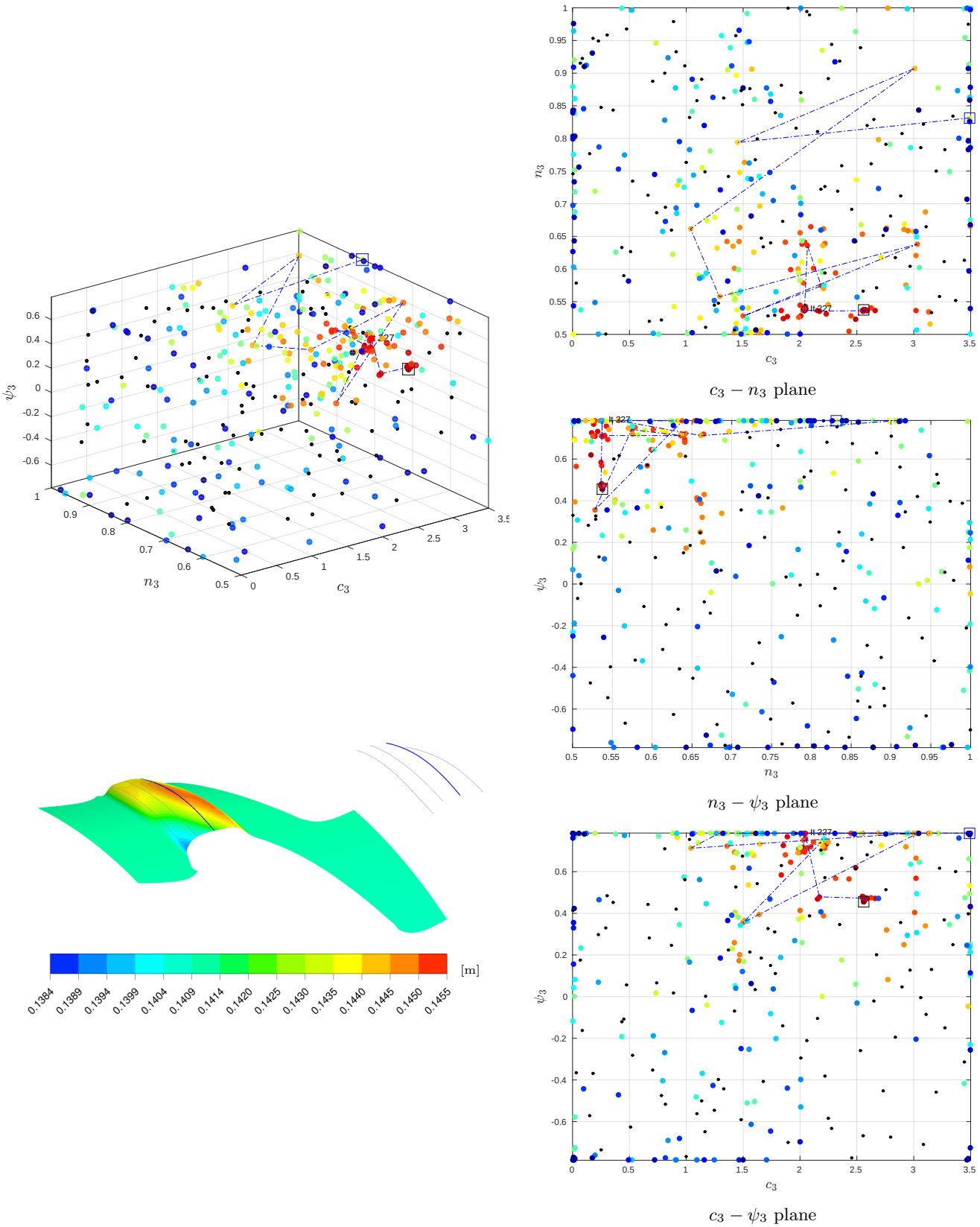

Fig. B.27: Infill history for circumferential curve 4 ($C_{ske,1} + \beta_{dev,0.7}$-based endwall)

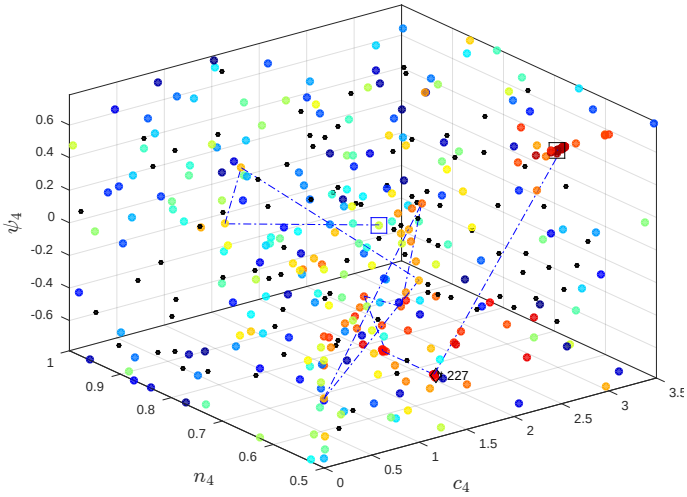

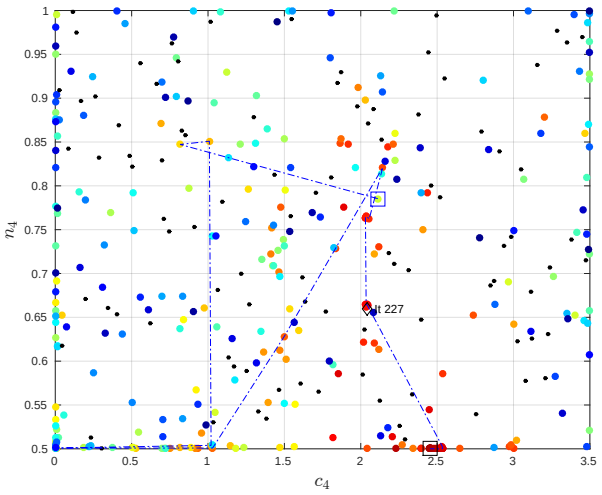

$c_4 - n_4$ plane

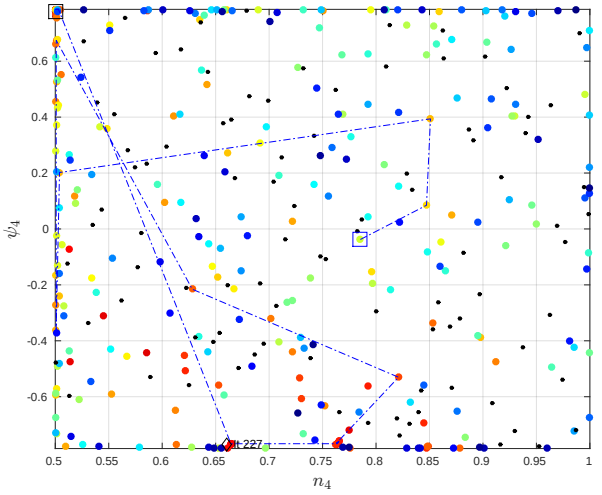

$n_4 - \psi_4$ plane

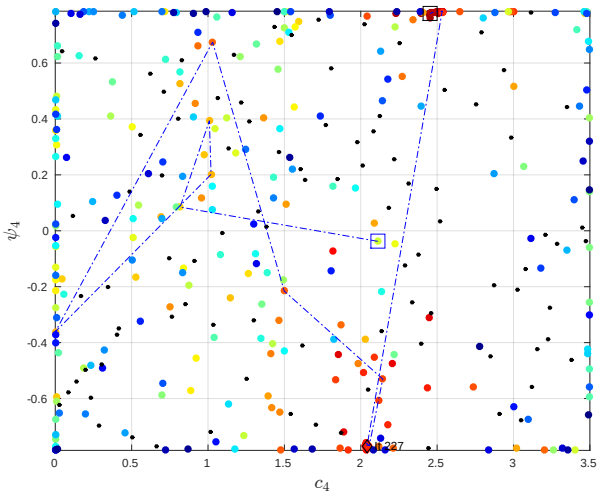

$c_4 - \psi_4$ plane

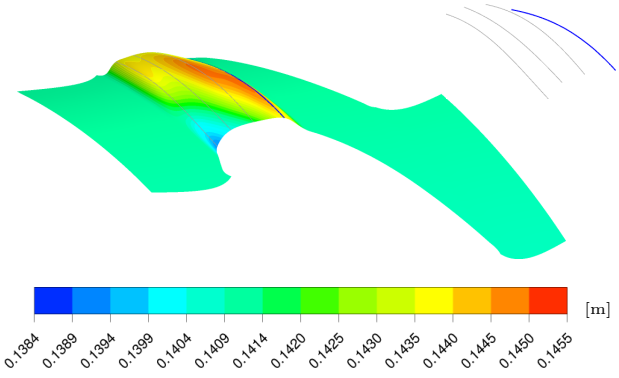

Fig. B.28: Infill history for circumferential curve 5 ($C_{ske,1} + \beta_{dev,0.7}$-based endwall)

H $C_{p0,rel,1} + \beta_{dev,0.7}$-based endwall

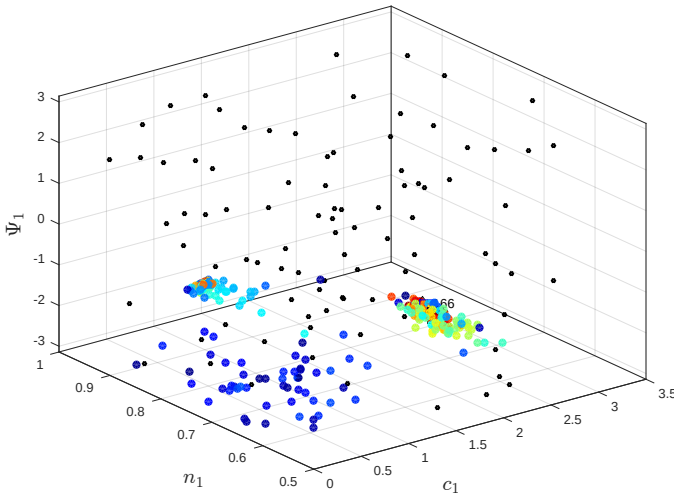

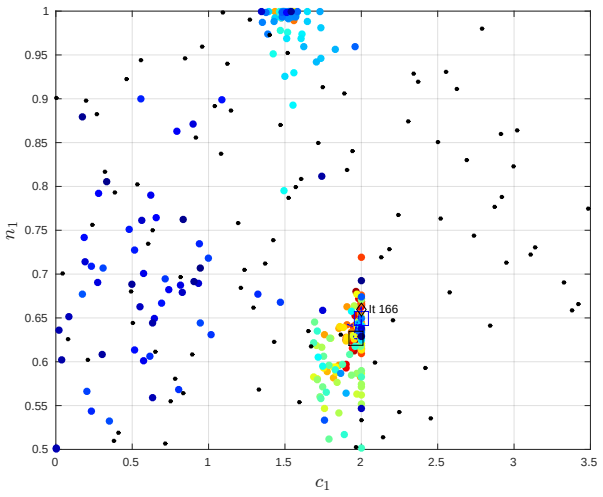

$c_1 - n_1$ plane

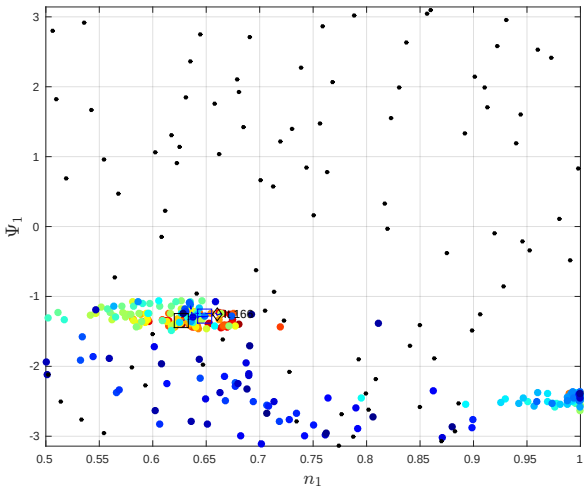

$n_1 - \Psi_1$ plane

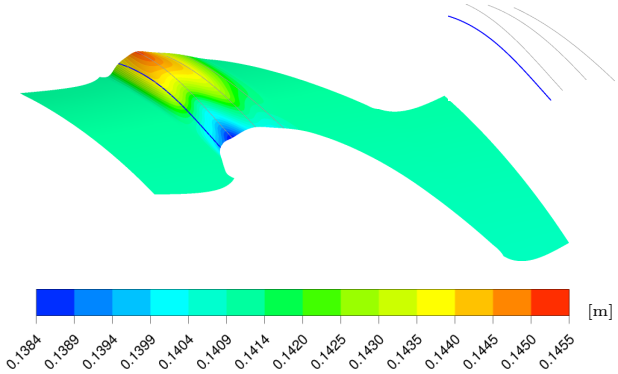

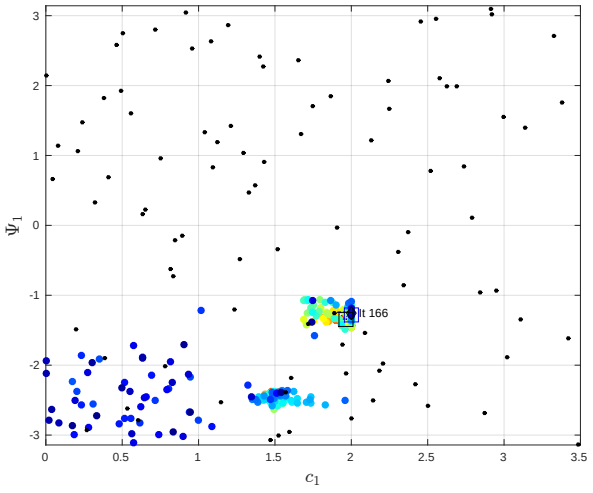

$c_1 - \Psi_1$ plane

Fig. B.29: Infill history for circumferential curve 2 ($C_{p0,rel,1} + \beta_{dev,0.7}$-based endwall)

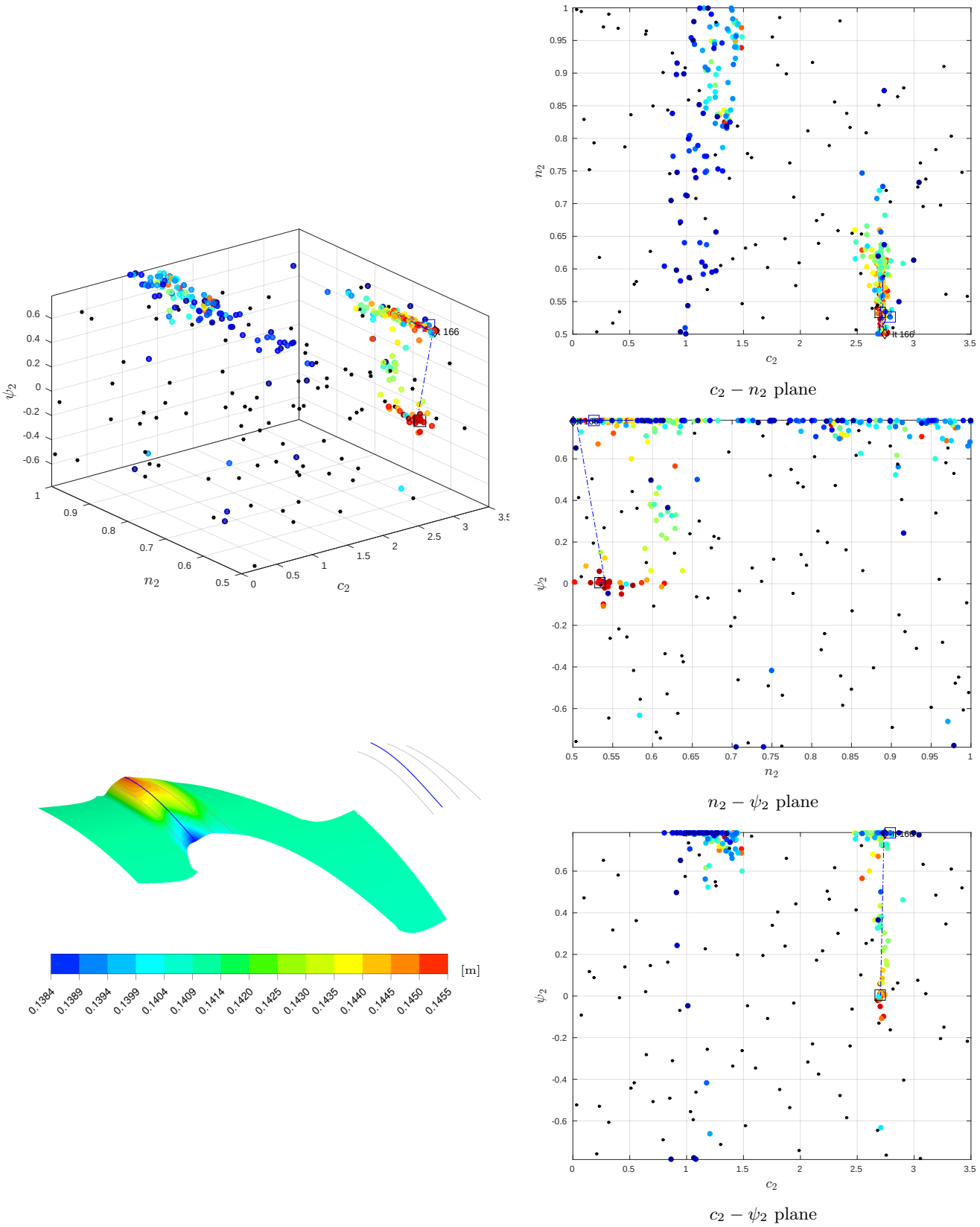

Fig. B.30: Infill history for circumferential curve 3 ($C_{p0,rel,1} + \beta_{dev,0.7}$-based endwall)

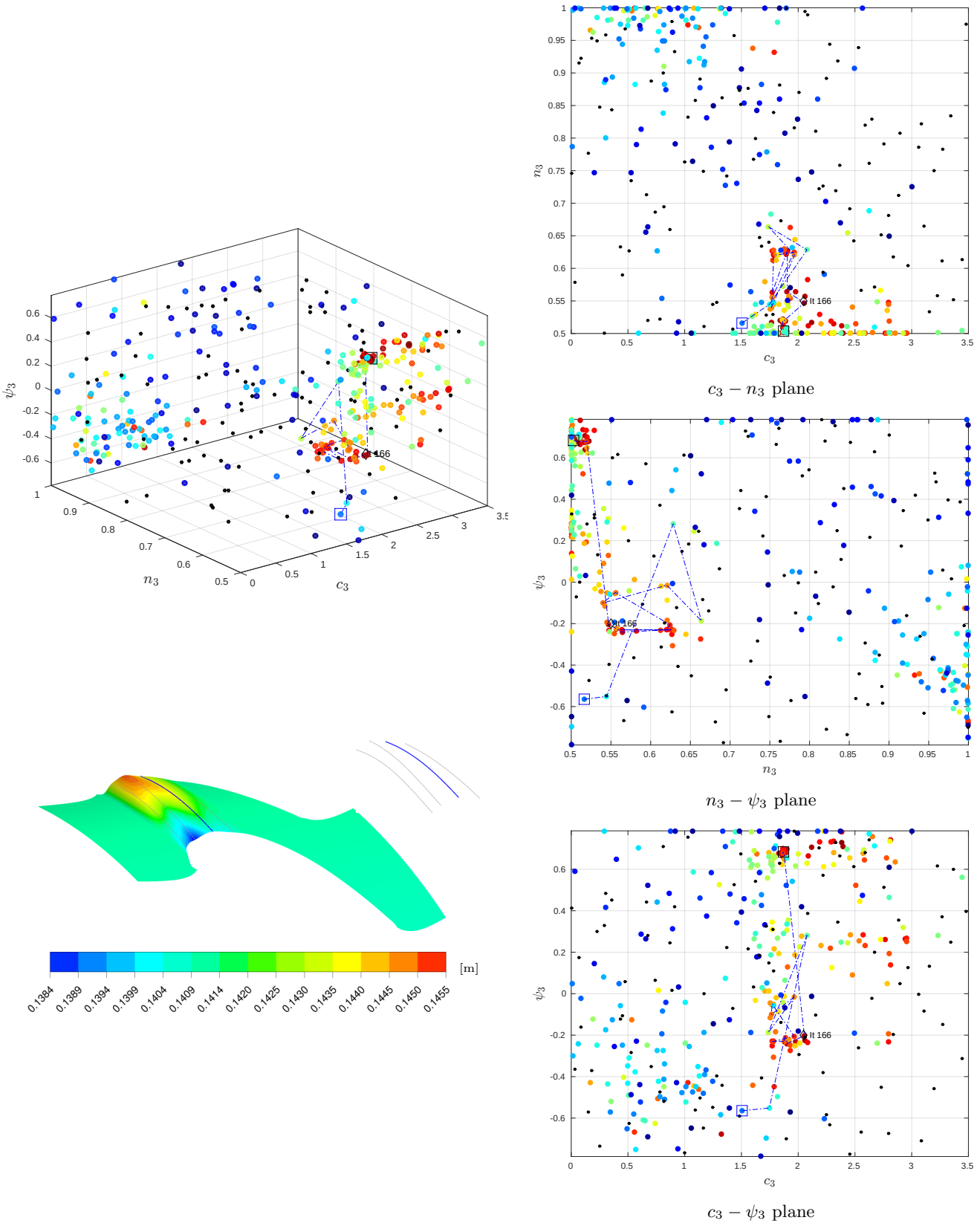

Fig. B.31: Infill history for circumferential curve 4 ($C_{p0,rel,1} + \beta_{dev,0.7}$-based endwall)

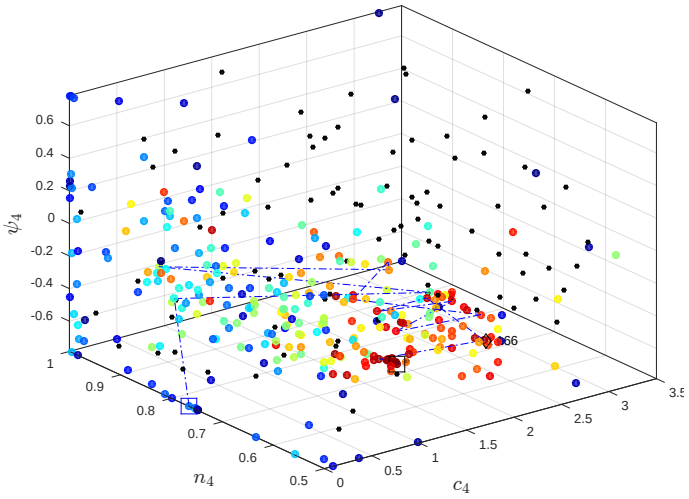

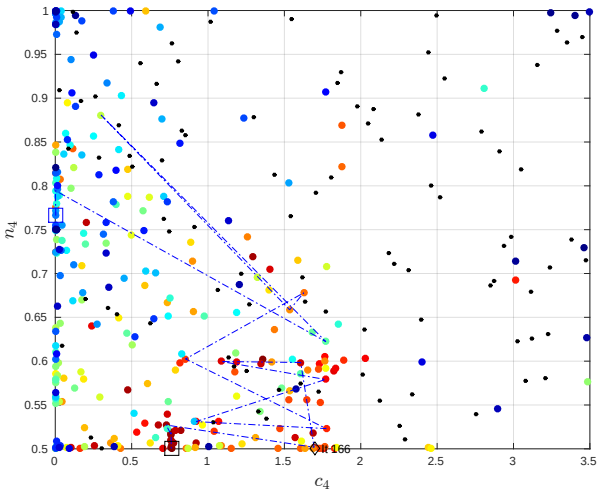

$c_4 - n_4$ plane

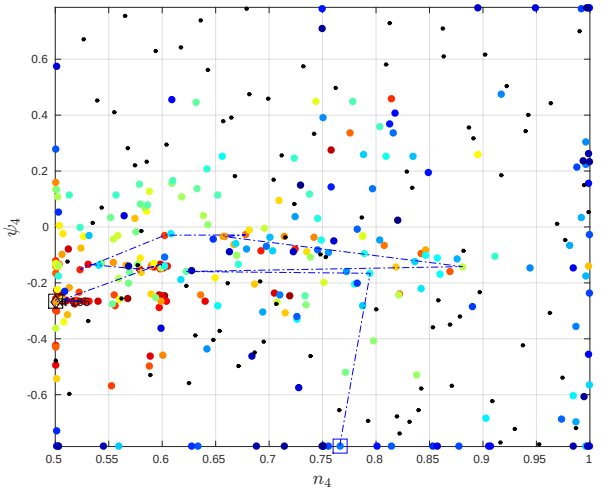

$n_4 - \psi_4$ plane

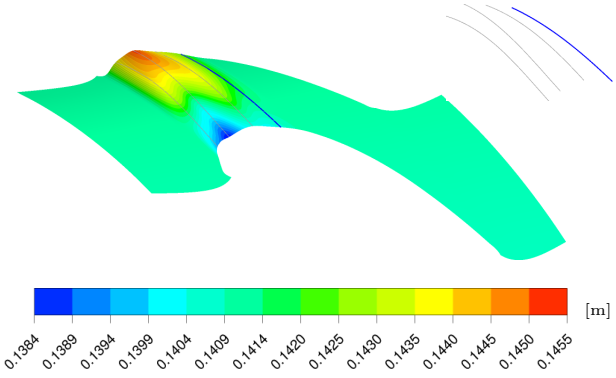

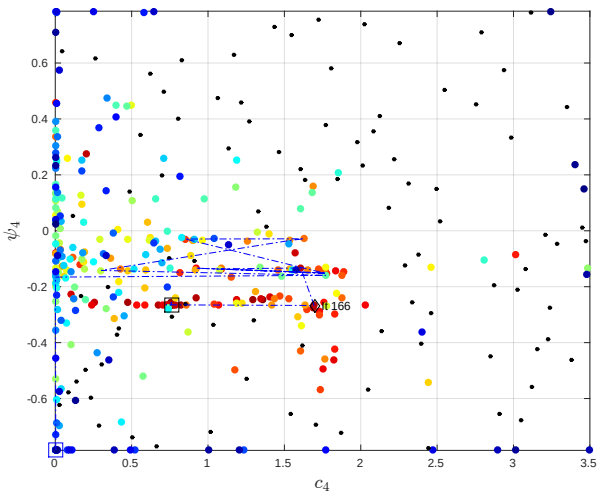

$c_4 - \psi_4$ plane

Fig. B.32: Infill history for circumferential curve 5 ($C_{p0,rel,1} + \beta_{dev,0.7}$-based endwall)

C

Cross-validation results for initial *DACE* model databases

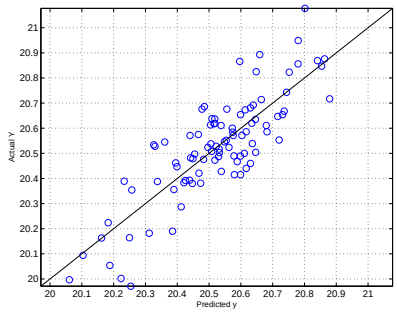

(a)

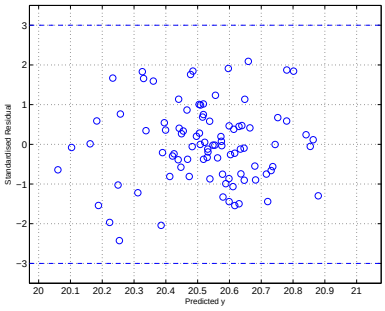

(b)

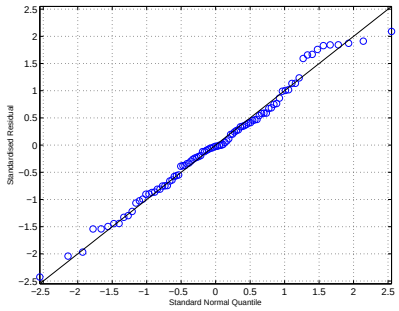

(c)

n_{points}	*RMSE*	*Max Error*	*Max* R_{std}
93	0.55% (0.11)	1.38% (0.28)	$^{2.43}/_{3.00}$

(d)

Fig. C.1: Cross-validation metrics for the initial η_{tt}-based design database

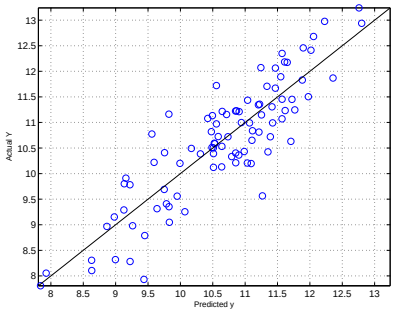

(a)

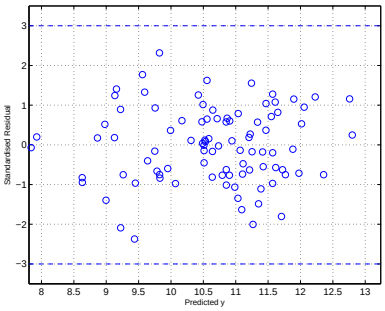

(b)

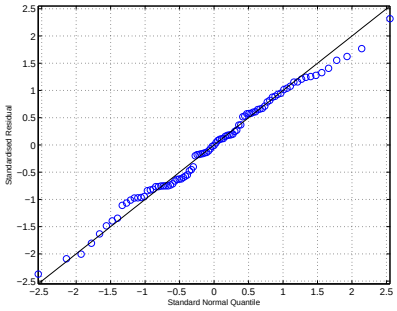

(c)

n_{points}	*RMSE*	*Max Error*	*Max* R_{std}
93	5.39% (0.57)	16.04% (1.70)	$^{2.37}/_{3.00}$

(d)

Fig. C.2: Cross-validation metrics for the initial C_{ske}-based design database

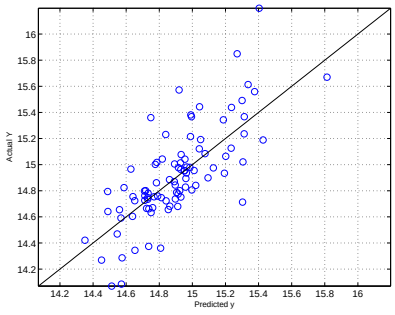

(a)

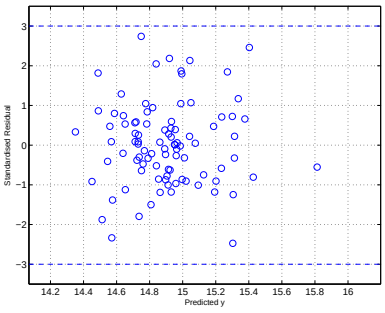

(b)

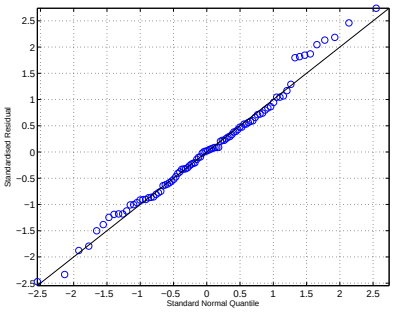

(c)

n_{points}	*RMSE*	*Max Error*	*Max* R_{std}
92	1.36% (0.20)	4.10% (0.61)	$^{2.74}/_{3.00}$

(d)

Fig. C.3: Cross-validation metrics for the initial $C_{p0,rel}$-based design database

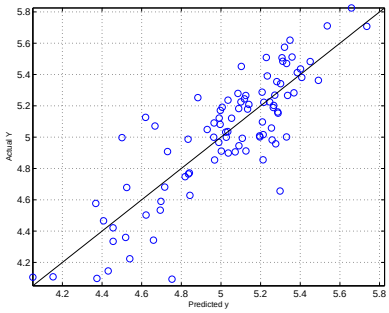

(a)

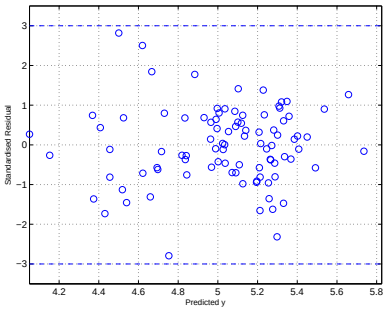

(b)

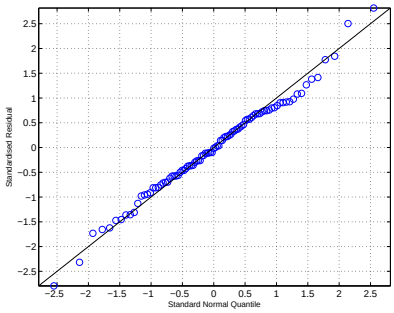

(c)

n_{points}	*RMSE*	*Max Error*	*Max* R_{std}
93	4.08% (0.20)	13.13% (0.65)	$^{2.82}/_{3.00}$

(d)

Fig. C.4: Cross-validation metrics for the initial β_{dev}-based design database

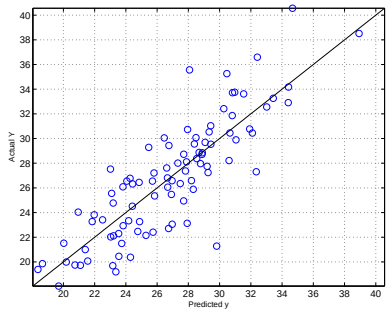

(a)

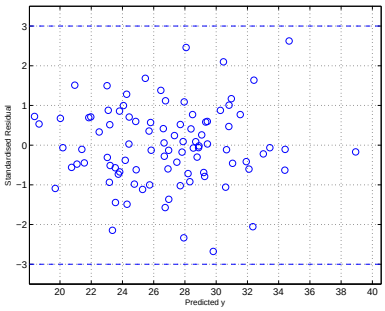

(b)

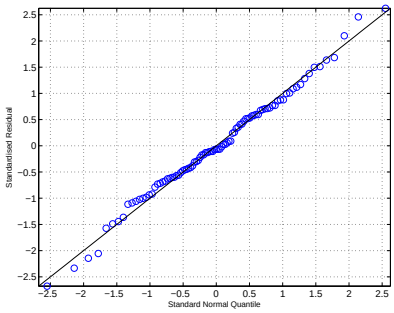

(c)

n_{points}	*RMSE*	*Max Error*	*Max* R_{std}
93	7.81% (2.23)	22.37% (6.39)	$^{2.68}/_{3.00}$

(d)

Fig. C.5: Cross-validation metrics for the initial $SKEH$-based database

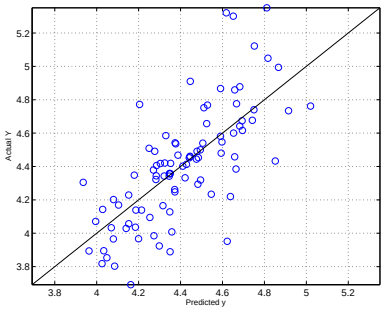

(a)

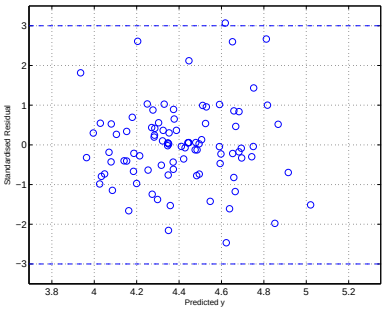

(b)

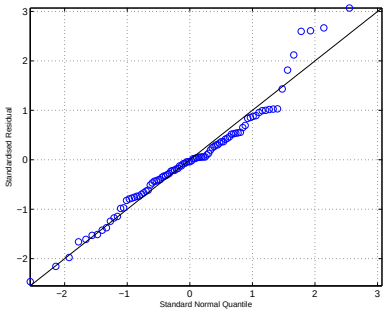

(c)

n_{points}	*RMSE*	*Max Error*	*Max* R_{std}
93	5.36% (0.23)	15.22% (0.67)	$^{3.06}/_{3.00}$

(d)

Fig. C.6: Cross-validation metrics for the initial η_{de}-based database

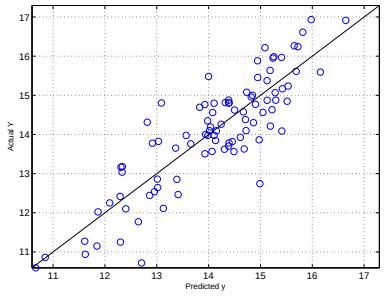

(a)

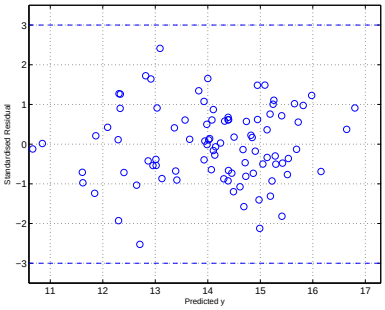

(b)

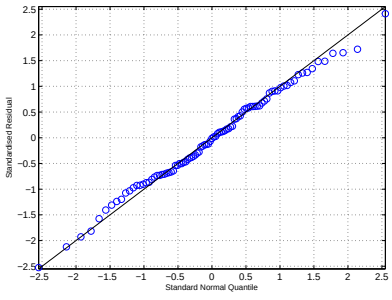

(c)

n_{points}	*RMSE*	*Max Error*	*Max* R_{std}
93	5.04% (0.71)	15.93% (2.24)	$^{2.53}/_{3.00}$

(d)

Fig. C.7: Cross-validation metrics for the initial $C_{ske,1} + \beta_{dev,0.7}$-based design database

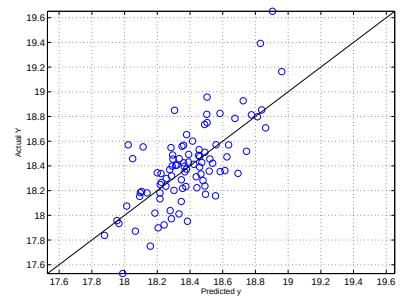

(a)

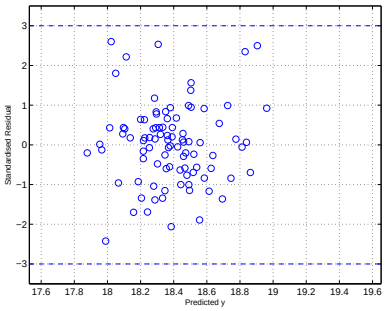

(b)

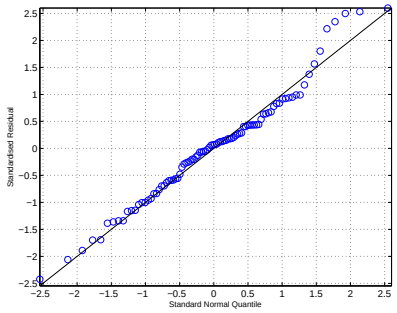

(c)

n_{points}	*RMSE*	*Max Error*	*Max* R_{std}
92	1.25% (0.23)	2.50% (0.46)	$^{2.60}/_{3.00}$

(d)

Fig. C.8: Cross-validation metrics for the initial $C_{p0,rel,1} + \beta_{dev,0.7}$-based design database